22023

Image Tubes

Illes P. Csorba

Illes P. Csorba is a graduate of the Technical University of Budapest with Diplom Ingenieur degrees in electrical, communications and warfare engineering.

During a creative quarter-century, he led the development of X-ray, electromagnetically focused, generations 1, 2 and 3 image intensifier tubes, cathode ray tubes and photomultiplier tubes.

In addition to designing the 19-inch rectangular black and white tv picture tube, Mr. Csorba is credited with developing the first high-gain, high-resolution image intensifier tube for low light-level intensification. He also led design and development of the 23-inch rectangular color kinescope.

During his career, Mr. Csorba has contributed to the statistical theory of low light-level resolution, developed the theory of resolution and MTF of electron lenses and other components and the theory of time resolution of image tubes.

The Howard W. Sams Engineering-Reference Book Series

IMAGE
TUBES

by

Illes P. Csorba

CONTENTS

FOREWORD

Five decades have passed since the appearance of the first electronic imaging tubes. During this time, electronic imaging rapidly advanced to become a flourishing industry producing a large variety of imaging tubes for many different purposes and applications. As this trend in growth continues, a need emerges for a better understanding of the design principles and the operation of electronic imaging tubes. This is a complex subject area extending over a large area of modern science which includes optics, imaging, electron lenses, aberration of electron lenses, image transfer characteristics of electron lenses and image tubes, low light level intensification, photocathodes, photoconductors, secondary electron emitters, phosphor screens, microchannel and fiber-optic plates, and a variety of electronic imaging systems. Because of the interdependence of the subject material, a coherent discussion of image tubes in a single volume is presented, providing the reader with a useful introduction to, and reference material for, image tubes.

The contents of this book may be classified into the following major sections:

1 Image intensifier tubes, image intensifier systems, image intensification, image tubes measurements, and photometry
2 Technology section, which includes photocathodes, photoconductors, secondary-electron emitters, phosphor screens, microchannel plates, and fiber-optic plates
3 Photomultiplier tubes
4 Camera tubes
5 Electron guns and electron beam deflection methods
6 Appendixes containing derivations related to imaging and electron optics

This volume was designed to reach all those who have an elementary background in optics, electron optics, electron physics, semiconductor physics and engineering mathematics. Nevertheless, most of the material is comprehensible without any specialized background.

The book is dedicated to the memory of scientists, engineers, industrialists, and other workers whose collective efforts produced the currently used image tubes.

ACKNOWLEDGMENTS

PREFACE

The first visual aids which improved daylight vision (telescope, microscope) were invented and developed at the beginning of the 17th century. Science and technology, however, became advanced enough to produce the first night vision aids only in this century. It all started with the discovery and explanation of the photoelectric effect by Hertz, Hallwachs, Lenard, Einstein, and others. This important discovery was a significant step of modern physics and led to the development of the photocathodes, photomultiplier tubes, camera tubes, and finally to the development of the image intensifier tube family.

Another important event leading to the electronic imaging was Busch's demonstration of the electron lens in 1926. The explanation of the lens action of axially symmetric focusing fields was given few years later by Davisson, Calbick, Brueche, and Johannson in 1931 and 1932. Thereafter, electronic imaging rapidly advanced mostly by means of industrial research and development.

Image intensification is obtained with image intensifier tubes, photomultiplier tube arrays, and thermal imaging systems.

Image intensifier tubes image and intensify a natural scene produced by light reflection in a manner similar to that of the eye. The contrast and the color of the natural scene is due to the difference of the spectral reflectivity of the objects of the scene.

The thermal imaging systems, on the other hand, utilize the thermal radiation of the scene. The contrast of the scene is due to the differences of the radiation of the objects of the scene.

X-ray and gamma-ray intensifier systems represent the third type of imaging systems. X-ray and gamma-ray converter tubes convert the X-ray or gamma-ray radiation pattern to a light image for intensification purposes. The contrast of an X-ray radiation pattern is due to a nonhomogeneous X-

ray absorption of objects under inspection. In gamma-ray imaging the contrast may be due to a nonhomogeneous absorption of radioactive drugs by human organs giving rise to a distinct gamma-ray radiation pattern that permits the visualization of those organs.

Image intensifiers are a burgeoning field of optical devices. They are used for night vision, as night blindness aids, to see through smoke and fog, astronomy, X-ray and gamma-ray intensification, electron microscopy, spectroscopy, medical research, radiology, and high-resolution lithography, etc. The yearly production figure of image intensifier systems has already surpassed the $500 million mark and production is forecasted to be doubled or tripled in the current decade.

Photomultiplier tubes are used to detect and measure radiant energy in the ultraviolet, visible, and near infrared regions of the electromagnetic spectrum. With scintillators and Cerenkov radiators, photomultipliers are also used to detect and measure X-rays, gamma rays and nuclear particles. Accordingly, photomultipliers find wide usage in nuclear research, oil-well logging, industrial controls, laboratory instrumentations, Raman spectroscopy, laser ranging and communication, and home entertainment in video playback equipment.

The extensive use of photomultiplier tubes led to the development of many different types of photomultiplier tubes for different purposes and requirements. This trend still continues with extensive research and development efforts to improve sensitivity, life, gain, temperature stability, production yield, ruggedness of certain types, and other performance characteristics required in new applications.

Television is a continuously advancing field. To meet the increasing demand for improved quality and new applications, a great variety of camera tubes was introduced and used for televising optical images. The early iconoscope and orthicon tubes were superseded by the more sensitive image orthicon tube and later on by the photoconduction type tubes. For low light level applications the secondary electron conduction target, the silicon intensifier target tube, and the image isocon tube were developed. Very high resolutions, required in aerial photography, were obtained with the return-beam vidicon. During the recent decade, development efforts produced new vidicon targets having higher quantum efficiency and greater spectral sensitivity range. The electron gun of the vidicon was also improved to provide an electron beam with low beam temperatures for low beam discharge lag.

Currently, a large variety of image tubes are in service and being manufactured yearly. As this trend continues, a greater need emerges for a better understanding of the operation and the complexity of the image intensifier systems. This book is directed to the practicing engineers, managers, scientists, and students of science and engineering who have an interest in

image tubes and their design and application. It is the author's hope that this volume will serve as a useful introduction and guide for image tubes.

The book concentrates on the fundamental aspects of image intensification, electron optics and construction of image tubes, and visual acuity improvements with the aid of image intensifiers and night vision systems. Additional sections include the theory and technology of photocathodes, photoconductors, secondary-electron emitters, fluorescent screens, microchannel plates, fiber-optic plates, and power supplies. Finally, the book has a section on photomultiplier tubes, camera tubes and electron guns, which are essential parts of electronically imaging systems.

The photomultiplier tubes section describes the construction and optics of photomultiplier tubes, noise in photomultiplier tubes, signal-to-noise ratio, gain variance, pulse height distribution, and applications.

The camera tubes section details the operation and the performance characteristics of the various types of camera tubes.

The electron gun and electron beam deflection chapters introduce the reader to the cathode-ray tube and camera tube gun and deflection systems. The operation, construction, and design principles are discussed.

The appendixes contain material related to imaging and electron optics. The motion of electrons in various types of electron lenses consisting of electric and/or magnetic fields is discussed and derived.

The author strived to keep this book concise while still presenting the essential information of image tubes. For additional information the reader is referred to the literature cited at the end of each chapter of the book.

The contents of the book have been generated during the author's long association first with RCA at Lancaster, Pennsylvania, and later with ITT Electro-Optical Products Division at Roanoke, Virginia.

ILLES P. CSORBA

1

INTRODUCTION

1.1 The Need for Image Intensification

The human eye is an extremely versatile adaptable optical instrument capable of night vision. It functions in the brightness range of less than 10^{-6} to 10^{1} fL (footlamberts). Satisfactory vision for normal human functioning, however, is obtained only at daylight levels. At night the visual acuity is limited by the small amount of available light, by the statistical variation of the light level, and by the relatively small quantum efficiency of the eye. As will be shown in Chapter 8 the quantum efficiency of the eye is on the order of about 1% at very low illumination levels, which indicates that for the resolution of a contrasty object at least 100 photons must reach the retina during the storage time of the eye, which may be on the order of about 0.2 second* at the threshold of vision. Accordingly, at starlight illumination levels there is enough light to resolve large contrasty objects only, and fine detail and low contrast, which are needed for daylight human functioning, are not resolved.

Apparently for night vision the light gathering power of the eye is of great importance. The quantity of light intercepted by the unaided eye is proportional to the area of the pupil or the square of the pupillary diameter. The function of the pupil is to regulate the quantity of light entering the eye. It automatically dilates at low field luminance levels and contracts when the brightness is increased. This process, which is known as *adaption*, makes it possible to gather more light from the scene at low field luminance levels

---

* This value was first established by Albert Rose. See *Vision: Human and Electronic*, (Plenum) 1973, for additional information.

and, thus, improve the acuity of night vision. The dark adapted eye has a diameter of approximately 7.6 mm, which sets an upper limit to the light gathering power of the eye.

To summarize the above, the visual acuity at low light level is limited by the light gathering power of the eye which is regulated by the pupillary diameter, and by the quantum efficiency and storage time of the eye. Consequently, the visual acuity, and night vision in general, can be improved by night vision aids which can collect more light and have a greater quantum efficiency and longer storage time than the eye.

1.2   The Telescopic Night Vision Aid

The telescope is one of the earliest night vision aids which extends the region of vision toward lower light levels by gathering more light from the scene with a larger diameter objective lens than the diameter of the unaided eye and by magnifying the scene. Figure 1.1 shows the schematic diagram of an astronomical telescope for which the scene is in infinity and the image of the scene formed by the objective lens is in the focal plane of the objective and ocular lenses. The ocular lens forms the final image of the scene at infinity and the eye looks at this final image. Since both the object and the final images are at infinity, the power of the telescope from figure 1.1 is

$$M = \theta'/\theta = f_o/f_e, \qquad (1.1)$$

where θ and θ' are the object and image field angles, respectively, and f_o and f_e are the objective and ocular lens focal lengths, respectively.

Under normal magnification, the diameter of the exit pupil of the telescope equals the pupillary diameter of the eye and the power of the telescope
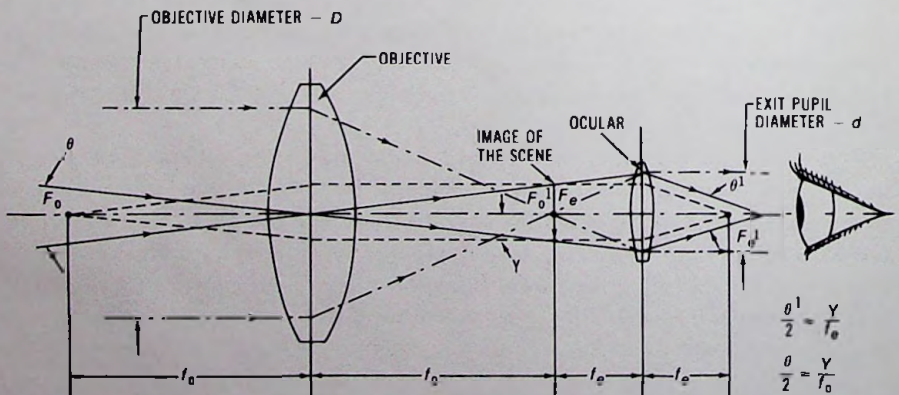
Fig. 1.1   The astronomical telescope.

is the ratio of the objective lens diameter to the exit pupil diameter. Since all light that enters the objective lens and is refracted by the ocular lens must pass through the exit pupil of the telescope, the quantity of light reaching the retina from an object on the telescope axis is proportional to the square of the ratio of the objective lens diameter to the pupillary diameter. For example, if the diameter of the objective lens is 10 times that of the pupil of the eye ($M = 10$), the objective lens admits 100 times as much light as does the unaided eye. However, since the linear dimensions of the retinal image are increased by the magnification, the telescope does not increase the apparent brightness of the scene, which is the same with the telescope at normal magnification as with the unaided eye. In other words, the telescope improves the visual acuity by a factor equal to the magnification of the instrument without altering the apparent brightness of the scene.

From the above, it is also apparent that a larger objective lens can be used with the eye only in a magnifying system and, therefore, at the expense of angular field of view, which is reduced by a factor equal to the power of the telescope. For example, a 7-power telescope reduces a 42° angular field of view to $42°/7 = 6°$.

1.3   Image Intensifier Systems

A true extension of the region of sharp vision toward lower light levels and in the domain of the electromagnetic spectrum can be obtained without a restriction of the field of view by use of an image intensifier telescope such as that shown in figure 1.2. Here, the input of the image intensifier tube
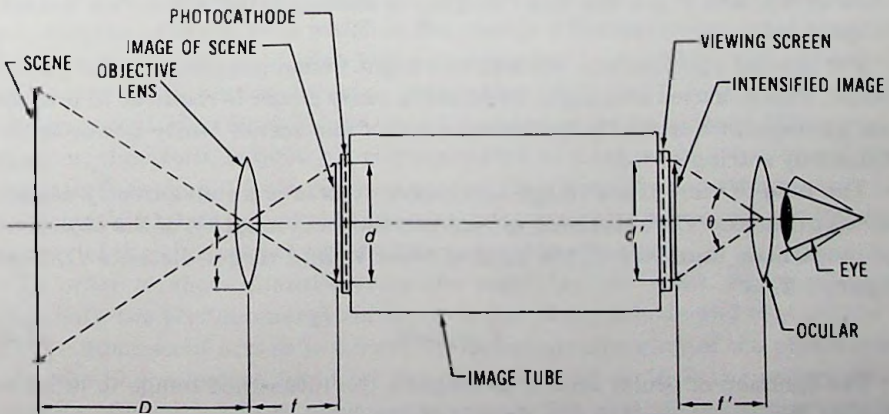
Fig. 1.2   Diagram of an image intensifier.

(brightness intensifier, brightness amplifier) is placed in the focal plane of the objective lens, and the intensified output is at the focal plane of the ocular lens. In this system the visual threshold is greatly lowered by use of a photocathode that has a high quantum efficiency and broader spectral response than the eye, and by use of a large objective lens with a wide angle view which gathers more light from the scene than the unaided eye. The extension of the visual threshold toward lower light levels with the image intensifier in a first-order approximation, therefore, may be related by the following equation:

$$\frac{B_e}{B_i} = \frac{D^2 \gamma_i N_i}{d^2 \gamma_i N_i},$$ (1.2)

where B_e is the visual threshold of the unaided eye, B_i is the visual aid threshold, d and D are the pupillary and objective diameters, respectively, γ_c and γ_r are the quantum efficiency of the photocathode and eye, respectively, and N_e and N_i are the photon quantities in the photocathode spectral response range and in the visible spectrum, respectively.

From equation 1.2, with $d = 2.5$ mm, $D = 25$ mm, $\gamma_i = 0.2$, $\gamma_i = 0.01$ and $N_e = N_i$, the scene brightness may be reduced from B_e for the unaided eye to B_i with the intensifier by a factor of 2000.

The insertion of the image intensifier tube in the optical system of the telescope increases the brightness of the image without altering the telescope principle. The power of the image intensifier, therefore, is the product of the magnifications of the telescope and the image intensifier tube:

$$M_r = M_i f_o / f_e,$$ (1.3)

where M_r is the angular magnification, M_i is the magnification of the image tube and f_o and f_e are the focal lengths of the objective and ocular lenses, respectively.

For special applications, such as the night vision goggles and the pocket scope, which is used as a night blind aid, a unity power is required to provide an unmagnified spatially unaltered view of the scene. Unity power is obtained by setting $f_o = f_e$.

The field of view of the image intensifier system is a conveniently adjustable parameter. The relationship between the focal length f_o of the objective, photocathode diameter d, the field of view V, and target distance D, from figure 1.2, is

$$V = Dd/f_o.$$ (1.4)

The function of ocular lens is to magnify the intensified image in order to enable the eye to resolve fine details of the intensified scene. The relationship between the focal length f_e of the ocular lens, the diameter of the

viewing screen d', and the field of view θ and magnification M, from figure 1.2, is

$$M = 250/f_e = (500/d') \tan (\theta/2). \tag{1.5}$$

1.4 The Operation of Image Intensifiers

The operation of image intensifiers is based on the photoelectric effect, (Hertz, Stoljetov 1897, Hallwacks 1898), amplification of the photelectric energy, and generation of light by the cathodoluminescent effect. The diagram of figure 1.3 shows how the photoelectric effect, electron transport via
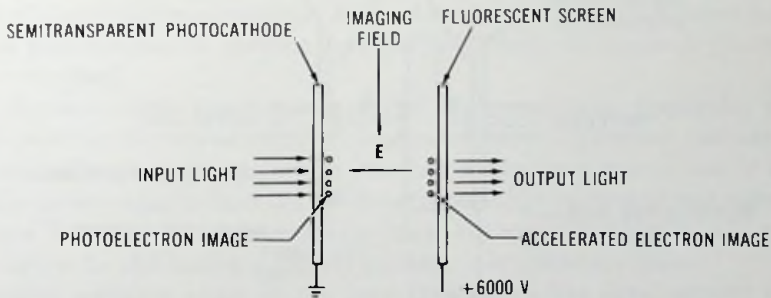
Fig. 1.3   Diagram of image intensification.

the imaging field, and the cathodoluminescent effect lead to image intensification. In these processes a semitransparent cathode converts the input light energy to electrical energy with a photoemission energy spread of usually less than 0.3 eV. The energy of the photoelectrons is amplified via an imaging electron lens which is frequently a homogeneous axial electric field, or an electric field with focusing properties, or combined electric and magnetic fields having focusing properties. In figure 1.3 the fluorescent screen potential is 6000 V. The final kinetic energy of electrons after acceleration, therefore, is 6000 eV, corresponding to a large amplification of the initially less than 0.3-eV electron energy. This amplified electron energy is sufficiently high to penetrate the screen structure and to convert the kinetic energy of the electrons to light with reasonable efficiency.

In order to show quantitatively the amplification effect, let us assume that both the photon energy incident on the photocathode and that emitted by the fluorescent screen is 2.5 eV, the quantum efficiency of the photocathode (the photoelectron yield per incident photons) is 10%, the energy conversion efficiency of the phosphor screen is 5%, and the phosphor screen voltage is 15 000 V. For these conditions, a photoelectron generates 15 000

× 0.05 = 750-eV radiant energy corresponding to 750 eV/2.5 eV = 300 photons. With 10% photocathode quantum efficiency, ten photons generate, on an average, one photoelectron. Therefore the photon gain of the image intensifier is $0.1 \times 300 = 30$. By cascading three of the above intensifier systems a photon gain of $30^3 = 27\,000$ is feasible and is frequently obtained in cascaded image tubes of the generation 1 family.

Another approach to high intensifier gain is obtained through photoelectron multiplication by a microchannel plate (MCP). The diagram of figure 1.4 shows the principle of the operation of a microchannel plate type image
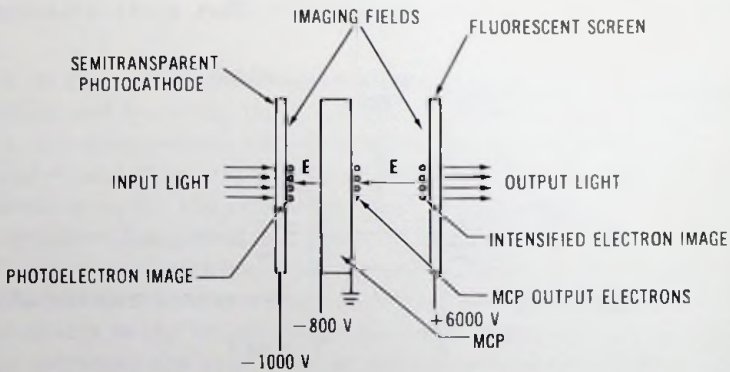
Fig. 1.4   Diagram of MCP image intensification.

intensifier. The photoelectrons, after a few hundred volts of acceleration, strike the input of the microchannel plate. The microchannel plate multiplies the photoelectron image so that for each input electron 1000 or more output electrons are obtained. The output electrons of the microchannel plate are accelerated to 6000 V fluorescent screen potential to provide additional gain and to convert the kinetic energy of the accelerated electrons to light. The gain of MCP image intensifiers is in the range of 10 000 to 30 000.

1.5   The History of Image Intensification

Historically, a great variety of image tubes were developed for many applications. The family of image tubes that are used for direct viewing and for intensification of optical images are called *image intensifier tubes*. On the other hand, image tubes used for image pickup in television cameras are classified as *camera tubes*. The first image intensifier tube was built by

G. Holst in 1932. This tube consisted of a plane photocathode and plane fluorescent screen in close proximity.

In the U.S.A. the first image intensifier tube was developed at the RCA laboratories in the mid-1930s. This tube utilized an electrostatic lens to focus a spherical cathode on a spherical screen. Spherical surfaces were used to minimize off-axial aberrations. This design was the front-runner of the generation 0 infrared image intensifier tube which used an S-1 photocathode surface and a P-20 phosphor screen. The generation 0 infrared telescope built with this tube was an active night vision aid working with infrared light illumination of the scene.

High-performance image intensifiers with sufficient gain and low light level resolution arrived, however, only in the early 1960s with the development of the electromagnetically focused cascaded image intensifier tube in which high-resolution screens and high-efficiency multialkali photocathodes were used.

In the mid-1960s the development of high-resolution fiber-optic plates made possible the introduction of the electrostatically focused cascaded image tube. The electrostatic image tube has a smaller size and weight and a simpler power supply than the electromagnetically focused image tube, and because it is insensitive to supply voltage variation and ripple it is a suitable device for the incorporation of automatic brightness control.

Further advance came in the late 1960s with the development of the generation 2 wafer tube, which operates by using a microchannel plate for internal current multiplication. The wafer tube represents a major advance in performance and reduction in physical size of image intensifier tubes.

Most recently, work has been concentrated in the image tube industry toward the development of more efficient photocathodes, improvement of noise, gain and life characteristics of image tubes and further reduction of physical size and weight of image intensifier systems. These improvements are incorporated in the generation 3 wafer tube.

Television has made tremendous advances since the end of World War II. To meet the increasing demand of improved quality and new applications, a great variety of camera tubes in many different sizes and forms were introduced and used for televising optical images. The early iconoscope and orthicon tubes were superseded by the more sensitive image orthicon tube and later on by the photoconduction type tubes. For low light level applications, pickup tubes with the secondary electron conduction target, silicon intensifier target, and the image isocon tube were developed. Very high resolutions, required in aerial photography, were obtained with the return-beam vidicon.

Since the mid-1930s when the photomultiplier tube development started, many different types of photomultiplier tubes were developed for different

purposes and requirements. In the last decade, work has been done to improve the photosensitivity, speed of response, gain stability, signal-to-noise ratio, light collection efficiency, and ruggedness of the multiplier structure of certain types. The introduction of gallium-arsenide–cesium (GaAs·Cs) cathodes and gallium phosphide (GaP) dynodes in the photomultiplier tube gave a new impetus to the development of the photomultiplier tube.

References

Blackwell, H. R. "Contrast Thresholds of the Human Eye," *J. Opt. Soc. America*, (36), (11), November 1946.

Busch, H. *Arch. Electrotech.*, (Berlin) 18, p. 583, 1927.

Csorba, I. P. "Contrast Thresholds of Image Intensifier-Aided Eye at Low Field-Luminance Levels," *RCA Review*, Vol. 32, p. 297, June 1971.

———. "Analytical Approach to the Modulation Transfer Function of the Generation 2 Wafer Tube," *Proceedings of the Electro-Optical Systems Design Conference*, September 1976, New York (Industrial and Scientific Conference Management, Inc., Chicago), p. 646.

———. "Long Life Goggle Tube Product Improvement Program for AN/ PVS-5," Final Engineering Report, Contract DAAG53-76-C-0203, U.S. Army Electronic Research and Development Command Night Vision and Electro-Optical Laboratories, Fort Belvoir, Virginia, 15 March 1979.

———. "Recent Advancements in the Field of Image Intensification: The Generation 3 Wafer Tube," *Applied Optics*, Vol. 18, 1979.

Csorba, I. P., et al. "Development of a Three-Stage Cascaded Image Tube," Final Report Contract No. DA44-009-Eng.-3914, NVL, Fort Belvoir, Virginia, No. 1962.

Holst, G., et al. "An Apparatus for the Transformation of Light of Long Wavelength into Light of Short Wavelength," *Physics*, Vol. 1, p. 297, 1934.

Morton, G. A. "Image Intensifiers and the Scotoscope," *Applied Optics*, Vol. 3, No. 6, June 1964.

———, and E. G. Ramberg, "Electron Optics of an Image Tube," *Physics*, Vol. 7, p. 451, December 1936.

Rose, A. "The Sensitivity Performance of the Human Eye on an Absolute Scale," *J. Optical Soc. America*, Vol. 38, No. 2, February 1948.

2

IMAGE INTENSIFIER TUBE TYPES

2.1 General Description

Image tubes are electro-optical devices that are used to detect, intensify, and shutter optical images in the near ultraviolet, visible, near infrared, X-ray and gamma-ray regions of the electromagnetic spectrum and for televising optical images. Accordingly, they are used for night vision, night blindness aid, astronomy, X-ray and gamma-ray intensification, electron microscopy, medical research, radiology and as high-speed light shutters, etc. Today a variety of image tubes is available on the market in single-stage and multistage tube configurations.

In general terms, a single-stage image intensifier tube consists of an image sensor (usually a photocathode or, in the case of X-ray and gamma-ray radiations, a phosphor screen overlaid by a photocathode) for the conversion of the incident radiant image to a low-energy electron image, of an electron lens for the production of a high-energy electron image, and of a phosphor screen for the conversion of the high-energy electron image to a light image. A multistage tube consists of two to four single-stage tubes in cascade.

With image tubes the visibility may be extended to very low light levels and in the invisible region of the spectrum. The photon gain of image intensifier tubes may range from less than unity to several millions, depending on the incident radiation wavelength and number of image tube stages.

In photography, image tubes are used as an "active" light shutter device permitting very short exposure time, intensifying the image, and converting the spectrum of radiation to a desired color. High-speed light shutter

tubes are also used to observe and analyze photoevents of very short dura-
tion and to measure time and distance accurately.

2.2   The Biplanar Image Tube

The most simple device is the biplanar image tube. It consists of a photo-
cathode and phosphor screen in close proximity as shown in figure 2.1. By
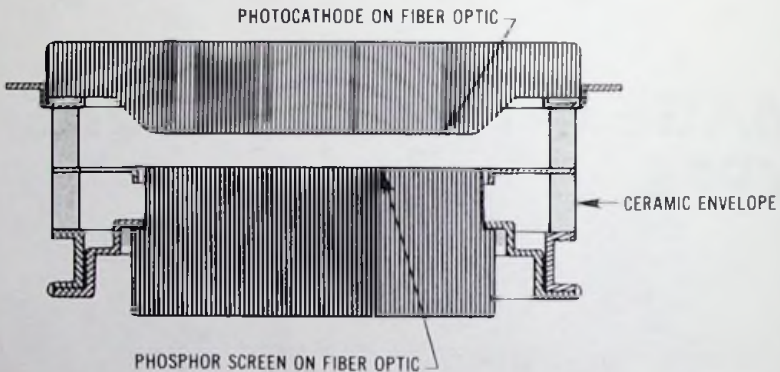
Fig. 2.1   The biplanar image tube.

application of a positive voltage between the phosphor screen and the pho-
tocathode, a homogeneous axial electric field is produced which proximity
focuses the photoelectron image on the phosphor screen. The biplanar image
tube has an important application as a distortion-free device.

2.3   The Electromagnetically Focused Image Tube

The electromagnetic image tube gained application in the areas where
superior image quality is required. A single-stage electromagnetically fo-
cused image tube consists of a plane photocathode and a plane phosphor
screen separated by the accelerator rings structure. The image tube is en-
closed by a magnet as shown in figure 2.2. The accelerator rings and the
magnet produce a set of homogeneous axial electric and magnetic fields
which focus an erect image of the photocathode on the phosphor screen with
unity magnification.

In a multistage tube a thin mica interstage coupler (5 to 10 μm) is used
for supporting the phosphor screen and the photocathode in close proximity
and for coupling the light image from the phosphor screen to the photocath-
ode of the following stage. A current gain of 50 to 100 may be obtained
across the mica target in the process of conversion of electron beam energy
into light and then the light into a low-energy photoelectron image. Because
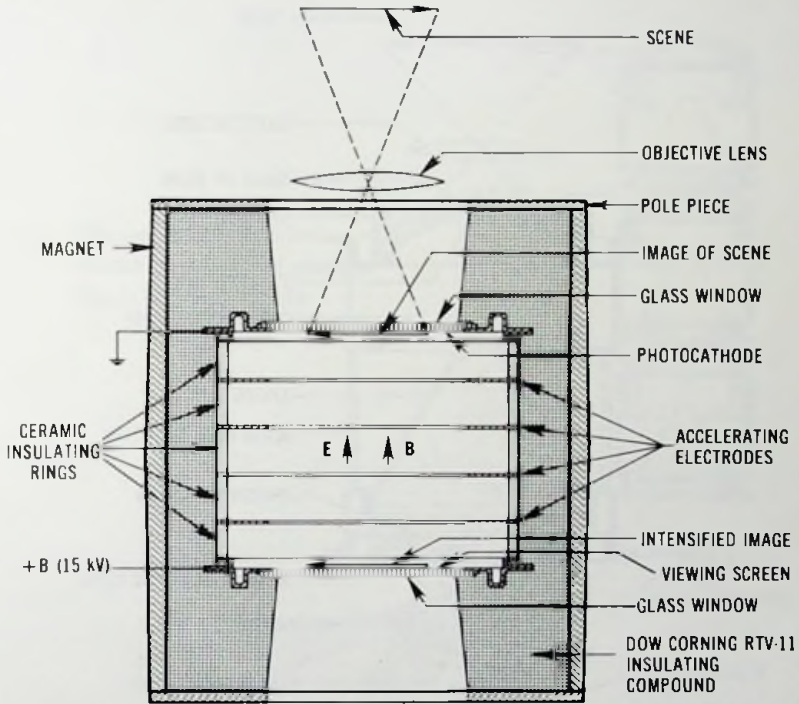
Fig. 2.2   The electromagnetically focused image tube.

of the internal current multiplication, a three-stage tube may have a luminous gain in excess of 10^6. Usually it is between 25 000 and 100 000.

The resolution of a three-stage tube may be in the range of 30 to 45 1p/mm, depending on mica thickness and phosphor screen resolutions.

2.4   The Electrostatically Focused Image Tube

The electrostatically focused image tube is mostly used in the areas where minimum weight and size, and an inverted image, often with other than unity magnification, is required. The electrostatically focused image tube has a spherical cathode and spherical screen and a conical anode with the anode aperture placed near the center of curvature of the photocathode, as shown in figure 2.3. The screen is at a certain distance beyond the anode aperture to provide the desired image magnification. Sharp focusing is obtained by an initial adjustment of the cathode aperture diameter. The boundary of the front section of the image tube is shaped to produce (to a close approximation) a central field between the anode cone and the cathode sphere. The central field and the anode aperture lens focus an inverted
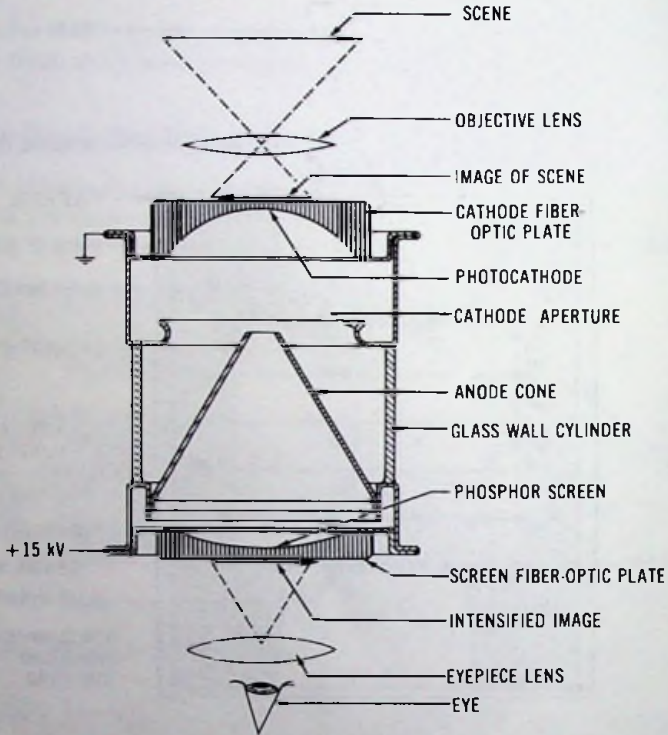
Fig. 2.3   The electrostatically focused image tube.

image of the photocathode on the phosphor screen. Because the photocathode and the screen are on curved surfaces, the input and output windows are often made of fiber optics for translation of curved images into plane images and for direct coupling of input and output images to other optical elements, such as a photographic film, a camera tube, etc.

For high intensification requirements, two or three single-stage tubes may be used in cascade as shown in figure 2.4.

2.5   Gated Image Tubes

Gated image tubes are used as electronic shutters to photograph and sense photoevents of extremely short duration. In one type the cathode aperture electrode (see figure 2.5) is isolated from the cathode. During the' operation, the cathode aperture is biased to a negative potential with respect to the cathode in order to cut off the cathode current. The tube is gated by pulsing the cathode aperture potential from the cutoff value to the focus

Fig. 2.4 **Three-stage electro-static intensifier assembly.** (*Courtesy RCA*)

0

+12 kV

+24 kV

+36 kV

IMAGE
CATHODE
FIBER-OPTIC PLATE

PHOTOCATHODE

GATING GRID

BASE METAL
EVAPORATOR

ALKALI CHANNEL

CATHODE APERTURE

ANODE CONE

(FOCUS) +150 V
(CUTOFF) −1500 V

CERAMIC WALL
CYLINDER

PHOSPHOR SCREEN

+15 kV

SCREEN FIBER-OPTIC
PLATE

INTENSIFIED IMAGE
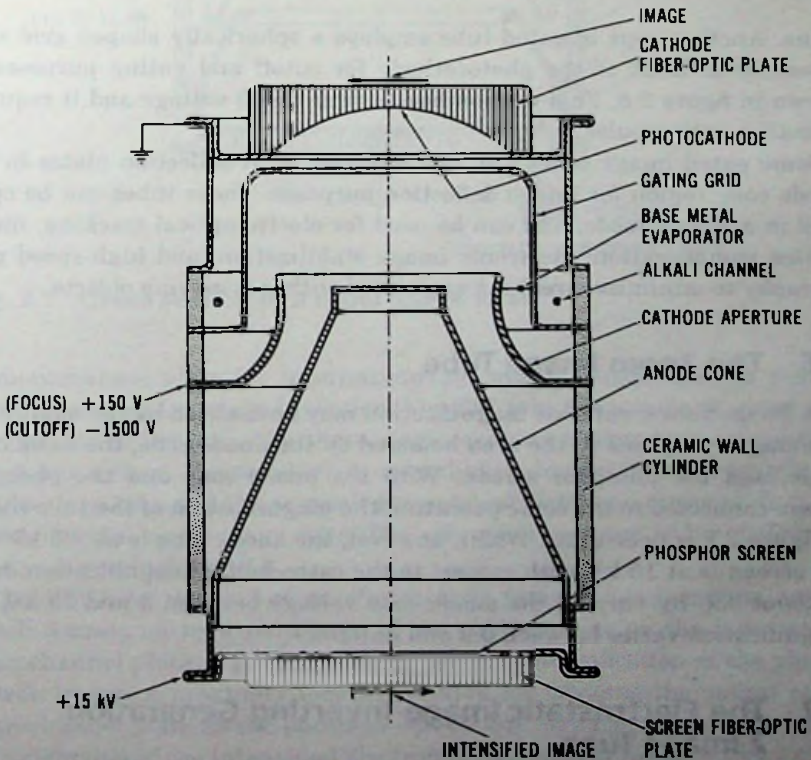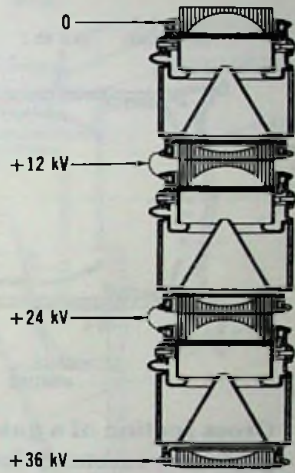
Fig. 2.5 **Cross section of a gated image tube.**
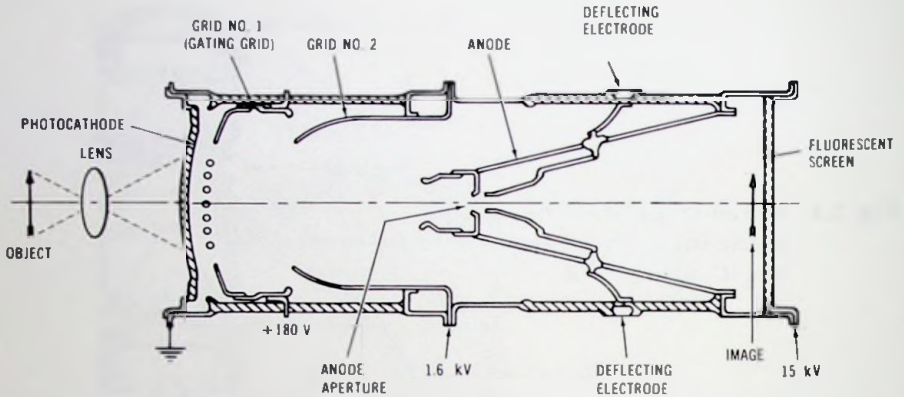
Fig. 2.6   Cross section of a gated image tube employing a spherical
grid wire assembly for gating.

value. Another type of gated tube employs a spherically shaped grid wire
assembly in front of the photocathode for cutoff and gating purposes as
shown in figure 2.6. This version has a lower cutoff voltage and it requires
a smaller gating pulse.

Some gated image tubes are also equipped with deflection plates in the
anode cone region for image deflection purposes. These tubes can be oper-
ated in a streak mode, and can be used for electro-optical tracking, image
motion compensation, electronic image stabilization, and high-speed pho-
tography to minimize streaking associated with fast moving objects.

2.6   The Zoom Image Tube

In image tubes, variable magnification may be realized by the addition of
a demagnifying lens in the area bounded by the anode cone, the zoom elec-
trode, and the phosphor screen. With the anode cone and the phosphor
screen connected to the same potential, the magnification of the tube shown
in figure 2.7 is near unity. When, however, the anode cone is at $+3$ kV and
the screen is at 15 kV with respect to the cathode, the magnification drops
to about 0.2. By varying the anode cone voltage between 3 and 15 kV, the
magnification varies between 0.2 and unity.

2.7   The Electrostatic Image-Inverting Generation
2 Image Tube

The electrostatic image-inverting generation 2 image tube (ESI tube) is a
high-gain, single-envelope image intensifier tube which operates by using
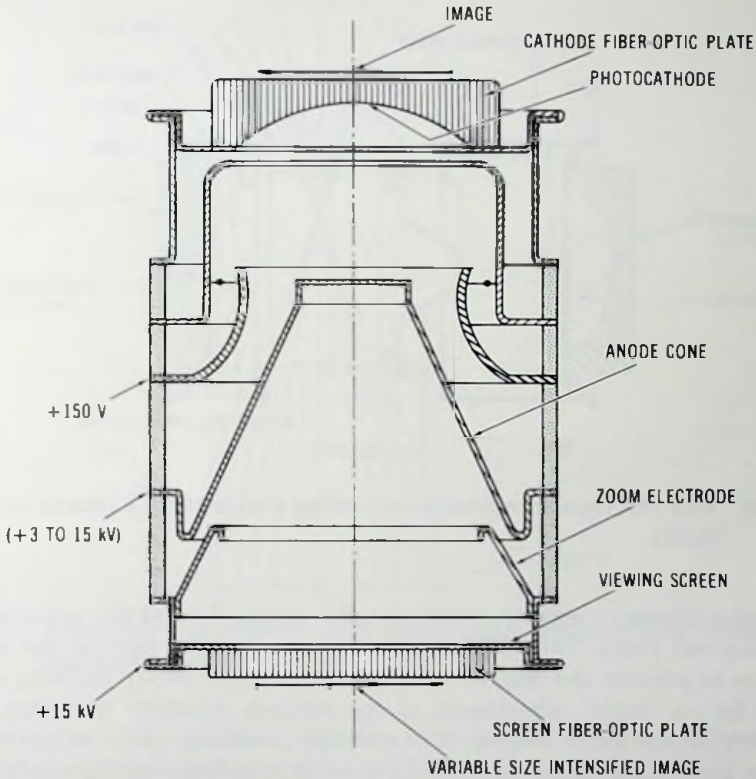
Fig. 2.7   Cross section of a zoom image tube.

a microchannel plate for internal current multiplication and an electrostatic focus lens for image inversion. The ESI tube has a radiant power gain comparable to the gain of a three-stage cascaded electrostatic image tube, but it has a short length which is only slightly longer than the length of a single-stage tube and it has small geometrical distortion comparable to the distortion of a single-stage tube. The schematic diagram of the ESI image tube is shown in figure 2.8.

The ESI tube consists of an electrostatic focus image-inverting section which focuses an inverted image of the photocathode on the input of the microchannel plate, a microchannel plate for intensification of the photoelectron image, a proximity focusing section for focusing the output of the microchannel plate on the phosphor screen and an output fiber-optic screen for conversion of the intensified electron image to light image.

The image-inverting optics has a spherical cathode and a conical anode with the anode aperture placed slightly beyond the center of curvature of
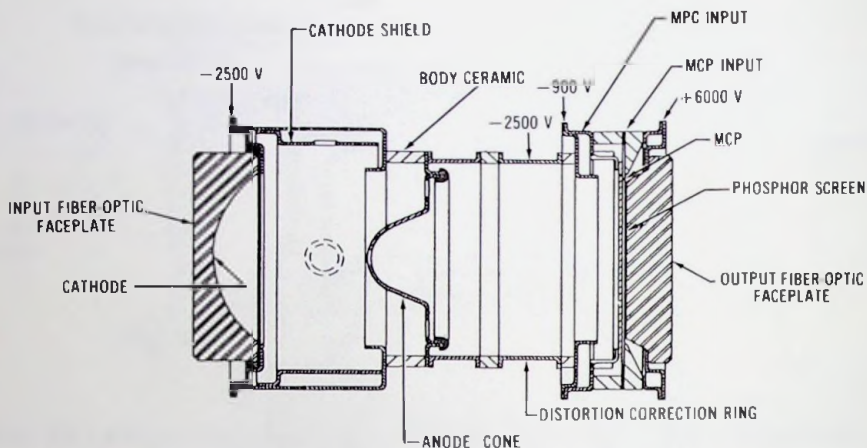
Fig. 2.8   The electrostatic image-inverting generation 2 image tube (ESI).

the photocathode in order to produce a flat image field at the input of the microchannel plate. The MCP is at a certain distance beyond the anode aperture to provide the desired image magnification. Sharp focusing is obtained by an initial adjustment of the cathode aperture diameter. The boundary of the front section of the image-inverting optics is shaped to produce (to a close approximation), a central field between the anode cone aperture and the cathode sphere. The central field and the anode aperture lens focus an inverted image of the photocathode on the input of the microchannel plate. The short cylindrical electrode at the input of the microchannel plate is for reducing the distortion of the optics and for ensuring perpendicular beam landing, which is critical for acceptable brightness uniformity.

Figure 2.9 shows the electron trajectories of a distortion-corrected electrostatic image-inverting electron optic. The central field accelerates the electrons toward the center of the centrally symmetric system. The anode aperture lens refracts the electron beam to give a new direction and focus for the electron rays. Finally, the distortion correction ring collimates the electron beam.

The ESI image-inverting optics also serves as a positive-ion barrier for the ions originating in the microchannel plate. A positive-ion barrier is obtained by placing the input of the microchannel plate at a lower potential with respect to the cathode than the anode cone potential. Energetic positive ions, if not stopped, reduce the life of the photocathode. The positive-ion
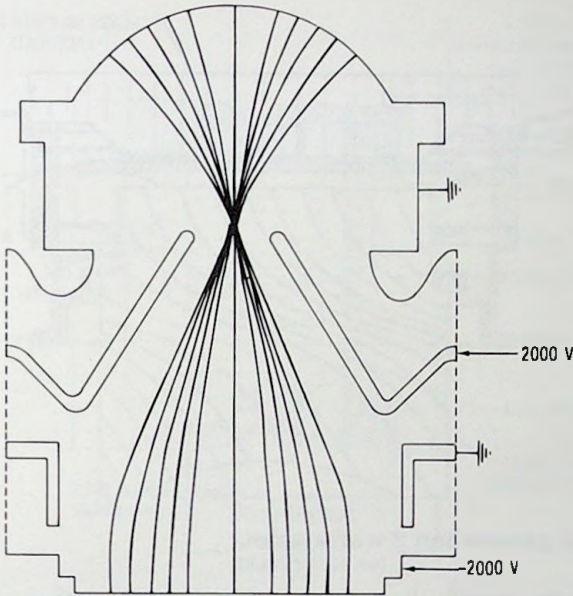
Fig. 2.9   Electron trajectories of a distortion-corrected electrostatic image-inverting electron optic.

barrier optics also eliminates halation by collection of the secondary electrons originating at the input of the MCP.

2.8   The Generation 2 Wafer Tube

The generation 2 wafer tube is a high-gain single-envelope very short image intensifier tube suitable for night vision goggle application using available light from night sky. The wafer tube is a geometrical distortion-free device. The cross-sectional view of the ITT generation 2 wafer tube is shown in figure 2.10. The wafer tube consists of a screen fiber-optic plate, ceramic metal body which contains the microchannel plate, and a metallized cathode fiber-optic faceplate wedge. The photocathode and the output of the microchannel plate are proximity focused on the microchannel plate input and output phosphor screen, respectively, to provide a very short distance between the photocathode and the output phosphor screen. Image inversion is obtained by a fiber-optic twist. To provide pumping during the exhaust and photocathode processing an indium seal configuration is used at the photocathode end of the tube. The luminous gain of the wafer tube is typically in the range of 10 000 to 15 000.
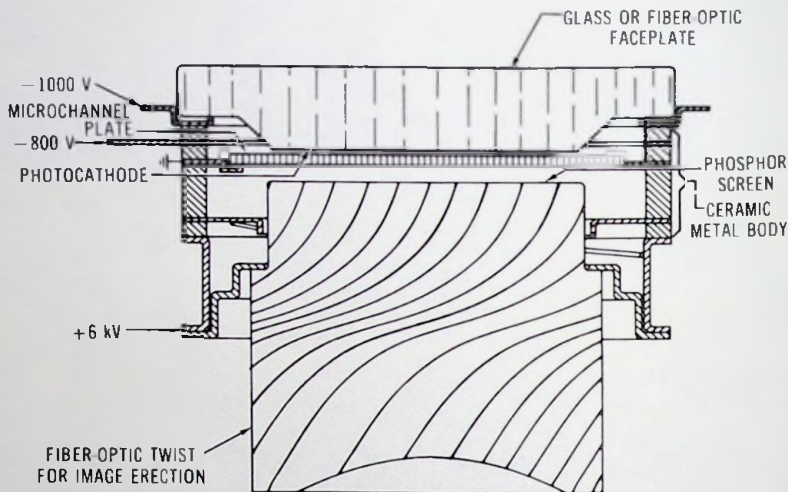
Fig. 2.10   The generation 2 wafer tube.

The wafer tube operates by use of a microchannel plate for internal current multiplication. Physically, a microchannel plate is a two-dimensional array of hollow glass fibers fused together into a thin disk. The inside surface of the hollow glass fibers is covered by a resistive secondary electron emission film which is electrically connected to the input and the output electroding of the channel plate. The hollow glass fibers, generally termed as microchannels, have an inside diameter in the 8- to 12-μm range. The channel length to diameter ratio (L/D) is typically on the order of 40 to 48 for plates used in image intensifier tubes. The microchannels are not perpendicular to the input and output surfaces but typically are at a 5° bias angle. The purpose of the bias angle is to ensure a first electron impact near the channel entrance, reduce light feedback from the phosphor screen, reduce ion feedback in the electrostatic image inverting tube types, and improve the uniformity of image transmission. For long life wafer tube applications the MCP has an ion barrier. The ion barrier is a continuous thin-film membrane of aluminum oxide (Al_2O_3) which covers the input surface of a standard microchannel plate. This thin-film membrane acts as a barrier to positive ions and neutral gas molecules, which are generated in the channels of the MCP as a result of electron impacts, while permitting free passage of electrons.

2.9   The Generation 3 Wafer Tube

The generation 3 wafer tube is a high-gain, high-photosensitivity image intensifier tube suitable for passive night vision with superior low light
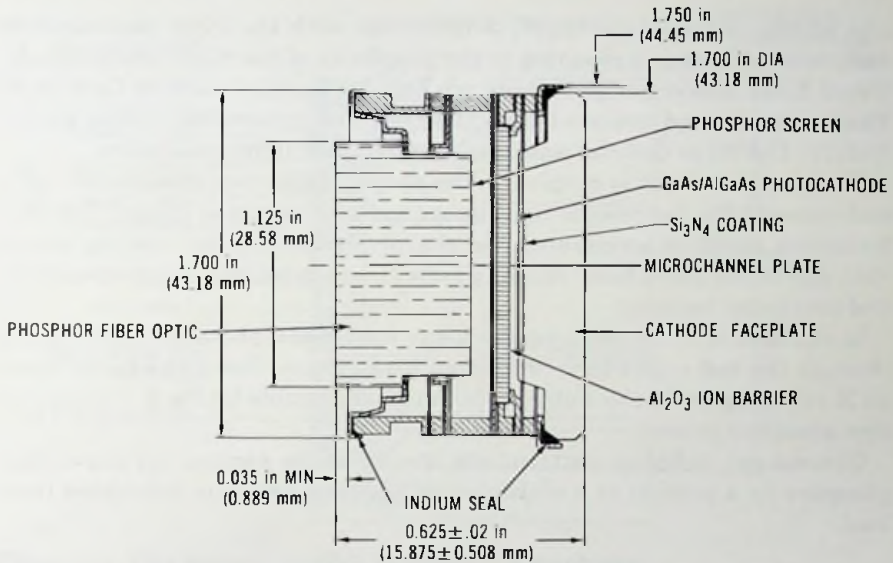
Fig. 2.11   The 25-mm generation 3 intensifier tube.

level resolution. Figure 2.11 shows the cross-sectional view of the ITT generation 3 wafer tube. The major difference between the generation 2 and the generation 3 wafer tubes is the photocathode. Generation 2 tubes use the multialkali photocathode, which has a luminous sensitivity in the range of 250 to 550 μA/lm. In the generation 3 wafer tube, the high-photosensitivity GaAs/AlGaAs photocathode is used. The typical luminous sensitivity of the gallium arsenide (GaAs) cathode is above 1000 μA/lm. The gallium arsenide cathode of the generation 3 tube is bonded to the cathode glass faceplate wedge as shown in figure 2.11.

To accommodate improved pumping during the exhaust and microchannel plate scrubbing, a double indium seal configuration is used at both photocathode and phosphor screen ends of the tube. Ion etching of the photocathode and exposure of the photocathode to gases emanating from the MCP during operation are prevented by use of an Al_2O_3 film at the input of the microchannel plate. The Al_2O_3 film is transparent to the photoelectrons. The lower MCP support and the MCP configuration are designed to provide a hermetic seal between the photocathode and the phosphor screen.

2.10   X-Ray and Gamma-Ray Converter Tubes

In X-ray and gamma-ray converter tubes the incident radiation pattern is absorbed and converted to a light image by a fluorescent phosphor mate-

rial which, in some tube types, is in contact with the input photocathode
and, in other types, is mounted in the proximity of the input photocathode.
Usual X-ray conversion phosphors are $ZnS:Ag$, $ZnS \cdot CdS:Ag$ and $CaWO4:W$.
Thallium-activated cesium-iodine [$CsI(Tl)$] and gamma-ray tubes utilize
$NaI(Tl)$, $CsI(Tl)$ or $CsI(Na)$ scintillator crystals for light generation.

The phosphor light is coupled to the photocathode that absorbs the light
and converts the fluorescent light image to a photoelectron image. The pho-
toelectron image is accelerated and sharply focused on the viewing screen
with any of the three basic imaging systems: electrostatic, electromagnetic,
and proximity focusing.

In the case of X-ray imaging the X-ray conversion phosphor is irradiated
through the test object by a collimated X-ray beam. The X-ray beam forms
an X-ray image of the test object which is made visible by the X-ray conver-
sion phosphor screen.

Gamma-ray radiation patterns are imaged on the gamma-ray conversion
phosphor by a pinhole or a multipinhole imaging structure fabricated from
lead.

2.11   The Hybrid Image Intensifier Tube

The hybrid image intensifier tube is a two-stage image intensifier tube
which consists of a generation 2 or generation 3 wafer image intensifier
tube coupled to a generation 1 electrostatically focused image tube and
packaged with a power supply into a rugged unit identical in form and fit
with the electrostatic generation 2 inverter tube (ESI). Figure 2.12 shows
the cross section of the hybrid tube. The hybrid tube is available in the 18-
mm and 25-mm formats. See Fig. 2.13.

The hybrid tube has been developed for superior low light level resolution,
high output brightness, and long life requirements. The hybrid tube, with
its wafer tube input, has a distinct advantage in its high signal-to-noise
ratio. The high signal-to-noise ratio is the result of the high photocathode
sensitivity of the wafer tube, which is in the range of 240 to 500 µA/lm for
the generation 2 wafer tube and typically 900 µA/lm for the generation 3
tube. Because the luminous gain of the hybrid tube is in excess of 100 000,
each photoelectron can produce a visual sensation, thus extending the re-
gion of vision to the lowest levels. The output of the hybrid tube is a gener-
ation 1 tube which enables the hybrid to operate at high output brightness
levels without loss of resolution or damage to the image tube.

The hybrid tube gained an important application as a gated image tube.
Gated image tubes are used as electronic shutters to photograph or sense
photoevents of extremely short duration. On and off gating of the hybrid
tube is accomplished by pulsing the wafer tube cathode potential from the
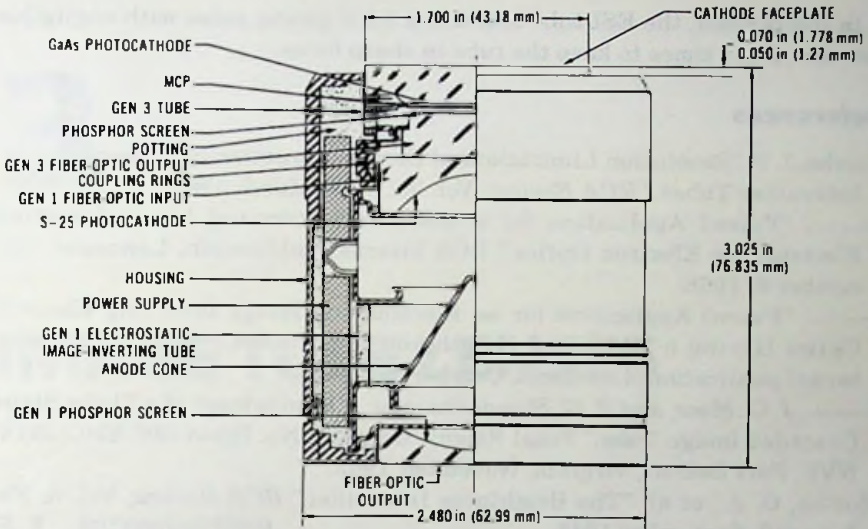
Fig. 2.12 The generation 3/1 MX9644/UV package.

Fig. 2.13 Two 18-mm generation 2 packaged image intensifier tubes.

cutoff value to the operational value. Since the MCP-to-cathode voltage is only about 200 V, the required pulse amplitude is less than or equal to 200 V. The rise and decay time of the gating pulses is not a rigorously critical parameter because the wafer tube remains in acceptable focus down to about 20 V cathode-to-MCP voltage value.

In comparison, the ESI tube requires a 3-kV gating pulse with negligible rise and decay times to keep the tube in sharp focus.

References

Csorba, I. P. "Resolution Limitations of Electromagnetically Focused Image-Intensifier Tubes," *RCA Review*, Vol. 30, p. 36, March 1969.

———. "Patent Application for a Distortion Corrected Image Inverting Electrostatic Electron Optics," RCA internal publication, Lancaster, December 6, 1968.

———. "Patent Application for an Electrostatic Image Inverting Electron Optics Having a Minimized Length and Distortion Correction," RCA internal publication, Lancaster, October 18, 1968.

———, J. C. Moor, and R. G. Stoudenheimer. "Development of a Three-Stage Cascaded Image Tube," Final Report, Contract No. DA44-009-ENG-3914, NVL, Fort Belvoir, Virginia, November 1962.

Morton, G. A., et al. "The Brightness Intensifier," *RCA Review*, Vol. 9, No. 3, p. 419, September 1948.

Niklas, W. F. "X-Ray Image Intensification with a Large Diameter Image Intensifier Tube," *American Journal of Roentgenology, Radiology, and Nuclear Science*, Vol. 85, No. 2, p. 323, February 1961.

Stoudenheimer, R. G., et al. "Image Intensifiers for Nuclear Track Imaging," *IRE Transactions on Nuclear Science*, No. 57, p. 136, 1960.

Stoudenheimer, R. G., and R. D. Faulkner. "Night Surveillance Systems for Law Enforcement," *Proceedings of the 1970 Carnahan Conference on Electronic Crime Counter Measures*, University of Kentucky, Lexington, Kentucky, April 16-18, 1970.

Teves, M. C., and T. Tol. "Electronic Intensification of Fluoroscopic Images," *Philips Technical Review*, Vol. 14, p. 33, 1952.

3

IMAGE TUBE LENSES

3.1   Introduction

Image tube lenses in analogy to light focusing lenses are able to produce a sharp electron image of an electron-emitting extended object. There are various ways and means for producing electrostatic and magnetostatic fields with focusing properties. The theory and description of focusing fields is the subject of electron optics and is covered in appendix E and in additional detail in the references. Before entering the discussion of electron lenses it is, however, appropriate that the reader be reminded that an analogy exists between the path of a ray of light passing through a refractive medium and the path of an electron passing through a conservative field of force. This analogy in a particular case shows that Snell's law of refraction of physical lenses has its counterpart in electron optics and the refractive index n is analogous to the electron velocity. The analogy in the general case may be seen from the principles of least time for geometrical optics (Fermat's principle) and of least action for electron optics.

The principle of least time states that the path of a light ray from one point to another is that which requires the least time. Thus,

$$T = \int \frac{ds}{v} = \frac{1}{c} \int n \, ds = \text{minimum}, \tag{3.1}$$

where T is time, s is distance, v is the velocity of light in a medium of index of refraction n, and c is the velocity of light in a vacuum.

The principle of least action for electron optics states that the path of an electron from one point to another is that which requires the least action:

$$\text{action} = \int mv \, ds = \text{minimum}, \tag{3.2}$$

where v is the electron velocity and m is the electron mass. From the above it may be seen that the counterpart of index of refraction is electron velocity.

The groundwork for electron optics was laid down more than 100 years ago by Hamilton, Maupertius, and Lagrange, who recognized the analogy between the principles of least time and least action. It was, however, Bush who showed in 1926 that the action of a short, axially symmetric magnetic field on electron beams is similar to that of a glass lens on light rays. Since then many outstanding books and articles have appeared on the subject of electron optics. In this chapter the special case governing the electron motion in the most commonly used electron lenses in image tubes will be treated and discussed.

In image tubes the requirement is to focus electron beams of large cross section with as little aberration as possible. The three most frequently used image tube lenses which meet this requirement are: (1) the biplanar lens consisting of a homogeneous axial electric field, (2) the electromagnetic lens consisting of homogeneous axial electric and magnetic fields, and (3) the centrally symmetric type of electrostatic lens.

3.2   The Biplanar Lens

In the biplanar lens the electrons, which are emitted by a point source with small radial and axial emission energies, travel on a parabolic path. The transit time t of the electrons is approximately equal to

$$t = L\sqrt{2m/eV_s},\tag{3.3}$$

where L is the screen-to-photocathode separation, and e and m are the charge and mass of an electron, respectively, and V_s is the screen voltage. The radial velocity v_r of an electron emitted at an angle θ is

$$v_r = \sqrt{2eV_i/m}\,\sin\theta,\tag{3.4}$$

where V_i is the voltage equivalent of the emission energy.

The transverse displacement of an electron may be obtained by multiplication of the radial emission velocity with the transit time:

$$r = tv_r = 2L\sqrt{V_i/V_s}\,\sin\theta.\tag{3.5}$$

From equation 3.5 the image of a point can be made sufficiently small by use of small L and large V_s values.

In a typical proximity focused diode the voltage equivalent of maximum emission energy spread is $V_{im} = 0.3$ V, $\theta = 90°$, $V_s = 10\ 000$ V and $L = 1.5$ mm, yielding, from equation 3.5, $r = 16.4 \times 10^{-3}$ mm.

3.3   The Electromagnetically Focused Electron Lens

In electromagnetic image intensifiers the electric and magnetic fields are sufficiently uniform over the useful beam diameter. Hence, for the electromagnetic lens the ideal conditions of homogeneous axial electric and magnetic fields may be assumed.

In homogeneous axial electric and magnetic fields the electrons are accelerated in the axial direction by a constant electrical force. The axial motion, therefore, from Newton's law is

$$m \frac{d^2z}{dt^2} = -eE,$$

(3.6)

where E is the electric field, e and m are the electron charge and mass, respectively, t is the time and z is the axial distance. The axial distance z traveled by the electron in the uniform electric field may be obtained by integration of equation 3.6:

$$z = -\frac{e}{2m} Et^2 + v_a t,$$

(3.7)

where v_a is the axial emission velocity.

The transverse motion of electrons in the homogeneous magnetic field of the lens is associated with a magnetic force having a value of eBv_r and acting at right angles to the transverse emission velocity v_r and to the magnetic flux density B. Since the magnetic deflection force is constant and it is always perpendicular to the transverse motion, it meets the requirements of a uniform circular motion and, therefore, it causes the electron to move on a circle in a plane perpendicular to the electric and magnetic fields and moving with the electron in the axial direction. The diameter D of the circular motion may be obtained by equating the centripetal and centrifugal forces of the circular motion:

$$eBv_r = 2mv_r^2/D.$$

(3.8)

From equation 3.8 the diameter in centimeters is

$$D = 2mv_r/eB = 6.74\sqrt{V_r}/B,$$

(3.9)

where B is the magnetic flux density in gausses, and V_r is the voltage equivalent of the transverse emission energy.

The period T of the circular motion may be obtained by division of the circumference (πD) by the transverse component of the emission velocity. By multiplication of equation 3.9 by π and division by v_r the period T in seconds is

$$T = 2\pi m/eB = (0.355/B) \times 10^{-6}.$$

(3.10)

The axial distance from the photocathode, at which an electron completes its period of rotation, may be obtained by substitution of the value of T in equation 3.7:

$$L = T(v_a - \pi E/B), \tag{3.11}$$

where L is the loop focus distance of v_a axial emission velocity electrons.

The approximate value of the loop focus distance, L_o, may be obtained by omission of the term v_a in equation 3.11 and by substitution of $E = -V_s/L_o$ for the electric field. By combination of equations 3.10 and 3.11 and upon rearrangement, L_o becomes

$$L_o = \pi\sqrt{2m/e} \sqrt{V_s} /B = 10.58\sqrt{V_s} /B. \tag{3.12}$$

In equation 3.12 the screen voltage V_s is in volts, B is in gausses and L_o is in centimeters.

The electron transit time is identical for magnetic fields that produce single or multiloop paths. For multiloop focusing, therefore, the loop focus distance is

$$L_o = 10.58n\sqrt{V_s} /B, \tag{3.13}$$

where n is the number of loops.

In a typical magnetically focused image tube, $V_s = 10\,000$ V and $B = 200$ gausses, yielding from equation 3.12 a loop focus distance of $L_o = 5.29$ cm.

3.4　The Centrally Symmetric Electrostatic Electron Lens

In the electrostatically focused image-inverting tubes the boundary of the electron optic of the image tube is shaped to produce to a close approximation a central field between the anode cone and the cathode sphere. Hence for the electrostatic image-inverting lens the ideal conditions of a centrally symmetric lens may be assumed.

In an ideally centrally symmetric system consisting of two concentric spheres, the electrons travel in a central field up to the anode sphere.

Consider an electron leaving the cathode sphere with an emission velocity v_i and direction θ as indicated in figure 3.1. In the central field region the electron path is determined by Kepler's law of equal areas:

$$r^2\frac{d\phi}{dt} = c, \tag{3.14}$$

where r and ϕ are the spherical coordinates of the centrally symmetric system and c is a constant. The velocity of the electron may be described by the following equation:
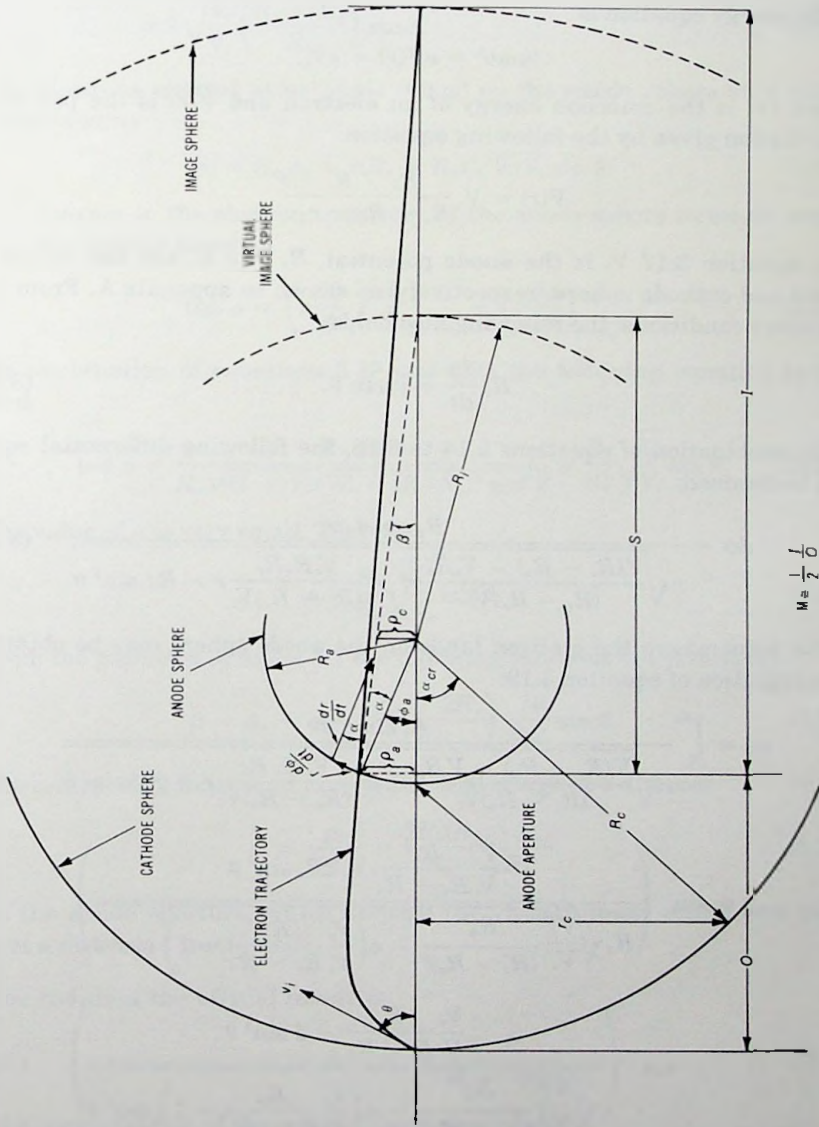
Fig. 3.1   Schematic diagram of a centrally symmetric electrostatic
            lens.

$$v^2 = \left(\frac{dr}{dt}\right)^2 + \left(r\frac{d\phi}{dt}\right)^2. \tag{3.15}$$

The energy equation is

$$\tfrac{1}{2}mv^2 = eV(r) + eV_i, \tag{3.16}$$

where eV_i is the emission energy of an electron and $V(r)$ is the potential distribution given by the following equation:

$$V(r) = V_s \frac{R_a}{R_c - R_a} \frac{R_c - r}{r}. \tag{3.17}$$

In equation 3.17 V_s is the anode potential, R_a and R_c are the radius of anode and cathode sphere, respectively, as shown in appendix A. From the boundary conditions, the following also holds:

$$R_c \frac{d\phi}{dt} = v_i \sin\theta. \tag{3.18}$$

By combination of equations 3.14 to 3.18, the following differential equation is obtained:

$$d\phi = \frac{R_c \sin\theta \, dr}{r\sqrt{\dfrac{V_i(R_s - R_a) - V_sR_a}{(R_c - R_a)V_i} r^2 + \dfrac{V_sR_aR_c}{(R_c - R_a)V_i} r - R_c^2 \sin^2\theta}}. \tag{3.19}$$

The point where the electron lands on the anode sphere may be obtained by integration of equation 3.19:

$$\phi_a = \int_{R_c}^{R_a} \frac{R_c \sin\theta \, dr}{r\sqrt{\dfrac{V_i(R_c - R_a) - V_sR_a}{(R_c - R_a)V_i} r^2 + \dfrac{V_s R_a R_c}{(R_c - R_a)V_i} r - R_c^2 \sin^2\theta}}$$

$$= \sin^{-1}\left(\frac{\dfrac{V_s}{V_i}\dfrac{R_a^2}{R_c - R_a} - 2R_c \sin^2\theta}{R_a\sqrt{\dfrac{V_s^2}{V_i^2}\dfrac{R_a^2}{(R_c - R_a)^2} - 4\left(\dfrac{V_s}{V_i}\dfrac{R_a}{R_c - R_a} - 1\right)\sin^2\theta}}\right)$$

$$- \sin^{-1}\left(\frac{\dfrac{V_s}{V_i}\dfrac{R_a}{R_c - R_a} - 2\sin^2\theta}{\sqrt{\dfrac{V_s^2}{V_i^2}\dfrac{R_a^2}{(R_c - R_a)^2} - 4\left(\dfrac{V_s}{V_i}\dfrac{R_a}{R_c - R_a} - 1\right)\sin^2\theta}}\right). \tag{3.20}$$

For $V_s \gg V_i$, and in the Gaussian image plane, equation 3.20 reduces to the following equation:

$$\phi_a = \sin^{-1}\left(2\sqrt{\frac{V_i}{V_s}}\frac{R_c - R_a}{R_a}\sin\theta - \frac{V_i}{V_s}\frac{R_c - R_a}{R_a}\sin\theta\cos\theta\right)$$

$$\cong 2\sqrt{\frac{V_i}{V_s}}\left(\frac{R_c - R_a}{R_a}\right)\sin\theta. \tag{3.21}$$

The electrons emitted at an angle θ land on the anode sphere on a circle having a radius

$$\rho_a = R_a\,\phi_a \cong 2(R_c - R_a)\sqrt{V_i/V_s}\,\sin\theta. \tag{3.22}$$

The tangent to the electron trajectory at the anode sphere forms an angle α with the normal given by

$$\tan\alpha = \left(r\frac{d\phi}{dt}\Big/\frac{dr}{dt}\right)_{r=R_a} = \left(r\frac{d\phi}{dr}\right)_{r=R_a}. \tag{3.23}$$

By combination of equations 3.19 and 3.23 the following equation is obtained:

$$\tan\alpha = \frac{R_c\sin\theta}{R_a\sqrt{(1 + V_s/V_i) - (R_c/R_a)^2\sin^2\theta}} \cong \frac{R_c}{R_a}\sqrt{\frac{V_i}{V_s}}\sin\theta. \tag{3.24}$$

The value of α is very small. Therefore

$$\alpha \cong \frac{R_c}{R_a}\sqrt{\frac{V_i}{V_s}}\sin\theta. \tag{3.25}$$

From the geometry of figure 3.1 the following relations are obtained:

$$\beta = \phi_a - \alpha = \left(\frac{R_c - 2R_a}{R_a}\right)\sqrt{\frac{V_i}{V_s}}\sin\theta. \tag{3.26}$$

The central field focuses an inverted virtual image at a distance

$$S = \frac{\rho_a}{\tan\beta} = \frac{2R_a(R_c - R_a)}{R_c - 2R_a}. \tag{3.27}$$

from the anode aperture, which projects the virtual image into a new position at a distance I from itself.

The radius of the virtual image is

$$R_i = S - R_a = \frac{R_a R_c}{R_c - 2R_a}. \tag{3.28}$$

The magnification of the centrally symmetric lens is

$$M_P = \frac{R_i}{R_c} = \frac{R_a}{R_c - 2R_a}. \tag{3.29}$$

3.5   The Anode Aperture Lens

In image tubes the electron beam is sharply focused on the phosphor screen by the central field and the anode aperture lens. The anode aperture lens is a divergent lens which modifies the location and the radius of the image sphere of the centrally symmetric lens. The image position of the modified system may be obtained by calculation of the focal length of the anode aperture lens immersed in a central field and by application of the thin lens equation to the anode aperture lens and the virtual image of the centrally symmetric lens.

The electric field E_a at the anode sphere may be given by the following equation (see appendix A):

$$E_a = \frac{R_c\,V_s}{R_a(R_c - R_a)}. \tag{3.30}$$

From Gauss's dielectric flux theorem the following integral is obtained for the small cylindrical volume shown in figure 3.2:

$$\pi d\int_{z_1}^{z_2} E_r\,dz = E_a\frac{d^2\pi}{4} = \frac{\pi d^2}{4}\frac{R_c\,V_s}{R_a(R_c - R_a)}. \tag{3.31}$$
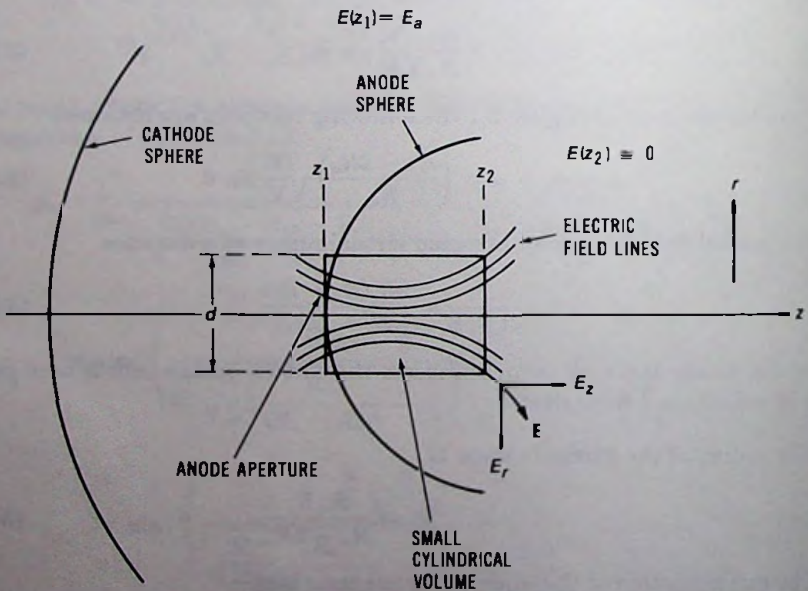
Fig. 3.2   Diagram for the derivation of the focal length of the anode aperture lens.

By combination of equations 3.30 and 3.31, the following equation is obtained:

$$\int_{z_1}^{z_2} E_r \, dz = \frac{d}{4} \frac{R_c \, V_a}{R_a(R_c - R_a)}. \tag{3.32}$$

The change of the radial velocity of an electron traversing through the anode aperture lens region is

$$\Delta v_r = -\frac{e}{m} \int_{t_1}^{t_2} E_r \, dt = -\frac{e}{m v_z} \int_{z_1}^{z_2} E_r \, dz = \frac{ed}{m v_z} \frac{R_c \, V_a}{R_a(R_c - R_a)}, \tag{3.33}$$

where

$$v_z \equiv \sqrt{2eV_a/m}. \tag{3.34}$$

The change of the direction of motion from equation 3.33 is

$$\tan \delta = \frac{\Delta v_r}{v_z} = \frac{d}{8} \frac{R_c}{R_a(R_c - R_a)}. \tag{3.35}$$

The focal length from the geometry of figure 3.2 is

$$f = \frac{d}{2 \tan \delta} = 4 \frac{R_a}{R_c}(R_c - R_a). \tag{3.36}$$

The anode aperture lens projects the virtual image of the cathode produced by the central field into a new position, forming there a real image. The distance of the real image position from the anode aperture may be found by the application of the thin lens formula to the anode aperture lens and the virtual image:

$$I = \frac{fS}{f - S} = 4R_a \frac{R_c - R_a}{R_c - 4R_a}, \tag{3.37}$$

where I and S are the image distance of real and virtual images, respectively.

The magnification M_n of the anode aperture lens is

$$M_n = I/S. \tag{3.38}$$

The system magnification M is the product of the magnifications of the symmetric and anode aperture lenses:

$$M = M_p \, M_n = \frac{2R_a}{R_c - 4R_a} = \frac{1}{2} \frac{I}{O}. \tag{3.39}$$

where O is the cathode distance measured from the anode aperture.

Equation 3.39 is especially useful for designing a pseudo centrally symmetric lens such as is employed in the generation 1 image tubes (see figure

2.3). In order to illustrate this let us assume that the required length of the optics is $L = I + O = 2.138$ in and $M = 0.92$. By combination of L and M values with equation 3.39, $I = 1.385$ in and $O = 0.753$ in are obtained. For the initial design, which must be refined by computerized electron trajectory calculation methods or cut-and-try building of electron optics study tubes, the cathode radius can be chosen to be $R_c = O$ cathode distance, and the phosphor screen radius may have a value of $R_s = I$. For comparison it is noteworthy that an optimized design obtained by computer calculation of electron trajectories yielded $I = 1.365$ in, $O = 0.773$ in, $R_c = 0.700$ in, and $R_s = 1.400$ in.

References

Brueche, E., and O. Scherzer. *Geometrische Electronenoptk*, Julius Springer, Berlin, 1934.

Brueche, E., and H. Johannson. *Naturewissenschaften*, p. 353, 1932.

Csorba, I. P. "Transit-Time-Spread-Limited Time Resolution of Image Tubes in Streak Operation," *RCA Review*, Vol. 32, p. 650, December 1971.

———. "Resolution Limitations of Electromagnetically Focused Image-Intensifier Tubes," *RCA Review*, Vol. 30, p. 36, March 1969.

———. "Anode Aperture Lens of the Electrostatic Image Converter Type 101C-5-F," Chicago, The Rauland Corporation internal publication, December 1957.

Davisson, C. J., and C. I. Calbick. "Electron Lenses," *Physical Review*, Vol. 38, p. 585, 1931.

———. "Electron Lenses: A Correction," *Physical Review*, Vol. 42, p. 580, 1932.

Faragó, P., and J. Pócza. *Electron Physics*, Academic Press, Budapest, 1954.

Glaser, W., *Grundlagen der Electronenoptic*, Julius Springer, Vienna, 1952.

Grivet, P. *Electron Optics*, Pergamon Press, Oxford 1965.

Kelman, V. M., and Sz. Ja. Javor. *Electron Optics*, Academic Press, Budapest, 1965.

Klemperer, O. *Electron Optics*, Cambridge University Press, London, 1939.

Maloff, I. G., and D. W. Epstein. *Electron Optics in Television*, McGraw-Hill Book Co., Inc., New York, 1938.

Rose, A. "Electron Optics of Cylindrical Electric and Magnetic Fields," *Proc. IRE*, Vol. 28, p. 30, January 1940.

Ruska, E. "Focusing of Cathode-Ray Beams of Large Cross Section," *Z. Physik*, Vol. 83, p. 684, July 1933.

Schagen, P., et al. "A Simple Electrostatic Electron-Optical System with Only One Voltage," *Philips Res. Rev.*, Vol. 7, p. 119, 1952.

Septier, A. *Focusing of Charged Particles*, Academic Press, New York and London, 1967.

Spangenberg, K. R. *Vacuum Tubes*, McGraw-Hill Book Co., Inc., New York, 1949.

Zworykin, V. K., et al. *Electron Optics and the Electron Microscope*, John Wiley & Sons, Inc., New York, 1945.

4

ABERRATIONS

4.1   Introduction

Image tube lenses under ideal conditions are free from geometrical aberrations. The imaging quality of ideal lenses, therefore, is determined by the chromatic aberrations only. Image tubes, however, are often built with electron lenses that slightly deviate from the ideal lens. These lenses, therefore, may have geometrical aberrations. The five geometrical aberrations that may exist in electron lenses are: (1) distortion of image, (2) astigmatism, (3) curvature of image field, (4) spherical aberration, and (5) coma. In image tubes, only the first three aberrations are of significance.

4.2   Chromatic Aberration

4.2.1   Focusing Error of an Electron Lens Consisting of Homogeneous Axial Electric and Magnetic Fields

In general, a photoelectron emitted from the photocathode enters the electron lens with small initial transverse and axial components of velocity. The transverse velocity component causes the electron to move on a circle in a plane perpendicular to the electric and magnetic fields. The period of the circular motion from equation 3.10 is

$$T = 2\pi m/eB, \tag{4.1}$$

where m is the electron mass, B the magnetic flux density, and e the elec-

tron's charge. The axial distance from the photocathode at which the electron completes its period of rotation is

$$L = T(v_a - \pi E/B), \tag{4.2}$$

where v_a is the axial emission velocity and E is the electric field.

In the case of a monoenergetic Lambertian electron emitter, if the phosphor screen is placed in the image plane of the electrons emitted at an angle θ_f, the axial focusing error may be obtained from equation 4.2 by calculating the electron image distance difference of the electrons emitted at angles θ and θ_f:

$$\Delta L = \pm Tv_i(\cos \theta_f - \cos \theta), \tag{4.3}$$

where v_i is the emission velocity of photoelectrons.

The electrons that complete a period of rotation a distance ΔL in front of the screen continue their transverse motion on a circular path for an additional time, ΔT. These electrons strike the screen at an arc length ΔTv_r from the image center, where v_r is the transverse emission velocity, as shown in figure 4.1. The situation is similar for the electrons completing a period of rotation behind the screen, except in this case ΔT has a negative value. The transverse focusing error of the electrons associated with particular values of v_i, θ_f, and θ from the geometry of figure 4.1 is given by

$$\Delta r = D \sin (v_r \Delta T/D), \tag{4.4}$$

where D is the diameter of circular motion.

$$\Delta r = D \sin \left(\frac{\psi}{2}\right) = D \sin \left(\frac{v_r \Delta T}{D}\right)$$

TRANSVERSE DISPLACEMENT
OF ELECTRON AT $t = \Delta T, T + \Delta T, \ldots$

ARC LENGTH $= \Delta Tv_r$

THE POSITION OF ELECTRON
AT THE PHOTOCATHODE AND IN
EXACT FOCUS ($t = 0, T, 2T \ldots$)
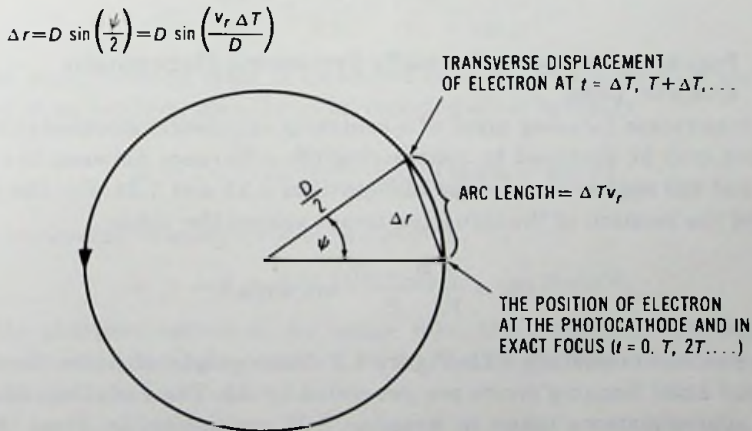
Fig. 4.1 **Transverse orbit of an electron in a plane perpendicular to the electric and magnetic fields and moving with the electron in the axial direction.**

From the equation of electron motion in a uniform electric field,

$$v_s^2 t^2 + 4L_o v_a t - 4L_o^2 = 0,\qquad (4.5)$$

the transit time difference ΔT may be obtained as

$$\Delta T = (2L_o/v_s^2)\left[v_i(\cos \theta_f - \cos \theta) - \sqrt{v_i^2 \cos^2 \theta_f + v_s^2}\right.$$
$$\left. + \sqrt{v_i^2 \cos^2 \theta + v_s^2}\right], \qquad (4.6)$$

where t is the transit time and v_s is the electron velocity corresponding to an accelerating voltage (screen-to-photocathode) V_s. For $v_s >> v_i$ equation 4.6 reduces to

$$\Delta T = L_o(\sqrt{V_i}/V_s)\sqrt{2m/e}\,(\cos \theta_f - \cos \theta). \qquad (4.7)$$

From the geometry of figure 4.2 and by use of equations 4.4 and 4.7, the first-order transverse focusing error is

$$\Delta r = (2L_o V_i/V_s)(\cos \theta_f - \cos \theta)\sin \theta, \qquad (4.8)$$

where L_o is the screen-to-photocathode distance and V_i is the accelerating voltage required for a photoelectron at rest to acquire its emission energy.

The electron transit time is identical for magnetic fields that produce single or multiloop paths. Therefore, in a first-order approximation, Δr is also identical in both modes of operation.

4.2.2   Focusing Error of a Centrally Symmetric Electrostatic Electron Lens

The transverse focusing error of a centrally symmetric electrostatic electron lens may be obtained by considering the difference between the exact value and the approximate value of equations 3.21 and 3.24. For the calculation of the location of the Gaussian image sphere the value

$$\Delta \phi_a = \frac{V_i}{V_s}\frac{R_c - R_a}{R_a}\sin \theta \cos \theta \qquad (4.9)$$

was neglected in equation 3.21. Figure 4.2 shows graphically how the transverse and axial focusing errors are generated by $\Delta \phi$. The variations of α due to the approximations taken in equation 3.24 are negligible. From the geometry of figure 4.2 the first-order transverse focusing error is

$$\Delta r = R_i \Delta \phi_a = 2\frac{V_i}{V_s}\frac{R_c}{R_a}\left(R_c - R_a\right)M_p \sin \theta \cos \theta. \qquad (4.10)$$
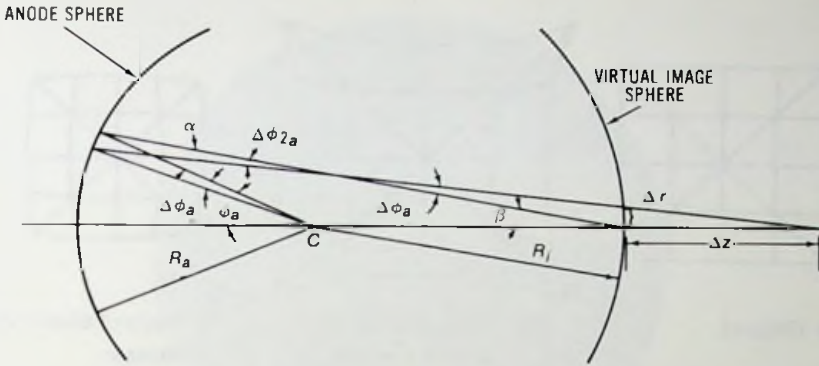
Fig. 4.2   Diagram for the derivation of the first-order focusing error.

The cathode field strength (see appendix A) is

$$E_c = V_s R_a / R_c (R_c - R_a).$$ (4.11)

By combination of equations 4.10 and 4.11, the transverse focusing error becomes

$$\Delta r = (2M_p V_i / E_c) \sin \theta \cos \theta.$$ (4.12)

The axial focusing error may be obtained by division of Δr by β:

$$\Delta z = \frac{\Delta r}{\beta} = 2 \sqrt{\frac{V_i}{V_s}} R_a \frac{R_c (R_c - R_a)}{(R_c - 2R_a)^2} \cos \theta.$$ (4.13)

If the axial focusing error is measured from the image plane of electrons emitted at an angle θ_f, then the axial focusing error becomes

$$\Delta z = 2 \sqrt{\frac{V_i}{V_s}} R_a \frac{R_c (R_c - R_a)}{(R_c - 2R_a)^2} \left(\cos \theta_f - \cos \theta \right).$$ (4.14)

The transverse focusing error in this case is

$$\Delta r = \Delta z \beta = (2M_p V_i / E_c)(\cos \theta_f - \cos \theta) \sin \theta.$$ (4.15)

At the phosphor sphere of the image tube, the transverse focusing error may be obtained by replacement of M_p by the image tube magnification M in equation 4.15.

4.3   Distortion of Image

Distortion of image of an electrostatically focused image tube is caused by the variation of the linear magnification along the radial distance.

| (A) Object. | (B) Pincushion dis- | (C) Barrel distorted |
| | torted image. | image. |
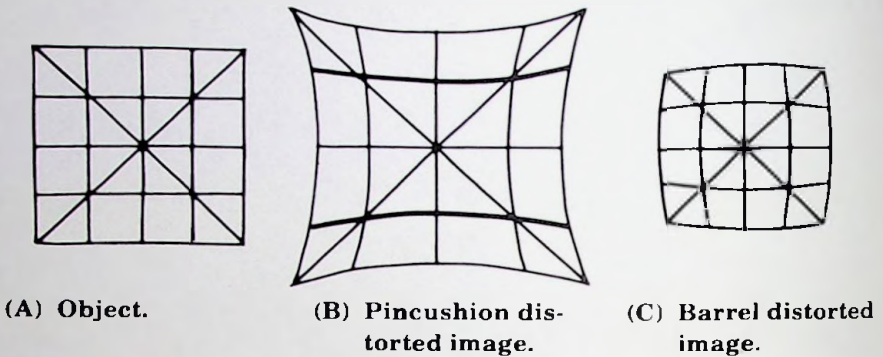
Fig. 4.3   Distortion of the image.

When the magnification increases with the radial distance the image has a pincushion distortion as shown in figure 4.3. Conversely, the image has a barrel distortion for decreasing magnification with the radial distance.

In an electromagnetically focused image tube, nonhomogeneous electric and magnetic fields may cause a radial line to be imaged with image rotation and spiral distortion as shown in figure 4.4. Figure 4.5 shows the spiral distortion of a two-stage 38-mm useful diameter magnetically focused image tube.

4.3.1   Distortion of the Image of the Electrostatically Focused Image Tube

The magnification of an electrostatically focused centrally symmetric image tube lens is constant over the entire spherical surface. Usually, the curved image and object fields are translated into flat fields by the input
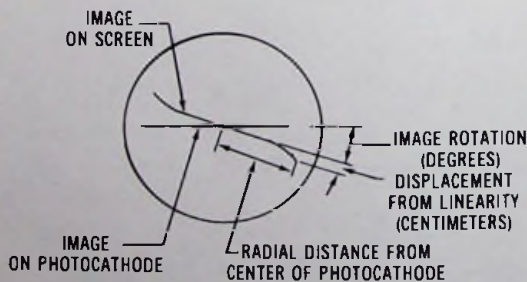
Fig. 4.4   Image rotation and spiral distortion of a magnetically focused image tube.
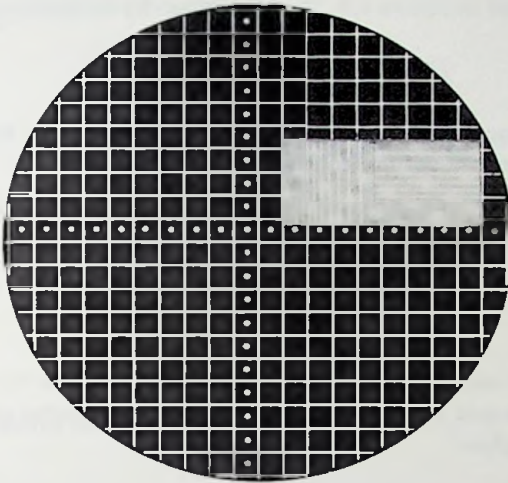
Fig. 4.5   Spiral distortion of an electromagnetically focused image
tube.

and output fiber-optic plates. The zonal magnification M_z along the flat fiber-optic surface from figure 4.6, is

$$M_z = r_s/r_c = I \sin \alpha_2/O \sin \alpha_1 = M_c/\cos (\alpha_1/2), \qquad (4.16)$$

where M_c is the center magnification, α_1 and α_2 are the angles subtending the electron beam at the cathode and screen, respectively, and I and O are
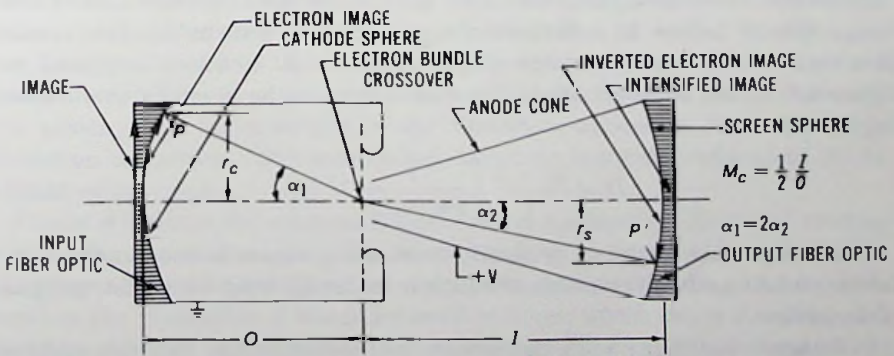
Fig. 4.6   Geometrical relations between the image and the object of
an image-inverting electrostatic diode.

distances indicated in figure 4.6. The distortion by definition is

$$D = \frac{M_z - M_c}{M_c} = \frac{1}{\cos(\alpha_1/2)} - 1.$$
(4.17)

When the photocathode is focused on a plane phosphor screen or microchannel plate the zonal magnification becomes

$$M_z = r_a'/r_c = 2M_c \tan \alpha_2/\sin \alpha_1 = 2M_c \tan(\alpha_1/2)/\sin \alpha_1.$$
(4.18)

The distortion is

$$D = \frac{1}{\cos^2(\alpha_1/2)} - 1.$$
(4.19)

Equations 4.17 and 4.19 are plotted in figure 4.7. The data of figure 4.7 are in good agreement with the distortion figures measured on commercially available image tubes.
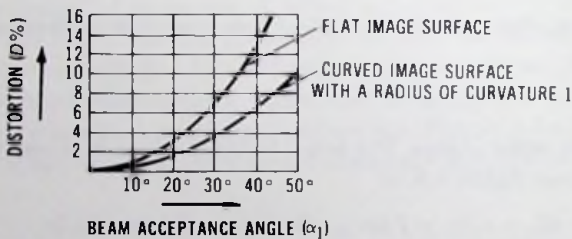
Fig. 4.7   Pincushion distortion as a function of beam angle α_1.

From the above analysis, distortion may be reduced by reduction of the image sphere radius. In a first-order approximation a distortion-free condition may exist when the image sphere radius is $R = I/2$ as indicated in figure 4.8. In the limit $I/2 < R < I$, the distortion may be given by the following equation:

$$D = \frac{2r - 1}{I}\left[\frac{1}{\cos(\alpha_1/2)} - 1\right].$$
(4.20)

The image tube designer generally must compromise between edge resolution and distortion, the result of which is an image tube with a few percent of distortion.

In image tubes that have a flat image field and therefore large pincushion distortion, distortion may be corrected by addition of an electron lens to the image-inverting optics which has a gradually decreasing magnification
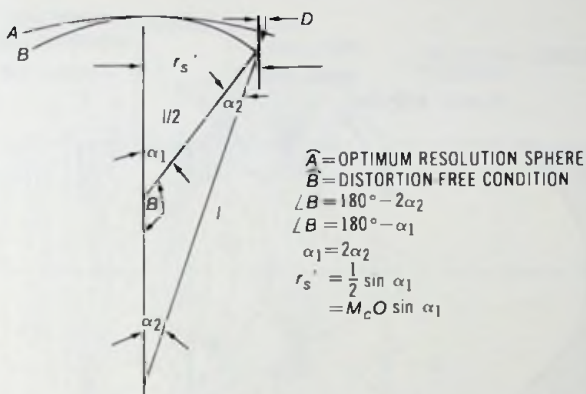
Fig. 4.8 Derivation of distortion.

along the radial distance. An electron lens which has this property may be obtained by addition of a short cylindrical electrode (distortion-correction electrode) between the anode cone and the screen or microchannel plate input of the image tube. By connection of the anode cone and the screen to an approximately equal potential, and the distortion-correction electrode to the cathode potential, a divergent lens is formed in the space of the anode cone while a saddle lens (positive lens) exists within the region bounded by the distortion-correction electrode and the screen as shown in figure 4.8. Along the axis of the optics the combined focusing action of the divergent and saddle lenses does not alter the magnification significantly. Off axis, however, the magnification decreases with the radial distance because the saddle lens, which is a demagnifying lens, has a higher power at the edge than in the center. The off-axis magnification may be varied by adjusting the axial position and the zonal strength of the saddle lens. The critical parameters of the structure are length, diameter, position with respect to the screen, and the potential of the distortion-correction electrode. With distortion correction, 12% uncorrected distortion has been reduced to 3% to 4% distortion values.

Figure 4.9 shows the electron trajectories of a distortion-corrected electrostatic image-inverting optic. The beam landing is nearly perpendicular to the plane image surface. The near perpendicular beam landing is a requirement in the generation 2 image intensifier tubes, which use a microchannel plate for current multiplication, to avoid zonal gain variation along radial distance of the microchannel plate.

Figure 4.10 shows an alternative version of distortion correction.
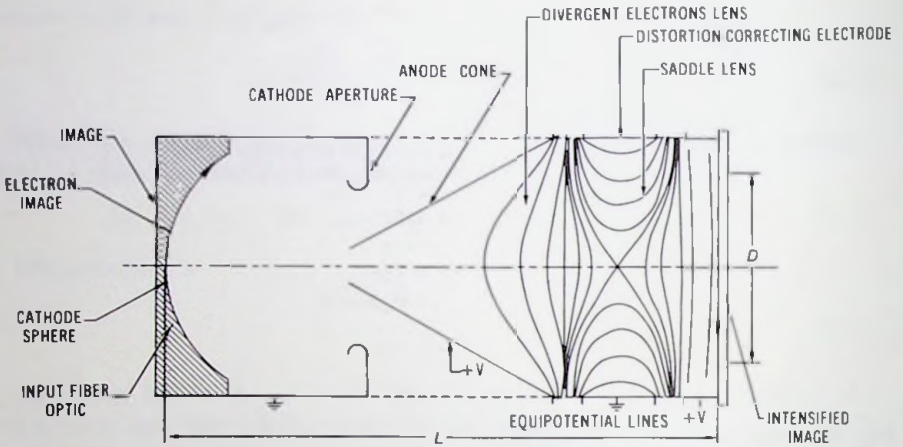
Fig. 4.9   Scheme of a distortion-corrected image-inverting electron optic.

4.3.2   Distortion of the Image of the Electromagnetically Focused Image Tube

In the electromagnetic image tube, such as that shown in figure 2.2, the accelerator rings and the magnet produce a set of nearly homogeneous axial electric and magnetic fields which focus an erect image of the photocathode on the phosphor screen with unity magnification. Even in the best designs, however, the nonhomogeneity of the fields is discernible at points away from the axis. This means that the electric and magnetic fields have small radial components. The radial component of the electric field deflects the electrons in the radial direction, producing distortion. In addition, the radial motion of electrons in the magnetic field and the presence of the radial magnetic field component produce image rotation that, in general, is not constant for all image points along a radial line. Characteristically, therefore, a radial line is imaged with spiral distortion, as shown in figure 4.4.

4.4   Astigmatism and Curvature of Field

Astigmatism and curvature of field are off-axial aberrations. Astigmatism causes the tangential and sagittal rays of an off-axial point to converge at two different axial distances. Curvature of field, on the other hand, causes the image of a plane perpendicular to the optical axis to lie on a curved surface. Figure 4.11 shows the astigmatic image off an off-axial point. In this figure the tangential and sagittal rays reconstruct the image of Q at
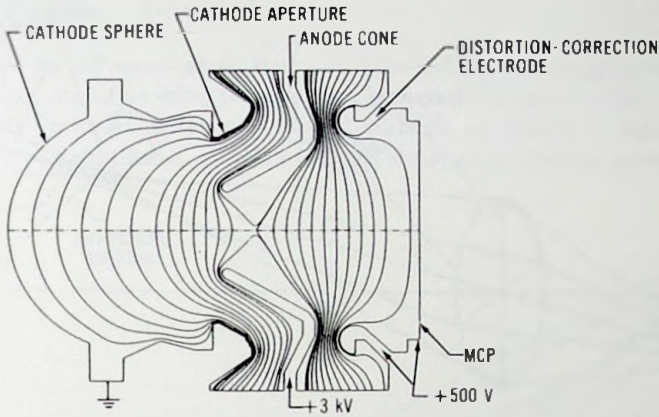
(A) **Equipotential plot.**

(B) **Trajectory plot—image conversion tube CMK.**
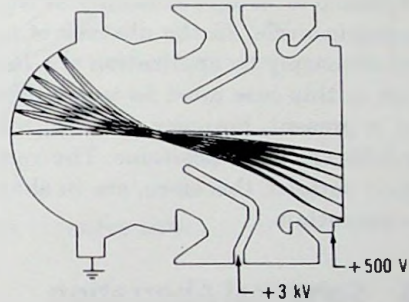
Fig. 4.10   Equipotential plot and electron trajectories of a distortion corrected electrostatic image-inverting electron optic.

the tangential and sagittal surfaces, respectively. The tangential and sagittal surfaces are approximate paraboloids of revolution.

Astigmatism and curvature of field problems are minimal in image tubes whose design is based on centrally symmetric principles. Yet both astigmatism and curvature of field are a limiting factor for edge resolution of image tubes designed with a flat image surface (phosphor screen or microchannel plate) and in tubes whose cathode or screen radius deviates from the radius required by the central symmetry. Image tubes designed prior to the development of fiber-optic plates were often made for existing glass optical systems requiring greater cathode and screen radius than the electron optically optimum curvatures. In such tubes the cathode image lies on a curved sur-
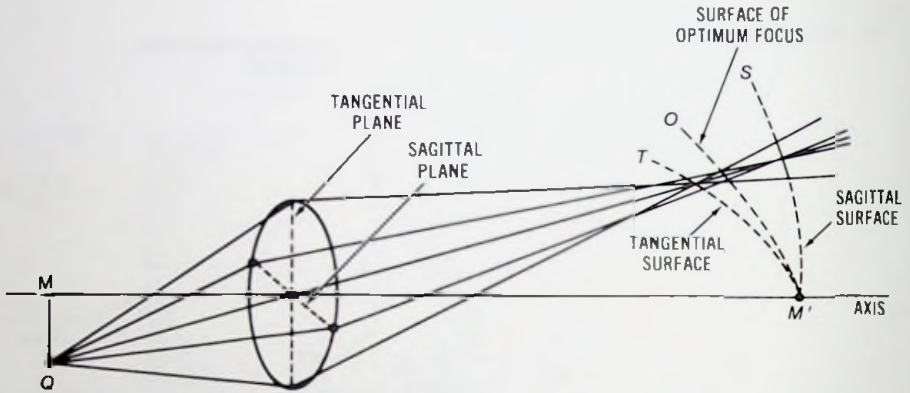
Fig. 4.11   Astigmatic image of an off-axial point Q.

face. Sharp focusing exists only at the center of the phosphor screen or on a concentric circle. In the absence of astigmatism an off-axial point may be focused sharply by application of a focusing voltage to the cathode aperture which in this case must be isolated from the photocathode. When astigmatism is present, however, the tangential and the sagittal rays converge at two different axial positions. The vertical and the horizontal lines of a resolution pattern, therefore, are in sharp focus at two different cathode aperture potentials.

4.5   Spherical Aberration

Spherical aberration is an axial aberration that appears when a point lying on the axis is imaged. Spherical aberration causes the rays passing through the lens at different circular zones about the axis to focus at different axial distances, as shown in figure 4.12. In image tubes the diameter of the electron beam of a cathode point is sufficiently small at operational voltages and therefore spherical aberration is not a problem.
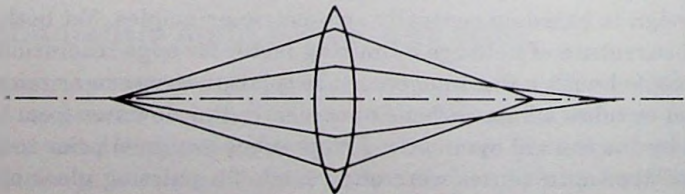
Fig. 4.12   Spherical aberration.

4.6   Coma

Coma is an off-axial aberration. It causes the rays originating from an off-axial point and passing through the lens at different circular zones about the axis to focus at different radial distances, as shown in figure 4.13. In figure 4.13A an off-axial point is imaged through a circular zone. The point
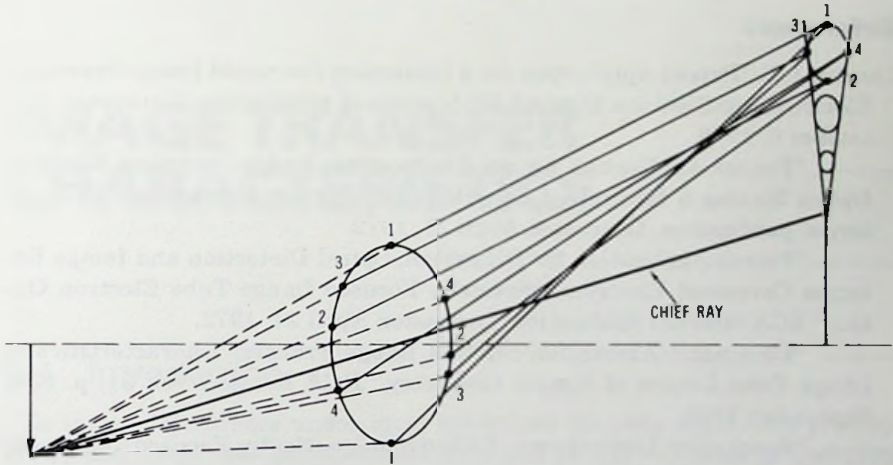
(A)   Off-axial point imaged through circular zone.
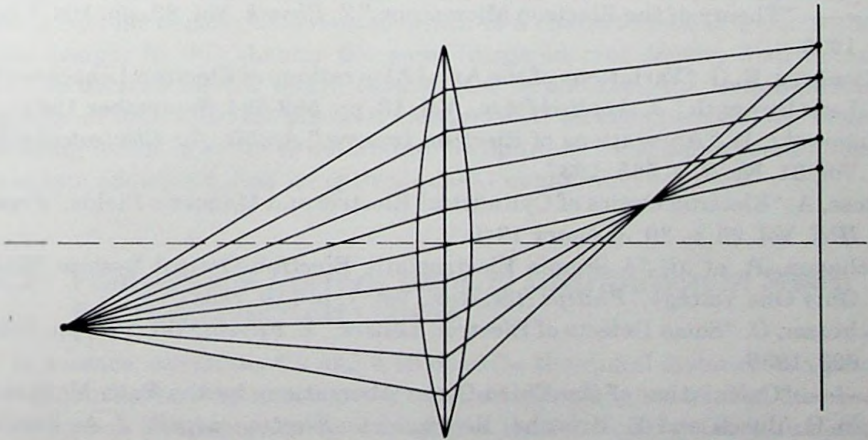
(B)   Off-axial point imaged by rays in plane of paper.

Fig. 4.13   Coma.

image lies on a comatic circle. Circular zones with radii smaller than indicated in figure 4.3A image the point on smaller comatic circles lying between the graphically obtained circle and the chief ray. Thus the point image has a cometlike shape. In figure 14.3B an off-axial point is imaged by rays lying in the plane of the page. The image lies on a line.

In image tubes the diameter of the electron beam of a cathode point is sufficiently small and therefore coma is not a problem.

References

Csorba, I. P. "Patent Application for a Distortion Corrected Image-Inverting Electrostatic Electron Optics," RCA internal publication, Lancaster, December 6, 1968.

————. "Patent Application for an Electrostatic Image-Inverting Electron Optics Having a Minimized Length and Distortion Correction," RCA internal publication, Lancaster, April 24, 1972.

————. "Patent Application for Distortion, Spiral Distortion and Image Rotation Corrected Electromagnetically Focused Image Tube Electron Optics," RCA internal publication, Lancaster, April 24, 1972.

————. "Chromatic-Aberration-Limited Image Transfer Characteristics of Image Tube Lenses of Simple Geometry," *RCA Review*, Vol. 31, p. 534, September 1970.

————. "Resolution Limitations of Electromagnetically Focused Image Intensifier Tubes," *RCA Review*, Vol. 30, pp. 36-52, March 1969.

Glaser, W. "Chromatic Aberration of Electron Lenses," *Z. Physik*, Vol. 116, pp. 56-67, June 1940.

————. "Theory of the Electron Microscope," *Z. Physik*, Vol. 83, pp. 104, 122, 1933.

Ramberg, E. G. "Variations of the Axial Aberrations of Electron Lenses with Lens Strength," *J. Applied Phys.*, Vol. 13, pp. 582-594, September 1942.

Rogowski, W. "Aberrations of Electron Images," *Archiv. für Electrotechnik*, Vol. 31, No. 9, p. 555, 1937.

Rose, A. "Electron Optics of Cylindrical Electric and Magnetic Fields," *Proc. IRE*, Vol. 28, p. 30, January 1940.

Schagen, P., et al. "A Simple Electrostatic Electron-Optical System With Only One Voltage," *Philips Res. Rev.*, Vol. 7, p. 119, 1952.

Scherzer, O. "Some Defects of Electron Lenses," *Z. Physik*, Vol. 101, pp. 593-603, 1936.

————. "Calculation of the Third-Order Aberrations by the Path Method," in H. Busch and E. Brueche, *Beitrage zur Electronenoptik*, J. A. Barth, Leipzig, pp. 33-41, 1937.

Zworykin, V. K., et al. *Electron Optics and the Electron Microscope*, John Wiley & Sons, Inc., New York, 1945.

5

IMAGE TRANSFER CHARACTERISTICS

5.1 Introduction

In image tube lenses under ideal conditions the only aberration present is the chromatic aberration, which is caused by the variation of emission energy of photoelectrons. Because of the variation of emission energy the image of a point at the photocathode is a small spot at the plane of the phosphor screen. The small image spot, hereafter called the *point image*, has a current density distribution which is a characteristic of a particular lens design. In this chapter the point-image current density distribution will be derived for the image tube lenses. In addition, the image-current density of disk and line electron emitters will be computed for the sharp focusing lenses in order to determine the optimum focal plane position and to obtain additional data for optical quality evaluation.

5.2 Point-Image Current Density Distribution of Sharp Focusing Electron Lenses

In essence, equations 4.8 and 4.10 describe the radial distance in a point image where the electrons emitted at an emission angle θ land at the phosphor screen. The image-current density is then derived by the assumption that ΔA is an infinitesimal element of area A on the surface of the photocathode. It is further assumed that a monoenergetic emission of electrons is produced from ΔA with an angular distribution obeying Lambert's law.

67

Based on these assumptions, the incremental current di_θ emitted between angles θ and $\theta + d\theta$ from ΔA is given by

$$di_\theta = 2I\Delta A \sin\theta \cos\theta \, d\theta, \tag{5.1}$$

where I is the emission-current density.

The incremental current di_θ strikes the phosphor screen over an annular element having a radius Δr. The current density j in this annular element may be obtained by division of di_θ by the area of the annular element, as follows:

$$j = \frac{I\Delta A \sin\theta \cos\theta \, d\theta}{\pi \Delta r d(\Delta r)}, \tag{5.2}$$

where $d(\Delta r)$ is the width of the annular element.

In the Gaussian image plane the focusing error Δr is given by equation 4.12. Differentiation of equation 4.12 leads to the following equation:

$$\frac{d(\Delta r)}{d\theta} = (2MV_i/E_c) \cos 2\theta. \tag{5.3}$$

By combination of equations 5.2, 5.3, and 4.12 the point-image current density becomes

$$j = \frac{I\Delta A}{4\pi\Delta r_m} \frac{1}{\sqrt{\Delta r_m^2 - \Delta r^2}}, \tag{5.4}$$

where Δr_m is the maximum value of the focusing error:

$$\Delta r_m = MV_i/E_c. \tag{5.5}$$

For a V_{af} axial emission energy image plane the transverse focusing error is given by equation 4.15. The point-image current density for this case can be obtained by a similar process as shown above leading to the following equation:

$$j = \frac{\Delta A \, I}{4\pi M^2 V_i} \frac{E_z^2 \sqrt{V_a}}{(\sqrt{V_{af}} - \sqrt{V_a})(\sqrt{V_{af} V_a} - \sqrt{V_i^2 - 4V_a(V_i - V_a)})}, \tag{5.6}$$

where V_a is the axial emission energy.

5.3 Image-Current Density Distribution of a Disk of Uniform Emission Current

For an extended Lambertian emitter at the cathode the current density distribution in the plane of the phosphor screen may be obtained by integration of j over the extended current-emitting surface. Therefore the image-

$$\beta = \cos^{-1}\left(\frac{\Delta r^2 + R^2 - r_0^2}{2R\Delta r}\right)$$

$$\Delta r = 2\frac{V_l}{E_c}(\cos\theta_l - \cos\theta)\sin\theta$$

$$dA = \Delta r\, d(\Delta r)\, d\phi$$
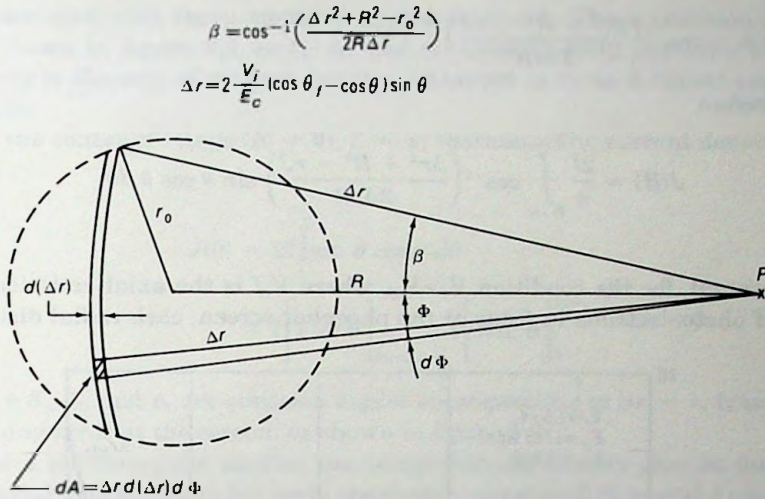
Fig. 5.1 Projection of a circular object on the plane of the phosphor screen (point P is at a radial distance R from the center of the disk).

current density distribution of a sine-wave resolution pattern and from that the modulation transfer function (MTF) of an electron lens may be derived by integration of equation 5.2 over the resolution pattern.

The computation is straightforward for a biplanar lens. However, for the electromagnetic or the two concentric-sphere type lenses, it is more complicated to find the optimum image plane where the MTF has a maximum value. The computation of the MTF for these lenses may be simplified by calculation of the image-current density distribution of disks of uniform emission current and then by transformation of these data into MTF. Figure 5.1 shows the geometrical outline for derivation of the image-current density distribution of a disk having a uniform emission current. By use of the notations in figure 5.1 the image-current density $J(R)$ at point P of the phosphor screen may be written

$$J(R) = \int_A \frac{I\sin\theta\cos\theta\,d\theta}{\pi\Delta r\,d(\Delta r)}\,dA$$

$$= \int_{R-r_0}^{R+r_0}\int_{\phi=-\beta}^{+\beta} \frac{I\sin\theta\cos\theta\,d\theta\,\Delta r\,d(\Delta r)\,d\phi}{\pi\Delta r\,d(\Delta r)}$$

$$= \frac{2I}{\pi}\int_{R-r_0}^{R+r_0} \beta\sin\theta\cos\theta\,d\theta, \tag{5.7}$$

where $\beta = \cos^{-1}\left(\dfrac{\Delta r^2 + R^2 - r_o^2}{2\Delta rR}\right)$.

Therefore

$$J(R) = \frac{2I}{\pi} \int\limits_{R-r_0}^{R+r_0} \cos^{-1}\left(\frac{\Delta r^2 + R^2 - r_o^2}{2\Delta rR}\right) \sin\theta\cos\theta\,d\theta. \tag{5.8}$$

In general, for the condition $V_i > V_{af}$, where $V_{a}f$ is the axial emission energy of photoelectrons in focus at the phosphor screen, each radial distance
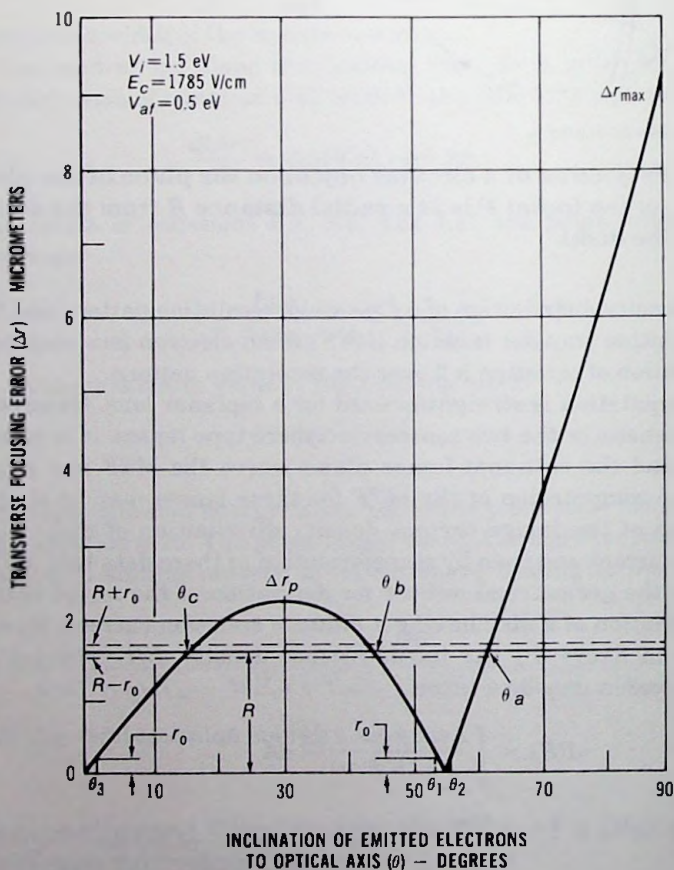
Fig. 5.2 Transverse focusing error as a function of the emission angle.

is associated with three emission angles up to Δr_p. These emission angles are shown in figure 5.2 as θ_a, θ_b, and θ_c. Consequently, the total current density is the sum of current densities obtained at three different emission angles.

In the center of image ($R = 0$), $\beta = \pi$; therefore, the current density $J(0)$ is

$$J(0) = 2I \int_0^{r_a} \sin \theta \cos \theta \, d\theta$$

$$= I \left[\sin^2 \theta \right]_{\theta_1(r_a)}^{\theta_2(r_a)} + I \left[\sin^2 \theta \right]_0^{\theta_3(r_a)}, \quad (5.9)$$

where θ_1, θ_2, and θ_3 are emission angles corresponding to $\Delta r = r_a$ transverse focusing error at the screen, as shown in figure 5.2.

For a polyenergetic emitter the image-current density may be found by integration of equation 5.8 (or in the center, equation 5.9) over the emission-energy distribution curve.

5.4 Calculation of Image-Current Density of Disk and Line Electron Emitters

In the following calculations it is assumed that the electron source has an emission-energy distribution with a maximum emission energy of $eV_{im} = 2$ eV. The fraction dN of electrons emitted in a voltage interval $d(V_i/V_{im})$ is then

$$dN = \frac{\pi^2}{2(\pi - 2)} \frac{V_i}{V_{im}} \cos \left(\frac{\pi}{2} \frac{V_i}{V_{im}} \right) d\left(\frac{V_i}{V_{im}} \right). \quad (5.10)$$

The distribution given by this equation is a normalized energy distribution similar to that measured by typical photocathodes. The focusing conditions are adjusted to yield a maximum peak current density in the image of a small disk.

The image plane where the maximum current density occurs may be found by successive placement of the phosphor screen in the image planes of various axial-emission energy groups and by calculation of the sum of current densities at each plane produced by the different monoenergetic groups, as described next.

For very small disks the $\sin \theta \cos \theta$ product in equation 5.9 is nearly constant between the emission angles θ_1 and θ_2 that correspond to a transverse displacement r_a at the phosphor screen. Therefore this product may be brought outside of the integral. In addition, if the second term of equation

5.9 (which provides only a minor contribution to the image-current density at $\theta_f = 0$) is omitted, the image-center current density becomes

$$J(0) = 2I \sin \theta_f \cos \theta_f \int_0^{r_a} d\theta = I \sin 2\theta_f (\theta_2 - \theta_1)$$

$$= 2I \sqrt{\frac{V_{af}}{V_i}} \sqrt{1 - \frac{V_{af}}{V_i}} (\theta_2 - \theta_1). \tag{5.11}$$

The value of $\theta_2 - \theta_1$ may be obtained by calculation of the slope of the transverse-focusing-error curve at the point of θ equal to θ_f from equation 4.15:

$$\left[\frac{d(\Delta r)}{d\theta}\right]_{\theta=\theta_f} = \frac{2(V_i - V_{af})}{E} = \frac{2r_a}{\theta_2 - \theta_1}. \tag{5.12}$$

By combination of equations 5.11 and 5.12 the image-current density becomes

$$J(0) = \frac{2IEr_a}{V_i} \sqrt{\frac{V_{af}}{V_i - V_{af}}}. \tag{5.13}$$

For an emission-energy distribution given by equation 5.10 the image-center current density is

$$J'(0) = \int_{V_{af}/V_{im}}^1 \frac{2I'Er_a}{V_i} \sqrt{\frac{V_{af}}{V_i + V_{af}}} dN$$

$$= \frac{2\pi^2 I'r_a}{\pi - 2} \frac{E}{V_{im}} \sqrt{\frac{V_{af}}{V_{im}}} \left[\cos\left(\frac{\pi}{2}\frac{V_{af}}{V_{im}}\right) C\left(\sqrt{1 - \frac{V_{af}}{V_{im}}}\right) \right.$$

$$\left. - \sin\left(\frac{\pi}{2}\frac{V_{af}}{V_{im}}\right) S\left(\sqrt{1 - \frac{V_{af}}{V_{im}}}\right) \right], \tag{5.14}$$

where C and S are the familiar Fresnel integrals and I' is the emission current density of the polyenergetic electron emitter. Figure 5.3 shows the plot of equation 5.14.

Figure 5.3 shows the image-current density as a function of the axial emission energy, V_{af}, that produces a sharp focus at the phosphor screen. In figure 5.3 a maximum occurs in the image plane of 0.5-V axial-emission-energy electrons. In the remaining discussion, therefore, the phosphor screen is assumed to be in the image plane of 0.5-V axial-emission-energy electrons.

By use of equations 5.8 and 5.9 and the above assumed emission-energy
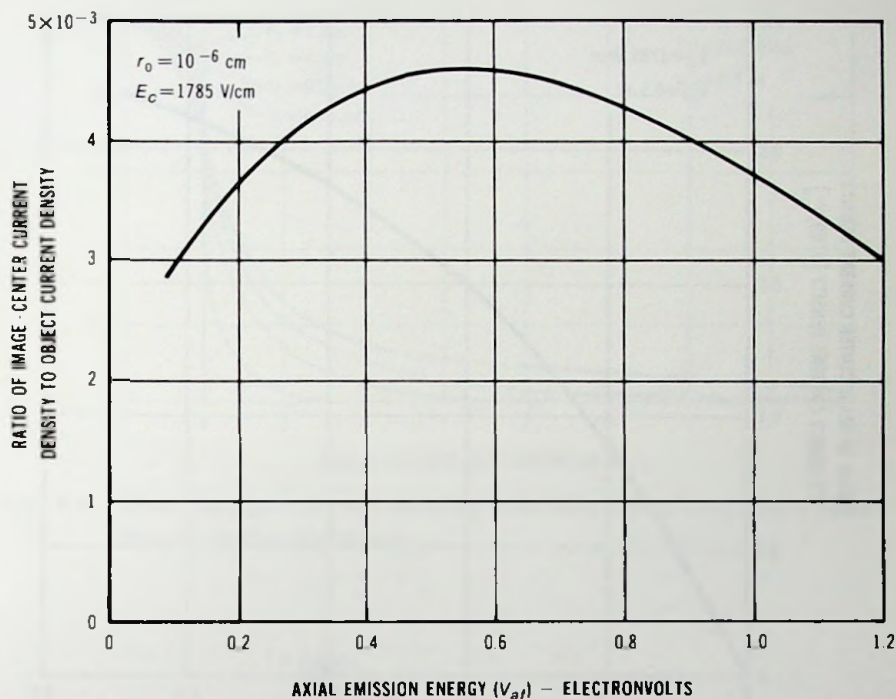
Fig. 5.3   Ratio of image-center current density to object current
            density of a disk as a function of axial emission energy of
            electrons in sharp focus at the phosphor screen.

distribution, the image-current density was calculated for disks of uniform
emission current. Figures 5.4 and 5.5 show the results of the calculation,
where $J'(R)$ and $J'(0)$ designate the image-current density at the radial
distance R and in the center, respectively.

For transformation of the image-current density distribution of disks into
MTF it is necessary to form a line image. By movement of a disk of uniform
emission current along a straight line in the object plane, a line may be
formed with an elliptic emission-current density distribution in the cross
section of the line. The image of this line may be generated by division of
the image of the stationary disk into disk sections of uniform image current,
as shown in figure 5.6, and, as in the object plane, by transformation of
these disk sections into lines with elliptic current-density distribution.

The line image is obtained by a summation of the current density pro-
duced by the individual disk segments. However, the current density of each

Fig. 5.5 **Zonal image-current density distribution of disks as a function of radial distance.**

Fig. 5.6 **Zonal image-current density distribution of a disk as a function of radial distance.**
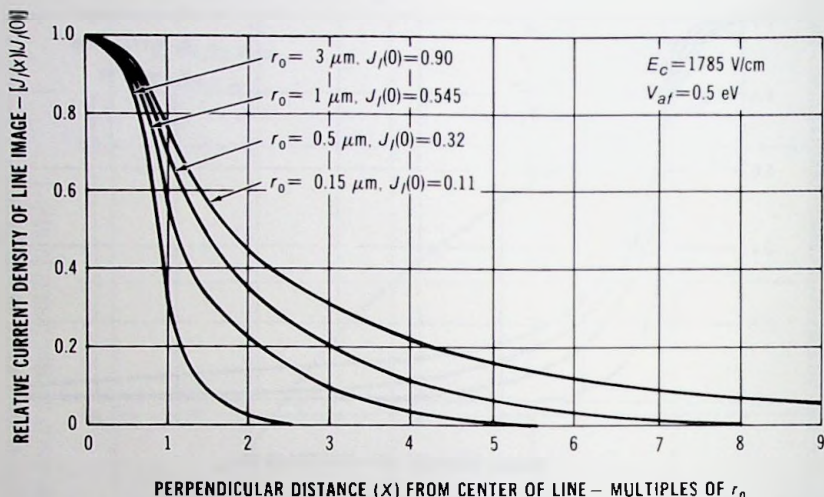
Fig. 5.7   Current density distribution in the cross section of the image of a line having eliptical emission current-density distribution and width $2r_o$.

The value of $d(\Delta r)$ in equation 5.15 was obtained by differentiation of equation 3.5.

In the case of a polyenergetic electron emitter having an emission-energy distribution described by equation 5.10, the incremental image-current density dJ is as follows:

$$dJ = jdN = \frac{\pi\Delta AI'}{8(\pi - 2)L^2}\frac{V_s}{V_{im}}\cos\left(\frac{\pi V_i}{2V_{im}}\right)d\left(\frac{V_i}{V_{im}}\right), \tag{5.16}$$

where I' is the emission-current density of the polyenergetic electron emitter. The point-image current density distribution $J(\Delta r)$ is given by

$$J(\Delta r) = \int_{V_i}^{V_{im}} \frac{\pi\Delta AI'}{8(\pi - 2)L^2}\frac{V_s}{V_{im}}\cos\left(\frac{\pi V_i}{2V_{im}}\right)d\left(\frac{V_i}{V_{im}}\right)$$

$$= \frac{\Delta AI'}{4(\pi - 2)L^2}\frac{V_s}{V_{im}}\left[1 - \sin\left(\frac{\pi}{2}\frac{V_i}{V_{im}}\right)\right]. \tag{5.17}$$

In the center of the point image the current density is

$$J(0) = \int_0^{V_{im}} dJ = \frac{\Delta AI'}{4(\pi - 2)L^2}\frac{V_s}{V_{im}}. \tag{5.18}$$

The relative image-current density distribution of the point image is then

$$\frac{J(\Delta r)}{J(0)} = 1 - \sin\left(\frac{\pi}{2}\frac{V_i}{V_{im}}\right). \tag{5.19}$$

In this equation $\Delta r = 2L\sqrt{V_i/V_s}$. Equation 5.19 then may be expressed in terms of Δr as

$$\frac{J(\Delta r)}{J(0)} = 1 - \sin\left(\frac{\pi}{8}\frac{V_s}{V_{im}}\frac{\Delta r^2}{L^2}\right). \tag{5.20}$$

The Maxwellian emission-energy distribution is another distribution frequently in use, and it is given by the following equation:

$$dN = \left(\frac{V}{\epsilon}\right)\exp\left[-\left(\frac{V}{\epsilon}\right)\right]d\left(\frac{V}{\epsilon}\right), \tag{5.21}$$

where ϵ is the voltage equivalent of the most probable emission energy.

For a Maxwellian emission energy distribution the incremental image-current density is

$$dJ = JdN = \frac{I\Delta A V_s}{4\pi L^2\epsilon}\exp\left[-\left(\frac{V}{\epsilon}\right)\right]d\left(\frac{V}{\epsilon}\right). \tag{5.22}$$

The point-image current density distribution is

$$J(\Delta r) = \int_V^\infty dJ = \frac{I\Delta A V_s}{4\pi L^2\epsilon}\exp\left[-\left(\frac{V}{\epsilon}\right)\right]. \tag{5.23}$$

In the center of point image the current density is

$$J(0) = \int_0^\infty dJ = I\Delta A V_s/4\pi L^2\epsilon. \tag{5.24}$$

The relative image-current density distribution is

$$J(\Delta r)/J(0) = \exp\left(-V/\epsilon\right). \tag{5.25}$$

The focusing error Δr is

$$\Delta r = 2L(V/V_s)^{1/2}. \tag{5.26}$$

By combination of equations 5.25 and 5.26 the relative image-current density becomes

$$\frac{J(\Delta r)}{J(0)} = \exp\left[-\frac{1}{4}\frac{V_s}{\epsilon}\left(\frac{\Delta r}{L}\right)^2\right]. \tag{5.27}$$

After normalization of equation 5.27, the normalized point spread function $j\Delta r$ becomes

$$j(\Delta r) = \frac{V_a}{4\pi L^2 \epsilon} \exp\left[-\frac{V_a}{4\epsilon}\left(\frac{\Delta r}{L}\right)^2 \right] = \frac{1}{\pi\rho^2}\exp\left[-\left(\frac{\Delta r}{\rho}\right)^2 \right]. \tag{5.28}$$

In the above equation the value of the focusing-error coefficient ρ is

$$\rho = 2L(\epsilon/V_a)^{1/2}, \tag{5.29}$$

To summarize, the image-current density distribution of a biplanar lens is unambiguously determined by the emission energy distribution, lens voltage and spacing and it is Gaussian for a Maxwellian emission energy distribution. In the case of sharp focusing lenses, however, the image-current density is a function of the axial emission energy of electrons in sharp focus at the phosphor screen. A maximum current density is obtained in the focal plane of $V_{af} = 0.25V_{im}$ axial-emission-energy electrons.

The point image is the elementary building block of imaging. Hence the faithfulness of imaging is determined by the diameter and the current density distribution of the point image.

References

Beurle, R. L., and W. M. Wreathall. "Aberration in Magnetic Focus Systems," *Advances in Electronics and Electron Devices*, Vol. XVI, p. 333, Academic Press, Inc., New York, 1962.

Csorba, I. P. "Chromatic-Aberration-Limited Image Transfer Characteristics of Image Tube Lenses of Simple Geometry," *RCA Review*, Vol. 31, p. 534, September 1970.

———. "Modulation Transfer Function Calculation of Electrostatic Electron Lenses," *RCA Review*, Vol. 33, p. 399, June 1972.

———. "Theoretical Studies of Factors Limiting the Resolution of Magnetically Focused Image Intensifier Tubes," *IEEE Winter General Meetings on Imaging and Counter Tubes*, New York, January 30, 1963.

Papp, G. "Limits of Resolution in Magnetically-Focused Image Converter Tubes," *IRE Transactions on Nuclear Science*, Vol. NS-9, p. 91, April 1962.

Wendt, G. "Sur Le Pouvoir Separateur Du Convertisseur D'Images A Champs Homogenes Electrostatique Et Magnetique," (Resolution of an Image Converter with Homogeneous Electric and Magnetic Fields), *Annales de Radioelectricite*, Vol. 10, p. 74, January 1955.

6

MTF OF IMAGE INTENSIFIER TUBES

6.1   Introduction

In an elementary approach, optical quality can be specified by the point or line image intensity distributions of optical systems. The energy spread of the point and line images is due to optical aberrations and the diffraction effect.

A more elaborate objective method for the assessment of imaging quality is specification by the modulation transfer function (MTF). With the MTF the resolution and contrast, the amount of perceivable detail, and the sharpness of the image are specified in the entire spatial frequency domain.

The MTF is the response of imaging systems to a variable spatial-frequency, constant-amplitude, sine-wave input. At a particular spatial frequency the MTF is defined by the following equation:

$$\text{MTF} = \frac{B_{max} - B_{min}}{B_{max} + B_{min}}, \tag{6.1}$$

where B_{max} and B_{min} are the maximum and minimum luminance values of the image of a sine-wave pattern, respectively, as shown in figure 6.1. In figure 6.1 the modulation M_o of the sine-wave input pattern is unity. If the modulation of the pattern is less than unity, the modulation transfer function of an imaging system is the ratio of the modulation in the image (M_i) to the modulation of the input pattern (M_o):

$$\text{MTF} = \frac{M_i}{M_o} = \frac{\text{modulation in image}}{\text{modulation in object}}. \tag{6.2}$$

$$\text{MTF} = \frac{B_{max} - B_{min}}{B_{max} + B_{min}}$$

(A) Input wave.   (B) Output wave.
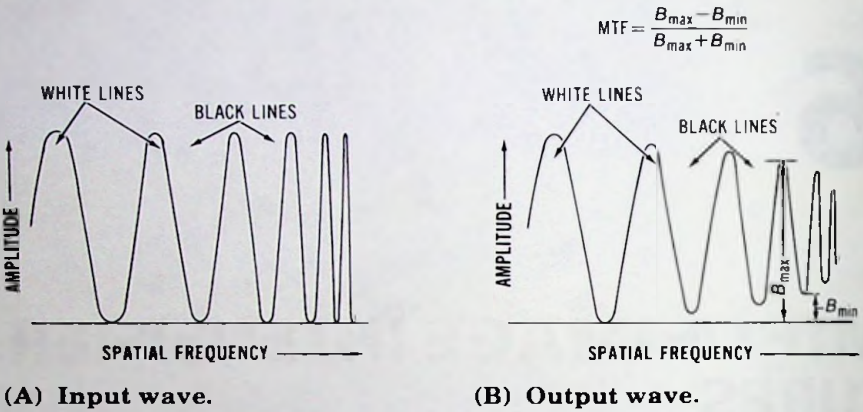
Fig. 6.1   Luminance variation of a sine-wave pattern at the input
and the output, respectively, of an optical system.

The limiting resolution is usually defined as the spatial frequency at which the modulation transfer function is 3%. Table 6.1 shows the limiting resolution for image tubes and image tube components.

One of the advantages of MTF, which has led to its widespread use for the specification of imaging quality, is that in the case of components in cascade, the total response (MTF) is the product of the response of the individual components.

Mathematically, the spatial frequency response can be derived from the image-current density or image brightness distribution of a sine-wave input pattern obtained by integration of the point or line spread functions over the sine-wave pattern. The results of such computation show that the spatial frequency response can be obtained from the point and line spread functions by a Fourier transform which gives the frequency spectrum of aperiodic functions. Accordingly, the optical transfer function (OTF) is the Fourier transform of the normalized point image (point spread function). For asymmetrical images the OTF is a complex function. The absolute value of OTF is the MTF which describes the transfer of contrast from the object to the image. The argument of the OTF is the spatial phase shift. The two-dimensional expression for the MTF is

$$\text{MTF} = \left| \frac{\int_{-\infty}^{\infty} \int_{-\infty}^{\infty} J(x,y) e^{-2\pi j (f_x x \,+\, f_y y)} \, dx \, dy}{\int_{-\infty}^{\infty} \int_{-\infty}^{\infty} J(x,y) \, dx \, dy} \right|, \tag{6.3}$$

where $J(x,y)$ is the point-image intensity distribution and f_x and f_y are the spatial frequency components in the x and y directions, respectively.

Table 6.1   Limiting Resolution of Image Intensifier Tubes and Image Tube Components

Image Tube or Component	Resolution (lp/mm)
magnetically focused single-stage module	80-120
magnetically focused two-stage tube	55-65
magnetically focused three-stage tube	32-45
generation 1 single-stage module	65-80
generation 1 three-stage module	25-36
ESI	28-36
generation 2 wafer tube	25-32
generation 3 wafer tube	28-40
wafer diode	45-65
phosphor screen	100-130
mica spacer (5 to 10 μm thick)	80-160
fiber-optic plate (6 μm diameter fiber)	100
fiber-optic twister plate (10 μm diameter fiber)	58
MCP (10-μm channel center to center spacing)	58
MCP (15-μm channel center to center spacing	40

The line-image intensity distribution $L(x)$ can be calculated from the point-image intensity distribution as shown in the next equation:

$$L(x) = \int_{-\infty}^{\infty} J(x,y)\, dy. \tag{6.4}$$

By combination of equations 6.3 and 6.4 and with substitution of $f_y = 0$ and $f_x = f$, the MTF expressed with the line-image intensity distribution becomes

$$\text{MTF} = \left| \frac{\int_{-\infty}^{\infty} L(x) e^{-2\pi j f x}\, dx}{\int_{-\infty}^{\infty} L(x)\, dx} \right|$$

$$= \left| A_1(f) - jA_2(f) \right|, \tag{6.5}$$

where in equation 6.5

$$A_1(f) = \frac{\int_{-\infty}^{\infty} L(x) \cos 2\pi f x\, dx}{\int_{-\infty}^{\infty} L(x)\, dx} \tag{6.6}$$

and

$$A_2(f) = \frac{\int_{-\infty}^{\infty} L(x) \sin 2\pi f x\, dx}{\int_{-\infty}^{\infty} L(x)\, dx}. \tag{6.7}$$

The spatial phase shift α, with which the pattern is shifted, is

$$\alpha = \tan^{-1}[A_2(f)/A_1(f)]. \tag{6.8}$$

For symmetric line images A_2 and α are zero.

For the evaluation of MTF, $L(x)$ can be obtained by direct measurement of the line-image intensity distribution or by derivation from the knife-edge response $E(x)$. The line image is the derivative of the edge response:

$$L(x) = \frac{dE(x)}{dx}. \tag{6.9}$$

An alternative method to MTF is specification of imaging quality by response to a variable spatial-frequency, high-contrast, square-wave input which gives the contrast transfer function (CTF). At a particular spatial frequency the CTF is defined by the following equation:

$$\text{CTF} = \frac{B_{max} - B_{min}}{B_{max} + B_{min}} \tag{6.10}$$

where B_{max} and B_{min} are the maximum and minimum luminance values of the image of a square-wave pattern as shown in figure 6.2.

The relationship between the sine-wave response $R(n)$ and square-wave response $r(n)$ may be obtained by Fourier analysis as shown in appendix B and is given below:

$$r(n) = \frac{4}{\pi}\left[R(n) - \frac{R(3n)}{3} + \frac{R(5n)}{5} - \frac{R(7n)}{7} + \frac{R(9n)}{9} - \cdots\right] \tag{6.11}$$

(A) Input wave.   (B) Output wave.
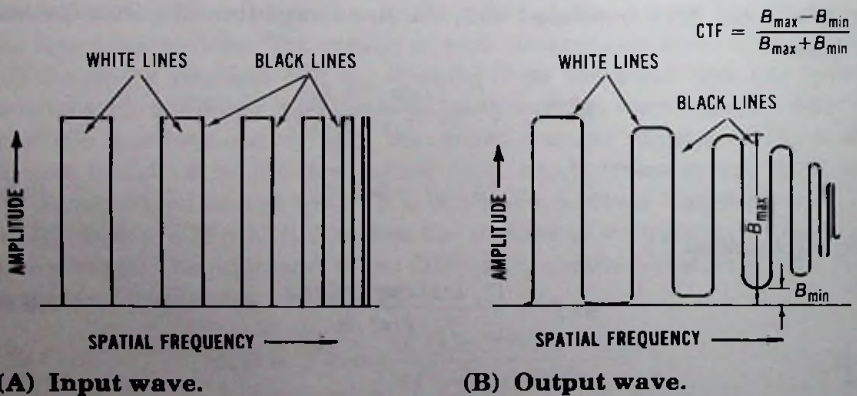
Fig. 6.2   Input and output waves of a square-wave pattern transmitted through an optical element.

or

$$R(n) = \frac{\pi}{4}\left[r(n) + \frac{r(3n)}{3} - \frac{r(5n)}{5} + \frac{r(7n)}{7} \right.$$
$$\left. - \frac{r(9n)}{9} + \frac{r(11n)}{11} - \frac{r(13n)}{13} + \frac{r(15n)}{15} \right], \qquad (6.12)$$

where n is the spatial frequency.

When the sine-wave response of an optical element is known, the square-wave response may be obtained by use of equation 6.11. Conversely, from equation 6.12, the sine-wave response may be calculated.

6.2 MTF of Image Tube Lenses

6.2.1 MTF of a Biplanar Lens

For a Maxwellian emission energy distribution given by equation 5.21, the MTF of the biplanar lens is the Fourier transform of the normalized point spread function given by equation 5.28. By changing to new variables satisfying the following equations

$$\Delta r^2 = x^2 + y^2 \qquad (6.13)$$

and

$$a^2 = V_s/2\epsilon L^2, \qquad (6.14)$$

the point spread function becomes

$$j(x,y) = \frac{a^2}{2\pi} e^{-a^2(x^2 + y^2)/2}. \qquad (6.15)$$

The point spread function has a Gaussian distribution which has a Fourier transform given by the following equation:

$$\text{MTF} = \frac{a^2}{2\pi} \int e^{-a^2 y^2/2} e^{-j2\pi f_y y} \, dy \int e^{-a^2 x^2/2} e^{-j2\pi f_x x} \, dx$$
$$= e^{-\omega_y^2 + \omega_x^2/2a^2} = e^{-\omega^2/2a^2}$$
$$= e^{-4\pi^2 \epsilon L^2 f^2/V_s}. \qquad (6.16)$$

The resolution at 3% response from equation 6.16 is

$$R = 0.3 \frac{1}{L} \left(\frac{V_s}{\epsilon} \right)^{1/2}. \qquad (6.17)$$

In the above equations, L is in millimeters, and f and R are in cycles per millimeter. For example, in a typical proximity focused diode, $L = 1.5$ mm,

$\epsilon = 0.1$ V, $V_s = 10\ 000$ V, yielding an MTF value of 70% at $f = 20$ line pairs per millimeter.

For a cosine energy distribution given by equation 5.10 the square-wave response may be obtained by integration of the point image distribution $J(\Delta r)$ over the square-wave resolution pattern.

Figure 6.3 may be used to derive the image-current density distribution of a line pattern at the photocathode with uniform emission current in the white lines. The figure is indicative for the calculation of image-current density in the center of a white line, where Δr_m is the maximum value of

$$dA = 2\Delta r \cos^{-1}\left(\frac{3W}{2\Delta r}\right)d\,(\Delta r) \qquad\qquad dA = 2\Delta r \cos^{-1}\left(\frac{W}{2\Delta r}\right)d\,(\Delta r)$$
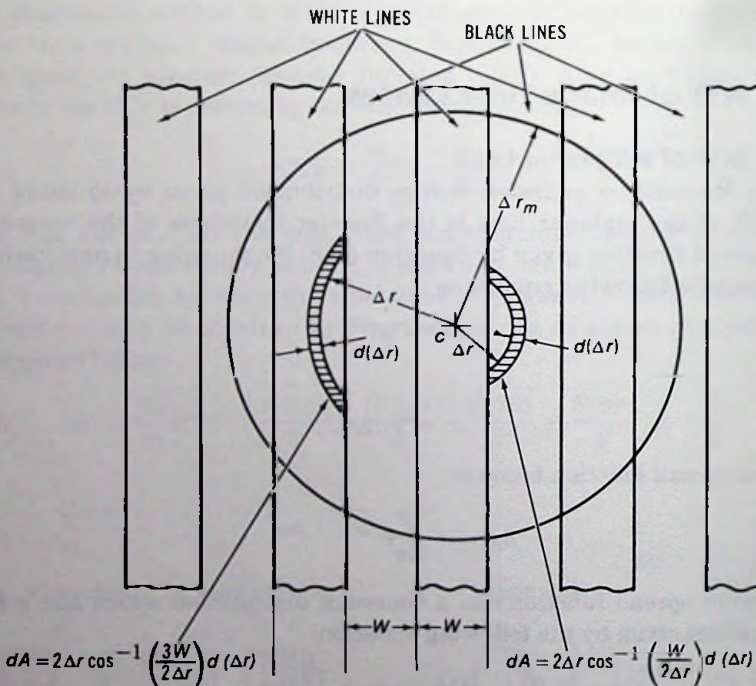
Fig. 6.3   Schematic diagram for deriving the image-current density distribution of a line pattern at the photocathode with uniform emission current in the white lines.

transverse focusing error. Thus the image-current density i_w in the center of a white line is

$$i_w = I' - 4\int_{w/2}^{\Delta r_m} J(\Delta r)\Delta r \cos^{-1}\frac{w}{2\Delta r}\,d(\Delta r) + 4\int_{3/2w}^{\Delta r_m} J(\Delta r)\Delta r \cos^{-1}\frac{3w}{2\Delta r}\,d(\Delta r). \quad (6.18)$$

The image-current density i_b in the center of a black line is expressed as

$$i_b = 4 \int_{w/2}^{\Delta r_m} J(\Delta r)\Delta r \cos^{-1} \frac{w}{2\Delta r} \, d(\Delta r) - 4 \int_{3/2w}^{\Delta r_m} J(\Delta r)\Delta r \cos^{-1} \frac{3w}{2\Delta r} \, d(\Delta r). \quad (6.19)$$

The square-wave response C is, then,

$$C = \frac{i_w - i_b}{i_w + i_b} = 1 - 8/I' \int_{w/2}^{\Delta r_m} J(\Delta r)\Delta r \cos^{-1} \frac{w}{2\Delta r} \, d(\Delta r)$$

$$+ 8/I' \int_{3w/2}^{\Delta r_m} J(\Delta r)\Delta r \cos^{-1} \frac{3w}{2\Delta r} \, d(\Delta r). \quad (6.20)$$

Figure 6.4 shows the calculated square-wave response curve for conditions of screen-to-cathode separation of $L = 1$ mm, screen voltage $V_s = 10\,000$ volts, and maximum emission energy $V_{im} = 2$ V. For different values of screen-to-cathode separation, L', screen voltage V'_s and maximum emission energy V'_{im} the abscissa of figure 6.4 is multiplied by L/L', $\sqrt{V'_s/V_s}$ and $\sqrt{V_{im}/V'_{im}}$ respectively. With all these considerations figure 6.4 also reveals that the MTF (sine-wave response) of the biplanar lens may well be approximated by

$$\text{MTF} \cong \exp\left[-12(V_{im}/V_s)(nL)^2\right], \quad (6.21)$$

where L is given in millimeters and n is in cycles per millimeter.
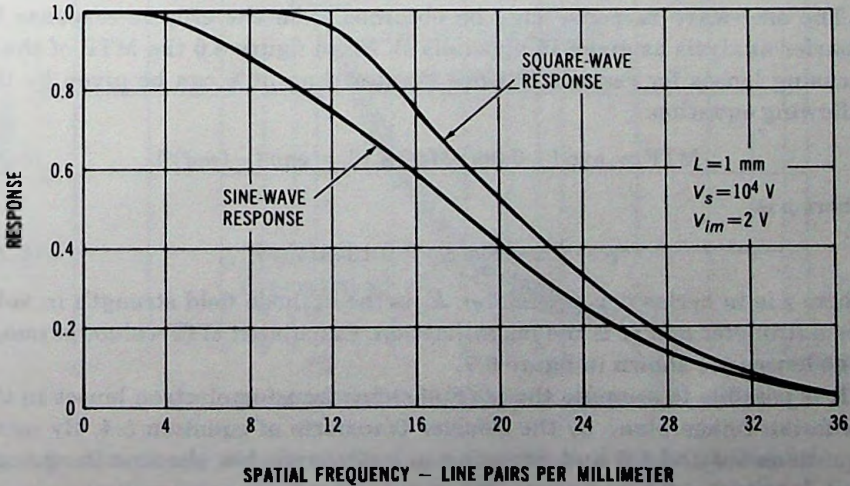
Fig. 6.4 Response curves of a biplanar electron lens.

The resolution at 3% response from equation 6.21 is

$$R = 0.4 \frac{1}{L}\left(\frac{V_s}{\epsilon}\right)^{1/2} = 0.54 \frac{1}{L}\left(\frac{V_s}{V_{im}}\right)^{1/2}. \tag{6.22}$$

In a typical proximity focused diode, $L = 1.5$ mm, $V_{im} = 0.3$ V, $V_s = 10\,000$ V, yielding $R = 65.7$ lp/mm resolution.

6.2.2   MTF of Sharp Focusing Electron Lenses

The sharp focusing electron lens group consists of the electrostatic image-inverting lens and the electromagnetic lens. The MTF of these lenses can be computed from the image-current density distributions of lines having an elliptical emission current density distribution as shown in figure 5.7.

An elliptic-wave pattern at the photocathode of an image tube may be generated by superimposition of alternating black and white lines of amplitude B_1 over a uniform illumination B_1 with the elliptical distribution of light in the cross section, as shown in figure 6.5. At each point of a line in the image plane the image-current density is jointly established by the image current of the particular line plus the current contributions of all neighboring lines that are within the circle of maximum transverse-focusing error. The elliptic-wave response r, therefore, is simply

$$r = \Delta B / B_2, \tag{6.23}$$

where ΔB is the amplitude of the wave pattern at the image plane. Figure 6.6 shows the calculated elliptic-wave response curve obtained by use of the line-image curves of figure 5.7.

The sine-wave response may be obtained from the elliptic response by Fourier analysis as given in appendix B. From figure 6.6 the MTF of sharp focusing lenses for response values greater than 30% can be given by the following equation:

$$\text{MTF} = \exp\left[-0.06(\pi M \epsilon f / E_c)^2\right] = \exp\left[-(\pi \rho f)^2\right], \tag{6.24}$$

where ρ is

$$\rho = 0.245 M \epsilon / E_c = 0.134 M V_m / E_c, \tag{6.25}$$

where f is in cycles per millimeter, E_c is the cathode field strength in volts per millimeter and M is the magnification. Calculated MTF values of image tube lenses are shown in figure 6.7.

It is possible to compute the MTF of sharp focusing electron lenses in the Gaussian image plane by the Fourier transform of equation 5.4. By using equations 5.4 and 5.5 and changing to a new variable, the line-image current density $j(x)$ for monoenergetic emission becomes

$$y = B_1 \left(1 + \sqrt{1 - \left(\frac{4x}{T} \right)^2} \right) : -\frac{T}{4} < x < \frac{T}{4}$$

$$y = B_1 \left(1 - \sqrt{1 - \left(\frac{4x}{T} - 2 \right)^2} \right) : \frac{T}{4} < x < \frac{3}{4}T$$
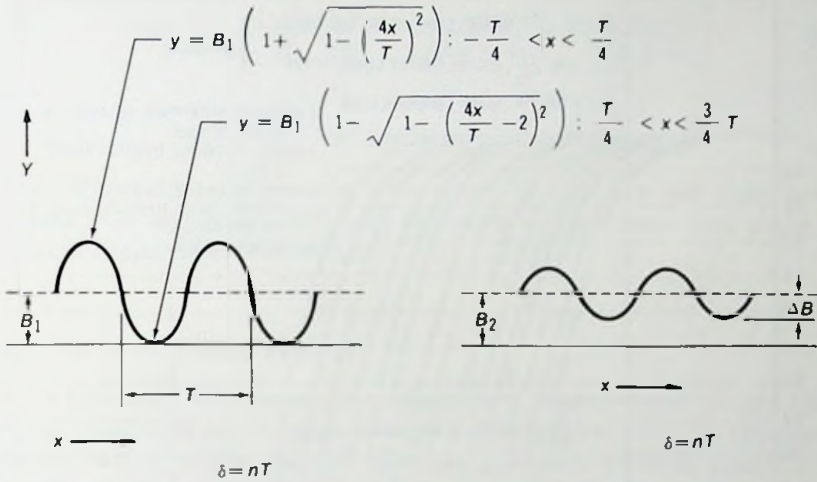
(A) Input wave.   (B) Output wave.

Fig. 6.5   Input and output waves of an elliptic-wave pattern.
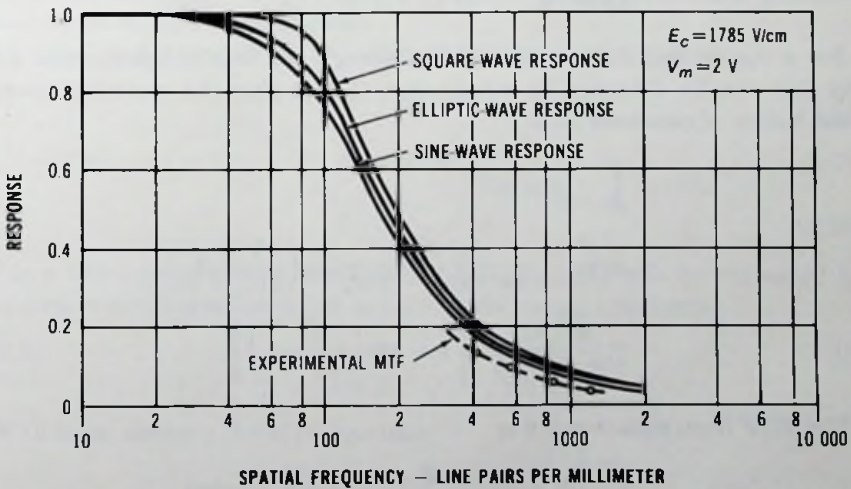
Fig. 6.6   Response curves of electromagnetic and two-concentric-
sphere type electron lenses.
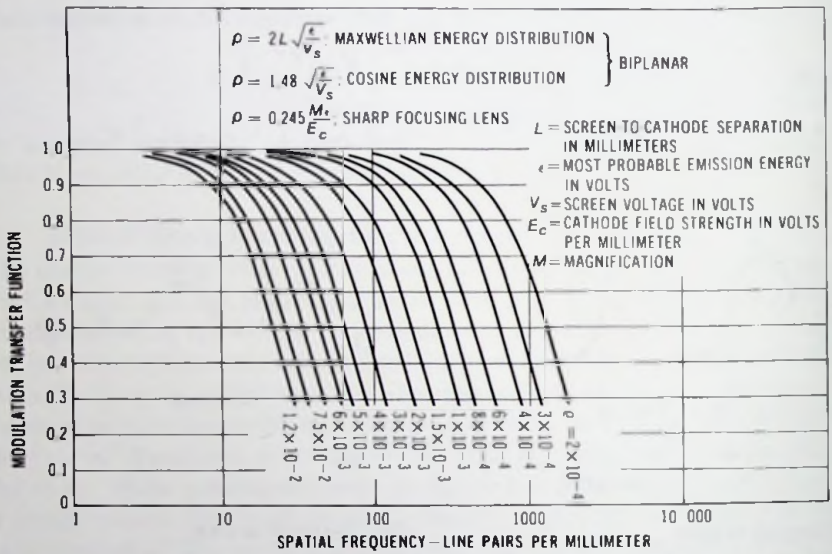
Fig. 6.7 Modulation transfer function of image tube lenses.

$$j_i(x) = dx \frac{2I}{4\pi\Delta r_m} \int_{y_0}^{\sqrt{\Delta r_m^2 - x^2}} \frac{1}{\sqrt{\Delta r_m^2 - x^2 - y^2}} \, dy = \frac{IE_c}{4MV_i} \, dx. \tag{6.26}$$

For a cosine distribution of emission energy, the line-image current density $J(x)$ can be obtained by integration of $j_i(x)$ over the emission energy distribution of equation 5.10:

$$J(x) = \int_{V_i/x V_m}^{1} j_i(x) \, dN$$

$$= dx \int_{V_i/x V_m}^{1} \frac{I\pi^2 E_c V_i}{4MV_i 2(\pi - 2)V_m} \cos\left(\frac{\pi V_i}{2V_m}\right) d\left(\frac{V_i}{V_m}\right)$$

$$= \frac{\pi E_c I dx}{4(\pi - 2)MV_m} \left[1 - \sin\left(\frac{\pi E_c}{2MV_m} x\right) \right]. \tag{6.27}$$

The MTF from equation 6.6 is

$$\text{MTF} = \frac{\displaystyle\int_0^{\Delta r_m} \left[1 - \sin\left(\frac{\pi E_c}{2MV_m} x\right) \right] \cos 2\pi n x \, dx}{\displaystyle\int_0^{\Delta r_m} \left[1 - \sin\left(\frac{\pi E_c}{2MV_m} x\right) \right] dx}$$

$$\text{MTF} = \frac{\pi}{\pi - 2}\left[\frac{\sin kn}{kn} + \frac{1 - \sin kn}{2kn - \pi} - \frac{1 + \sin kn}{2kn + \pi}\right], \qquad (6.28)$$

where

$$k = 2\pi M V_m / E_c. \qquad (6.29)$$

The MTF values computable from equation 6.28 are less than can be obtained from equation 6.24 which represent the optimum focal plane conditions as explained in section 5.4.

6.3 MTF of Fiber Plates

Round-channel fiber-optic (FO) plates and microchannel plates (MCP) have a cylindrical point-image intensity distribution with the cylinder diameter D equal to the channel diameter and with a radial shift r at the object plane. As a consequence of the radial shift there is an identical disk of confusion at the input with the disk of confusion at output of the channel. Now, the imaging errors at the input and output planes occur in the same imaging process. Therefore the diameters of the disk of confusion are additive and the total process approaches a $2D$ diameter cylindrical intensity distribution aperture process. The MTF of round-channel plates, therefore, can be approximated by taking the Fourier transform of a $2D$ diameter constant-intensity round aperture.

In equation 6.3 the variables satisfy the following equations:

$$x^2 + y^2 = r^2, \qquad (6.30)$$

$$f_x^2 + f_y^2 = f^2, \qquad (6.31)$$

$$f_x x + f_y y = rf. \qquad (6.32)$$

For a rotationally symmetrical point image the MTF can be expressed by changing to new variables which satisfy the following equations:

$$\begin{aligned} x = r\cos\theta, \quad & y = r\sin\theta, \\ f_x = f\cos\psi, \quad & f_y = f\sin\psi. \end{aligned} \qquad (6.33)$$

With these changes the MTF becomes

$$\text{MTF} = \left|\frac{\int_0^\infty \int_0^{2\pi} i(r)\, e^{-j2\pi fr\cos(\theta - \phi)}\, r\, dr\, d\theta}{\int_0^\infty \int_0^{2\pi} i(r)\, r\, dr\, d\theta}\right|$$

$$= \left|\frac{\int_0^\infty i(r)\,[\int_0^{2\pi} e^{-j2\pi fr\cos(\theta - \phi)}\, d\theta]\, r\, dr}{2\pi \int_0^\infty i(r)\, r\, dr}\right|$$

$$\text{MTF} = \left| \frac{\int_0^\infty i(r) \, J_0(2\pi fr) \, r \, dr}{\int_0^\infty i(r) \, r \, dr} \right|. \tag{6.34}$$

By use of equation 6.34 the MTF of fiber plates becomes

$$\text{MTF} = 2|J_1(2\pi fD)/2\pi fD|, \tag{6.35}$$

where J_1 is the first-order Bessel function.
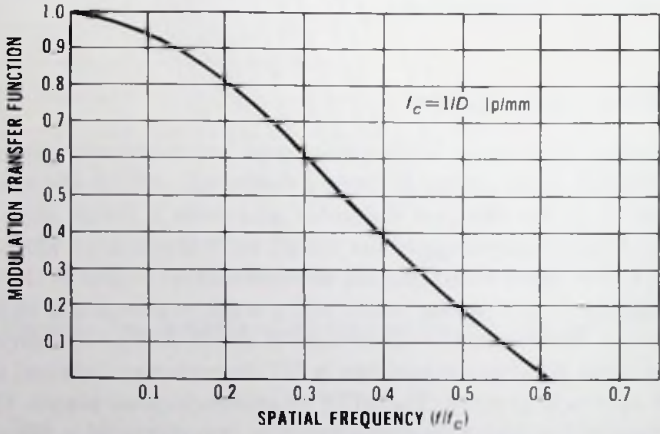
(A) MTF of round channel plate.
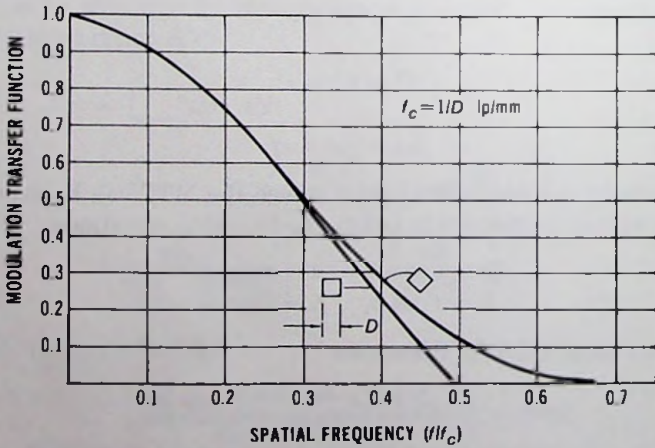
(B) MTF of square channel plate.

Fig. 6.8   Plots of equations 6.35 and 6.36
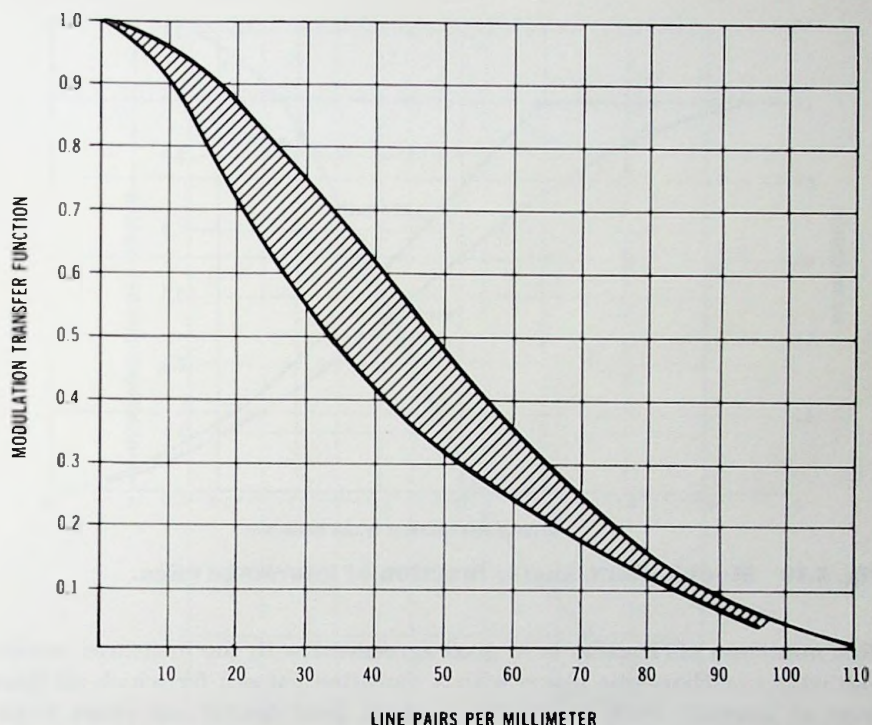
Fig. 6.9 Modulation transfer function spread of phosphor screens.

The MTF of square channels can be derived by the same analogy with the following end result:

$$\text{MTF} = |(\sin 2\pi fD)/2\pi fD|. \tag{6.36}$$

Plots of equations 6.35 and 6.36 are shown in figures 6.8A and 6.8B, respectively.

It should be pointed out that equation 6.35 represents the MTF of an ideally random spatial distribution of fibers. For a regular fiber-optic plate which has a line structure the apparent resolution and MTF is a function of the direction of the scan and orthogonal position. By alignment of the input sine-wave pattern with the line structure of the fiber-optic plate and shifting the pattern perpendicularly to the alignment, the MTF varies between a maximum and a minimum value as a function of position of the sine-wave pattern. When the sine-wave pattern is not aligned with the fiber-optic line structure smaller MTF maximums are obtained. Equation 6.35 corresponds to the minimum MTF values obtained by the above scanning experiment.
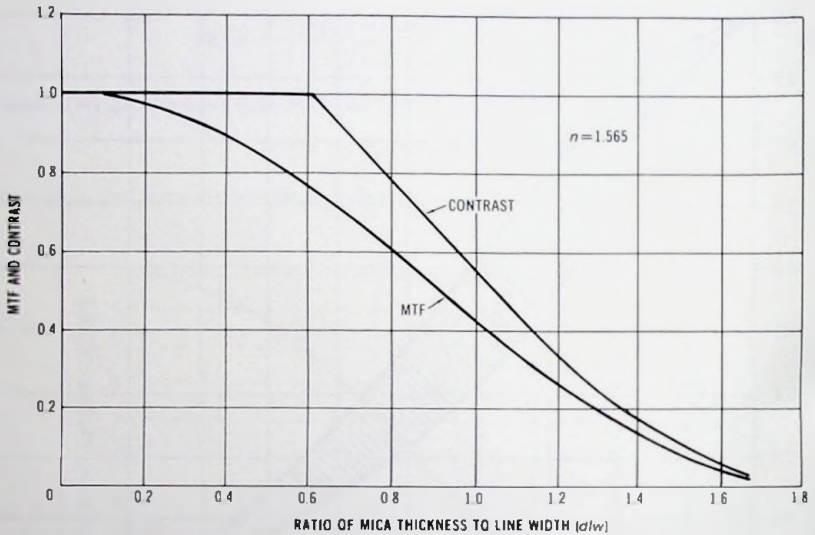
Fig. 6.10   Modulation transfer function of interstage mica.

This minimum MTF value is in good agreement with the measured resolution values of fiber-optic plates with a multiline pattern for which all lines must be resolved. With a multiline pattern, good spatial and phase alignment is possible only for a limited number of lines, giving a tendency to read a resolution corresponding to the minimum MTF value. For instance, the resolution of 6-μm fiber diameter fiber-optic plates is 100 lp/mm; the 10-μm plates have 58 lp/mm resolution and the 15-μm plates have 40 lp/mm measured resolution, in good agreement with equation 6.35.

6.4   MTF of Phosphor Screens

The resolution and MTF characteristics of a phosphor screen are determined by the thickness of the phosphor film and by the particle or aggregate size. When the phosphor screen is thicker than a monolayer it is often difficult to control the aggregate size. This may result in a considerable spread of the MTF of image tube screens. Figure 6.9 shows a typical MTF spread for image tube screens. A more detailed discussion of resolution is given in chapter 10.

6.5   MTF of the Mica-Coupled Image

In electromagnetically focused cascaded image intensifier tubes, 5-μm to 10-μm thick mica spacers are used as supports for the interstage phosphor
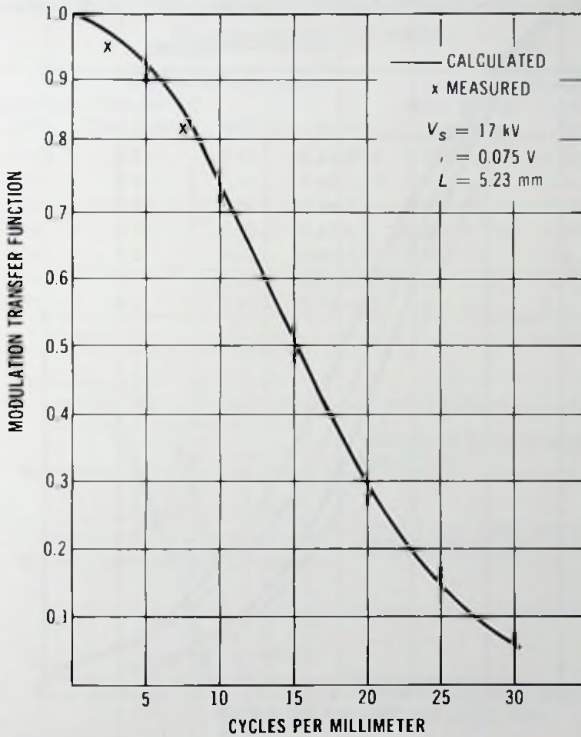
Fig. 6.11   Wafer tube response.

screens and photocathodes. The calculated MTF of the mica-coupled image is shown in figure 6.10. The exact value of the contrast transfer function is given by equation D.7 of appendix D. The MTF values from the CTF values were obtained by use of equation 6.12.

6.6   MTF of the Wafer Diode

The previously discussed theory is now applied to the proximity focused wafer diode, which consists of a glass faceplate input and a phosphored and aluminized fiber-optic output. The MTF of the wafer tube is the product of the sine-wave response of the fiber-optic screen and electron optic (EO). Figure 6.11 shows the calculated and measured response values of the wafer tube which had been obtained with a GaAs:Cs·O photocathode. The MTF of the electron optics was obtained by use of equation 6.21. The MTFs of the 6-μm fiber diameter fiber optics and phosphor screen were obtained from figure 6.8 and figure 6.9, respectively.
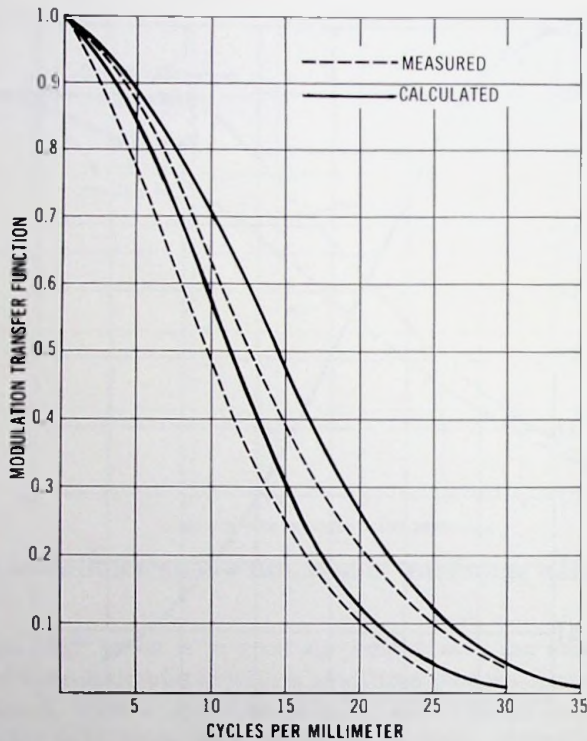
Fig. 6.12   Modulation transfer function of F4791 generation 2 wafer tube.

6.7   MTF of the Generation 2 Wafer Tube

The MTF of the generation 2 wafer tube is a product of the sine-wave response of the optical components of the wafer tube. The major components of the MTF are a 6-μm fiber diameter input fiber-optic, a 10-μm fiber diameter fiber-optic twister, and the electron optics of the input and output MCP spacings. The wafer tube response is shown in figure 6.12. Numerical values for component and tube response are shown in table 6.2.

For comparison, figure 6.13 shows the MTF of the other members of the low light level image-intensifier tube family. These include the electromagnetically focused cascaded image (generations 1 and 2), the electrostatic cascaded image tube (generation 1), and the generation 2 electrostatic image-inverting image tube (ESI).

Table 6.2   Response of Generation 2 Wafer Tube
Components for F4791

Cycles per Millimeter	Input Fiber Optic	Twister Fiber Optic	MCP	Screen	Electron-Optic Screen Spacing	Electron-Optic Cathode Spacing	Wafer Tube
2	0.995	0.99	0.99	0.99-0.98	0.996-0.995	0.995-0.99	0.956-0.94
6	0.99	0.97	0.96	0.98-0.95	0.973-0.953	0.985-0.96	0.86 -0.80
10	0.98	0.95	0.88	0.96-0.9	0.928-0.878	0.97 -0.9	0.70 -0.58
15	0.96	0.88	0.78	0.92-0.8	0.855-0.744	0.95 -0.8	0.49 -0.31
20	0.92	0.8	0.62	0.86-0.7	0.748-0.6	0.9 -0.66	0.26 -0.12
25	0.88	0.7	0.47	0.8 -0.63	0.63 -0.44	0.86 -0.54	0.12 -0.04
30	0.82	0.6	0.28	0.74-0.55	0.517-0.3	0.8 -0.41	0.04 -0.01
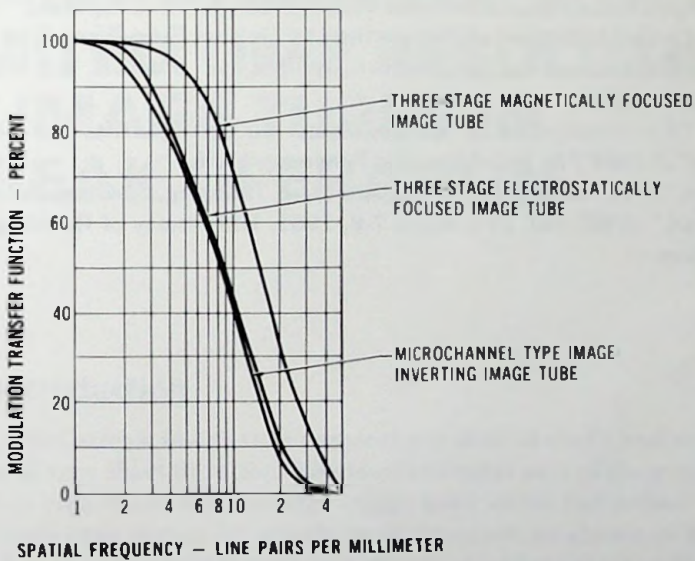
Fig. 6.13   Modulation transfer function of image tubes.

References

Born, M., and E. Wolf, *Principles of Optics*, Macmillan, New York, 1964.

Coltman, J. M. "The Specification of Imaging Properties by Response to a Sine Wave Input," *Jour. Opt. Soc. of America*, Vol. 7, No. 2, p. 121, April 1960.

Csorba, I. P. "Modulation Transfer Function Calculation of Electrostatic Electron Lenses," *RCA Review*, Vol. 33, p. 393, 1972.

———. "Modulation Transfer Function of Image Tube Lenses," *Applied Optics*, Vol. 16, p. 2647, 1977.

————. "Chromatic Aberration Limited Image Transfer Characteristics of Image Tube Lenses of Simple Geometry," *RCA Review*, Vol. 31, p. 535, 1970.

————. "Analytical Approach to the Modulation Transfer Function of the Generation 2 Wafer Tube," *Proceedings of Electro-Optical Systems Design Conference*, September 1976, New York (Industrial and Scientific Conference Management, Inc., Chicago), p. 646.

————. "Resolution Limitation of Electromagnetically Focused Image Intensifier Tubes," *RCA Review*, Vol. 30, p. 36, 1969.

————. "MTF of Image Intensifier Tubes," *SPIE*, Vol. 274, pp. 42-50.

Hopkins, H. H. "Modern Methods of Image Assessment," *SPIE*, Vol. 274, pp. 2-11, April 7-9, 1981. University of Reading, United Kingdom.

Schade, O. H. "A Method of Measuring the Optical Sine-Wave Spatial Spectrum of Television Image Display Devices," *J. SMPTE*, Vol. 67, No. 9, September 1958.

————. "An Evaluation of Photographic Image Quality and Resolving Power," *J. SMPTE*, Vol. 73, p. 81, February 1964.

Williams, T. L., ed. SIRA. "Assessment of Imaging Systems: Visible and Infrared," *SPIE*, Vol. 274, April 7-9, 1981, University of Reading, United Kingdom.

7

TRANSIT-TIME-SPREAD-LIMITED TIME RESOLUTION OF IMAGE TUBES IN STREAK OPERATION

7.1 Introduction

High-speed streak image tube cameras are used to study and record pho-toevents of very short duration. The most essential part of their instrumen-tation is a high-speed light-shutter image tube which has deflection plates in the anode cone region for streak mode operation as shown in figure 2.6. In streak mode operation the electron image of a photoevent is deflected in order to display the light intensity variation as a function of time at the phosphor screen.

Transit-time spread produced by the emission spread of photoelectrons is one of the fundamental limitations of time resolution of high-speed image tube cameras. Because of transit-time spread a point image of a photoevent of very short duration is imaged by the camera as a line in streak mode operation. The length of the line is proportional to the transit-time spread. Obviously, the shorter the length of the line at a given streak velocity, the better the time resolution of the camera. In various types of image tubes an electron may travel in a uniform electric field, in a central field, or in a field-free region during the imaging process. In this section the transit-time spread in each region will be analyzed.

7.2   Uniform Electric Field

In the case of a uniform electric field the transit time difference between two electrons, one having a zero emission velocity and another having an axial emission velocity v_s, may be obtained from the equation of electron motion in a uniform electric field:

$$v_s^2 t^2 + 4L v_a t - 4L^2 = 0, \tag{7.1}$$

where t is the transit time, L is the screen-to-cathode separation, v_a is the electron velocity corresponding to zero emission velocity, and v_s is the electron velocity corresponding to an accelerating voltage V_s. For $v_s \gg v_a$ the transit-time difference $\varDelta T$ from equation 7.1 is given by

$$\varDelta T = 2L v_a / v_s^2 = T_r \sqrt{V_a / V_s} = \sqrt{2m/e} \, \sqrt{V_a} / E, \tag{7.2}$$

where T_r is the transit time of zero-emission-velocity electrons, V_a is the accelerating voltage required for an electron at rest to acquire its emission energy, E is the electric-field strength, and e and m are the charge and mass of an electron, respectively.

The numerical value of transit-time difference from equation 7.2 is given by

$$\varDelta T = 3.37 \times 10^{-8} L \sqrt{V_a} / V_s = 3.37 \times 10^{-8} \sqrt{V_a} / E, \tag{7.3}$$

where L is in centimeters, V_s and V_a are in volts, and E is in volts per centimeter.

7.3   Field-Free Region

Assume that two electrons, one having zero emission energy and another having eV_a axial emission energy, are accelerated across a very small distance to potential V_s. Then let the electrons travel in a field-free region through a distance L. Denote the transit time of the zero-emission-energy electron by T_r.

The transit-time difference of two electrons then becomes

$$
\begin{aligned}
\varDelta T &= \frac{L}{\sqrt{2eV_s/m}} - \frac{L}{\sqrt{2e(V_a + V_s)/m}} \\
&= \frac{L}{\sqrt{2eV_s/m}} \left(1 - \sqrt{\frac{V_s}{V_s + V_a}} \right).
\end{aligned} \tag{7.4}
$$

For $V_s \gg V_a$, equation 7.4 reduces to

$$\Delta T = \frac{L}{\sqrt{2eV_s/m}} \frac{V_a}{2V_s} = \frac{T_r}{2} \frac{V_a}{V_s} = 0.84 \times 10^{-8} \, LV_a/V_s \sqrt{V_s}, \qquad (7.5)$$

where L is in centimeters and V_a and V_s are in volts.

7.4   Central-Field Region

In a two-concentric-sphere type image-inverting diode the electrons travel in a central field up to the anode aperture, then from the anode aperture to the screen in a field-free region. Consider an electron leaving the cathode sphere with an emission velocity v_i and direction θ as indicated in figure 3.1. In the central-field region the electron path is determined by Kepler's law of equal areas (eq. 3.14):

$$r^2 \frac{d\phi}{dt} = c, \qquad (7.6)$$

where r and ϕ are the radius and angle, respectively, of the spherical coordinates of the centrally symmetric system and c is a constant. The velocity v of the electron may be described by the following equation (eq. 3.15):

$$v^2 = \left(\frac{dr}{dt}\right)^2 + \left(r\frac{d\phi}{dt}\right)^2. \qquad (7.7)$$

The energy equation was given as equation 3.16:

$$\tfrac{1}{2}mv^2 = eV(r) + eV_i, \qquad (7.8)$$

where eV_i is the emission energy of the electron and $V(r)$ is the potential distribution given by the following equation (eq. 3.17):

$$V(r) = V_s \frac{R_a}{R_c - R_a} \frac{R_c - r}{r}. \qquad (7.9)$$

In equation 7.9, V_s is the anode potential and R_a and R_c are the radius of the anode and cathode spheres, respectively. From the boundary conditions the following (eq. 3.18) also holds:

$$R_c \frac{d\phi}{dt} = v_i \sin \theta, \qquad (7.10)$$

where the terms are shown in figure 3.1.

By combining equations 7.6 to 7.10 the following differential equation is obtained:

$$dt = \sqrt{\frac{m}{2e}} \frac{r\,dr}{\sqrt{\left(V_i - V_s \dfrac{R_a}{R_c - R_a}\right)r^2 + V_s \dfrac{R_a R_c}{R_c - R_a} r - R_c^2 V_i \sin^2 \theta}}. \quad (7.11)$$

The transit time of an electron now may be obtained by integration of equation 7.11:

$$\int_0^T dt = -\sqrt{\frac{m}{2e}} \int_{R_c}^{R_a} \frac{r\,dr}{\sqrt{\left(V_i - V_s \dfrac{R_a}{R_c - R_a}\right)r^2 + V_s \dfrac{R_a R_c}{R_c - R_a} r - R_c^2 V_i \sin^2 \theta}}. \quad (7.12)$$

The result is

$$T = -\sqrt{\frac{m}{2e}} \Bigg\{ \frac{\sqrt{V_i(R_a^2 - R_c^2 \sin^2 \theta) + V_s R_a^2} - \sqrt{V_i R_c^2(1 - \sin^2 \theta)}}{V_s R_c - (V_s + V_i)R_a}(R_c - R_a)$$

$$- \frac{V_s R_a R_c \sqrt{R_c - R_a}}{2[V_s R_a - V_i(R_c - R_a)]\sqrt{V_s R_a - V_i(R_c - R_a)}}$$

$$\left[\sin^{-1}\left(\frac{V_s R_a(R_c - 2R_a) + 2V_i R_a(R_c - R_a)}{\sqrt{R_a^2 R_c^2 V_s^2 - 4R_c^2 V_i(R_c - R_a)[V_s R_a - V_i(R_c - R_a)]\sin^2 \theta}} \right) \right.$$

$$\left. + \sin^{-1}\left(\frac{V_s R_a R_c - 2V_i(R_c - R_a)R_c}{\sqrt{R_a^2 R_c^2 V_s^2 - 4R_c^2 V_i(R_c - R_a)[V_s R_a - V_i(R_c - R_a)]\sin^2 \theta}} \right) \right] \Bigg\} \quad (7.13)$$

For $V_s \gg V_i$ and $R_c > 2R_a$, equation 7.13 reduces to the following equation:

$$T = \sqrt{\frac{m}{2e}} \Bigg\{ \frac{R_c - R_a}{\sqrt{V_s}} + \frac{R_c}{2}\sqrt{\frac{R_c - R_a}{V_s R_a}} \left[\pi - \sin^{-1}\left(\frac{2\sqrt{R_a(R_c - R_a)}}{R_c} \right.\right.$$

$$\left.\left. + \frac{2(R_c - 2R_a)}{R_c}\sqrt{\frac{R_c - R_a}{R_a}}\sqrt{\frac{V_i}{V_s}}\cos \theta \right) \right] - \frac{R_c}{R_a}(R_c - R_a)\frac{\sqrt{V_i}}{V_s}\cos \theta \Bigg\}. \quad (7.14)$$

Expanding the inverse sine function in a Taylor's series gives

$$T = \sqrt{\frac{m}{2e}} \Bigg\{ \frac{R_c - R_a}{\sqrt{V_s}} + \pi\frac{R_c}{2}\sqrt{\frac{R_c - R_a}{V_s R_a}} - \frac{R_c}{2}\sqrt{\frac{R_c - R_a}{V_s R_a}} \times$$

$$\sin^{-1}\left(\frac{2\sqrt{R_a(R_c - R_a)}}{R_c} \right) - \frac{2R_c}{R_a}(R_c - R_a)\frac{\sqrt{V_i}}{V_s}\cos \theta \Bigg\}. \quad (7.15)$$

The transit-time difference between a zero-emission energy electron and an eV_i emission-energy electron from equation 7.15 is given by

$$\Delta T = -\sqrt{\frac{2m}{e}}\frac{R_c}{R_a}(R_c - R_a)\frac{\sqrt{V_i}}{V_s}\cos\theta. \tag{7.16}$$

The relationship between the anode voltage V_s and cathode field strength E_c is given by

$$V_s = E_c R_c (R_c - R_a)/R_a. \tag{7.17}$$

By combining equations 7.16 and 7.17 the transit-time difference in seconds, expressed with the cathode field strength, becomes

$$\Delta T = -\sqrt{\frac{2m}{e}}\frac{\sqrt{V_i}}{E_c}\cos\theta = -\sqrt{\frac{2m}{e}}\frac{\sqrt{V_a}}{E_c} = -3.37\times10^{-8}\frac{\sqrt{V_i}}{E_c}\cos\theta, \tag{7.18}$$

where V_i is in volts and E_c is in volts per centimeter. Equation 7.18 is identical with equation 7.3.

7.5 Image-Current Distribution as a Function of Transit-Time Difference

Assume a Lambertian emitter with the emission-energy distribution of equation 5.10. The fraction dN_θ of electrons emitted between angles θ and $\theta + d\theta$ then may be given by the following equation:

$$dN_\theta = \frac{\pi^2}{\pi - 2}\frac{V_i}{V_{im}}\cos\left(\frac{\pi}{2}\frac{V_i}{V_{im}}\right)d\left(\frac{V_i}{V_{im}}\right)\cos\theta\sin\theta\,d\theta. \tag{7.19}$$

With substitution of

$$x = \sqrt{V_a/V_{im}} \quad \text{and} \quad y = \sqrt{V_r/V_{im}} \tag{7.20}$$

in equation 7.19 the following is obtained:

$$dN_\theta = \frac{2\pi^2}{\pi - 2}\cos\left[\frac{\pi}{2}(x^2 + y^2)\right]xy\,dx\,dy. \tag{7.21}$$

where eV_r is the transverse emission energy. The axial emission-energy distribution is

$$dN_a = \frac{2\pi^2}{\pi - 2}x\,dx\int_0^{\sqrt{1-x^2}}\cos\left[\frac{\pi}{2}(x^2 + y^2)\right]y\,dy$$

$$= \frac{2\pi}{\pi - 2}x\left[1 - \sin\left(\frac{\pi}{2}x^2\right)\right]dx. \tag{7.22}$$

Combining equations 7.18, 7.20, and 7.22 gives

$$dN_a = \frac{\pi}{\pi - 2} \frac{E_c^2 e}{m V_{im}} \Delta T \left[1 - \sin\left(\frac{\pi}{4} \frac{E_c^2 \Delta T^2 e}{m V_{im}} \right) \right] d(\Delta T). \qquad (7.23)$$

Equation 7.23 is plotted in figure 7.1.

7.6 Time Resolution

The time resolution can be derived from figure 7.1. It is 33 ps, which is the time difference between the 50% image-current density points.
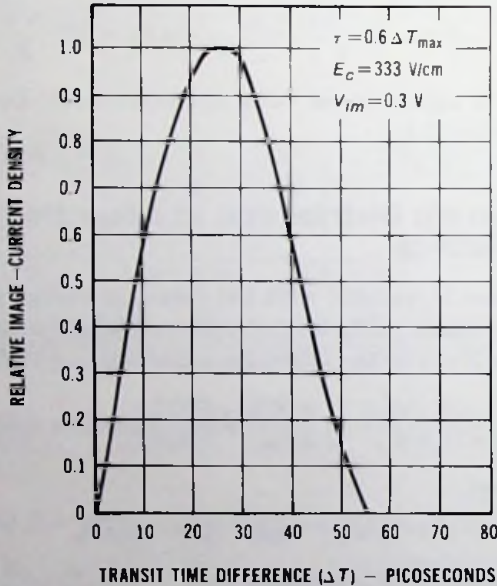
Fig. 7.1 Image-current density as a function of transit-time difference.

If the time resolution calculations were carried out for a different value of emission-energy spread eV_{im} or a different value of cathode field strength E_c, only the values of ΔT on the abscissa of figure 7.1 would change. The transit-time difference ΔT is proportional to the square root of emission energy and inversely proportional to the cathode field strength. Therefore the time resolution in seconds may be expressed as

$$\tau = k\sqrt{V_{im}}/E_c = 2 \times 10^{-8}\sqrt{V_{im}}/E_c, \qquad (7.24)$$

where V_{im} is in volts and E_c is in volts per centimeter. The value of $k = 2 \times 10^{-8}$ was obtained by substitution in equation 7.24 of $\tau = 33 \times 10^{-12}$ s, $V_{im} = 0.3$ V, and $E_c = 333$ V/cm. Because of the identity of equations 7.3

and 7.18, equation 7.24 is also valid for electromagnetic image tubes (uniform electric and magnetic fields).

References

Csorba, I. P. "Resolution Limitations of Electromagnetically Focused Image Intensifier Tubes," *RCA Review*, Vol. 30, p. 36, March 1969.
———. "Transit-Time-Limited Time Resolution of Image Tubes in Streak Operation," *RCA Review*, December 1971.
Weber, E. *Electromagnetic Fields*, p. 151, John Wiley & Sons, Inc., New York, 1950.

8

IMAGE INTENSIFICATION

8.1 Introduction

It is a common experience that at night only large contrasty objects are visible, whereas fine detail and low contrast are not resolvable for the naked eye. The visual acuity impairment is due to the insufficient quantity of visible light needed for sharp vision. Experimental study of human vision indicates that the photoreceptors of the eye (cones and rods) must receive a large number of visible light photons from an object point to register visual sensation. In comparison, electronic light amplifiers can sense less light. The extension of the region of vision toward lower light levels, therefore, is feasible by use of light amplifying devices which require less light for response than the eye and can detect infrared and ultraviolet light. The most commonly used light amplifying device is an image intensifier tube, which extends the visibility by gathering more light from the scene with an objective lens than the unaided eye and uses a photocathode that has a higher quantum efficiency and broader spectral response than the eye.

The objective lens extends the visibility toward lower light levels by a factor of the square of the ratio of the objective lens diameter to the pupil diameter. Photocathodes lower the visual threshold in proportion to their quantum efficiency. The quantum efficiency of the most efficient photocathodes is in the neighborhood of 20% in the visible spectrum, whereas the quantum efficiency of the fully dark adapted eye is only 1%.

The visible spectrum extends from about 420 nm of wavelength to 700 nm of wavelength. In contrast, multialkali cathodes with extended red response respond to light in the region of 300 nm to 900 nm. In the infrared region the quantum efficiency of the photocathode may be significantly less than

in the visible spectrum, but the emission efficiency loss is compensated by the greater number of photons available in the infrared region of the spectrum. Figure 8.1 shows the natural night-sky spectral irradiance on the earth's horizontal surface. The photon rate is five to seven times greater in the region of 800 to 900 nm than in the visible region in the neighborhood of 500 nm.
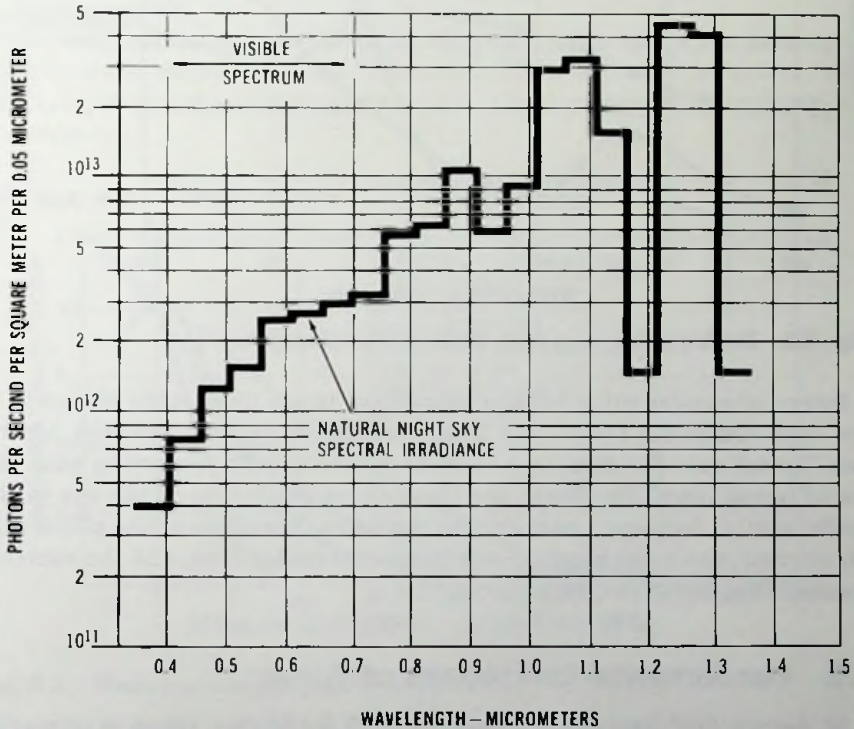
Fig. 8.1   Natural night-sky spectral irradiance on horizontal earth surface.

For passive night vision with image intensifier tubes the superior near-IR sensitivity is an important factor in conjunction with the spectral irradiance of the night-sky and target reflectivity. As shown in figure 8.2 the target reflectivity of a variety of materials and scenes is on the rise in the IR region. Therefore, on one hand more light is available in the IR; on the other hand, against certain backgrounds more contrast is available. The third generation GaAs:Cs·O/AlGaAs cathode has a photoresponse in the 600-nm to 900-nm wavelength range, taking full advantage of the above described situation.
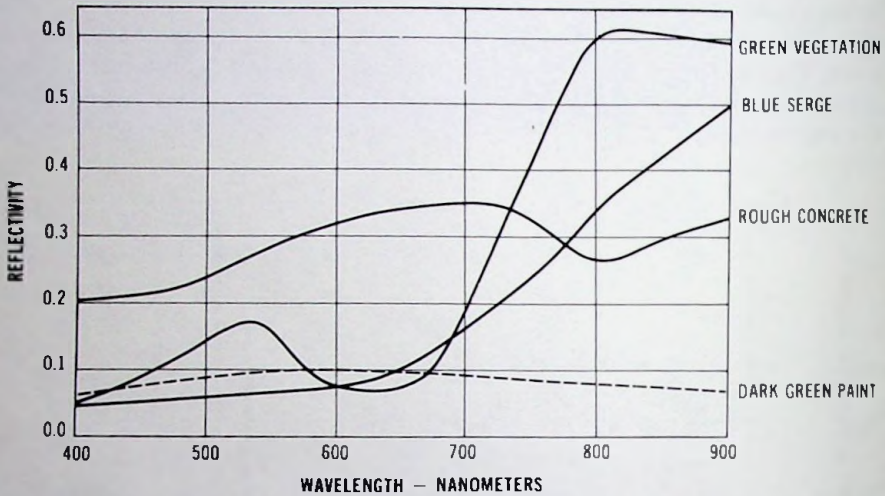
Fig. 8.2   Reflectivity as a function of wavelength.

Image intensifier tubes aid the human eye to see fine details of objects at low field luminance levels. The image intensifier system, however, has its own limitations. Fundamental limitations of visibility occurring with the use of image intensifier tubes are the contrast sensitivity of the eye in the useful spatial frequency domain, the statistical variation of the photocathode current, the noise figure of the image intensifier tube, and the contrast transfer function of the image intensifier.

8.2   Fundamental Limitations of Vision

At normal field luminance levels (10 to 20 fL) human vision is primarily limited by the contrast loss which is caused by the diffraction effect, the fiber structure of the retina, the light spread in the retina, and aberrations.

Diffraction is the result of the modification which light undergoes in passing through the lens aperture. It causes a beam spread at the plane of sharp focus which is proportional to the wavelength and inversely proportional to the pupil diameter.

The fiber structure of the retina limits resolution due to its granular nature. The *fovea centralis*, which is the region of sharpest vision, has a photoreceptor density of about 147 000 per square millimeter. The center to center spacing of photoreceptors varies from less than 2 μm to 5.4 μm.

The third serious loss to resolution is the light spread in the retina. The length of the photoreceptors is on the order of 34 μm. Light transmission

through the photoreceptors is associated with fiber crosstalk, which in a first order should be proportional to the beam angle and consequently to the pupil diameter. The cone shape of the photoreceptors is for reduction of the crosstalk at the expense of sensitivity. Now, with a linear absorption of light along the length of photoreceptors, it is estimated that about 50% light may participate in the crosstalk. Crosstalk is significant only at the far end of the photoreceptors.

The computed modulation transfer function of the eye is the product of the sine-wave response of the diffraction effect, granular structure, and retinal light spread as shown in figure 8.3. The measured MTF is shown for comparison.
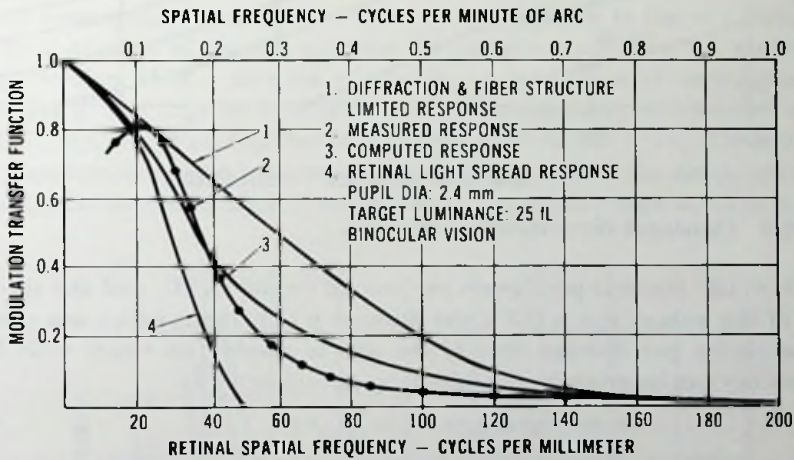
Fig. 8.3   Sine-wave response of the eye.

The limiting resolution of the eye is in the range of 12 to 14 line pairs per millimeter at a normal viewing distance of 25 cm. This resolution value is in good agreement with the generally adapted value of resolution of 1 minute of arc, which corresponds to 13.75 lp/mm of resolution.

At low illumination levels, in addition to the eye response characteristics, resolution is also limited by the statistical variation of the light level. Figure 8.4 shows the angular resolution as a function of illumination as reported by Blackwell. The dark adapted eye begins to resolve large, contrasty objects at about 10^{-5} fL field luminance levels. For instance, at 10^{-5} fL adaption brightness and $C = 10$, the resolution of the eye is about 8 minutes of arc and the resolved object has 1.1×10^{-4} fL brightness. By assumption that the resolved object has a Lambertian light emission with a photon rate
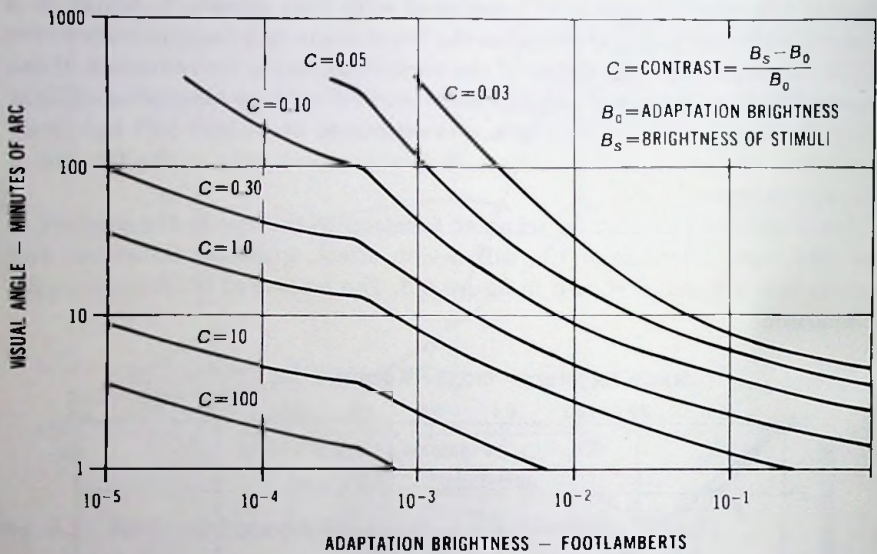
Fig. 8.4 Contrast thresholds of the eye.

of 1.3×10^{16} photons per lumen per second (white light), and the storage time of the human eye is 0.2 s, the number n of photons which are needed at the retina per storage time of the eye to resolve an object with 50% probability can be given by the following equation:

$$n = 6.5 \times 10^{14} D^2 \alpha^2 L^2, \tag{8.1}$$

where D is the pupil diameter in centimeters, α is the visual angle in radians, and L is the luminance of object in lumens per square centimeter. Table 8.1 was obtained from equation 8.1 by use of Blackwell's contrast threshold data for α and L and Flamant's data for D.

In table 8.1 the target contrast is $C = 10$ and N represents the number of photoreceptors receiving the n photons. From table 8.1 the retina sensitivity

Table 8.1   Number of Photons Needed for Resolution With 50% Probability

L	α	D	n	N
6×10^{-5}	1′	0.4	524	3.5
1×10^{-5}	2.2′	0.45	535	17.6
1×10^{-6}	4.5′	0.55	334	73
1×10^{-7}	8.3′	0.55	113	248

is greater by a factor of about 4.7 at 1×10^{-7} lm/cm² level than at the 6×10^{-5} lm/cm² level.

For a 90% resolution probability the photon number n is greater by a factor of 1.62 than that given in table 8.1.

8.3   The Ocular and the Eye Response

The function of the ocular is to magnify the intensified image so that the contrast loss caused by the eye response is minimized. By use of a $10 \times$ ocular the contrast loss resulting from the eye response is at a moderate level up to 20 lp/mm at the output screen. It appears that a further increase of magnification may completely eliminate the contrast loss caused by the eye at high spatial frequencies. However, in addition to the eye response, the field of view of the ocular must be considered. Figure 8.5 shows the magnification M of a number of oculars as a function of viewing-screen diameter d' and angular field of view θ. The human eye, with motion of the eyeball, can accept an angular field of view of about 60° to 70°. Therefore, if the requirements were to view a 40-mm output screen, the ocular magnification, as shown in figure 8.5, would have to be in the range of 7.2 to 8.7.

$$M = 500 (d')^{-1} \tan (\theta/2)$$
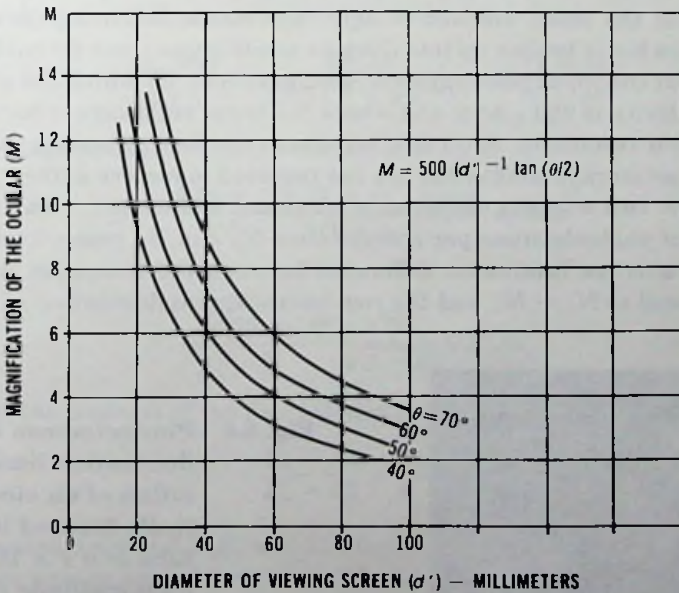
Fig. 8.5   Magnification of a number of oculars as a function of viewing screen diameter and angular field of view.

8.4   Field of View

The angular field of view is related to the angular resolution of the image intensifier system. This relation can be shown by considering that the total amount of image detail transferred through the image intensifier tube is determined by the resolution and diameter of the image intensifier tube. Thus the total highlight resolution of an 18-mm-format image intensifier tube having 30 lp/mm limiting resolution is 30 × 18 = 540 line pairs. Accordingly, the total field resolution is 540 line pairs per field of view. The angular resolution can be obtained by division of the total field resolution with the angular field of view. For example, for a 6° angular field of view and 540 line pairs total field resolution, the angular resolution γ_R is

$$\gamma_R = \frac{540}{6 \times 60} = 1.5 \text{ line pairs/minute of arc}. \tag{8.2}$$

8.5   Resolution at Low Photocathode Illumination Levels

At very low levels of photocathode illumination the resolution of a high-gain image intensifier is primarily limited by the finite number of photoelectrons released at the photocathode during the storage time of the eye. Because of the small amount of light, the intensified image is no longer continuous but is broken up into discrete scintillations, one for each electron released at the input photocathode (see figure 8.6), for which the photocathode sensitivity is 280 μA/lm and where the lower right-corner bars indicate 7.13 lp/mm resolution. A certain minimum number of perceivable flashes per line per storage time of the eye are required to resolve a line.

Consider two adjacent elements, a white and a black bar, with an average number of photoelectrons per storage time N_w and N_b, respectively. In this case the average luminance difference between the images of the bars is proportional to $N_w - N_b$, and the root-mean-square fluctuation of the lumi-

Fig. 8.6   **Photoelectron current fluctuation limited resolution of an electrostatically focused image tube at a 1 × 10⁻⁷ fc photocathode illumination.**

nance is proportional to $\sqrt{\overline{N}_w + \overline{N}_b}$. For the bars to be resolved the average luminance difference must exceed the fluctuation by a factor of K:

$$\overline{N}_w - \overline{N}_b = K\sqrt{\overline{N}_w + \overline{N}_b}. \tag{8.3}$$

The larger the value of K in equation 8.3, the greater the certainty for resolving the bars. By substituting $N_b = \rho N_w$ in equation 8.3 and rearranging terms, the average number of electrons in a white bar becomes

$$\overline{N}_w = K^2\frac{(1 + \rho)}{(1 - \rho)^2}, \tag{8.4}$$

where ρ is the ratio of the average luminances of a black and a white line.

Because the average number of emitted electrons is proportional to the illumination, the emitting area, and the storage time, it may also be expressed as

$$\overline{N}_w = E'_w Stlw/e, \tag{8.5}$$

where l and w are the length and width of a line, e is the electron charge in coulombs, E' is the illumination in lumens per square centimeter, S is the photocathode sensitivity in amperes per lumen, and t is the storage time.

If a resolution pattern, in which $l = 5w$ (U.S. Air Force resolution pattern) is used, and if $w = l/2R_l$, equation 8.5 becomes

$$N_w = \frac{5E'_w Stw^2}{e} = \frac{5E'_w St}{4R_l^2(1.6 \times 10^{-19})} = K^2\frac{(1 + \rho)}{(1 - \rho)^2}. \tag{8.6}$$

On rearrangement of terms, the resolution R_l is

$$R_l = \frac{2.79 \times 10^8}{K} \frac{(1 - \rho)}{\sqrt{1 + \rho}} \sqrt{E'_w St} \text{ lp/mm} \tag{8.7}$$

or

$$R_l = \frac{2.79 \times 10^8}{K} \frac{\sqrt{2}C}{\sqrt{1 + C}} \sqrt{E'_w St}, \tag{8.8}$$

where C is the contrast of the line pattern at the photocathode defined by

$$C = \frac{E'_w - E'_b}{E'_w + E'_b} = \frac{1 - \rho}{1 + \rho}. \tag{8.9}$$

In equations 8.8 and 8.9, E'_b and E'_w are the photocathode illumination (in lumens per square centimeter) of the black and white lines, respectively, S is the photocathode sensitivity (amperes per lumen), t is the storage time (seconds), and K is the signal-to-noise ratio having a threshold value of about 3.1 per line length to width ratio of 5.

ILLUMINATION OF PHOTOCATHODE – FOOTCANDLES

RESOLUTION (R) – LINE PAIRS PER MILLIMETER

100 μA/lm
175 μA/lm
200 μA/lm
250 μA/lm
300 μA/lm
400 μA/lm

OVERCAST STARLIGHT

STARLIGHT

QUARTER MOON

FULL MOON

$$R = \frac{2.79 \times 10^8}{K} \sqrt{ESt}$$

$K = 3.1$
$t = 0.20$

ILLUMINATION (E) OF PHOTOCATHODE – LUMENS PER SQUARE CENTIMETER
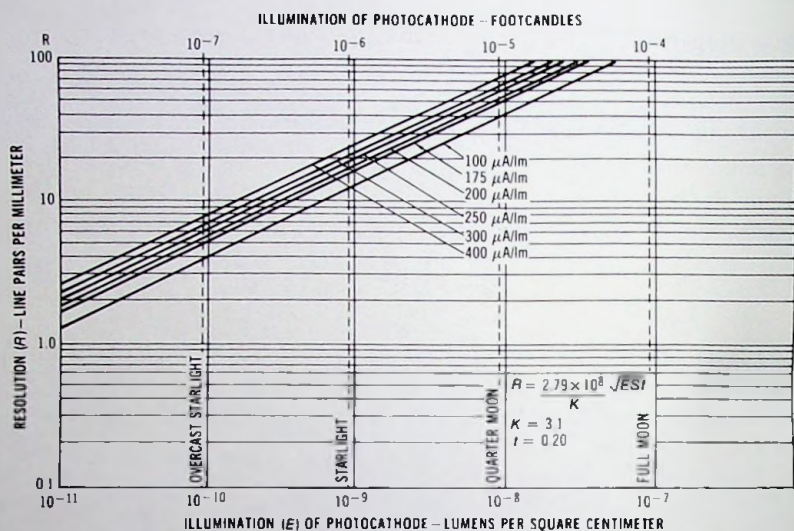
Fig. 8.7   Photoelectron current fluctuation limited cathode resolution for different photocathode sensitivities.

ILLUMINATION OF PHOTOCATHODE – FOOTCANDLES

RESOLUTION (R) – LINE PAIRS PER MILLIMETER

C·1.0
0.8
0.6
0.5
0.4
0.3
0.2
0.1
0.03

$$R = \frac{2.79 \times 10^8 C}{K \sqrt{1+C}} \sqrt{2\,ESt}$$

$K = 3.1$
$t = 0.2$
$S = 10^{-3}$ A/lm

ILLUMINATION (E) OF PHOTOCATHODE – LUMENS PER SQUARE CENTIMETER
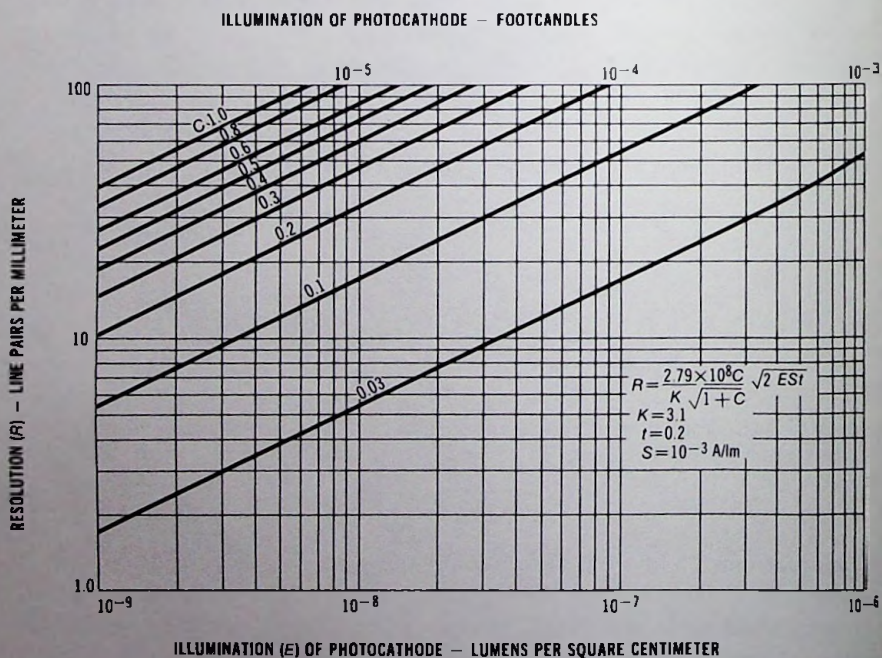
Fig. 8.8   Photoelectron current fluctuation limited cathode resolution for different contrasts.

Figures 8.7 and 8.8 show the photoelectron current fluctuation limited cathode resolution as a function of photocathode illumination.

Usually the photocathode resolution is observed at the output screen of the image-intensifier tube. At the output screen the input contrast is modified by the contrast transfer of the image tube. In this case, therefore, the output image contrast must be used for the value of C in equation 8.8. The output image contrast is the product of the input image contrast C_f and the contrast transfer function C_i of the image intensifier tube as shown in appendix C:

$$R_i = \frac{2.79 \times 10^3 \sqrt{2}\, C_f C_i}{K N_f \sqrt{1 + C_f C_i}} \sqrt{E'_{w} S t}, \tag{8.10}$$

where N_f is the noise figure of the image intensifier tube.

Figure 8.9 shows the photoelectron current fluctuation limited resolution of a generation 3 image intensifier tube as a function of photocathode illumination. The resolution was obtained by use of typical contrast transfer function values for the computation of E'_{w} values in equation 8.10. The resolution curves show saturation above the limiting resolution points of the image tube.

When a square-wave grating is viewed through an image intensifier, the field resolution as a function of field luminance and field contrast may be obtained by multiplication of equation 8.8 with the magnification of the
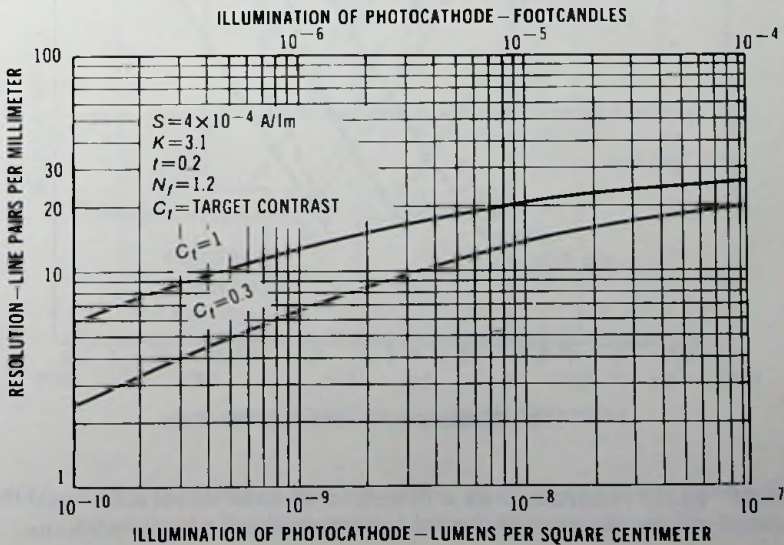
Fig. 8.9 Resolution as a function of photocathode illumination.
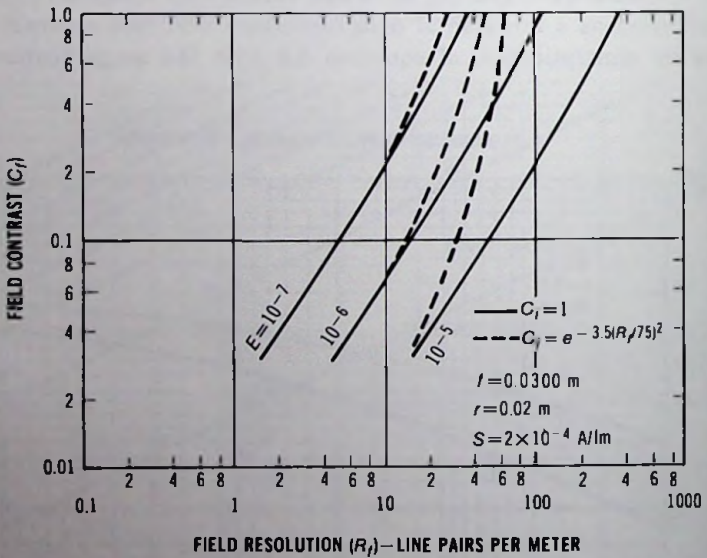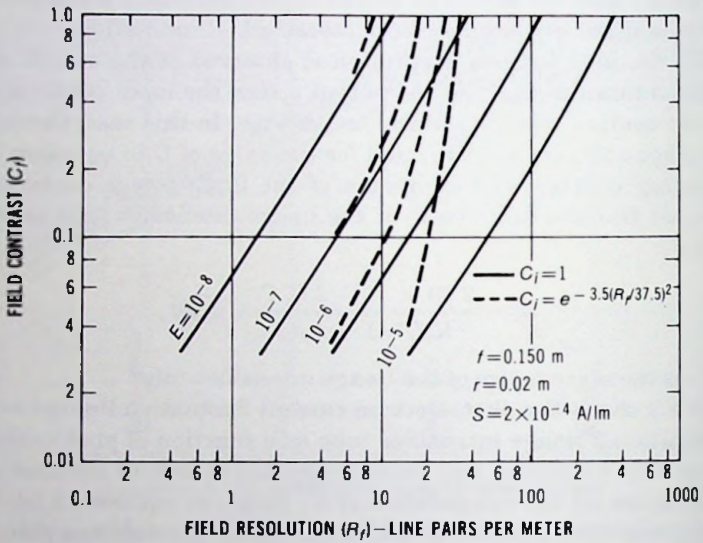
Fig. 8.10 Field resolution as a function of field contrast C and field luminance for the first two different objective lenses.
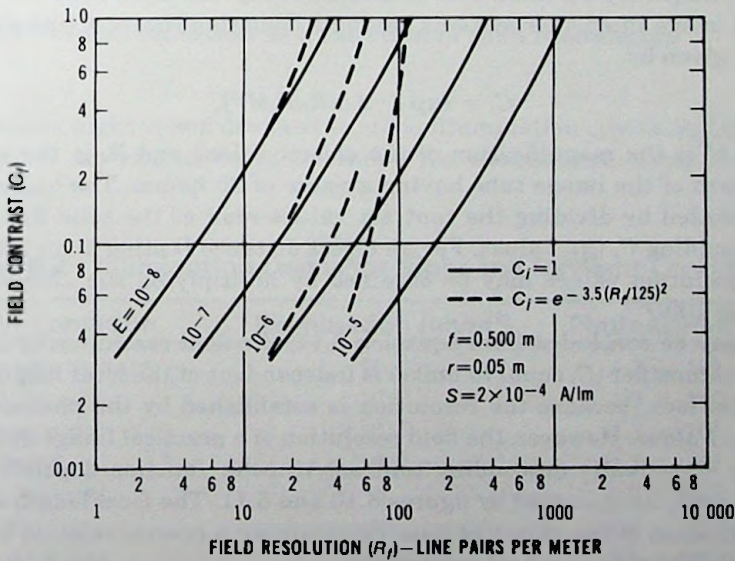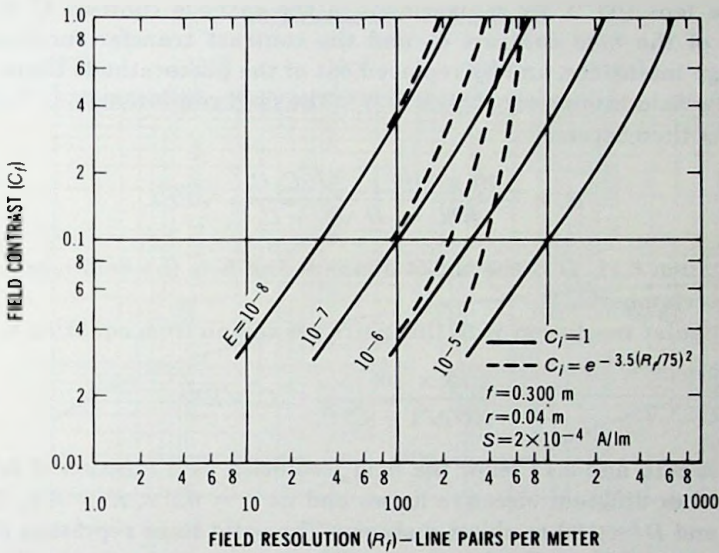
Fig. 8.11 Field resolution as a function of field contrast C and field luminance for the second two different objective lenses.

objective lens (fD^{-1}), by replacement of the cathode contrast C with the product of the field contrast C_f and the contrast transfer function C_i of the image intensifier, and by replacement of the photocathode illumination E'_{ar} by the field luminance $E = E'_{ar}{}^{-2}f^2$. The field resolution R_f in line pairs per meter then becomes

$$R_f = \frac{2.79 \times 10^{11}}{KN_f} \frac{r}{D} \frac{\sqrt{2C_f C_i}}{\sqrt{1 + C_f C_i}} \sqrt{ESt}. \tag{8.11}$$

In equation 8.11, D is the object distance and E is the field luminance in centimeterlamberts.

The angular resolution γ_R in line pairs per radian from equation 8.11 is

$$\gamma_R = \frac{2.79 \times 10^{11} r\sqrt{2}}{KN_f\sqrt{1 + C_f C_i}} C_f C_i \sqrt{ESt}. \tag{8.12}$$

Figures 8.10 and 8.11 show the field resolution as a function of field contrast for four different objective lenses and for $t = 0.2$ s, $K = 3.1$, $R_i = 25$ lp/mm, and $D = 100$-m object distance. The solid lines represent the contrast thresholds for a C_i of unity (constant-contrast transfer in the useful spatial-frequency domain). The broken lines represent the contrast thresholds of image intensifier systems having a Gaussian contrast transfer function C_i given by

$$C_i = \exp\left[-3.5(R_f/R_i M)^2\right], \tag{8.13}$$

where M is the magnification of the objective lens and R_i is the limiting resolution of the image tube having a value of 25 lp/mm. The broken lines were plotted by dividing the contrast values read at the solid line by the corresponding $C_i (R_f)$ values. For an object distance D other than 100 m the field-resolution values may be obtained by multiplying the abscissa by a factor of $100D^{-1}$.

As may be concluded from equation 8.11, the field resolution of an ideal image intensifier (C_i equal to unity) is independent of the focal length of the objective lens, because the resolution is established by the photoemission statistics alone. However, the field resolution of a practical image intensifier having a gradually descending contrast transfer function depends on the focal length, as indicated by figures 8.10 and 8.11. The focal length sets the magnification of the objective lens, determining a precise relation between the highlight tube and field resolutions.

Figure 8.12 shows the field resolution of an image intensifier telescope as a function of field luminance. For comparison, the resolution of the eye is also shown.
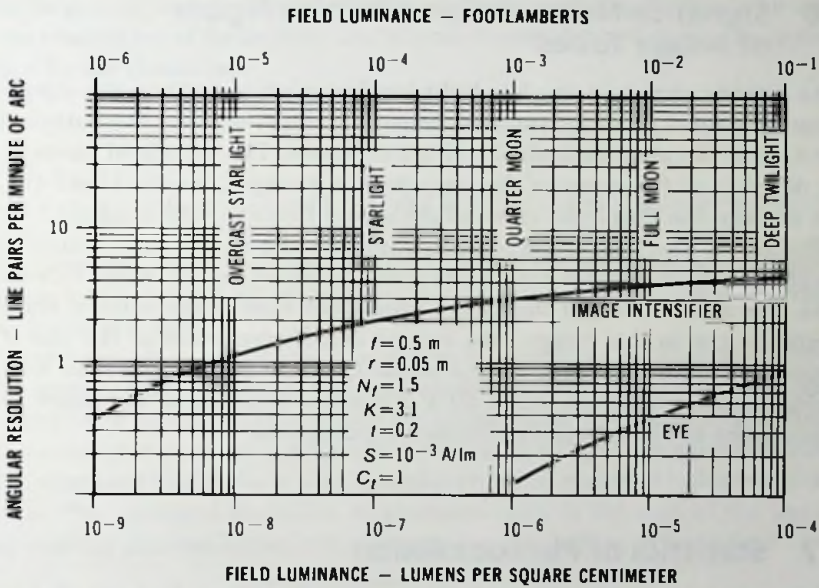
Fig. 8.12   Field resolution as a function of field luminance.

In passive night vision devices the scene illumination is provided through starlight or moonlight. Table 8.2 shows the illumination levels for night conditions.

Table 8.2   Illumination Levels for Night and Daylight Conditions

Night Condition	Illumination (lm/m²)	Photons/mm²/s
overcast starlight	10^{-4}	1.3×10^{6}
starlight	10^{-3}	1.3×10^{7}
quarter moon	10^{-2}	1.3×10^{8}
full moon	10^{-1}	1.3×10^{9}
deep twilight	1	1.3×10^{10}
twilight	10	1.3×10^{11}
very dark day	10^{2}	1.3×10^{12}
overcast day	10^{3}	1.3×10^{13}
daylight	10^{4}	1.3×10^{14}
direct sunlight	10^{5}	1.3×10^{15}

8.6 Signal-to-Noise Ratio and Noise Figure of Image Tubes

As already shown in the low light level resolution section, the signal-to-noise ratio (snr) is a fundamental factor which determines the pattern recognition at low photocathode illumination levels. The threshold value of the snr depends on the shape of the pattern. For example, for the USAF resolution pattern the threshold value of the signal-to-noise ratio is about 3.1.

The snr of an image tube is determined by the statistical fluctuation of the photocathode current and by the noise figure (N_f) of the image intensifier tube. The noise figure of the image intensifier tube is the ratio of the photocathode snr to the image tube output snr. Degradation of the snr of an image tube may be caused by the current loss at the opaque area and the multiplication statistics of the MCP. Phosphor screens, on the other hand, improve the snr by integration of the output signal.

8.7 Statistics of Photoemission

Photoemission is a statistical phenomenon to which the basic Bernoulli trials are applicable. If the probability of emission on a single trial corresponding to one photon is p, then the probability that exactly r electrons are emitted by n photons can be obtained from the Bernoulli distribution (binomial probability law):

$$P_r = \frac{n!\, p^r (1 - p)^{n - r}}{r!(n - r)!}. \tag{8.14}$$

In the above equation the arithmetic mean μ is

$$\mu = np \tag{8.15}$$

and the standard deviation σ is

$$\sigma = \sqrt{np(1 - p)}. \tag{8.16}$$

For small p and $r \ll n$ values, the binominal probability law can be approximated by the Poisson law, which is given by the following equation:

$$P_r = \frac{\mu^r e^{-\mu}}{r!}. \tag{8.17}$$

Since p is small, $1 - p \cong 1$, and

$$\sigma \cong \sqrt{np}. \tag{8.18}$$

For large r, n, and $n-r$ values (large enough to use the Stirling's formula for the evaluation of factorials), the binomial probability law can be approximated by the Gauss law:

$$P_r = \frac{e^{-(\delta/2\sigma)^2}}{\sigma\sqrt{2\pi}},$$

(8.19)

where $\delta = r - np$, $\sigma = \sqrt{np(1-p)}$ and $\mu = np$. Again, for small p values $\sigma \cong \sqrt{\mu}$.

The Gaussian or normal distribution is a bell-shaped curve which has its maximum at $\delta = 0$. In the normal approximation r assumes its most probable value at $r = np$.

Usually the photon flux is not noiseless but contains its own fluctuation. If the photon flux originates from a broadband thermal source, a Poisson distribution of photoemission can be assumed. If the thermal source radiates on the average n photons in a time interval of Δt, the photon noise expressed by the standard deviation is $\sqrt{n}$. The photon noise generated photoemission is $p\sqrt{n}$. The standard deviation of photoemission is the sum of the photon noise and the photoemission noise as given in the following equation:

$$\sigma = \sqrt{np(1-p) + np^2} = \sqrt{np} = \sqrt{\mu}.$$

(8.20)

The signal-to-noise ratio at the photocathode may be obtained by computation of μ and σ. The value of the photocurrent I_c is

$$I_c = E\Delta A S,$$

(8.21)

where E is the photocathode illumination, ΔA is an area of the photocathode and S is the luminous sensitivity.

The number of electrons emitted during Δt time interval from ΔA is

$$\mu = E\Delta A S \Delta t/e,$$

(8.22)

where e is the electron charge. The rms deviation is

$$\sigma = \sqrt{\mu}.$$

(8.23)

The signal-to-noise ratio is

$$(\text{snr})_c = \mu/\sigma = \sqrt{E\Delta A S \Delta t/e} = \sqrt{I_c\Delta t/e} = \sqrt{I_c/2e\Delta f}.$$

(8.24)

where Δf is the bandpass of the image intensifier system established by the storage time of the phosphor screen. Figure 8.13 shows the signal-to-noise ratio as a function of luminous sensitivity.
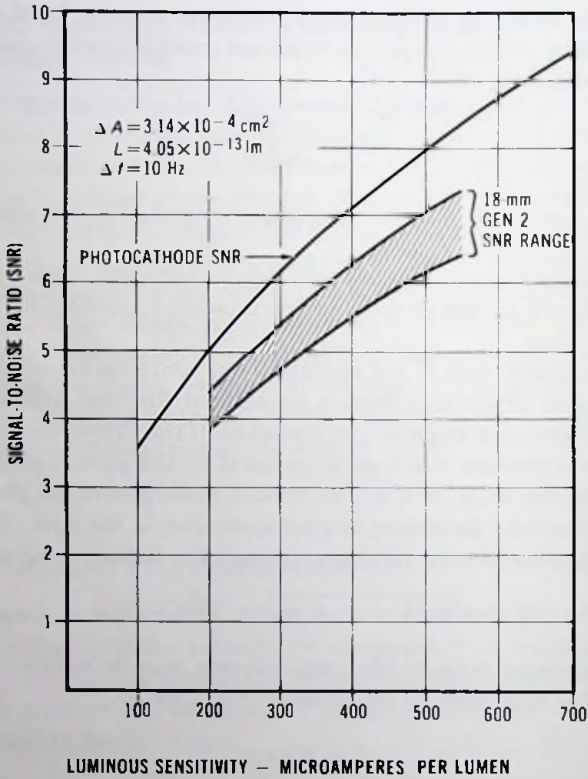
Fig. 8.13   Signal-to-noise-ratio range as a function of luminous
            sensitivity at the output of the MCP.

8.8   Noise Figure

The snr of an image intensifier tube utilizing an MCP for current multi-
plication is degraded by the noise figure of the MCP.

The noise figure of the MCP is the ratio of the MCP input snr to the MCP
output snr. The snr loss of the MCP is caused by the multiplication statistics
and the current loss at the opaque area of the MCP. Accordingly, the noise
figure N of the MCP can be given by the following equation:

$$N = M/\sqrt{F}, \qquad (8.25)$$

where F is the fraction of photoelectrons which enter the microchannels and
participate in the multiplication process and M is a noise figure factor estab-

lished by the multiplication statistics of the continuous resistive strip dynode.

As will be shown, F is a function of MCP application.

In the generation 2 wafer tube the photoelectron image is proximity focused on the input of the MCP by an approximately 200-V acceleration voltage which is present between the photocathode and the input of the MCP. A large portion of the secondary electrons which are generated at the opaque area of the MCP are returned by the cathode electric field to the neighboring channels. The result is an increase in the effective open area ratio. Measurements in the generation 2 wafer tube indicate that the noise figure of MCPs is the range of 1.4 to 1.6.

In electrostatic image-inverting generation 2 tubes (ESI) the secondary electrons generated at the opaque area of the MCP and the backward emitted electrons are collected by the anode cone, which is at a positive potential with respect to the MCP input in order to form a positive-ion barrier. Because of the secondary electron current loss at the MCP input, the noise figure is in the range of 1.5 to 1.95.

In the case of aluminum oxide (Al_2O_3) ion barrier coated MCPs, the secondary electrons generated at the opaque MCP area cannot participate in the multiplication process because the aluminum oxide film blocks their entrance to the channels. In addition, the snr is reduced by the primary beam reflection at the aluminum oxide film; about 10-15% of the primary electrons are returned toward the photocathode. Signal-to-noise ratio measurements on wafer image intensifier tubes with the aluminum oxide coated MCPs indicate that the aluminum oxide film reduces the snr on an average to a factor of 0.8–0.85. The noise figure of the aluminum oxide ion barrier coated MCPs is in the range of 1.76 to 2.0.

The snr of the aluminum oxide coated MCPs is a function of the dead voltage characteristics of the aluminum oxide field. Figure 8.14 shows the dead voltage characteristics of an aluminum oxide film as measured in an image intensifier tube. At beam energies less than the dead voltage the photoelectrons partially penetrate the aluminum oxide film. At beam energies greater than the dead voltage the photoelectrons traverse the aluminum oxide film and lose a kinetic energy equal to the dead voltage, which is on the order of about 100 to 150 V. The rising output current characteristic is primarily due to the increase of the first-impact secondary-electron emission coefficient of the 8161 glass.

The stiffness of the upper knee of the dead voltage curve and the location of the knee on the V_1 voltage axis are primarily determined by the secondary electron emission characteristics of the 8161 glass and by the thickness of the aluminum oxide film.
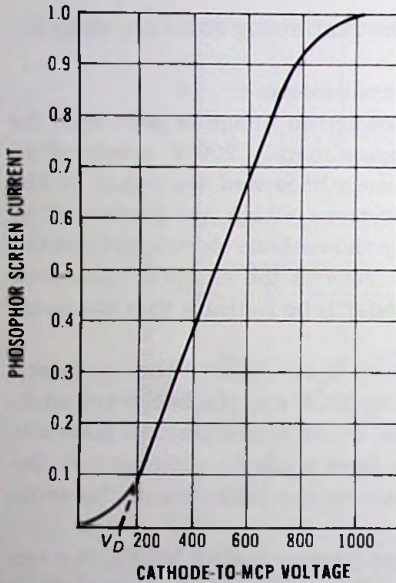
Fig. 8.14   Dead voltage curve.

Figure 8.15 shows the secondary-electron emission coefficient δ of the 8161 glass as a function of beam energy for perpendicular beam landing. The term δ has a maximum value at about 300 V primary-electron beam-landing energy.

For comparison, figure 8.16 shows the relative value of δ in terms of
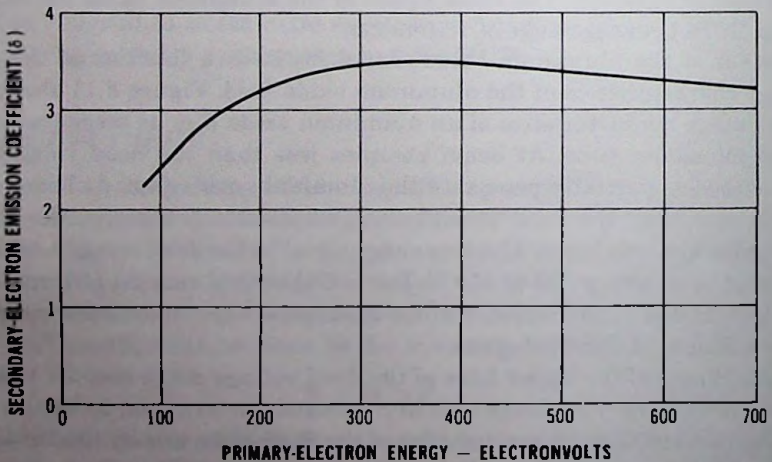
Fig. 8.15   Secondary-electron emission yield of 8161 glass.
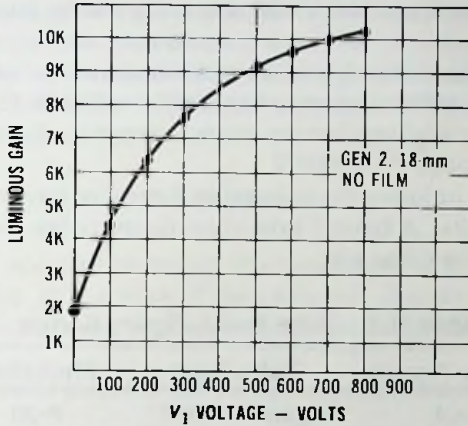
Fig. 8.16 Luminous gain of a generation 2 wafer tube as a function of voltage V_1.

luminous gain for beam landing at grazing angles as occur in generation 2 image intensifier tubes which do not have aluminum oxide coating. As may be concluded from figure 8.16, δ has a maximum value above 800 V beam energy for beam landings at grazing angles. For aluminum oxide coated MCPs, therefore, the maximum should occur at primary-electron beam
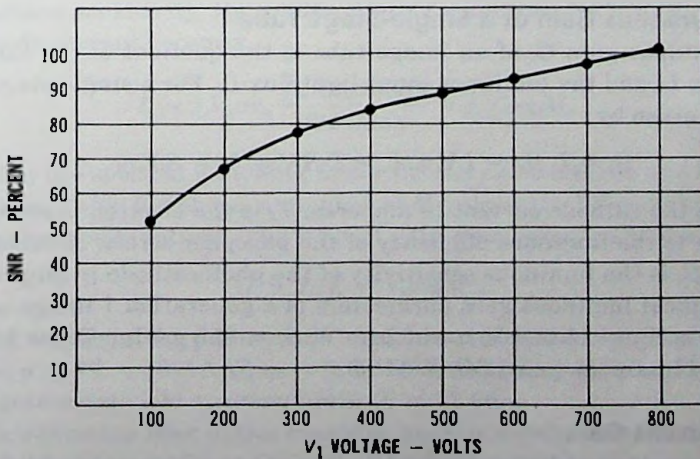
Fig. 8.17 Signal-to-noise-ratio percentage as a function of voltage V_1.

energies greater than $V_D = 800$ V and this is the reason for the dead voltage curve saturation.

From the above discussion δ is at its maximum and the snr losses are at minimum when the MCP is operated above $V_D = 800$ V. Figure 8.17 shows the snr as a function of photoelectron beam energy (V_1) for a 30 Å thick film. The snr saturates above $V_D = 800$ V.

Phosphor screens improve the tube noise figure by integration of the output signal (*cf.* eq. 8.24). A typical tube noise figure range for P-20 and 10-52 phosphors is shown in table 8.3.

Table 8.3 **Tube Noise Figure Range**

Noise Figure	Tube Type	Phosphor
<1	generation 1	P-20
1.15–1.3	generation 2	10-52
1.5–1.7	generation 3	P-20

8.9 The Gain of Image Tubes

An image intensifier tube can perform its function satisfactorily only if it has a sufficient luminous or radiant power gain. In this section the gain characteristics of the various types of image intensifiers will be derived and numerical examples for the gain of actual working devices will be given.

8.9.1 Luminous Gain of a Single-Stage Tube

The luminous gain G_l of an image tube is the quotient of the luminous output flux L_o and the luminous input light flux L_i. For a single-stage tube, G_l may be given by

$$G_l = L_o/L_i = I_c V_a \eta_l / L_i = L_i S_l V_a \eta_l / L_i = S_l V_a \eta_l, \qquad (8.26)$$

where I_c is the cathode current in amperes, V_a is the electron beam voltage in volts, η_l is the luminous efficiency of the phosphor screen in lumens per watt, and S_l is the luminous sensitivity of the photocathode in amperes per lumen. Typical luminous gain parameters of a generation 1 image intensifier tube are: $V_a = 15\,000$ V, $\eta_l = 22$ lm/W, $S_l = 350$ μA/lm. These parameters yield a luminous gain of $G_l = 115.5$.

8.9.2 Current Gain

In the case of a multistage tube the luminous gain may be obtained by multiplication of equation 8.26 by the current gain of the image tube. Note, however, that S_l is related to the input photocathode, and V_a and η_l are

related to the output phosphor screen of the multistage tube. The current gain across an interstage mica coupler, or across an interstage fiber optics, may be obtained by conversion of the radiant power of the interstage phosphor screen into electron current. The average radiant power P of the phosphor screen may be given by

$$\bar{P} = \hat{P} \int_0^\infty P(\lambda)d\lambda, \tag{8.27}$$

where $P(\lambda)$ is the spectral radiation characteristics of the phosphor screen normalized to unity at the peak of the radiation characteristics curve, and $\hat{P}$ is the peak radiant power of the phosphor screen in watts per unit wavelength.

The average radiant power of the phosphor screen may also be given by

$$\bar{P} = I_s V_s \eta_a, \tag{8.28}$$

where I_s is the interstage screen current, V_s is the electron beam voltage, and η_a is the absolute conversion efficiency of the phosphor screen including the substrate losses in the case of fiber optics. The interstage cathode current is

$$I_c = \hat{P}\sigma \int_0^\infty P(\lambda)R(\lambda)d\lambda, \tag{8.29}$$

where $R(\lambda)$ is the spectral response characteristic of the interstage cathode normalized to unity at the wavelength of maximum sensitivity, and σ is the peak radiant sensitivity. By combination of equations 8.27, 8.28, and 8.29 the cathode current becomes

$$I_c = I_s V_s \sigma \eta_a \frac{\int_0^\infty P(\lambda)R(\lambda)d\lambda}{\int_0^\infty P(\lambda)d\lambda} = I_s V_s \sigma \eta_a M, \tag{8.30}$$

where M is the spectral matching factor for the photocathode and the phosphor screen. Table 8.4 shows a number of M values for different photocathode phosphor combinations. The current gain from equation 8.30 is

$$G_c = I_c/I_s = V_s \sigma \eta_a M. \tag{8.31}$$

Typical current gain parameters of a mica interstage target are: $V_s = 15\,000$ V, $\sigma = 70 \times 10^{-3}$ A/W, $\eta_a = 0.08$ W/W, and from table 8.4 $M = 0.877$. These parameters yield a current gain $G_c = 73.66$.

For an interstage fiber-optics coupling, such as exists between two generation 1 image tube modules, the typical current gain parameters are: $V_s = 15\,000$ V, $\sigma = 40 \times 10^{-3}$ A/W, $\eta_a = 0.04$ W/W and $M = 0.877$. These parameters yield an interstage current gain of $G_c = 21$.

<div align="center">Table 8.4   Spectral Matching Factors*</div>

| Phosphors | Notes | Photocathodes | | | | | | | Other Detectors | |
		S-1 k	S-4 k	S-10 k	S-11 k	S-17 k	S-20 k	S-25 k	Photopic eye l	Scotopic eye m
P-1	a	0.278	0.498	0.807	0.687	0.892	0.700	0.853	0.768	0.743
P-4	a,b	0.310	0.549	0.767	0.661	0.734	0.724	0.861	0.402	0.452
P-7	a	0.312	0.611	0.805	0.709	0.773	0.771	0.882	0.411	0.388
P-11	a	0.217	0.816	0.949	0.914	0.954	0.877	0.953	0.201	0.601
P-15	a	0.385	0.701	0.855	0.787	0.871	0.802	0.904	0.376	0.495
P-16	a	0.830	0.970	0.853	0.830	0.855	0.902	0.922	0.003	0.042
P-20	a	0.395	0.284	0.612	0.427	0.563	0.583	0.782	0.707	0.354
P-22B	c	0.217	0.893	0.974	0.960	0.948	0.927	0.979	0.808	0.477
P-22G	c	0.278	0.495	0.807	0.686	0.896	0.699	0.855	0.784	0.747
P-22R	c	0.632	0.036	0.264	0.055	0.077	0.363	0.623	0.225	0.008
P-24	a	0.279	0.545	0.806	0.696	0.827	0.725	0.869	0.540	0.621
P-31	a,d	0.276	0.533	0.811	0.698	0.853	0.722	0.863	0.626	0.651
NaI	e	0.534	0.923	0.885	0.889	0.889	0.900	0.933	0.046	0.224

*Data from E. H. Eberhardt, "Source-Detector Spectral Matching Factors," *Applied Optics*, Vol. 1, p. 2037, 1968.

8.9.3   Luminous Gain of a Multistage Tube

The luminous gain of a multistage image intensifier tube from equations 8.31 and 8.26 becomes

$$G_l = S_l G_c^n V_s \eta_l, \tag{8.32}$$

where n is the number of interstage couplings, S_l is the input cathode luminous sensitivity, V_s is the output screen voltage and η_l is the luminous efficiency of the output screen.

Typical parameters of a three-stage magnetically focused image intensifier tube are: $S_l = 250$ µA/lm, $V_s = 15\,000$ V, $\eta_l = 45$ lm/W, $G_c = 73$, and $n = 2$. These parameters yield a luminous gain $G_l = 8.99 \times 10^5$ fL/fc.

For a generation 2 wafer tube the typical luminous gain parameters are: $S_l = 350$ µA/lm, the current gain of the microchannel plate is $G_c = 500$, $V_s = 6000$ V, and $\eta_l = 12$ lm/W. These parameters yield a luminous gain of 12 600.

Typical luminous gain parameters of a generation 3 tube are: $S_l = 1000$ µA/lm, the current gain of the MCP is $G_c = 175$, $V_s = 6000$ V, and $\eta_l = 12$ lm/W. The luminous gain is 12 600.

8.9.4   Radiant Power Gain of a Single-Stage Tube

The radiant power gain G_p of an image tube is the quotient of the output radiant power P_o and the input radiant power P_i. For a monochromatic illumination the radiant power gain of a single-stage tube is

$$G_p = P_o/P_i = I_c V_s \eta_a/P_i = P_i S_r V_s \eta_a/P_i = S_r V_s \eta_a, \tag{8.33}$$

where S_r is the radiant sensitivity of the photocathode in amperes per watt at the wavelength of the input radiation.

Typical radiant power parameters of a generation 1 image intensifier tube at $\lambda = 600$ nm are: $S_r = 50 \times 10^{-3}$ A/W, $V_s = 15\,000$ V, $\eta_a = 0.04$ W/W. These parameters yield a radiant power gain of $G_p = 30$.

8.9.5   Radiant Power Gain of a Multistage Tube

For a multistage tube the power gain may be obtained by multiplication of equation 8.33 by the current gain of the image tube. Note, however, that S_r is related to the input photocathode and V_s and η_a are related to the output phosphor screen of the multistage tube. The radiant power gain of a multistage tube thus becomes

$$G_p = S_r G_c^n V_s \eta_a, \tag{8.34}$$

where n is the number of interstage couplings, S_r is the radiant sensitivity of the input photocathode, V_s is the output screen voltage, and η_a is the absolute conversion efficiency of the output phosphor screen in watts per watt.

Typical parameters of a three stage generation 1 image intensifier tube at $\lambda = 800$ nm are: $S_r = 40 \times 10^{-3}$ A/W, $G_c = 21$, $V_s = 15\,000$ V, $\eta_a = 0.04$ W/W and $n = 2$. The radiant power gain is $G_p = 1.058 \times 10^4$ W/W.

Typical parameters of a three-stage magnetically focused image intensifier tube at $\lambda = 420$ nm are: $S_r = 80 \times 10^{-3}$ A/W, $V_s = 15\,000$ V, $\eta_a = 0.08$ W/W, and $G_c = 73$. These parameters yield a power gain of $G_p = 5.1 \times 10^5$ W/W.

When the input illumination is generated by a light source which is filtered by a filter $T(\lambda)$, the radiant power gain may be given by

$$G_p = \frac{P_o}{P_i} = \frac{I_c V_s \eta_a}{W_p \int W(\lambda)T(\lambda)d\lambda} = \sigma V_s \eta_a \frac{\int W(\lambda)R(\lambda)T(\lambda)d\lambda}{\int W(\lambda)T(\lambda)d\lambda}, \tag{8.35}$$

where $W(\lambda)$ is the spectral radiation characteristics of the light source normalized to unity at the peak of the radiation characteristics curve, W_p is the peak radiant power of the light source in watts per unit wavelength, $T(\lambda)$ is the spectral transmittance of the filter, and $R(\lambda)$ is the spectral response of the input photocathode.

8.9.6   Infrared Conversion Index

For the specification of the gain characteristics of infrared image tubes which convert the invisible infrared radiation to a visible image, the infrared conversion index has been used. The infrared conversion index is obtained by illumination of the photocathode through a Corning no. 2540 infrared filter with a tungsten filament lamp operated at a color temperature of 2854 K, and by the measurement of the image tube output luminous flux. The value of the infrared conversion index is

$$CI = \frac{\text{output luminous flux}}{L_i T}, \qquad (8.36)$$

where L_i is the input light flux supplied by the tungsten lamp, and T is the infrared filter factor given by

$$T = \frac{\int W(\lambda)R(\lambda)T(\lambda)d\lambda}{\int W(\lambda)R(\lambda)d\lambda} = 0.116, \qquad (8.37)$$

where $W(\lambda)$ is the spectral radiation characteristics of the tungsten lamp, $R(\lambda)$ is the spectral response characteristics of the standard S-1 photocathode surface, and $T(\lambda)$ is the spectral transmission characteristic of Corning no. 2540 filter.

By expressing the output luminous flux with the image tube parameters, the conversion index becomes

$$CI = \frac{I_c V_a \eta_l}{L_i T} = \frac{L_i S_{ir} V_a \eta_l}{0.116 L_i} = \frac{S_{ir} V_a \eta_l}{0.116}, \qquad (8.38)$$

where S_{ir} is the infrared sensitivity of the photocathode.

Typical parameters of an infrared image tube are: $S_{ir} = 4 \ \mu A/lm$, $V_a = 16\,000 \ V$, and $\eta_l = 45 \ lm/W$. The corresponding conversion index is $CI = 24.8$.

8.9.7   Luminous Gain Requirement

In order to take full advantage of the greater light-gathering power of the objective lens and of the greater quantum efficiency of the photocathode, the image intensifier must have sufficient gain to ensure that each photoelectron may produce a visual sensation at the eye, thus extending the region of vision to the lowest light levels. From table 8.1, at 6×10^{-2} fL adaption brightness, the pupil diameter is 4 mm and 524 photons per storage time of the eye are needed to reach the retina to resolve a contrasty object. If a 10-power magnifier is used which has an $f = 25$-mm focal length, the fraction α of light of a point source which may enter the eye is proportional to square

of the angle defined by the pupil diameter D and the focal length f of the ocular as given below:

$$\alpha = \frac{D}{2f} = \frac{4}{50} = 0.08 . \tag{8.39}$$

Assuming a Lambertian emission of light, a point on the screen must radiate the following number N of photons in order to be resolved:

$$N = \frac{524}{\alpha^2} = \frac{524}{(0.08)^2} = 81\ 875 . \tag{8.40}$$

The average photon energy of an RCA 10-52 phosphor screen is on the order of 2.25 eV and consequently the radiant energy is 81 875 × 2.25 = 184 218 eV.

The absolute conversion efficiency of fiber-optic phosphor screens at 6 kV screen potential is typically 2.5%. The electron beam energy producing the radiant energy, therefore, is 184 218/0.025 = 7 371 120 eV.

At 6 kV screen potential the number n of electrons which generate the beam energy is

$$n = \frac{7\ 371\ 120}{6\ 000} = 1\ 228 . \tag{8.41}$$

The luminous gain of the image intensifier with $S = 300$ μA/lm $V_s = 6$ kV, and $\eta = 12$ lm/W is

$$G = SV_s\eta n = 26\ 525 . \tag{8.42}$$

At this gain level the individual electron scintillations are resolved by the dark adapted eye. Note that at $S = 1000$ μA/lm the luminous gain for electron scintillation resolution is $G = 88\ 416$. This indicates that the extension of vision toward lower light levels needs a higher photocathode sensitivity and also a higher gain.

References

Amon, M., et al. "Large Objective for Night Observation," *Applied Optics*, Vol. 10, No. 3, p. 490, March, 1971.

————. "Large Objective for Night Observation," *Applied Optics*, Vol. 10, No. 3, p. 490, March 1971.

Blackwell, H. R. "Contrast Thresholds of the Human Eye," *J. Optical Soc. America*, Vol. 36, No. 11, November 1946.

Csorba, I. P. "Contrast Thresholds of Image-Intensifier-Aided Eye at Low Field-Luminance Levels," *RCA Review*, June 1971.

————. "Current Status of Image Intensification," *Miltronics*, March and May 1981.

————. "Resolution Limitation of Electromagnetically Focused Image Intensifier Tubes," *RCA Review*, March 1969.

————. "Recent Advancements in the Field of Image Intensification: The Generation 3 Wafer Tube," *Applied Optics*, July 15, 1979.

Eberhardt, E. H. "Source-Detector Spectral Matching Factors," *Applied Optics*, Vol. 7, p. 2037, 1968.

Engstrom, R. W. "Calculation of Radiant Photoelectric Sensitivity From Luminous Sensitivity," *RCA Review*, p. 116, March 1955.

Epstein, D. W. "Photometry in Television Engineering," *Electronics*, p. 110, July 1948.

Flamant, F. "Variation du Diametre de la Pupille de L'oeil en Function de la Brilliance," *Rev. Opt.*, Vol. 27, pp. 751-758.

Gardiner, F. T., ed. *Electro-Optics Handbook*, RCA Commercial Engineering, Harrison, NJ, 1968.

Johnson, C. B. "The Influence of High Magnetic Flux Densities on Electromagnetic Focusing of Electrons," *IEEE Transactions on Electron Devices*, p. 1187, December 1971.

Pollehn, H. K. "Statistical Processes and Noise in Image Intensifier Tubes," private communication.

Richards, E. A. "Fundamental Limitations in the Low Light Level Performance of Direct-View Image-Intensifier Systems," *Infrared Physics*, Pergamon Press, London, U. K., Vol. 8, p. 101, 1968.

————. "Limitations in Optical Imaging Devices at Low Light Levels," *Applied Optics*, Vol. 8, No. 10, p. 1999, October 1969.

Rose, A. "The Sensitivity Performance of the Human Eye on an Absolute Scale," *J. Optical Soc. America*, Vol. 38, No. 2, February 1948.

Schade, O. H. "Optical and Photoelectric Analog of the Eye," *J. Optical Soc. America*, Vol. 46, No. 9, September 1956.

Schagen, P. "Electronic Aid to Night Vision," *Television Society Journal*, Vol. 10, No. 7, 1963.

Schober, H. A. W., and R. Hilz, "Contrast Sensitivity of the Human Eye for Square-Wave Gratings," *J. Optical Soc. America*, Vol. 55, No. 9, 1965.

9

IMAGE INTENSIFIER SYSTEMS

9.1 Introduction

The extensive use of image intensifier tubes for intensification of optical images led to the development of a variety of image intensifier tubes and systems. The most frequent applications, however, are night vision, astronomy, research, and medicine. This chapter covers the most important applications of image intensifier tubes and introduces the reader to the image intensifier systems.

Historically, the first family of image intensifier tubes, the generation 0 device, was developed for the infrared telescope. Almost parallel with this effort, the X-ray image intensifier tube was developed first in Europe and later in the United States. The next step in the early effort was the development of the light shutter tube.

A new era in image intensification started with the development of the high-performance electromagnetically focused image intensifier tubes for aerospace, high-resolution aerial photography, astronomy, and extremely low light level intensifications. This development was shortly followed by the development of the generation 1 and 2 and 3 devices.

In this chapter no effort was made to discuss and group the image intensifier systems in historical order or according to their scientific merit. Rather, the frequency of present-day applications took precedence.

9.2   Night Vision Aids

9.2.1   Night Vision Goggles

The night vision goggles are a head-mounted binocular night vision aid for such nighttime tasks as driving, mobile equipment operations, patrol, surveillance, reading, crew use in a helicopter, and other general purpose viewing. The goggles have a 40° field of view and a unity power to provide an unmagnified view of the scene. Individual diopter adjustment for each eye is provided, and bifocal and plane focus versions are also available. The focus range is from 20 cm to infinity. The weight of the goggles is 850 g. Figure 9.1 is a photograph of the night vision goggles.
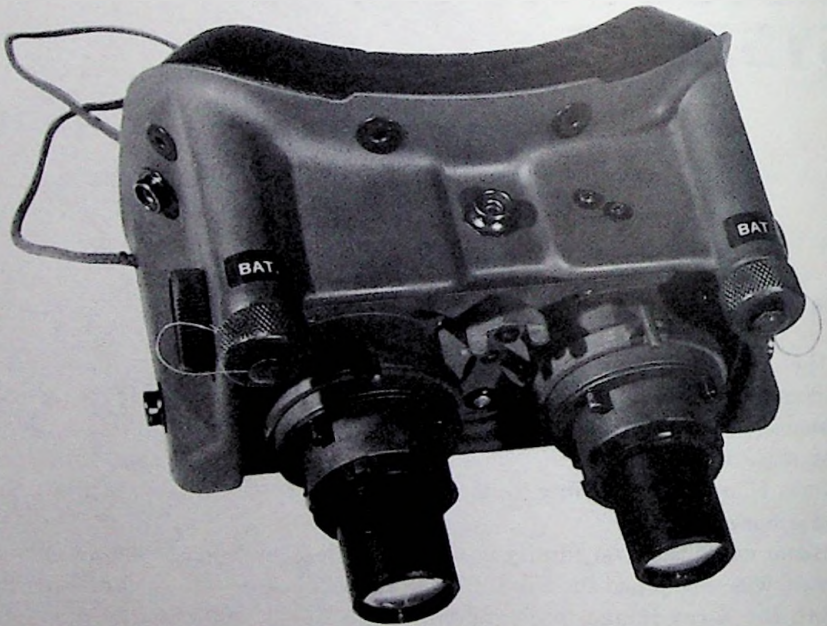
Fig. 9.1   Night vision goggles.

The system of the night vision goggles consists of a pair of 1-power telescopes as shown in figure 9.2. Each telescope consists of an 18-mm-format generation 2 wafer image intensifier tube and an objective (f/1.4; $f = 26.6$ mm) and an eyepiece ($f = 26.9$ mm) lens.

The objective lens focuses the image of the scene on the planocathode fiber optics of the generation 2 wafer tube. The schematic of the generation 2 wafer tube is shown in figure 2.10. Image erection is obtained by the fiber
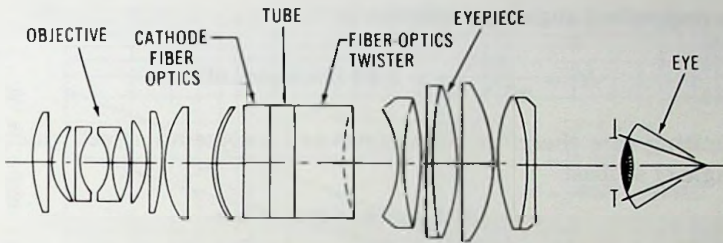
Fig. 9.2   Schematic of night vision goggles.

optics twister to give proper orientation to the observer. The fiber-optics twister has a concave output to simplify the eyepiece design. The objective lens is designed to incorporate 7.0% barrel distortion, which is compensated by 8% pincushion distortion of the eyepiece.

The MTF characteristic of the night vision goggles (AN/PVS-5A) is shown in figure 9.3. The design of the optical system of night vision aids is a compromise between the field of view and resolution. For goggle and pocketscope application a 40° field of view yields a reasonable compromise.

The field resolution of goggles or a pocketscope, utilizing an 18-mm-format image intensifier tube which has a typical limiting resolution of 28 lp/mm, is

$$R_f = 18 \times 28 = 504 \text{ lp}. \tag{9.1}$$
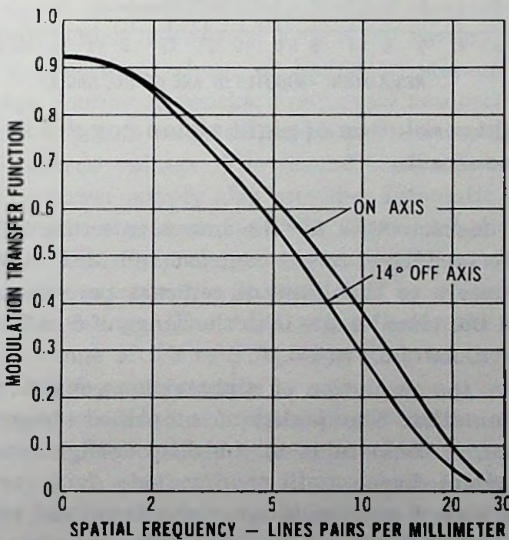
Fig. 9.3   MTF of night vision goggles.

The corresponding angular resolution is

$$R_\gamma = \frac{504}{40 \times 60} = 0.20 \text{ lp/minute of arc}. \tag{9.2}$$

In a limiting case therefore the goggles can resolve an object which has a visual angle of at least

$$\alpha = 1/0.2 = 5 \text{ minutes of arc}. \tag{9.3}$$

For comparison, the limiting resolution of the eye is 1 minute of arc.

The resolution of the goggles is also a function of target contrast as shown in figure 9.4. The functional relationship of figure 9.4 was obtained by use
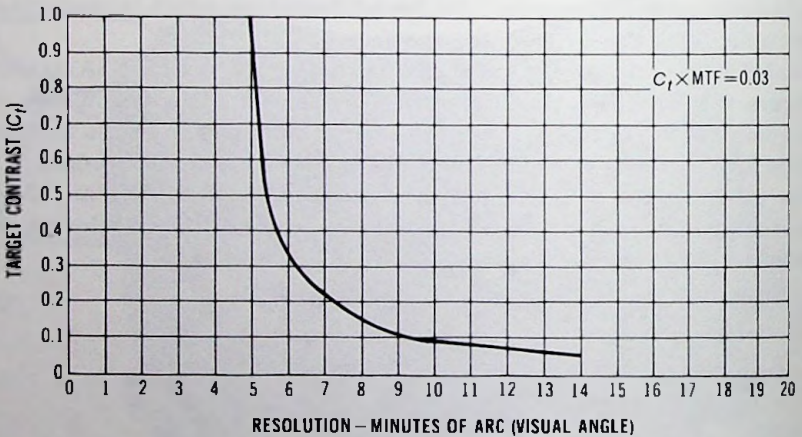
Fig. 9.4 Highlight resolution of night vision goggles as a function of target contrast.

of a typical MTF characteristic for the image intensifier. At each spatial frequency point the product of target contrast and MTF is 0.03, which corresponds approximately to the limit of contrast perception (liminal contrast). In figure 9.4 the visual angle is in the range of 5 to 9.4 minutes of arc for target contrast values of 0.1 to 1.0.

Figure 9.5 shows the resolution of night vision goggles as a function of photocathode illumination. The quality of intensified image, as far as resolution is concerned, is comparable to the deep twilight conditions for the unaided and dark adapted eye.

With 8° field of view 1 minute of arc night-vision aid resolution can be obtained with image intensifier binoculars. The sharpness of the image,
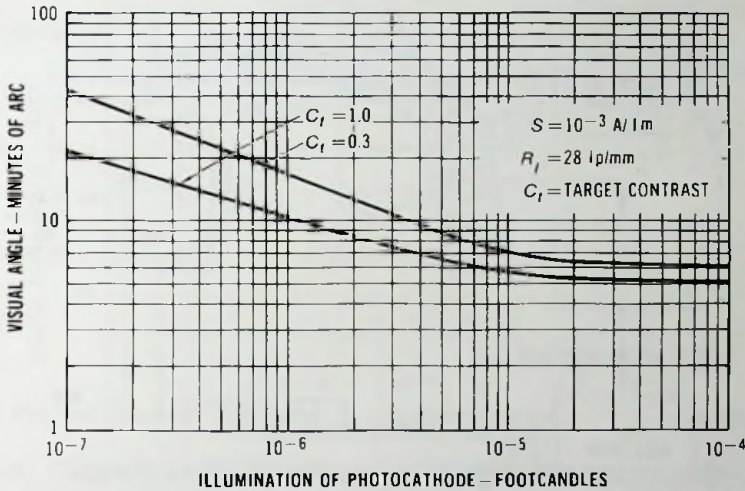
Fig. 9.5   **Resolution of night vision goggles as a function of photo-cathode illumination.**

under these conditions, equals the sharpness of the naked eye. The view of the scene, however, is magnified and the peripheral view of the scene is lost.

As far as operation is concerned, the image tube voltages (cathode, MCP, and screen voltages) are supplied by a rugged wraparound voltage-regulated power supply which is powered by a 2.7-V battery. The power supply operates by a conventional chain of oscillator, step-up transformer and multistage voltage doubler networks. Frequently two oscillators are present as shown in figure 9.6. One oscillator supplies a positive 6-kV screen voltage and a −200-V cathode voltage. The second oscillator supplies a variable MCP voltage. The power supply also provides automatic brightness control (ABC) and bright source protection (BSP). Figure 9.7 shows a typical gain saturation characteristic of a packaged generation 2 wafer tube.

Automatic brightness control is accomplished by automatic control of the microchannel plate voltage. The ABC action holds the maximum output brightness in the range of 0.3 to 3 fL, depending on the maximum output brightness and tube life requirements.

Bright source protection is accomplished by reduction of the cathode voltage above a certain photocathode current level as shown, for example, in figure 9.8. At very high photocathode illumination levels, image transmission is ensured by holding the cathode voltage at a level of a few volts.

The gain saturation characteristics of the microchannel plate are an ad-
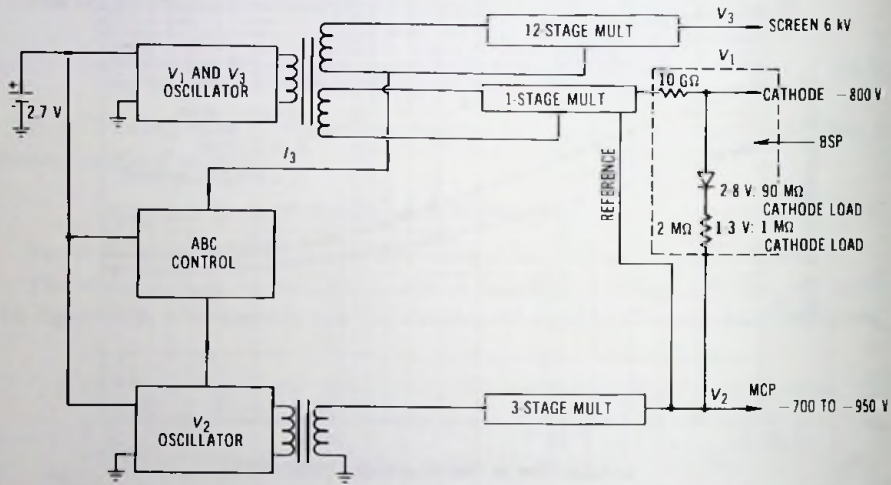
Fig. 9.6 Generation 2 power supply block diagram.

Fig. 9.7 Gain/saturation characteristics.
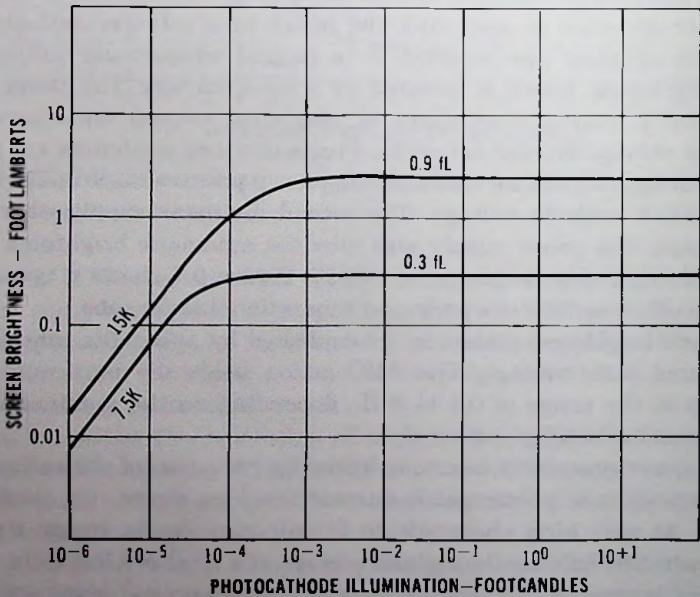
PHOTOCATHODE CURRENT — AMPERES
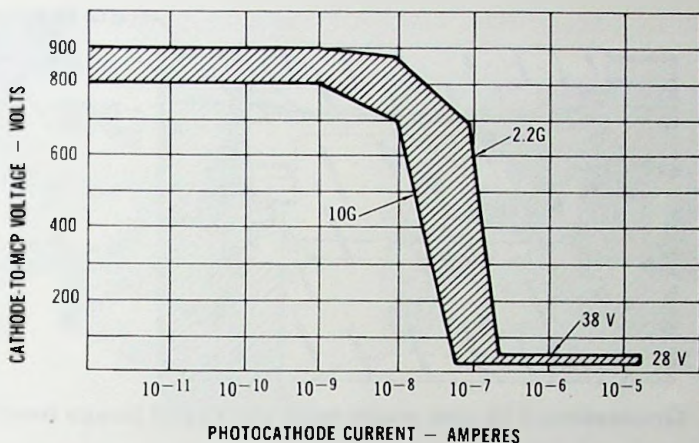
Fig. 9.8   Cathode-to-MCP voltage for bright source protection.

ditional parameter which is utilized in the wafer image intensifier tube system for the brightness reduction of small bright sources, such as, for example, automobile lights. The combined action of ABC, BSP, and microchannel plate gain saturation may, for example, reduce a 5000-fc, 1-mm^2 input light spot to approximately a 100-fL output luminance, thus providing the necessary eye relief against bright sources.

Hermetic sealing and packaging protect the image intensifier tube and power supply assemblies from moisture and provide insulation. For sealing, the assemblies are primed with an adhesive. Insulation is provided by a deaired and activated silicon rubber potting compound. The outline of a packaged generation 2 wafer tube and power supply assembly is shown in figure 9.9. The image tube, power supply, and housing are joined together by components of the generation 2 and generation 3 image intensifier assemblies. Figure 9.10 shows the components of the generation 2 and generation 3 image intensifier assemblies. From left to right are the generation 3 power supply, the generation 2 power supply, the generation 3 packaged image intensifier, the generation 2 image intensifier tube, the generation 3 image intensifier tube, and a 2.7-V battery.

9.2.2   Pocketscope

The pocketscope is a hand-held, monocular night-vision aid small enough to be carried in a pocket. It has been developed for patients suffering from night blindness. Figure 9.11 shows a picture of pocketscopes in use.

The pocketscope utilizes an 18-mm generation 2 wafer image intensifier tube with a wraparound 6-V rechargeable battery power supply. The 26-mm
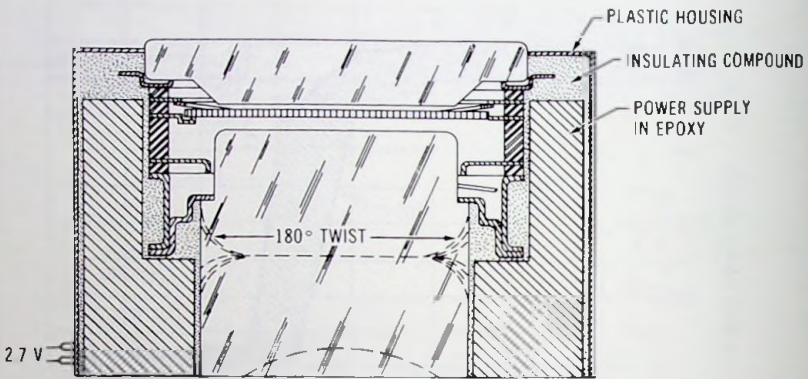
Fig. 9.9 Generation 2 18-mm wafer tube packaged image intensifier.

Fig. 9.10 Generation 2 and 3 image intensifier components.

focal length objective and eyepiece lenses provide a 40° field of view and unity power magnification.

The optical system of the pocketscope is identical with the telescopic system of the night vision goggles.

9.2.3 Generation 1 Starlight Scope Assembly

The generation 1 image intensifier starlight scope utilizes a three-stage cascaded image intensifier tube for night vision. The schematic arrangement of the cascade image tube and power supply is shown in figure 9.12. The generation 1 single-stage modules are coupled and sealed together to provide a three-stage tube by a thin layer of laminating resin used for bonding glass to glass elements. The image tube voltages are supplied by a rugged wraparound power supply powered by a battery. The image tube and the power supply are potted with silicon rubber to provide insulation and hermetic sealing of the image intensifier assembly.

The advantage of the cascaded generation 1 image tube over the generation 2 and 3 tubes is the less than unity noise figure, which enables it to
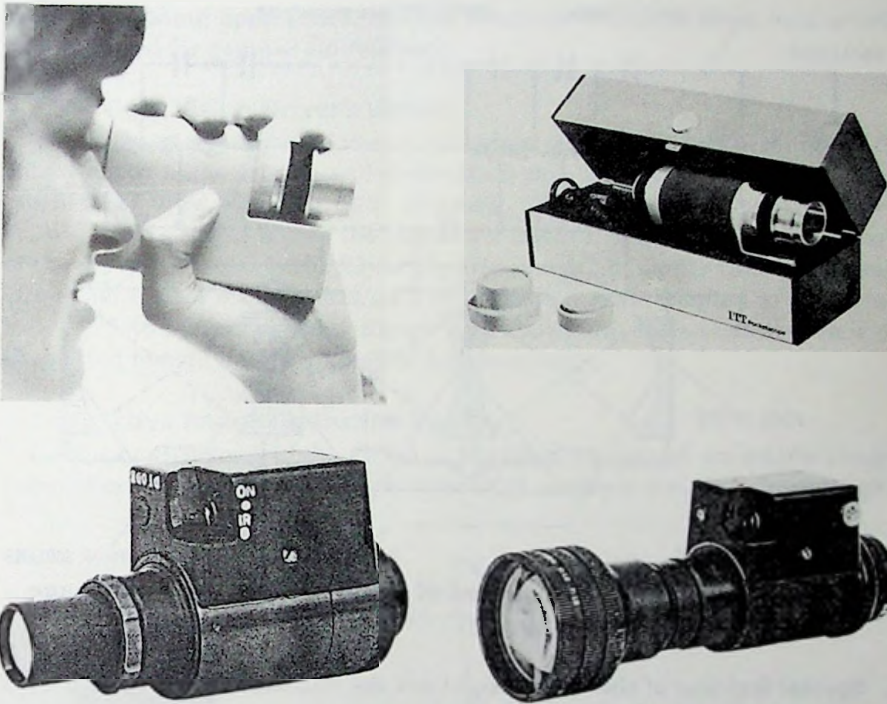
Fig. 9.11   Four night viewing pocketscopes.

provide a superior low light level resolution at relatively low photocathode sensitivity values.

9.2.4   Night Vision Weaponsight

Figure 9.13 shows the second-generation Night Owl night-vision weaponsight, which provides the soldier with night observation and weaponfire capabilities under battlefield conditions.

The major components of the weaponsight are the 155-mm, six-element objective lens assembly, the 25-mm microchannel image intensifier tube, and an eight-element eyepiece lens assembly.

The night vision weaponsight operates by using light from the night sky. The objective lens focuses the image of scene on the photocathode of the image intensifier tube, which amplifies the input image approximately 20 000 times for display on the tube's phosphor screen. The output image is viewed through the eyepiece lens, which magnifies and focuses the displayed image to the naked eye.
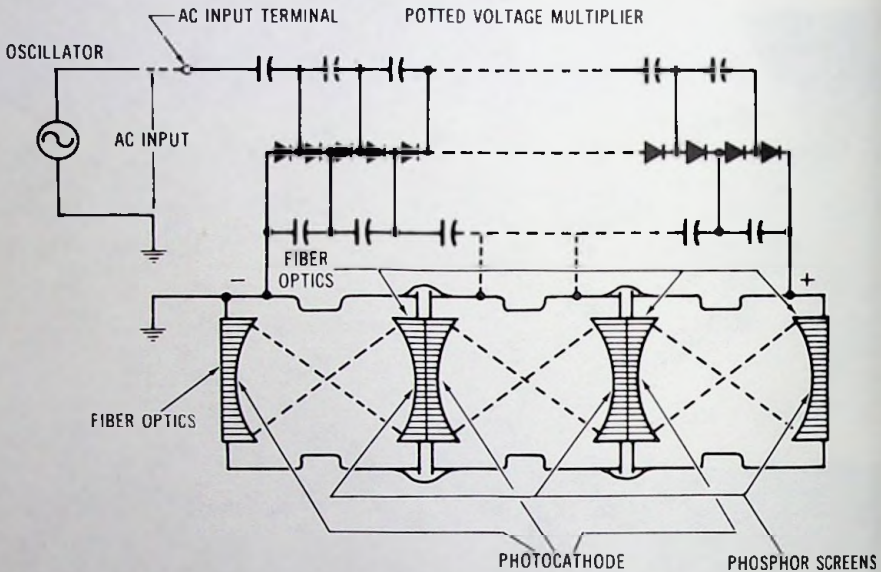
Fig. 9.12   Schematic arrangement of a three-stage cascaded image tube and power supply.

Special features of the weaponsight are the automatic brightness control and flash suppression. The flash suppression circuit ensures good image transmission by suppression of flashes when explosion, fires, or tracers occur in the field of view. In addition, the presence of only one phosphor screen in the second generation image intensifier allows the system to operate without image smear when one is observing a moving target.

The sight is attached and zeroed to weapons (machine guns, recoilless
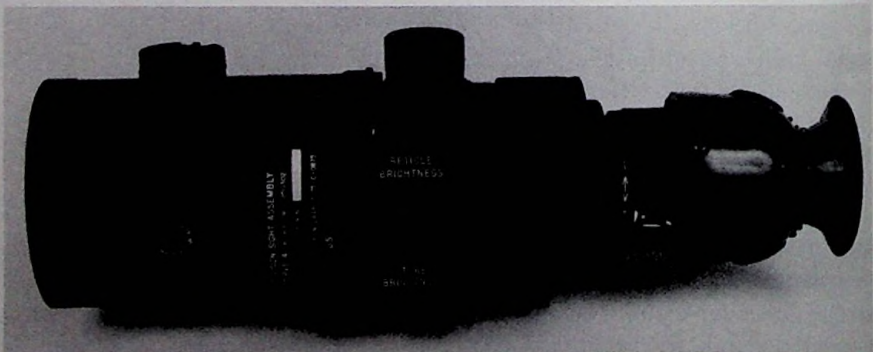
Fig. 9.13   Night vision sight. (*Courtesy Applied Services Corporation*)

rifles, etc.) using appropriate adapter brackets. It can be hand-held or tri-pod-mounted for general surveillance.

9.2.5   Night Vision Driver's Viewer

The night vision driver's viewer provides combat vehicle personnel with closed-hatch night driving and observation capabilities. It has a 45° rotata-ble field of view allowing 135° scanning. The viewer is shown in figure 9.14A. Figure 9.14B shows the schematic of the driver's viewer. The heart of the driver's viewer is the 25-mm hybrid image intensifier tube consisting of a generation 2 or a generation 3 wafer tube module coupled to a genera-tion 1, 25:46 magnifier tube. Figure 9.15 shows the cross-sectional view of the potted hybrid image intensifier tube assembly.

9.2.6   Active Image Intensifier System

Exceptionally good night vision is obtained by use of an active image intensifier system. Active image intensifier systems use an infrared light
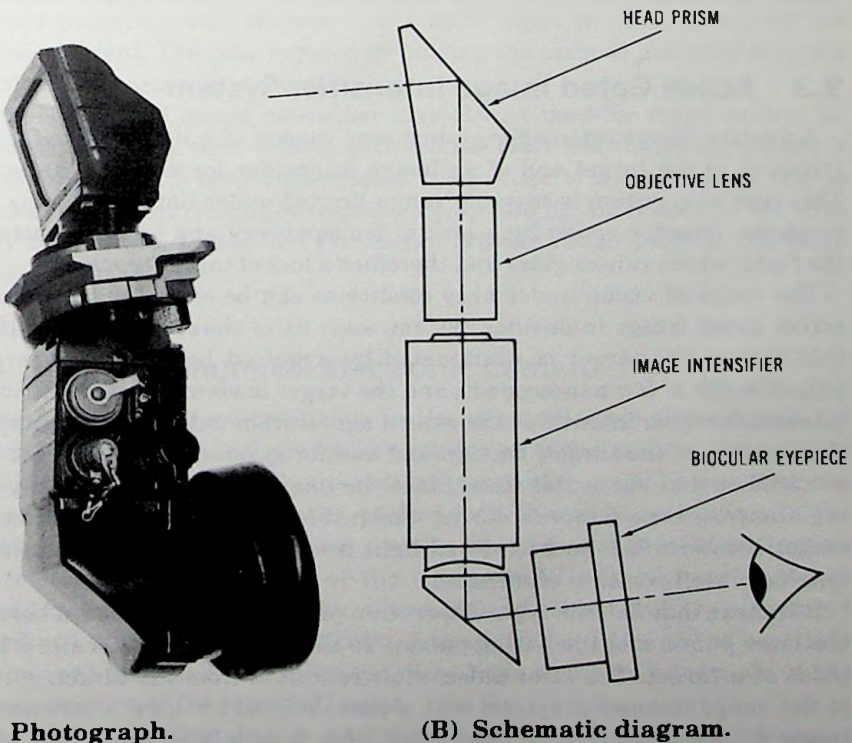
(A) Photograph.   (B) Schematic diagram.

Fig. 9.14   Night vision driver's viewer. (*Courtesy Applied Devices Cor-poration*)
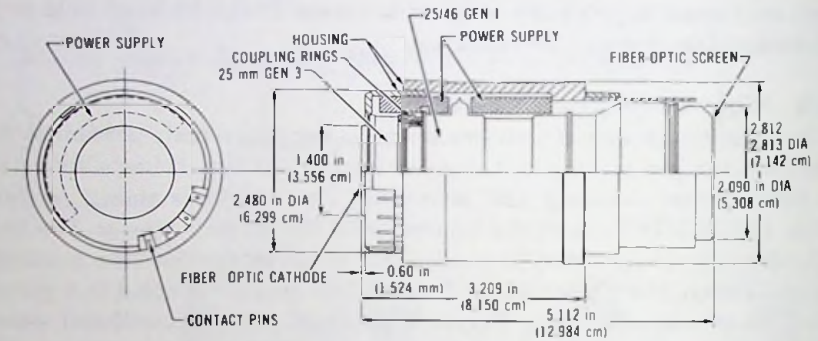
Fig. 9.15   Cross section of a potted hybrid image intensifier tube.

source (an infrared lamp or a laser) to illuminate the target. The target is viewed through an infrared image intensifier consisting of an image converter tube having an S-1 cathode and an objective and an eyepiece lens.

9.3   Active Gated Image Intensifier System

An active image intensifier system may consist of a light source for illumination of the target and of an image intensifier for viewing the target. This type of a system is severely range limited under hazy conditions. Fog or smoke impedes vision by a lack of transparency and by backscattering the light, which causes glare and therefore a loss of target contrast.

The range of vision under hazy conditions can be extended by use of an active gated image intensifier system, such as is shown in figure 9.16. In this system the target is illuminated by a pulsed laser beam, having a pulsed width of few nanoseconds, and the target is viewed by a gated image intensifier which intensifies the return signal from only a narrow range in the vicinity of the target; background and foreground objects are not illuminated at that particular time. Since the image intensifier is on only during a narrow time interval, during which the laser light reflected from the target is intensified, backscattered light from haze arriving during the intensifier cutoff period is eliminated.

It is clear that for this type of operation precise timing is needed between the laser pulses and the gating pulses. To illustrate this, let us aim a laser pulse at a target. The laser pulse, after reflection from the target, returns to the image intensifier system with a time delay of $t = 2d/c$, where d is the target distance and c is the velocity of light. Precisely at the arrival of the laser pulse, the image intensifier is gated for a short period and the target
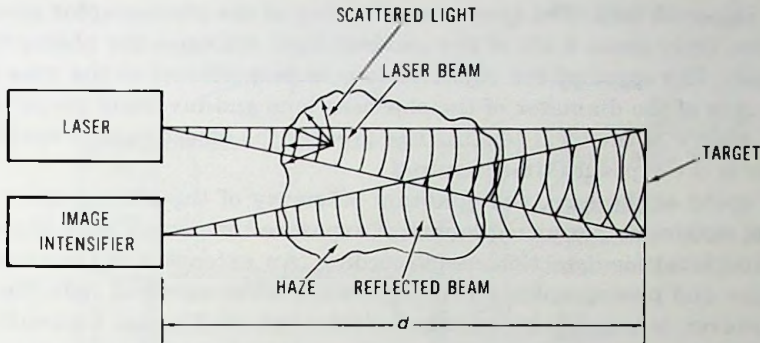
Fig. 9.16   Active gated image intensifier system.

image is intensified. The depth Δd of the field is proportional to the width W of the gating pulse: $\Delta d = cW$.

Gating of the image intensifier is accomplished by biasing the wafer tube cathode potential with respect to the MCP input in order to cut off the cathode current. The tube is gated by pulsing the cathode potential from the cutoff value to the transmission value.

An active gated image intensifier may also be used for range finding. As outlined above, the time delay t, between the laser and the gating pulses, is proportional to the target distance d. The range of a target thus can be obtained by measurement of the time delay and by conversion of the time delay to distance. Picosecond pulses can provide range gates in the millimeter dimension.

9.4   The Astronomical Electronic Camera

The optical telescope operating in the ultraviolet visible and infrared region of the electromagnetic spectrum was one of the earliest instruments used by astronomers to study the radiant image of celestial bodies. With the use of the optical telescope the preliminary observations leading to the setting up of the experiment are usually done by simply looking through the telescope. The main part of the astronomical work, however, is performed by means of photographic exposures and other auxiliary equipment recordings of the celestial radiation. Indeed, without the use of auxiliary equipment attached to the telescope, very little would be known about the physical nature of the celestial bodies.

In simple telescope photography the efficiency of the recording is determined by the quantum efficiency of the photographic plate and by the speed

of the objective lens. The quantum efficiency of the photographic plates is very low. Only about 0.5% of the incident light activates the photographic emulsion. The speed of the objective lens is proportional to the area or to the square of the diameter of the objective lens and inversely proportional to the square of the focal length. The greater the objective lens speed, the smaller is the exposure time required.

The speed of the lens, the quantum efficiency of the photographic film, and the maximum permitted length of exposure time establish a threshold radiation level for detection and recording. An extension of the region of detection and photographic recording toward lower celestial radiation levels, however, is possible by means of electro-optical devices. Currently the most efficient method of recording weak celestial light is by means of electronic image intensification through the use of an image intensifier tube. With the use of image intensifier tubes, exposures are speeded up by a factor of 100 or more.

For the electronic intensification of starlight the electromagnetically focused image intensifier is most frequently used. The electromagnetically focused image intensifier tubes are favored by the astronomers over the other types of image intensifier tubes because of their superior performance, resulting in very low image tube background noise, small geometrical distortion, excellent uniformity and shading characteristics, freedom from the microchannel plate and fiber-optic pattern, and high resolution and intensification.

Figure 9.17 shows the schematic of a two-stage electromagnetically focused image intensifier tube system. The objective lens focuses the image of a celestial body on the plane input photocathode of the image intensifier tube, producing a photoelectron image. The photoelectron image is focused on the interstage phosphor screen by a set of homogeneous axial electric and magnetic fields, producing an intensified light image which is coupled through the mica to the photocathode of the second stage. The electron image of the interstage photocathode is sharply focused on the viewing screen by the homogeneous axial electric and magnetic fields to provide the final intensified light image, which is transmitted on the photographic plate by a relay lens for recording the radiant image of the celestial body.

The luminous gain of a two-stage electromagnetically focused image tube is typically 5000 to 12 000, the typical resolution is 55 lp/mm and the EBI is less than 10^{-14} W/cm^2 for a multialkali photocathode input and is in the range of 10^{-16} W/cm^2 to 10^{-15} W/cm^2 for the bialkali photocathode input.

Ion scintillations are part of the residual screen radiation. Although they do not contribute measurably to the EBI, they are a great concern in image tube cameras at long exposure times. Because of their greater brilliance, ion scintillations are more noticeable on the photographic film than the
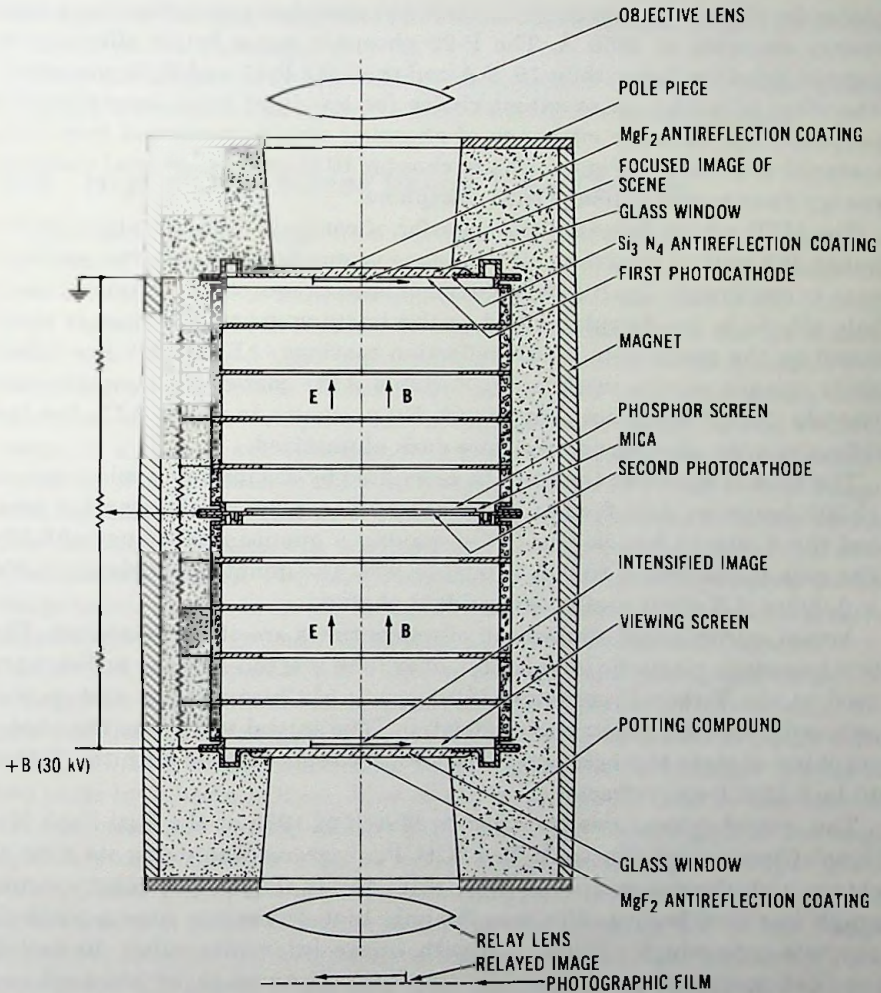
Fig. 9.17   Astronomical electronic camera.

electron scintillations. Ion scintillations, therefore, may limit the exposure time by fogging the film. The ion count of magnetically focused image intensifier tubes is typically less than 0.1 ions per second per square centimeter.

When the output of the image tube is photographed, a good match to the film response is obtained by the use of a P-11 (ZnS:Ag) phosphor. The peak of the spectral emission characteristics of this phosphor is in the blue region at 4600 Å. Therefore the luminous efficiency is only about 10 lm/W. Another

choice for photography is the P-22 (ZnS:Ag) phosphor screen that has a peak energy emission at 4450 Å. The P-22 phosphor has a better efficiency at current densities lower than 10^{-10} A/cm^2 than the P-11 and P-20 phosphors. Therefore it is also an excellent choice for low light level intensification purposes. The absolute efficiency of phosphor screens processed from P-22 material is about 9%. Figure 10.4 in chapter 10 shows the spectral emission energy distribution of image tube phosphors.

The MTF, which describes the transfer of contrast from the object to the image, is a critical parameter of the image intensifier tube as far as performance is concerned. Quality image transmission requires the elimination of halo effects in the faceplates and in the imaging space. Halation is minimized by the application of antireflection coatings (ARC) and a low-reflectivity opaque screen metalizing. Suitable ARC coatings are magnesium flouride (MgF$_2$) and silicon nitride (Si$_3$N$_4$) as shown in figure 9.17. For low reflectivity the phosphor screens are dark aluminized.

The gain in exposure time can be estimated by assuming a typical case of 10 000 luminous gain for the image intensifier, a 3% efficiency relay lens, and the Eastman Kodak II a-O film having a quantum efficiency of 0.5%. The gain to the film is 10 000 × 0.03 = 300. The quantum efficiency is 300 × 0.005 = 1.5 silver grains per incident photon.

Actual astronomical application of image tubes are of great interest. The first two-stage magnetic image intensifier tube was put into use in February 1965 at the Yerkes Observatory (University of Chicago). The system was primarily used for spectral classification. The initial work was the photographing of stars through narrow-band interference filters with the Yerkes 40-inch (101.6-cm) refractor.

The second system was installed in March of 1965 at the Kitt Peak National Observatory (Tucson). The Kitt Peak group was using its tube to obtain high-dispersion spectra from interstellar clouds. The solar spectrograph was used because this was the only high-dispersion spectrograph on any telescope which can be used with image intensifier tubes. In earlier recorded spectrographs a calcium line was observed to be smeared and broad. With the image intensifier tubes and the solar high-resolution spectrograph, this smeared line was resolved into finer components. The interpretation of these fine components was that there are clouds in interstellar space which are moving with various velocities toward and away from the earth which cause different Doppler shifts in the calcium lines.

Another intensifier system was installed at Lowell Observatory at Flagstaff, Arizona, and has been used to study the spectra of quasars. Because of the increased red sensitivity of the image intensifier over that of film, the astronomers have been able to obtain more lines extending farther into the

red region of the spectrum than have been obtained on the 200-in (508-cm) telescope on Mt. Palomar.

After the above early pioneering work, image intensifier tubes gained wide applications in astronomy in many locations around the world.

9.5   High-Speed Streak Image Tube Camera

High-speed streak image tube cameras are used to study and record photoevents of very short duration, such as occur in nuclear fusion research, laser research, plasma radiation research, and in other intense electromagnetic radiation research studies. The most essential part of the instrumentation is a high-speed light shutter image tube which has a spherical grid for gating and deflection plates in the anode cone region for streak mode operation as shown in figure 2.6. In streak mode operation the electron image of a photoevent is deflected in order to display the light intensity variation as a function of time at the phosphor screen. The streak image, after suitable intensification, is photographed and the light intensity versus time function is obtained by scanning the developed photographic film with a microdensitometer. The time resolution capability of high-speed streak image tube cameras is on the order of 1 to a few picoseconds, which is more than an order of magnitude faster than any other photoelectric device.

In streak mode operation the photoevent and the gating and deflection voltages are synchronous. Time concurrence is obtained by derivation of the gate and deflection triggers from the same source as shown in figure 9.18. In figure 9.18 a mode-locked laser beam of picoseconds duration is split in two parts by a beam splitter. Half of the laser light is used to synchronize the deflection and gating voltage generators. The second half of the laser light is passed through a pulse delay device consisting of wedged glass plates. These plates are spaced and arranged to reflect and converge the light to form a narrow luminous line at the entrance slit of the image intensifier system, and to provide a train of delayed light pulses for each laser pulse. The length of the light path determines the pulse delay and the spacings between the wedged plates establish the time delay between two successive reflected light pulses.

The recording of picoseconds duration pulses requires a high streak velocity that is usually on the order of 2×10^{11} mm/s. Even then, the width of a picosecond pulse is only 0.2 mm as displayed on the phosphor screen. It is clear, therefore, that the image intensifier system must have a sufficiently high resolution and deflection speed to be able to display picosecond duration pulses. In absence of transit-time spread limitation of time resolution, two photoevents can be resolved in streak mode when they are spatially at
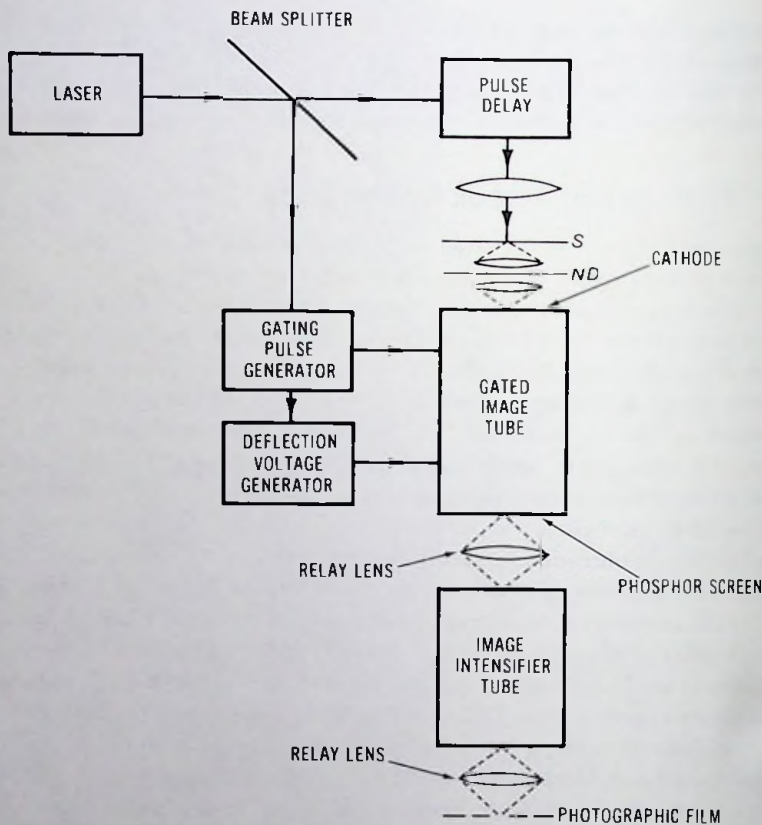
Fig. 9.18   Streak image tube camera.

a minimum distance of $1/R$ from each other, where R is the spatial resolution of the image intensifier system in line pairs per millimeter. The resolution distance, in the limiting case, is equal to the progression of the streak:

$$1/R = v\tau, \tag{9.4}$$

or

$$\tau = 1/Rv, \tag{9.5}$$

where v is the streak velocity in millimeters per second and τ is the time resolution of the image intensifier system in seconds.

From the above equations a time resolution of 1 ps requires 2×10^{11} mm/s streak velocity and 5 lp/mm spatial resolution.

For time intervals greater than τ the contrast of the streak image is determined by the MTF of the streak image camera system.

At a streak velocity of 2×10^{11} mm/s, loss of deflection sensitivity due to high-frequency effects is not negligible. High reactive currents which are present between the deflection plates are also significant. Deflection power and frequency can be reduced or deflection speed can be increased by use of an x (horizontal) and y (vertical) deflection system. The beam deflection structure consists of two pairs of deflection plates set at right angles and placed along the axis of the image tube in the field-free region of the anode cone. One pair of deflection plates deflects in the x direction and the other pair in the y direction. Circular deflection is obtained by two phase-related sinusoidal voltages applied to each pair of deflection plates. The advantages of the x,y deflection system over single-pair deflection are that it produces π times more deflection speed per applied voltage than a single-pair system and that it is easier to produce sine-wave voltage than sawtooth voltages.

For time intervals greater than τ the contrast of the streak image is determined by the MTF of the streak image camera system.

In addition to the streak velocity and spatial resolution, time resolution is also limited by the transit-time spread of photoelectrons traveling from the photocathode to the phosphor screen. This limitation is discussed in greater detail in chapter 7. Accordingly the transit-time spread limited time resolution produced by the emission energy spread of photoelectrons is

$$\tau = 2 \times 10^{-8}\sqrt{V_{im}}/E_c, \tag{9.6}$$

where V_{im} is the voltage equivalent of the emission energy spread in volts and E_c is the cathode field strength in volts per centimeter.

From equation 9.6, 1 ps transit-time limited time resolution for $V_{im} = 0.3$ V requires a cathode field strength of approximately 10 000 V/cm.

Quantum noise is another limiting factor affecting the time resolution at picosecond pulse time duration. This phenomenon is the same as experienced at low light level, whereas photoelectron statistics limit resolution. Because of the shortness of the pulse time duration even at very intense light levels, only few electrons might be emitted by a resolution element. To show this, let us assume bright light pulses generating 10^{-2} A/cm^2 photocathode current density in a resolution element of 10^{-4} cm^2 during 10^{-12} s. The total charge per pulse and per resolution elements is $Q = 10^{-2} \times 10^{-12} \times 10^{-4} = 10^{-18}$ C, corresponding to 6.28 electrons. Since a human observer needs at least 10 electrons to consistently resolve a resolution element, the above conditions produce quantum noise limitation of spatial resolution which may affect time resolution as explained in connection with equation 9.5. Quantum noise limitation may be avoided by streaking the light pulses

across the screen repetitively over many light pulses with successive traces accurately superimposed.

A streak image can be photographed only if there is enough gain. Eastman Kodak's 2485 film requires 6.243×10^7 eV/mm^2 from a P-11 phosphor in order to be developed to a density 1. Suppose that the area of a resolution element is 0.1 mm^2, the phosphor efficiency is 5% and the electron beam voltage is 15 kV. The number of electrons required for the development of a 0.1 mm^2 area then becomes

$$N = \frac{0.1 \times 6.243 \times 10^7}{15 \times 10^3 \times 0.05} = 8.324 \times 10^4 \text{ electrons.} \qquad (9.7)$$

The above number also gives the electron gain of the image intensifier system required to record individual photoelectron scintillation.

9.6   X-Ray Image Conversion and Intensification

Because of their great penetrating ability, X-rays are often used for imaging the hidden structural details of objects such as the human body, a transistor, an image tube, etc. Roentgen demonstrated in 1895 that X-rays are able to penetrate dense objects and form a latent image of these objects. The latent image can be made visible on a fluorescent screen.

Figure 9.19 shows the diagram of X-ray imaging. In this process the object is illuminated by a uniform X-ray beam. The X-rays penetrate the object and experience absorption, which is a function of the thickness and the absorption coefficient of the material. Therefore an object that has a varying thickness or contains nonhomogeneity in its structure translates a homogeneous X-ray beam into local intensity variations. The beam-intensity
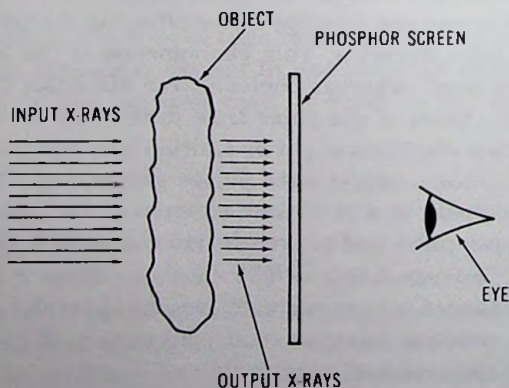
Fig. 9.19   X-ray imaging.

pattern produced by these variations is made visible by conversion of the X-rays into visible light by a fluorescent screen. In this manner the structural details of the object are displayed in terms of brightness variation.

Simple X-ray fluoroscopy, as described above, has the drawback of requiring a high-intensity X-ray source, and, in addition, the fluorescent image is brightness and quantum noise limited.

In the case of medical roentgenoscopy the brightness of the fluorescent screen is comparable to the full-moon illumination of a scene, because the X-ray doses used for this application may not exceed certain limits as otherwise physiologic and genetic damage results. At such a low brightness level, human vision is seriously limited by the small amount of light available and by the statistical variation of the light level leading to a loss of fine detail and low contrast that is contained in the X-ray image.

The fluoroscopic process can be improved by use of an image intensifier which has a sufficient quantum efficiency and gain to eliminate the physiologic limitations of the eye and to enable the observer to perceive all information present in the X-ray image. Figure 9.20 shows the schematic diagram of an electrostatically focused minifying type of X-ray image intensifier system. The X-rays after passing through the object are absorbed and converted to light by a relatively thick X-ray phosphor screen which is supported by a thin aluminum dome mounted on the vacuum side of the
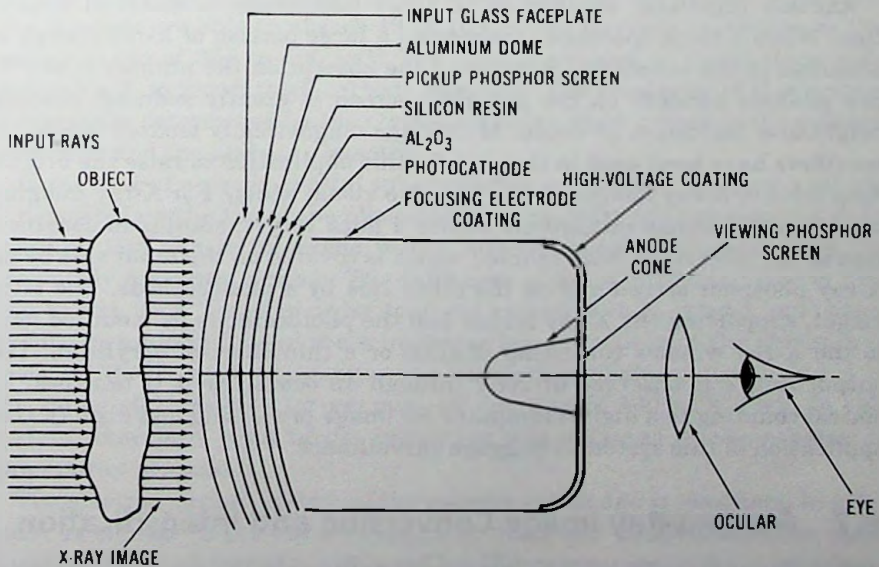
Fig. 9.20   Schematic diagram of an X-ray image intensifier system.

input glass window. The phosphor layer is covered with a transparent thin layer of silicon resin coating to make the phosphor surface as smooth as possible, and with a thin layer of aluminum oxide (Al_2O_3) coating to provide a transparent barrier layer between the silicon resin and the photocathode. The semitransparent photocathode of Cs_3Sb or Na_2KSb type is deposited over the aluminum oxide coating. The photocathode converts the fluorescent light image into a photoelectron image. The photoelectron image is imaged on the viewing screen by a minifying centrally symmetric electrostatic electron lens which minifies the image by a factor of about 8:1 and therefore increases the brightness of the output image by $8 \times 8 = 64$. The brightness gain of the image intensifier is the product of the gain due to geometrical minification and the genuine light flux gain.

At a screen potential of 25 kV, therefore, the brightness gain is typically more than 1000. This gain is sufficiently high to provide the observer with a bright output image suitable for normal daylight vision. At present, however, rarely does one observe the output of the X-ray intensifier with the eye; the output image is televised by optical coupling to a television camera tube and then to a digital computer for image processing, image storage, and display. This is called *digital radiography*. Simple image processing procedures involve edge enhancement, size discrimination, and contrast enhancement. With these manipulations, details in image can be displayed and examined which were not discernible in the original image.

Another important application of X-ray fluoroscopy is material inspection. When a thick specimen is inspected a large portion of X-ray energy is absorbed in the substance. Because of the absorption the number of the X-ray photons incident on the phosphor screen is greatly reduced, causing brightness limitation of vision. Multistage magnetically focused image intensifiers have been used in the past for this application to raise the brightness level of X-ray images and to improve visual acuity. For X-ray imaging the magnetic image intensifiers utilize a mica target, similar in construction to the interstage mica coupler, which is covered on the input side by an X-ray phosphor screen and on the other side by a photocathode. The mica target, supporting the X-ray screen and the photocathode, is mounted next to the X-ray window consisting of glass or a thin sheet of beryllium. The output image is observed directly through an ocular, or it is televised by optical coupling to a digital computer for image processing and display. One application of this system is baggage surveillance.

9.7 Gamma-Ray Image Conversion and Intensification

The penetrating ability of gamma rays made possible the development of other types of imaging systems for the visualization of organs beneath the skin surface of the human body. An organ within the living body can be

made radiant by a radioactive isotope administered by mouth or intravenously. Some organs absorb more radioactive drug than others, giving rise to a distinct gamma-ray radiation pattern that permits the visualization of the organs.

For the safety of the patient the intensity of the gamma-ray radiation must be minimized, which leads to a weak radiation field. The weak radiation pattern needs amplification for detection and recording. A frequent recording technique, which can provide the user with fast and reliable results, is photography. A photograph of the radiation pattern can be obtained by use of a gamma-ray image intensifier tube camera which converts the gamma-ray radiation pattern to light and sufficiently intensifies the image for short exposure times. Exposure times can be short enough to effectively stop the motion of heart and lungs.

In order to obtain an intensified image of a gamma-ray pattern, first it must be imaged on the input of the image intensifier tube. Since sharp focusing gamma-ray lenses are not available, imaging is accomplished by a pinhole as shown in figure 9.21. The gamma rays admitted by the pinhole irradiate a thallium-activated sodium iodine [NaI(Tl)] scintillator mosaic packed on the atmospheric side of the photocathode faceplate, or in another type, a CsI(Tl) single-crystal spherical disk scintillator mounted on the vacuum side of the input faceplate.

In one version of the mosaic type of input targets, the gamma rays are heavily absorbed in a 25-mm thick, 5-mm size, mosaic crystal structure. The crystals are able to absorb 49 to 70% of the incident radiations in the energy range of 365 to 500 keV. The light is coupled to the photocathode through a 2- to 3-mm thick cathode faceplate. The resolution of this system is primarily determined by the crystal diameter, light spread in the cathode faceplate, and the pinhole diameter.

In the case of a single-crystal spherical-disk scintillator, the photocathode is deposited on the top of the phosphor layer in order to eliminate the light coupling loss and light spread in the cathode faceplate drawbacks of the previously described system. The thickness of the scintillator layer is limited to less than 2 mm in order to avoid excessive light spread and consequently resolution loss in the scintillator layer. Because of the thinness of the scintillator layer, the gamma-ray absorption efficiency is low and is in the range of 10 to 35% for gamma-ray energies of 140 to 270 kV. In this system, therefore, high target resolution was obtained at the expense of gamma-ray absorption.

The electron optical system of the gamma-ray image intensifiers, in principle, is similar to the electron optics of the X-ray image intensifier tube, namely, the photocathode is focused on the output screen by a minifying electrostatic electron lens.

The gain requirement is an important consideration of gamma-ray cam-
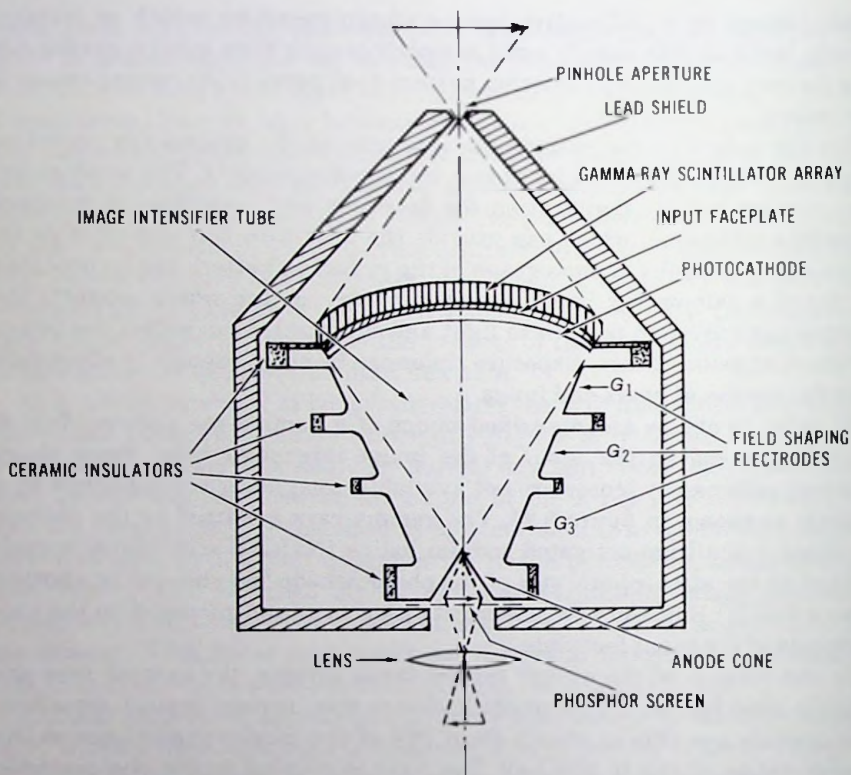
Fig. 9.21 Schematic diagram of a gamma-ray image intensifier
system.

eras. It is estimated that for photographic recording of a gamma-ray scintil-
lation about 2.3×10^7 photons are needed to fully expose a 1-mm² area of
the photographic plate (Kodak 2485 exposed to P-11 phosphor radiation).

If an iodine-131 radioisotope is used, which has a 365-keV gamma-ray
photon energy, and the conversion efficiency of the scintillator phosphor is
10%, a gamma-ray photon can yield 1.2×10^4 light photons of 3-eV energy.
For photography, therefore, the required intensifier gain is 1.9×10^3.

It is obvious that a single-stage intensifier tube cannot yield the required
gain. Additional gain is obtained by coupling the output of the gamma-ray
image converter tube to a multistage image intensifier tube. Two- or three-
stage magnetically focused gated image intensifier tubes may be used for
this application. The output image of the gamma-ray tube is split into two
routes. The first route is through the magnetic image intensifier and the

second to a photomultiplier coupled to a pulse amplitude analyzer system. The pulse amplitude analyzer gates the magnetic image intensifier long enough to record the scintillation and shuts off the magnetic image intensifier during the rest of the time. Shuttering is necessary to eliminate the thermal background and ion scintillations of the first stage which otherwise fog the film.

For gamma-ray imaging, hospitals frequently use an Anger camera which is a combination of a NaI(Tl) crystal on the back of which an array of many (16, 32, 48,. . .) photomultipliers is mounted. This provides even images of dynamic processes. At first sight it would appear that only 16, 32, 48,. . . element resolution would be obtained, corresponding to the number of photomultiplier tubes. But this is not so. The light produced by the scintillations is scattered through the crystal, but the photomultipliers nearest the scintillation receive the largest fraction of this light. Thus, by comparing the relative pulse heights of the photomultipliers, it is possible to assess the scintillation position with quite good accuracy. Anger cameras now offer near optimal performance with the use of digital image processing.

9.8   Image Enhancing System for Light-Focusing Gradient-Index Optical Fibers

9.8.1   Introduction

Light-focusing gradient-index optical fibers can be used for image transmission from the interior of the human body and from other not easily accessible locations and cavitations. For these applications the diameter of the imaging fibers can be made so small that it is possible to insert them in a human vein for illumination when looking at the internal structure of the vein.

Gradient-index optical fibers transmit a light image with unity magnification. For small fiber diameters, therefore, a detailed observation of the transmitted image requires magnification. Magnification together with a small fiber transmission efficiency reduces the brightness of the retinal image creating a need for image intensification. As will be shown, an image intensifier tube can be used as an integral part of a gradient-index optical fiber imaging system. In this capacity the image intensifier converts the infrared radiation of the scene to visible light, provides screen presentation, and supplies luminous gain.

9.8.2   Image Enhancing System

The schematic of the image enhancing gradient-index system is shown in figure 9.22. The illumination of the scene is provided by a gallium arsenide
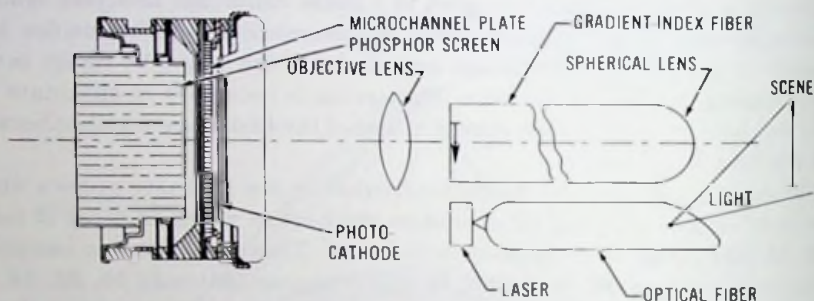
Fig. 9.22   Image enhancing system.

laser diode from which the radiation is transmitted to the scene by an optical fiber. An erect image of the scene is formed at the photocathode of the image intensifier tube by the combined actions of the spherical lens, the gradient-index optical fiber, and the objective lens of the image-intensifier tube. The objective lens magnifies the image to cover the entire useful diameter of the image tube.

The image tube shown in figure 9.22 is a generation 2 wafer image intensifier tube that operates by use of a microchannel plate for internal current multiplication. The photocathode and the output of the microchannel plate are proximity focused on the microchannel input and phosphor screen, respectively. Figures 12.1 and 10.4 show the spectral response of photocathodes and the spectral emission characteristics of phosphor screens frequently used on image intensifier tubes. The improved multialkali cathode and the gallium arsenide cathode have a sufficient response at the 0.83-μm wavelength where the laser diode operates. The P-20 phosphor provides a good match to the eye-response curve.

9.8.3   Image Transmission Losses

In the process of imaging the scene on the photocathode of the image tube, the radiant flux density is greatly reduced by the transmission efficiency of the spherical lens, transmission losses of fiber glass and objective lens glass, and magnification of the objective lens.

From the geometry of figure 9.23, the following holds:

$$\sin \alpha_1 = nm_1 \sin \alpha_2, \tag{9.8}$$

where n is the refraction index of the fiber, and m_1 is the magnification of the spherical lens.
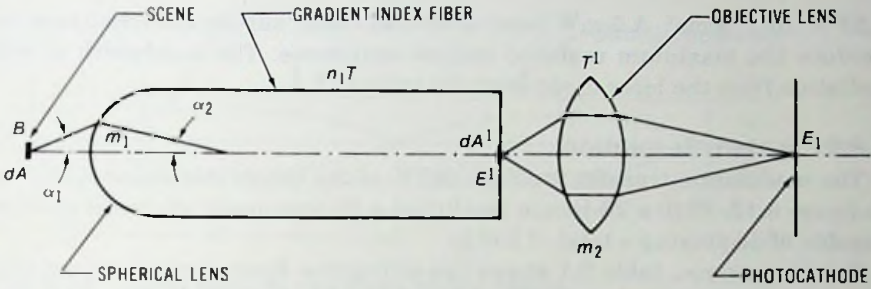
Fig. 9.23   Gradient-index fiber imaging system.

Assuming an angular distribution of light obeying Lambert's law, the light flux L from an area dA of the scene is

$$L = dAB \sin^2 \alpha_1, \tag{9.9}$$

where B is the luminous emittance of the scene.

The illumination in the image of the scene at the end of the fiber is

$$E' = T\frac{L}{dA'} = T\frac{dA}{dA'} B \sin^2 \alpha_1 = \frac{TB}{m_1^2} \sin^2 \alpha_1,$$

$$= TBn^2 \sin^2 \alpha_2, \tag{9.10}$$

where T is the transmission loss of the fiber.

With $\alpha_2 = \gamma_p$, where γ_p is the maximum beam angle in the fiber, the illumination at the photocathode becomes

$$E_1 = \frac{T'E'}{m_2^2} = \frac{TT'Bn^2 \sin^2 \gamma_p}{m_2^2}, \tag{9.11}$$

where T' is the glass transmission loss and m_2 is the magnification of the objective lens.

9.8.4   Scene Illumination Requirement

In normal use of the image intensifier tube the input illumination is 10^{-4} fc $\leq 10^{-7}$ lm/cm^2. At this illumination level the snr in a resolution element, corresponding to 6 lp/mm resolution, is about 50:1 (34 dB). The input current density with cathode sensitivity $s = 300$ μA/lm is $J = 10^{-7} \times 3 \times 10^{-4}$ $= 3 \times 10^{-11}$ A/cm^2. An equivalent input current can be obtained by illumination of the photocathode with a 0.83 μm wavelength laser diode. The input power density with $R = 30$ mA/W radiant sensitivity is $E = 3 \times 10^{-11}/30 \times 10^{-3} = 1 \times 10^{-9}$ W/cm^2. The radiant emittance of the scene by use of the highest B/E ratio from table 9.1 is $B = 1 \times 10^{-9} \times 8.53 \times 10^{8} =$

8.53×10^{-4} W/cm². A 5-mW laser diode can easily supply the irradiance to produce the maximum required radiant emittance. The bandwidth of the radiation from the laser diode is on the order of 1 Å.

9.8.5 System Resolution

The modulation transfer function (MTF) of the image intensifier is shown in figure 6.12. With a 28-lp/mm resolution a 25-mm-useful-diameter tube is capable of displaying a total of 700 lp.

For comparison, table 9.1 shows the diffraction-limited resolution of the fiber system. The resolution was obtained from the following equation:

$$R = 0.41 \frac{D\gamma_p n}{\gamma} \text{ in line pairs,} \tag{9.12}$$

where λ is the wavelength of light, D is the diameter of the fiber, and $n = 1.55$. The input image size is $D/2$. It is apparent that even for this ideal case, the image intensifier becomes a limiting factor only for large-diameter, high-N.A. fibers.

Table 9.1   Diffraction-Limited Resolution of the Fiber System

γ_p (°)	N.A.	$\dfrac{n_o - n_p}{n_o}$	Diameter (mm)	P (mm)	m_2	B/E	R
5	0.135	0.003 8	0.5	18	100	3.4×10^6	33.4
5	0.135	0.003 8	1.0	36	50	8.53×10^5	66.5
5	0.135	0.003 8	1.5	54	33.33	3.79×10^5	100
5	0.135	0.003 8	2.0	72	25	2.13×10^5	133.5
10	0.27	0.015 2	0.5	9	100	8.53×10^5	66.5
10	0.27	0.015 2	1.0	18	50	2.13×10^5	133.5
10	0.27	0.015 2	1.5	27	33.33	9.48×10^4	200
10	0.27	0.015 2	2.0	36	25	5.32×10^4	267
15	0.40	0.034 2	0.5	6	100	3.78×10^5	100
15	0.40	0.034 2	1.0	12	50	9.48×10^4	200
15	0.40	0.034 2	1.5	18	33.33	4.2×10^4	300
15	0.40	0.034 2	2.0	24	25	2.36×10^4	400
20	0.54	0.060 87	1.0	9	50	5.35×10^4	267
20	0.54	0.060 87	2.0	18	25	1.34×10^3	534

9.8.6 Focal Characteristics of Gradient-Index Fibers

In gradient-index glass fibers, light focusing is obtained by transverse variation of the index of refraction of the optical transmission medium. The
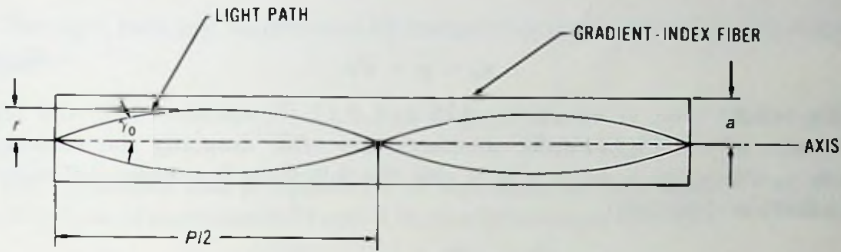
Fig. 9.24 Light path in gradient-index fibers.
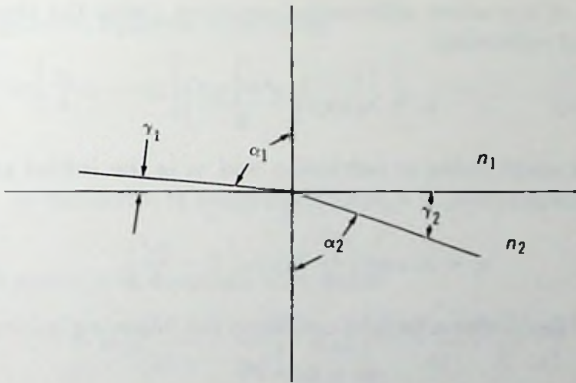
Fig. 9.25 Refraction of a light ray at a boundary.

index of refraction decreases continuously from the axis to the periphery. The focusing action of a gradient-index fiber is shown in figure 9.24.

The focal characteristics of a gradient-index fiber can be derived by ray tracing. Figure 9.25 shows the refraction of a light ray at a boundary with indexes of refraction n_1 and n_2 on the two sides of the boundary. From Snell's law, the following equation is obtained:

$$n_1 \cos \gamma_1 = n_2 \cos \gamma_2. \qquad (9.13)$$

For the paraxial case

$$\cos \gamma = 1 - \gamma^2/2. \qquad (9.14)$$

By substitution of equation 9.14 in equation 9.13, the following equation is obtained:

$$n_1(1 - \gamma_1^2/2) = n_2(1 - \gamma_2^2/2). \qquad (9.15)$$

For a gradient-index material,

$$n_2 = n_1 + dn \qquad (9.16)$$

and

$$\gamma_2 = \gamma_1 + d\gamma. \tag{9.17}$$

By substitution of equations 9.16 and 9.17 in equation 9.15 and after omission of the higher-order members and after dropping the subscripts from n_1 and γ_1 ($n_1 = n$; $n_2 = n + dn$), the following first-order differential equation is obtained:

$$\frac{dn}{d\gamma} = n\gamma. \tag{9.18}$$

The solution of the above differential equation yields the transverse variation of index of refraction:

$$n_r = n_0 \exp\left(\frac{\gamma^2 - \gamma_0^2}{2}\right), \tag{9.19}$$

where n_0 is the axial index of refraction and γ_0 is the initial angle. At the antinode of the light path, $\gamma = 0$, and the index of refraction is

$$n_r = n_0 \exp\left(\frac{\gamma_0^2}{2}\right) \cong n_0\left(1 - \frac{\gamma_0^2}{2}\right). \tag{9.20}$$

For a general ray under a focused condition the following holds:

$$\gamma_0 = 4c(r/P), \tag{9.21}$$

where r is the radial distance at the antinode, P is the period of focusing as shown in figure 9.24, and c is a constant.

By substitution of equation 9.21 in equation 9.20, the following two equations are obtained:

$$\frac{n_0 - n_r}{n_0} \cong 8c^2\left(\frac{r}{P}\right)^2 \tag{9.22}$$

and

$$\frac{n_0 - n_P}{n_0} \cong 8c^2\left(\frac{a}{P}\right)^2, \tag{9.23}$$

where n_p is the peripheral index of refraction and a is the radius of the glass.

By division of equation 9.22 by equation 9.23 and after rearrangement of terms, the following is obtained:

$$n_r = n_0\left[1 - \frac{n_0 - n_p}{n_0}\left(\frac{r}{a}\right)^2\right]. \tag{9.24}$$

Equation 9.24 describes the transverse variation of the index of refraction as a function of radial distance for sharp focusing.

The light path can be obtained by integration of the following differential equation:

$$\frac{dr}{dz} = \gamma = \left(\gamma_0^2 + 2 \ln \frac{n_r}{n_0} \right)^{1/2}$$

(9.25)

The right-hand side of equation 9.25 was obtained from equation 9.19. By combination of equations 9.24 and 9.25, the following is obtained:

$$\int_{r_0}^{r} dr \left/ \left\{ \gamma_0 \left[1 - \frac{2(n_0 - n_p)}{n_0} \frac{r^2}{\gamma_0^2} \right]^{1/2} \right\} \right. = \int_{z_0}^{z} dz .$$

(9.26)

After integration, equation 9.26 yields

$$a \frac{\gamma_0}{\gamma_p} \sin\left[\frac{\gamma_p}{a} (z - z_0) \right] = r \left[1 - \left(\frac{r_0}{a} \frac{\gamma_p}{\gamma_0} \right)^2 \right]^{1/2} - r_0 \left[1 - \left(\frac{r}{a} \frac{\gamma_p}{\gamma_0} \right)^2 \right],$$

(9.27)

where

$$\gamma_p = \left(2 \frac{n_0 - n_p}{n_0} \right)^{1/2}$$

(9.28)

For $z_0 = 0$ and $r_0 = 0$, equation 9.27 yields

$$r = a\gamma_0 \left[\frac{n_0}{2(n_0 - n_p)} \right]^{1/2} \sin\left\{ \left[\frac{2(n_0 - n_p)}{n_0} \right]^{1/2} \frac{z}{a} \right\}$$

$$= \frac{a\gamma_0}{\gamma_p} \sin\left(\frac{\gamma_p z}{a} \right).$$

(9.29)

At the peak of the light path the following holds:

$$\frac{z}{a} \left[\frac{2(n_0 - n_p)}{n_0} \right]^{1/2} = \frac{\pi}{2}.$$

(9.30)

From equation 9.30

$$P = z = 2\pi a \left[\frac{n_0}{2(n_0 - n_p)} \right]^{1/2} = 2 \frac{\pi a}{\gamma_p}.$$

(9.31)

The independence of P from γ_0 indicates sharp focusing for all angles for the paraxial case. The same conclusion can be drawn for an off-axial point from equation 9.27.

The focal length of a shorter than a quarter-period fiber slab can be derived from the diagram of figure 9.26. After the refraction at the exit plane, the direction of the light path is described by the following equation:

$$\tan \alpha = -n \frac{dr}{dz} = -n\gamma_p \sin(\gamma_p Z/a).$$

(9.32)
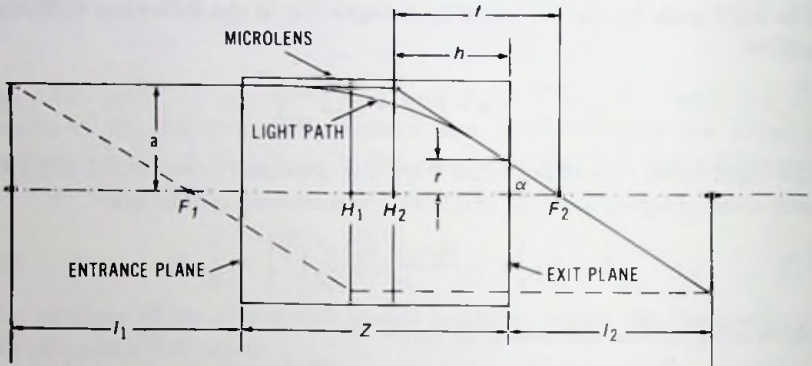
Fig. 9.26 Diagram for the derivation of the cardinal points of a
microlens.

The focal length is

$$f = -\frac{a}{\tan \alpha} = \frac{a}{n\gamma_p \sin (\gamma_p Z/a)}.$$ (9.33)

The principal plane position from figure 9.26 is

$$h = f\left[1 - \cos (\gamma_p Z/a) = \frac{a \tan (\gamma_p Z/2a)}{n\gamma_p} \right.$$ (9.34)

The relationship between the objects and image distances l_1 and l_2 is

$$\frac{1}{l_1 + h} + \frac{1}{l_2 + h} = \frac{1}{f}.$$ (9.35)

By combination of equations 9.33, 9.34 and 9.35, the object distance l_1 is

$$l_1 = \frac{a}{n\gamma_p}\left[\frac{n\gamma_p l_2 \cos (\gamma_p Z/a) + a \sin (\gamma_p Z/a)}{n\gamma_p l_2 \sin (\gamma_p Z/a) - a \cos (\gamma_p Z/a)} \right].$$ (9.36)

9.9   Forward-Looking Infrared System

The forward-looking infrared system (FLIR) is a new technological ad-
vancement for night vision and heat-sensing applications. Instead of using
visible light, the FLIR system utilizes heat rays which provide a thermal
image of objects.

Visible imagery is obtained by reflected light from the scene. When the
scene is illuminated by an external light source, such as the sun, night sky,
or a lamp, the brightness and color distribution (radiation distribution) is

determined by the reflectivity of the objects of the scene. The visible image, therefore, is the result of reflected light.

In thermal imaging, the thermal radiation of the scenery is used for imaging. The thermal radiation of material objects varies according to their temperature and emissivity, the result of which is the formation of a distinct thermal image of a scene. The thermal radiation of an object can be given by Planck's radiation law:

$$W(\lambda,T) = \frac{C_1 \, \epsilon(\lambda) \, \lambda^{-5}}{\exp{(hc/\lambda k T)} - 1},$$

(9.37)

where C_1 is a physical constant, $\epsilon(\lambda)$ is the emissivity function, λ is the wavelength of the radiation, k is the Boltzmann constant, h is Planck's constant, c is the velocity of light, and T is the absolute temperature of the body. Figure 9.27 shows the spectral radiance of a blackbody at temperatures 273 K (0°C) and 335 K (61.8°C).

For a blackbody, ϵ is unity for all wavelengths. If the body is not black, ϵ is always less than 1 and usually is between 0.02 and 0.9 as shown in table 9.2. From Planck's radiation equation the peak of the radiation occurs at 10 μm wavelength at 300 K (normal scene temperature: 26.8°C) and the total blackbody power density is 450 W/m².

The above facts associated with the existence of an atmospheric transmission window in the 10-μm region as shown in figure 9.28 and suitable infrared detectors in the desired spectral range made thermal imaging
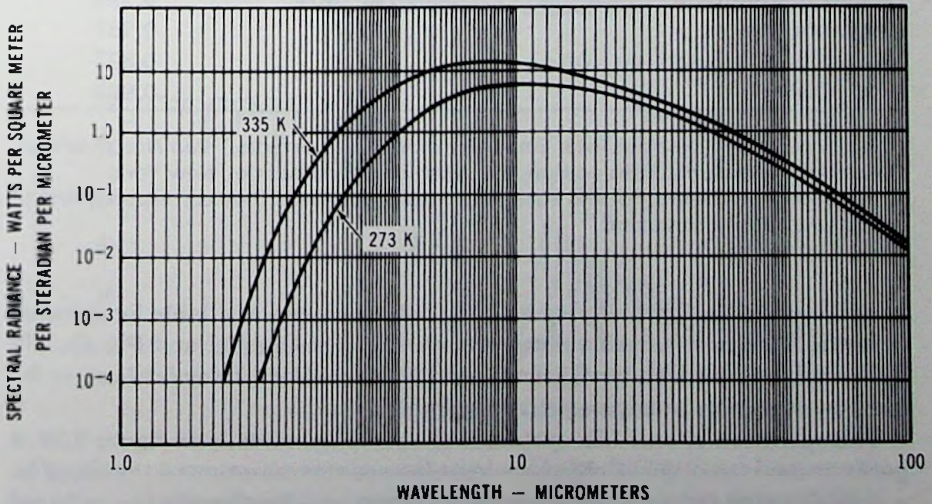
Fig. 9.27   Spectral radiance $W(\lambda, T)$ of a blackbody at 273 K and 335 K.

Table 9.2   Total Emissivity of Various Surfaces*

Surface	Temperature °C**	Emissivity**
aluminum, highly polished	210-577	0.039-0.057
aluminum, oxidized (at 599°C)	199-599	0.11-0.19
brass, highly polished	247-357	0.028-0.031
brass rolled plate, natural surface	22.2	0.06
brass dull plate	49-349	0.22
brass, oxidized (at 599°C)	199-599	0.61-0.59
copper, polished electrolytic	80	0.018
copper, shiny (but not mirror finish)	22.2	0.072
cast plate iron, smooth	22.8	0.80
cast iron, rough, oxidized	38-249	0.95
cast iron, molten	1299-1399	0.29
lead, pure, unoxidized	127-227	0.057-0.075
lead, oxidized (at 199°C)	199	0.63
mercury	0-100	0.90-0.12
molybdenum filament	727-2593	0.096-0.292
nickel, electroplated on iron,		
polished	23.3	0.045
nickel oxide	649-1254	0.59-0.86
asbestos board	23.3	0.96
brick, silica, glazed, rough	593	0.85
carbon filament	1038-1404	0.526
glass, smooth	22.2	0.937
enamel, white-fused, on iron	18.9	0.897
oak, planed	21.1	0.903

*Reprinted from "Normal Total Emissivity of Various Surfaces," *Van Nostrand's Scientific Encyclopedia*, fifth edition, Van Nostrand Reinhold Co., New York.
**When two temperatures and two emissivities are given, they correspond, first to first and second to second.

possible and a reality today. Among the detector types available for infrared imaging, the most suitable detectors are the $Hg_{0.8}Cd_{0.2}Te$, and $Pb_{0.2}Sn_{0.8}Te$ semiconductor materials which are used for photodiode array fabrication for the 10-μm spectral region as shown in table 9.3.

The operation of an FLIR system is shown schematically in figure 9.29. A germanium-coated glass objective lens focuses the radiation of the scene on a liquid-cooled infrared detector diode array which converts the infrared radiation to a video signal. Vertical scanning is obtained by a scanning mirror. The video signal, after amplification, is displayed by a light-emit-
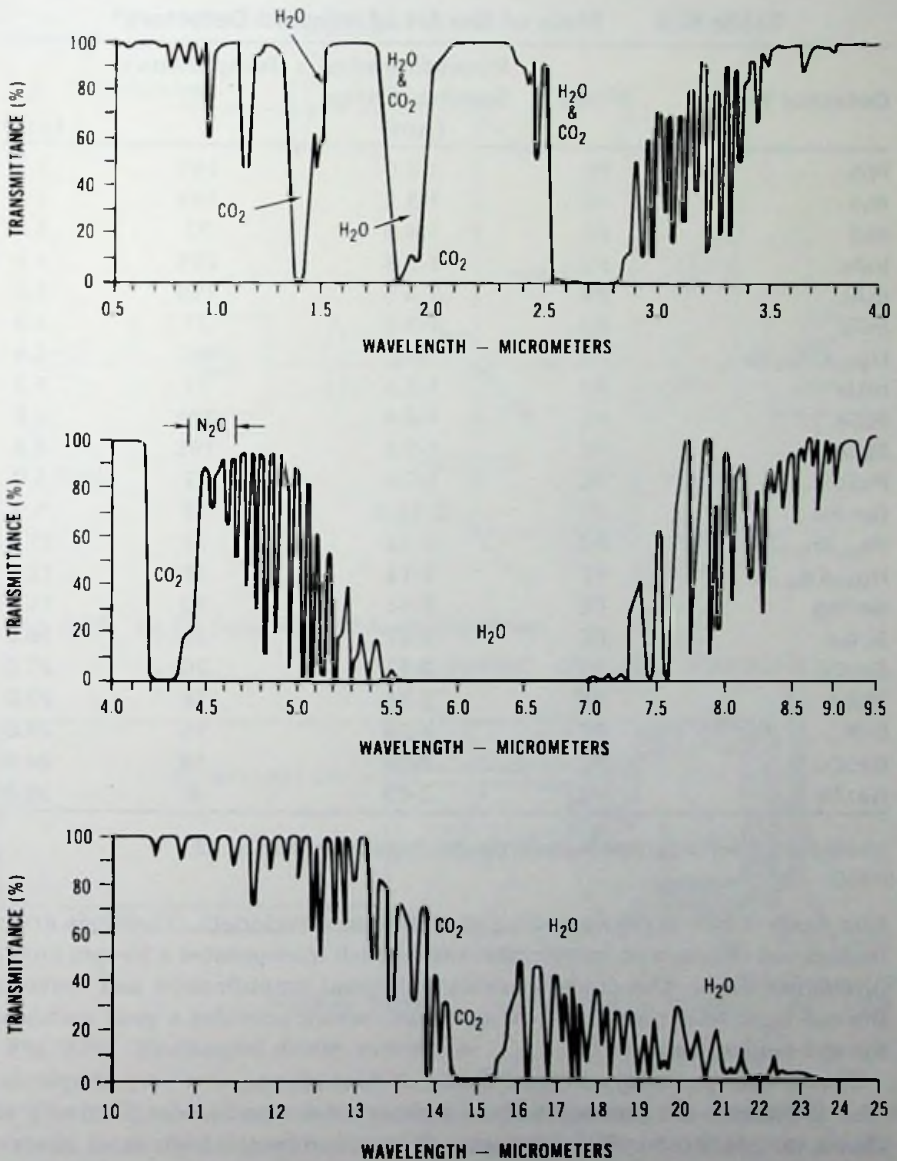
Fig. 9.28   Atmospheric transmission of 1000-ft (304.8-m) horizontal airpath at sea level, 5.7-mm precipitable water at 79°F (26.2°C or 299.3 K). (*Reprinted with permission of Santa Barbara Research Center*)

Table 9.3   State of the Art of Infrared Detectors*

Detector Type	Mode	Recommended Spectral Range (μm)	Temperature (K)	λ (μm)
PbS	PC	1-3.0	295	2.4
PbS	PC	1-3.5	195	2.8
PbS	PC	1-4.0	77	3.2
InAs	PV	1-3.8	295	3.4
InAs	PV	1-3.5	195	3.2
InAs	PV	1-3.2	77	3.0
$Hg_{0.7}Cd_{0.3}Te$	PC	1-5	192	4.6
InSb	PV	1-5.4	77	5.3
PbSe	PC	1-4.4	295	3.8
PbSe	PC	1-5.1	195	4.8
PbSe	PC	1-7.0	77	5.0
Ge:Au	PC	2-10.6	77	5.5
$Pb_{0.2}Sn_{0.8}Te$	PC	1-12	77	11.0
$Hg_{0.8}Cd_{0.2}Te$	PC	1-13	77	12.0
Ge:Hg	PC	2-14	30	11.0
Si:Ga	PC	2-17	23	16.0
Ge:Cd	PC	2-22	20	21.0
Si:As	PC	2-23	18	22.0
Si:P	PC	2-28	15	23.0
Ge:Cu	PC	2-30	14	24.0
Ge:Zn	PC	2-40	8	38.0

*Data from *Electro-Optical Systems Design*, December 1976, p. 43.

ting diode (LED) array operating at a 650-nm wavelength. The diode array is observed through an image intensifier which incorporates a 25-mm image intensifier diode. The diode provides additional amplification and converts the red light (650 nm) to a P-20 spectrum, which provides a good match to the eye response curve.

The 25-mm proximity focused diode, at first glance, is a very simple device. It consists of a photocathode and phosphor screen in close proximity as shown in figure 9.30. Sharp imaging is obtained by the high axial electric field which prevents the radial spreading of an electron beam. The diode supplies an erect, distortion-free image of the photocathode with unity magnification, with a luminous gain of 70 to 100 and with a 60% modulation transfer function (MTF) at a spatial frequency of 20 c/mm.
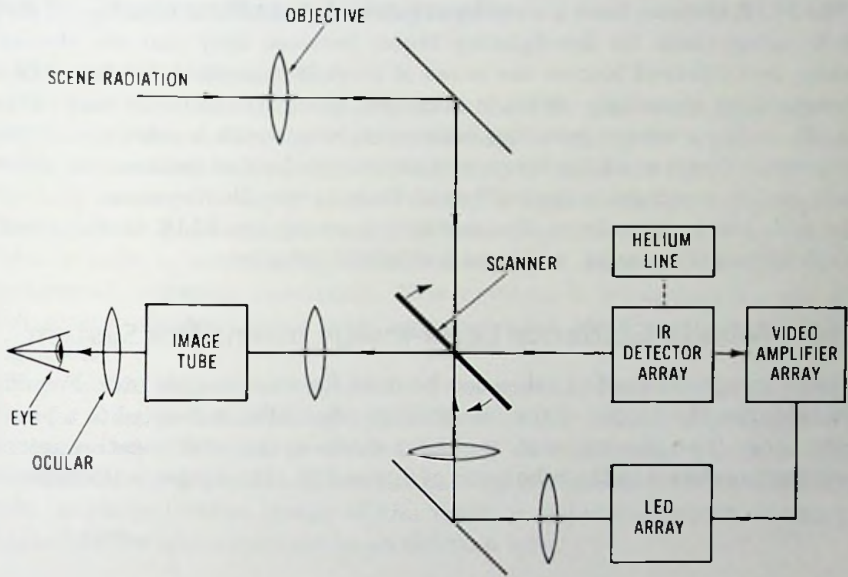
Fig. 9.29   FLIR functional block diagram.
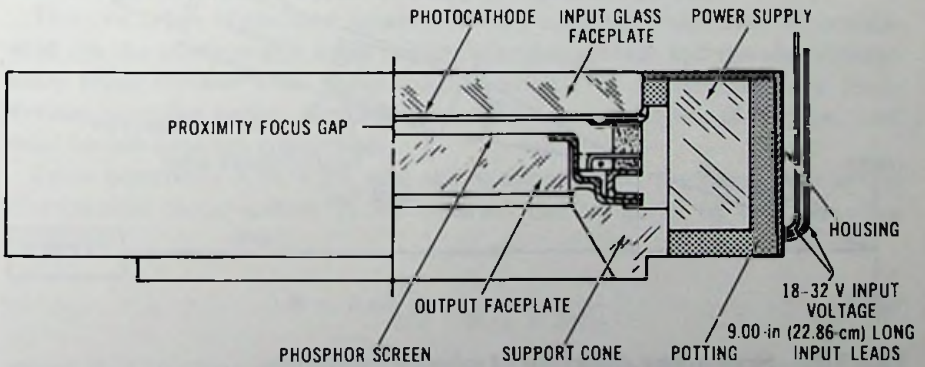
Fig. 9.30   Packaged diode assembly.

The MTF, which describes the transfer of contrast from the object to the image, is a critical parameter of the diode as far as performance is concerned. Quality image transmission requires the elimination of halo effects in the faceplates and in the proximity focus gap. Halation is minimized in a high-quality, fully developed diode by application of antireflection coatings (Si_3N_4; MgF_2) and a low-reflectivity opaque screen metalizing.

The FLIR systems have a number of interesting applications. Forest service is using them for fire-fighting teams because they can see through smoke, and infrared locates the areas of most intense heat for dumping of fire-retardant chemicals. Wildlife managers use them to count night-grazing elk in their winter grounds; oceanographers watch warm-up currents; cattlemen inspect stock for fever; and physicians look at patients for abnormally cool or warm spots that will alert them to specific illnesses.

In addition to the above, the military is using the FLIR in the army's attack helicopters, tanks, and most battlefield vehicles.

9.10   Missile Guidance Laser-Image Intensifier System

Gated image intensifier tubes can be used for missile guidance. For missile guidance the output of the image intensifier tube is coupled to a photodiode array (two dimensional, or linear diode array with rotative mirror scanning) as shown in the schematic of figure 9.31. The target is illuminated
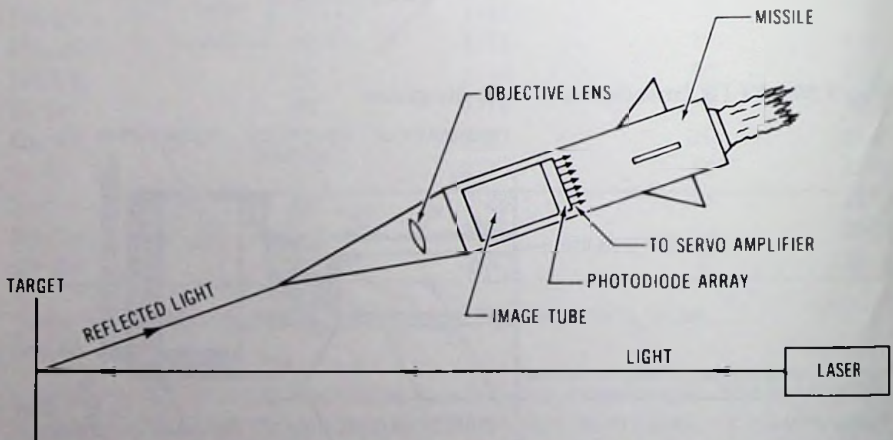
Fig. 9.31   Schematic diagram of missile guidance.

with coded laser pulses. The image intensifier views the target by receiving the reflected laser light. When the missile is on the right course the target image is on the axis of the image intensifier system. When the image is off center the missile is off the target course and the photodiode array produces an error signal which defines the missile target error. The error signal is fed to the missile guidance system (servo amplifiers) to steer the missile on the correct course.

9.11   Electron Beam Lithography

9.11.1   General Description

The electron beam printing process is used for photoetching metal substrates. In this process the metal substrate is coated by a photoresist on which the desired etch pattern is imprinted by means of an electron beam. Electron beam printing is used to obtain a higher resolution than can be obtained with photochemical etching. In a photochemical etching process, light is used to activate the photoresist. Light, however, spreads in the photoresist, reducing resolution. This problem is minimized by use of a high-energy electron beam printing process for which the beam spread is negligible.

Figure 9.32 shows the schematic of an electron image projector system used for electron beam lithography. The required pattern is evaporated on the quartz input window, producing a mask. Over the mask a cesium-iodine photocathode is deposited. When the pattern is illuminated with ultraviolet light, a photoelectron image of the mask is generated which is sharply focused on the etch substrate by an electron lens.

9.11.2   Resolution of Electron Image Projector Systems

The two types of electron image projector systems which may be considered are the electrostatic focus image inversion system and the electromagnetic focus system with unity magnification. The electromagnetic focus system provides better performance as far as resolution, distortion, and total usable area are concerned.

From equations 3.39, 6.24, and A.7 of appendix A, the resolution of the electrostatic focus system at 3% contrast can be given by the following equation:

$$R = 2.43\frac{E_c}{M\epsilon} = \frac{V}{R_c(2 + 3M)\epsilon},\tag{9.38}$$

where V is the lens potential, R_c is the radius of the cathode sphere, M is the magnification of the lens, ϵ is the voltage equivalent of the most probable emission energy, and E_c is cathode field strength.

Equation 9.38 shows that small M values provide higher resolution.

As an example, assume an 18-mm useful cathode diameter tube for which the maximum voltage breakdown characteristics are known. This tube can be operated at a 15-kV anode potential. With $R_c = 20$ mm, $\epsilon = 0.2$ V, and $M = 0.1$, equation 9.38 yields $R = 3962$ lp/mm resolution. The line width for this resolution is 0.126 μm. This resolution may be satisfactory for lithog-

UV LIGHT BEAM
QUARTZ SUBSTRATE
MASK
CsI PHOTOCATHODE
MASKED ELECTRON BEAM
ELECTRON LENS
PHOTORESIST
ETCH SUBSTRATE
SILICA WAFER

E

B

+20 kV
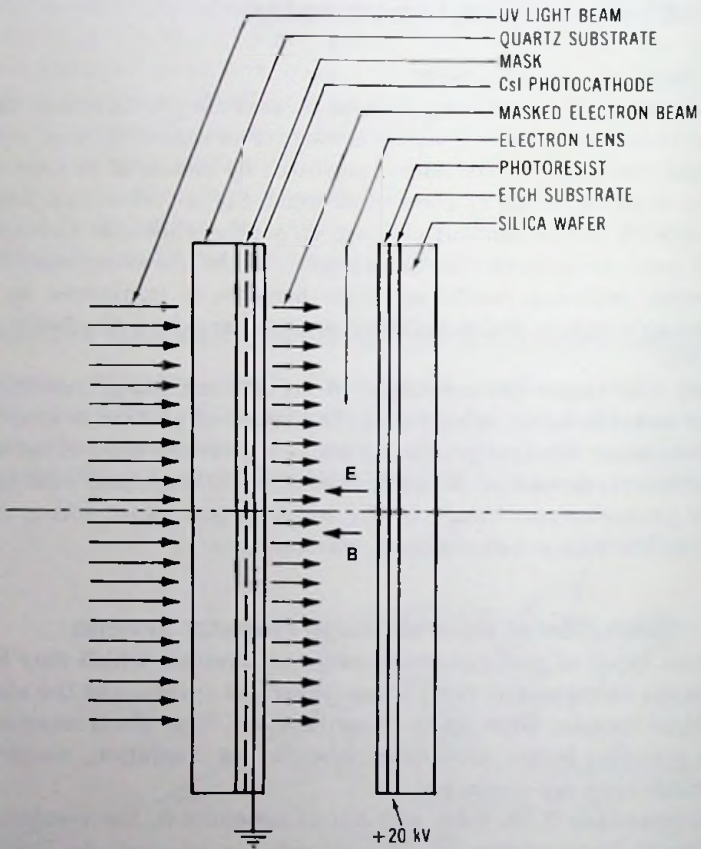
Fig. 9.32 Schematic of an electron beam lithography system.

raphy applications, but it yields an extremely small useful diameter for small distortions. In lithography the users usually worry about a distortion of 1 μm.

The resolution of an electromagnetically focused system consisting of homogeneous axial electric and magnetic fields is

$$R = 2.43\, E_c/\epsilon, \tag{9.39}$$

where E_c is the cathode field strength.

For existing projection systems, E_c is 2000 V/mm and $\epsilon = 0.2$ V, yielding a resolution of 24 300 lp/mm. The resolved line width is 0.020 0 μm = 200 Å.

The magnetic system under ideal conditions (parallel input and output plates and homogeneous magnetic field) is free from geometrical distortions.

There are existing systems with a 75-mm useful diameter which yield 0.15 μm resolution. The resolution of the electromagnetic system is limited by the depth of focus effect. For high resolution it is important to control the target and the mask flatness within a few micrometers.

Existing electron image projection systems use a cesium-iodine photocathode mask which is electromagnetically focused on the target. The target and mask separation is on the order of 1 cm and the lens voltage is 20 kV. The resolution is on the order of 0.15 μm.

References

Alcock, A. J., et al. "Application of Laser-Triggered Spark Gaps to Electro-Optical Image Converter Cameras," Ninth International Congress on High-Speed Photography, Denver, August 1970. Copyright by SMPTE.

"Atmospheric Transmission," *Electro-Optical Systems Design*, September 1977.

Biberman, L. C., and S. Nudelman, eds. *Photoelectronic Imaging Devices*, Plenum Press, New York and London, 1971.

Bode, D. E. "Infrared Detector Technology—Today and Tomorrow," *Electro-Optical Systems Design*, December, 1976.

———. "Infrared Detector Technology—Today and Tomorrow," *Electro-Optical System Design*, September 1977.

Bradley, D. J., et al. "Nanosecond Gating of an Image Intensifier Capable of Triggered Picosecond Photography," *Applied Physics Letters*, Vol. 16, No. 2, p. 53, January 15, 1970.

Chartier, G., et al. "Elaboration of Gradient Index in Glass by Chemical or Electrical Exchange and Migration of Ions," Topical Meeting on Gradient Index Optical Imaging Systems at the Institute of Optics, University of Rochester, May 15-16, 1979.

Csorba, I. P. "Contrast Characteristics of X-Ray Images," *RCA Review*, March 1971.

———. "Image Enhancement for Light Focusing Gradient Index Optical Fibers," *Applied Optics*, January 15, 1980.

———. "Transit-Time-Limited Time Resolution of Image Tubes in Streak Operation," *RCA Review*, December 1971.

———. et al. "Patent Application for X-Y Deflection Image Shutter Tube," RCA internal publication, Lancaster, August 7, 1972.

———. "Image Enhancement For Light Focusing Graded Index Optical Fibers," Topical Meeting on Gradient Index Optical Imaging Systems at the Institute of Optics, University of Rochester, May 15-16, 1979.

Iga, K. "Theory for Gradient Index Imaging," Topical Meeting on Gradient Index Optical Imaging Systems at the Institute of Optics, University of Rochester, May 15-16, 1979.

Jenkins, J. A., and R. A. Chippendale. "High Speed Photography by Means of the Image Converter," *Philips Technical Review*, Vol. 14, No. 8, p. 213, February 1953.

Kohashi, T., et al. "DC-Controlled Solid-State X-Ray Image Converter," *IEEE Transactions on Electron Devices*, Vol. ED-19, No. 2, February 1972.
———. et al. "A Solid-State Infrared Image Converter," *IEEE Transactions on Electron Devices*, Vol. ED-19, No. 1, January 1972.

Korobkin, V. V., et al. "Time Resolution of an Image Converter Camera in Streak Operation," *Journal of Photographic Science*, Vol. 17, 1969.

Linden, B. R., and P. A. Snell, "Shutter Image Converter Tubes," *Proc. IRE*, Vol. 8, p. 513, April, 1957.

Livesay, W. R. "Imaging and Alignment Tests on Electron Projection Systems," *J. Vac. Sci. Technical*, 15 (3), May/June, 1978.

Moody, N. F., et al. "A Survey of Medical Gamma-Ray Cameras," *Proc. IEEE*, Vol. 58, No. 2, February 1970.

Moor, D. T. "Current Status Of Gradient Index Imaging Lenses," Topical Meeting on Gradient Index Optical Imaging Systems at the Institute of Optics, University of Rochester, May 15-16, 1979.

Niklas, W. F., "X-Ray Image Intensification with a Large Diameter Image Intensifier Tube," *American Journal of Roentgenology, Radiology, and Nuclear Science*, Vol. 85, No. 2, p. 323, February 1961.

Nishizawa, K. "Study on Chromatic Aberration of Selfoc Micro Lens in Imaging Systems," Topical Meeting on Gradient Index Optical Imaging Systems at the Institute of Optics, University of Rochester, May 15-16, 1979.

Norton, G. A., et al. "The Brightness Intensifier," *RCA Review*, Vol. 9, No. 3, p. 419, September 1948.

Nudelman, S., et al. "A Study of Photoelectronic-Digital Radiology," *Proceedings of the IEEE*, Vol. 70, No. 7, July 1982.

Roehrig, H., et al. "Photoelectronic Imaging For Radiology," *IEEE Transactions on Nuclear Science*, Vol. NS-28, No. 1, February 1981.

Roziere, G., et al. "Large Field of View Image Intensifier Gamma Camera Detectors Using a Silicon X-Y Scintillation Localizer," *IEEE Transactions on Nuclear Science*, Vol. NS-28, No. 1, February 1981.

Schelev, M. Ya., et al. "Image-Converter Streak Camera with Picosecond Resolution," *Applied Physics Letters*, Vol. 18, No. 8, p. 354, 1970.

Scott, J. P., "Photocathodes for Use in an Electron Image Projector," *Journal of Applied Physics*, Vol. 46, No. 2, February 1975.
———. "An Electron Image Projector with Automatic Alignment," *IEEE Transactions on Electron Devices*, p. 409, 1975.

Stoudenheimer, R. C., et al. "An Image-Converter Tube for High-Speed Photographic Shutter Service," *RCA Review*, Vol. 18, No. 3, p. 322, September 1957.

————, and R. D. Faulkner. "Night Surveillance Systems for Law Enforcement," *Proceedings of the 1970 Carnahan Conference on Electronic Crime Countermeasures*, University of Kentucky, Lexington, April 16–18, 1970.

Teves, M. C., and T. Tol. "Electronic Intensification of Fluoroscopic Images," *Philips Technical Review*, Vol. 14, p. 33, 1952.

10

PHOSPHOR SCREENS

10.1   The Preparation for Conventional Phosphor Screens

Image tube phosphor screens are relatively smooth layers of luminescent material less than 10 μm thick and frequently water settled phosphor particles from 1 to 5 μm in size. The phosphor screens are coated with a thin opaque film of aluminum (about 1000 Å thick) as shown in figure 10.1.

In water settling the phosphor particles are allowed to settle out on a gelatin coated substrate under the influence of gravity from a water suspension of phosphor powder to which potassium silicate and sodium silicate compounds are added as screen binders and barium acetate as electrolyte. Barium acetate is a gelling agent which promotes adhesion between the individual phosphor granules and the substrate; it is usually added to the settling water after the phosphor particles are settled. At the end of the settling period the liquid is drained and the phosphor layer is air dried and baked. The phosphor screen is then placed in water and coated with a thin
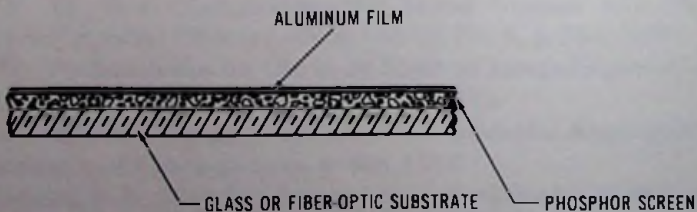
Fig. 10.1   Aluminized phosphor screen.

organic film by a water flotation technique; a drop of organic film solution is allowed to form a thin film on the water surface which, by draining the water, settles on the phosphor screen. The screen is then dried and aluminized in a high vacuum by evaporation of aluminum on the organic film. Finally, the aluminized phosphor screen assembly is air baked to decompose the organic lacquer film and to allow the aluminum film to settle on the phosphor screen and to adhere by electrostatic forces.

The aluminum film has a triple role. First, it holds the phosphor screen at a uniform potential by providing it with a conductive layer; second, it prevents light feedback from the phosphor screen to the photocathode; third, it serves as a light reflector for the phosphor screen, thus improving its efficiency. In addition to regular aluminizing, in some cases the screen is dark aluminized in order to improve contrast by elimination of light reflections from the screen to the photocathode. A dark aluminum film is usually deposited by evaporation of aluminum in argon in the pressure range of 5 $\times$ 10^{-2} to 10^{-1} torr.

An alternative method of screen deposition is the brushing operation. In the brushing type of screen deposition the screen substrate is coated with a thin thermoplastic film by spinning as the first step of the fabrication. As the next step the plastic film is baked and the temperature is raised for the brushing operation. The brushing operation consists of depositing a phosphor material on the plastic film by dusting and of embedding the phosphor particles in the plastic film. The brushed screen is air baked to remove the organic film. Finally, the screen is sprayed with a suitable screen binder for binding the phosphor particles. The screen prepared this way is filmed and aluminized by conventional techniques used for image tube screens.

Usual screen substrates are: a plane of optical quality Corning 7056 glass or a fiber-optic plate.

10.2   Luminescence

The basic function of the phosphor screen is to convert the electron beam energy to light. The exact details of energy conversion to light may be different for different phosphors. But, in general, part of the electron beam energy is used to produce excited states within the material. Light emission occurs when the excited states return to their normal state. The light emitted simultaneously with the introduction of excitation energy is called *fluorescence*. In contrast, *phosphorescence* is light that persists after the excitation is removed.

Figure 10.2 shows the energy band diagram of a phosphor in a general case. Luminescence is associated with the presence of localized energy levels in the normally forbidden energy gap. The localized energy levels, called
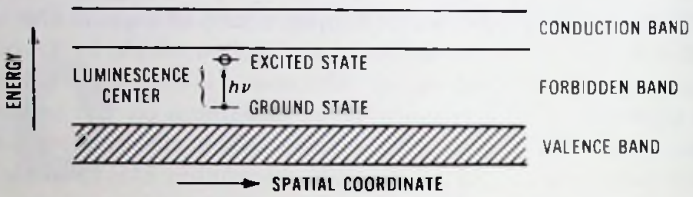
Fig. 10.2   Simplified energy-band diagram of a phosphor.

the *luminescent center*, are produced by an activator atom, which is an imperfection usually intentionally added to a pure crystal. In self activated phosphors, however, the imperfections are caused by interstitials or vacancies. In the ground state the luminescent center is occupied by an electron and in the excited state it is empty. The excitation of the luminescent center may be accomplished in three different ways: (*a*) The incident energy (a photon or the energy of an energetic electron) may be directly absorbed by the luminescent center, resulting in excitation of the electron; (*b*) The excitation may be caused by an *exciton*. An exciton is produced by raising an electron from the filled band to a level below the conduction band. In this transition the atom is not completely ionized. Therefore the electron is still bound to some extent by the Coulomb field produced by the hole it left behind. The excited electron and the associated hole together are called an exciton; the unit as a whole is neutral. (*c*) The luminescent center may be excited by a hole-electron pair. The hole-electron pair is produced by energetic incident electrons or photons by lifting an electron from the filled band to the conduction band. The electrons and holes wander through the crystal until they are trapped in the luminescent center. This excitation process is associated with conductivity in contrast with processes (*a*) and (*b*).

Within the three excitation processes discussed above, still two different cases may be distinguished. In one process the excited electron remains in the domain of the center from which it originated and eventually returns to its ground state with the emission of light. In the other, any of the excited electrons may recombine with any other empty luminescent center. The first process is called a *monomolecular process*, the second a *bimolecular process*.

In the case of a monomolecular process the number L of emission processes per second, in absence of excitation, is the rate of change of the number N of the excited states.

$$L = \frac{dN}{dt} = \frac{N}{T} \tag{10.1}$$

or in integrated form

$$L = L_0 e^{-t/T}, \tag{10.2}$$

where L_0 is the initial rate of light emission, t is time in seconds, and T is the time in which L drops to the value of L_0/e ($e = 2.72$).

For the photoconductive phosphors the recombining electrons and holes are independent. Therefore the rate of emission is proportional to the product of the number of the excited electrons and holes. The number of holes equals the number of excited electrons, so that the rate of recombination is

$$L = \frac{dN}{dt} = KN^2. \tag{10.3}$$

The number of excited centers at time t may be obtained from equation 10.3 by integration:

$$N = \frac{N_0}{1 + KN_0t}. \tag{10.4}$$

By combination of equations 10.3 and 10.4 the following equation is obtained:

$$L = \frac{L_0}{(1 + \gamma t)^2}, \tag{10.5}$$

where $L_0 = KN_0^2$ and $\gamma = L_0/N_0 = KN_0$.

From the simplified luminescence model of figure 10.2 one may get the impression that all photons will be emitted at a single frequency. This is, however, not the case. Consider figure 10.3, which shows the energy levels as a function of position of the activator atom with respect to the surrounding neighbors. The activator atom vibrates about its equilibrium position. Thus the energy of a photon during transition to the ground state may be any value between $h\nu_1$ and $h\nu_2$, and depends on the phase of the vibration of the activator atom. Consequently, a broad band of light is emitted. Figure 10.4 shows the spectral emission of phosphors used frequently in image tubes, and tables 10.1 and 10.2 show the characteristics and applications of phosphor screens.

10.3   Sulfide Phosphors

The two most frequently used phosphors in image tubes are the zinc sulfide (ZnS:Ag,Cl) and the zinc cadmium sulfide phosphors (ZnS·CdS:Ag,Cl). These phosphors are crystalline compounds with the zinc sulfide and zinc cadmium sulfide being the host lattice, and the silver (Ag) and chlorine (Cl) are the activator and coactivator, respectively. The amount of silver/chlorine is only about 0.15% by weight.

Zinc sulfide (ZnS) is usually obtained by precipitation from purified zinc
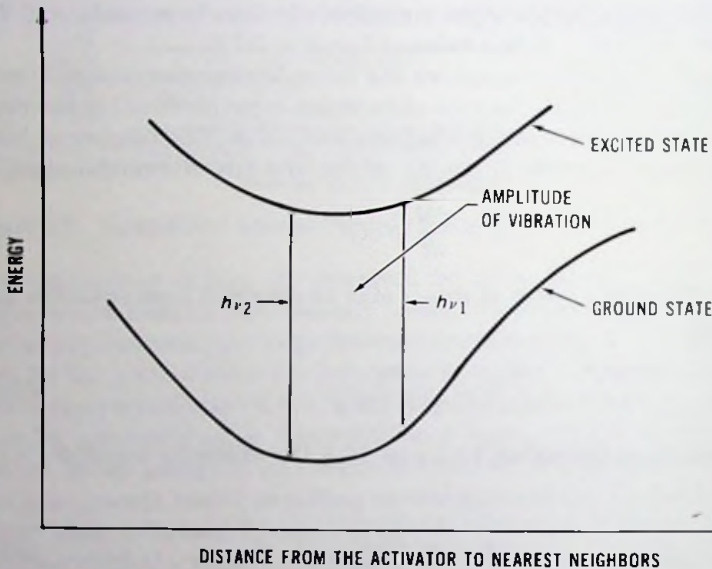
Fig. 10.3 **Energy levels as a function of the position of the activator atom with respect to its neighbors.**

sulfate with hydrogen sulfide (H_2S). The reaction by which zinc sulfide is made is

$$ZnSO_4 + H_2S \leftrightarrows ZnS \downarrow + H_2SO_4, \tag{10.6}$$
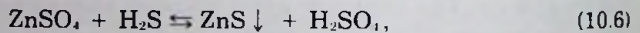
where the down arrow sign indicates that the particular reaction product is so insoluble that it precipitates out of solution. The precipitate is washed with distilled water and dried.

In a similar way as above, cadmium sulfide (CdS) may be obtained by precipitation from purified cadium sulfate with hydrogen sulfide.

The zinc sulfide phosphor may be prepared by adding to a water slurry of zinc sulfide placed in an acid cleaned quartz crucible, 0.015% by weight of silver as silver nitrate together with a flux in the form of purified sodium chloride. An intimate mixture is obtained by milling the ingredients in a pebble mill. The resultant phosphor mix is dried and then crystallized by firing in air at 800°C. As a next step the surface of the phosphor is cleaned to remove the portion that has been oxidized to zinc oxide.

The zinc cadmium sulfide phosphor may be prepared in a similar manner. Zinc sulfide and cadmium sulfide are mixed in a 1:1 weight ratio (for every gram of zinc sulfide, 1 gram of cadmium sulfide is added). To this mixture, silver nitrate and sodium chloride are added. A thoroughly ground mixture
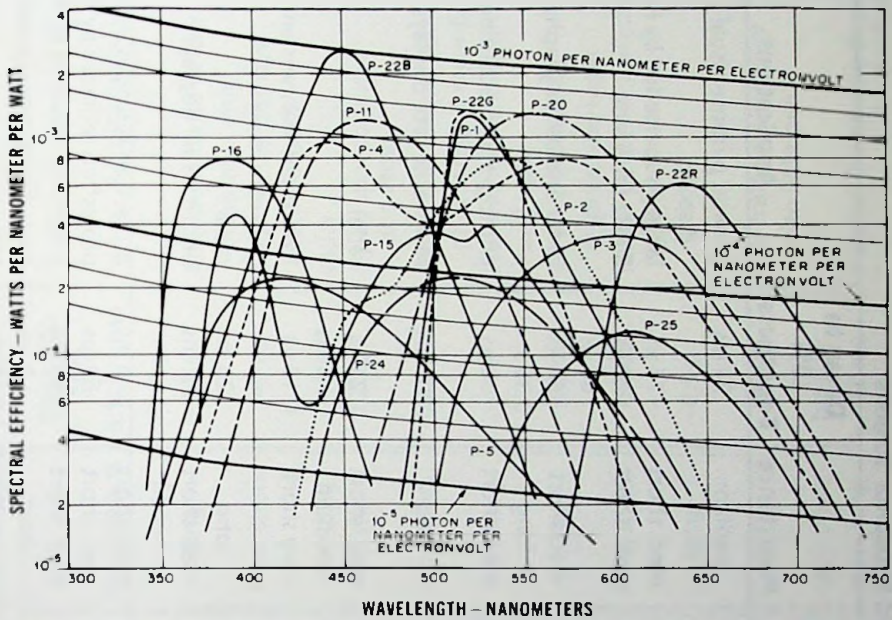
Fig. 10.4 **Typical spectral energy emission characteristics of aluminized phosphor screens.**

of the phosphor is then crystallized by firing in air at a suitable temperature.

By incorporation of silver and chlorine in the zinc sulfide lattice, the structure of the lattice will be modified as shown in figure 10.5. As shown, the monovalent positive Ag^+ ion enters the zinc sulfide lattice, where it substitutes for the doubly charged Zn^{++} ion. To neutralize the crystal a singly charged negative Cl^- ion substitutes for a doubly charged negative S^{--} ion. The situation is similar in the silver activated and charge compensated cadium sulfide.

Because the activator ion is singly charged, the electrons of the neighboring sulfur ion are not as strongly bound as in the case of a Zn^{++} ion. Therefore the energy levels of the S^{--} ions surrounding the activator will be slightly above the energy levels of normal sulfur atoms, thus producing occupied energy levels (acceptors) in the forbidden band near the top of the valence band. In a similar way the coactivator ions produce unoccupied energy levels (donors) close to the bottom of the conduction band. For more explanation, see figure 10.5, where the sulfur and zinc are tetrahedrally surrounded; the sulphur atoms by four zinc atoms and the zinc atoms by

Table 10.1 Standard Phosphor Screens

Type	Color (Kelly Chart)	Spectral Peak (angstroms)	CIE Coordinates		Persistence	Decay to 10% Brightness	Applications
P-1	yellowish-green	5250	0.218	0.712	medium	24 ms	general purpose visual displays
P-2	yellowish-green	5350	0.279	0.534	med. short	~75 μs	largely superseded by P-31
P-4	white	4600 5600	0.270	0.300	med. short	20 μs 60 μs	60-Hz television
P-7	blue	4400	0.151	0.032	med short	~50 μs	radar and oscillography
	yellow-green	5550	0.357	0.537	long	0.35 s	
P-11	blue	4600	0.139	0.148	med. short	~50 μs	photographic recording
P-12	orange	5900	0.605	0.394	long	200 ms	low frame rate displays and radar
P-14	purplish-blue	4400	0.150	0.093	med. short	25 μs	radar
	yellowish-orange	6000	0.504	0.443	medium	5 ms	
P-16	bluish-purple	3800	0.175	0.003	very short	0.12 μs	flying spot scanners and uv recording
P-19	orange	5900	0.572	0.442	long	220 ms	radar
P-20	yellow-green	5600	0.426	0.546	med. short	~0.2 ms	bright visual displays
P-22R	reddish-orange	6200	0.623	0.342	med. short	10 ms	projection replaced by P-56
P-22G	yellow-green	5200	0.343	0.591	med. short	60 ms	projection replaced by P-53
P-22B	blue	4500	0.155	0.067	med. short	60 ms	projection replaced by P-55
P-24	green	5100	0.245	0.441	short	~1.5 μs	color flying spot scanner
P-25	orange	6100	0.557	0.430	medium	45 ms	radar

Table 10.1—cont.   Standard Phosphor Screens

Type	Color (Kelly Chart)	Spectral Peak (angstroms)	CIE Coordinates	Persistence	Decay to 10% Brightness	Applications
P-26	orange	5950	0.582 0.416	very long	~10 s	radar
P-28	yellow-green	5500	0.370 0.540	long	~0.5 s	long persistance at low brightness only
P-31	green	5200	0.193 0.420	med. short	40 μs	bright visual displays oscillography
P-33	orange	5875	0.559 0.440	very long	~10 s	radar
P-36	yellow-green	5500	0.400 0.543	very short	0.25 μs	flying spot scanners
P-37	blue	4700	0.143 0.208	very short	0.15 μs	flying spot scanners and photographic recording
P-38	orange	6000	0.561 0.437	very long	1 s	low frame rate displays and radar
P-39	yellowish-green	5250	0.223 0.698	long	150 ms	medium frame rate displays and radar
P-40	white	4400	0.276 0.311	med. short	150 μs	longer persistence version of P-4
P-41	yellow-green	5500		long	~0.5 s	
	greenish-yellow	5900	0.541 0.456	long	200 ms	low frame rate display with light pen
P-42		3800	0.175 0.003	very short	0.12 μs	
	yellowish-green	5200	0.238 0.568	med. long	10 ms	medium frame rate display

Table 10.1—cont. Standard Phosphor Screens

Type	Color (Kelly Chart)	Spectral Peak (angstroms)	CIE Coordinates	Persistence	Decay to 10% Brightness	Applications
P-43	yellowish-green	5440	0.333 0.556	medium	1.2 ms	bright high-contrast displays with bandpass filter
P-44	yellowish-green	5440	0.300 0.596	medium	1.2 ms	bright high-contrast displays with bandpass filter
P-45	white	**	0.253 0.312	medium	1.7 ms	preferred alternative to P-4 for high-brightness white displays
P-46	yellow green	5300	0.365 0.595	very short	0.16 μs	flying spot scanners; preferred alternative to P-36
P-47	purplish-blue	4000	0.166 0.101	very short	0.08 μs	flying spot scanners; superior to P-16 in most applications
P-48	yellow-green	4000 5250	0.365 0.474	very short	0.12 μs	color flying spot scanner; superior to P-24 in most applications
P-49	red 10 kV green 17 kV	6150 5150	0.672 0.327 0.315 0.615	medium medium	1.2 ms 30 ms	high-resolution multicolor

Table 10.1—cont. Standard Phosphor Screens

Type	Color (Kelly Chart)	Spectral Peak (angstroms)	CIE Coordinates	Persistence	Decay to 10% Brightness	Applications
P-50	red 8 kV	6200	0.655 0.340	medium	5 ms	high-resolution multicolor
	yellow-green 15 kV	5450	0.398 0.546	med. short	20 μs	
P-51	red 6 kV	6225	0.675 0.325	medium	2.2 ms	high-resolution multicolor
	yellow-green 12 kV	5450	0.414 0.514	med. short	31 μs	
P-52	purplish-blue	4000	0.157 0.075	med. short	2.6 μs	photorecording
P-53	yellow-green	5450	0.368 0.539	medium	7 ms	high current density displays and projection
P-55	blue	4500	0.150 0.070	med. short	—	projection
P-56	red	6200	0.640 0.335	medium	—	projection
P-57	yellow-green	5200	0.218 0.712	medium	0.8 s	radar
	orange	5900	0.573 0.426	very long	20 s	

*Data taken from the Thomas Electronics, Inc., catalog with permission of Thomas Electronics, Inc., 100 Riverview Drive, Wayne, New Jersey 07470.
**Multiple peaks.

Table 10.2   Special Purpose Phosphor Screens*

Type	Color	Persistence	Comments
PT-309	infrared	short	peak emission at 1 μm
PT-328	orange-blue	very long	for radar with alphanumerics
PT-340	yellowish-green	long	for low refresh display with ir light pen
PT-346	orange	long	for low refresh display with ir light pen
PT-414	ultra violet	med. short	peak emission at 350 nm
PT-442	orange	very long	for low refresh display with blue-sensitive light pen
PT-443	amber	medium	for comfortable long-term viewing
PT-457	yellowish-green	very long	cascade screen for radar and medical displays
PT-462	yellowish-green	med. short	very high luminous efficiency
PT-478	yellowish-green	long	for low refresh rate display with blue-sensitive light pen
PT-498	orange-green	very long	for radar with alphanumerics
PT-452	red yellow-green	med. short	current-sensitive color shift
PT-582	yellow-green	very short	single-component version of P-48
PT-602	white	med. short	color recording with balanced r/g/b output
PT-609	white	med. short	high-efficiency white for projection
PT-615	red-green	med. short/ very long	voltage penetration multicolor, short-decay red, long-decay green
PT-621	red-green-blue	med. short	voltage penetration multicolor, three primary colors

*Data taken with permission from the catalog of Thomas Electronics, Inc., 100 Riverview Drive, Wayne, New Jersey 07470.

four sulphur atoms. For a covalent bond eight electrons are needed. Six electrons are provided by the sulphur and two electrons by zinc. Silver substitutes for the Zn^{++} ion. Because silver is monovalent one electron is missing from the bond. The silver activator therefore has the nature of an electron acceptor. Chlorine substitutes for the sulphur. Chlorine has one
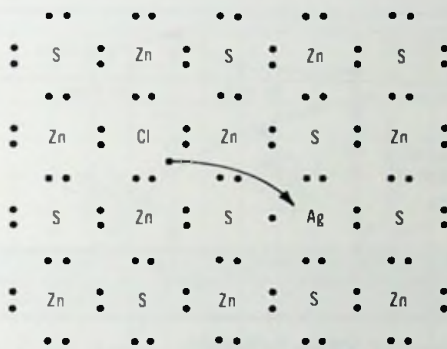
Fig. 10.5 ZnS:Ag,Cl crystal.

more electron than the sulphur; therefore it acts as an electron donor. In equilibrium, the electron trapped in the field of a coactivator is transferred to the activator. The activator and coactivator, then, each form four complete tetrahedral bonds. The activator has a negative charge and the coactivator a positive charge with respect to the perfect crystal.

In the case of sulfide phosphors the luminescence may be considered as a three-step process. First, free electrons and holes are generated by the absorbed energy. Second, the holes and electrons loose their energy to the lattice by phonon production, then by drifting through the crystal the holes are trapped in the activator centers and the electrons are trapped in the unoccupied energy levels below the bottom of the conduction band. Third, the trapped electrons are freed by thermal agitation and the free electrons recombine with the trapped holes at the activator centers by emission of light (figure 10.6).

Although most of the holes are trapped in the activator centers, the empty levels below the bottom of the conduction band may also act as recombination centers, thus allowing radiationless transitions. In some cases radiationless transitions may also occur in the activator centers. The efficiency of the phosphor, i.e., the conversion of the electron beam energy to radiant energy, depends on the competition between the radiative and radiationless transitions. The largest energy losses, however, occur in the process of hole-electron pair production followed by phonon generation. In the case of zinc sulfide the mean energy required for a free hole-electron pair production is $\bar{E} = 3E_G$. The band gap energy E_G is 3.7 eV. The mean energy of the emitted photon is $E_\mu = 2.7$ eV. The energy difference $\bar{E} - E_p$ is lost to the lattice by phonon generation. The efficiency of the luminescence process is

$$\eta = \frac{E_p}{\bar{E}} = \frac{2.7 \text{ eV}}{3 \times 3.7 \text{ eV}} = 0.243 = 24.3\%. \tag{10.7}$$
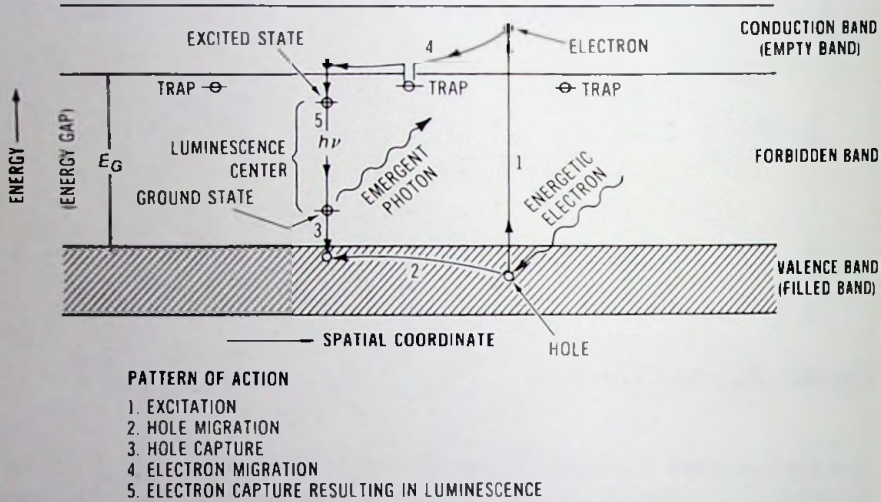
Fig. 10.6   Diagram for luminescence of sulfide phosphors with monovalent activator.

Bril and Klasens measured 25% phosphor efficiency for ZnS:Ag phosphor, which is in a good agreement with the theory based on a very simple model.

The efficiency of the phosphor screen, besides the bulk efficiency, is mostly determined by the thickness of the phosphor screen, by the losses in the aluminum film, by the particle size of the phosphor, and by the electron beam energy. In general, the larger the particle size of the phosphor, the greater the screen efficiency. The loss in the aluminum film may be minimized by keeping the aluminum film as thin as the opacity requirement allows it. The usual requirement is that the aluminum film must attenuate light by a factor of 100 to 1000, which can be met by a 1000-Å thick aluminum layer.

The thickness of the phosphor screen is critical as far as efficiency is concerned. If the phosphor screen is too thin, the electron beam is not stopped by the fluorescent material but passes through it, giving up energy to the glass substrate. Conversely, a phosphor layer thicker than the penetration depth of the electrons absorbs some light as it passes through the material which is not reached by the electron beam.

Figure 10.7 shows a typical image tube phosphor screen efficiency curve as a function of electron beam energy. At beam energies lower than 2.5 kV, the electrons do not penetrate the aluminum film, and therefore light is not produced. As the beam voltage is increased beyond 2.5 kV the efficiency increases rapidly because part of the beam energy is now used to excite the
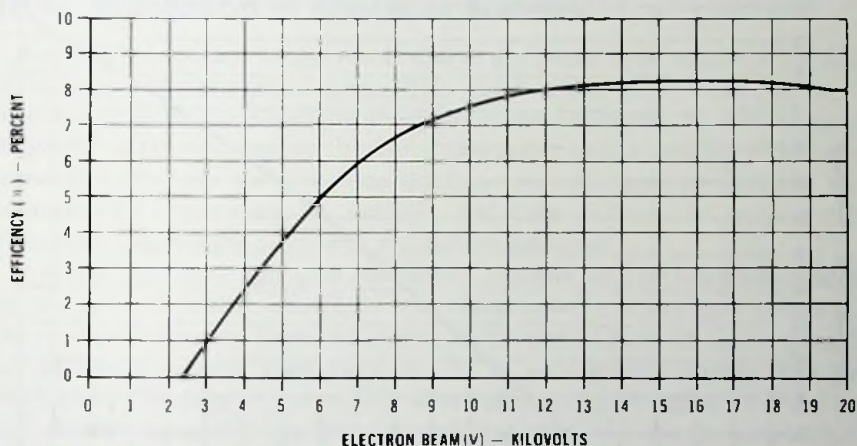
Fig. 10.7 Efficiency of a typical image tube phosphor screen on a glass substrate.

phosphor. The higher the beam voltage, the better the ratio of the energy used to excite the phosphor to the energy loss in the aluminum film. At higher voltages, however, the slope of the efficiency curve decreases because the electrons penetrating the phosphor layer lose part of their energy to the glass substrate. For the particular screen of figure 10.7 an optimum efficiency is obtained at about 15 kV. By making the screen thicker the loss caused by glass bombardment may be reduced and the efficiency somewhat improved, but only at the expense of losing resolution.

High-resolution sulfide screens currently used in image tubes have typically a conversion efficiency of 7 to 10% at operating voltages of 12 to 15 kV. Typical phosphor screen resolution is about 120 lp/mm.

Figure 10.8 shows the luminous output of the screen discussed above as a function of electron beam energy. As may be concluded from figure 10.8 the luminous output may be expressed to a close approximation by the following equation:

$$L \cong K(V - V_0), \tag{10.8}$$

where L is the luminous flux, K is a constant, and V and V_o are the electron beam voltage and the dead voltage required to penetrate the aluminum film, respectively.

In applications, where the output screen of the image intensifier tube is viewed by the eye, the luminous efficiency is a more meaningful term for the specification of the radiant characteristics of the phosphor screen. The
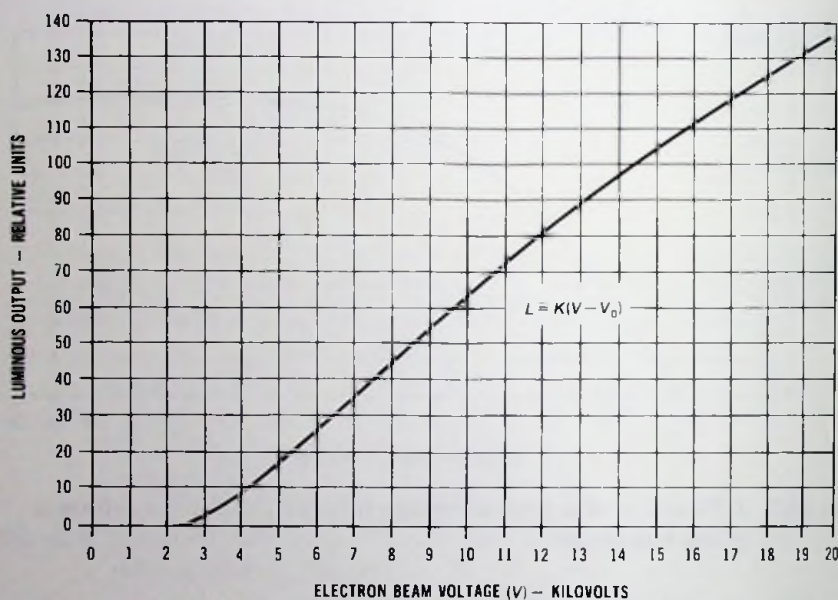
Fig. 10.8 **Luminous output of a phosphor screen as a function of beam voltage.**

luminous efficiency is usually expressed in lumens per watt of electron beam energy. Since the eye is most sensitive in the yellow-green region of the spectrum, the yellow-green phosphors have the highest luminous efficiency. Zinc cadmium sulfide activated with silver (P-20 screen designation) has a peak energy output near the maximum eye sensitivity (5600 Å). The luminous efficiency of aluminized phosphor screens from P-20 material is in the range of 40 to 50 lm/W.

When the output of the image tube is photographed, a good match to the film response is obtained by the use of a P-11 (ZnS:Ag) phosphor screen. The peak of the spectral emission characteristic of this phosphor is in the blue region at 4600 Å. Therefore the luminous efficiency is only about 10 lm/W. Another choice for photography is the P-22 (ZnS:Ag) phosphor screen that has a peak energy emission at 4450 Å. The P-22 phosphor has a better efficiency at current densities lower than 10^{-10} A/cm² than the P-11 and P-20 phosphors. Consequently it is also an excellent choice for purposes of low light level intensification. The absolute efficiency of phosphor screens processed from P-22 material is about 9% on glass substrates.

10.4   Resolution of Phosphor Screens

A serious limitation to the resolution of an image tube results from light scattering in the phosphor screen. The width of the white lines appears to increase as the thickness of the phosphor screen increases. To determine the relationship between screen thickness and resolution, a number of phosphor screens were made with various thicknesses, and their resolutions were measured by projecting an optical resolution pattern on each screen. Figure 10.9 shows the measured resolution obtained.

It is interesting to note that resolution depends only on thickness and not on screen particle size, except for very thin screens, where the thickness of the particle is greater than the average screen thickness. In these cases the use of larger-particle phosphors results in very grainy images and poor resolution. The data in figure 10.9 were taken using phosphors having particle diameters up to 3 μm. For a screen thickness of 4 μm the resolution is shown to be approximately 235 lp/mm. When larger-diameter particles (up to 8 μm) are used, for the same screen thickness, the resolution is reduced considerably. The reason is that the thickness of the particle becomes the limiting factor. For particle sizes up to 8 μm the best resolution is, therefore, obtained at a screen thickness of 8 μm.
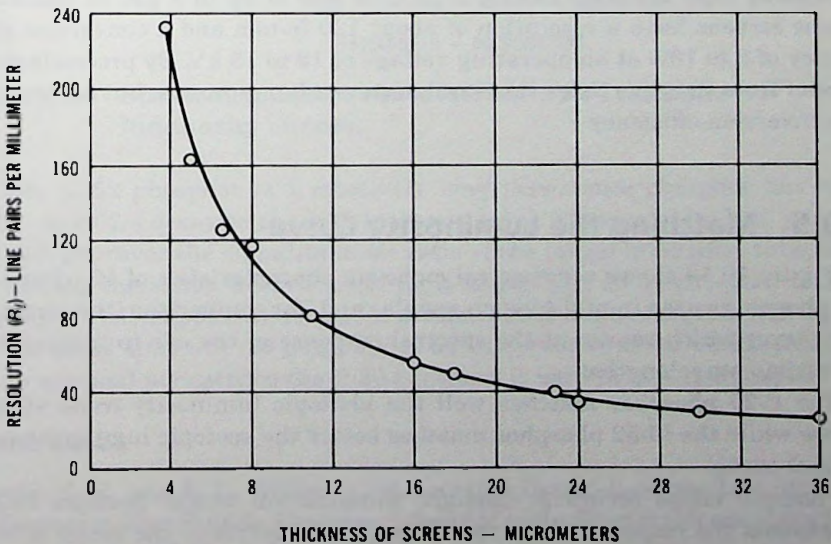

Fig. 10.9   **Measured values of limiting resolution as a function of screen thickness.**

Because the function of the phosphor screen is to convert electron kinetic energy into light energy, the conversion efficiency of the phosphor screen must also be considered in designing for the optimum thickness of the phosphor screen. In general, the larger the particle size of the phosphor, the greater the conversion efficiency. Because the use of a larger-particle phosphor with a thin screen results in a loss of resolution, however, an optimum balance of conversion efficiency and resolution requires a trade-off between the size of the phosphor particle and the thickness of the screen. A suitable compromise is to make the diameter of the phosphor particle equal to the thickness of the screen (essentially a monolayer screen). In such screens, however, the microscopic irregularities in the effective thickness reduce the performance of the screen somewhat. In usual practice, therefore, smaller particles are also included to provide a smooth screen layer. An important characteristic of high-resolution screens is that their screen density is considerably higher than that of regular screens (such as, for example, those used in television picture tubes) in which the phosphor particles are loosely packed. Because of the higher screen density it is possible to reduce the screen thickness for a given screen weight, and thus to improve the resolution.

High-resolution screens used at present in image tube applications are processed from material having a particle size of up to 5 μm in diameter. These screens have a resolution of about 120 lp/mm and a conversion efficiency of 8 to 10% at an operating voltage of 12 to 15 kV. By processing the screen from finer particles this resolution can be improved, but with a loss of conversion efficiency.

10.5   Matching the Luminosity Curve

Figure 10.10 shows the spectral emission characteristics of 10-52 and P-20 phosphors used in night vision goggles and, for comparison, the luminosity curves which represent the spectral response of the eye to radiant flux at various wavelengths.

The P-20 phosphor matches well the photopic luminosity (cone vision) curve while the 10-52 phosphor matches better the scotopic luminosity (rod vision) curve.

Photopic vision occurs at daylight illumination levels. Scotopic vision represents the response of the eye at moonlight levels in the range of 10^{-1} to 10^{-5} fL brightness levels. The scotopic curve shown in Figure 10.10 is thus representative for very low brightness levels. At higher brightness levels the scotopic luminosity curve shifts toward the photopic luminosity curve.
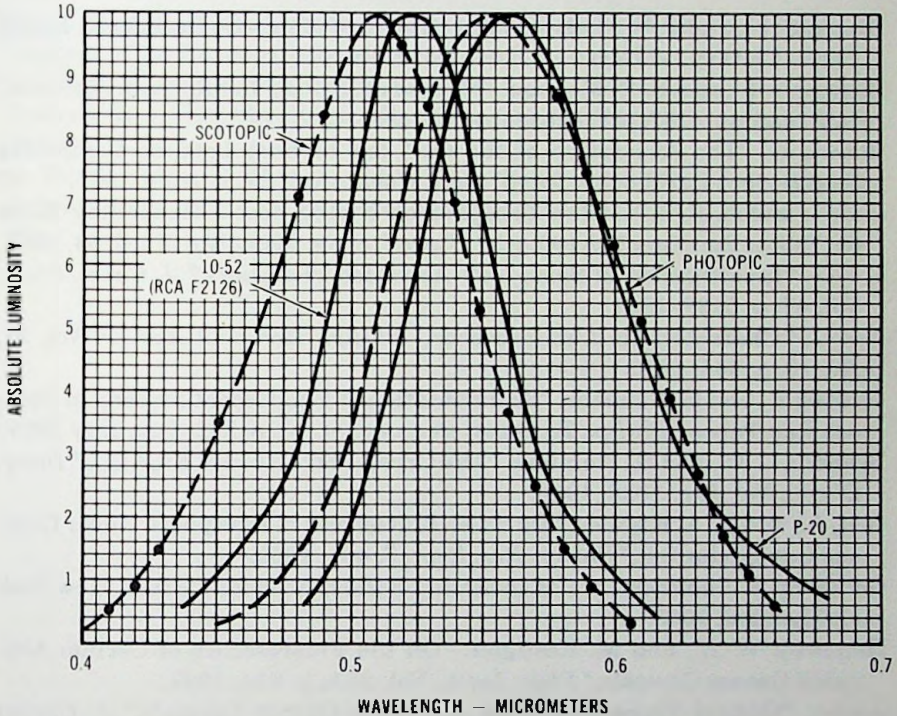
**Fig. 10.10   Spectral emission characteristics and absolute
luminosity curves.**

The 10-52 phosphor is a relatively long persistence phosphor having a
0.01- to 0.02-s decay to the 10% intensity level. Because of its long persist-
ence it improves the signal-to-noise ratio of the image intensifier tube, thus
extending the vision toward lower light levels. The 10-52 phosphor is used
for night vision applications where persistence is not a critical factor.

The decay time of P-20 phosphor is on the order of about 60 μs. Because
of its minimal persistence the P-20 phosphor is used in avionics goggles.

References

Apple, E. F., and F. E. Williams. "Associated Donor-Acceptor Luminescent
Centers in Zinc Sulfide Phosphor," *Journal of the Electro Chemical Society*,
p. 224, Vol. 106, No. 3, March 1959.

Benderskii, L. A., et al. "Synthesis and Luminescence Properties of Solid
Solutions in the System YAG:CeGdAG:Ce," *Bull. Acad. Sciences USSR
Phys.*, Vol. 38, p. 72, 1974.

Blank, S. L., and J. W. Nielsen. "The Growth of Magnetic Garnets by Liquid Phase Epitaxy," *J. Cryst. Growth*, Vol. 17, p. 302, 1972.

Bishop, A. E., and E. E. Mayaud. "Method of Making Luminescent Screens," U. S. patent 3,287,151, November 22, 1966.

Blasse, G. "The Absorption of the Ce^{3+} Ion in Host Lattices Containing Pentavalent Cations," *J. Inorg. Nucl. Chem.*, Vol. 29, p. 1817, 1967.

――――, and A. Bril. "A New Phosphor for Flying Spot Cathode-Ray Tubes for Yellow Emitting $Y_3Al_5O_{12}:Ce^{3+}$," *Appl. Phys. Letts.*, Vol. 11, p. 53, 1967.

――――. "Investigation of Some Ce^{3+} Activated Phosphors," *J. Chem. Phys.*, Vol. 47, p. 5139, 1967.

――――. "Characteristic Luminescence," *Philips Technical Review*, Vol. 31, No. 10, p. 304, 1970.

de Boer, F., and H. Emmens. "Sedimentation of Fluorescent Screens in Cathode Ray Tubes," *Philips Technical Review*, Vol. 16, p. 232, February 1955.

Brandle, C. D., and H. Steinfink. "The Crystal Structure of $Eu_4Al_2O_9$," *Inorg. Chem.*, Vol. 8, p. 1320, 1969.

Bril, A., and H. A. Klasens. "Intrinsic Efficiencies of Phosphors Under Cathode Ray Excitation," *Philips Res. Rept. 7*, 401, 1952.

Goldberg, P. *Luminescence of Inorganic Solids*, Academic Press, New York and London, 1966.

Holloway, W. W., and M. Kestigan. "On the Fluorescence of Cerium Activated Garnet Crystals," *Phys. Letts.*, Vol. 25A, p. 614, 1967.

――――. "Optical Properties of Ce Activated Garnet Crystals," *J. Optical Society of America*, Vol. 59, p. 60, 1969.

Jørgensen, C. J. "Differences Between the Four Halide Ligands and Discussion Remarks of Trigonal-Bipyramidal Complexes, on Oxidation States, and Diagonal Elements of One Electron Energy," *Coord. Chem Rev.*, Vol. 1, p. 164, 1966.

Leverenz, H. W., *An Introduction to Luminescence of Solids*, Dover Publications, Inc., New York, 1968.

Prener, J. S., and F. E. Williams. "Activator Systems in Zinc Sulfide Phosphors," *Journal of the Electro Chemical Society*, Vol. 103, No. 6, p. 342, June 1956.

Reed, J. W., and A. B. Chase. "The Unit Cell and Space Group of $2Y_2O_3:Al_2O_3$," *Acta Cryst.*, Vol. 15, p. 312, 1962.

Robertson, J. M., and M. W. van Tol. "Epitaxially Grown Monocrystalline Garnet Cathode Ray Tube Phosphor Screens," *Appl. Phys. Letts.*, Vol. 37, No. 5, p. 471, 1980.

――――, et al. "Thin Single Crystalline Phosphor Layers Grown by Liquid Phase Epitaxy," *Philips J. Res.*, to be published.

――――, et al. "Color Shift of Ce^{3+} Emission in Monocrystalline Epitaxially Grown Garnet Layers," *Philips J. Res.*, Vol. 36, p. 15, 1981.

Tien, T. Y., et al. "Ce^{3+} Activated Y$_3$Al$_5$O$_{12}$ and Some of Its Solid Solutions," *Journal of the Electro Chemical Society,* Vol. 120, p. 278, 1973.

van Tol, M. W., and J. Van Esdonk. "A High Luminescence, High Resolution Cathode-Ray Tube for Special Purposes," *IEEE Transactions,* to be published.

van Tol, M. W., and W. F. van der Weg, "Saturation Effects of Cathodo-luminescence in Rare Earth Activated Epitaxial Y$_3$Al$_5$O$_{12}$ Layers," *Appl. Phys. Letts.,* to be published.

11

X-RAY IMAGES

11.1   Introduction

Image intensifiers are often used to convert and intensify X-ray images that are obtained by irradiation of an X-ray converting screen with X-rays through a specimen under observation. The quality of such a system depends on its ability to display contrast between two elements under observation and to resolve small details. The contrast and the resolution of an X-ray image are largely determined by the electrical and physical properties of the X-ray converting screen, the spectral emission characteristics of the X-ray source, and the X-ray attenuation of the specimen under observation. In the following discussion, the relative importance of each of these parameters in the formation of the X-ray image will be examined.

11.2   Absorption of X-Rays

When X-rays are traversing a homogeneous substance their intensity is reduced by a constant fraction per unit length. Thus the beam intensity I of the radiation may be given by

$$I = I_0 \exp\left[-\left(\frac{\mu}{\rho}\right)\rho t \right], \tag{11.1}$$

where I_0 is the X-ray intensity incident on the material, and ρ, t, and μ are the density, thickness, and absorption coefficient of the material, respectively.

The linear absorption coefficient μ of a substance is a function of the X-ray wavelength, the atomic numbers of the constituent elements, and the

physical state of the substance. The mass absorption coefficient (μ/ρ) is a more commonly used term and has the useful property of being independent of the physical state of the material. (Tables of μ/ρ values for pure elements are available in the literature.)

Equation 11.1 indicates that a test object that has a varying thickness or contains nonhomogeneity in its structure translates a homogeneous X-ray beam into local intensity variations. The beam intensity pattern produced by these variations is made visible by conversion of the X-rays into visible light by use of a fluorescent screen. In this manner the structural details of the object under test are displayed in terms of brightness variation.

11.3   X-Ray Phosphor Screens

The conversion of X-ray energy to light occurs in two stages. In the first stage the absorbed X-ray energy is converted to high-energy electrons. In the second stage the kinetic energy of the released electrons is converted to light. The fraction α_p of X-ray absorption of a screen at a particular wavelength is given by the following expression:

$$\alpha_p = 1 - \exp\left[-\left(\frac{\mu}{\rho}\right)\rho t \right], \tag{11.2}$$

where μ/ρ and t are the mass absorption coefficient and thickness of the phosphor screen, respectively.

The mass absorption coefficient of a material consisting of several elements is the sum of the mass absorption coefficients of the individual elements multiplied by their appropriate weight fractions. This rule follows directly from the fact that the mass-absorption coefficient is independent of the physical state of the absorbing material (i.e., whether the element exists in a pure state or as a compound constituent).

The mass absorption coefficient (μ/ρ) of a compound consisting of n elements is given by

$$\left(\frac{\mu}{\rho}\right) = W_1\left(\frac{\mu}{\rho}\right)_1 + W_2\left(\frac{\mu}{\rho}\right)_2 + \ldots + W_n\left(\frac{\mu}{\rho}\right)_n, \tag{11.3}$$

where W_n and $(\mu/\rho)_n$ are the weight fraction and the mass absorption coefficient, respectively, of the nth element of the compound.

Absorption coefficients have been calculated for the three most widely used X-ray phosphors: zinc sulfide (ZnS), zinc cadmium sulfide (ZnS·CdS), and calcium tungstate ($CaWO_4$) by the procedure outlined below. The mass compositions and densities of the three phosphors are given in table 11.1.

Table 11.1   Mass Compositions and Densities of Three Phosphors

Phosphor	Mass Composition	Density (g/cm^3)
ZnS	$0.67Zn + 0.33S$	4.1
ZnS·CdS	$0.341Zn + 0.382Cd + 0.277S$	4.46
CaWO$_4$	$0.142Ca + 0.634W + 0.224O$	6.06

The linear absorption coefficients μ of these three phosphors are calculated as follows:

$$\mu_{ZnS} = 4.1\left[0.67\left(\frac{\mu}{\rho}\right)_{Zn} + 0.33\left(\frac{\mu}{\rho}\right)_S\right],$$

$$\mu_{ZnS\cdot CdS} = 4.46\left[0.341\left(\frac{\mu}{\rho}\right)_{Zn} + 0.382\left(\frac{\mu}{\rho}\right)_{Cd} + 0.277\left(\frac{\mu}{\rho}\right)_S\right],$$

$$\mu_{CaWO_4} = 6.06\left[0.142\left(\frac{\mu}{\rho}\right)_{Ca} + 0.634\left(\frac{\mu}{\rho}\right)_W + 0.224\left(\frac{\mu}{\rho}\right)_O\right]. \tag{11.4}$$

Figure 11.1 shows the absorption coefficients for these three phosphors as a function of wavelength, as calculated by use of published data for the
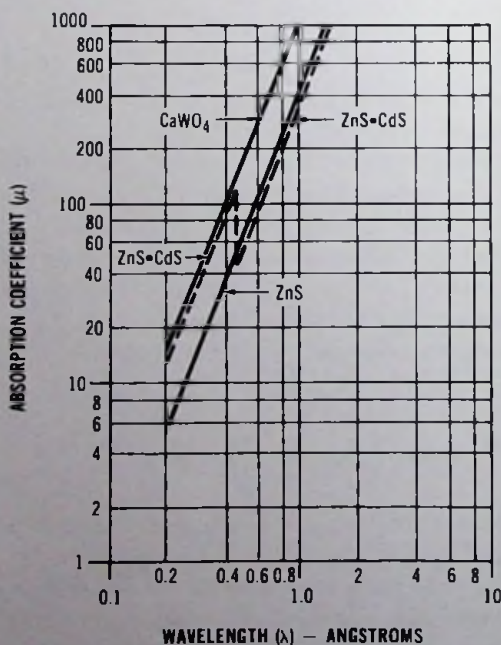
Fig. 11.1   Absorption coefficient as a function of wavelength for three phosphor compounds.

value of (μ/ρ). With μ known, the fraction α_p of X-ray absorption of a solid-layer screen can be determined by equation 11.2. Figure 11.2 shows the results of these calculations.

Because the density of the microsettled screens approximately equals the density of a solid-layer screen, it is justifiable to carry over the calculations for a solid layer without considerable error.

As mentioned earlier, the energy of an absorbed X-ray quantum is partially converted into the kinetic energy of the released electron. The kinetic energy E_k of the released electron is given by

$$E_k = E_p - E_b, \tag{11.5}$$

where E_p is the energy of the X-ray photon and E_b is the energy required for the complete removal of the electron from a particular shell of the converting atom.
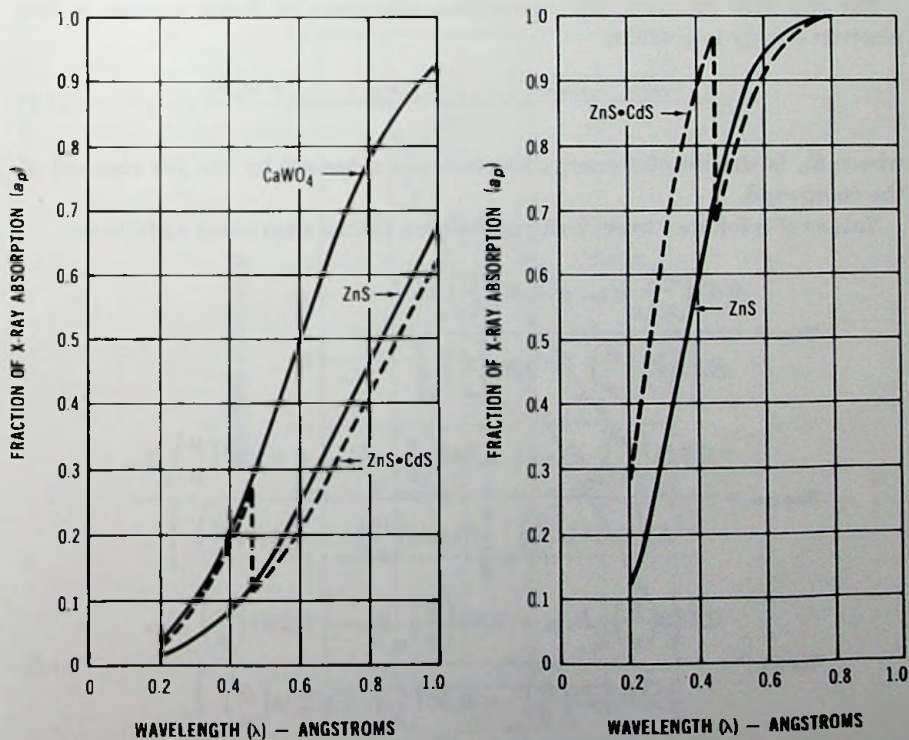
(A) 2.5×10^{-3} cm thick phosphor screen.

(B) 2.5×10^{-2} cm thick phosphor screen.

Fig. 11.2   Fraction of X-ray absorption of the phosphor screens as a function of wavelength.

In general, when the X-ray photon is energetic enough to liberate an electron from the K shell, the probability is high that the K electron is released; otherwise, electrons are freed from subsequent shells.

It follows from equation 11.5 that, for identical X-ray photon energies, the electrons released by different atoms of a compound possess different kinetic energies. Therefore it is important to know the partial absorption of an element in the compound. From equation 11.3 the partial absorption α, of an element at a particular wavelength expressed as a fraction of total absorption of the compound is given by

$$\alpha_j = \frac{W_j \left(\frac{\mu}{\rho}\right)_j}{W_1 \left(\frac{\mu}{\rho}\right)_1 + W_2 \left(\frac{\mu}{\rho}\right)_2 + \ldots + W_j \left(\frac{\mu}{\rho}\right)_j + \ldots + W_n \left(\frac{\mu}{\rho}\right)_n}. \tag{11.6}$$

For the first electron, the conversion efficiency of X-ray energy η into electron energy is given by

$$\eta = \frac{\alpha_1 E_{k1} + \alpha_2 E_{k2} + \ldots + \alpha_j E_{kj} + \ldots + \alpha_n E_{kn}}{E_p}, \tag{11.7}$$

where E_{kj} is the kinetic energy of electrons released by the jth element of the compound.

Values of η for the three X-ray phosphors can be expressed as follows:

$$\eta_{ZnS} = \frac{0.67 \left(\frac{\mu}{\rho}\right)_{Zn} E_{k,Zn} + 0.33 \left(\frac{\mu}{\rho}\right)_{S} E_{k,S}}{E_p \left[0.67 \left(\frac{\mu}{\rho}\right)_{Zn} + 0.33 \left(\frac{\mu}{\rho}\right)_{S}\right]},$$

$$\eta_{ZnS.CdS} = \frac{0.341 \left(\frac{\mu}{\rho}\right)_{Zn} E_{k,Zn} + 0.382 \left(\frac{\mu}{\rho}\right)_{Cd} E_{k,Cd} + 0.277 \left(\frac{\mu}{\rho}\right)_{S} E_{k,S}}{E_p \left[0.341 \left(\frac{\mu}{\rho}\right)_{Zn} + 0.382 \left(\frac{\mu}{\rho}\right)_{Cd} + 0.277 \left(\frac{\mu}{\rho}\right)_{S}\right]},$$

$$\eta_{CaWO_4} = \frac{0.142 \left(\frac{\mu}{\rho}\right)_{Ca} E_{k,Ca} + 0.63 \left(\frac{\mu}{\rho}\right)_{W} E_{k,W} + 0.224 \left(\frac{\mu}{\rho}\right)_{O} E_{k,O}}{E_p \left[0.142 \left(\frac{\mu}{\rho}\right)_{Ca} + 0.63 \left(\frac{\mu}{\rho}\right)_{W} + 0.224 \left(\frac{\mu}{\rho}\right)_{O}\right]}. \tag{11.8}$$

where

$E_{k,Zn} = (E_p - 9.662)$ keV for $\lambda < 1.29$ Å,
$E_{k,S} = (E_p - 2.469)$ keV for $\lambda < 5$ Å,

$E_{k,Cd} = (E_p - 26.712)$ keV for $\lambda > 0.465$ Å,

$E_{k,Cd} = (E_p - 4.019)$ keV for $\lambda = (0.465 - 2.97)$ Å,

$E_{k,Cs} = (E_p - 4.038)$ keV for $\lambda < 2.83$ Å,

$E_{k,w} = (E_p - 12.094$ keV for $\lambda = (0.18 - 1.025)$ Å

$E_{k,O} = (E_p - 0.532)$ keV for $\lambda < 23.3$ Å.

Numerical values calculated from these equations are shown in figure 11.3.

For purposes of energy conversion, only the energy of the first electron has been taken into account. When the excited atom containing a surplus E_b of energy returns to the ground state it either radiates an X-ray quantum or emits an Auger electron. The first process has a high probability in heavy elements, the second process in light elements. In relatively thin screens, however, both of these processes are so inefficient that they can be neglected. The reason for this inefficiency is the low velocity of the Auger or second-
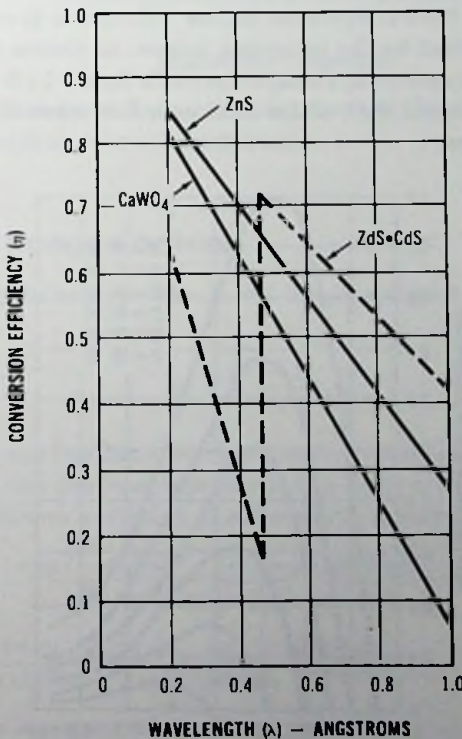
Fig. 11.3   Conversion efficiency of X-ray energy into electron energy for thin screens.

generation electrons (electrons produced by the X-ray radiation of the screen) and the low self-absorption of the screens. The curves of figure 11.3, therefore, are representative of the energy conversion of a thin screen. When the conversion efficiency of X-ray energy into electron energy is known, the conversion efficiency for light is obtained as the product of η and the absolute electron-energy-to-light conversion efficiency of the screen.

11.4   X-Ray Source

One of the commonly used X-ray sources is an X-ray tube having a tungsten target. Figure 11.4 shows the continuous X-ray spectrum of this target for various tube voltages. As the tube voltage decreases, the energy radiation shifts towards longer wavelengths. Figure 11.5 shows the X-ray spectrum change when the radiation passes through sheets of aluminum. Aluminum attenuates the radiation and shifts it toward shorter wavelengths. Both of these shifts are important for contrast.

When the X-ray tube is operated at low voltages a greater portion of X-ray energy is absorbed by the phosphor screen, as shown in figure 11.2. On the other hand, the spectrum change shown in figure 11.5 provides contrast percentage that exceeds that of the thickness variation of the specimen, as figure 11.2 indicates.
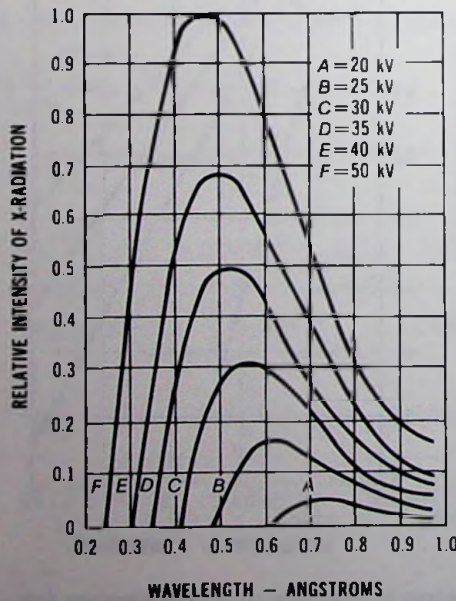
Fig. 11.4   The continuous X-ray spectrum of a tungsten target for various tube voltages.
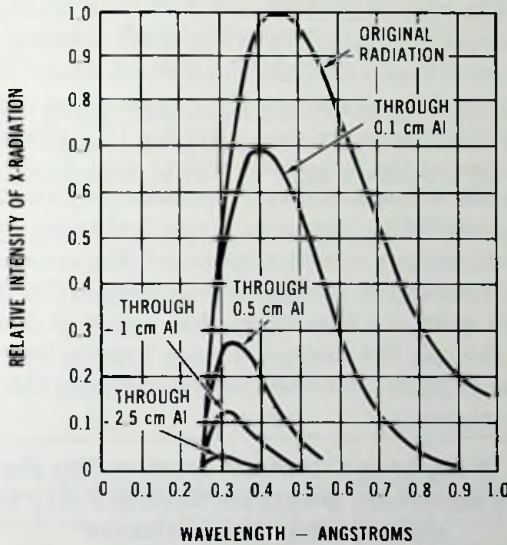
Fig. 11.5   The change of X-ray spectrum after the radiation passes
through sheets of aluminum.

11.5   X-Ray Image Contrast

It is customary to express the X-ray image contrast C by the following
equation:

$$C = \frac{B_1 - B_2}{B_1},\qquad(11.9)$$

where B_1 and B_2 are the luminance of two information elements under ob-
servation. When the contrast represents the X-ray intensity variation pro-
duced by the thickness variation of a specimen, it may be expressed as

$$C = \frac{\int I_0(\lambda)\alpha_p(\lambda)\eta(\lambda)\exp(-\mu t_1)\,d\lambda - \int I_0(\lambda)\alpha_p(\lambda)\eta(\lambda)\exp[-\mu(t_1+\Delta t)]\,d\lambda}{\int I_0(\lambda)\alpha_p(\lambda)\eta(\lambda)\exp(-\mu t_1)\,d\lambda}$$

$$= \frac{\int I_0(\lambda)\alpha_p(\lambda)\eta(\lambda)\exp(-\mu t_1)(1-\exp[-\mu\Delta t])\,d\lambda}{\int I_0(\lambda)\alpha_p(\lambda)\eta(\lambda)\exp(-\mu t_1)\,d\lambda},\qquad(11.10)$$

where $I_0(\lambda)$ is the intensity of the X-ray radiation, μ is the absorption coef-
ficient of the specimen, and t_1 and $t_1 + \Delta t$ are specimen thicknesses corre-
sponding to B_1 and B_2. Figure 11.4 shows the relative values of $I_0(\lambda)$ for
several values of X-ray tube voltages.

One of the requirements in industrial application of X-ray fluoroscopy is

to display a thickness variation of 2% of 0.6 cm thick aluminum layer with an observable contrast. The objective in the study involves selection of the best possible approach that will satisfy this requirement. For this reason, contrast was calculated by alteration of the parameters of equation 11.10. The results of this calculation are shown in table 11.2. Group 1 of table 11.2 shows the comparison of the three most widely used X-ray screens. In this group no appreciable contrast difference results from the use of different screens. Group 2 shows that a reduction of the X-ray tube voltage increases the value of the contrast by a significant amount. The reason for this change is the shift in the spectral-emission characteristics of the X-ray source, as shown in figure 11.4. Group 3 indicates that a tenfold increase in screen thickness hardly changes the contrast. Group 4 shows how the contrast is changed by alteration of the specimen thickness within the thickness variation at the 2% level.

Table 11.2 X-ray Image Contrast Produced by the Thickness Variation of Aluminum Sheets for Several X-Ray Screens at Various X-Ray Tube Voltages

Group	Screen	t_s	V_z	t_1	Δt	C
1	ZnS·CdS	2.5×10^{-3}	50	0.600	0.012	0.034
	ZnS	2.5×10^{-3}	50	0.600	0.012	0.036
	CaWO$_4$	2.5×10^{-3}	50	0.600	0.012	0.035
2	ZnS·CdS	2.5×10^{-3}	30	0.600	0.012	0.06
	ZnS	2.5×10^{-3}	30	0.600	0.012	0.058
3	ZnS·CdS	2.5×10^{-2}	50	0.600	0.012	0.032
	ZnS	2.5×10^{-2}	50	0.600	0.012	0.034
4	ZnS·CdS	2.5×10^{-3}	50	0.300	0.006	0.025
	ZnS·CdS	2.5×10^{-3}	50	1.00	0.020	0.044
5	ZnS·CdS	2.5×10^{-3}	50	0.600	0.200	0.42
	ZnS	2.5×10^{-3}	50	0.600	0.200	0.44
	ZnS·CdS	2.5×10^{-3}	30	0.600	0.200	0.62
	ZnS	2.5×10^{-3}	30	0.600	0.200	0.61

V_z = X-ray tube voltage in kilovolts
t_s = thickness of phosphor screen in centimeters
t_1 = thickness of aluminum sheet in centimeters
Δt = thickness variation of the aluminum in centimeters (only in positive direction)

Another important application of the X-ray fluoroscopy is inspection of small components. For example, in the case of transistors it is desirable to observe details comparable to a 0.0125 cm thick wire enclosed in a 0.03 cm

thick envelope. If both the wire and the envelope are made of iron, calculated contrast values are shown approximately in table 11.3. Table 11.3 also contains the contrast for a 1-mil wire (2.54×10^{-3} cm).

Table 11.3 X-Ray Image Contrast C of an Iron Sheet Having a Nominal Thickness of 0.06 cm Overlaid With an Iron Pattern of Thickness Δt (X-Ray Tube Voltage is 50 kV)

Δt	C	Screen
0.0125	0.386	ZnS
0.0125	0.364	ZnS·Cds
0.0125	0.38	CaWO$_4$
0.0025	0.097	ZnS
0.0025	0.09	ZnS·Cds
0.0025	0.095	CaWO$_4$

It can be concluded that an adequate contrast is present that resolves the 2% thickness variation of a 0.6 cm thick aluminum sheet by application of any one of three screens even at 50-kV X-ray tube voltage. Moreover, results show that a relatively thin screen produces practically as much contrast as a considerably thicker screen. This effect is very favorable from a slightly different point of view. For example, it is known that if two regions differ in luminance, it is difficult, if not impossible, for an observer to recognize the difference unless the luminance gradient or contrast gradient is sufficiently great. High-contrast gradients, however, can be obtained only by the application of relatively thin screens, which have high resolution.

11.6 X-Ray Absorption of Phosphor Screens in the Presence of a Specimen

As mentioned previously, the three phosphors under consideration display no distinct difference in contrast. Inspection of a thick specimen, however, indicates absorption of a large portion of X-ray energy in the substance. Because of this absorption the number of X-ray photons incident on the phosphor screen is greatly reduced, and the number of X-ray photons absorbed in the screen has a still lower value. Consequently, resolution may be limited by quantum noise, and it is important to consider the absorption of the phosphor screens that provides the greatest number of absorbed X-ray photons. The fraction a of X-ray absorption of a phosphor screen in the presence of a specimen with a thickness t is given by

$$a = \frac{\int I_0(\lambda)\alpha_p(\lambda) \exp{(-\mu t)}\, d\lambda}{\int I_0(\lambda) \exp{(-\mu t)}\, d\lambda}. \qquad (11.11)$$

Values of a calculated for several phosphors are shown in table 11.4. This table shows that calcium tungstate ($CaWO_4$) is the most efficient absorber. However, zinc cadmium sulfide absorbs only 17% less than the calcium tungstate screen; the difference is insignificant with respect to the signal-to-noise ratio.

Table 11.4   X-Ray Absorption a of 2×10^{-3}-cm Phosphor Screens in the Presence of an Aluminum Sheet of Thickness t Centimeters, Where the X-Ray Tube Voltage is 50 kV

t	a	Screen
0	0.214	ZnS
0	0.228	ZnS-Cds
0	0.413	$CaWO_4$
0.600	0.024	ZnS
0.600	0.049	ZnS-Cds
0.600	0.059	$CaWO_4$

11.7   Quantum Noise Limitation of Contrast

The expression for the signal-to-noise ratio produced by the statistical variation of X-ray photon flux absorbed by two information elements of the phosphor screen may be expressed as follows:

$$k = \frac{S}{N} = \frac{N_a - N_b}{\sqrt{N_a + N_b}}, \tag{11.12}$$

where N_a and N_b are the average numbers of X-ray quantum per storage time per information element from the high-light and low-light areas, respectively. For reliable detection k is about 5; the storage time of the human eye is 0.2 s.

For example, if the observed contrast is 2.5%, $N_b = 0.975N_a$. Substitution of this N_b value and $k = 5$ in equation 11.12 gives $N_a \equiv 80\ 000$ quanta per 0.2 second, or 400 000 quanta per second.

When the resolution is 5 lp/mm, the area A of a white bar of a standard USAF pattern is given by

$$A = 5W^2 = \frac{5}{4R_l^2} = 5 \times 10^{-4}\ cm^2. \tag{11.13}$$

The absorbed photon flux per square centimeter then becomes $400\ 000/(5 \times 10^{-4}) = 8 \times 10^8$ photons per square centimeter per second.

If, in addition to this information, the data of table 11.4 are used, the necessary minimum output power of the X-ray tube can be calculated as required for the inspection of a 0.6 cm thick aluminum specimen.

Table 11.5   X-Ray Image Contrast of Two Adjacent Aluminum Elements Having Thicknesses of 0.635 cm and 0.835 cm (V_z = 50 kV)

Screen	C
ZnS	0.46
ZnS·Cds	0.47
CaWO$_4$	0.48

The usefulness of the equations developed for the contrast calculations was tested with the following parameters:

t_1 = 0.635-cm aluminum sheet,

Δt = 0.2-cm aluminum sheet,

V_x = 50 kV.

First, the phosphor screen was excited through an aluminum sheet having a thickness t_1 = 0.635 cm, and the corresponding luminance B_1 was measured. Second, the luminance B_2 was measured by excitation of the phosphor screen through an aluminum layer with $t_1 + \Delta t$ = 0.635 + 0.2 = 0.835 cm. The contrast was obtained by use of equation 11.9. Table 11.5 shows the results of these measurements. These results are in reasonable agreement with the theoretical values of contrast given in table 11.1, group 5.

Additional experiments conducted to resolve a 2% thickness variation of a 0.6-cm aluminum sheet have demonstrated that any of the three phosphor screens displays a contrast large enough to be observable by the eye.

References

American Institute of Physics Handbook, 2nd Ed., McGraw-Hill Book Co., New York, 1963.

Csorba, I. P. "Contrast Characteristics of X-Ray Images," *RCA Review*, Vol. 32, No. 1, March 1971.

———. "Resolution Limitations of Electromagnetically Focused Image-Intensifier Tubes," *RCA Review*, Vol. 30, No. 3, 1969.

Handbook of Chemistry and Physics, 45th ed. Chemical Pub. Co., Cleveland, 1964–1965.

Richardson, D. A. "The X-Ray and Gamma-Ray Absorption Coefficients of a Number of Glasses," *British J. of App. Phys.*, Vol. 8, January 1957.

"The Low-Light-Level Performance of the Image Intensifier Orthicon," *Advances in Electronics and Electron Physics*, Vol. 13, 1960.

Ulrey, C. T. "An Experimental Investigation of the Energy in the Continuous X-Ray Spectral of Certain Elements," *Physical Review*, Vol. 11, 1918.

12

PHOTOCATHODES, PHOTOCONDUCTIVITY, AND SECONDARY-ELECTRON EMISSION

12.1 Photocathodes

12.1.1 Introduction

Image tube photocathodes are semitransparent photoemissive materials deposited on the vacuum side of the input faceplate of the image tube. At present, two major types exist. The first type consists of polycrystalline materials deposited in high vacuum on the input faceplate. To this group belong the alkali antimonides, the silver-oxygen-cesium cathode, and the solar-blind cesium-activated cathodes. These cathodes can be classified as positive electron affinity cathodes. The second type is the generation 3 GaAs:CsO/ALGaAs photocathode consisting of epitaxially grown single-crystal materials. The generation 3 cathode is a negative electron affinity cathode.

According to the spectral sensitivity characteristics, image tube cathodes may be classified into four major categories. The first category consists of cathodes responding to light in the visible and near ultraviolet region of the electromagnetic spectrum. The cesium-antimony and the bialkali cathodes belong to this group. The second category consists of multialkali cathodes and the generation 3 cathode responding to light in the region from 300 nm to 950 nm and 550 nm to 950 nm, respectively. The silver-oxygen-cesium

cathode belongs to the third category, responding to light in the region from 300 nm to 1200 nm. The solar-blind cathodes constitute the fourth category of cathodes which respond to light in the region of 120 nm to 320 nm. Figure 12.1 shows the spectral sensitivity characteristics of a variety of practical photocathodes.

12.1.2   Photoemission From Semiconductors

The operation of a photocathode is based on the photoelectric emission effect, which for semiconductors may be considered as a three-step process. In the first step, photoelectrons are excited from the valence band to the vacuum level by absorption of light in a thin semiconductor film. The second step is the transport of the excited electrons through the semiconductor film to the semiconductor-vacuum interface. The third step is escape over the surface barrier into the vacuum. Because each of the above steps contains losses, the efficiency of the photoelectric emission is determined by the efficiency of all three steps.

Photoemission may be explained in terms of the band theory of solids. Consider the semiconductor energy band model of figure 12.2. The horizontal coordinate represents the spatial coordinate perpendicular to the surface, and the vertical coordinate represents energy. The valence band is completely filled with electrons and the conduction band is empty. The conduction band and the valence band are separated by the forbidden band E_G which is the energy difference between the bottom of the conduction band and the top of the valence band. The Fermi level lies in the forbidden zone at a distance below the vacuum level, where ϕ is the thermionic work function of the semiconductor. An incident photon with an energy $E_P = h\nu$ just slightly greater than E_G (where h is the Planck's constant and ν is the frequency of radiation), on absorption, can excite an electron from the valence band to the conduction band. The electron produced by this process is free to migrate through the solid, but because of the electron affinity E_A, it cannot escape from the solid. Photoemission, therefore, may occur only if the absorbed photon energy E_p is greater than $\phi_0 = E_A + E_G$. Here ϕ_0 is the photoelectric work function or long-wavelength threshold.

The relationship between the energy E_p of a light quantum and the wavelength (λ) of the radiation may be given by the following equation:

$$E_p = h\nu = \frac{hc}{\lambda} = \frac{12\ 395}{\lambda}, \qquad (12.1)$$

where E_p is in electronvolts, λ is in angstroms, and c is the velocity of light.

When the energy of the light quantum is just sufficient to produce photoemission, the following relationships exist:

$$E_p = \phi_0 = E_A + E_G, \qquad (12.2)$$

and

$$\lambda_0 = \frac{12\ 395}{\phi_0} = \frac{12\ 395}{E_A + E_G},$$ (12.3)

where λ_0 is the threshold wavelength of photoemission.

By illumination of the photocathode with a light wavelength shorter than λ_0, the energy of the absorbed light quantum is partially converted into the kinetic energy of the released electron. The maximum emission energy E_{im} of the released electron may be given by

$$E_{im} = E_p - (E_A + E_G).$$ (12.4)

Most electrons, however, lose part of their energy by collision. For energetic electrons (hot electrons) the major energy loss process is the hole-electron pair production by excitation of valence band electrons. Because of energy loss processes the emission energy corresponding to a monochromatic radiation ranges from zero to a maximum emission energy given by equation 12.4.

12.1.3 Band Bending

In the preceding discussion it was assumed that the energy band edges are straight horizontal lines. For most photoemitters, however, this is only true in the bulk of the material. At the surface of the semiconductor there is always some bending of the energy bands due to the presence of donors or acceptors with energy levels in the forbidden zone.

Consider the case of a p-type semiconductor with a large concentration of donor levels at the surface (n-type surface states). Before equilibrium is established the n-type surface states lie above the Fermi level of the semiconductor. A state of equilibrium is established by the donors giving up electrons to the acceptors in the bulk of the semiconductor. This process gives rise to a negative space charge region near the surface combined with a positive space charge. Thus the potential at the surface drops and the bands at the surface are bent downward. It can be shown that acceptor states which lie below the Fermi level before the equilibrium is established (n-type semiconductor p-type surface states) will bend the bands upward at the surface. Figure 12.3 illustrates the two possibilities for band bending and the cases where no bending takes place. From figure 12.3 we may conclude that bending the bands downward reduces the effective value of electron affinity, while upward bending increases it. Thus downward bending aids the photoemission whereas upward bending hinders it. It has been found that the most efficient photoemitters, $(Na_2KSb)Cs$, Cs_3Sb, and $GaAs:Cs\cdot O$, are p-type in bulk conductivity. It is also possible that the effect
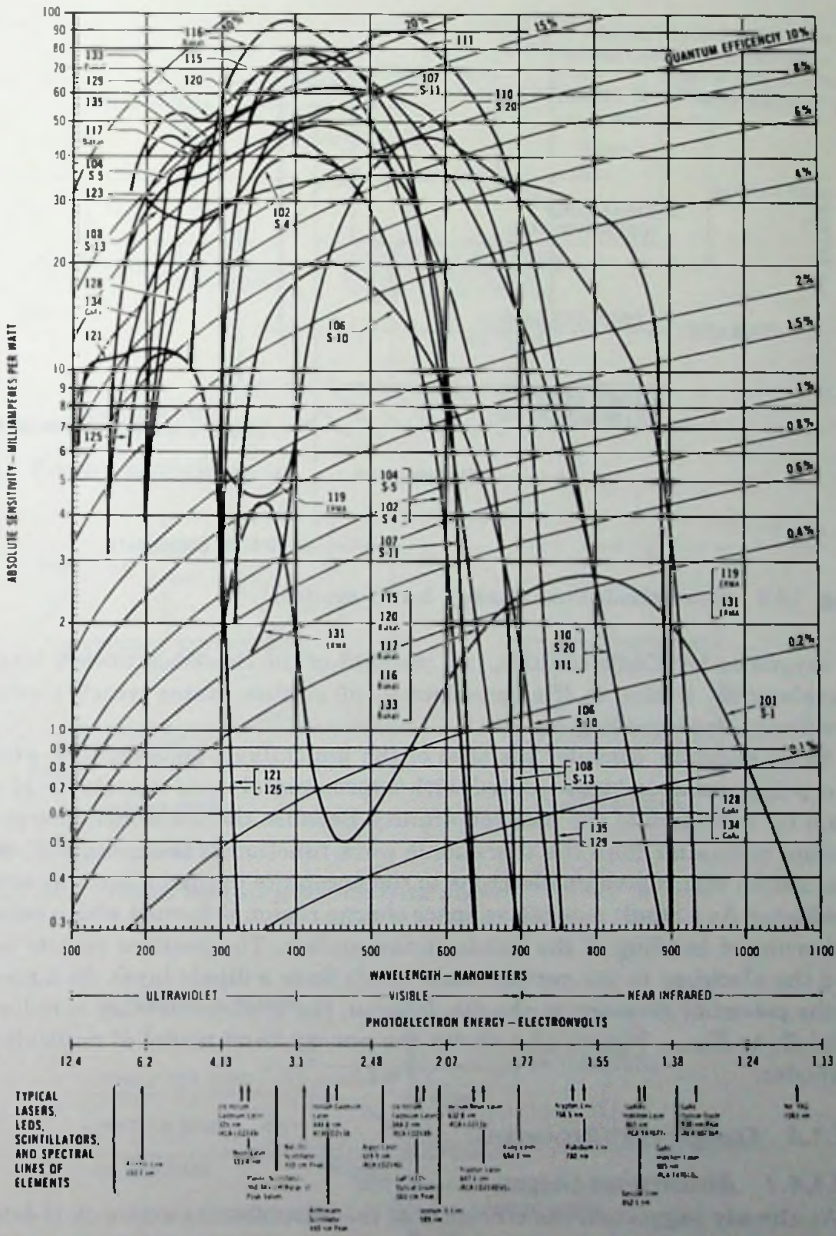
Fig. 12.1   Typical photocathode spectral response characteristics.
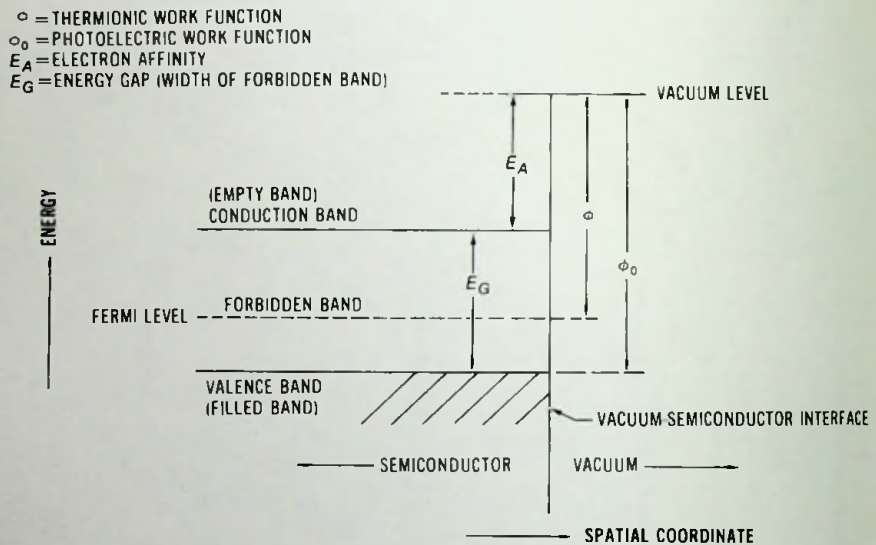(*Courtesy RCA*)

○ = THERMIONIC WORK FUNCTION
○₀ = PHOTOELECTRIC WORK FUNCTION
E_A = ELECTRON AFFINITY
E_G = ENERGY GAP (WIDTH OF FORBIDDEN BAND)

Fig. 12.2   Semiconductor energy band model.

of oxygen on the Cs_3Sb cathode, i.e., the shift of the threshold toward longer wavelengths, is due to the introduction of surface states which produce downward band bending.

As an example, consider the case of the multialkali photocathode which is a p-type semiconductor coated with approximately one monolayer of cesium for reduction of the electron affinity. Because the ionization energy of cesium is smaller than the thermionic work function of the semiconductor, the cesium atoms give up electrons to the acceptors in the bulk of the semiconductor. As a result a negative space charge region is formed which causes a downward bending of the bands at the surface. The positive cesium ions and the electrons in the surface state levels form a dipole layer. As a result of the potential drop across the dipole layer, the electron affinity is reduced from E_A to $E_{A(\text{true})}$. Figure 12.4 shows the energy band model of multialkali cathodes.

12.1.4   Energy Loss Processes

12.1.4.1   Absorption Losses

As already suggested, the efficiency of the photoelectric emission is determined by the energy loss processes occurring in the three basic steps of the emission process. The energy loss processes occurring in the first step are due to imperfect absorption of light within the absorption band of the pho-
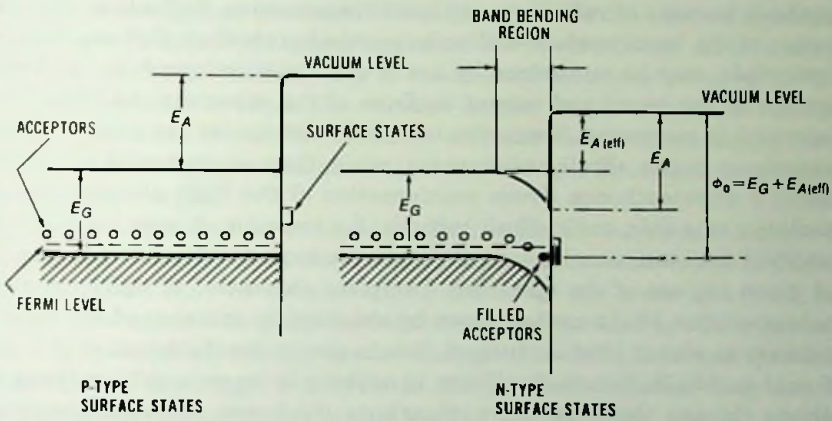
(A) P-type material.
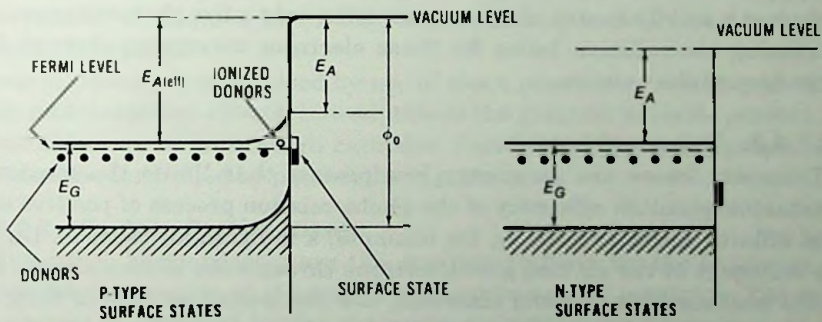
(B) N-type material.

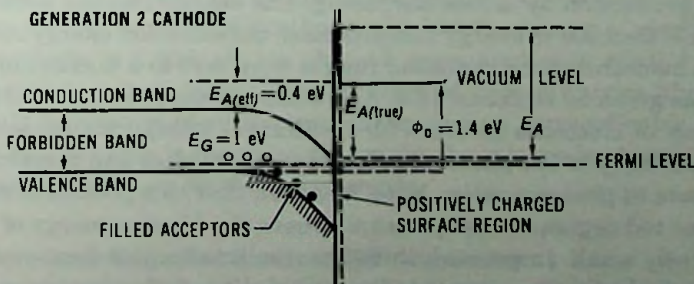Fig. 12.3   Band bending by surface states.

Fig. 12.4   Energy band model of multialkali cathodes.

tocathode because of reflection and light transmission. Reflection losses are present at the input surface of the photocathode interface. Reflection losses, in principle, may be minimized by use of quarter-wavelength antireflection coatings at the input and output surfaces of the substrate. As far as light absorption is concerned, losses due to light transmission are a major energy loss process in the alkali antimonides, while they are minimal in the generation 3 photocathodes. From consideration of the light absorption characteristics of a thin multialkali cathode, for example, it may be concluded that light transmission losses are due to inadequate absorption in the red and green regions of the spectrum. Complete absorption of light across the whole spectrum of the cathode may be obtained by increase of the cathode thickness to about 1200 Å. Indeed, this is about the thickness of the most efficient multialkali cathode. There is nothing to be gained by making the cathode thicker than the fully absorbing thickness, because absorption losses begin to kill the response over the full spectrum. In cathodes thicker than optimum the surplus layer at the photocathode-vacuum interface absorbs just a small amount of light, generating only a few photoelectrons and increasing the collision losses for those electrons traversing through this layer toward the vacuum.

12.1.4.2 Transport Losses

Transport losses are an energy loss process that limits the maximum obtainable quantum efficiency of the photoemission process of positive electron affinity cathodes such as, for example, a multialkali cathode. During the transport of the excited photoelectrons through the semiconductor film to the photocathode-vacuum interface, the electrons lose part of their energy by collision with the lattice. For energetic electrons (hot electrons) the major energy loss process is the hole-electron pair production by excitation of valence band electrons. The threshold energy for pair production in the alkali antimonides is $3E_G$ and the energy loss per event is E_G. For electrons with insufficient energy for pair production, the energy loss mechanism is phonon production by lattice scattering. The energy loss per event is 0.005 to 0.01 eV. Because of energy loss processes the emission energy corresponding to a monochromatic radiation ranges from zero to a maximum emission energy as given by equation 12.4. As a consequence of energy loss processes a fraction of electrons arrive with insufficient energy for overcoming the electron affinity to the photocathode-vacuum interface and therefore cannot participate in photoemission. Note, however, that this process is more critical in the red region of the spectrum, where the kinetic energy of electrons is relatively small. In general, therefore, the smaller the electron affinity of the photocathode, the greater is the probability of photoemission. For this reason efficient photocathodes must have a small electron affinity to allow a substantial fraction of photoelectrons for emission.

Because of energy loss processes it is important that the emitted electrons originate from a thin layer at the surface of the photocathode. As a result of interaction with the lattice, only a fraction of electrons proportional to $\exp(-x/d)$ are able to reach the vacuum from a depth x from the surface. Here d is the escape depth. Therefore, for efficient photoemission, light must be heavily absorbed in a thin photocathode having a thickness comparable with the escape depth.

Transport losses can be reduced by limitation of the mean number of collisions the electrons must make before emission. A reduction in the number of collisions may be obtained by increase of the mean free path for collision. The mean free path for collision is established by the following factors: (a) phonon scattering due to thermal vibration of lattice; (b) ionic scattering due to foreign materials in the crystals; (c) scattering due to crystal imperfections; (d) scattering due to stress in the crystal; and (e) scattering at the grain boundaries.

The first factor can be minimized by cooling the cathode. If, however, no improvement is obtained by cooling, the remaining four factors determine the mean free path.

Ionic scattering is minimized by use of clean processes, resulting in minimum contamination effects. Indeed, this is the greatest variable present in the manufacture of multialkali cathodes. Factors c, d, and e are properties which can be controlled by photocathode processing.

12.1.4.3   Surface Barrier Losses

The surface barrier losses are the greatest problem for the extension of efficient photoemission in the region of electromagnetic spectrum. The surface barrier is produced by the restraining electrostatic forces present at the photocathode vacuum interface. For example, the surface barrier potential or electron affinity is in the range of 0.3 to 0.4 eV for the multialkali cathode. This means that a mobile electron inside the photocathode must have a greater kinetic energy perpendicular to the photocathode-vacuum interface than 0.3 to 0.4 eV for escape to the vacuum. By considering a 1-eV energy gap for the multialkali cathode, the kinetic energy of electrons in the photocathode is 0.458 eV for photons associated with 8500 Å wavelength. For an isotropic velocity distribution of photoelectrons, therefore, only a small fraction of photoelectrons have enough perpendicular kinetic energy for escape. This is the main reason for the relatively sharp cutoff of photoresponse beyond an 8500 Å wavelength.

12.1.5   Zero and Negative Electron Affinity Emitters

In the case of the GaAs:Cs photocathode the heavily p-doped gallium arsenide is cesium coated. Because the ionization energy E_i of cesium is smaller than the thermionic work function of the semiconductor, the cesium

atoms give up electrons to the acceptors in the bulk of the semiconductor. As a result a negative space charge region is formed which causes a downward bending of the bands at the surface. At optimum cesium coating and after equilibrium is established, the Fermi level is stabilized to the level of the surface states. (Further bending does not occur, because the electrons coming from the cesium atoms may enter the surface states in which the number of the available states is comparatively large.) The positive cesium ions and the electrons in the filled surface state levels form a dipole layer. As a result of the potential drop across the dipole layer the electron affinity is reduced from E_A to $E_{A(true)}$. The effective electron affinity, which is the energy difference between the bottom of the conduction band in the bulk of the semiconductor and the vacuum level, is zero.

The work function and the electron affinity is further reduced by coating the cesiated gallium arsenide surface with layers of cesium oxide. Cesium oxide is a low electron affinity material which modifies the dipole layer and the surface conditions in such a manner that the composite work function becomes less than E_G. Thus the vacuum level is below the level of the bottom of the conduction band in the bulk material, resulting in a negative electron affinity.

In negative electron affinity electron emitters, electrons excited into the conduction band may relax to the bottom of the conduction band after interaction with the lattice and still be emitted because of the absence of the surface barrier. The transport to the surface is via minority carrier diffusion and is not hot-electron transport. The escape depth which for hot electrons is on the order of few hundred angstroms is now the minority diffusion length, which can be on the order of 3 μm. The great escape depth allows the light to be heavily absorbed in a relatively thick layer. The overall result is a significant increase in emission efficiency and decrease in the emission energy spread. The energy distribution of the emitted electrons is narrower than that from the other type of emitters, because most of the emitted electrons come from the bottom of the conduction band.

The typical luminous sensitivity of the $GaAs:Cs_2O$ cathode is above 900 μA/lm in the generation 3 image tube.

12.1.6   Antireflection Coating

Among the energy loss processes associated with photoelectric emission, reflection losses have a special significance as they influence photosensitivity, sharpness of the image, and low light level detectability. Reflection losses are present at the input surface of the cathode faceplate and at the photocathode glass interface. These losses, in principle, can be minimized by use of quarter-wavelength antireflection coatings (ARC) at the glass input and output surfaces. Ideally the ARC material should have an index

of reflection of $n = (n_1 n_2)^{1/2}$, where n_1 and n_2 are the indexes of refraction of the two light propagating media to be matched. The desired thickness d of the ARC is given by $d = \lambda/4n$, where λ is the wavelength at which the minimum in reflectivity is desired.

At the input of glass faceplate the materials to be matched are air and glass, with $n_1 = 1$ and $n_2 = 1.5$, respectively. The antireflection coating thus should have a refractive index of 1.22. Magnesium fluoride (MgF_2) has an index of refraction of 1.38 and is often used as antireflection coating on glass.

In the case of an input fiber-optic plate, the materials to be matched are air and glass with $n_1 = 1$ and $n_2 = 1.78$, respectively. The antireflection coating thus should have a refractive index of $n = 1.33$. The suitable antireflection coating, therefore, is again magnesium fluoride (MgF_2).

The multialkali cathode has an index of refraction of $n \geq 2.9$ in the wavelength range of interest. At the photocathode glass interface, therefore, the ARC should have an index of refraction of $n = 2.085$ for a glass faceplace and 2.27 for a fiber-optic plate.

Table 12.1 shows the indexes of refraction of a few materials which may be considered as antireflection coatings.

Table 12.1   Indexes of Refraction

Material	Index of Refraction
MnO	2.16
SnO_2	2.0
Sb_2O_3	2.09
Si_3N_4	2.18

Manganese oxide (MnO) and tin oxide (SnO_2) can be used as underlays for the cesium-antimony photocathode, which has a process temperature of 160°C. These materials, however, are not as compatible with the multialkali cathode for which the process temperature is in the neighborhood of 200°C. At 200°C antimony reacts with the underlays. Antimony oxide (Sb_2O_3) does not adversely affect the multialkali photocathode processing. It provides the cathode with a buffer layer against minor substrate contaminations, thus providing an improved red response, but because of its reaction with the photocathode it may lose its effectiveness as an antireflection coating.

The remaining material, which is stable at the multialkali photocathode processing temperature and provides a suitable surface for high-sensitivity photocathode fabrication, is silicon nitride (Si_3N_4). Silicon nitride can be deposited with accurate control by rf bias sputtering. This process has been proved to give high-quality, low-impurity films with an index of refraction

of $n = 2.18$. This material can provide a reasonably good match between the glass and the multialkali photocathode. The desired thickness is 100 nm.

12.1.7 Image Tube Background

In addition to photoemission, photocathodes also produce thermionic emission. Thermionic emission at room temperature is the main cause of image tube background that presents itself as a residual phosphor screen luminance in absence of photocathode illumination. The magnitude of the thermionic emission is determined by the thermionic work function of the photocathode, which is the energy difference between the vacuum level and the Fermi level. The Fermi level usually coincides with the dominant defect levels present in the forbidden band which for p-type material are near the conduction band. Defect levels are also responsible for the conductivity of the photocathode.

Ion scintillations are part of the residual screen radiation. Although they do not contribute measurably to the equivalent background input (EBI) they are a great concern in image tube cameras at long exposure times. Because of their brilliance, ion scintillations are more noticeable on the photographic film than the electron scintillations. Ion scintillations, therefore, may limit the exposure time by fogging the film. Ion scintillations are produced by positive ions striking the photocathode surface and producing a multiple number of secondary electrons. Positive ions may be generated by several different mechanisms in image tubes, chiefly these: (a) high-energy electrons colliding with free gas molecules; (b) high-energy electrons bombarding the screen and alkali atoms and gases absorbed on tube surfaces; (c) ionization induced by wall charging; and (d) field stripping of ions from positively charged electrodes due to high electric field stresses.

In addition to ion scintillations, multielectron emission events are also produced by cosmic particles traversing the photocathode substrate and generating light in the form of Cerenkov radiation.

12.1.8 Cathode Field Effect

In the wafer-type tube the cathode to microchannel plate spacing is in the range of 0.01 cm to 0.02 cm. Correspondingly, the cathode field is in the range of 1 to 20 kV/cm for a cathode to microchannel plate voltage difference of 20 to 200 V. The effect of the cathode field is, on one hand, a reduction in the work function of the photocathode analogous to the Schottky effect. On the other hand, since the photocathode is partly a dielectric, there is also some penetration of the field into the photocathode, which bends the energy levels downward near the surface and causes additional reduction in the work function. The result is an increase in the photosensitivity. Figure 12.5
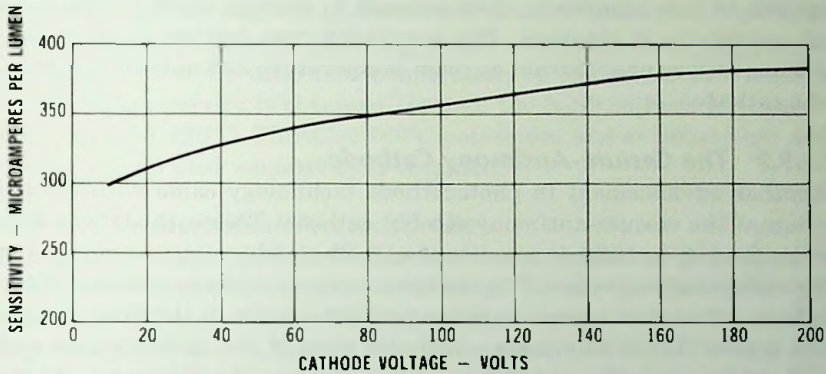
Fig. 12.5   Luminous sensitivity as a function of cathode voltage.

shows the luminous sensitivity as a function of cathode voltage for a typical photocathode.

12.1.9   Types of Image Tube Photocathodes

12.1.9.1   The Silver-Oxygen-Cesium Cathode

The silver-oxygen-cesium photocathode discovered in 1930 is the first photocathode which gained wide application in image tubes. At wavelengths longer than 950 nm the silver-oxygen-cesium cathode is still the only usable cathode. Although work is being done in the area of three-five compounds, these cathodes have so far a limited use in image tubes. The silver-oxygen-cesium cathode provides the S-1 response. The response curve has two peaks, one in the ultraviolet region and the other in the infrared. In the ultraviolet region the electrons are believed to be excited from the valence band of the cesium oxide (CsO). The long-wavelength response, on the other hand, is believed to be associated with the silver. Accordingly, the absorption of long-wavelength light and the conversion into photoelectrons takes place in the silver. The photoelectrons are able to escape from the silver into the surrounding cesium oxide containing a small stoichiometric excess of cesium. Cesium oxide has a low surface barrier potential that enables the electrons to escape into the vacuum.

The maximum luminous sensitivity of the S-1 cathode is only about 60 μA/lm, and the maximum quantum efficiency is in the neighborhood of 1.0% in the ultraviolet region, and 0.5% in the infrared region.

The silver-oxygen-cesium cathode is processed by evaporation of a transparent silver layer that has a light transmission in the range of 50 to 70%. This silver layer is oxidized by glow discharge in oxygen. After oxidation a small amount of silver is evaporated again. The silver oxide (AgO) layer

prepared in this manner is then exposed to cesium vapor at 175°C until peak sensitivity is obtained. The sensitivity may further be improved by additional silver evaporation at room temperature and subsequent heating of the cathode.

12.1.9.2 The Cesium-Antimony Cathode

Another advancement in photocathode technology came with the introduction of the cesium-antimony (Cs·Sb) cathode. This cathode was discovered by Görlich in 1936. It consists of a Cs_3Sb stoichiometric compound with semiconducting properties. The cesium-antimony cathode provides the S-11 response, which has a maximum spectral sensitivity in the blue and ultraviolet region. The S-11 response includes most of the visible region with a threshold wavelength near 650 nm. The maximum luminous sensitivity of the S-11 cathode is approximately 80 μA/lm and the maximum quantum efficiency is in the neighborhood of 20%. The cesium-antimony cathode is an inexpensive and relatively simple to process cathode. But because of the superior performance of more complex alkali antimonides this cathode is now only rarely used in image tubes. The Cs_3Sb cathode is processed by exposure of a thin, evaporated antimony layer, which has about 85% light transmission, to cesium vapor at 160°C in high vacuum until a peak sensitivity is obtained.

12.1.9.3 The Bialkali Antimonide Cathodes

Investigation of the properties of alkali antimonides by Sommer led to the development of the bialkali antimonide cathodes of the potassium-cesium-antimony type (K_2CsSb) and the sodium-potassium-antimony type (Na_2KSb), which have higher peak quantum efficiency and more red response than the Cs_3Sb cathode. These cathodes are noted for their very low thermionic emission which is in the order of 10^{-17} A/cm^2 or lower. The K_2CsSb cathode, however, is very resistive and for over 10^{-9} A/cm^2 current density can be used only with a conductive substrate.

The maximum spectral sensitivity is in the blue and ultraviolet region for both bialkali cathodes. The response curves include most of the visible region with a threshold wavelength in the range of 660 to 700 nm. The maximum luminous sensitivity of the K_2CsSb cathode is about 100 μA/lm, and of the Na_2KSb cathode is about 130 μA/lm. The maximum quantum efficiency is in the neighborhood of 30% for both photocathodes.

The K_2CsSb cathode is processed by exposure of a thin evaporated antimony layer which has about 80% light transmission to potassium (K) vapor at 190°C, until a peak sensitivity is obtained. The potassium-antimony cathode (K_3Sb) obtained in this manner is cesiated to peak sensitivity at 160°C.

The process of the Na_2KSb photocathode is more elaborate. First a K_3Sb cathode is formed either by exposing a thin antimony layer to potassium vapor at 160°C, or by alternate evaporation of potassium and antimony until a peak sensitivity is obtained. Second, the K_3Sb cathode is exposed to sodium vapor at 220°C. Third, at 160°C potassium and antimony are added alternately until peak sensitivity is obtained.

12.1.9.4   *The Multialkali Photocathode*

Multialkali image tube cathodes are semitransparent polycrystalline semiconductor films that are deposited in high vacuum on the input window of the image intensifier tube. The approximate composition of the multialkali photocathode is $(Na_2KSb)Cs$. The bulk material of the cathode film is a sodium, potassium and antimony semiconducting compound alloyed by a small quantity of cesium. The cathode film is coated with cesium for reduction of electron affinity. The multialkali cathode is p-type in bulk conductivity due to a stoichiometric excess of antimony. The film thickness is a few hundred angstroms for the relatively thin multialkali cathodes having an S-20 spectral response, and about 1200 Å for the extended red response multialkali cathodes. Multialkali cathodes have a cubic lattice structure.

The first step in the multialkali cathode fabrication is the fabrication of a thin layer of potassium-antimony cathode having an approximate composition of K_3Sb. This cathode is obtained by deposition of antimony on the photocathode substrate and by exposure of the deposited antimony to potassium vapor at elevated temperatures. Frequent manufacturing methods are alternate evaporation of potassium and antimony until peak sensitivity is obtained, or coevaporation of potassium and antimony to peak sensitivity.

The second step is the formation of an Na_2KSb type bialkali cathode. The bialkali cathode is obtained by exposure of K_3Sb cathode to sodium vapor and subsequent alternate evaporation or coevaporation of potassium and antimony until a peak sensitivity is obtained. In the case of extended red response cathodes the second step may be repeated several times until a desired cathode thickness is obtained. The thickness of the cathode is usually estimated by the amount of the photosensitivity loss in the blue region.

In the third major step the Na_2KSb cathode is exposed to cesium vapor. Cesium reduces the electron affinity of the photocathode, providing high quantum and luminous efficiency, and extends the photoresponse in the red region. The lowest electron affinity and the most stable cathodes are obtained by processing the cesium layer with several alternate evaporations of cesium and antimony until a peak sensitivity is obtained. The presence of cesium in the photocathode is twofold: the incorporation of cesium and antimony, during the cesium-antimony yo-yo, produces a p-type doping in the bulk of the cathode, and the positive cesium ions at the surface form a

dipole layer with the electrons in the filled acceptors of the cathode reducing the electron affinity.

Additional reduction of electron affinity and improvement of photosensitivity can be obtained by oxidation of cesium to cesium oxide. The effect is similar to the effect experienced in the generation 3 GaAs:Cs-O cathodes.

12.1.9.5 The Solar-Blind Cathode

For solar-blind imaging the cesium-telluride (Cs·Te) cathode is used most frequently because this cathode has good quantum efficiency at wavelengths shorter than 3000 Å and it has a negligible light absorption and photoresponse in the visible part of the spectrum. The cesium-telluride cathode is deposited on quartz or lithium fluoride windows which are transparent in the ultraviolet spectrum. The substrates are coated with an 85% transmission platinum layer for conduction because the cesium-telluride cathode is very resistive.

12.1.9.6 The Generation 3 Photocathode

The generation 3 photocathode is a high-photosensitivity GaAs:Cs-O/ AlGaAs cathode which has a photoresponse in the 600-nm to 900-nm wavelength range. The typical luminous sensitivity of the generation 3 cathode is above 900 μA/lm. Figure 12.6 shows the structure of the generation 3 photocathode bonded to a cathode glass faceplate wedge.

In the generation 3 photocathode structure the quarter-wavelength silicon-nitride (Si_3N_4) antireflection coating between the AlGaAs window layer and glass is for the minimization of reflection losses. The epitaxially grown 5 μm thick window layer serves a dual purpose: it supports the active layer and acts as a high-pass filter allowing light transmission wavelengths beyond 600 nm only. The heavily zinc-doped gallium-arsenide active layer is an epitaxially grown single-crystal layer which has a thickness in the range
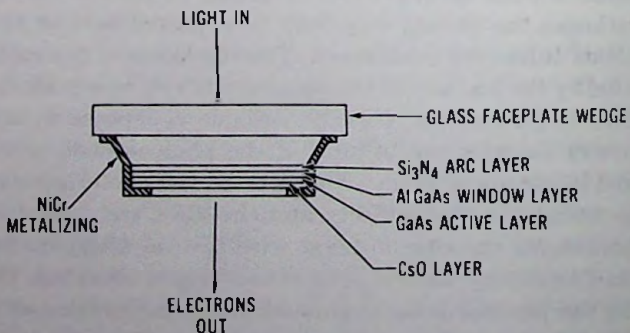

Fig. 12.6   Generation 3 photocathode structure.

of 1.0 to 1.8 μm. The thickness of the active layer is adjusted to absorb all available light while permitting an efficient escape of photoelectrons over the entire thickness.

Gallium arsenide (GaAs) is a high work function material. It has a forbidden band gap of $E_G = 1.4$ eV and an even higher electron affinity. High photosensitivity in the wavelength range of interest is obtained by coating the gallium arsenide surface with approximately one monolayer of cesium oxide. Cesium oxide (Cs·O) is a low electron affinity material which modifies the surface conditions in such a manner that the composite work function becomes less than E_G. Thus the vacuum level is below the level of the bottom of the conduction band of the bulk material, resulting in a negative effective electron affinity as shown in figure 12.7.

Conventional photocathodes have a positive electron affinity. This means that the photoelectrons lose kinetic energy by passing through the positive surface barrier. Therefore only those electrons are emitted which have a sufficient kinetic energy to overcome the positive surface barrier. As far as emission is concerned, more favorable conditions exist in a negative electron affinity emitter, in which the electrons gain kinetic energy in the process of transport from the bulk to the vacuum. In a negative electron affinity emitter, electrons excited into the conduction band, therefore, may relax to the bottom of the conduction band after interaction with the lattice and still be emitted.

The overall result is a significant increase in emission efficiency. Typical spectral response characteristics of GaAs:Cs·O/AlGaAs photocathodes and, for comparison, the spectral responses of multialkali cathodes are shown in figure 12.8.

The first step in the generation 3 photocathode fabrication is the processing of the multilayer GaAs/AlGaAs crystal structure as shown in figure 12.9. This structure can be obtained by a liquid-phase epitaxy (LPE) or by metallorganic vapor-phase epitaxy (MO-VPE) processes.
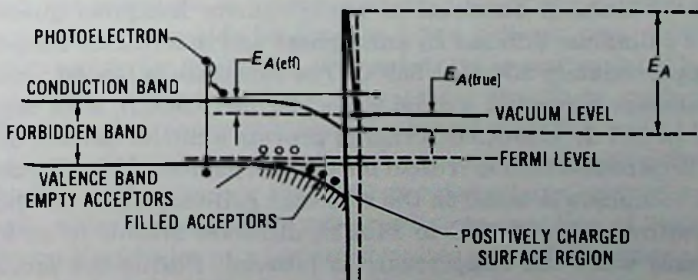

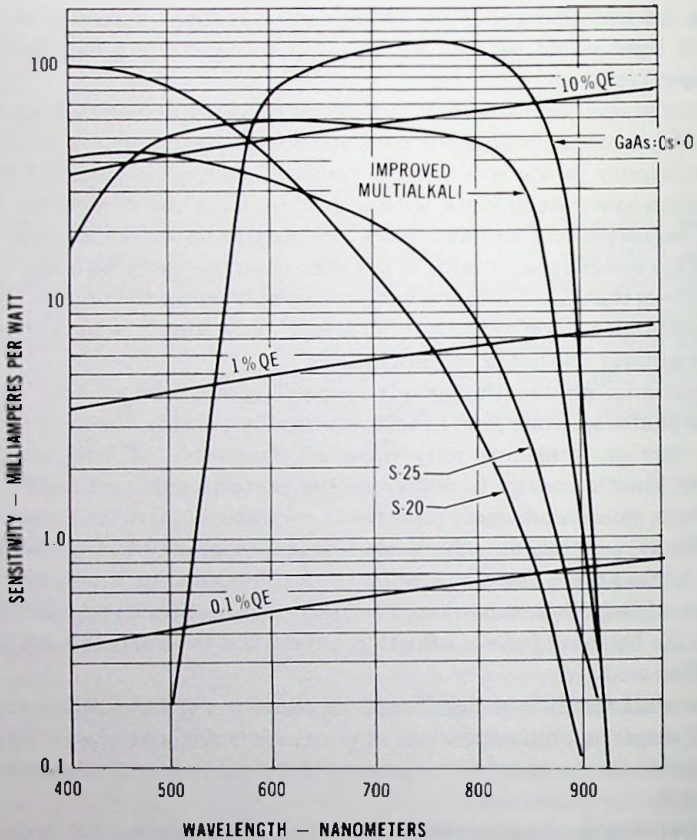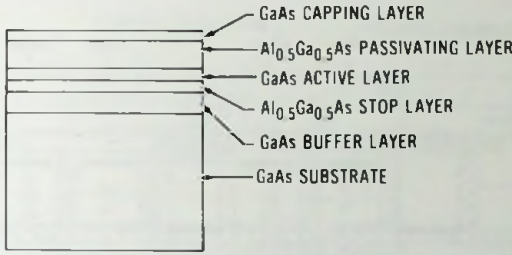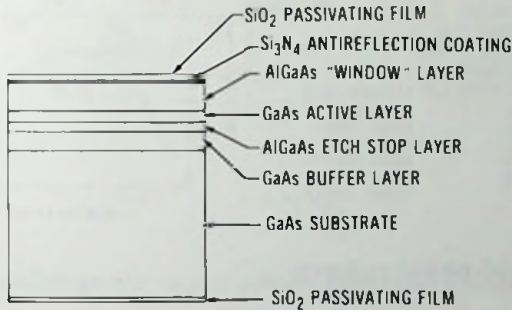**Fig. 12.7   Energy band model of a GaAs:Cs·O cathode.**

Fig. 12.8 Spectral response of photocathodes.

In the case of an LPE process the crystalline microstructure is grown on (111) oriented GaAs:Si substrate in a high-purity leakproof quartz tube reactor in a palladium diffused H_2 atmosphere and in a reactor temperature range of approximately 830°C to 850°C. The substrate is lapped, chemopolished by colloidal silica and sodium hypochloride (NaOCl), then degreased and etched in (5:1:1): H_2SO_4:H_2O_2:H_2O to provide a mirror-smooth damage-free crystalline base which is critical for the fabrication of microstructures.

The LPE technique is based on the rule that gallium, which is a liquid in the temperature range of 30°C to 2400°C, dissolves arsenic in an amount that decreases when the temperature is lowered. During the process the substrate is brought into contact with a melt of gallium saturated with arsenic which contains the required quantity of dopant at a temperature of

GaAs CAPPING LAYER
$Al_{0.5}Ga_{0.5}As$ PASSIVATING LAYER
GaAs ACTIVE LAYER
$Al_{0.5}Ga_{0.5}As$ STOP LAYER
GaAs BUFFER LAYER
GaAs SUBSTRATE

(A) Grown generation 3 photocathode structure.

SiO_2 PASSIVATING FILM
Si_3N_4 ANTIREFLECTION COATING
AlGaAs "WINDOW" LAYER
GaAs ACTIVE LAYER
AlGaAs ETCH STOP LAYER
GaAs BUFFER LAYER
GaAs SUBSTRATE
SiO_2 PASSIVATING FILM

(B) Photocathode prepared for 7056 glass sealing.

Fig. 12.9   Photocathode fabrication in prebonding stage.

850°C. As the temperature is slowly lowered, the solubility of arsenic decreases and excess arsenic deposits on the substrate as a gallium arsenide epitaxial layer. By bringing the substrate into contact with melts of gallium, which contains an appropriate amount of aluminum, an AlGaAs epitaxial layer can be grown. Thus, by bringing the substrate into contact with different melts of gallium in succession, it is possible to grow a multilayer structure sequentially. Figure 12.10 shows the diagram of the graphite boat in which the substrate is loaded with an appropriate amount of gallium, zinc, and gallium arsenide for position 1 and gallium, zinc, aluminum, and gallium arsenide for position 2. The substrate is manipulated between position 1 and position 2 during the epitaxial growth by push rods which extend outside the reactor through a leakproof seal. Figure 12.11 shows the liquid-phase epitaxial growth system for generation 3 photocathodes.

In the MO-VPE technique the (100) oriented microstructure is grown in a cold-wall, water-cooled quartz tube reactor by reaction of metal organics with Group V hydrides at a hot substrate on a graphite pedestal heated by high-frequency induction to a temperature ranging between 700°C and 780°C. Epitaxial GaAs:Zn growth is obtained by reaction of trimethylgal-
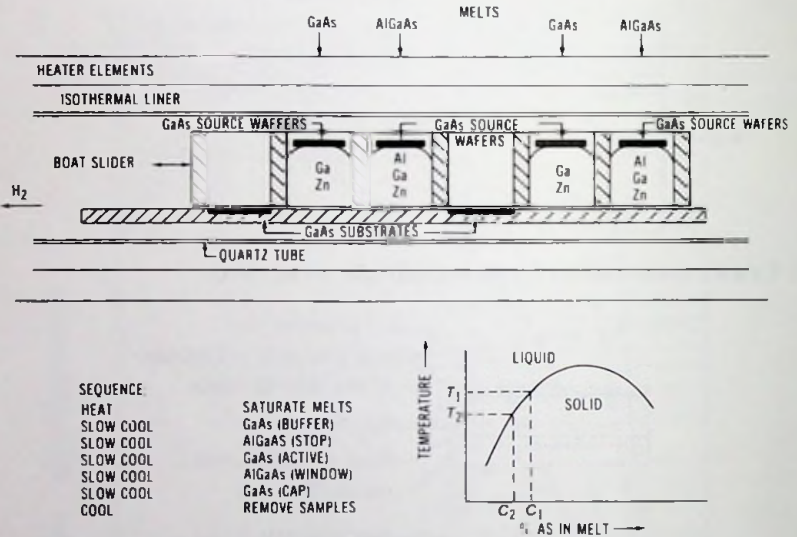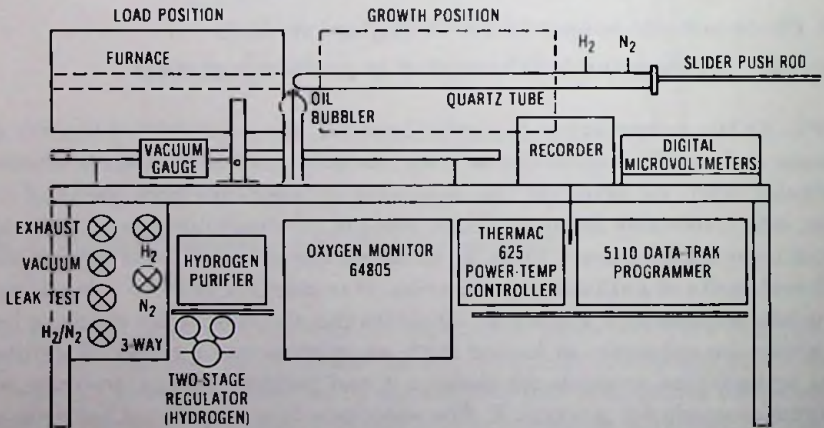
Fig. 12.10 Liquid-phase epitaxy.

Fig. 12.11 Liquid-phase epitaxial growth system for generation 3
photocathodes.

lium (TMG), arsine (AsH_3), and diethylzinc (DEZ) transported by palladium
diffused hydrogen. Epitaxial AlGaAs:Zn is grown by reacting trimethylal-
uminum (TMAl), TMG, AsH_3, and DEZ. Figure 12.12 shows the metallor-
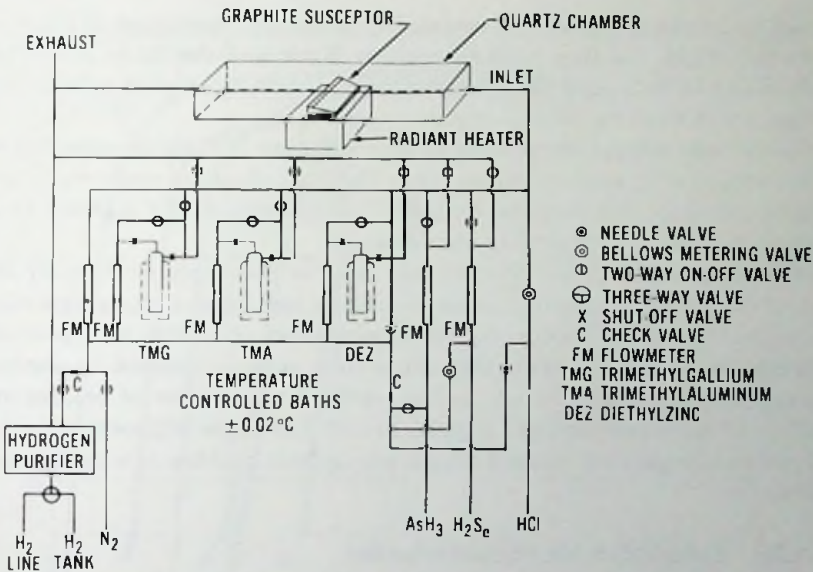ganic vapor-phase epitaxial system.

Fig. 12.12   Metallorganic vapor-phase epitaxial system.

The multilayer GaAs/AlGaAs wafer must be processed into a photocath-ode structure such that it will be an integral part of the input faceplate window of the generation 3 image intensifier tube. This involves the re-moval of nonactive layers, the deposition of an antireflection coating, and the bonding of the remaining active and window layers to the glass face-plate.

As a first step of the wafer processing procedure a circular wafer is cut from the rectangular wafer structure. From the sealing surface the gallium arsenide capping layer is removed by a sulfuric acid, hydrogen peroxide, and water mixture.

Following this operation the silicon nitride and silicon dioxide films are deposited to obtain the structure shown in figure 12.9B.

For bonding purposes the cathode is placed in a graphite bonding fixture. A cathode faceplate is laid on top of the coated layer of the cathode. Heat is applied from the cathode side of the fixture and pressure bonding is done, at approximately 680°C. Complete sealing takes 5 to 10 minutes.

During the postbonding process, selective etches are used to remove the nonactive epitaxial layers and the substrate from the bonded cathode. The silicon dioxide layer is removed from the surface with hydrogen fluoride (HF). The gallium arsenide substrate and buffer layer is removed by a 10:1:1 H_2SO_4:H_2O_2:H_2O solution and the AlGaAs stop layer with a concen-

trated hydrogen fluoride. The remaining structure, consisting of glass face-plate SiO_2/Si_3N_4 coating, AlGaAs window layer, and the GaAs active layer is final etched in a 5:1:1 $H_2SO_4:H_2O_2:H_2O$ solution to provide a fresh, clean surface for the activation.

The cathode activation consists of heat cleaning in high vacuum, followed by activation with cesium and oxygen. The heat cleaning cycle consists of a rapid heating of the cathode to 630°C, outgassing of the cathode at this temperature for a few minutes and cooling.

Activation is done after the cathode cools to room temperature by exposure of the gallium arsenide layer to cesium and oxygen. As a first step of the activation cycle, approximately a monolayer of cesium is deposited on the cathode surface. Subsequently, the cesium layer is oxidized by admission of oxygen to form a layer of cesium oxide. A monolayer of cesium oxide consists of more cesium than oxygen atoms. Consequently, several cesium-oxygen admissions are needed for an asymptotic buildup of a cesium oxide monolayer.

12.1.10 Substrates for Photocathodes

Usual substrates for cathodes in the visible and infrared region are Corning 7056 glass and fiber optics. In the near ultraviolet region Corning 9741 or 9823 uv transmitting glass or uv-grade sapphire are used, depending on the requirements. Figure 12.13 shows typical transmission characteristics of substrate materials.

In operations where the current density does not exceed 1 $\mu A/cm^2$, practical photocathodes (with the exception of Cs·Te and K_2CsSb cathodes) have sufficient conductivity, so that a conductive substrate is not necessary. In light-shutter image tubes, however, the cathode current density in pulsed operation may exceed 1 mA/cm^2. In this application a sufficient pulsed resolution may be obtained only by use of conductive substrates. Usual conductive layers are a 50% light transmission nickel or platinum layer, or an 85% light transmission tin oxide (SnO_2) layer. The resistivity of these layers is in the range of 100 to 300 ohms/square.

12.1.11 Photocathode Materials

As we already have seen, photocathodes are often processed by use of alkali metals (cesium, potassium, sodium) in elementary form. However, because of their great reactivity, pure alkali metals cannot be exposed to air but must be handled in vacuum during the whole process. In usual practice, therefore, elementary alkali metals are produced in the evacuated image tube (or in an appendage of the image tube) by reducing a salt of the alkali metal by reaction with a suitable reducing agent. As alkali metal salts, Cs_2CrO_4, K_2CrO_4 and Na_2CrO_4 compounds are used almost exclusively be-
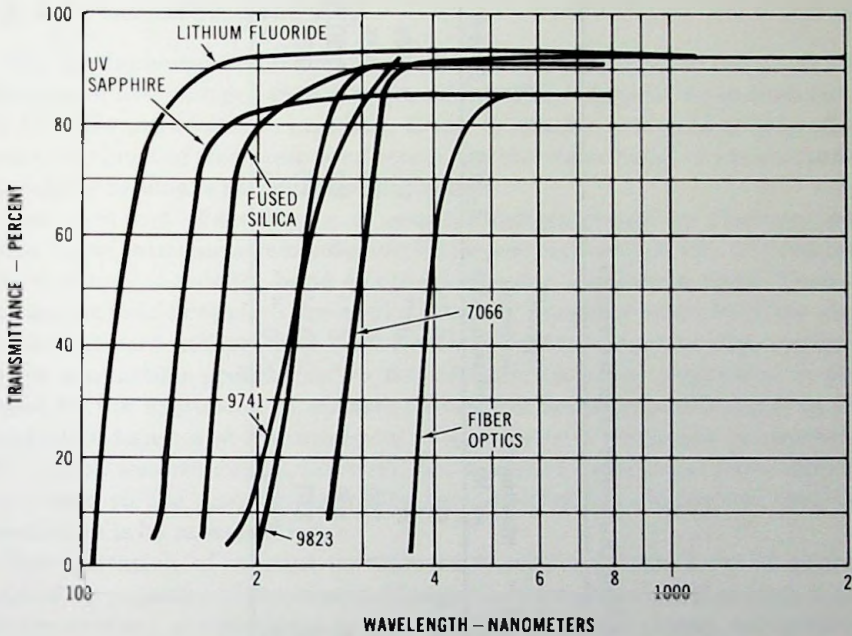
Fig. 12.13   Typical transmission characteristics of substrate
             materials.

cause these materials are not hygroscopic. Zirconium, silicon, and alumi-
num are used as reducing agents. Tungsten is frequently added to the
mixture of the alkali metal salt as the reducing agent to slow down the
reaction. The intimate powder mixture of these materials is placed in a 30
to 40 mm long and 1 to 2 mm diameter nichrome, nickel or tantalum con-
tainers (channels). By passing a current through these channels the chan-
nels can be heated to the reaction temperature. During the chemical
reaction the alkali vapor is able to escape through the exit slit of the chan-
nel, but the solid residue is retained.

The base metal evaporators (antimony, silver, indium telluride) consist of
thin (about 0.2 mm diameter) platinum-clad wire with a 10- to 30-mg base
metal bead on it. (For the cesium-telluride cathode, tellurium is obtained
from an indium-telluride bead because indium telluride decomposes above
500°C, thus permitting a high degassing bake of the image tube. Tellurium
beads limit the degassing temperature to below 200°C.) The base metal is
evaporated by passing a current through the wire.

Table 12.2 is a summary of photocathode characteristics.

Table 12.2 Summary of Photocathode Characteristics

Cathode	λ(peaks)	Maximum Quantum Yield at λ(peak) in %	λ₀ [1% of λ (peak)]	Maximum μA/lm	Typical Thermionic Emission (A/cm²)	E_G (eV)	E_A (eV)
Ag-O-Cs	8000 Å	0.5	$\cong$12 000 Å	60	10^{-12}		
Cs$_3$Sb on MnO	4000	20	6500	80	10^{-15}	1.6	0.45
(Cs)Na$_2$KSb	4000	30	9500	550	10^{-15}	1.0	0.35
K$_2$CsSb	4000	30	6600	100	$<10^{-17}$	1.0	0.90
Na$_2$KSb	4000	30	6600	130	$<10^{-17}$	1.0	0.75
GaAs:Cs-O	7800	>20	9500	>1000	$<10^{-14}$	1.4	< 0

12.2   Photoconductivity

The fundamental requirement of electrical conduction in solids is the presence of free charge carriers of electricity. The charge carriers of electricity in solids are electrons and ions. If the electricity is transported by electrons, we speak of *electronic conduction*. On the other hand, the transport of electricity by ions is called *ionic conduction*.

The transport of electricity in semiconductors occurs by electrons and holes. In an intrinsic semiconductor, electronic conduction may be produced by excitation of valence band electrons into the conduction band. Then, if an electric field is applied across the intrinsic semiconductor, both the electrons in the conduction band and the holes in the valence band participate in the conduction process. In an n-type semiconductor, conduction is produced by the excitation of electrons from the donor impurity level to the conduction band, and the transport of electricity is by means of electrons. In a p-type semiconductor, however, the electrons are excited from the valence band to the acceptor impurity level to produce conduction, and the conduction is by means of holes.

The excitation of current carriers in a semiconductor may be accomplished by exposure of the semiconductor to different forms of energy. If the charge carriers are produced by the action of thermal energy, we speak of *thermal conduction*. In contrast, *photoconductivity* is the phenomenon of light being used to produce conduction.

Photoconduction can be produced only if the energy of the absorbed photons is equal to or greater than the energy required to produce a charge carrier. The semiconductors, in which the electrons are excited from the valence band into the conduction band by the action of light, are *intrinsic photoconductors*. On the other hand, the semiconductors in which the electrons are excited from the impurity levels or to the impurity level, are the *impurity photoconductors*.

The spectral response of the photoconductor and the long wave threshold of photoconduction is dependent on the energy band structure of the photoconductor. The determining factor in the intrinsic photoconductors is the forbidden band energy E_G, which is the difference between the bottom of the conduction band and the top of the valence band. Table 12.3 gives the long wave threshold and the forbidden band energy E_G for several intrinsic photoconductors.

In the most simple case of photoconduction process one electronic charge flows through the photoconductor for each photon absorbed. Such a simple process, however, can occur only with nearly perfect crystals. For many materials the quantum efficiency is low due to the existence of transitions which do not free bound charge carriers by absorption of light. Other com-

Table 12.3   Long Wave Threshold and Forbidden Band Energy of Photoconductors*

Photoconductor	Gap Width E_G (electronvolts)	Long Wave Threshold (micrometers)
Sb_2S_3	1.6	0.75
PbTe	0.25	5.0 (at 90 K)
PbSe	0.27	4.5
CdS	2.4	0.51
Tl_2S	1.0	1.25
PbS	0.4	3.0
Ge	0.72	1.72
Si	1.13	1.08
Se (amorphous)	2.4	0.51
Se (black, crystalline)	1.5	0.80

*Data from T. S. Moss, *Photoconductivity in the Elements*, Academic Press, 1952.

plications, which may exist, are space charge in the crystal, localized fields at the contacting electrodes, and trapping of holes and electrons.

Traps are localized empty quantum states introduced by an interstitial, by a negative ion vacancy, or by a chemical impurity. The traps are located in the forbidden band near the bottom of the conduction band. During the conduction process an electron excited into the conduction band may lose its energy by interaction with the lattice and become immobilized in a trap until it again acquires a sufficient energy to escape. If the trapped electron is thermally released, the time of the release is determined by the Boltzmann factor $\exp\,(-E_t/kT)$ where E_t is the energy difference between the trap level and the bottom of the conduction band, k is the Boltzmann constant and T is the temperature. For large values of E_t, the electron spends a long time in the trap before release.

Recombination is a process which reduces the quantum efficiency of a photoconductor. It is caused by deep traps. An atom with a trapped electron having a negative charge can trap a hole, thus causing electron hole recombination. The recombination process removes an electron and a hole from the conduction process.

The fraction of photons which cause transitions giving rise to photoconduction is the primary quantum efficiency of the photoconductor. For many materials the quantum efficiency is low due to the presence of transitions which do not cause conduction. Good photoconductors, on the other hand, have a peak quantum efficiency close to unity. The primary quantum efficiency cannot exceed unity. Photoconductors with gain mechanism, how-

ever, may have an apparent quantum efficiency greater than unity. One process with gain mechanism works the following way. An incident photon produces a hole and a free electron. The electron moves quickly out of the crystal and the hole becomes trapped, creating a positive space charge. Another electron moves into the crystal from the negative electrode in order to neutralize the space charge and flows through the crystal. The process continues until an electron recombines with the hole. The current gain of this process is the ratio of the lifetime of the trapped hole to the transit time of an electron.

Photoconductors have an important application in the photoconduction type of camera tubes as light sensors. In these devices a thin layer of photoconductor is utilized for conversion of the light image into an electrical signal to be televised.

12.3   Secondary-Electron Emission

Secondary-electron emission takes place when solid materials are bombarded by primary electrons of sufficiently high energy for entering the material. The process of secondary-electron production is similar to the process of photoemission, except that in the case of secondary-electron emission energetic electrons are used to raise the energy levels of the electrons of the solid material. The mechanism of the secondary-electron production is different in metals from that observed in insulators and semiconductors. When a clean metal surface is exposed to energetic primary electrons, secondary-electron emission occurs by raising the energy level of conduction band electrons to the vacuum level. One primary electron of sufficiently high kinetic energy may excite a multiple number of low-energy secondary electrons on its way in the solid material. Each time the primary electron excites a secondary electron it loses on an average as much kinetic energy as is required for the production of a secondary electron. The *secondary emission ratio* of a material is defined as the total number of secondary electrons produced per primary electron. Clean metals are poor secondary-electron emitters. Semiconductors and insulators are efficient secondary-electron emitters.

The secondary emission of semiconductors may be considered as a three-step process. In the first step, electrons are excited from the valence band to the vacuum level by absorption of the primary-electron beam energy. The efficiency of this process depends on the mean energy required to produce an electron-hole pair. (In the alkali antimonides this energy is $3E_G$.) The second step is the transport of the excited electrons through the material to the semiconductor-vacuum interface. In this step the migrating electrons lose part of their energy by collision. The third step is escape over the

surface barrier into the vacuum. In conventional secondary-electron emitters only those electrons can escape that have a sufficiently high energy to overcome the surface barrier. The efficiency of this step is therefore dependent on the magnitude of the electron affinity of the secondary-electron emitter, on the physical depth of the secondary-electron excitation, and on the energy of the escaping electrons. The electrons generated at greater depths, on an average, lose more of their energy by phonon production than those generated near to the semiconductor-vacuum interface. Consequently, only those electrons may escape that are generated at depths smaller than the escape depth. (The electrons generated at depths greater than the escape depth, due to numerous collisions, arrive at the semiconductor-vacuum interface with insufficient energy to overcome the surface barrier.)

The situation is different in the negative or zero electron affinity emitters. In the negative or zero electron affinity semiconductors, such as a cesium-activated gallium-phosphide material, a surface barrier is not present. Therefore all electrons arriving to the semiconductor vacuum interface may freely enter into the vacuum. This is the primary reason for the greater secondary emission efficiency of the negative or zero electron affinity secondary-electron emitters as compared to the conventional secondary-electron emitters. Instead of secondary emission ratios of 4 to 6 as obtained with conventional dynode materials, gains of 50 to 100 or more are obtained with cesium-activated gallium phosphide.

The secondary emission ratio δ would be proportional to the primary-electron beam energy if all secondary electrons had an equal chance of escape. This is, however, not the case. Figure 12.14 shows δ as a function of
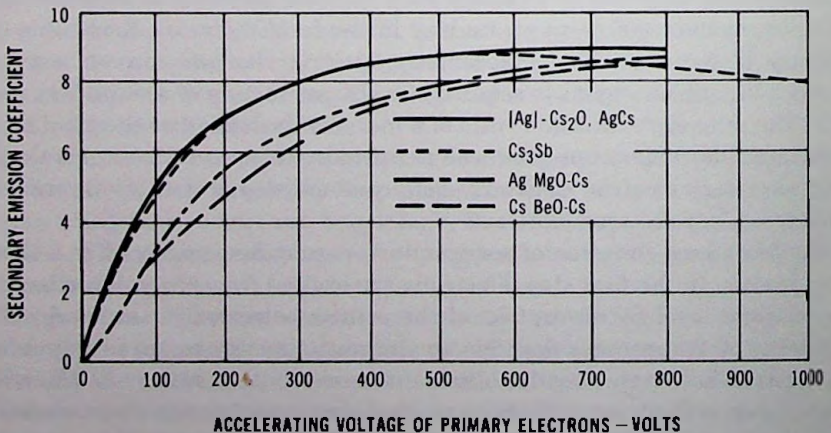
Fig. 12.14   Secondary emission ratio of materials.

primary-electron energy for several materials. As may be seen, for small primary-electron energies, δ reaches a maximum, then it stays constant or declines. The reason for the departure from the linear relationship is that at higher beam energies more secondary electrons are generated at greater depths. From greater depths an electron has a smaller chance to arrive to the semiconductor-vacuum interface.

Another important portion of the secondary emission curve, utilized in camera and storage tubes, is the portion near zero primary-electron energy. Figure 12.15 shows that at primary-electron energies less than the first crossover, δ decreases to a minimum, then it reverses, rising to a value of unity at zero primary-electron energy. The reversed part of the curve is due to reflected primary electrons. When the primary-electron energy is less than the minimum energy needed for the hole-electron pair production plus the energy necessary to overcome the electron affinity, true secondaries cannot be produced anymore.

An important characteristic of a secondary-electron emitter is the velocity or kinetic energy distribution of the secondary electrons. As may be seen from figure 12.16, where the primary-electron energy is approximately 150 V, the velocity or energy distribution curve has two peaks. The first peak corresponds to the useful low-velocity group of electrons. The bulk of elec-

$$\delta_c = \frac{i_c}{i_p} \qquad i_c = \text{COLLECTED CURRENT}$$

$$\delta = \frac{i_s}{i_p} \qquad i_s = \text{SECONDARY-ELECTRON CURRENT}$$

$$i_p = \text{PRIMARY-ELECTRON CURRENT}$$

QUASISTABLE
EQUILIBRIUM
POINT

V_{cr1} = FIRST CROSSOVER POTENTIAL

V_{cr2} = SECOND CROSSOVER POTENTIAL
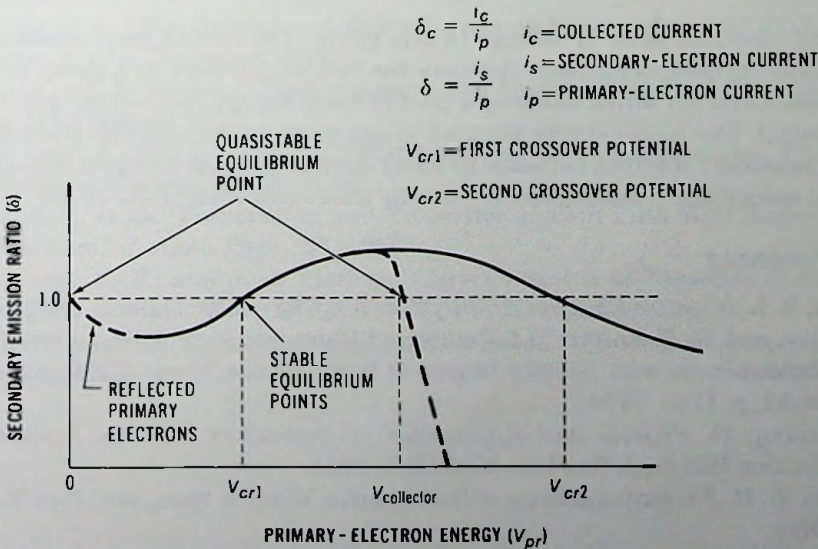
Fig. 12.15   Secondary emission ratio as a function of bombarding primary-electron energy at the target.
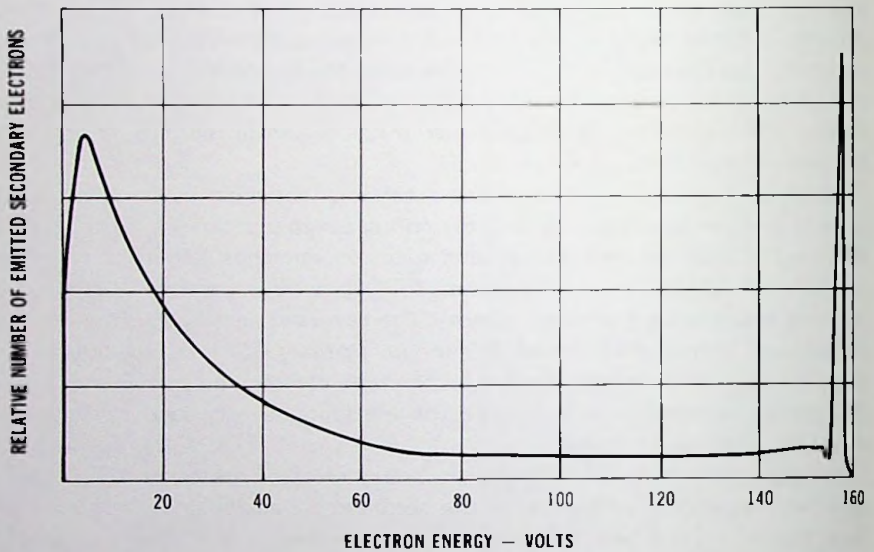
Fig. 12.16   Typical secondary-electron energy distribution for a silver target.

trons (about 80 to 85%) belongs to this group. The second peak consists of reflected primary electrons. Between the two peaks there is a group of reflected electrons which lost only a part of their energy interacting with the material. The high-velocity electron group is an undesirable by-product of the secondary-electron emission in many devices because it causes transient time spread and consequently lowers the time resolution of the device.

References

Bell, R. L. *Negative Electron Affinity Devices*, Clarendon, Oxford, 1973.
———, and W. E. Spicer, "3-5 Compound Photocathodes: A New Family of Photoemitters with Greatly Improved Performance," *Proc. IEEE*, Vol. 58, No. 11, p. 1788, 1970.
Bruining, N. *Physics and Application of Secondary Electron Emission*, McGraw Hill Book Co., Inc., New York, 1954.
Bube, R. H. *Photoconductivity of Solids*, John Wiley & Sons, Inc., New York, 1960.
Carroll, W. H., et al. "Role of Cesium in the $(Cs)Na_2KSb$ Multialkali Photocathode," *Journal of Applied Physics*, Vol. 42, No. 2, p. 569, February 1971.

Csorba, I. P. "P. E. M. for Automatic Production for Multialkali Photocathode Processing," Final Engineering Report, Contract DAAAB05-74-C-2521, U. S. Army Electronics Command, Fort Monmouth, NJ, December 1975.

———. "State of the Art in Automated Multialkali Photocathode Processing," Electro-Optics/Laser '76 Conference, New York Hilton, September 14-16, 1976.

Fisher, D. G., and R. U. Martinelli. "Negative Electron Affinity Materials for Imaging Devices," *Advances in Image Pickup and Display*, Vol. 1, B. Kazan, ed., Academic Press, New York, 1974.

Martinelli, R. U., and D. G. Fisher. *Proc. IEEE*, Vol. 62, p. 1339, 1974.

Moss, T. S. *Photoconductivity in the Elements*, Academic Press, New York, 1952.

McVay, K. G. "Secondary Electron Emission," *Advances in Electronics*, 1, 1948.

Rappaport, P. "Methods of Processing Silver-Magnesium Secondary Emitters for Electron Tubes," *J. Appl. Phys.*, 25, 1954.

Rose, A. "An Outline of Some Photoconductive Processes," *RCA Review*, 12, 1951.

Simon, R. E., et al. "Secondary Electron Emission," *IEEE Transactions on Nuclear Science*, Vol. NS-15, No. 3, p. 167, 1968.

Sommer, A. H. *Photoemissive Materials*, John Wiley & Sons, Inc., New York, 1968.

Spicer, W. E. "The Influence of Defect Levels on Photoemissions," *RCA Review*, p. 444, December 1958.

———, and F. Wooten. "Photoemission and Photomultipliers," *Proc. IEEE*, p. 1119, August 1973.

Van Laar, J., and J. J. Scheer. "Photoemission of Semiconductors," *Philips Technical Review*, Vol. 29, p. 54.

Wargo, P., et al. "Preparation and Properties of Thin-Film MgO Secondary Emitters," *J. Appl. Phys.*, 27, 1956.

Williams, B. F., and J. J. Tietjen, "Current Status of Negative Electron Affinity Devices," *Proc. IEEE*, Vol. 59, No. 10, October 1971.

Wooldrige, D. E. "Theory of Secondary Emission," *Physical Review*, Vol. 56, pp. 562–578, 1939.

13

MICROCHANNEL AND FIBER-OPTIC PLATES

13.1   Microchannel Plates

Microchannel plates (MCPs) are current-multiplying optical devices frequently used in image intensifier tubes for intensification of the photoelectron image. Other applications include high-speed photomultiplier tubes, cathode-ray tubes, storage tubes, camera tubes, and electron, ion, X-ray, and ultraviolet radiation detectors and imaging.

The microchannel plates are characterized by high electron gain, low noise, high spatial resolution, high speed, small weight, relatively low power consumption, and long operational life. Their self-saturating property also makes them an ideal device for output current limiting applications.

Physically, a microchannel plate is a two-dimensional array of hollow glass fibers fused together into a thin disk as shown in figure 13.1. The inside surface of the hollow glass fibers is covered by a resistive secondary electron emission film which is electrically connected to the input and the output electrodes of the channel plate. The hollow glass fibers, generally termed *microchannels*, have an inside diameter in the 8- to 45-μm range. The channel length to diameter ratio (L/D) is typically on the order of 40 to 48 for plates used in image intensifier tubes.

The microchannels are not perpendicular to the input and output surfaces but typically are at a 5° to 10° bias angle. The purpose of the bias angle is to ensure a first electron impact near the channel entrance, reduce light feedback from the phosphor screen, reduce ion feedback, and, in the electro-
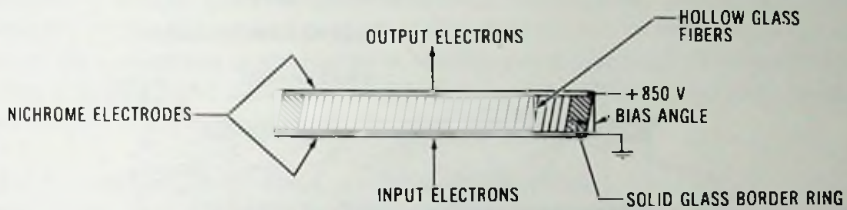
Fig. 13.1   Microchannel plate.

static image inverting tube types, improve the uniformity of image transmission.

The solid border rim is for ruggedness and for mounting purposes. The thickness of the MCP is determined by the channel diameter and the L/D ratio.

The *open area ratio* of the MCP is the ratio of the open area to the total area of the microchannel plate. It is typically about 55% for the regular plates and greater than 75% for the funneled plates. Funneling reduces the opaque MCP area at the input of the MCP.

The material of the microchannel plate is lead-silicate glass. The fabrication technique of the MCP is similar to the process used in manufacturing of fiber-optic plates. In this method etchable glass rods (cores) are clad with lead-silicate glass. The clad rods, after being drawn smaller, are fused into hexagonal array bundles. The bundles are packed into a glass tube and are fused into a *boule*, which is sliced into thin wafers and ground and polished to the final dimensions of the microchannel plate. The microchannels are obtained by etching the core glass out from the lead-silicate glass structure.

The resistive secondary emission film covering the inside surface of the microchannels is obtained by hydrogen firing the MCP structure. Hydrogen firing reduces the lead-oxide glass to lead and water. The finely dispersed lead produces semiconduction in the lead oxide. The stability of the conductive film is improved by leaching the lead oxide from the glass surface by a very dilute solution of hydrochloric acid prior to hydrogen firing. Leaching produces a silica-rich surface layer as shown in figure 13.2.

For long-life wafer tube applications the MCP has an ion barrier. The ion barrier is a continuous thin-film membrane of aluminum oxide (Al_2O_3) which covers the input of a standard microchannel plate. This thin-film membrane acts as a barrier to positive ions and neutral gas molecules, which are generated in the channels of the MCP as a result of electron impacts, while permitting free passage of electrons. Energetic positive ions, if not stopped, produce surface etching of the photocathode and ion scintillations.
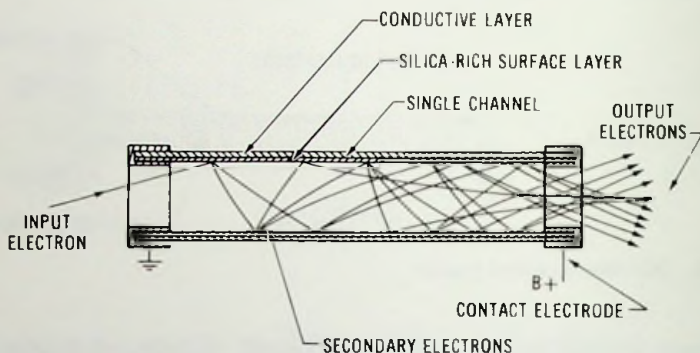
Fig. 13.2   Operation of a single microchannel.

The purpose of the ion barrier film coating, therefore, is to improve the operational life of generation 2 and generation 3 image intensifier tubes and to reduce the signal induced noise produced by ionized gasses originating in the microchannel plates.

The process of coating of microchannel plate input with a thin layer of strongly adherent aluminum oxide film consists of steps of placing a thin self-supporting organic lacquer film in contact with the input surface of the MCP on which the aluminum oxide film is deposited in a vacuum, and of an air bake to decompose the organic film material and to allow the aluminum oxide film to settle on the input of the MCP and to adhere by electrostatic forces. The self-supporting organic film is obtained by a water flotation technique in which a drop of lacquer on the water surface is allowed to spread uniformly over the surface and, by draining the water, allowed to settle on a lacquering fixture ring. The self-supporting lacquer film after drying and hardening is transferred and attached to the input of the MCP.

13.1.1   Principle of Operation

The operation of the microchannel electron multiplier is based on the concept of a continuous resistive strip diode. By impression of a voltage across the microchannel, a homogeneous axially oriented electric field is produced in the channel. A primary electron striking the input end of the channel produces a multiple number of secondary electrons. The secondary electrons enter the axial electric field with a small initial component of transverse velocity causing the electrons to move on a parabolic path along the length of the channel until, due to the transverse motion, the secondary electrons collide with the channel wall again and generate more secondary electrons as shown in figure 13.2. The multiplication process continues along the channel until the end of the channel is reached or current gain

saturation occurs. Current gain saturation results from the reduced field strength in the output end portion of the channel due to high channel currents. This situation is analogous to that in a conventional photomultiplier when a bright light pulse reduces the interstage voltages near the output end so that the secondary emission coefficents are reduced.

13.1.2 Derivation of the Current Gain Equation

The current gain of a continuous resistive channel can be derived by consideration of the measured current gain, which is shown in figure 13.3. The straight line on the log-log paper indicates an exponential relation between the MCP voltage and current gain. Obviously a similar functional relation exists for a section of the channel length (hereafter designated *stage length*). Accordingly, the stage gain G_s can be given by the following equation:

$$G_s = \left(\frac{V_s}{K}\right)^m = \left(\frac{V}{Kn}\right)^m, \tag{13.1}$$
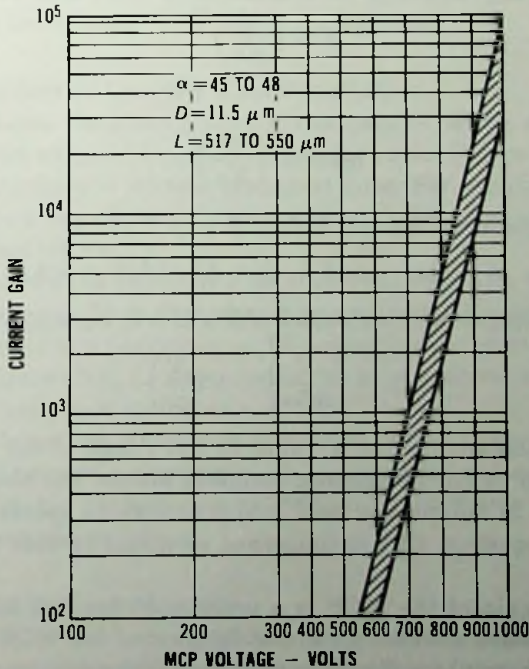
Fig. 13.3   Measured current gain range as a function of MCP voltage for unscrubbed 18-mm generation 2 MCPs.

where n is the number of stages along the channel, V_s is stage voltage, V is the MCP voltage, K and m are constants determined by the stage length and the secondary electron emitter.

The current gain G_c of a continuous resistive channel is the product of the gain of the individual stages:

$$G_c = G_s{}^n. \tag{13.2}$$

Here n is proportional to the length L of the channel and inversely proportional to the stage length l, i.e., $n = L/l$. By combination of equations 13.1 and 13.2 the current gain becomes

$$G_c = \left(\frac{V}{Kn}\right)^{mn}. \tag{13.3}$$

The values of K and n can be obtained from equation 13.3 by use of measured current gain values. For example, for a channel length-to-diameter ratio of $\alpha = 40$, the measured current gain at $V = 340$ V is $G = 1$ and at $V = 800$ V, $G = 5201$. Substitution of these values in equation 13.3 leads to the following two equations:

$$1 = \left(\frac{340}{Kn}\right)^{mn} \tag{13.4}$$

and

$$5201 = \left(\frac{800}{Kn}\right)^{mn}. \tag{13.5}$$

Solution of equations 13.4 and 13.5 with $m = 1$ yields

$$K = 34 \qquad \text{and} \qquad n = 10 = L/l = \alpha/4. \tag{13.6}$$

Finally, substitution of these values of K and n in equation 13.3 yields

$$G_c = \left(\frac{V}{8.5\alpha}\right)^{\alpha/4} = \left(\frac{V}{c\alpha}\right)^{\alpha/4}, \tag{13.7}$$

where c is a constant having a value in the range of 8.5 for unscrubbed plates and 9.5 to 10 for the electron-scrubbed plates. The electron scrubbing process is used to outgas the MCP and increase its operational life. Note that as far as equation 13.7 is concerned identical results can be obtained with $m = 1$.

The current gain of the MCP is a product of the first impact gain, the continuous resistive channel gain, the fraction of the MCP open area, and the end spoiling gain loss. For the evaluation of the first impact gain, let us consider an MCP with a 7° bias. For this case the input current strikes two continuous 4-diameter/length stages approximately. The output current I_o expressed with the current I_i is

$$I_0 = F\left(\frac{I_i}{2}\delta_1 G_s{}^n + \frac{I_i}{2}\delta_1 G_s{}^{n-1}\right) = FI_i\delta_1 G_s{}^n \frac{G_s + 1}{2G_s}, \tag{13.8}$$

where δ_1 is the secondary emission coefficient of the first impact, and F is the effective value of the fraction of the MCP open area. End spoiling decreases the output current by the following experimental gain-loss factor:

$$G_r = \exp(-0.65h), \tag{13.9}$$

where h is the end spoiling length in channel diameters. From equations 13.8 and 13.9, the current gain G_p of an MCP becomes

$$G_p = F\delta_1 G_s{}^n \frac{G_s + 1}{2G_s} \exp(-0.65h). \tag{13.10}$$

By combination of equations 13.2, 13.3, 13.7, and 13.10, the MCP gain becomes

$$G_p = F\frac{\delta_1}{2}\left(\frac{V}{c\alpha}\right)^{\alpha/4}\left(\frac{V + c\alpha}{V}\right)\exp(-0.65h). \tag{13.11}$$

Equation 13.11 is a general expression for the MCP gain and gives the current gain for any channel length-to-diameter ratio.

13.1.3 Evaluation of Current Gain Parameters

Table 13.1 shows the calculated current gain of MCPs as a function of MCP voltage and channel length-to-diameter ratio. Figure 13.4 shows the data of table 13.1 for $\alpha = 46$ in a graphical form. For comparison see figure 13.3, which shows the measured current gain range for the 18-mm generation 2 unscrubbed MCPs.

Figure 13.5 shows the calculated MCP current gain as a function of α for several MCP voltages. Note that at each operative MCP voltage a maximum current gain occurs at a particular α. The maximum current gain conditions are plotted in figure 13.6. As an example, for an operative voltage of 1000 V, a maximum current gain occurs at $\alpha = 45$.

Figure 13.7 shows the maximum obtainable current gain as a function of MCP voltage. Again as an example, at an operative voltage of 800 V, the maximum obtainable current gain is 7887, and from figure 13.6 the voltage is obtained by use of $\alpha = 36$.

13.1.4 Current Gain Uniformity

The uniformity of the current gain over the entire active microchannel plate area is an important requirement in the image intensifier application. Channel plates are fabricated which are close to this ideal performance. In imperfect plates, nonuniform image transmission is usually the result of bundle-to-bundle gain variation and gain variation at the bundles' bounda-

Table 13.1   Current Gain as a Function of MCP Voltage

V	α = 30		α = 36		α = 40		α = 44		α = 46		α = 48		α = 52		α = 60	
	G_c	G_p	G_c	G_p	G_c	G_p	G_c	G_p	G_c	G_p	G_c	G_p	G_c	G_p	G_c	G_p
300	3.38	6.25	0.836	1.69	0.28	0.59	0.09	0.2	0.047	0.1	0.025	0.06	0.006	0.015	0.00034	0.0009
400	29	47	11.1	19.6	5.32	9.84	2.1	4.06	1.3	2.57	0.788	1.6	0.27	0.67	.026	.06
500	156	235	83	133.8	47	79	24	42	16.9	30	11.47	20.8	1.96	9.34	0.74	1.37
600	612	872	428	646	292	457	181	293	137	226	102	171	53	92	11.5	21.3
700	1946	2654	1715	2464	1368	2032	987	1514	810	1262	650	1028	394	642	115	198
800	5298	6986	5705	7887	5201	7411	4289	6294	3762	5600	3229	4875	2237	3472	856	1401
900	12 816	16 447	16 469	22 068	16 890	23 270	15 670	22 181	14 579	20 912	13 273	19 290	10 343	15 422	5012	7852
1000	28 245	35 447	42 511	55 519	48 440	64 909	49 935	68 610	48 974	68 122	46 997	66 171	40 692	58 678	24 347	36 764

$F\delta_1 = 4$; $\exp(-0.65\tilde{n}) = 0.5$
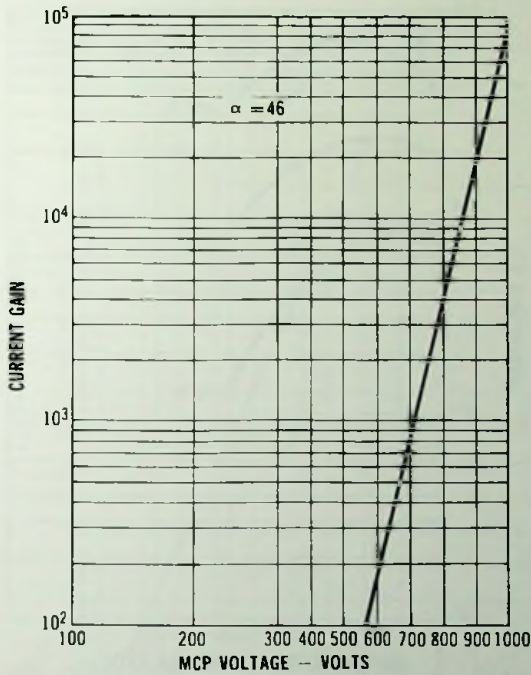
Fig. 13.4   Current gain as a function of MCP voltages.

ries. The nonuniform image transmission of this nature is often referred to as *spatial noise* or *fixed pattern noise*. The value of fixed pattern noise, however, is less than 5% for gain range of 10 to 10 000.

The current gain of the MCP is greatly determined by the secondary-electron emission coefficient of the resistive secondary-electron emission film. Figure 8.15 of chapter 8 shows the secondary-electron emission coefficient of 8161 glass for perpendicular beam landing, which is used in ITT MCPs. For grazing angles the primary-electron beam penetration of the secondary-electron emission film is substantially smaller and, therefore, the secondary-electron emission yield is substantially greater.

An additional improvement of electron gain is possible by increasing the open area ratio by funneling and by use of magnesium oxide (MgO) coating at the input of the channels. Magnesium oxide has a greater secondary electron emission yield than the 8161 glass.

13.1.5   Equivalent Electron Input

The background noise of the MCP with no input signal is another key parameter and it is usually defined by the term of *equivalent electron input*
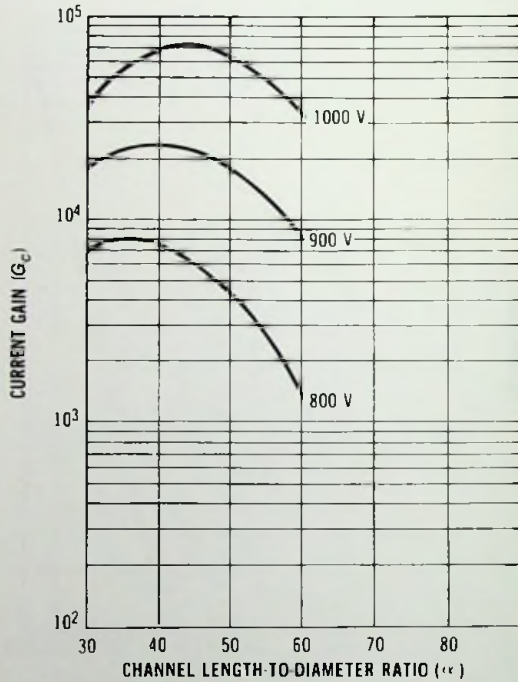
Fig. 13.5   Current gain as a function of channel length/diameter ratio.

(EEI). The EEI of an MCP is the ratio of the dark output current density to the MCP current gain at a given MCP voltage.

In image tubes the maximum acceptable value of EEI is about 1×10^{-15} A/cm^2. Typical EEI values are much lower than this value.

13.1.6   Resolution and MTF

The resolution of microchannel plates is primarily limited by the microchannel center-to-center spacing. In a first-order approximation, resolution is inversely proportional to the microchannel center-to-center spacing. The MTF of microchannel plates is shown in figure 6.8, chapter 6.

In image intensifier tubes the output of the MCP is proximity focused on the phosphor screen. The resolution and MTF of the image intensifier tube, therefore, depend on the radial emission energy spread of the MCP. The radial emission energy can be reduced by end spoiling the output end of the microchannels. End spoiling allows only the small radial emission energy electrons to escape from the channel. In addition, it forms a microlens at
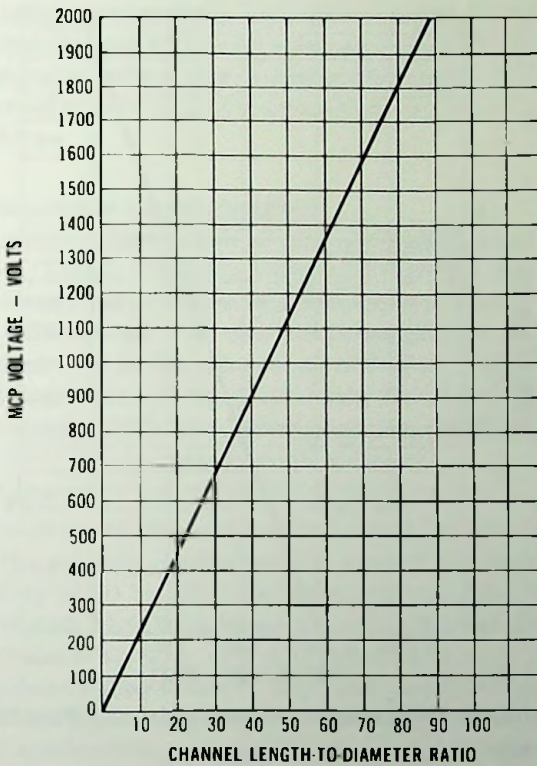
Fig. 13.6 Maximum current gain conditions at operative MCP voltages as a function of channel length/diameter ratio.

the exit end of channel which has a strong collimation effect on the microchannel beamlets.

At low input current densities, resolution is also limited by the multiplication statistics of the MCP.

At high output current density values, current gain saturation is a serious limitation to resolution. Current gain saturation reduces the contrast of the image.

13.1.7 Current Gain Saturation

Current gain saturation results from the reduced field strength in the output end portion of the channels due to high channel currents. This situation causes the input current versus the output current characteristics to
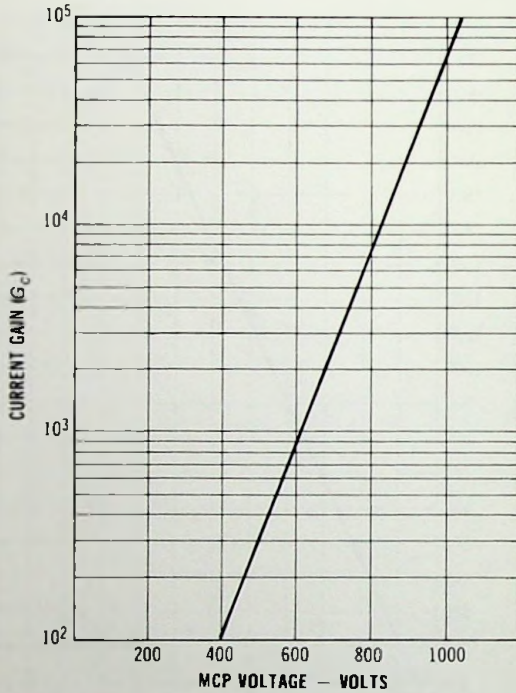
Fig. 13.7 **Maximum obtainable current gain as a function of MCP voltage.**

deviate from the ideally linear relationship. Current gain saturation reduces the MTF.

The primary factor which governs MCP saturation is the strip current. Secondary factors are the capacitance of the adjacent annulars of the channels and the thickness of the secondary-electron emitting surface.

Under unsaturated conditions the maximum MCP output current is about 5% of the strip current. In the generation 2 tube, the MCP output current is in the range of 10 to 20 nA/cm². Consequently, for an 18-mm-diameter MCP which has a useful area of 2.54 cm², the minimum strip current is 1 μA. The maximum value of the strip current is established by the power consumption of the MCP and it is usually less than 6 μA for an 18-mm-format MCP.

MCPs are suitable devices for detection and multiplication of high-speed events. The electron transit time of an MCP is typically less than 1 ns and the transit time spread is approximately 0.1 ns. In pulse applications, the MCP instantaneous currents can be orders of magnitude higher than the strip current for linear amplification.

The self-saturating feature of the MCP is utilized in the generation 2

wafer tube for bright sources protection. The combined action of automatic brightness control circuits and MCP saturation can reduce a 5000-fc input light spot to approximately a 100-fL output luminance, thus providing the necessary eye relief against bright sources, such as, for example, automobile lights or light flares.

13.1.8   Environmental Characteristics

In image intensifier tube applications the operational temperature is $+45°C$ to $-45°C$. Stable operation requires a minimal electron gain, EBI, and plate resistance change within this temperature range.

The current gain change from the room temperature value to $+45°C$ is typically less than 25% in the gain range of 200 to 1000. The plate resistance at $+45°C$ decreases less than 25% from the room temperature value and at $-45°C$ increases less than 75% of the room temperature value.

13.1.9   Life Cycle

The life cycle of an MCP is primarily limited by the outgassing of the MCP. During the electron multiplication process the secondary electrons acquire an energy of 50 to 100 V between each multiplication step. This energy is sufficiently high to progressively dislodge the gas molecules absorbed at the channel surface. In microchannel plates in which the water vapor has been desorbed by bakeout, the main gasses released are CO, CO_2, H_2, and CH_4. A small fraction of the released gasses is in an ionized state. The ions, after acceleration, may strike the channel wall, causing an ion burn effect which is associated with gain loss. The usual methods for the stabilization of the MCP gain is electron scrubbing of the MCP. Electron scrubbing decreases the rate of gain loss per specified time interval. It also decreases the electron gain of the MCP.

13.1.10   Physical Properties of the Aluminum Oxide Ion Barrier Film

The ion barrier film is a very thin aluminum oxide (Al_2O_3) film that is deposited over the input side of the microchannel plate. It prevents positive ions which are generated within the channels of the MCP from reaching the photocathode surface but allows the transmittance of photoelectrons.

To be effective the aluminum oxide film must be relatively free of holes, uniform in thickness, and must adhere strongly to the MCP, or separation will occur when voltage is applied or during shock or vibration. The thickness must be controlled to approximately 30 Å in order to avoid excessive beam energy loss. Figure 13.8 shows the dead voltage of aluminum oxide film as a function of film thickness. A 30-Å film thickness corresponds to 120 V dead voltage. Films thinner than 30 Å have less dead voltage but are too fragile to handle, show poor adherence, and have too many holes.
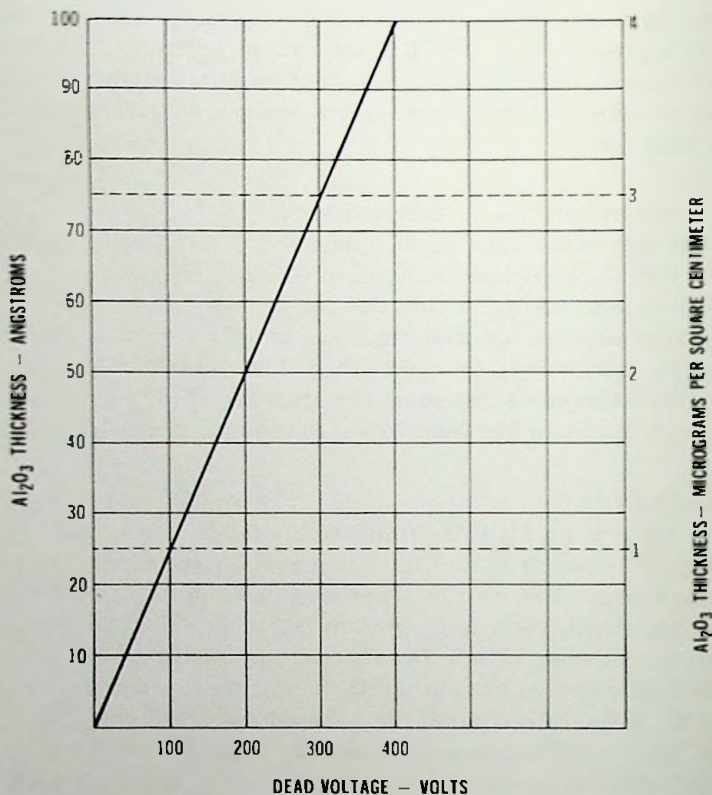
Fig. 13.8   Dead voltage as a function of film thickness.

Another important characteristic of the film is the first secondary emission crossover. At high illumination levels, bright source protection in the wafer tube is accomplished by reduction of the cathode voltage. Image transmission is ensured by clamping the cathode voltage above the first crossover voltage which is less than 28 V. If the clamp voltage is adjusted below the first crossover of the film, image transmission ceases to exist because the ion barrier film discharges to the cathode potential.

The quality of the ion barrier film is greatly determined by the "A" and "B" type hole defects. The "A" defect is a pinhole in the ion barrier film which has an apparent dimension of one channel of the MCP. The "B" hole defect is a hole in the ion barrier film which exists over a string of channels with dimensions no longer than 25 µm by 125 µm or a hole in the ion barrier film which exists over a cluster of channels with a diameter no larger than 50 µm.

In normal operation the "A" and "B" type holes are not resolvable at the output of the phosphor screen of an image tube because of their very low contrast. "A" type holes become resolvable only by reduction of the V_1 voltage to about 5 V and at photocathode illumination levels greater than 10^{-4} fc.

The adherence of aluminum oxide film is an important parameter. In wafer tubes it is required that with an input electric field of 4000V/mm, there shall be no electrical or physical breakdown of the ion barrier MCP.

13.2 Fiber-Optic Plates

13.2.1 General Description of Fiber-Optic Plates

Fiber-optic plates are optical devices for transmission and transformation of luminous images from the input to the output ends of the fiber-optic bundles. The operation of the fiber-optic plates is based on the concept of total internal light reflection in thin fibers. A very thin, transparent, homogeneous fiber of glass that is enclosed by a material of lower index of refraction transmits light through its length by internal reflection. A bundle of such fibers can be used to transmit complete optical images.

Physically a fiber-optic plate is a two-dimensional array of light-propagating glass fibers fused together with a precise orientation of fibers to constitute a solid vacuum-tight plate. Each fiber of the plate consists of a core glass clad with a jacket glass of a lower index of refraction and with an absorbing coating for prevention of light crosstalk between the adjacent channels as shown in figure 13.9. The diameter of the glass fibers is in the
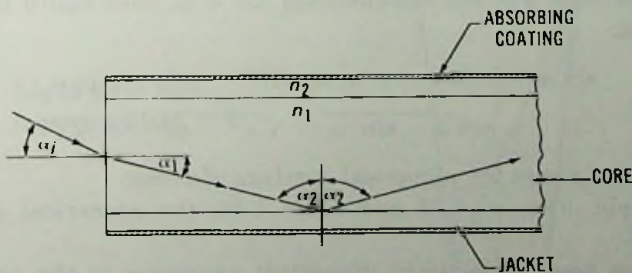
Fig. 13.9 Light propagation in a fiber.

range of 3 to 10 μm. The fabrication technique of fiber-optic plates consists of drawing the clad rods smaller and fusing them into a solid vacuum-tight bundle, then slicing the bundle and polishing the input and output surfaces to the final shape of the fiber-optic plate.

With fiber-optic plates, complex input image surfaces can be transferred into any desired output surface shape. The three most frequently used input and output surface combinations are the plano-plano, plano-concave, and the convex-concave shapes.

According to the desired image transfer characteristics, fiber-optic plates are fabricated from cylindrical, tapered, and twisted rods. Fiber optics fabricated from axially oriented cylindrical rods transmit an erect image with unity magnification. Tapered fiber optics consisting of tapered rods transmit a magnified erect image ($M > 1$). The fiber-optic twister plates invert the transmitted image. The radial position of the output fibers of the twister plate is twisted $180°$ with respect to the radial position of the input fibers.

13.2.2 Cylindrical Fibers

In fiber bundles in which the diameter of individual fibers are on the order of magnitude of the wavelength of light, the fibers behave as waveguides as far as light propagation is concerned. A transparent dielectric rod thus serves as a waveguide for the light in the same way that a hollow metal pipe does for the electromagnetic waves, and it has similar properties. In fiber-optic plates that are used in imaging devices the diameter of the individual fibers is much larger than the wavelength of light. In such fibers light propagates by total internal reflection. When light passes from an optically dense medium to an optically less dense medium, the angle of refraction is always greater than the angle of incidence. As the angle of incidence is increased, a critical angle, α_c, is reached at which the angle of refraction is $90°$. For angles of incidence larger than this critical angle no refracted ray exists but all light is trapped in the fiber, giving rise to total internal reflection. For the extreme case, $\alpha_2 = \alpha_c$, from figure 13.9 the following holds:

$$\sin \alpha_i = n_1 \sin \alpha_1 = n_1 \sin (90° - \alpha_c) = n_1 \cos \alpha_c$$

$$= n_1\sqrt{1 - \sin^2 \alpha_c} = \sqrt{n_1{}^2 - n_2{}^2} = \text{N.A.}, \tag{13.12}$$

where N.A. designates the numerical aperture of a fiber.

For example, if $n_1 = 1.78$ and $n_2 = 1.48$, the numerical aperture is N.A. $= 0.98$.

Image-tube fiber optics have numerical apertures in the range of 0.9 to 1.0.

For a Lambertian light source, in the absence of crosstalk between the fibers and reflection losses at the core-jacket interface and the input and output surface of the fiber, the fraction of light transmitted by the fiber is

$$\sin^2 \alpha_i = (\text{N.A.})^2. \tag{13.13}$$

The diffused light transmission (Lambertian light source) of image tube fiber-optic plates supplied by different manufacturers is in the range of 50 to 60%. Much of the loss is due to the fact that the area of the mosaic occupied by the light-transmitting fiber cores is a fraction of the total area (about 70%).

13.2.3 Tapered Fibers

Light propagation in tapered fibers is similar to that experienced in cylindrical fibers. But because tapered fibers magnify the transmitted image, important characteristics of the light transmission are modified in correspondence with the general laws of optics. Let us examine first the relationship between the lateral and angular magnification in tapered fibers. In order to find the relation between the angular and lateral magnifications it is enough to examine two successive light reflections at the wall of the tapered fiber. Consider a light ray entering a fiber (or being reflected from the tapered wall of the fiber) at an angle as shown in figure 13.10. The axial distance Z_1 between two successive reflections is

$$Z_1 = \frac{D_0}{\tan \alpha_1 - \tan \gamma}. \tag{13.14}$$
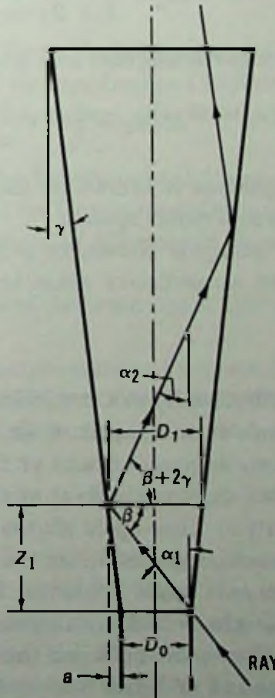
Fig. 13.10 Light path in a tapered fiber.

The diameter of the fiber at a reflection expressed with the diameter of the previous reflection is

$$D_1 = D_0 + 2a = D_0 \left(1 + \frac{2 \tan \gamma}{\tan \alpha_1 - \tan \gamma} \right). \tag{13.15}$$

The lateral magnification is

$$M_l = \frac{D_1}{D_0} = 1 + \frac{2 \tan \gamma}{\tan \alpha_1 - \tan \gamma}. \tag{13.16}$$

The angular magnification is

$$M_a = \frac{\alpha_2}{\alpha_1} = \frac{\alpha_2}{\alpha_2 + 2\gamma} = \frac{1}{1 + 2\gamma/\alpha_2}. \tag{13.17}$$

For the paraxial condition and for $\alpha_1 \gg \gamma$ the magnifications become

$$M_l = 1 + \frac{2\gamma}{\alpha_1 - \gamma} \cong 1 + \frac{2\gamma}{\alpha_1} \tag{13.18}$$

and

$$M_a = \frac{1}{1 + 2\gamma/(\alpha_1 - 2\gamma)} = \frac{1}{1 + 2\gamma/\alpha_1}. \tag{13.19}$$

The product of the angular and lateral magnifications is

$$M_l M_a = \left(1 + \frac{2\gamma}{\alpha_1} \right) \left(\frac{1}{1 + 2\gamma/\alpha_1} \right) = 1. \tag{13.20}$$

The last equation is known as Lagrange's law for equal refractive indexes for the image and object spaces.

The above analysis shows, in a first-order approximation, that a tapered fiber acts like an ordinary glass lens as far as image transmission is concerned.

13.2.4 Luminous Gain Considerations

Assume that at the input of an image intensifier tube a demagnifying fiber-optic plate is present, and at the output a magnifying fiber-optic plate is also present. Assume also that the product of the magnifications of the input and output fiber-optic plates is unity. In this case, if the maximum light acceptance angle is α_1, at the entrance of the input fiber-optic plate, the maximum exit angle is also α_1. However, an exit angle α_1 corresponds to an entrance angle $\alpha_2 = M_l \alpha_1$ (Lagrange's law), which indicates that all light entering the fiber optic between the angles α_2 and α_1 is lost in the fiber optic. Since the amount of light flux at the photocathode is proportional to the

square of α_2 (or more precisely to the $\sin^2 \alpha_2$) the light loss is proportional to M_l^2. This means that for $M_l = 0.5$, only one-fourth of the entrance light flux arrives to the photocathode from a Lambertian emitter which is in contact with the input fiber optic. Because of the light loss the illumination at the photocathode is identical with the illumination at the entrance of the fiber optic. Thus the output fiber optic acts similar to an eyepiece having a normal magnification, i.e., the output image is magnified without a change in the apparent brightness.

For a tapered fiber-optic plate and lens combination at the input of the image tube, light loss in the fiber-optic plate does not occur when the lens acts as an aperture stop. In this case it is possible to increase the amount of light flux per unit area at the photocathode. However, the apparent brightness at the entrance and at the exit of the fiber-optic plate will remain identical if transmission losses are excluded. This phenomenon follows from Lagrange's law, which relates the angular and lateral magnifications.

References

Adams, J., and B. W. Manley. "The Mechanism of Channel Electron Multiplication," *IEEE Transactions on Nuclear Science*, Vol. NS-13, No. 3, p. 88, June 1966.

Asam, A. R. "Advances in Microchannel Plate Technology and Application," *Proceedings of the 1976 Electro Optical System Design Conferences*, Industrial and Scientific Conference Management, Inc., 222 West Adams Street, Chicago, Illinois 60606.

Chuiko, G. A., and A. M. Yakobson. "The Fundamental Characteristics of High Lead Content Glasses as Material for Continuous Dynode Secondary Electron Multiplier," *Radio Engineering and Electronic Physics*, Vol. 11, No. 9, p. 1471, 1966.

Csorba, I. P. "Current Gain Parameters of Microchannel Plates," *Applied Optics*, November 15, 1980.

————. "Long Life Goggle Tube Product Improvement Program for AN/PVS-5," Final Engineering Report, Contract DAAAG53-76-C-0203, U. S. Army Electronic Research and Development Command, Fort Belvoir, Virginia 22060 (March 15, 1979).

Eberhardt, E. H. "Gain Model for Microchannel Plates," *Applied Optics*, Vol. 18, p. 1418, 1979.

Eschard, G., and B. W. Manley. "Principles and Characteristics of Channel Electron Multipliers," *Acta Electronica*, 14, p. 19, 1971.

Green, R. L., and K. B. Blodgett. "Electrically Conducting Glasses," *The Journal of the American Ceramic Society*, Vol. 31, p. 89, April 1, 1948.

Kapany, N. S. *Fiberoptics*, Academic Press, New York and London, 1967.

Lampton, M. "The Microchannel Image Intensifier," *Scientific American*, Vol. 245, No. 5, November 1981.

Patric, E. V., and A. R. Asam. "Microchannel Plates with High Open Area Ratio," *Proceedings of the 1976 Electro-Optical System Design Conference*, New York, September 1976.

Peifer, W. K. "Present Life Status of Proximity Focused Generation 2 Wafer Tube," *Proceedings of the 1976 Electro-Optical Systems Design Conference*, New York, 1976.

Pollen, H. K. "Noise in Second Generation Image Intensifier Tubes," *Proceedings of the Electro-Optical System Design Conference*, New York, 1972.

Ruggieri, D. "Microchannel Plate Image Detectors," *IEEE Transactions on Nuclear Science*, pp. 74-84, 1972.

Stefanik, R. "Imaging Characteristics of Image Intensifiers at Low Spatial Frequencies," *Proceedings of the 1976 Electro-Optical Systems Design Conference*, New York, 1976.

Wiley, W. C., and C. F. Hendee. "Electron Multipliers Utilizing Continuous Strip Surfaces," *IRE Transactions on Nuclear Science*, Vol. NS-9, No. 3, p. 103, June 1962.

14

BASIC IMAGE TUBE MEASUREMENTS

Among the many measurements an image tube goes through to guarantee a satisfactory product, the most frequently measured characteristics are:

1. Photocathode sensitivity
2. Gain
3. Equivalent background input
4. Ion scintillations
5. Resolution
6. Modulation transfer function
7. Distortion

In the following paragraphs each of these measurements is briefly defined.

14.1   Photocathode Sensitivity

The photocathode sensitivity of an image tube is measured by exposure of the photocathode to a known quantity of radiant flux and by measurement of the photocathode current. The usual equipment is a light source and 100-V battery, which is connected through a microammeter to the cathode and the anode of the image tube as shown in figure 14.1. In this illustration the photocathode of the image tube is illuminated by a tungsten lamp through a calibrated aperture. The photoelectron current is measured by a microammeter at the screen.

The light source for photocathode sensitivity measurements is a tungsten
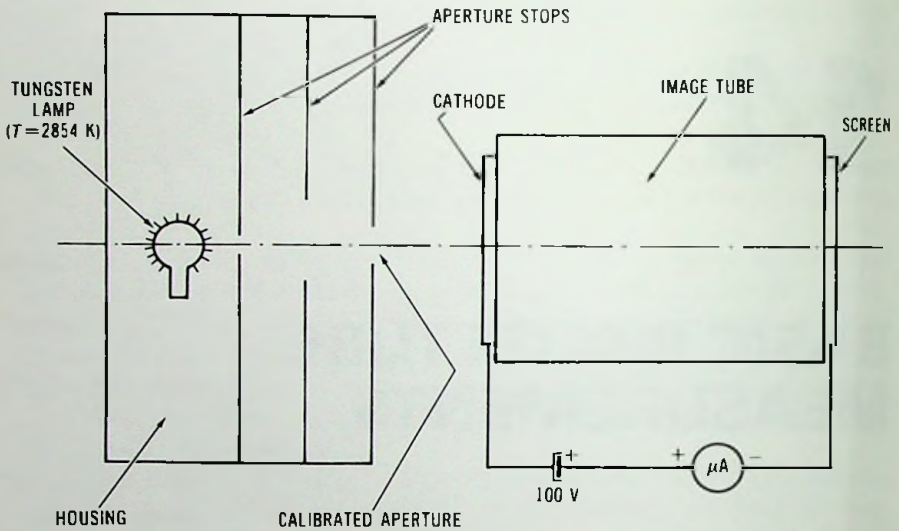
Fig. 14.1   Diagram of a photocathode sensitivity-measuring
            equipment.

lamp operated at a color temperature of 2854 K. With calibration aperture
stops, the light flux may be varied from 10^{-1} to 10^{-3} lm.

14.2   Luminous Sensitivity

The luminous sensitivity of the photocathode is measured by illumination
of the photocathode with a known quantity of unfiltered radiation of a
tungsten lamp and by the measurements of the photocathode current; it
is expressed in amperes per lumen. For example, if the photocathode is
illuminated with a 0.01-lm luminous flux and the measured photo-
cathode current is 3 μA, the luminous sensitivity is $S_l = 3$ μA/0.01 lm =
300 μA/lm.

14.3   Blue Sensitivity

For image tubes having a P-11 output phosphor screen (blue phosphor),
an important characteristic is the blue sensitivity of the photocathode
which determines the blue radiant power gain of the image tube. The blue
sensitivity of the photocathode is measured by the illumination of the photo-
cathode through a Corning No. 5113 blue filter with a tungsten lamp (see
figure 14.2); it is expressed in amperes per lumen. For example, if the photo-
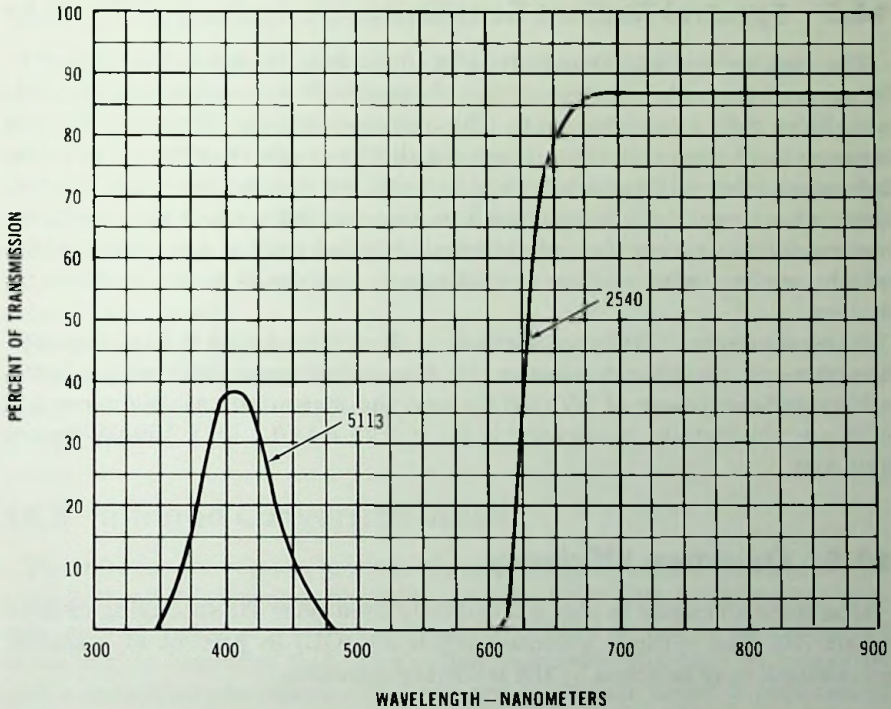
Fig. 14.2   Transmission characteristics of Corning no. 5113 and 2540 filters.

cathode is illuminated with a 0.1-lm luminous flux through a 5113 blue filter and the measured photocathode current is 1.0 μA, the blue sensitivity is $S_b = 1$ μA/0.1 lm $= 10$ μA/lm.

14.4   Infrared Sensitivity

For specification of the photosensitivity of infrared image tubes which convert the infrared radiation to a visible image, the infrared sensitivity is often used. The infrared sensitivity of a photocathode is measured by illumination of the photocathode through a Corning No. 2540 infrared filter with a tungsten lamp (see figure 14.2); it is expressed in amperes per lumen. The unit of amperes per lumen is the result of tungsten lamp calibration, which is given in lumens.

For example, if the photocathode is illuminated with 0.1 lm luminous flux through a 2540 infrared filter and the measured photocathode current is 0.5 μA, the infrared sensitivity is $S_{ir} = 0.5$ μA/0.1 lm $= 5$ μA/lm.

14.5   Spectral Radiant Sensitivity

The spectral radiant sensitivity of a photocathode at a wavelength may be measured by illumination of the photocathode through a narrow-bandpass filter with a tungsten lamp. The narrow-bandpass filters used for this measurement are calibrated by use of a thermocouple in terms of transmitted radiant flux of a tungsten lamp in watts per lumen. The radiant sensitivity at a wavelength is expressed in amperes per watt. A more accurate method for measuring the radiant sensitivity is by use of a monochromator, which supplies (with a prism or grating) an essentially monochromatic radiation.

As an example, if the photocathode is illuminated with 0.1 lm luminous flux through an 800-nm-wavelength narrow-bandpass filter which transmits a radiant power of 150 μW/lm and the measured cathode current is 0.75 μA, the radiant sensitivity is S_R = 0.75 μA/(0.1 lm x 150 μW/lm) = 0.05 A/W.

14.6   Quantum Efficiency

Quantum efficiency is also a frequently used term for specifying cathode sensitivity. The cathode quantum efficiency (QE) in percent at a specific wavelength may be given by the following equation:

$$QE = 123\,950 S_R / \lambda, \tag{14.1}$$

where λ is the wavelength in nanometers and S_R is radiant sensitivity in amperes per watt.

For example, if the radiant sensitivity at λ = 800 nm is S_R = 0.0645 A/W, the quantum efficiency is 10%.

14.7   Luminous Gain

The luminous gain of an image tube is measured by illumination of the photocathode by a calibrated tungsten lamp operated at a color temperature of 2854 K and by measurement of the output brightness of the image tube. With the use of a calibrated light source the input illumination is known, and it is, therefore, necessary only to measure the output brightness of the image tube. The output brightness may be measured with a spot brightness meter. The luminous gain is the ratio of the output brightness to the input illumination.

For example, if the input illumination is 10^{-5} fc and the measured output luminance is 1 fL, the luminous gain is G_l = 1 fL/10^{-6} fc = 10^5 fL/fc.

14.8 Blue Radiant Power Gain

The blue radiant power gain is the most frequently used power gain measurement for image tubes having a P-11 output phosphor screen (blue phosphor). It is measured by illumination of the photocathode through a Corning No. 5113 blue filter with a calibrated tungsten lamp operated at a color temperature of 2854 K and by measurement of the radiant output power of the image tube. The radiant output power (and also the radiant input power) may be measured with a calibrated photodiode having an S-20 response. The radiant power gain is the ratio of the radiant output power to the radiant input power.

For example, if the input illumination through a 5113 filter yields 10^{-8} W calibrated radiant power input and the measured radiant output power is 3×10^{-4} W, the blue radiant power gain is $G_p = 3 \times 10^{-4}\text{W}/10^{-8}\text{W} = 3 \times 10^4$ W/W.

14.9 Infrared Conversion Index

The infrared conversion index is measured by illumination of the photocathode through a Corning No. 2540 infrared filter with a calibrated tungsten lamp operated at a color temperature of 2854 K and by measurement of the output luminous flux. The output luminous flux may be measured with a calibrated photodiode. The infrared conversion index is obtained as defined by equation 8.36.

For example, if the input of the image tube is illuminated through a 2540 infrared filter with 0.01 lm luminous flux and the measured output luminous flux is 0.0348 lm the infrared conversion index from equation 8.36 is 30.

14.10 Equivalent Background Input

The equivalent background input (EBI) is the ratio of the residual output screen radiation and the gain of the image tube in absence of photocathode illumination. The residual screen radiation is usually measured with a calibrated photomultiplier tube or by a spot brightness meter. By division of the residual luminance with the luminous gain or the residual radiant power with the power gain, the EBI is obtained in lumens per square centimeter or in watts per square centimeter, respectively.

For example, if the luminous gain of an image intensifier tube is 40 000 fL/fc and the measured residual screen luminance is 4×10^{-7} lm/cm², the equivalent background input is 4×10^{-7} lm/cm²/$4 \times 10^4 = 1 \times 10^{-11}$ lm/cm². As another example, if the radiant power gain of an image intensifier

tube is 30 000 W/W and the measured residual screen radiant power is 3×10^{-11} W/cm^2, the EBI is 3×10^{-11} W/cm^2/3×10^4 W/W $= 1 \times 10^{-15}$ W/cm^2.

14.11   Ion Scintillations

Ion scintillations are part of the residual screen radiation. Although they do not contribute measurably to the EBI, they are a great concern in image tube cameras at long exposure times. Because of their greater brilliance, ion scintillations are more noticeable on the photographic film than the electron scintillations. Ion scintillations, therefore, may limit the exposure time by fogging the film. Ion scintillations are produced by positive ions striking the photocathode surface and producing a number of secondary electrons. Positive ions may be generated by several different mechanisms in image tubes, chiefly these: (1) high-energy electrons colliding with free gas molecules; (2) high-energy electrons bombarding alkali atoms and gasses absorbed on tube surfaces; (3) ionization induced by bulb wall charging; and (4) field stripping of ions from positively charged electrodes due to high electric field stresses.

The number of ion scintillations per second per useful area of image tube is usually counted by photographing the viewing screen of the image tube with a high-gain image tube camera.

14.12   Limiting Resolution

The limiting resolution of an image tube is measured by projection of a high-contrast resolution pattern, such as shown in figure 14.3, on the photocathode of the image tube and by reading the intensified resolution pattern by a microscope. A resolution element (a pair of three horizontal and three vertical bars) is considered to be resolved when the observer counts three vertical and three horizontal bars. At the limiting resolution the output image contrast is only about 3% for monocular vision. Therefore, special care must be exercised to avoid contrast limitations by the glass optics of the projector and microscope. Consequently, for critical measurements the combined resolution of the glass optics should be in excess of 200 lp/mm.

14.13   Pulsed Resolution

The pulsed resolution of gated image tubes is measured with the same arrangement as explained above except the tube is pulsed on and off. The length of a gating pulse is often in the nanosecond range with a repetition rate of a few cycles per second. Therefore, to obtain a visible output image of the resolution pattern, a high-intensity stroboscope lamp in synchronism with the gating pulse is used as a projector light source.
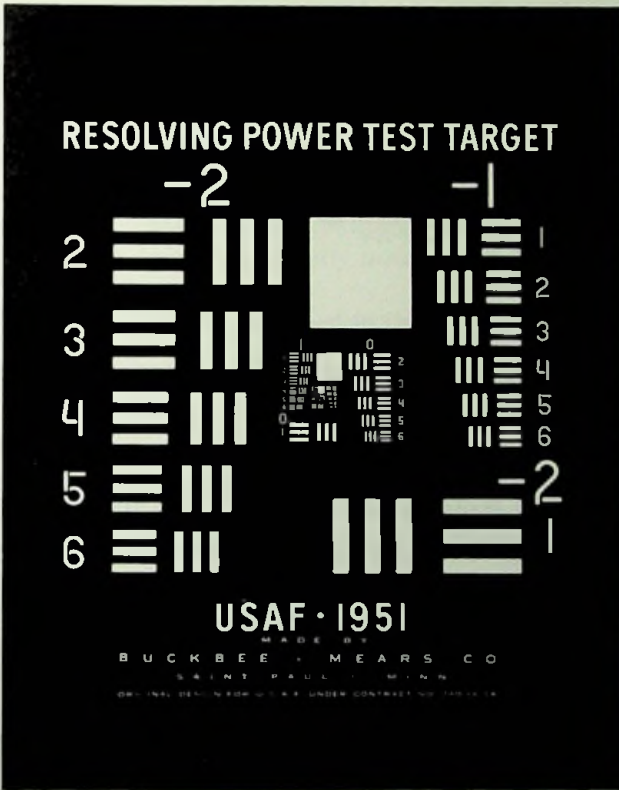
Fig. 14.3   USAF 1951 resolving-power test target. (*Courtesy USAF*)

14.14   Low Light Level Resolution

The low light level resolution of image tubes is measured by projecting the resolution pattern with a calibrated low light level projector. The output image may be read by a microscope or photographed with 0.2-s exposure time with an image tube camera.

14.15   Modulation Transfer Function

The modulation transfer function (MTF) of an image tube may be measured by projection of a sine-wave pattern of varying spatial frequency on the photocathode and by measuring the output luminance variations of the sine-wave pattern as shown in figure 14.4. In figure 14.4 the output image luminance variation is measured by producing an image formed in the air
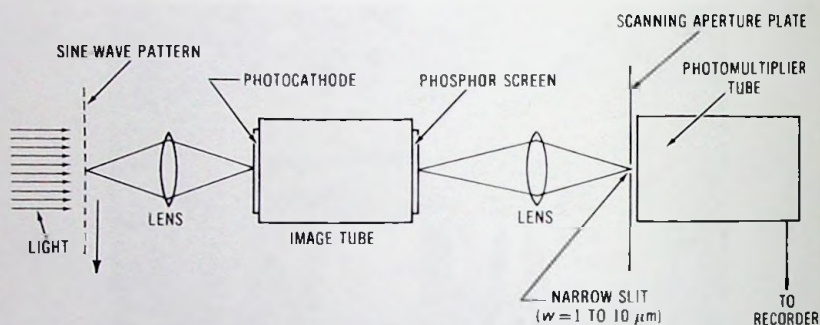
Fig. 14.4   Schematic diagram of a spatial frequency response test apparatus.

of the viewing screen with a lens, and by scanning this image with a narrow slit, which acts as an entrance aperture to a photomultiplier tube. From the recorded luminance variation the MTF is obtained by use of equation 6.1.

14.16   Contrast Transfer Function

The contrast transfer function (CTF) is measured similarly to the MTF measurements with the exception that a square-wave pattern is used.

For both measurements (MTF and CTF) a reasonable degree of accuracy may be obtained by using a slit width not greater than $W = 1/20f$; where f is the spatial frequency in line pairs per millimeter and W is the slit width in millimeters.

14.17   Distortion of an Image Tube

The distortion of an image tube is measured by projection of a millimeter scale on the photocathode and by measurements of the magnification of the intensified image of the millimeter scale as a function of radial distance with a microscope micrometer. By measuring the center and zonal magnifications the distortion as a function of zone diameter may be obtained by substitution of the center and zonal magnifications in equation 4.17.

14.18   Signal-to-Noise-Ratio Measurements

When measuring the signal-to-noise ratio one has to account for four quantities: (1) the dc signal current I_s, produced by the photocathode illumination; (2) the statistical fluctuation of the signal current, i_n, which is noise within the signal; (3) the dark dc current, I_d, produced mostly by

thermionic emission; and (4) the dark noise, i_{dn}, produced by the statistical fluctuation of the dark current.

The signal-to-noise ratio (snr) within the signal may be obtained from the following equation:

$$\text{snr} = \frac{I_s - I_d}{\sqrt{i_s^2 - i_{dn}^2}} = \frac{I_s - I_d}{i_n}. \tag{14.2}$$

In equation 14.2 i_s is the noise current, produced by the signal and dark currents. The noise current i_s is directly measurable during the photocathode illumination.

When the dark noise is also included in the signal-to-noise ratio the snr becomes

$$\text{snr} = \frac{I_s - I_d}{i_s}. \tag{14.3}$$

14.19   Luminous Efficiency of Phosphor Screens

The luminous efficiency of aluminized phosphor screens at a particular set of beam voltage and beam current may be measured by measurement of the luminous flux of the phosphor screen. It is expressed in lumens per watt.

For example, if the beam voltage is $V_s = 6000$ V and the beam current is $I_s = 10^{-8}$ A and the measured luminous flux of the phosphor screen is 6×10^{-4} lm, the luminous efficiency is $\eta = 6 \times 10^{-4}$ lm/6000 V $\times 10^{-8}$ A = 10 lm/W.

14.20   Absolute Conversion Efficiency of Phosphor Screens

The absolute conversion efficiency of aluminized phosphor screens at a particular set of beam voltage and beam current may be measured by measurement of the radiant flux of the phosphor screen. It is expressed in watts per watt.

For example, if the beam voltage is $V_s = 6000$ V and the beam current is $I_s = 10^{-8}$ A and the measured radiant flux is 2.4×10^{-6} W, the absolute conversion efficiency is $\eta = 2.4 \times 10^{-6}$ W /6000 V $\times 10^{-8}$ A = 0.04 W/W.

References

Eberhardt, E. H. "Source-Detector Spectral Matching Factors," *Applied Optics*, 7, p. 2037, 1968.

Engstrom, R. W. "Calculation of Radiant Photoelectric Sensitivity from Luminous Sensitivity," *RCA Review*, p. 116, March 1955.

RCA. *Electro-Optics Handbook*, 1968.

15

PHOTOMETRIC QUANTITIES

In the preceding chapters we have dealt with radiant flux, radiant energy, luminance, illumination and other photometric quantities. The precise definition of these quantities is the subject of photometry. This chapter is a summary of photometric quantities used through this book.

15.1   The Lambertian Radiator

Lambert's law states that if an area ΔA emits radiation at the rate I_0 per unit area, then the intensity of the radiation in the direction of θ is

$$I_\theta = (I_0/\pi)\Delta A \cos \theta. \qquad (15.1)$$

The area of the shaded zone in figure 15.1 is

$$\Delta F = 2\pi r^2 \sin \theta \, d\theta. \qquad (15.2)$$

The solid angle it subtends at ΔA is

$$d\omega = 4\pi(\Delta F/F) = 4\pi(2\pi r^2 \sin \theta \, d\theta/4\pi r^2) = 2\pi \sin \theta \, d\theta, \qquad (15.3)$$

where F is the area of the sphere.

The radiation crossing the zone between θ and $\theta + d\theta$ is

$$di_\theta = I_\theta d\omega = 2I_0 \, \Delta A \sin \theta \cos \theta \, d\theta = I_0 \, \Delta A \sin 2\theta \, d\theta. \qquad (15.4)$$

The radiation emitted in a zone having an apex angle θ is

$$i_\theta = \int_0^\theta di_\theta = I_0 \, \Delta A \sin^2 \theta. \qquad (15.5)$$

264
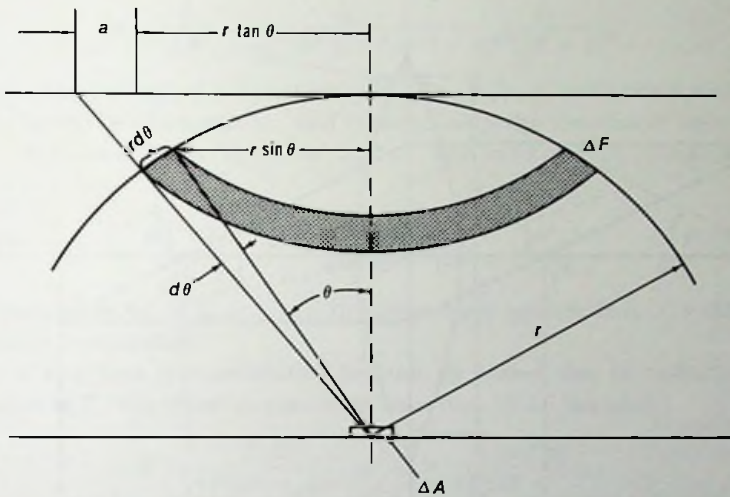
Fig. 15.1   Lambertian radiator.

The off-axial illumination at a plane positioned at a distance r from ΔA can be obtained by division of the radiation crossing the zone between θ and $\theta + d\theta$ with the elemental ring area $\Delta F'$, which is

$$\Delta F' = 2\pi r a \tan \theta = 2\pi r^2 \sin \theta \, d\theta / \cos^3 \theta. \tag{15.6}$$

By dividing equation 15.4 by equation 15.6 the illumination becomes

$$E = (I_0/\pi r^2)\Delta A \cos^4 \theta. \tag{15.7}$$

15.2   Photometry of Lenses

Assume that an elemental area ΔA, whose angular distribution of radiation obeys Lambert's law, is imaged by a lens. In the absence of light transmission losses the quantity of light which passes through the lens is, from equation 15.5,

$$L = I_0 \, \Delta A \sin^2 \theta_1 = M^2 I_0 \, \Delta A \sin^2 \theta_2 \tag{15.8}$$

where θ_1 and θ_2 are as shown in figure 15.2. The value of $\sin^2 \theta_2$, from the geometry of figure 15.2, is

$$\sin^2 \theta_2 = \frac{1}{4(S'/D)^2 + 1}, \tag{15.9}$$
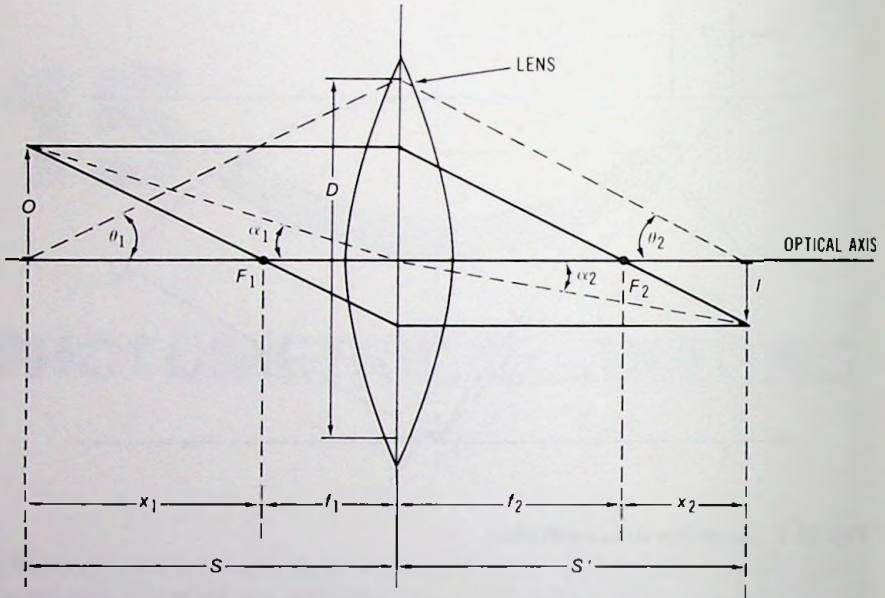
Fig. 15.2 Diagram of a lens for photometric calculations.

The magnification of the lens is

$$M = \frac{S' - f_2}{f_2}.$$ (15.10)

By combining equations 15.9 and 15.10 we obtain

$$\sin^2 \theta_2 = \frac{D^2}{4f_2^2(M + 1)^2 + D^2} = \frac{1}{4F^2(M + 1)^2 + 1},$$ (15.11)

where $F = f_2/D$ is the f-number of the lens.

With substitution of equation 15.11 in equation 15.8, L becomes

$$L = \frac{M^2 I_0 \,\Delta A}{4F^2(M + 1)^2 + 1}.$$ (15.12)

The above quantity of light illuminates an area $\Delta A'$ in the image plane. The relationship between $\Delta A'$ and ΔA is

$$\Delta A' = M^2 \Delta A.$$ (15.13)

By combining of equations 15.12 and 15.13 the illumination in the image plane becomes

$$E = \frac{L}{\Delta A'} = \frac{I_0}{4F^2(M + 1)^2 + 1} \cong \frac{I_0}{4F^2(M + 1)^2}. \tag{15.14}$$

For an off-axial object point subtending an angle α_1 with the optical axis, the lens aperture illumination, and consequently the amount of light transmitted, decreases by a factor of $\cos^4 \alpha$. The off-axial illumination then becomes

$$E = \frac{I_0 \cos^4 \alpha_1}{4F^2(M + 1)^2}. \tag{15.15}$$

In equation 15.15, if I_0 is given in lumens per square foot (fL) then E is obtained in footcandles.

Now, if the lens transmittance limited by losses due to reflection and absorption is T_r, the illumination from equation 15.15 becomes

$$E = \frac{T_r I_0}{4F^2(M + 1)^2} \cos^4 \alpha_1 = \frac{I_0 \cos^4 \alpha_1}{4T^2(M + 1)^2}, \tag{15.16}$$

Where T is the f-number of the lens given by the following equation:

$$T = \frac{\text{f-number}}{\sqrt{T_r}} = \frac{F}{\sqrt{T_r}}. \tag{15.17}$$

15.3 Radiometric and Photometric Definitions

15.3.1 Radiometry

The *radiant energy* is energy traveling in the form of electromagnetic waves; it is expressed in joules.

The *radiant flux* is the time rate of flow of radiant energy; it is expressed in watts.

The *radiant emittance* is the radiant flux emitted per unit area; it is expressed in watts per square meter, watts per square centimeter, and watts per square foot.

The *radiant intensity* is the radiant flux emitted in a unit solid angle; it is expressed in watts per steradian.

The *radiance* is the radiant flux emitted in a unit solid angle per unit area; it is expressed in watts per steradian per square meter, watts per steradian per square centimeter, and watts/per steradian per square foot.

The *irradiance* is the radiant flux incident per unit area; it is expressed in watts per square meter, watts per square centimeter, and watts per square foot.

15.3.2   Photometry

The *luminous energy* is the radiant energy which stimulates visual sensation; it is expressed in lumen-seconds (talbots).

The *luminous flux* is the time rate of flow of luminous energy (light); it is expressed in lumens.

The *lumen* is 1/60th of the luminous flux radiated by one square centimeter of area of a blackbody radiator per steradian at the solidification temperature of platinum, 2042 K.

The *luminous emittance* is the luminous flux emitted per unit area; it is expressed in lumens per square meter, lumens per square centimeter, and lumens per square foot. If the surface is Lambertian, then the lumens per square meter are called meterlamberts, the lumens per square centimeter are called centimeterlamberts, and the lumens per square foot are called footlamberts.

The *luminous intensity* is the luminous flux emitted in a unit solid angle; it is expressed in lumens per steradian or candelas.

The *luminance* is the luminous flux emitted in a unit solid angle per unit area; it is expressed in candelas per square meter, candelas per square centimeter, candelas per square foot.

The *illuminance* is the luminous flux incident per unit area; it is expressed in lumens per square meter, lumens per square centimeter, lumens per square foot (footcandles).

The *luminous efficiency* of a light source is the rate of emission of luminous energy per watt of input power; it is expressed in lumens per watt.

The *luminous coefficient* is the ratio of luminous energy to the radiant energy of a light source; it is expressed in lumens per watt.

One *steradian* is the solid angle subtended at the center of a sphere by an area of arbitrary shape on the surface of the sphere equal to the square of the radius of the sphere.

15.3.3   The Luminosity Function

Tables 15.1, 15.2, and 15.3 show the nomenclature and symbols used in photometry and the conversion factors for units of luminance and illuminance.

Any radiometric unit in table 15.1 may be converted into a corresponding photometric unit by evaluating it with respect to the standard luminosity function $\overline{Y}(\lambda)$. The standard luminosity curve, shown in figure 15.3, shows the relative effectiveness of various wavelengths of energy to evoke visual sensation. This curve represents an average of a number of observations. Thus, if $P(\lambda)$ is the spectral radiant power (in watts per nanometer) distrib-

Table 15.1   Nomenclature and Symbols Used in Photometry

Radiometry			Photometry		
Name	Symbol	MKS Unit	Name	Symbol	MKS Unit
radiant energy	U	joules	luminous energy	Q	talbots
radiant flux	P	watts	luminous flux	F	lumens
radiant emittance	W	watts per square meter	luminous emittance	L	lumens per square meter
radiant intensity	J	watts per steradian	luminous intensity	I	lumens per steradian (candelas)
radiance	N	watts per steradian per square meter	luminance	B	lumens per steradian per square meter (candelas per square meter)
irradiance	H	watts per square meter	illuminance	E	lumens per square meter (lux)
	m	meter		Ω	steradian

uted over a continuous spectrum extending between λ_1, and λ_2, then the luminous flux F in lumens is

$$F = 680 \int_{\lambda_1}^{\lambda_2} P(\lambda)\, \overline{Y}(\lambda) d\lambda, \qquad (15.18)$$

where λ is measured in nanometers.

The ratio of the luminous energy to the radiant energy, that is, the luminous coefficient K is given by the following equation:

$$K = 680 \frac{\int_{\lambda_1}^{\lambda_2} P(\lambda)\overline{Y}(\lambda) d\lambda}{\int_{\lambda_1}^{\lambda_2} P(\lambda)\, d\lambda}. \qquad (15.19)$$

In equations 15.18 and 15.19 the number 680 signifies that at 555 nm (peak of the standard luminosity curve) 1 W of monochromatic radiant flux is equivalent to 680 lm.

Table 15.2   Conversion Factors for Units of Luminance

Units	Candelas per Square Centimeter	Candelas per Square Inch	Candelas per Square Foot	Candelas per Square Meter	Centimeter-lamberts	Footlamberts	Millilamberts	Meter-lamberts
candelas per square centimeter or stilb	1	6.452	929	10 000	3.142	2 919	3 142	31 420
candelas per square inch	0.155 0	1	144	1 550	0.486 9	452.4	486.9	4 869
candelas per square foot	0.001 08	0.006 94	1	10.764	0.003 38	3.142	3.38	33.82
candelas per square meter	0.000 1	0.000 645	0.092 9	1	0.000 314 2	0.291 9	0.314 2	3.142
centimeter-lamberts	0.318 3	2.054	295.7	3 183	1	929	1 000	10 000
footlamberts	0.000 343	0.002 21	0.318 3	3.426	0.001 076 4	1	1.076 4	10.764
millilamberts	0.000 318	.002 054	0.295 7	3.183	0.001	0.929	1	10
meterlamberts	0.000 031 8	0.000 205 4	0.029 57	0.318 3	0.000 1	0.092 9	0.1	1

Table 15.3   Conversion Factors for Units of Illuminance

Unit	Lumen per Square Meter or Meter-candle or lux	Lumen per Square Foot or Foot-candle	Lumen per Square Centi-meter or Phot	Millilumen per Square Centi-meter or Milliphot
lumen per square meter or metercandle or lux	1	0.092 9	0.000 1	0.1
lumen per square foot or footcandle	10.76	1	0.001 076	1.076
lumen per square centimeter or phot	10 000	929	1	1000
millilumen per square centi-meter or milliphot	10	0.929	0.001	1
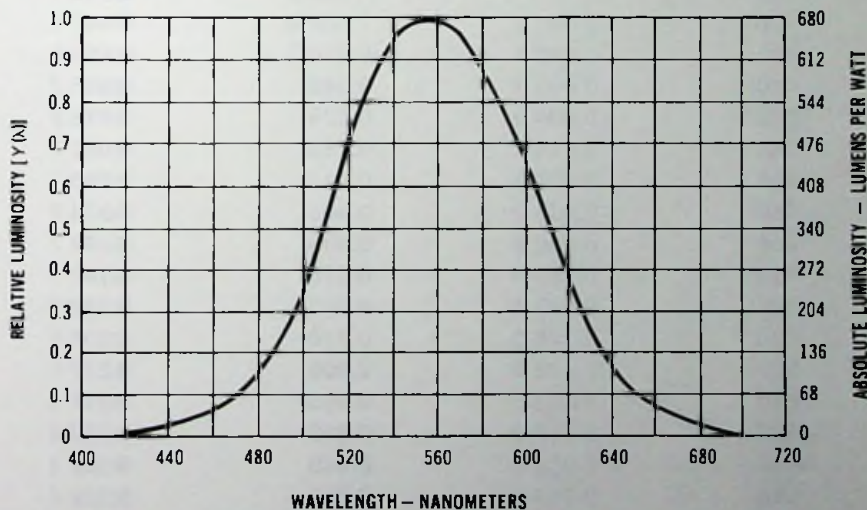
Fig. 15.3   Standard luminosity curve.

15.3.4   The Quantum Efficacy

The *quantum efficacy* of radiant power is the rate of emission of radiant quanta per watt of radiant power. It is expressed in quanta per watt.

The quantum efficacy of radiant power is

$$E_Q = \frac{1}{hc} \frac{\int_{\lambda_1}^{\lambda_2} \lambda P(\lambda)d\lambda}{\int_{\lambda_1}^{\lambda_2} P(\lambda)d\lambda}. \tag{15.20}$$

The term hc/λ is the energy of the quantum.

Table 15.4   Relative Luminosity Values for Photopic and
Scotopic Vision and Relative Radiant Power of a Tungsten Lamp
at 2854 K*

Wavelength (nanometers)	Photopic vision $Y(\lambda)$	Scotopic vision $Y(\lambda)$	Tungsten Lamp $W(\lambda)$
300			0.000 4
310			0.001 7
320			0.004 4
330			0.007 8
340			0.011 7
350			0.016 4
360			0.022 1
370			0.028 5
380			0.036 1
390	0.000 1		0.044 9
400	0.000 4	0.018 5	0.055 0
410	0.001 2	0.040	0.066 2
420	0.004 0	0.076	0.078 8
430	0.011 6	0.132	0.092 7
440	0.023 0	0.212	0.108 1
450	0.038 0	0.302	0.124 8
460	0.060 0	0.406	0.142 7
470	0.091 0	0.520	0.162 1
480	0.139 0	0.650	0.182 8
490	0.208 0	0.770	0.204 6
500	0.323 0	0.900	0.227 6
510	0.503 0	0.985	0.251 5
520	0.710 0	0.960	0.276 4
530	0.862 0	0.840	0.302 3
540	0.954 0	0.680	0.328 4
550	0.995 0	0.500	0.355 4
560	0.995 0	0.350	0.382 4
570	0.952 0	0.228	0.409 5
580	0.870 0	0.140	0.436 5
590	0.757 0	0.083	0.463 3
600	0.631 0	0.049 0	0.490 3
610	0.503 0	0.030 0	0.517 6
620	0.381 0	0.017 5	0.544 6
630	0.265 0	0.010 0	0.571 4
640	0.175 0	0.005 7	0.598 1
650	0.107 0	0.003 1	0.624 6
660	0.061 0	0.001 7	0.649 7

Table 15.4—cont.   Relative Luminosity Values for Photopic and
Scotopic Vision and Relative Radiant Power of a Tungsten Lamp
at 2854 K*

Wavelength (nanometers)	Photopic vision $Y(\lambda)$	Scotopic vision $Y(\lambda)$	Tungsten Lamp $W(\lambda)$
670	0.032 0	0.000 87	0.674 4
680	0.017 0	0.000 44	0.698 5
690	0.008 2	0.000 21	0.721 7
700	0.004 1	0.000 10	0.743 6
710	0.002 1		0.764 7
720	0.001 0		0.785 8
730	0.000 5		0.805 2
740	0.000 3		0.823 1
750	0.000 1		0.840 0
760	0.000 1		0.855 5
770			0.871 7
780			0.885 9
790			0.899 1
800			0.911 2
850			0.962 3
900			0.989 2
950			0.999 0
1 000			0.993 4
1 050			0.974 8
1 100			0.945 8
1 150			0.911 2
1 200			0.870 6
1 250			0.828 3
1 300			0.784 3
1 350			0.740 1
1 400			0.695 8
1 450			0.653 2
1 500			0.611 5
1 600			0.534 6
1 700			0.466 2
1 800			0.405 6
1 900			0.352 7
2 000			0.306 8
2 100			0.266 6
2 200			0.231 4
2 300			0.201 2
2 400			0.176 3

Table 15.4—cont. Relative Luminosity Values for Photopic and Scotopic Vision and Relative Radiant Power of a Tungsten Lamp at 2854 K*

Wavelength (nanometers)	Photopic vision $Y(\lambda)$	Scotopic vision $Y(\lambda)$	Tungsten Lamp $W(\lambda)$
2 500			0.155 2
2 600			0.136 4
2 700			0.118 9
2 800			0.074 2
2 900			0.062 2
3 000			0.056 4

*From R. W. Engstrom, "Values of Relative Power of a Tungsten Lamp at 2854 K," *RCA Review*, September 1967.

15.3.5 The Blackbody Radiator

The thermal radiation of a blackbody is given by Planck's radiation law:

$$dW(\lambda,T) = \frac{C_1 \lambda^{-5}}{\exp{(C_2/\lambda T)} - 1}\, d\lambda . \tag{15.21}$$

If mks units are used, λ and $d\lambda$ are expressed in meters and dW in watts per square meter. The numerical values of C_1 and C_2 are then

$$C_1 = 3.740 \times 10^{-16} \quad \text{and} \quad C_2 = 1.4385 \times 10^{-2}. \tag{15.22}$$

If λ and $d\lambda$ are expressed in nanometers and dW in watts per square meter, the values of C_1 and C_2 become

$$C_1 = 3.740 \times 10^{20} \quad \text{and} \quad C_2 = 1.4385 \times 10^{7}. \tag{15.23}$$

15.4 Colorimetry

15.4.1 Colorimetric Quantities

Colorimetric quantities ("tristimulus values") are computed from three similar integrations of the measured spectral distribution data:

$$X = \int P(\lambda)\, \bar{x}(\lambda)\, d\lambda .$$

$$Y = \int P(\lambda)\, \bar{y}(\lambda)\, d\lambda .$$

$$Z = \int P(\lambda)\, \bar{z}(\lambda)\, d\lambda .$$

where $P(\lambda)$ is the measured spectral power distribution, and $\bar{x}(\lambda)$, $\bar{y}(\lambda)$, and $\bar{z}(\lambda)$ are the CIE 1931 color-matching functions.
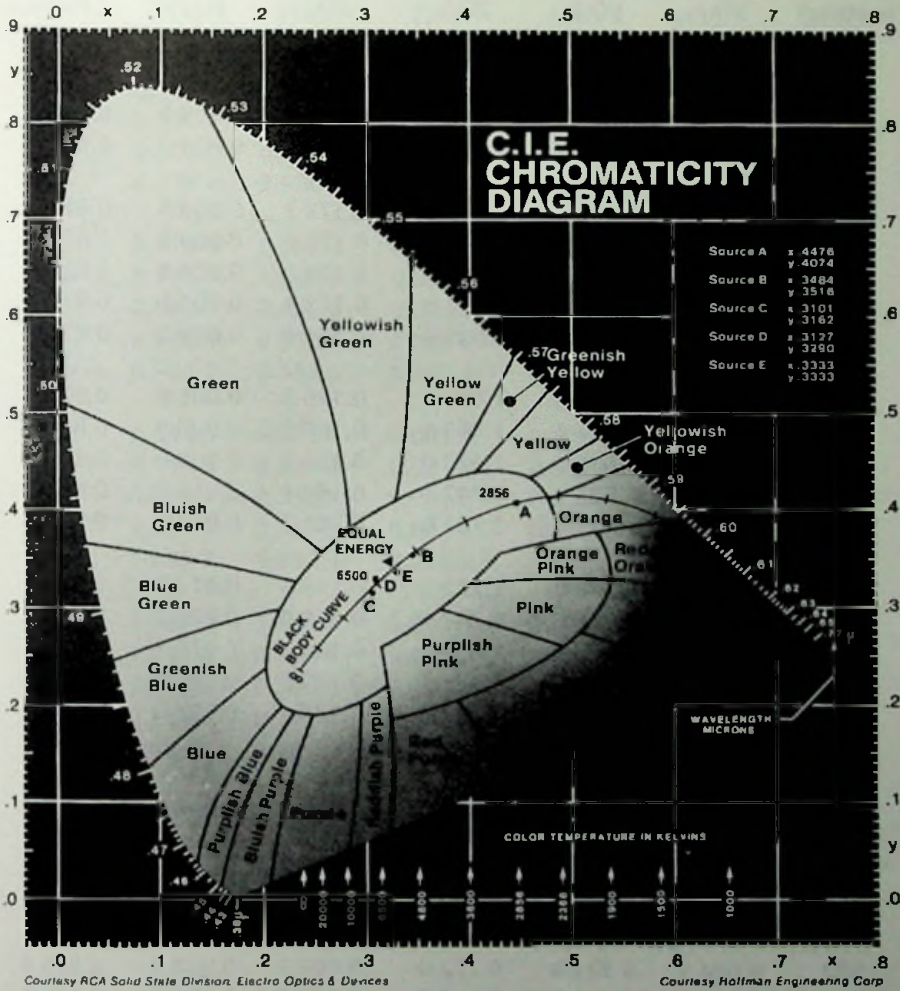
Fig. 15.4   **CIE chromaticity diagram.** (*Courtesy Photo Research, Div. of Kollmorgen Corp.*)

Table 15.5 Spectral Tristimulus Values Defining CIE 1931 Standard
Colorimetric Observer and Chromaticity Coordinates
Derived From Them

λ (nano-meters)	Spectral Tristimulus Values			Chromaticity Coordinates		
	$\bar{x}(\lambda)$	$\bar{y}(\lambda)$	$\bar{z}(\lambda)$	$x(\lambda)$	$y(\lambda)$	$z(\lambda)$
380	0.001 4	0.000 0	0.006 5	0.174 1	0.005 0	0.820 9
385	0.002 2	0.000 1	0.010 5	0.174 0	0.005 0	0.821 0
390	0.004 2	0.000 1	0.020 1	0.173 8	0.004 9	0.821 3
395	0.007 6	0.000 2	0.036 2	0.173 6	0.004 9	0.821 5
400	0.014 3	0.000 4	0.067 9	0.173 3	0.004 8	0.821 9
405	0.023 2	0.000 6	0.110 2	0.173 0	0.004 8	0.822 2
410	0.043 5	0.001 2	0.207 4	0.172 6	0.004 8	0.822 6
415	0.077 6	0.002 2	0.371 3	0.172 1	0.004 8	0.823 1
420	0.134 4	0.004 0	0.645 6	0.171 4	0.005 1	0.823 5
425	0.214 8	0.007 3	1.039 1	0.170 3	0.005 8	0.823 9
430	0.283 9	0.011 6	1.385 6	0.168 9	0.006 9	0.824 2
435	0.328 5	0.016 8	1.623 0	0.166 9	0.008 6	0.824 5
440	0.348 3	0.023 0	1.747 1	0.164 4	0.010 9	0.824 7
445	0.348 1	0.029 8	1.782 6	0.161 1	0.013 8	0.825 1
450	0.336 2	0.038 0	1.772 1	0.156 6	0.017 7	0.825 7
455	0.318 7	0.048 0	1.744 1	0.151 0	0.022 7	0.826 3
460	0.290 8	0.060 0	1.669 2	0.144 0	0.029 7	0.826 3
465	0.251 1	0.073 9	1.528 1	0.135 5	0.039 9	0.824 6
470	0.195 4	0.091 0	1.287 6	0.124 1	0.057 8	0.818 1
475	0.142 1	0.112 6	1.041 9	0.109 6	0.086 8	0.803 6
480	0.095 6	0.139 0	0.813 0	0.091 3	0.132 7	0.776 0
485	0.058 0	0.169 3	0.616 2	0.068 7	0.200 7	0.730 6
490	0.032 0	0.208 0	0.465 2	0.045 4	0.295 0	0.659 6
495	0.014 7	0.258 6	0.353 3	0.023 5	0.412 7	0.563 8
500	0.004 9	0.323 0	0.272 0	0.008 2	0.538 4	0.453 4
505	0.002 4	0.407 3	0.212 3	0.003 9	0.654 8	0.341 3
510	0.009 3	0.503 0	0.158 2	0.013 9	0.750 2	0.235 9
515	0.029 1	0.608 2	0.111 7	0.038 9	0.812 0	0.149 1
520	0.063 3	0.710 0	0.078 2	0.074 3	0.833 8	0.091 9

Table 15.5—cont.   Spectral Tristimulus Values Defining CIE 1931 Standard Colorimetric Observer and Chromaticity Coordinates Derived From Them

λ (nano-meters)	Spectral Tristimulus Values			Chromaticity Coordinates		
	$\bar{x}(\lambda)$	$\bar{y}(\lambda)$	$\bar{z}(\lambda)$	$x(\lambda)$	$y(\lambda)$	$z(\lambda)$
525	0.109 6	0.793 2	0.057 3	0.114 2	0.826 2	0.059 6
530	0.165 5	0.862 0	0.042 2	0.154 7	0.805 9	0.039 4
535	0.225 7	0.914 9	0.029 8	0.192 9	0.781 6	0.025 5
540	0.290 4	0.954 0	0.020 3	0.229 6	0.754 3	0.016 1
545	0.359 7	0.980 3	0.013 4	0.265 8	0.724 3	0.009 9
550	0.433 4	0.995 0	0.008 7	0.301 6	0.692 3	0.006 1
555	0.512 1	1.000 0	0.005 7	0.337 3	0.658 9	0.003 8
560	0.594 5	0.995 0	0.003 9	0.373 1	0.624 5	0.002 4
565	0.678 4	0.978 6	0.002 7	0.408 7	0.589 6	0.001 7
570	0.762 1	0.952 0	0.002 1	0.444 1	0.554 7	0.001 2
575	0.842 5	0.915 4	0.001 8	0.478 8	0.520 2	0.001 0
580	0.916 8	0.870 0	0.001 7	0.512 5	0.486 6	0.000 9
585	0.978 6	0.816 3	0.001 4	0.544 8	0.454 4	0.000 8
590	1.026 3	0.757 0	0.001 1	0.575 2	0.424 2	0.000 6
595	1.056 7	0.694 9	0.001 0	0.602 9	0.396 5	0.000 6
600	1.062 2	0.631 0	0.000 8	0.627 0	0.372 5	0.000 5
605	1.045 6	0.566 8	0.000 6	0.648 2	0.351 4	0.000 4
610	1.002 6	0.503 0	0.000 3	0.665 8	0.334 0	0.000 2
615	0.938 4	0.441 2	0.000 2	0.680 1	0.319 7	0.000 2
620	0.854 4	0.381 0	0.000 2	0.691 5	0.308 3	0.000 2
625	0.751 4	0.321 0	0.000 1	0.700 6	0.299 3	0.000 1
630	0.642 4	0.265 0	0.000 0	0.707 9	0.292 0	0.000 1
635	0.541 9	0.217 0	0.000 0	0.714 0	0.285 9	0.000 1
640	0.447 9	0.175 0	0.000 0	0.719 0	0.280 9	0.000 1
645	0.360 8	0.138 2	0.000 0	0.723 0	0.277 0	0.000 0
650	0.283 5	0.107 0	0.000 0	0.726 0	0.274 0	0.000 0
655	0.218 7	0.081 6	0.000 0	0.728 3	0.271 7	0.000 0
660	0.164 9	0.061 0	0.000 0	0.730 0	0.270 0	0.000 0
665	0.121 2	0.044 6	0.000 0	0.731 1	0.268 9	0.000 0

Table 15.5—cont. Spectral Tristimulus Values Defining CIE 1931
Standard Colorimetric Observer and Chromaticity
Coordinates Derived From Them

λ (nano-meters)	Spectral Tristimulus Values			Chromaticity Coordinates		
	$\bar{x}(\lambda)$	$\bar{y}(\lambda)$	$\bar{z}(\lambda)$	$x(\lambda)$	$y(\lambda)$	$z(\lambda)$
670	0.087 4	0.032 0	0.000 0	0.732 0	0.268 0	0.000 0
675	0.063 6	0.023 2	0.000 0	0.732 7	0.267 3	0.000 0
680	0.046 8	0.017 0	0.000 0	0.733 4	0.266 6	0.000 0
685	0.032 9	0.011 9	0.000 0	0.734 0	0.266 0	0.000 0
690	0.022 7	0.998 2	0.000 0	0.734 4	0.265 6	0.000 0
695	0.015 8	0.005 7	0.000 0	0.734 6	0.265 4	0.000 0
700	0.011 4	0.004 1	0.000 0	0.734 7	0.265 3	0.000 0
705	0.008 1	0.002 9	0.000 0	0.734 7	0.265 3	0.000 0
710	0.005 8	0.002 1	0.000 0	0.734 7	0.265 3	0.000 0
715	0.004 1	0.001 5	0.000 0	0.734 7	0.265 3	0.000 0
720	0.002 9	0.001 0	0.000 0	0.734 7	0.265 3	0.000 0
725	0.002 0	0.000 7	0.000 0	0.734 7	0.265 3	0.000 0
730	0.001 4	0.000 5	0.000 0	0.734 7	0.265 3	0.000 0
735	0.001 0	0.000 4	0.000 0	0.734 7	0.265 3	0.000 0
740	0.000 7	0.000 2	0.000 0	0.734 7	0.265 3	0.000 0
745	0.000 5	0.000 2	0.000 0	0.734 7	0.265 3	0.000 0
750	0.000 3	0.000 1	0.000 0	0.734 7	0.265 3	0.000 0
755	0.000 2	0.000 1	0.000 0	0.734 7	0.265 3	0.000 0
760	0.000 2	0.000 1	0.000 0	0.734 7	0.265 3	0.000 0
765	0.000 1	0.000 0	0.000 0	0.734 7	0.265 3	0.000 0
770	0.000 1	0.000 0	0.000 0	0.734 7	0.265 3	0.000 0
775	0.000 1	0.000 0	0.000 0	0.734 7	0.265 3	0.000 0
780	˙0.000 0	0.000 0	0.000 0	0.734 7	0.265 3	0.000 0

Table 15.6   Spectral Tristimulus Values Defining CIE 1964 Supplementary Standard Colorimetric Observer and Chromaticity Coordinates Derived From Them

λ (nano-meters)	Spectral Tristimulus Values			Chromaticity Coordinates		
	$\bar{x}_{10}(\lambda)$	$\bar{y}_{10}(\lambda)$	$\bar{z}_{10}(\lambda)$	$x_{10}(\lambda)$	$y_{10}(\lambda)$	$z_{10}(\lambda)$
380	0.000 2	0.000 0	0.000 7	0.181 3	0.019 7	0.799 0
385	0.000 7	0.000 1	0.002 9	0.180 9	0.019 5	0.799 6
390	0.002 4	0.000 3	0.010 5	0.180 3	0.019 4	0.800 3
395	0.007 2	0.000 8	0.032 3	0.179 5	0.019 0	0.801 5
400	0.019 1	0.002 0	0.086 0	0.178 4	0.018 7	0.802 9
405	0.043 4	0.004 5	0.197 1	0.177 1	0.018 4	0.804 5
410	0.084 7	0.008 8	0.389 4	0.175 5	0.018 1	0.806 4
415	0.140 6	0.014 5	0.656 8	0.173 2	0.017 8	0.809 0
420	0.204 5	0.021 4	0.972 5	0.170 6	0.017 9	0.811 5
425	0.264 7	0.029 5	1.282 5	0.167 9	0.018 7	0.813 4
430	0.314 7	0.038 7	1.553 5	0.165 0	0.020 3	0.814 7
435	0.357 7	0.049 6	1.798 5	0.162 2	0.022 5	0.815 3
440	0.383 7	0.062 1	1.967 3	0.159 0	0.025 7	0.815 3
445	0.386 7	0.074 7	2.027 3	0.155 4	0.030 0	0.814 6
450	0.370 7	0.089 5	1.994 8	0.151 0	0.036 4	0.812 6
455	0.343 0	0.106 3	1.900 7	0.145 9	0.045 2	0.808 8
460	0.302 3	0.128 2	1.745 4	0.138 9	0.058 9	0.802 2
465	0.254 1	0.152 8	1.554 9	0.129 5	0.077 9	0.792 6
470	0.195 6	0.185 2	1.317 6	6.115 2	0.109 0	0.775 8
475	0.132 3	0.219 9	1.030 2	0.095 7	0.159 1	0.745 2
480	0.080 5	0.253 6	0.772 1	0.072 8	0.229 2	0.698 0
485	0.041 1	0.297 7	0.570 1	0.045 2	0.327 5	0.627 3
490	0.016 2	0.339 1	0.415 3	0.021 0	0.440 1	0.538 9
495	0.005 1	0.395 4	0.302 4	0.007 3	0.562 5	0.430 2
500	0.003 8	0.460 8	0.218 5	0.005 6	0.674 5	0.319 9
505	0.015 4	0.531 4	0.159 2	0.021 9	0.752 6	0.225 6
510	0.037 5	0.606 7	0.112 0	0.049 5	0.802 3	0.148 2
515	0.071 4	0.685 7	0.082 2	0.085 0	0.817 0	0.098 0
520	0.117 7	0.761 8	0.060 7	0.125 2	0.810 2	0.064 6

Table 15.6—cont.   Spectral Tristimulus Values Defining CIE 1964
Supplementary Standard Colorimetric Observer and Chromaticity
Coordinates Derived From Them

λ (nano-meters)	Spectral Tristimulus Values			Chromaticity Coordinates		
	$\bar{x}_{10}(\lambda)$	$\bar{y}_{10}(\lambda)$	$\bar{z}_{10}(\lambda)$	$x_{10}(\lambda)$	$y_{10}(\lambda)$	$z_{10}(\lambda)$
525	0.173 0	0.823 3	0.043 1	0.166 4	0.792 2	0.041 4
530	0.236 5	0.875 2	0.030 5	0.207 1	0.766 3	0.026 7
535	0.304 2	0.923 8	0.020 6	0.243 6	0.739 9	0.016 5
540	0.376 8	0.962 0	0.013 7	0.278 6	0.711 3	0.010 1
545	0.451 6	0.982 2	0.007 9	0.313 2	0.681 3	0.005 5
550	0.529 8	0.991 8	0.004 0	0.347 3	0.650 1	0.002 6
555	0.616 1	0.999 1	0.001 1	0.381 2	0.618 2	0.000 7
560	0.705 2	0.997 3	0.000 0	0.414 2	0.585 8	0.000 0
565	0.793 8	0.982 4	0.000 0	0.446 9	0.553 1	0.000 0
570	0.878 7	0.955 6	0.000 0	0.479 0	0.521 0	0.000 0
575	0.951 2	0.915 2	0.000 0	0.509 6	0.490 4	0.000 0
580	1.014 2	0.868 9	0.000 0	0.538 6	0.461 4	0.000 0
585	1.074 3	0.825 6	0.000 0	0.565 4	0.434 6	0.000 0
590	1.118 5	0.777 4	0.000 0	0.590 0	0.410 0	0.000 0
595	1.134 3	0.720 4	0.000 0	0.611 6	0.388 4	0.000 0
600	1.124 0	0.658 3	0.000 0	0.630 6	0.369 4	0.000 0
605	1.089 1	0.593 9	0.000 0	0.647 1	0.352 9	0.000 0
610	1.030 5	0.528 0	0.000 0	0.661 2	0.338 8	0.000 0
615	0.950 7	0.461 8	0.000 0	0.673 1	0.326 9	0.000 0
620	0.856 3	0.398 1	0.000 0	0.682 7	0.317 3	0.000 0
625	0.754 9	0.339 6	0.000 0	0.689 8	0.310 2	0.000 0
630	0.647 5	0.283 5	0.000 0	0.695 5	0.304 5	0.000 0
635	0.535 1	0.228 3	0.000 0	0.701 0	0.299 0	0.000 0
640	0.431 6	0.179 8	0.000 0	0.705 9	0.294 1	0.000 0
645	0.343 7	0.140 2	0.000 0	0.710 3	0.289 8	0.000 0
650	0.268 3	0.107 6	0.000 0	0.713 7	0.286 3	0.000 0
655	0.204 3	0.081 2	0.000 0	0.715 6	0.284 4	0.000 0
660	0.152 6	0.060 3	0.000 0	0.716 8	0.283 2	0.000 0
665	0.112 2	0.044 1	0.000 0	0.717 9	0.282 1	0.000 0

Table 15.6—cont. Spectral Tristimulus Values Defining CIE 1964 Supplementary Standard Colorimetric Observer and Chromaticity Coordinates Derived From Them

λ (nanometers)	Spectral Tristimulus Values			Chromaticity Coordinates		
	$\bar{x}_{10}(\lambda)$	$\bar{y}_{10}(\lambda)$	$\bar{z}_{10}(\lambda)$	$x_{10}(\lambda)$	$y_{10}(\lambda)$	$z_{10}(\lambda)$
670	0.081 3	0.031 8	0.000 0	0.718 7	0.281 3	0.000 0
675	0.057 9	0.022 6	0.000 0	0.719 3	0.280 7	0.000 0
680	0.040 9	0.015 9	0.000 0	0.719 8	0.280 2	0.000 0
685	0.028 6	0.011 1	0.000 0	0.720 0	0.280 0	0.000 0
690	0.019 9	0.007 7	0.000 0	0.720 2	0.279 8	0.000 0
695	0.013 8	0.005 4	0.000 0	0.720 3	0.279 7	0.000 0
700	0.009 6	0.003 7	0.000 0	0.720 4	0.279 6	0.000 0
705	0.006 6	0.002 6	0.000 0	0.720 3	0.279 7	0.000 0
710	0.004 6	0.001 8	0.000 0	0.720 2	0.279 8	0.000 0
715	0.003 1	0.001 2	0.000 0	0.720 1	0.279 9	0.000 0
720	0.002 2	0.000 8	0.000 0	0.719 9	0.280 1	0.000 0
725	0.001 5	0.000 6	0.000 0	0.719 7	0.280 3	0.000 0
730	0.001 0	0.000 4	0.000 0	0.719 5	0.280 6	0.000 0
735	0.000 7	0.000 3	0.000 0	0.719 2	0.280 8	0.000 0
740	0.000 5	0.000 2	0.000 0	0.718 9	0.281 1	0.000 0
745	0.000 4	0.000 1	0.000 0	0.718 6	0.281 4	0.000 0
750	0.000 3	0.000 1	0.000 0	0.718 3	0.281 7	0.000 0
755	0.000 2	0.000 1	0.000 0	0.718 0	0.282 0	0.000 0
760	0.000 1	0.000 0	0.000 0	0.717 6	0.282 4	0.000 0
765	0.000 1	0.000 0	0.000 0	0.717 2	0.282 8	0.000 0
770	0.000 1	0.000 0	0.000 0	0.716 9	0.283 1	0.000 0
775	0.000 0	0.000 0	0.000 0	0.716 5	0.283 5	0.000 0
780	0.000 0	0.000 0	0.000 0	0.716 1	0.283 9	0.000 0

15.4.2   Colorimetric Calculations

Chromaticity coordinates are computed from tristimulus values (X, Y, Z) as follows:

1931 CIE: $x = X/(X + Y + Z)$

$y = Y/(X + Y + Z)$

$z = 1 - (x + y)$

1960 CIE: $u = \dfrac{4X}{X + 15Y + 3Z} = 4x/(-2x + 12y + 3)$

$v = \dfrac{6Y}{X + 15Y + 3Z} = 6y/(-2x + 12y + 3)$

1976 CIE: $u' = \dfrac{4X}{X + 15Y + 3Z} = 4x/(-2x + 12y + 3)$

$v' = \dfrac{9Y}{x + 15Y + 3z} = 9y/(-2x + 12y + 3)$

Color difference equations, where ΔE^* is the color difference, are computed as follows:

$$\Delta E^*(L^*\, u^*\, v^*) = [(\Delta L^*)^2 + (\Delta u^*)^2 + (A v^*)^2]^{1/2}$$

$$L^* = 116(Y/Y_0)^{1/3} - 16$$

$$u^* = 13L^*(u' - u'_0)$$

$$v^* = 13L^*(v' - v'_0)$$

$$\Delta E^*(L^* a^* b^*) = [(\Delta L^*)^2 + (\Delta a^*)^2 + (\Delta b^*)^2]^{1/2}$$

$$L^* = 116(Y/Y_0)^{1/3} - 16$$

$$a^* = 500[(X/X_0)^{1/3} - (Y/Y_0)^{1/3}]$$

$$b^* = 200[(Y/Y_0)^{1/3} - (Z/Z_0)^{1/3}]$$

where X_0, Y_0, Z_0, u'_0 and v'_0 are the coordinates of a CIE standard illuminant such as D_{65}. This illuminant is a CIE recommended spectral distribution of natural daylight.

The CIE chromaticity diagram is shown in figure 15.4 and tables 15.5 and 15.6 give the CIE 1931 and 1964 spectral tristimulus values.

References

Engstrom, R. W., and A. L. Morehead. "Standard Test-Lamp Temperature for Photosensitive Devices—Relationship of Absolute and Luminous Sensitivities." *RCA Review*, September 1967.

Epstein, D. W. "Photometry in Television Engineering," *Electronics*, p. 110, July 1948.

Sears, F. W. *Principles of Physics: Optics*, Addison-Wesley Publishing Company, Cambridge, MA, 1946.

Walker, R. R. "Spectrometry: Its Benefits, Its Uses," *Optical Spectra,* p. 54, October 1981.

Walsh, J. W. T. *Photometry*, Constable & Co., Ltd., London, 1953.

16

PHOTOELECTRON MULTIPLIER TUBES

16.1   Introduction

In addition to its fundamental role and use in a great variety of imaging devices, photoelectric emission also has an important application for the detection and measurement of radiant energy in the ultraviolet, visible, and near infrared regions of the electromagnetic spectrum. It gained its earliest application in the photodiode, consisting of a photocathode and a metallic electron collector (anode). The photodiode provides a stable and a relatively large and noise-free signal at high and medium illumination levels. At low light levels, however, the photodiode can be used only with special amplifying techniques suitable to raise the signal level.

A relatively noise free, very broad bandpass amplification of the photocathode current may be obtained by use of the photomultiplier tube. The photomultiplier tube can provide a current gain ranging from 10 to 10^9. It has a fast time response with a fraction of a nanosecond rise time in certain types. The photomultiplier tube is the most sensitive detector of radiant energy and its performance is limited only by the statistical fluctuation of the photocathode current. It is used with scintillators and Cerenkov radiators for the detection and measurement of X-rays, gamma rays, and energetic particles. It is also used in Raman spectroscopy and laser ranging and communication.

The operation of the photomultiplier tube is based on photoemission and secondary emission principles. In the photoelectron multiplier tube the photoelectron current, generated by the light, is accelerated and directed to

the first dynode, whose surface is an efficient secondary-electron emitter. At the first dynode each photoelectron produces a multiple number of secondary electrons, depending on the energy of the primary beam. The secondary electrons of the first dynode are accelerated and directed to the second dynode, where again the energetic electrons produce a multiple number of secondary electrons. The multiplication process is repeated on the following dynodes and finally the multiplied current is collected at the anode of the photomultiplier tube. The current gain m of the photomultiplier tube thus is the product of the current gain of the individual multiplier stages.

$$m = \delta_1 \times \delta_2 \times \cdots \times \delta_n, \tag{16.1}$$

where δ_1, δ_2, and δ_n are the secondary-electron emission ratios of the first, second, and the nth dynode. For an n-stage photomultiplier with equal stage gains, δ, the current gain is simply

$$m_n = \delta^n. \tag{16.2}$$

16.2   Photomultiplier Structures

A variety of different photomultiplier structures have been developed for different purposes and different requirements and applications. These structures may differ in speed of response, amplification, signal-to-noise ratio, cathode size, light collection efficiency from a scintillation counter crystal, electron collection efficiency, and in the ruggedness of the multiplier structure. All existing photomultiplier structures, however, utilize a convergent or a channeled-type electron optics between the consecutive stages to ensure high collection efficiency and minimum transit-time spread. A convergent optics causes a demagnification between the succeeding stages; that is, the current emission of each stage is directed into a smaller area on the following stage. In contrast, a divergent optics would cause magnification on successive stages, thus causing a skipping of the stages, electron loss to support structures, and loss of gain. The channeled type of optics is used in the venetian-blind tube, where the bulk of low-energy electrons of each vane is sharply reproduced on another vane of the next dynode. Although magnetic fields may be combined with electric fields to provide the desired electron optics, most multiplier structures are electrostatically focused. Typical photomultiplier structures are shown in figures 16.1 and 16.2.

The circular dynode structure is one of the earliest systems developed for photoelectron multiplication. In this system the incident light is directed through a glass window onto an opaque photocathode deposited or attached on the photocathode dynode. The circular arrangement of dynodes results in a compact layout, good collection efficiency, and a small transit-time dispersion. The relatively fast time response of this structure is due to its

small size and high interdynode field strengths. The circular structure is also used in head-on type photomultipliers as shown in figure 16.1.

The linear dynode structure is used in the head-on type photomultipliers. The front end of the photomultiplier consists of a semitransparent photocathode deposited on the inside of a spherical photocathode faceplate, and of a cylindrical focusing structure. The optics of the front end are designed
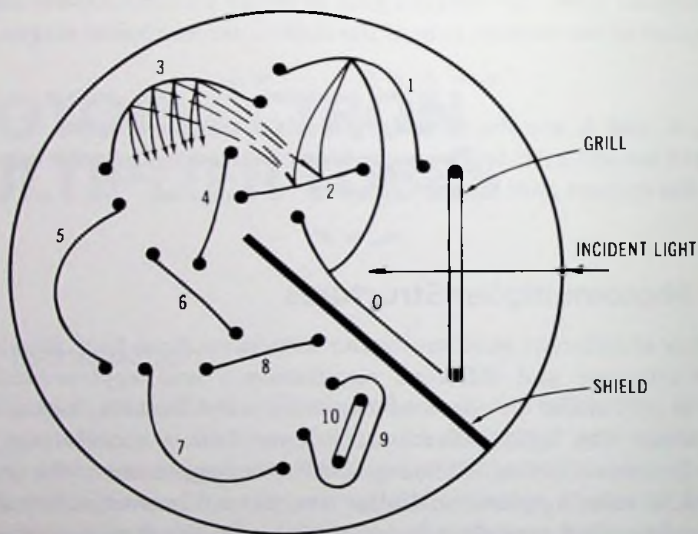
0 = PHOTOCATHODE; 1-9 = DYNODES ; 10 = ANODE

(A) Circular dynode structure.
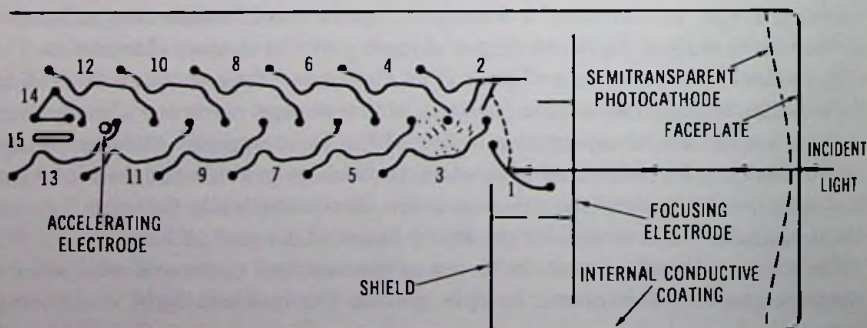
1-14 = DYNODES; 15 = ANODE

(B) Head-on type linear dynode structure.

Fig. 16.1 Typical

to approximate a centrally symmetric focusing system having a crossover in the vicinity of the first dynode. The electrode structure, equipotential lines, and electron trajectories of a typical front-end structure are shown in figure 16.3. As can be seen, even when initial velocities are involved, the size of the crossover is quite small, ensuring a small current spot on the first dynode. Note also that the electrons emitted by the focusing and wall electrodes miss the aperture, so they do not contribute to the dark current of the tube. The transit-time difference between the center and the periphery, judging by the path differences and by the equipotential lines, is quite small.
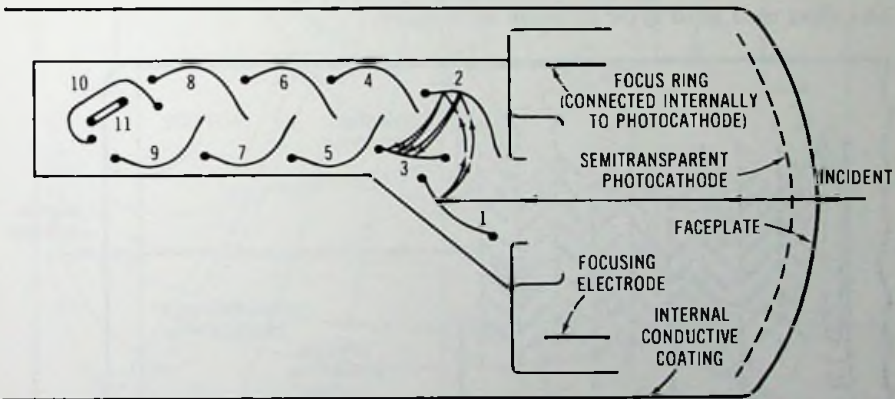
.1-10 = DYNODES; 11 = ANODE

(C) **Head-on linear dynode structure with focus ring.**
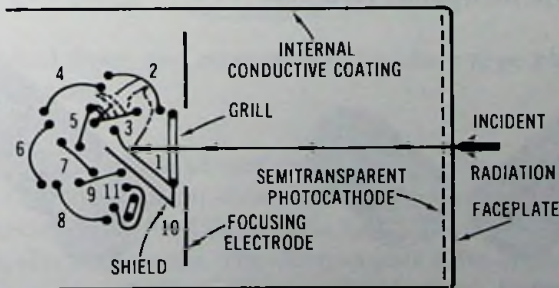
1-10: DYNODES = ELECTRON MULTIPLER
11. ANODE

(D) **Head-on type circular dynode structure.**

photomultiplier configurations.
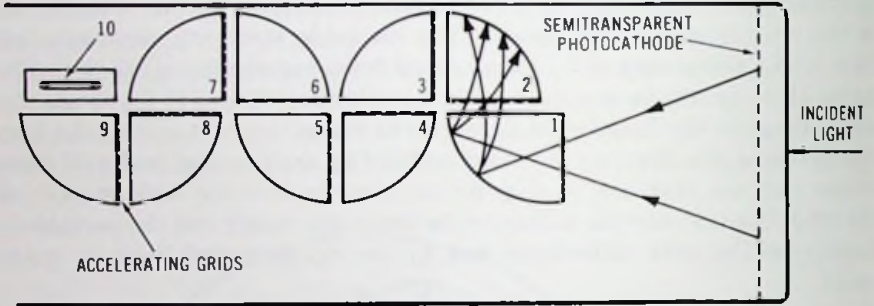
(A) Box and grid type dynode structure.
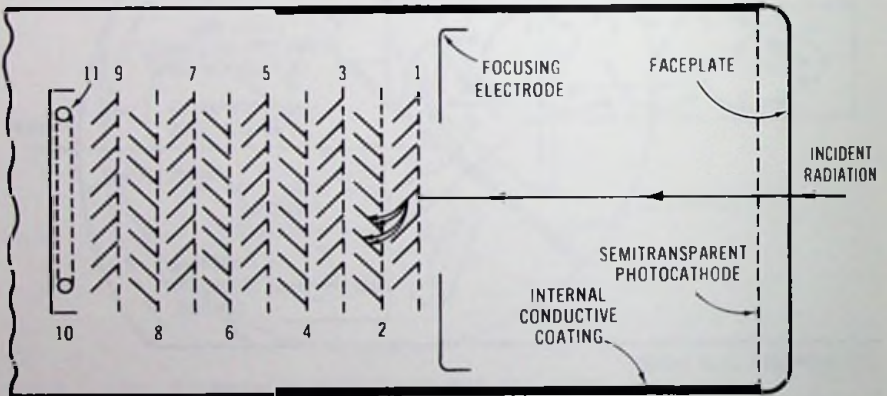
(B) Venetian-blind dynode structure.
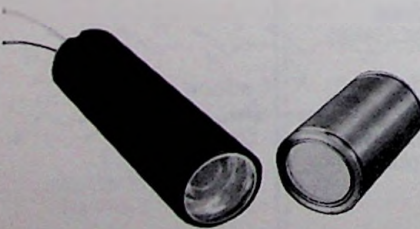
**(C) EMR-P potted, ruggedized
PMT with gamma scintilla-
tion crystal for use in oil-
well logging. (*Courtesy EMR
Photoelectric*)**

**(D) EMR-P ruggedized verte-
brate structure photomulti-
plier. (*Courtesy EMR
Photoelectric*)**

Fig. 16.2   Typical photomultiplier structures.
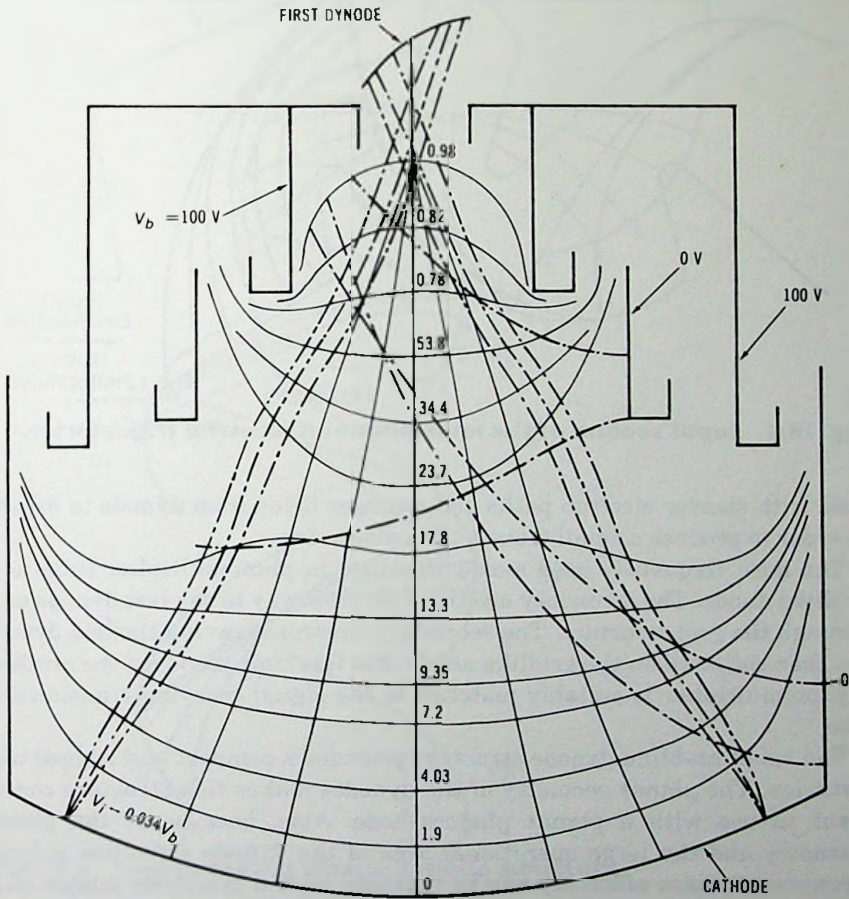
Fig. 16.3   Typical front-end structure of head-on type photomultiplier tubes.

Figure 16.4 shows the input section of a multiplier structure. The efficiency of the electron transfer between the first and second dynodes and between the second and third dynodes is high. The electron paths, in this system, are rapidly convergent. The electron path difference, assuming that the first dynode is covered full length by electrons, is quite large. This is the section which limits the speed of this structure.

The multiplier section consists of identical dynodes, similar to or identical with the third and fourth dynodes.

Figure 16.5 shows the structure of the compensated design multiplier. In the compensated design the longer electron paths and weaker fields alter-

SECOND DYNODE

FOCUSED
ELECTRON BEAM

FROM THE
PHOTOCATHODE

FIRST DYNODE
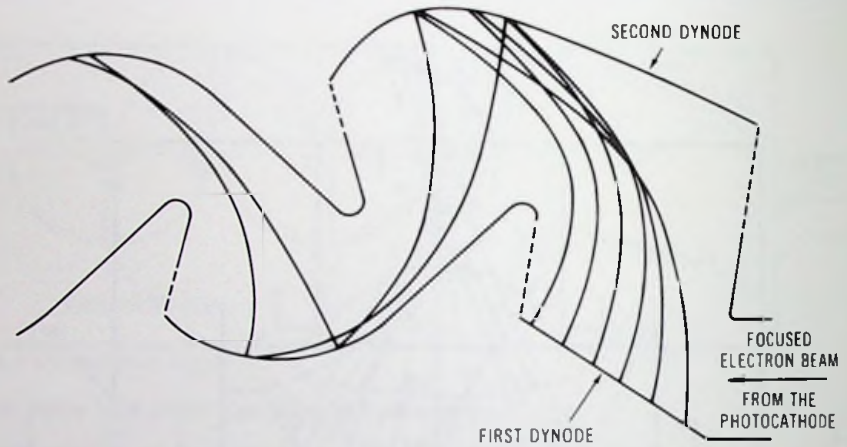
Fig. 16.4   Input section of the multiplier and electron trajectories.

nate with shorter electron paths and stronger fields from dynode to dynode
in order to produce a small transit-time dispersion.

   The most frequently used anode structure in photomultiplier tubes is a
gridlike anode. The secondary electrons on their way to the last dynode pass
through the grid structure. The secondary electrons leaving the last dynode
are then collected on the gridlike anode. For fast time response the anode of
a photomultiplier is suitably matched to the signal carrying transmission
line.

   The venetian-blind dynode structure provides a compact and rugged con-
struction. The planar geometry of the dynodes makes this structure conve-
nient to use with a planar photocathode. Also, because of the planar
geometry and the large operational area of the dynode structure, a large
electron collection efficiency can be obtained with a relatively simple elec-
tron optical input system. Figure 16.2 shows one of the commonly used input
systems. Another front end used with the venetian-blind multiplier struc-
ture is shown in figure 16.6. This front end has a larger cathode for improved
performance in scintillation counting.

   The operation and the focusing properties of the venetian-blind dynodes
can be followed from the diagram of figure 16.7. The primary photoelectron
beam is allowed to strike the vanes of the first dynode at full length. The
secondary electrons of each vane are directed to a vane of the next dynode.
The multiplier structure remains blind even when the emission energy is
in the order of 5 eV. With this structure it is ensured that the bulk of the
low-energy electrons do not contribute to the diffusion of the electron beam
during the multiplication process. Electrons emitted from the top of a vane
with high emission energy, however, can produce an enlargement of the
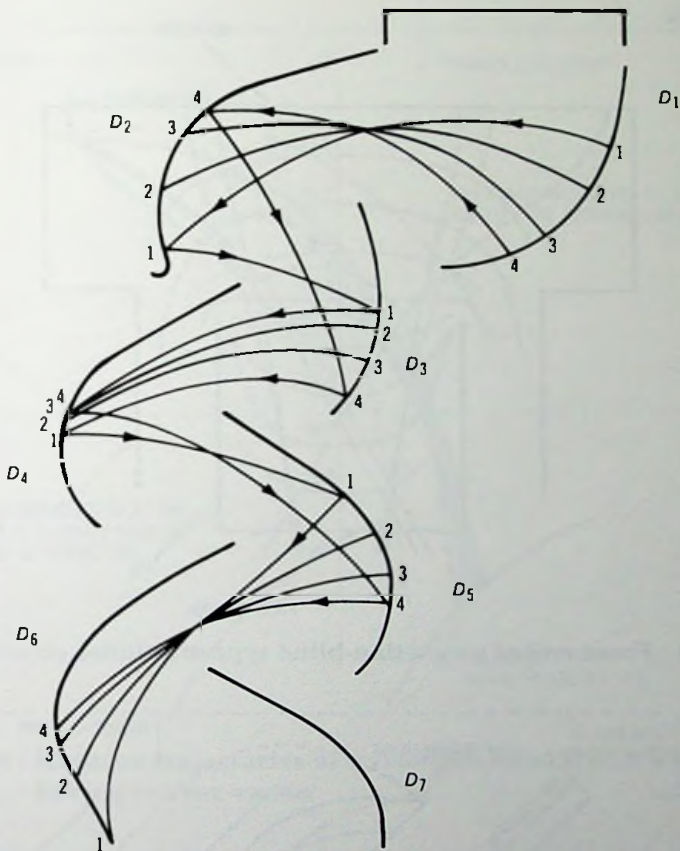
Fig. 16.5 Compensated design dynode structure.

electron beam by passing through the neighboring dynode slots. The beam enlargement occurring at several succeeding dynodes can produce a loss of gain and bombardment of the dynode insulators, thus limiting the number of usable multiplying stages. Other losses of electron transfer include the finite transparency of the secondary-electron emission from the top of the vane by the field of the preceding dynode.

A more rugged dynode structure may be obtained by curving the vanes. Curving of the vane can increase significantly its resonant frequency. Figure 16.8 shows the electron trajectories of the curved dynode vanes. The electron trajectories are similar to those of the straight structure.

The electron path difference from the top to the bottom of the vane is large, which results in relatively large transit-time dispersion. The vene-
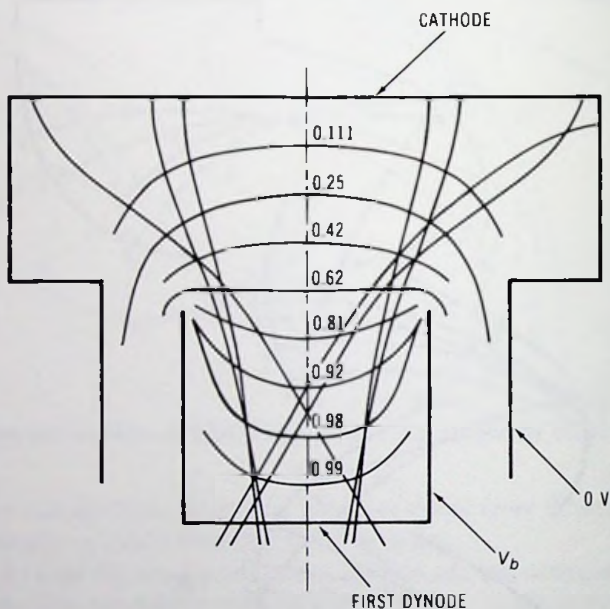
Fig. 16.6   Front end of a venetian-blind type multiplier structure.
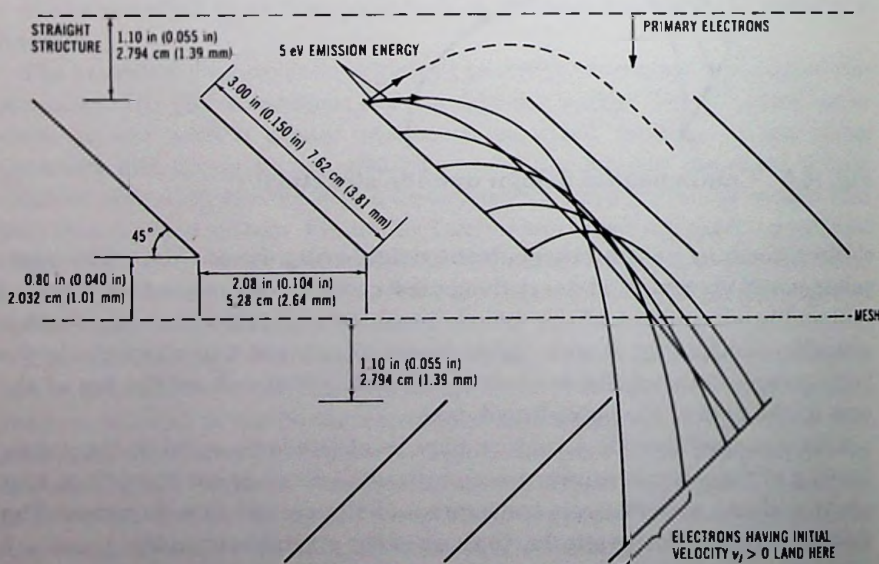
Fig. 16.7   Electron trajectories of a venetian-blind type multiplier structure.

MESH

"B" STRUCTURE

PRIMARY ELECTRONS

5-eV EMISSION ENERGY

THE VANES ARE CURVED BY 0.2 in (5.08 cm)
RADIUS. THE AVERAGE SLOPE IS 45°

NOTE:
THE VOLTAGE PENETRATION AT THE
TOP OF VANE IS SLIGHTLY WEAKER
THAN IN THE "A" STRUCTURE

ELECTRONS WITH
INITIAL VELOCITY $v_j > 0$
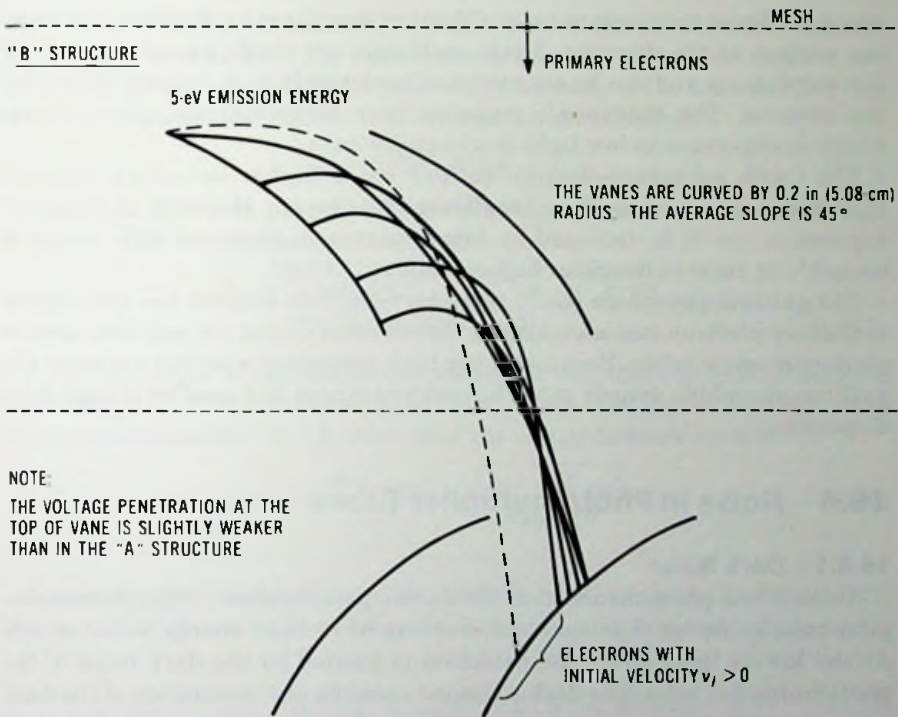
**Fig. 16.8   Electron trajectories of a venetian-blind type multiplier
having convex vanes.**

tian-blind photomultiplier tube gained a wide application for scintillation
counting, where speed is seldom important since most scintillators have
much larger time constants than even the slowest photomultiplier.

The box and grid type of multiplier structure, except for grid losses, has a
good electron transfer efficiency between the boxes. Because of the weak
electric field within the box and lack of focusing, the transit-time dispersion
is relatively large.

16.3   Dynode Materials

The most frequently used dynode materials are the copper beryllium alloy
containing about 2% beryllium, the silver-magnesium alloy containing ap-
proximately 2% magnesium, and the Cs_3Sb and gallium phosphide
secondary-electron emitters.

The silver-magnesium alloy and copper-beryllium dynodes are activated
by heating the dynodes in low-pressure water vapor. Oxidation by water

vapor produces magnesium oxide (MgO) or beryllium oxide (BeO) layers on the surface of the dynodes. These materials are stable at relatively high current density and can be outgassed at moderately high temperatures during exhaust. The thermionic emission from these materials is very low, which is important in low light level applications.

The Cs_3Sb secondary-electron emitter has a higher secondary emission than the magnesium oxide or beryllium oxide layers. However, it cannot be exposed to air, it is damaged by temperatures in excess of 75°C and it is unstable at current densities higher than 10^{-4} A/cm^2.

The gallium phosphide (GaP) secondary-electron emitter has the highest secondary-electron emission among the secondary-electron emitters used in photomultiplier tubes. Because of the high secondary-electron emission the gallium phosphide dynode tubes have fewer stages and smaller transit-time dispersion.

16.4   Noise in Photomultiplier Tubes

16.4.1   Dark Noise

Noise is one phenomenon that limits the performance of the photomultiplier tube as far as detection and measure of radiant energy is concerned. At the lowest light levels the detection is limited by the dark noise of the photomultiplier tube. The dark noise is caused by the fluctuation of the dark current which is present even though the photomultiplier tube is in complete darkness. Dark current originates from a number of sources in the photomultiplier tube. Thermionic emission from the photocathode and the first dynode is one of the most important sources of the dark current. Other sources include field emission; positive ion generation due to residual gas; field desorption and dark current bombardment of electrodes; ohmic leakage due to insufficient insulation between the electrodes; fluorescent effects due to the electron bombardment of the dynodes, the glass bulb, and the dynode insulators; electron luminescent effects due to the high electric field across the glass insulators; faceplate phosphorescence due to exposure to ultraviolet light; and Cerenkov radiation and faceplate scintillation due to radioactive materials, particularly potassium-40 and radium-226. With careful design and processing, with the exception of thermionic emission, the dark current effects can be restrained to a relatively low level. Under these conditions the noise which limits the detectability results from amplified thermionic emission of the photocathode. The thermionic emission or dark current I_d of the photocathode is associated with the following shot noise current:

$$I_n = \sqrt{2e\,\Delta f I_d},\qquad\qquad (16.3)$$

where e is the charge of electron, and Δf is the bandpass at the first dynode. At the first dynode both the dark current and the shot noise current are multiplied by the secondary-electron emission ratio of the dynode. The rms noise current after the first dynode multiplication becomes

$$I_{n_1} = \sqrt{2eI_d \, \Delta f \, \delta(\delta + 1)}. \tag{16.4}$$

Repeating the same process on the following dynodes, the rms noise current for n stage multiplications becomes

$$\begin{aligned} I_{nn} &= \sqrt{2eI_d \, \Delta f(\delta^{2n} + \delta^{2n-1} + \cdots + \delta^n)} \\ &= \delta^n \sqrt{2eI_d \, \Delta f[\delta/(\delta - 1)]} \end{aligned} \tag{16.5}$$

If the rms value of the modulated signal current (light is modulated by a light chopper) at the cathode is I_k (rms), then the signal current after n-stage multiplication is $\delta^n I_k$ (rms), and the signal-to-noise ratio is

$$snr = \frac{\delta^n \, I_{k(rms)}}{I_{nn}} = \sqrt{\frac{(\delta - 1) \, I_{k(rms)}^2}{2eI_d \, \Delta f \delta}}. \tag{16.6}$$

A typical pulse-height distribution of dark noise is shown in figure 16.9. The portion of the curve between pulse heights 1 and 4 corresponds to single
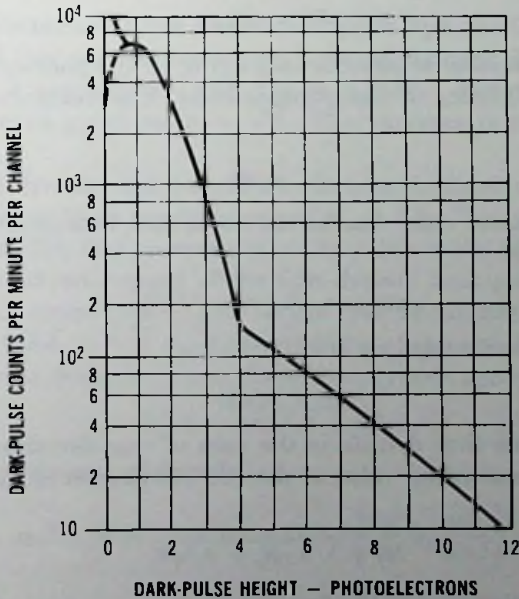
Fig. 16.9 **Pulse-height distribution of dark noise.**

electron events. The region greater than four electrons is believed to be caused by multiple electron-emission events, such as ionic bombardment of the photocathode. The region corresponding to less than one-half electron pulse-height is assumed to be caused by electron emission from the first and second dynode surfaces.

16.4.2   Afterpulsing

Afterpulsing is another spurious effect in photomultiplier tubes used for the detection of short light flashes. Afterpulses are minor secondary pulses that follow a main anode current pulse. They are caused by light feedback and by ionization of the residual gas in the region between the cathode and the first dynode. Afterpulses caused by light feedback are usually delayed by about 50 ns. The delay of the ionization type of afterpulses is usually in the range of 0.2 to 1 μs.

16.4.3   Noise Produced by the Statistical Fluctuation of the Signal Current

At photocurrents well in excess of the thermionic emission the signal-to-noise ratio at the output of the photomultiplier tube is determined by the statistical variation of the signal current. For the purpose of analysis assume that the average number $\bar{n}_e$ of photoelectrons in a time τ is

$$\bar{n}_e = \eta\bar{n}_p, \tag{16.7}$$

where $\bar{n}_p$ is the number of photons impinging on the photocathode, and η is the quantum efficiency of the photocathode. The variance of the photoelectrons is

$$\sigma_e^2 = \eta\bar{n}_p. \tag{16.8}$$

The signal-to-noise ratio due to the statistical fluctuation of the photoelectron current is

$$(\text{snr})_0 = \eta\bar{n}_p/\sigma_e = \sqrt{\eta\bar{n}_p}. \tag{16.9}$$

The signal at the first dynode is

$$s_1 = \delta_1\eta\bar{n}_p. \tag{16.10}$$

The noise at the first dynode is the sum of rms deviation of the signal current and the multiplied value of the rms fluctuation of the photoelectron current:

$$N_1 = \sqrt{\delta_1\eta\bar{n}_p + \delta_1^2\eta\bar{n}_p}. \tag{16.11}$$

The signal-to-noise ratio at the first dynode is

$$(\text{snr})_1 = \sqrt{\eta \overline{n}_p} \sqrt{\frac{\delta_1}{1 + \delta_1}}. \tag{16.12}$$

Continuing this process, the signal-to-noise ratio at the second dynode becomes

$$(\text{snr})_2 = \sqrt{\eta \overline{n}_p} \sqrt{\frac{\delta_1 \delta_2}{1 + \delta_2 + \delta_1 \delta_2}}. \tag{16.13}$$

For an n-stage multiplier the signal-to-noise ratio may then be given by the following equation:

$$(\text{snr})_n = \sqrt{\eta \overline{n}_p}$$
$$\times \sqrt{\frac{\delta_1 \delta_2 \delta_3 \cdots \delta_n}{1 + \delta_1 \delta_2 \delta_3 \cdots \delta_n + \delta_2 \delta_3 \cdots \delta_n + \delta_3 \delta_4 \cdots \delta_n + \cdots + \delta_{n-1} \delta_n + \delta_n}}. \tag{16.14}$$

If all stages are operated at a same secondary-electron emission ratio then equation 16.14 reduces to

$$(\text{snr})_n = \sqrt{\eta \overline{n}_p} \sqrt{\frac{\delta^n (\delta - 1)}{\delta^{n+1} - 1}} \cong \sqrt{\eta \overline{n}_p} \sqrt{\frac{\delta - 1}{\delta}}. \tag{16.15}$$

16.4.4 Gain Variance of the Photomultiplier Dynode Chain

It is assumed that one photoelectron striking the first dynode produces, on an average, δ_1 secondaries. The rms or standard deviation of a normal distribution is then given by $\sigma_1 = \sqrt{\delta_1}$. The variance is $\sigma_1^2 = \delta_1$, and the gain is $m_1 = \delta_1$.

At the second dynode each secondary electron produces on an average δ_2 tertiary electrons with an average gain of $m_2 = \delta_1 \delta_2$. The rms deviation has two components. The first component is the value of the rms fluctuation of the secondary electron current of the first dynode multiplied by δ_2, that is $\delta_2 \sigma_1$. The second component is due to the rms fluctuation of the average signal current, $\sqrt{\delta_1 \delta_2} = \sqrt{\delta_1} \, \sigma_2$. By summation of the rms deviation components the total rms deviation σ_{2t} at the second dynode becomes

$$\sigma_{2t} = \sqrt{\delta_2^2 \sigma_1^2 + \delta_1 \sigma_2^2}. \tag{16.16}$$

The variance at the second dynode is

$$\sigma_{2t}^2 = \delta_2^2 \sigma_1^2 + \delta_1^2 \sigma_2^2 = (\delta_1 \delta_2)^2 \left[\frac{\sigma_1^2}{\delta_1^2} + \frac{\sigma_2^2}{\delta_1 \delta_2^2} \right], \tag{16.17}$$

where $\sigma_2 = \sqrt{\delta_2}$.

At the third dynode the process is repeated:

$$\sigma_{3t} = \delta_3^2 \, \sigma_{2t}^2 + \delta_1 \delta_2 \sigma_3^2 = (\delta_1 \delta_2 \delta_3)^2 \left[\frac{\sigma_1^2}{\delta_1} + \frac{\sigma_2^2}{\delta_1 \delta_2^2} + \frac{\sigma_3^2}{\delta_1 \delta_2 \delta_3^2} \right]. \qquad (16.18)$$

The gain variance for a dynode chain of n dynodes from the above equation is

$$\sigma_{nt}^2 = (m_n)^2 \left[\frac{\sigma_1^2}{\delta_1^2} + \frac{\sigma_2^2}{\delta_1 \delta_2^2} + \frac{\sigma_3^2}{\delta_1 \delta_2 \delta_3^2} + \cdots + \frac{\sigma_n^2}{\delta_1 \delta_2 \delta_3 \cdots \delta_n^2} \right], \qquad (16.19)$$

where $m_n = \delta_1 \delta_2 \delta_3 \cdots \delta_n$ and $\sigma_n^2 = \delta_n^2$.

The signal-to-noise ratio of the photomultiplier dynode chain is

$$(\text{snr})_n = \frac{m_n}{\sigma_{nt}} = \left[\frac{\sigma_1^2}{\delta_1^2} + \frac{\sigma_2^2}{\delta_1 \delta_2^2} + \frac{\sigma_3^2}{\delta_1 \delta_2 \delta_3} + \cdots + \frac{\sigma_n^2}{\delta_1 \delta_2 \delta_3 \cdots \delta_n^2} \right]^{-1/2}. \qquad (16.20)$$

The relative gain variance of the dynode chain is

$$V_G = \frac{\sigma_{nt}^2}{m_n^2} = V_1 + \frac{V_2}{\delta_1} + \frac{V_3}{\delta_1 \delta_2} + \frac{V_4}{\delta_1 \delta_2 \delta_3} + \cdots + \frac{V_n}{\delta_1 \delta_2 \delta_3 \cdots \delta_{n-1}}, \qquad (16.21)$$

where $V_1 = \sigma_1^2/\delta_1^2$, $V_2 = \sigma_2^2/\delta_2^2$, . . ., $V_n = \sigma_n^2/\delta_n^2$ are the relative gain variances of the individual dynodes.

If all stages operate at the same gain δ, then

$$V_G = V \left(\frac{1}{\delta_1} + \frac{1}{\delta_1 \delta_2} + \cdots + \frac{1}{\delta_1 \delta_2 \cdots \delta_{n-1}} \right)$$

$$= \frac{V}{\delta^{n-1}} \left(1 + \delta + \delta^2 + \cdots + \delta^n - \delta^n \right)$$

$$= \frac{V}{\delta^{n-1}} \left(\frac{\delta^{n+1} - 1}{\delta - 1} - \delta^n \right) \cong V \frac{\delta}{\delta - 1}. \qquad (16.22)$$

If the first dynode is operated at a higher stage voltage in order to increase the signal-to-noise ratio, then the gain variance becomes

$$V_G = V_1 + \frac{V}{\delta - 1}. \qquad (16.23)$$

The pulse-height distribution of anode pulses, due to single electron inputs, may be calculated approximately from the Poisson statistics. Figure 16.10 shows the measured amplitude distribution of anode pulses due to single electron inputs for a photomultiplier tube. For comparison, the curve $y = xe^{-x}$ is included. Figure 16.11 shows the calculated amplitude distribution for a Poisson distribution of secondary-electron emission, assuming an equal average gain m per stage.
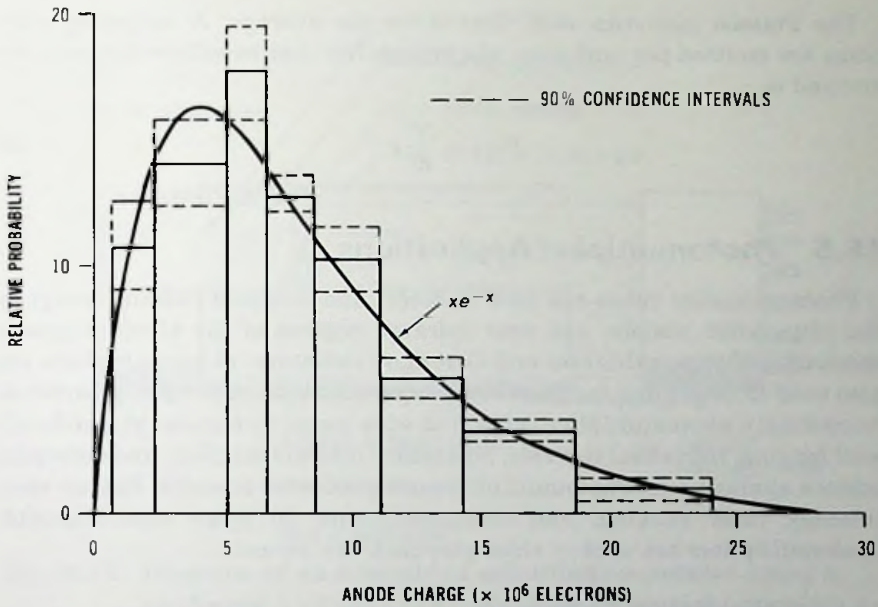
Fig. 16.10 Measured amplitude distribution of anode pulses due to single photoelectron inputs for a CL-1090 photomultiplier ($m \sim 3$).
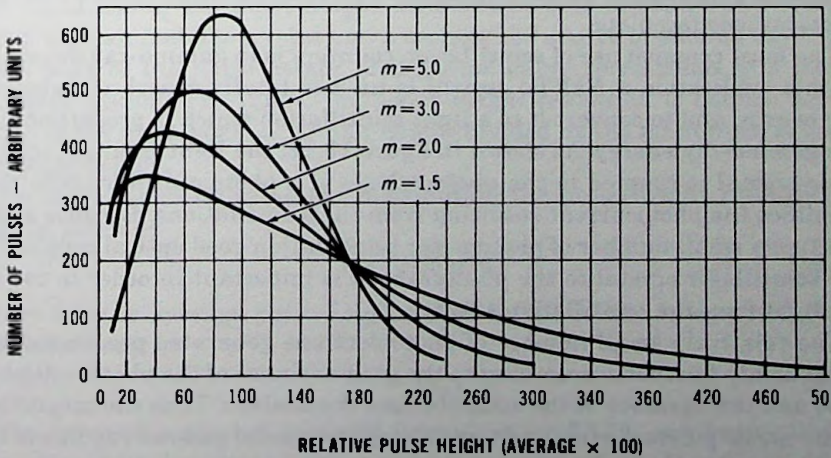
Fig. 16.11 Calculated amplitude distribution of pulses from an electron multiplier for single-electron inputs.

The Poisson statistics state that if, on the average, N secondary electrons are emitted per unit time, the probability that exactly n electrons are emitted is

$$P(n) = \frac{N^n}{n!} e^{-N}. \tag{16.24}$$

16.5   Photomultiplier Applications

Photomultiplier tubes are used to detect and measure radiant energy in the ultraviolet, visible, and near infrared regions of the electromagnetic spectrum. With scintillators and Cerenkov radiators, photomultipliers are also used to detect and measure X-rays, gamma rays, and nuclear particles. Accordingly, photomultiplier tubes find wide usage in nuclear research, oil-well logging, industrial controls, laboratory instrumentation, and aerospace science applications. Photomultipliers are used with lasers in Raman spectroscopy, laser ranging, and communications. In home entertainment, photomultipliers are used in video playback equipment.

16.5.1   Scintillation Counter

The scintillation counter consists of a solid, liquid, or gas scintillation detector and a photomultiplier tube. The scintillation detector, which produces light flashes on excitation by ionizing radiation, such as alpha particles, beta particles, neutrons or gamma rays, is mounted in contact with the photocathode faceplate.

The most common use of scintillation counters is in gamma-ray detection. In this application a NaI(Tl) crystal is used to totally absorb the gamma-ray energy, and to convert it to a light scintillation which is proportional to the gamma-ray energy. As shown in figure 16.12, the light from the scintillator crystal is coupled to the photocathode of a photomultiplier tube that amplifies the photocurrent resulting from the scintillations. Because of the relatively small number of photons per scintillation good optical coupling of the scintillator crystal to the photocathode is important in order to use all the light from the scintillation effectively.

The relatively small number of photoelectrons generated per photoevent statistically fluctuates according to the gain variance of the photomultiplier tube and the variance of the scintillations themselves. Thus the magnitude of the anode pulses corresponding to a monoenergetic gamma-ray flux is not constant but statistically varies about a mean value of pulse height. Because the pulse height is a direct measure of gamma-ray energy the ability to discriminate between pulses of various heights is an important requirement in nuclear spectrometry. Obviously, the smaller the variation of the

NaI (Tl) CRYSTAL

PACKED Al_2O_3 REFLECTOR

SPRAYED Al_2O_3 REFLECTOR

OPTICAL WINDOW

OPTICAL COUPLING FLUID

MUMETAL MAGNETIC SHIELD

SPUN ALUMINUM BODY

SPUN ALUMINUM CAP

TYPE 6292
PHOTOMULTIPLIER
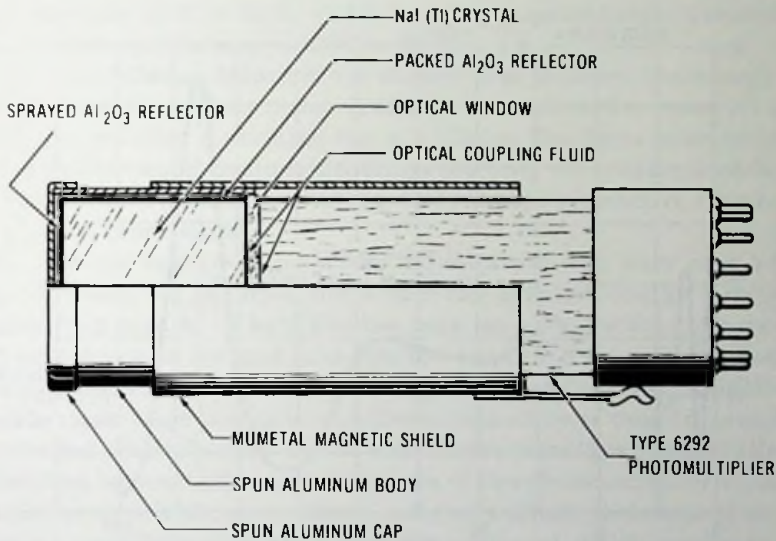
Fig. 16.12 Diagram of an assembled scintillation counter using a packaged 2×2-inch (5×5-cm) NaI(Tl) crystal optically coupled to a 6292 photomultiplier.

pulse height of a scintillation counting setup, the better its ability to resolve a pulse height. Hence the origin of the term "pulse-height resolution." Figure 16.13 shows the pulse-height distribution of a scintillation counting setup with an NaI(Tl) crystal and a cesium-137 source of gamma rays. The main peak of the pulse height distribution curve corresponds to a mono-energetic gamma-ray input. The *pulse-height resolution* is defined as the width of the main peak at its half height divided by the main peak value of the pulse height.

For a Gaussian pulse-height distribution the pulse-height resolution η may be given by

$$\eta = 2.35 \, \sigma/\bar{x}, \tag{16.25}$$

where $\bar{x}$ is the average pulse height given by the following equation for N photoelectrons:

$$\bar{x} = m_n N. \tag{16.26}$$

The value of σ can be computed from equation 16.19, and for a gallium-phosphide first dynode (δ_1) followed by copper-beryllium dynodes (δ) it reduces to

$$\sigma = m_n \sqrt{N} \sqrt{1 + \frac{\delta}{\delta_1(\delta - 1)}}. \tag{16.27}$$

$$RESOLUTION = \frac{92 - 81.5}{86.5} \times 100\%$$
$$= 12.1\%$$

FULL WIDTH AT HALF
MAX = 92 − 81.5 = 10.5 UNITS

PEAK MIDPOINT
POSITION
= 86.5 UNITS

COUNTS PER SECOND
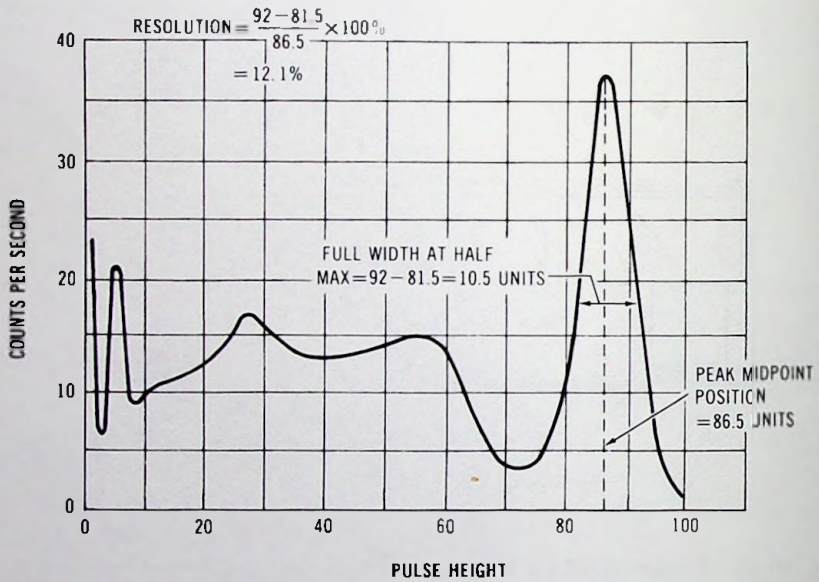
PULSE HEIGHT

Fig. 16.13 **Distribution of pulse heights observed in a scintillation counting experiment using gamma rays from cesium-137 to excite a NaI(Tl) crystal.**

By combination of equations 16.25, 16.26, and 16.27, the pulse-height resolution becomes

$$\eta = \frac{2.35}{\sqrt{N}} \sqrt{1 + \frac{a\delta}{\delta_1(\delta - 1)}}, \tag{16.28}$$

where a is an experimental factor having a value of 1 for the conventional photomultiplier and 1.6 for a gallium-phosphide first dynode multiplier.

For example, an NaI(Tl) scintillator and a cesium-137 source may produce $N = 4000$ electrons per scintillation. With $\delta_1 = 5 = \delta$, a conventional photomultiplier, from equation 16.28, has a pulse-height resolution of $\eta = 0.041 = 4.1\%$. In comparison, a gallium-phosphide first dynode photomultiplier with $\delta_1 = 50$ and $\delta = 5$ has a pulse-height resolution of $\eta = 0.038 = 3.8\%$.

For single-electron or multiple-electron emission events the statistical variations start at the first dynode. For this case equation 16.28 is modified to the following form:

$$\eta = \frac{2.35}{\sqrt{\delta_1 N}} \sqrt{1 + \frac{a}{\delta - 1}}, \tag{16.29}$$

where N is the number of multiple-electron emission events.

For example, if $N = 1$, $\delta_1 = 50$, $\delta = 5$, the pulse-height resolution of single-electron pulses is $\eta = 0.393 = 39.3\%$.

Liquid scintillation detectors are usually used to detect low-energy beta-rays produced by nuclear disintegrations. The radioactive material is dissolved in a solution containing the scintillator. The three most commonly used radioisotopes in liquid scintillation counting are tritium-3, carbon-14, and phosphorous-32. These elements are suitable radioactive tracers used in biological experiments.

The beta-ray energies from these radioisotopes may vary over a broad range. Tritium, for example, has a beta-ray emission energy distribution ranging from zero to 18 keV. For low beta-ray energies the corresponding light output is also low and falls into the amplitude range of random dark noise pulses. In order to separate the signal pulses (beta-ray scintillations) from the dark noise pulses a coincidence technique is used in most liquid scintillation spectrometers. In the coincidence technique the scintillator is sandwiched between the input faceplates of two photomultiplier tubes. The coincidence circuit allows an output pulse only if both photomultiplier tubes register a scintillation within a short time interval, which may be as small as 10 ns. Because the dark count of the photomultiplier tubes may be as low as 100 counts per second the coincidence resolving time of 10 ns is sufficiently small to remove all background noise effectively. Table 16.1 shows the characteristics of representative scintillation phosphors.

Cerenkov radiation detection is used for fast beta-ray detection. Cerenkov radiation is emitted by a charged particle moving through a medium at a velocity greater than the phase velocity of light in that medium. This radiation is due to the effect of the difference between the velocity of the particle and that of its associated electric and magnetic fields: the particle runs away from its own electromagnetic field. Since the effect is greater when the index of refraction of a dielectric is large, materials with high indexes of refraction are usually chosen for Cerenkov counters. The Cerenkov radiation is usually very low. Therefore the utilization of coincidence technique and a good ultraviolet transmission cathode faceplate is important.

Alpha particle scintillation counters consist of an aluminized zinc sulfide phosphor screen deposited on the photocathode faceplace of the photomultiplier tube.

Thermal neutrons can be detected with a mixture of zinc sulfide and boron. When a boron nucleus captures a slow neutron a nuclear reaction takes place during which an energy of 2.3 to 2.8 MeV is liberated. This energy is passed to the zinc sulfide, which transforms it to light flashes.

Fast neutrons can be converted to light flashes with a phosphor consisting of a suspension of zinc sulfide crystals in a transparent plastic material containing hydrogen.

Table 16.1   Characteristics of Representative Scintillation Phosphors

Material	Wavelength of Maximum Emission (angstroms)	Decay Constant (micro-seconds)	Density (grams per cubic centimeter)	Relative Pulse Height*
inorganic crystals				
NaI (Tl)	4100	.25	3.67	210
CsI (Tl)	4200-5700**	1.1	4.51	55
KI (Tl)	4100	1.0	3.13	50 (approx)
LiI (Eu)	4400	1.4	4.06	74
organic crystals				
anthracene	4400	0.032	1.25	100
trans-stilbene	4100	0.006	1.16	60
plastic phos-phors	3500 to 4500	0.003 to 0.005	1.06	28 to 48
liquid phos-phors	3550 to 4500	0.002 to 0.008	0.86	27 to 49

*With 10 μs anode time constant [Robert Swank, *Annual Review of Nuclear Science*, Vol. 4 (1954)].

**Unpublished data of Bonomomi and Rossel quoted by B. Hahn and J. Rossel in *Helv. Phys. Acta*, Vol. 26, 1953.

16.5.2   Oil-Well Logging

The scintillation counter obtained an important application as a detector in special instruments used to analyze oil wells. The oil companies, after drilling the well, need to do an analysis of the well. This analysis, called a *log*, is a foot-by-foot description of the rocks that the well has been drilled through. Important things to know are the kinds of rocks (sandstone, limestone, shale, etc.), the porosity of the rock, the percentage of oil and water found in the pore spaces, and the potential flow rate of oil through the rock.

The foot-by-foot description is obtained by dropping an instrument package, called a *sonde*, down the well on the end of a long cable. The instruments measure the properties of the rocks as the sonde is slowly cranked back uphole. The type of rock can often be determined by measuring the level of natural radioactivity, since shales and clays have higher levels than other rocks. A scintillation counter is used in the sonde to make this measurement. The scintillation counter measures the natural gamma radiation from the rocks surrounding the borehole.

The porosity is measured with a special sonde employing a radioactive source. Gamma rays leave the source, penetrate the rocks, and are reflected back to the scintillation counter. The attenuation of this reflected beam is a measure of the density, which is related to the porosity.

The oil saturation can be derived from measurements made with another sonde, which uses two scintillation counters and a neutron tube. The rocks are irradiated by fast neutrons. When the fast neutrons are finally slowed down and absorbed by the rocks and fluid, gamma rays are emitted which may be sensed by one of the scintillation counters. The absorption of the neutrons is related to the water saturation, to the porosity, and to certain elements dissolved in the water.

It can be seen that the scintillation counters are vital to the oil industry. Oil-well logging companies rely on the scintillation counters for many crucial measurements which must be reliable at high temperatures (175°C) and extreme vibration levels. Without such products the search for oil would be much more of a hit-or-miss affair, and gasoline would be much scarcer and more expensive.

16.5.3   Low Light Level Detection

At the lowest light levels light detection is limited by the dark noise of the photomultiplier tube. The dark noise is caused by the fluctuation of the dark current, which is present even though the photomultiplier tube is in complete darkness.

Dark noise can be minimized by cooling the photomultiplier in a refrigerant, such as dry ice, and by reduction of the bandwidth of the measuring system.

In one low light level detection technique the noise is minimized by chopping the light signal and by use of a narrow bandpass filter that transmits the signal but rejects the noise components out of bandpass. Extremely narrow bandwidths (4×10^{-1} Hz) and consequently a superior noise rejection may be obtained by use of a phase-sensitive lock-in amplifier system.

The lock-in amplifier is an ac voltmeter that accurately measures the amplitude of low-level signals in high-level background noise. The heart of a lock-in amplifier is a phase-sensitive detector that functions by detecting only that part of the input signal which is synchronous with the reference signal. In this case the reference signal is identical with the light chopper frequency and may be derived from the light chopper.

Another technique which is used for low light level detection is photon counting. In this method an amplitude discriminator circuit is present at the output of the photomultiplier tube. The amplitude discriminator and other associated circuits ensure that only those pulses are counted which correspond to a single electron at the photocathode. Two counts are made:

one with the light on and one with the light off. The signal is the difference of the two counts.

16.5.4   Instrumentation

An important application of photomultiplier tubes is in radiometry and photometry to measure radiometric and photometric quantities. Instruments for the measurements of luminous intensity, luminous flux density, and illumination are called *photometers*. A photometer is comprised of a transducer which transforms the electromagnetic waves into electric current and a current-measuring readout device. In its simplest form the instrument could be a voltage generating photocell connected to a microammeter. For precision work, however, photomultiplier tubes are commonly used as transducers.

Other applications are: atomic absorption spectrometry, spectrophotometry, colorimetry, fluorimetry, ellipsometry, densitometry, polorimetry, refractometry, and many other applications involving light measurements and light detection and conversion to an amplified electrical signal.

16.5.5   Power Supply Considerations

The input, output, and dynode voltages of a photomultiplier tube may be supplied by a high-voltage power supply which is connected to a resistance voltage-divider network as shown in figure 16.14. The voltage-divider network distributes the power supply voltage according to the needs of a par-
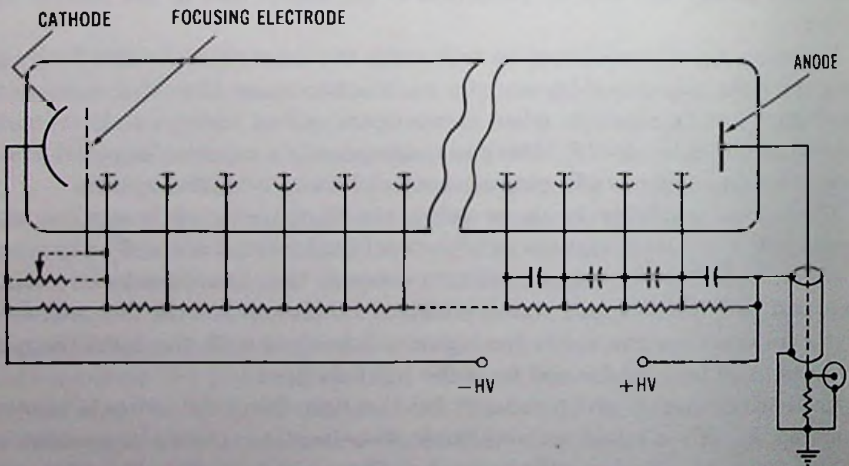
Fig. 16.14   Typical voltage-divider arrangement for fast pulse response and high peak current systems.

ticular application. In order to obtain a high first dynode gain, usually a high cathode to first dynode voltage is required which is approximately 600 to 800 V in photomultipliers having a gallium-phosphide first dynode. In modern photomultipliers the focusing electrode may be connected to the arm of a potentiometer, between the cathode and the first dynode, to permit adjustment for maximum anode current.

For common photomultiplier applications, equal voltages between dynode stages may be used. To prevent dynode voltage variation and to ensure linearity between the input light and the output current, the voltage divider current must be at least ten times the maximum anode current.

In the case of pulsed operation, when the input signal is from short pulses, the peak pulse current may be orders of magnitude higher than the average current. In this case nearly constant dynode potentials can be maintained by use of charge storage capacitors as shown in figure 16.14.

For some applications it is required that the photomultiplier deliver 0.2 A or more current for a short duration. The fundamental limitation on current output is space charge at the last few stages. The space-charge limitation can be overcome by a tapered voltage-divider network which allows an increased stage voltage across the last few stages.

For fast pulse application a proper impedance match between the anode and the transmission line is critical in order to preserve linearity and pulse shape. Impedance matching is accomplished by use of low-inductance strips as shown in figure 16.15. Note in this figure that the last dynode and the next to last dynode are capacitively coupled to the ground braid of the coaxial cable.

16.5.6   Time Response

Time response measurements of a photomultiplier tube are made by illumination of the entire photocathode with a delta-function light source, such as a light-emitting diode, mode-locked laser, or a small-spark source. At the anode of the photomultiplier tube a dispersed current pulse is obtained which is a direct indication of the time response of the photomultiplier tube. The two principal causes of anode pulse dispersion are the transit-time spread of electrons, and anode and transmission line mismatch, if they are not properly designed.

Frequently the time response of a photomultiplier tube is specified by the anode pulse rise time only. Figure 16.16 shows the anode current pulse of an RCA C70129 type photomultiplier tube operated at a 1000-V anode-to-cathode voltage. The photograph was obtained with a repetitive delta-function light source and a sampling oscilloscope. The sweep speed is 1 ns/cm. The anode pulse rise time is the time difference between the 10 and 90% amplitude points. In figure 16.16 the rise time is 1.4 ns.
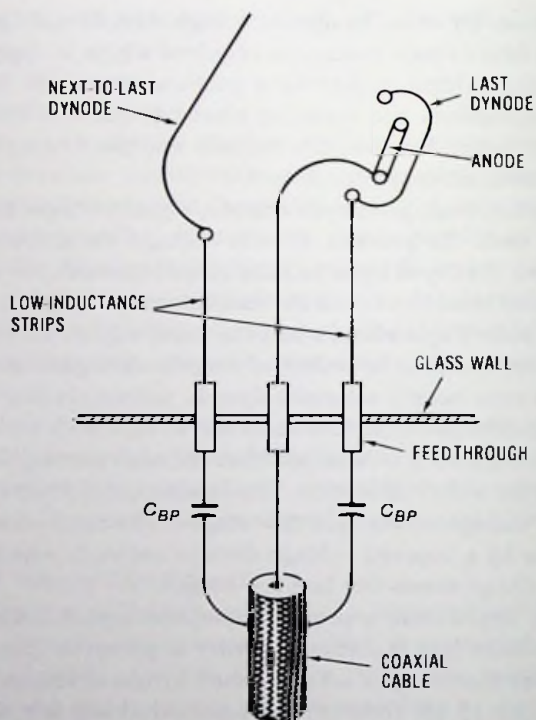
Fig. 16.15   Impedance matching by low-inductance strips between the anode and transmission line.
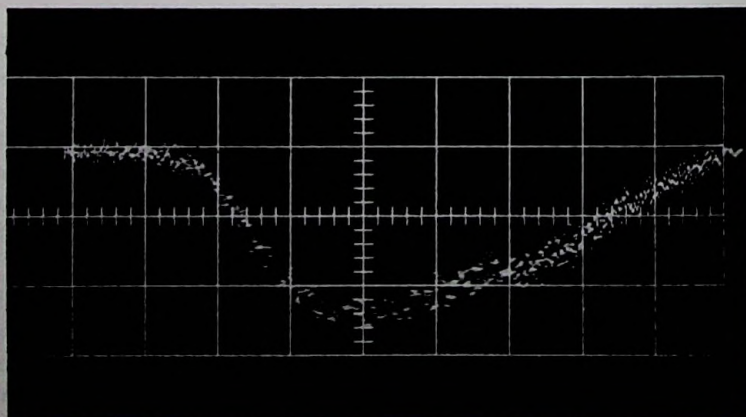
Fig. 16.16   Anode current pulse of a photomultiplier obtained with a delta-function light source.

Special high-speed photomultipliers are available with less than 0.5 ns rise time. The rise time of circular and in-line cage photomultipliers is in the range of 1.5 to 3 ns depending on the number of stages and size of the photomultiplier tube. The rise time of venetian blind types is in the range of 10 to 20 ns.

The frequency response of a photomultiplier tube is closely related to the anode pulse dispersion. Mathematically it is the Fourier transform of the normalized anode current pulse dispersion.

References

Allen, J. S. "An Improved Electron Multiplier Particle Counter," *Rev. of Sci. Instr.*, Vol. 18, 1947.

Barsukov, O. A. *Radioactive Investigations of Oil and Gas Wells*, Pergamon Press, New York, 1965

Breitenberger, E. "Scintillation Spectrometer Statistics," *Progress of Nuclear Physics*, Vol. 4, p. 56, 1955.

Duckett, S. W. "Miniature Photomultiplier for Scintillation and Space Use," *The Thirteenth Scintillation and Semiconductor Counter Symposium*, Shoreham Hotel, Washington, D.C., March 1972.

Encyclopedia of Chemical Technology, John Wiley & Sons, Inc., New York, 1968.

Engstrom, R. W., and R. M. Matheson. "Multiplier-Phototube Development Program at RCA-Lancaster," *IEEE Transactions on Nuclear Science*, NS-7, June 1960.

Helvy, F. A. "Photomultipliers for Scintillation Counting in Severe Environments," *IEEE Transactions on Nuclear Science*, Vol. NS-14, No. 1, February 1967.

Johnson, S. M. "Photomultiplier Tubes: Surviving the Rugged Life," *Electro-Optical Systems Design*, Vol. 4, No. 3, p. 20, March 1972.

Jorgensen, T. "On Probability Generating Functions," *Am. J. Phys.*, Vol. 16, p. 285, 1948.

Krall, H. R. "Extraneous Light Emission From Photomultipliers," *IEEE Transactions on Nuclear Science*, p. 455, February 1967.

Kramer, A. W. "Radiation Measurements," *Atomics*, November/December 1963.

Matheson, R. M. "High-Temperature Performance of Metal-Ceramic Photomultipliers," *IEEE Transactions on Nuclear Science*, Vol. NS-15, No. 3, June 1968.

———. "Recent Photomultiplier Developments at RCA," *IEEE Transactions on Nuclear Science*, p. 64, June 1964.

Morton, G. A. "Recent Developments in the Scintillation Counter Field," *IRE Transaction on Nuclear Science*, Vol. NS-3, p. 122, November 1956.

————, et al. "Design of Photomultipliers for the Submillimicrosecond Region," *IRE Transactions on Nuclear Science*, December 1958.

————, et al. "The Performance of High-Gain First-Dynode Photomultipliers," *Fifteenth IEEE Nuclear Science Symposium*, Montreal, October 23, 1968.

Photomultiplier Manual, RCA Technical Series PT-61.

Phototubes and Photocells, RCA Technical Series PT-60.

Pietri, G., and J. Nussli. "Design and Characteristics of Present-Day Photomultipliers," *Phillips Technical Review*, Vol. 29, No. 8/9, p. 267, 1968.

Rajchman, J. A., and R. L. Snyder, "An Electrically Focused Multiplier Phototube," *Electronics*, Vol. 13, pp. 20, 58, 60, December 1939.

Rappaport, P. "Methods of Processing Silver-Magnesium Secondary Emitters for Electron Tubes," *Journal of Applied Physics*, 25, 1954.

Sharpe, J. "Progress in Photomultiplier Tubes, Scintillation Instruments and Image Intensifiers," *IRE Transactions on Nuclear Science*, Vol. NS-7, June 1960.

Shockley, W., and J. R. Pierce. "Theory of Noise for Electron Multipliers," *Proc. IRE*, Vol. 26, No. 3, p. 321, March 1958.

Tusting, R. F., et al. "Photomultiplier Single-Electron Statistics," *IRE Transactions on Nuclear Science*, NS-9, 1962.

Wargo, P., et al. "Preparation and Properties of Thin Film MgO Secondary Emitters," *Journal of Applied Physics*, 27, 1956.

Widmaier, W., et al. "A New High-Gain Multiplier Phototube for Scintillation Counting," *IRE Transactions on Nuclear Science*, Vol. N5-3, No. 4, November 1956.

Zworykin, V. K., et al. "Silver Magnesium Alloy as a Secondary Electron Emitting Material," *Journal of Applied Physics*, 12, 1941.

————, and J. A. Rajchman. "The Electrostatic Electron Multiplier," *Proc. IRE*, Vol. 27, p. 558, September 1939.

17

CAMERA TUBES

17.1   Introduction

Camera tubes are electro-optical devices that are used to detect the optical image of a scene and to convert the detected image into electrical signals suitable to be televised. Historically, a great variety of camera tubes was introduced and successfully used for televising optical images. The most commonly used devices, however, operate on the charge image principle. A camera tube operating on the charge image principle, in general, consists of an image storage section for conversion of the incident radiant energy into an electrical charge image pattern corresponding to the imaged scene, and of an electron beam scanning section for reading out the charge pattern as a time-based video signal. In a most simple case the image storage section consists of an optically excitable camera tube target. In more sophisticated camera tubes, however, the storage target is in the image plane of an image intensifier tube, i.e., the optical image of the scene is either intensified or converted to a high-energy electron image, or both. The readout section consists of a biaxially deflected low-energy electron beam with the associated video output components. Frequently the video signal is obtained directly from the signal plate of the storage target. In other instances, however, the video signal is obtained as an amplitude modulation of the scanning beam that is returned by the storage target and amplified by an internally arranged photomultiplier tube. The return-beam devices are used in connection of the bisided target, or in cases when a large signal output is needed to overcome the video amplifier noise.

311

17.2   Camera Tube Targets

A charge image pattern may be produced in many different ways. Some targets have continuous surfaces, others are composed of a mosaic. The mosaic surfaces have lower light sensitivity than the continuous types due to the loss of useful area in the voids between the mosaic elements. Most targets have only one floating side where the charge pattern is stored, while the other side is held at a uniform potential: the potential of the signal plate. In a bisided target, however, both sides are floating, giving rise to a charge pattern on both sides of the target. Figure 17.1 shows the schematics of camera tube targets.

The target of the *CPS emitron* (figure 17.1A) consists of a mica or a glass insulator covered on one side by a transparent conductive signal electrode and on the other side by a geometric array of photoemissive islands prepared by evaporation of the basic photocathode material (S-20 cathode) through a fine mesh on the dielectric. The photoemissive islands and the signal plate form an array of capacitors that in the absence of light are uncharged. Due to photoemission from the photoemissive islands, when an optical image is focused on the mosaic, a positive charge proportional to the light intensity is accumulated on the mosaic capacitors. Thus an electrical charge pattern corresponding to the imaged scene is produced. The conversion of the charge pattern into electrical signals is done by scanning the target with a low-velocity electron beam. The low-velocity electron beam discharges the mosaic capacitors by deposition of electrons on the target. As the scanning beam moves across the target, the signal plate current is proportional to the accumulated charge of the scanned mosaic capacitors.

The construction and the operation of the *iconoscope* and *orthicon targets* (figures 17.1B and 17.1C) are similar to that of the CPS emitron, except that the photoemissive islands are composed of cesium and oxygen activated minute silver globes in a random pattern.

The disadvantage of mosaic surfaces of having voids between the mosaic elements may be corrected by use of continuous surface targets such as, for example, the image orthicon tube has. The *image orthicon target* (figure 17.1D) consists of a thin membrane of semiconducting glass or magnesium oxide. In operation, both sides of the target are floating, and the potentials of the two sides are determined by the interactions of the scanning and imaging electron beams with the target. The electrical charge pattern, corresponding to the imaged scene, is deposited by a high-energy (500-eV) photoelectron image on the image side of the target by secondary electron emission. On the average each photoelectron produces a multiple number of secondary electrons, allowing the target surface to charge positive. The positive charge pattern produced this way is capacitively coupled to the scan

side of the target, which is periodically charged by a low-energy scanning beam to the cathode potential of the electron gun (ground potential) by deposition of electrons.

The signal from the image orthicon target is obtained as an amplitude modulation of the scanning beam. The scanning beam deposits electrons proportionally to the positive charge pattern. If there is no positive charge on the target, all primary electrons are reflected and the return beam has the same value as the primary beam. If there is positive charge on the target, the scanning beam deposits a sufficient number of electrons to neutralize the positive charge and only the remaining electrons are reflected. In this way the return beam is amplitude modulated by the charge pattern.

The target capacitor C_t, which exists between the two faces of the target, and the target mesh to target capacitor C_m are charged periodically at the same rate by the scanning beam current. However, $C_t >> C_m$, and therefore most of the voltage drop is across C_m and only a small fraction of the target mesh voltage is on the target capacitor. Capacitor C_m is continuously discharged by the photoelectron current, preventing charge accumulation on C_m. The charge of target capacitor C_t, however, is accumulative. The scanning beam, by deposition of a sufficient amount of negative charge to neutralize the positive charge produced by the photoelectrons, charges capacitor C_t in the process of charging the scan side of the target to the ground potential. Therefore, to prevent charge accumulation on C_t, the target must have a sufficiently high conductivity to discharge the target capacitor during one frame time ($\frac{1}{30}$ s).

Operation and construction-wise a more simple device, with better lag and halation characteristics than the image orthicon has, may be obtained by use of a *secondary-electron conduction target* (SEC). The secondary-electron conduction target, with its high-gain characteristics, also extends the visibility toward lower light levels than the image orthicon. The target consists of a low-density layer of potassium chloride (KCl) supported by an aluminum oxide and a conductive aluminum layer. The conductive aluminum layer serves as a signal plate. The low-density potassium chloride is deposited on the support layers by evaporation in an argon atmosphere.

In operation, a positive voltage is applied to the signal plate and the scan side of the target is charged to the gun cathode potential by a low-velocity scanning beam. Thus the target capacitor between the signal plate and the scan side of the target is charged to the signal plate voltage. By focusing a high-energy photoelectron image (approximately 10 kV) on the image side of the target, the photoelectrons, after penetration of aluminum oxide and aluminum layers, dissipate most of their energy in the potassium chloride layer, creating many low-energy secondary electrons. Due to the electric field across the potassium chloride layer, a secondary-electron conduction
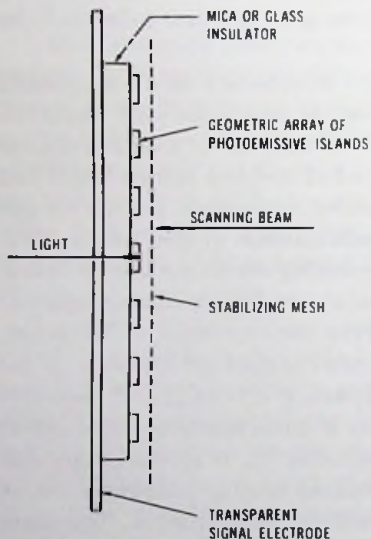
(A) CPS emitron mosaic.
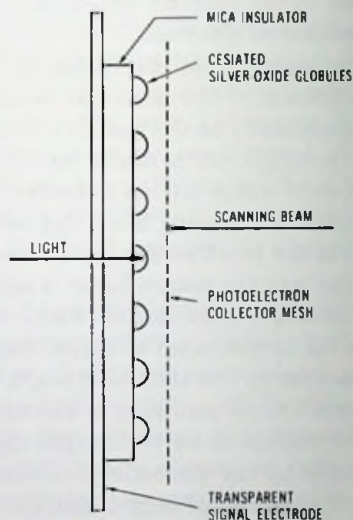
(B) Orthicon mosaic.
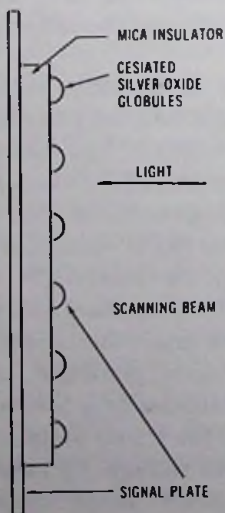
(C) Iconoscope mosaic.
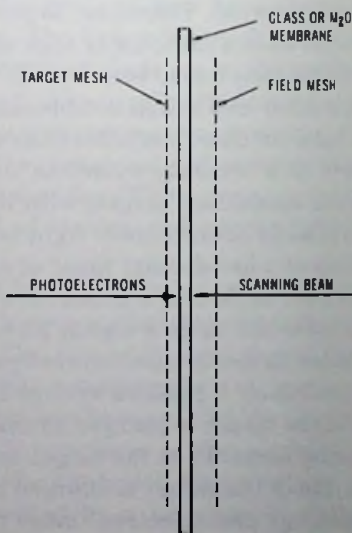
(D) Image orthicon or isocon target.

Fig. 17.1 Camera

occurs, discharging the target capacitor. In this manner a charge pattern, corresponding to the local intensity of the photoelectron image, is produced on the target. The charge pattern is read out by scanning the target by a low-velocity electron beam which returns the potential of the charged area to the gun cathode potential. Each time an elemental capacitor is charged
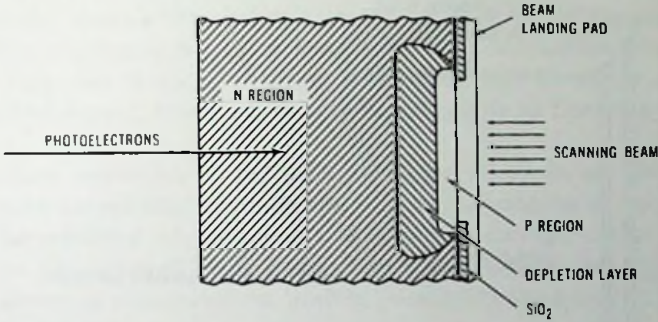
(E) Silicon intensifier target.
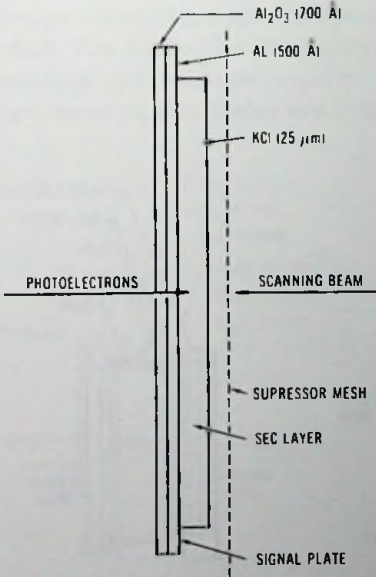
(F) SEC target.
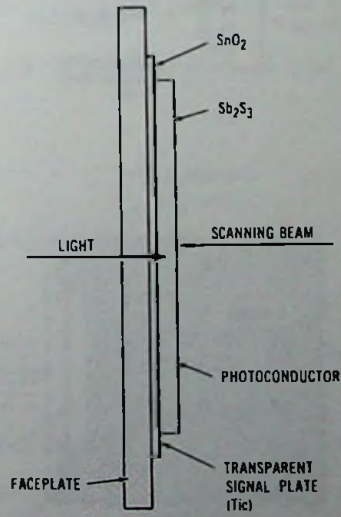
(G) Vidicon target.

tube targets.

by the scanning beam, a current pulse flows through the load resistor, producing the video signal.

In order to integrate during the exposure time (frame time) without loss of information available from the photocathode, the RC time constant of the target must be much larger than the exposure time. Large capacitance,
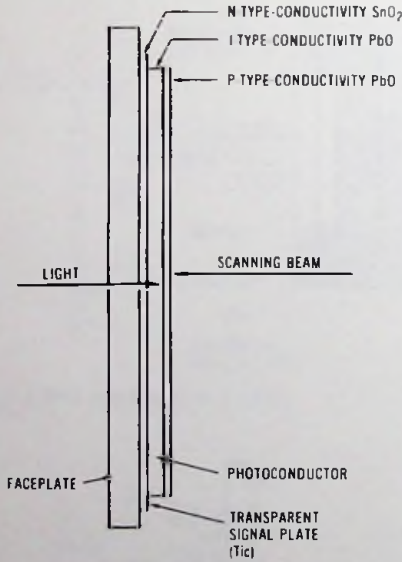
(H) Lead oxide target.
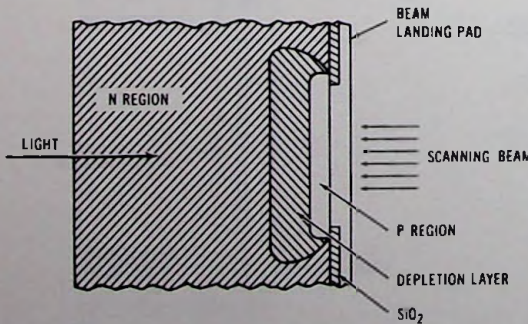
(I) Silicon diode array target.
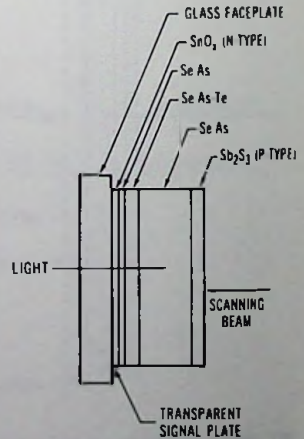
(J) Staticon target.

Fig. 17.1—cont.

however, introduces beam discharge lag. Therefore it is important to make the target resistivity as large as other parameters, such as, for example, resolution and high-energy beam penetration, allow it.

Lag is an important phenomenon in camera tubes. In general, there are two sources of lag in direct beam readout tubes. *Capacitive lag* is due to the final time it takes for the scanning electron beam to remove the charge accumulated on the target. *Conductive lag*, due to the slow decay of conduction process, occurs when charge carriers are trapped between the valence and conduction bands in states associated with impurities and imperfections. In the case of an SEC target when only free electrons are used to generate the signal, however, the conductive type of time lag should not occur.

The *silicon intensifier target* (SIT) of figure 17.1E is an advanced type camera tube target that extends the range of operation to very low light levels. The principal advantage of this device is the high target gain which may be on the order of 2000. This gain figure permits the SIT camera to operate closer to photoelectron limited conditions than any of the devices discussed above.

The silicon intensifier target consists of a two-dimensional array of diodes formed in an n-type silicon wafer. The diode array is produced by diffusion of p-type dopant through the openings of a silicon oxide film present on the surface. The oxide film separates the diode matrix and prevents the beam from striking the n-type material.

In operation, the diodes are reverse-biased by connecting the n-type sub-
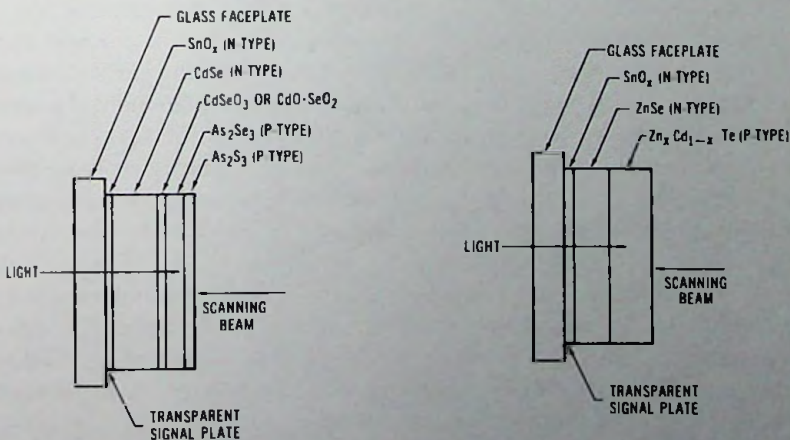
(K) Chalnicon/pasecon target.   **(L) Newvicon target.**

Camera tube targets.

strate to a positive potential and maintaining the scanned side at gun cathode potential (ground). Each diode constitutes an elemental storage capacitor. A charge image pattern is produced by focusing a high-energy (approximately 10-kV) photoelectron image on the diode array target. The photoelectrons produce a large number of hole-electron pairs for each primary electron by interacting with the silicon layer. The holes diffuse through the n region and pass through the depletion layer, discharging the storage capacitor. The video signal is generated by capacitive displacement current during the recharging of the elemental capacitors by the scanning beam.

The current gain of the target is determined by the energy required to produce a hole-electron pair production. Silicon requires an average energy of 3.5 eV for a hole-electron pair production. The overall efficiency is, however, reduced by recombination at the surface and in the bulk and through imperfect collection. Collection efficiencies as high as 85 to 90% have been reported.

The dark current of the target is 5 to 10 nA at normal operating bias voltage of 8 V. The maximum signal current is about 800 nA.

The *vidicon* (figure 17.1G) is the most simple camera tube as far as both construction and operation are concerned. It is also an inexpensive device. The target of the vidicon consists of a transparent signal plate overlaid by a photoconductive layer. In operation, the signal plate is connected to a positive potential and the scan side of the photoconductor is maintained at the gun cathode potential by a low-energy scanning beam.

The target may be considered to consist of many elemental capacitors parallel connected with elemental resistors. In dark the value of the elemental resistors is very high; thus the capacitors remain charged to the signal plate voltage. When a light image is focused on the target, however, photoconduction takes place, reducing the value of the elemental resistors in accordance with the light intensity distribution on the target. The conduction current discharges the elemental capacitors, giving rise to a charge image pattern. The video signal is generated by capacitive displacement current during the recharging of the elemental capacitors by the scanning beam.

The early types of vidicons suffered from the following problems: (1) high dark current causing signal loss and nonuniform background; (2) high capacitive and conductive lag as compared to other devices; and (3) relatively low luminous sensitivity. These problems were associated with the vidicon targets composed of antimony trisulfide (Sb_2S_3) material.

Better results may be obtained with the *lead oxide target vidicons* (figure 17.1H). The lead oxide target consists of a transparent, n-type conductivity signal plate overlaid by an intrinsic (i-type) conductivity type of lead oxide

layer which is covered by a thin layer of p-type conductivity lead oxide. In operation the signal plate is again connected to a positive potential (+ 50 V) and the p-type layer is maintained at ground potential by low-energy scanning. The barrier depletion layers formed between the n- and i-type materials and between the i-type and p-type materials prevent unwanted electrons and holes from entering the photoconductor. As a result the dark current of the photoconductor is extremely low. When a light image is focused on the target, electrons and holes are generated in the bulk of the photoconductor (in the i region) causing photoconduction. The conduction current produces a charge pattern which is read out by a low-energy scanning beam producing the video signal.

In addition to the low dark current due to the blocking contacts at the n-i and i-p interfaces, the lead oxide target also has satisfactory lag characteristics. The target voltage of 30 to 50 V applied across the target sweeps the electrons and the holes to their destination very rapidly before trapping or recombination can take place. As a result the target operates very fast and the photoconductive lag is at an acceptable level. The photoconductive layer of the lead oxide target is considerably thicker than the photoconductor of the vidicon. The thicker layer lowers the target capacitance, reducing the capacitive lag to a fairly low value.

In many respects comparable results to the lead-oxide target may be obtained by use of the *silicon diode array* as a photoconductive target (figure 17.1I). When a light image is focused on the silicon diode array target, hole-electron pairs are generated by the interaction of the light with the silicon layer. The holes diffuse through the n region and pass through the depletion layer, discharging the storage capacitors. The charge pattern produced this way is read out by a low-energy electron beam, charging the elemental capacitors and producing the video signal.

During the recent decade, development efforts produced three new vidicon targets as shown in figures 17.1J, 17.1K and 17.1L.

The *staticon* (figure 17.1J) announced by RCA in 1973 for color television has proved useful also for many other television camera applications. The staticon target is a multilayer structure selenium-arsenic-tellurium photoconductor. This photoconductor represents an improvement in resolution, stability, and reduction of optical flare over the lead oxide photoconductor. The spectral response of the staticon target extends from the blue region (400 nm) to beyond 800 nm. Although the quantum efficiency of the staticon photoconductor is somewhat less than the quantum efficiency of the lead oxide photoconductor in the wavelength bands of all three channels, it is yet comparable. The dark current of the staticon tube is very low, typically 0.5 nA, indicating the efficiency of the reversed-bias junction. Acceptable lag characteristics are obtained by use of bias lighting, in other words,

inserting a "dc" illumination level on top of the optical image which is later electrically subtracted from the signal. Bias lighting is particularly effective with staticon tubes because the photoconductor sensitivity is uniform.

The *chalnicon* (announced by Toshiba in 1972) and the *pasecon* (announced by Heiman in 1977) are panchromatic sensitive vidicons (see figure 17.1K). The spectral sensitivity range of these targets is in the wavelength range of 400 to 800 nm. These targets are much more sensitive than the lead-oxide target, having a quantum efficiency of greater than 90% in the wavelength range of 400 to 700 nm. The chalnicon target is a heterojunction construction with reverse bias capability for low dark current.

The *newicon* (figure 17.1L) was developed by Matsushita and announced in 1974. The spectral sensitivity range of the newicon extends from 400 nm to beyond 950 nm. The peak sensitivity is in the neighborhood of 700 nm and its quantum efficiency value approaches 100%.

Vidicons also found numerous applications for infrared imaging with special infrared radiation sensing photoconductors.

In the *pyroelectric vidicon* the radiation sensing layer is a single-crystal disk of triglycine sulphate $(NH_2CH_2COOH)_3 \cdot H_2SO_4$ abbreviated TGS, or triglycine fluoroberyllate $(CH_2NH_2COOH)_3 \cdot H_2BeF_4$, abbreviated TGFB. A semitransparent signal electrode is evaporated on the face of the single-crystal disk next to the infrared transmitting germanium faceplate. The pyroelectric crystal is mounted next to the germanium faceplate which is antireflection coated for maximum transmission in the 8- to 14-μm wavelength range.

The pyroelectric material senses only the temperature changes of a thermal image of a stationary scene. For televison purposes, therefore, the stationary radiation pattern must be modulated to make it detectable by the pyroelectric crystal. In a chopping-mode camera the thermal image of the scene is interrupted by a chopper wheel in synchronization with the electron beam scanning pattern. The desired temperature change is obtained by exposing the pyroelectric crystal target in alternate frames first to the scene radiation, then to the chopper blade. For a scene hotter than the chopper blade a positive charge pattern is produced on the radiation sensing crystal layer during the exposure to the scene and a negative charge pattern during the exposure to the chopper blade. The charge pattern is read from the target by a low-energy scanning electron beam. Since both a positive and also a negative charge pattern are present at the target in successive frames, for a continuous operation the target must be stabilized to a slightly higher potential than the thermionic cathode potential. This type of operation is usually called the *pedestal-current stabilized mode*, distinguishing it from the cathode-potential stabilized mode employed in conventional vidicons.

A pedestal-current stabilized-mode operation can be obtained by several methods. In one method a positive ion beam is produced by the scanning beam by ionization of a low-pressure hydrogen gas continuously maintained in the vidicon envelope. The positive ions charge the target positive. A stable operational potential is obtained when the ion beam just equals the current charge deposited by the scanning electron beam.

In another method the target is charged positive by means of secondary electron emission current during the horizontal retrace time. In this method the scanning electron beam energy is raised to about 80 V during the horizontal retrace time by pulsing the cathode to -80 V. At this energy level the secondary electron emission coefficient of the target is greater than unity, allowing the target to charge positive. Again a stable operating potential is obtained by balancing the charging and discharging currents of the scanning electron beam during the scan and retrace periods. It should be noted, however, that a linear retrace is necessary in order to avoid shading.

As far as performance is concerned, the responsivity of the Amperex S49xQB vidicon is reported as 5 μA/W. The sensitivity is 3 nA/°C in the scene. The maximum resolvable temperature is 0.3°C at 150 tv lines (tvl). The limiting resolution is 300 tvl. Lag after 50 ms is 25%.

The *IRicon*, a cooled lead-tellurium (PbTe) vidicon, was developed for infrared imaging in the wavelength range of up to 4 μm. The porous and amorphous lead-telluride target is deposited on a conducting sapphire faceplate by evaporation through an inert gas at low pressure. The operating temperature of the target is below 100 K, which is provided with liquid nitrogen cooling of the tube and lens housing. A 3.5-cm-format RCA vidicon provides 500 tvl resolution and scene temperature differences less than 1°C can be detected with f/1.2 optics.

17.3 Cathode-Potential Stabilized Emitron

The cathode-potential stabilized or CPS emitron is a medium sensitivity, storage-type camera tube used mostly for applications where the light level and the contrast range are adequately controlled for optimum picture transmission. For many years this device was successfully used in England primarily for studio broadcast service.

The CPS emitron operates on the photoemission produced charge integration principle. The charge integration occurs on the target consisting of a geometric array of capacitors formed by a mosaic-type semitransparent photocathode and by the transparent signal plate.

Figure 17.2 shows the cross section of the construction of the CPS emitron camera tube. The tube consists of a target for the conversion of the radiant image into an electrical charge pattern and of a low-velocity scanning beam
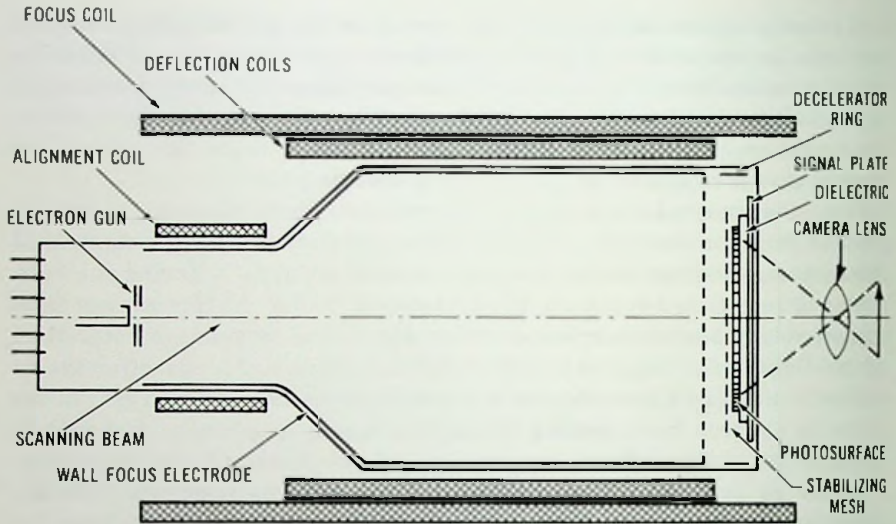
Fig. 17.2   Cross section of the CPS emitron camera.

section for reading out the stored image from the target as a time-based video signal.

The construction and the operation of the target are described in section 17.2. Briefly, when a light image is focused on the target, the photosensitive mosaic islands, due to photoemission, are charged during a frame time to a potential ranging from 0 to about +3 volts, depending on the light intensity distribution of the focused image. The positive charges integrated on the mosaic hold an equal charge of negative polarity on the signal plate. The video signal is generated by discharging the photoemissive islands to the ground potential by scanning the target with a low-velocity electron beam. The low-velocity beam deposits electrons on the target, because the secondary emission ratio δ is less than unity for beam energies corresponding to the target potential.

From the foregoing it is clear that the video signal consists of two components, opposite in sign. The first component is the useful, rapidly changing video signal corresponding to the imaged scene. The second component is due to the photocurrent continuously charging the capacitors. For steady illumination of the scene the second component is constant. If, however, the illumination changes during one frame period or between lines, a video signal distortion of the picture will appear, due to the unwanted signal component (second component) generated by the illumination change, unless the signal black level is properly clamped.

The scanning beam is produced by a low-velocity electron gun. The electron beam, after leaving the gun, is accelerated to the potential of wall focus electrode (about 300 V); it travels at this velocity through most of the length of the tube, then it is decelerated over a short distance in front of the mosaic to the potential of the mosaic surface. The electron beam is brought to sharp focus on the target after several loops by the action of the axial magnetic focus field and the accelerating and deceleration fields. Biaxial deflection of the electron beam is achieved by transverse magnetic fields produced by the horizontal and vertical deflection coils.

For a uniform discharge of the target the electron beam must land perpendicularly on the target. Perpendicular beam landing is obtained by the action of the deceleration lens formed by the short cylindrical electrode and the wall coating, and the mesh in front of the mosaic. The deceleration lens, immersed in the magnetic field, removes the tangential and the radial velocity components of the helical motion, thus causing the beam to land perpendicularly on the target. Because no current can pass through the dielectric, and the scanning beam lands perpendicularly on the target, no shading signals are generated.

The early version of this tube suffered from instability of the mosaic potential. At illumination levels sufficiently high to raise the potential of the mosaic above the level of greater secondary emission ratio δ than unity during one frame time, the tube ceased to operate in a correct manner until restabilized. The scanning beam drove the excessively illuminated areas progressively more positive by the secondary emission of the target, rather than negative. The same problem occurred by not fully discharging the target by the scanning beam during one frame time, causing charge accumulation and a runaway condition in few frame times. The serious fault of the early tube was corrected by introduction of a surface stabilizing fine-metal mesh in close proximity in front of the mosaic surface. By maintaining the mesh at $+15$ V with respect to the cathode, the tube is completely stable under excessive illumination.

The sensitivity of the CPS emitron is determined by the photosensitivity of the mosaic surface. In the early version of this tube the mosaic was composed of bismuth-silver-oxygen-cesium (S-10) photocathode. The S-10 cathode, however, was replaced by the more sensitive multialkali photocathode (S-20). Continuous surface multialkali cathodes have a luminous sensitivity in the range of 150 to 500 $\mu A/lm$, depending on the spectral response and manufacturing technology. The CPS emitron mosaic is produced by holding the surface stabilizing mesh in close contact with the dielectric during the photocathode fabrication. The photocathode, therefore, is produced only in the open areas of the mesh on the dielectric. Conse-

quently the photosensitivity of the mosaic will also be determined by the light transmission of the mesh.

The signal-to-noise ratio of the CPS emitron is determined by the magnitude of the target signal and by the video amplifier rms noise current. The amplifier rms noise current is about 1 nA. For a 100:1 (40-dB) peak-white signal-to-noise ratio, therefore, a 100-nA peak-white signal is necessary. With a 150-μA/lm target sensitivity and 15 sq cm target area, the target illumination E, for a 0.1-μA signal current is

$$E = \frac{0.1 \ \mu\text{A}}{150 \ \mu\text{A/lm} \times 15 \ \text{cm}^2} = 4.4 \times 10^{-5} \ \text{lm/cm}^2 \cong 0.048 \ \text{fc}. \quad (17.1)$$

The capacitance of the target is on the order of 1000 pF. For a uniform target illumination of 0.048 fc, the target capacitor accumulates the following charge during one frame time:

$$Q = 0.1 \ \mu\text{A} \times \frac{1}{30 \ \text{s}} = \frac{1}{3} \times 10^{-8} \ \text{C}. \quad (17.2)$$

The voltage across the capacitor becomes

$$V = \frac{Q}{C} = \frac{10 \ \text{C}}{3 \ \text{F}} \cong 3.3 \ \text{V}. \quad (17.3)$$

A larger peak voltage swing is not desirable because it would cause beam pulling and defocusing and consequently the loss of resolution. For larger signal currents than indicated above, an alternative course is to increase the capacitance of the target.

Because the signal, from any point of the target, is proportional to the illumination intensity, the device has a linear gamma. Therefore, in ordinary operations, gamma correction applied to the picture signal is necessary. Because of the charge integration during the frame time, all image movement, occurring between scans, is blurred.

17.4   The Image Orthicon

The image orthicon is a high-sensitivity, storage type camera tube used in television field and studio cameras. It is especially suitable for televising optical images with a wide range of light levels. While the CPS emitron, or its equivalent, the orthicon tube, operates best at medium light levels, the image orthicon extends the operating range toward lower illuminations by a factor of about 100. In addition, the image orthicon operates well at medium and high illumination levels.

The image orthicons are available in many different sizes and forms. There are 2-in (5.08-cm) types of compact, portable tv cameras, 3-in (7.62-cm) types for conventional image orthicon cameras, and 4.5-in (11.43-cm) types for tv pickup systems requiring exceptional resolution and signal-to-noise ratio.

The image orthicon, similar to the CPS emitron, operates on the charge integration principle. The charge integration is done on a bisided, continuous-surface dielectric, interacting on one side with the imaging electron beam and on the other side with the scanning beam. The imaging electron beam deposits a positive charge pattern on the target corresponding to the imaged scene. The scanning beam neutralizes the charge pattern by deposition of electrons and reads the charge pattern out as an amplitude modulation of the return beam.

The image orthicon tube consists of four main sections: (1) image section, (2) target, (3) scanning section, and (4) multiplier section. Refer to figure 17.3.

17.4.1 Image Tube Section

Essentially, the image tube section is a magnetically focused image tube having the target in its focal plane. It consists of a semitransparent photocathode deposited on the inside of the faceplate, an accelerating grid (grid no. 6) which, together with the photocathode and the target, establishes an axial electric field. Focusing is accomplished by the combined action of the electric and magnetic fields. The axial magnetic field is supplied by an external focusing coil. For uniform electric and magnetic fields the electron image of the cathode is erect and it has unity magnification at the target. For a nonuniform, graded magnetic field having a smaller value at the target than at the cathode, the cathode image is magnified.

The light image, being televised, is focused on the photocathode by an optical system. The photoelectrons generated by the light image are accelerated to about 500-eV energy by the electromagnetic lens. About 40% of the primary electrons are intercepted by the target mesh in front of the glass target. The remainder of electrons pass through the mesh apertures, striking the glass target and causing secondary electrons to be emitted. The secondary electrons are collected by the target mesh, which is held at about +2-V potential with respect to the gun cathode potential. The secondary-electron emission from the glass target produces a positive charge pattern on the target corresponding to the imaged scene.

17.4.2 Scanning Section

The positive charge pattern, being present on the image side of the glass target, is capacitively coupled to the scanning side by the elemental capac-

ACCELERATOR GRID NO.6 — PHOTOCATHODE — HORIZONTAL & VERTICAL DEFLECTING COILS — DECELERATOR GRID NO.5 — FOCUSING COIL — GRID NO.4 — ALIGNMENT COIL — GRID NO.2 & DYNODE NO.1 — GRID NO.3 — FIVE STAGE MULTIPLIER — TELEVISED SCENE — TARGET — SCANNING BEAM — RETURN BEAM — CAMERA LENS — FIELD MESH — SUPPRESSOR GRID — ELECTRON GUN

IMAGE SECTION — SCANNING SECTION — MULTIPLIER SECTION
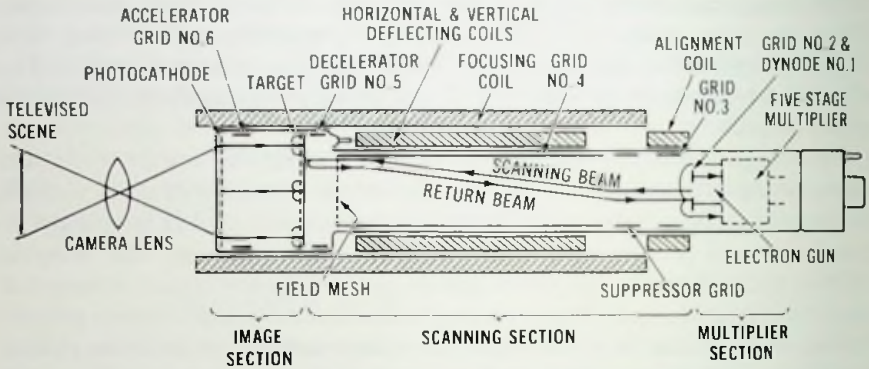
(A) The image section has approximately 0.85 magnification, and the field mesh is positioned on the target end of the grid no. 4 cylinder.

ACCELERATOR GRID NO.6 — DECELERATOR GRID NO.5 — ALIGNMENT COIL — FIVE STAGE ELECTRON MULTIPLIER — "PANCAKE" FOCUSING COIL (SEE NOTE) — FOCUSING COIL — TARGET — HORIZONTAL & VERTICAL DEFLECTING COILS — GRID NO.3 — GRID NO.2 & DYNODE NO.1 — TELEVISED SCENE — SCANNING BEAM — RETURN BEAM — CAMERA LENS — PHOTOCATHODE — FIELD MESH — ENVELOPE TERMINAL — GRID NO.4 INTERNAL CONDUCTIVE COATING — ELECTRON GUN

IMAGE SECTION — SCANNING SECTION — MULTIPLIER SECTION

NOTE: "PANCAKE FOCUSING COIL IS CONNECTED IN SERIES AIDING WITH MAIN FOCUSING COIL — (WITH SEPARATELY ADJUSTABLE FIELD MESH)

(B) The nonuniform graded magnetic field produced by the focusing coils magnifies the photocathode image approximately 1.5 times.

Fig. 17.3 Cross section of image orthicon camera tubes and associated components.

itors existing between the two sides of the glass film. In the process of video signal generation the positive charge pattern is neutralized by the scanning beam by deposition of an equal amount of negative charge on each elemental capacitor, discharging the scanning side to the gun cathode potential and charging the target capacitors. The conductivity of the glass is so chosen

that in one frame time ($1/30$ s) the charge can leak through the glass, but only a negligible amount can spread transversely. The video signal is derived as an amplitude modulation of the scanning beam. On each elemental capacitor the scanning beam deposits just a sufficient amount of negative charge to drive the target surface to the ground potential. Since the target cannot accept more electrons without becoming negative, the fraction of the electrons not deposited is repelled as a return beam, which is amplitude modulated by absorption of electrons at the target.

The scanning beam is produced by a low-velocity electron gun consisting of a thermionic cathode, a control grid (grid no. 1), and an accelerating grid (grid no. 2). The beam is brought to sharp focus on the target after several loops by the magnetic field of the external focusing coil and by the potential of the wall focus electrode (grid no. 4).

Biaxial deflection of the electron beam is achieved by transverse magnetic fields produced by external deflection coils. See figure 17.4.

Alignment of the beam is accomplished by a transverse magnetic field produced by external coils located at the gun end of the focusing coil.

The scanning beam is made to approach the target perpendicularly by proper adjustment of the decelerating ring (grid no. 5) and field mesh potentials. These electrodes and the wall coating constitute the deceleration lens, which, immersed in the magnetic field, removes the unwanted tangential and radial velocity components of the helical motion.

The field mesh is a high electron transmission fine-metal mesh placed in front of the target to increase the strength and improve the uniformity of the decelerating field at the target. The uniform decelerating field over the scanned area causes the beam electrons to land perpendicularly at all points on the target. The high field also prevents the charge pattern on the target from bending the beam away from its proper trajectory, thus allowing the tube to be operated at high values of target voltage. High target voltage thereby improves the signal-to-noise ratio. Finally, the field mesh defocuses the return beam, ensuring that the texture of the first dynode does not appear in the background of the picture.

17.4.3 Electron-Multiplier Section

The purpose of electron multiplication in the image orthicon is to raise the level of the small signal that modulates the returned beam sufficiently above the noise level of the first stage of the video amplifier by a relatively noiseless process. For this reason the return beam is directed to the first dynode of a five-stage electrostatically focused multiplier. The first dynode is an apertured disk at the end of the electron gun. The return beam returns along nearly the same path as it followed on its outward journey. However, since the transit time of an electron from the gun to the target and back is
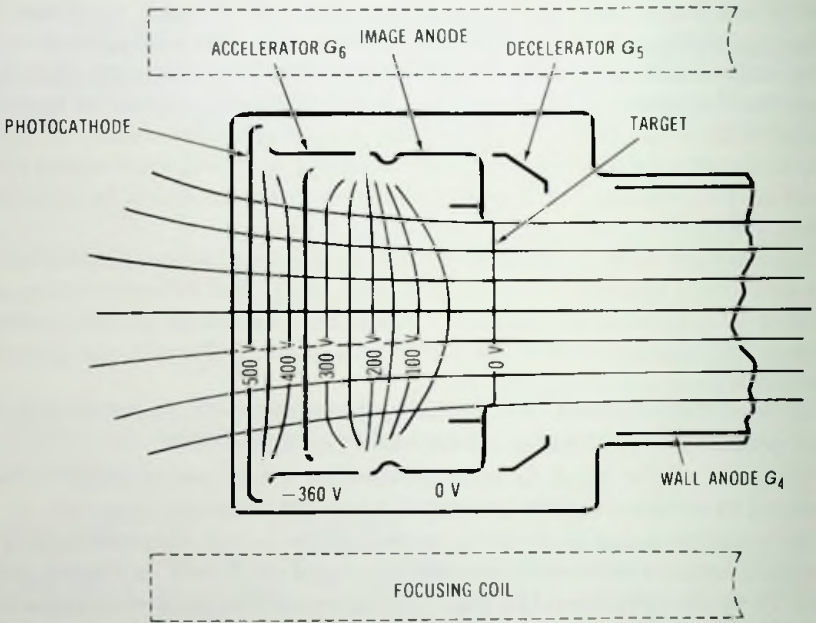
(A) Demagnifying lens.
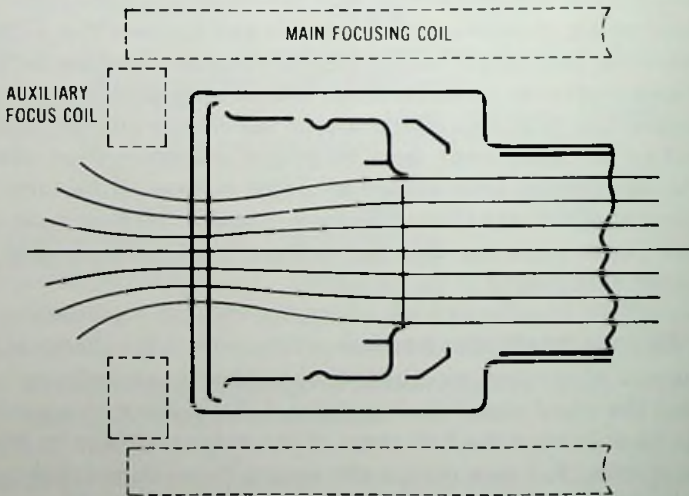
(B) Magnifying lens.

Fig. 17.4   Principle of electronic image magnification in the image
orthicon tubes; the photoelectrons follow the magnetic
lines of force.

in the order of 0.1 μs, the return beam does not pass through the first dynode aperture but strikes the dynode surface. The surface of the first dynode is an efficient secondary-electron emitter and it is operated at about 300 V positive with respect to the target. From the first dynode the secondary electrons are directed to a pinwheel type second dynode by the electric field configuration produced by the potential difference between the first and second dynodes and the G_3 electrode. The secondary electrons from the second dynode pass to the third dynode. A coarse screen between the second and the third dynode and connected to the third dynode potential prevents the field of the second dynode from suppressing the emission from the third dynode. The fourth and fifth stage of the multiplier is similar to the screen pinwheel combination of the third dynode.

A frequently used dynode material is the silver-magnesium alloy containing approximately 2% of magnesium. Oxidation by low-pressure water vapor produces a magnesium oxide layer on the surface which is an efficient and stable secondary electron emitter.

The multiplier section amplifies the video signal more than 500 times without significant reduction of the signal-to-noise ratio established by the random noise of the electronic beam.

17.4.4 Targets

The first target material used in image orthicon was an optical-quality soda lime glass film about 5 μm thick. This material, however, had serious limitations as far as performance is concerned due to the low secondary emission ratio and lack of relatively high lateral resistivity needed for high-resolution systems. In addition, the life of this type of target is limited by the ionic conduction through the glass sheet largely by sodium ions. In time a sufficient amount of sodium is transferred from the front surface of the glass plate to the back surface to change its conductivity and the secondary emission coefficient. This change causes image persistence, thus limiting the useful life of the tube.

The magnesium oxide target has a high secondary emission coefficient, about four times that of the glass. It has the high lateral resistivity needed for high resolution and it has a long life. The magnesium oxide target, however, suffers from noise and graininess at high light levels, while its performance at low and medium light levels is superior to the glass.

The electronically conducting glass target overcame the limitations (life problem and sticking pictures) of the early ionic conduction glass. This target provides high-quality pictures at medium and high light levels and it has a long life. The secondary emission coefficient and the resolution of the electronically conducting glass are lower than those of magnesium oxide.

17.4.5 Light Transfer Characteristics

The light transfer characteristic of the image orthicon has a rather complex nature. It is determined primarily by such factors as the target to target-mesh spacing and voltage, the secondary emission properties of the target material, and electron redistribution effects. Figure 17.5 shows the light transfer characteristics of the close and wide spaced tubes. In the close spaced tube the mesh to target spacing is 0.001 in (25.4 μm). The wide spaced tube has a 0.0025- to 0.003-in (63.5- to 76.2-μm) mesh to target spacing. The difference between the light transfer characteristics of the close and wide spaced tubes is caused by the difference of the mesh to target capacitance. Beginning with low light levels the signal rises linearly with illumination until intermediate light levels are reached. Beyond intermediate levels the light transfer characteristic has an almost flat portion, corresponding to signal saturation. The knee of the transfer characteristics corresponds to a target potential charged up to the mesh potential.

The special and complex light transfer characteristics of the image orthicon may be explained by consideration of the charge buildup mechanism on the target. At low light levels the potential rise of the target surface is small. Consequently most of the secondary electrons are captured by the target mesh, and the target surface is charged almost linearly with the light flux. A small fraction of secondary electrons having a high initial velocity
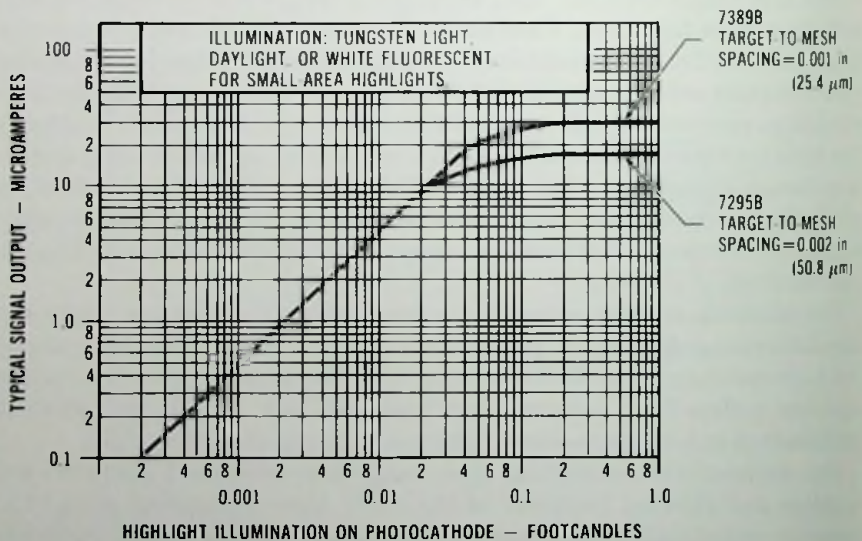
Fig. 17.5   Light transfer characteristic of wide and close spaced image orthicon tubes.

can pass through the mesh openings and enter the retarding field on the photocathode side of the mesh. After traveling a short distance, however, these electrons are forced back by the retarding field to the target at varying distances from their points of origin causing the electron redistribution phenomenon. This effect can show up as a spurious signal under certain circumstances by transferring negative charges from the positively charged areas, corresponding to the illuminated areas, to the neighboring unilluminated areas of the image. In the linear portion of the light transfer curve the electron redistribution effect, however, does not cause a serious problem.

At light levels approaching the knee, and beyond the knee, the target potential approaches the mesh potential and the capture of the secondary electrons by the mesh becomes very inefficient. Because no atttracting force is present between the target and the mesh to collect the secondary electrons, the electrons are free to travel past the mesh into the negative field and are redistributed over the adjacent areas. The returned secondary electrons, on one hand, stabilize the target surface to the mesh potential; on the other hand, if their velocity is high enough to cause these electrons to land outside of the highlight area from which they originate, they discharge the adjacent areas and cause black borders around the bright area. If the secondary electrons have a sufficient energy to produce a positive charge on landing on the target, a white halo around a black border will be present. A small fraction of the secondary electrons are high-energy reflected electrons. The reflected electrons have enough energy to return to the vicinity of the photosurface and then turn around and travel to the target. These electrons are fairly well focused as a ghost image on the target. Ghost images, however, can be brought to coincidence with the picture by proper image section design.

As far as performance is concerned two types of operation may be considered: (1) operation on the linear portion of the characteristic, and (2) operation with the highlights above the knee of the characteristic.

The tube performs satisfactorily on the linear portion up to the knee. The resolution, picture gradation, and contrast range are good. The picture has a photographic quality, i.e., there are no exaggerated brightness distortions, black borders or white halos. The picture, however, is unnatural because it is not corrected for the third-power response of the picture tube.

Operation with the highlights above the knee of the light transfer characteristic produces a picture on the monitor which is close in tones to the original scene. When the camera tube is operated with twice the amount of highlights necessary to operate the tube at the knee, a light transfer characteristic is produced that is nearly complementary to the picture tube response. The average gamma, for this case, is 0.5 to 0.6. Operation above the knee of the light transfer characteristic has advantages and disadvantages.

If the highlights are greatly over the knee, an excessive amount of black border may appear around white objects due to electron redistribution. A moderate amount of electron redistribution, however, makes a picture appear somewhat sharper and clearer.

The value of target voltage is one of the influential parameters affecting the picture characteristics. The useful target voltage is in the range of 1.5 to 3 V above the target cutoff point. Target voltages lower than 1.5 V produce muddy and noisy pictures. High target voltage produces a long linear characteristic and a high signal-to-noise ratio. It also produces exaggerated edging effects and poor resolution. The field-mesh type tube permits operation at a somewhat higher target voltage without edging effects.

17.4.6 Resolution

Typical square-wave response curves of image orthicon tubes are shown in figure 17.6. These responses were measured with highlights one stop
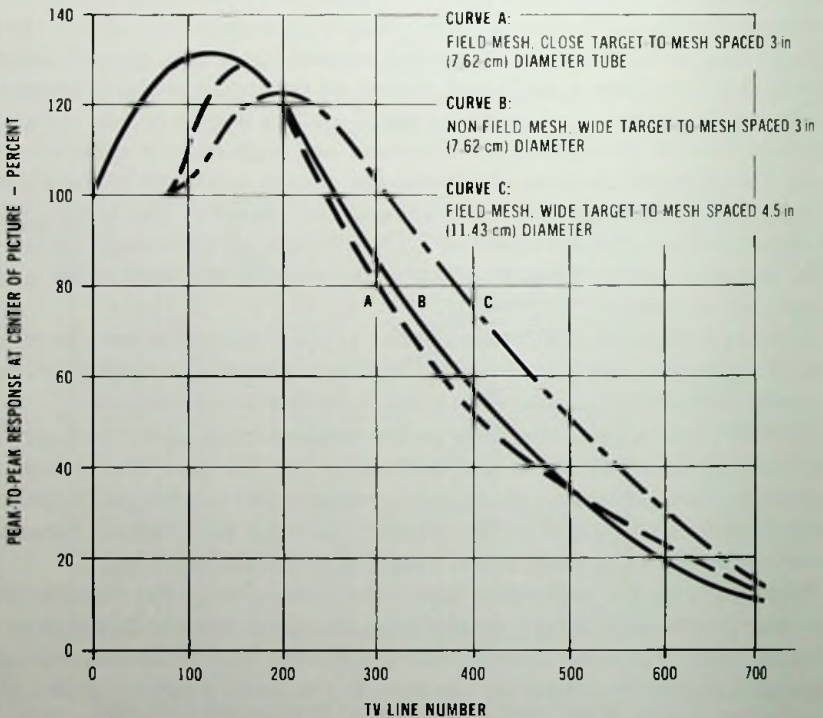
Fig. 17.6 **Typical square-wave response curves of image orthicon tubes.**

above the knee of light transfer characteristics in a system having a 10-MHz bandwidth.

17.4.7   Photocathodes

The light energy is converted to electrons by the photocathode. The type of photocathode used determines the spectral response of image orthicon and it also determines the photosensitivity. Figure 17.7 shows typical spectral response curves of photocathodes used in image orthicons.

17.4.8   Signal-to-Noise Ratio

The signal-to-noise ratio of different types of image orthicons is in the range of 30 to 39.5 dB, depending on the mesh-to-target capacitance, target voltage and type of tube, etc. The upper limit is obtained in the 4.5-in (11.43-cm) high-capacitance, high-quality image orthicons. The signal-to-noise ratio is measured with a noise equivalent bandwidth of 4.5 MHz. Peak signal output is measured with respect to picture black. The video gain controls are adjusted to obtain a specific peak-to-peak signal current (or voltage)—usually from a test pattern highlight. The rms noise current (or voltage) is then measured by capping the lens. In this way, readings are obtained under the circumstances of full return-beam maximum noise conditions. A cutaway view of the image orthicon is shown in figure 17.8.
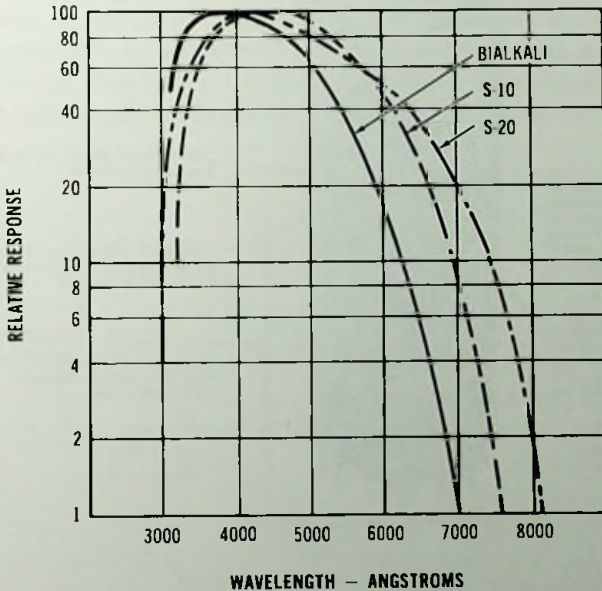
Fig. 17.7   Typical spectral response curves.

"ANTI-GHOST" IMAGE SECTION—A specially designed image section used in certain RCA Image Orthicons. Provides proper geometry and suppresses highlight flare or "ghost" that occurs when field-mesh image-orthicon types are operated above the knee.

PRECISION CONSTRUCTION—Employed in the manufacture of certain RCA Image Orthicons. All tube parts including the envelope are precision made, precision spaced, and precision aligned. Provides tubes having excellent registration capability and uniformity of tube characteristics.

FIELD-MESH — A fine mesh screen employed in certain image orthicons which causes the scanning beam to approach the target perpendicularly at all points and prevents "beam-bending" due to charge pattern on the target. Provides a picture that is relatively free of unwanted bright edges or "overshoots" at the boundary of brightly illuminated portions of a scene. Improves dynamic registration in color pickup applications and provides superior picture sharpness.

PHOTOCATHODES—Individually processed in each tube to provide maximum sensitivity and uniformity.

OPTICAL-GLASS FACE-PLATES — Made of the finest optical-quality glass to eliminate optical distortion. Image Orthicons having fiber-optics faceplates can also be provided.

TARGETS — Made of electronically conducting glass to provide long life, stable sensitivity, and maximum resistance to raster burn in, semiconductive material for high gain, and specially selected blemish-free optical glass.

MICROMESH—A delicate, precision, electroformed mesh having 750 openings per linear inch. Prevents mesh-pattern and moiré effects without the need for defocusing. Improves picture detail when used with aperture-correction to provide full response.

SUPER DYNODE — The first dynode of the multiplier section in non-field mesh tubes designed to provide freedom from grainy background and to minimize dynode burn.

HIGH-GAIN DYNODE — The first dynode of the multiplier section in field-mesh tubes designed to increase the output signal-to-noise ratio and signal-output level.
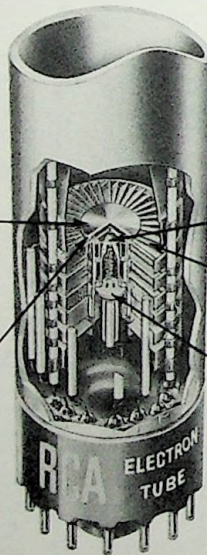
CONTROL GRIDS—Gold-plated to reduce thermionic emission.

DYNODES — Precision formed, spaced, and aligned to assure uniformity of signal gain in the multiplier section.

X-RADIATION INSPECTED GUN ASSEMBLY—Assures accurate alignment of parts and spacing of electrodes.

Fig. 17.8 Cutaway view of image orthicon tube. (*Courtesy RCA*)

17.5   Image Isocon

The image isocon was developed with the purpose of improving the signal-to-noise ratio of the image orthicon tube. In many aspects the image isocon is similar to the image orthicon tube. As far as operation, construction, and performance are concerned, however, there are some fundamental differences between the two tubes. The differences arise mainly from the beam separation techniques employed in this tube.

The most significant source of noise in the image orthicon is the shot noise associated with the current in the return beam. Because of the reversed polarity of the signal, the return beam current is maximum in the dark, causing the noise to appear most prominently in the darker parts of the picture. An additional cause of beam noise is the low percentage of return beam modulation (25 to 30%) obtainable in usual operations. The aim in the development of the image isocon, therefore, was the elimination of the beam noise component by separation of unwanted parts of the return beam.

The return beam consists of scattered and specularly reflected electrons as shown in figure 17.9. In the image orthicon the entire return beam is directed into the electron multiplier. In the image isocon, however, the reflected electrons are isolated and only the scattered electrons are received by the electron multiplier. The scattered portion of the return beam is proportional to the charge on the target. Because of the near to unity secondary emission ratio at the target, for each electron entering the target to neutralize the positive charge several electrons are scattered, giving rise to a gain mechanism. The closer the secondary emission ratio is to unity, the greater the scatter gain. Figure 17.10 shows the comparison of the image

$$I_P = I_C + I_R + I_S$$
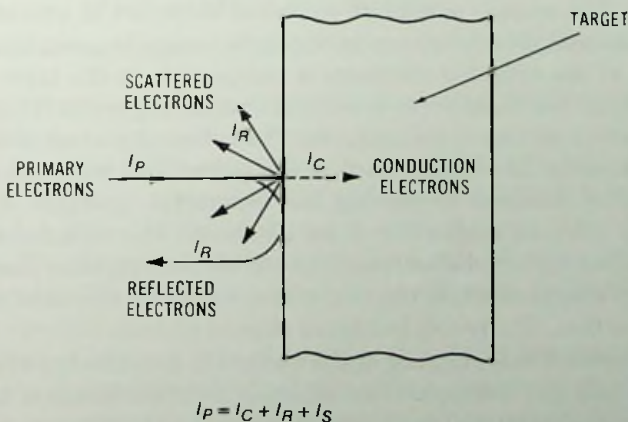
Fig. 17.9   Distribution of the primary electron beam.
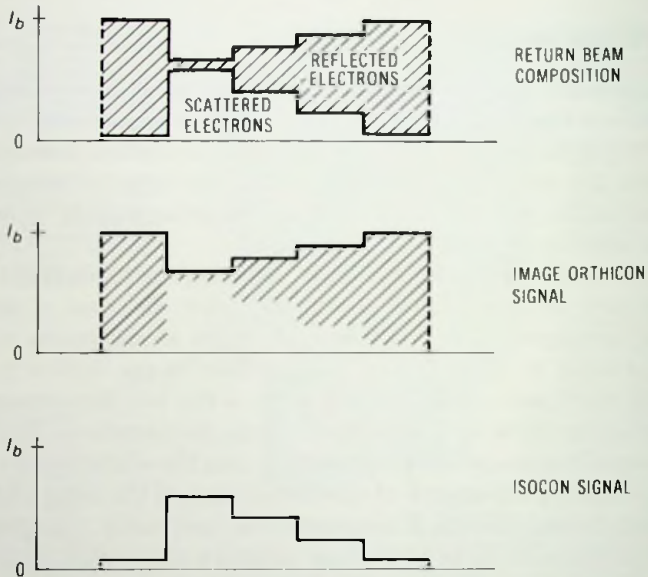
Fig. 17.10   Image orthicon and isocon signals.

orthicon and the isocon signals. The image isocon signal is maximum for highlights and minimum for dark areas. The image isocon signal is also greater than the image orthicon signal, thus giving a greater percentage modulation of the total return beam.

Because of the difference in the energy distribution between the reflected and scattered electrons, the reflected electrons can be separated from the return beam. The energy spread of scattered electrons is greatest in the highlight areas and it is minimum in the dark areas. The maximum transverse energy of the reflected electrons is comparable to the transverse energy of scattered electrons from low-signal areas. Figure 17.11 shows the return-beam cross section at an antinode. The reflected portion of the return beam is situated in the center part of the beam. The reflected electrons therefore can be removed by placing the separation aperture of the first dynode of the electron multiplier at an antinode. The reflected electrons, together with the scattered electrons from the dark areas, thus pass through the separation aperture while the rest of the scattered electrons strike the first dynode surface. The result is a black clipped picture.

In order to avoid black clipping of the picture it is necessary to move the reflected electrons and the separation aperture from the center of the return beam into a radial position, as shown in figure 17.11. This can be accomplished by providing the reflected electrons with the same transverse energy
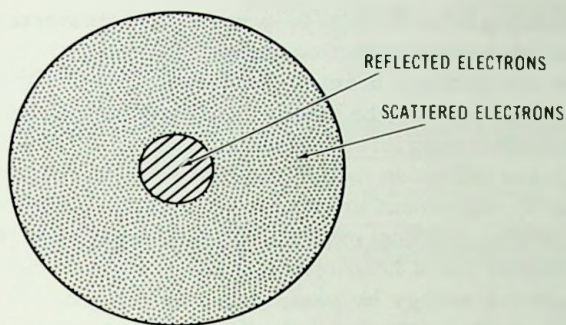
(A) **Return beam of image isocon.**
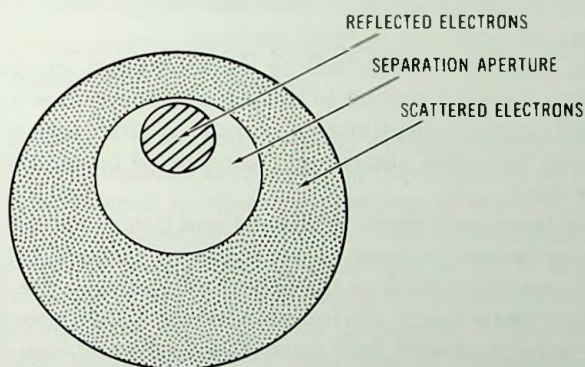
(B) **Reflected electrons are moved from the center over the
separated aperture of the first dynode.**

Fig. 17.11 Cross section of the return electron beam at an antinode.

the scattered electrons have at a particular radial position within the scattered beam.

In practice, the beam separation is done with two sets of vertical and horizontal deflection plates (total of eight plates). The first set of horizontal and vertical plates is placed at a $\lambda/4$ axial distance from the separation aperture. The second set of plates is at $3\lambda/4$ axial distance from the separation aperture. The separation aperture is $\lambda/2$ axial distance from the gun limiting aperture.

The effect of the two sets of horizontal deflection plates (misalignment plates) is to provide the primary beam with a transverse energy component. Since the two sets of horizontal deflection plates are at $\lambda/2$ axial distance from each other, balanced dc voltages of reverse polarity are applied to the

two sets of deflection plates in order to increase the transverse energy of the primary beam at each set of deflection plates.

Let us follow the primary beam on its journey toward the target. The primary beam emerging from the limiting aperture of the gun, after passing through the separation aperture, gains a transverse velocity component by passing through the deflection field of the first set of horizontal plates. The transverse velocity component and the axial magnetic field cause the primary beam to move on a helical path. After a half-loop period ($\lambda/2$) the beam arrives at the second set of horizontal deflection plates, where it gains an additional transverse energy by passing through a deflection field which has a polarity opposite to that of deflection fields of the first plates. The primary beam then spirals toward the target through the magnetic deflection fields and lands on the target with a small inclination to the normal of the target. In usual operations the transverse energy of the landing beam is not greater than about 0.7 eV to avoid shading.

The reflected beam on its way back to the separation aperture spirals in the opposite direction with respect to the primary beam. Due to the opposite direction spiraling, the helical motion is removed from the reflected beam by the horizontal deflection plates and the reflected beam is aligned at the separation aperture.

The scattered beam as a whole is aligned and it does not contain a transverse energy component common to all scattered electrons. Therefore the scattered electrons travel back to the deflection plates on the same path as an aligned return beam has in the image orthicon. The horizontal deflection fields and the axial magnetic field cause the scattered beam to move on a helical path. The axial positioning of deflection plates from the separation aperture is designed to yield the greatest separation of the scattered beam from the reflected beam.

To the vertical sets of deflection plates, or steering plates, a balanced dc voltage of the same magnitude and polarity is applied. The effect of the same polarity vertical deflection fields is to produce a radial displacement of the beams in the horizontal direction by the production of a helical motion over an axial distance of $\lambda/2$ between the two sets of deflection plates. Since the vertical deflection fields are of same polarity, the transverse energy introduced by one set of plates is removed by the other set and the net result is a horizontally displaced aligned beam. The steering plates are used to properly position the scattered beam over the separation aperture.

Figure 17.12 shows the cross section of the image isocon camera. With the exception of special accessories required for proper beam separation, it is similar to the image orthicon. The tube consists of an image section, target, scanning and beam separation section, and an electron multiplier section. Focusing is done by a long magnetic focus coil supplying a field strength of
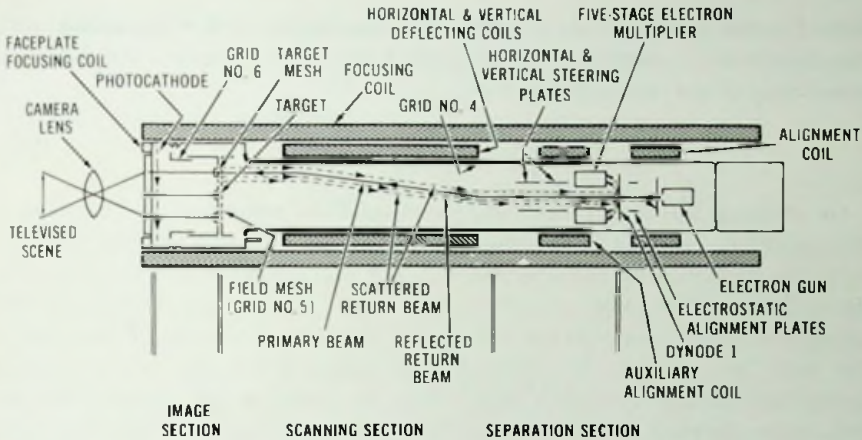
Fig. 17.12   **Cross section of the image isocon camera tube and associated components.**

about 70 G. Deflection is done by specially designed deflection coils suitable to accommodate the uniform beam landing requirements on the target.

As far as performance is concerned, because of the absence of reflected electrons in the video signal the signal-to-noise ratio is greater in the dark regions of the picture than in the highlight regions. In the highlight regions the noise level of the image isocon is nearly the same as the image orthicon has. The signal-to-noise ratio, however, is superior in the image isocon because the isocon signal is greater than that of the image orthicon. Also, because of the absence of beam noise the signal-to-noise ratio in the dark areas of image isocon is superior to that of the image orthicon. Sensitivity, light transfer characteristics, and resolution of the image isocon are similar to those of image orthicon.

17.6   Signal-to-Noise Ratio of the Image Orthicon and Isocon Tubes

A fundamental source of noise in electronic imaging is the camera tube itself in which the noise is generated as a by-product of the imaging process. Consider the noise in the image orthicon tube. The noise in the image orthicon is generated by the statistical fluctuation of the signal and scanning beam currents. The fraction TI of the photocathode current that strikes the target of the image orthicon is associated with the following shot noise current I_{ni}:

$$I_{ni} = \sqrt{2e\Delta f TI}. \tag{17.4}$$

Here I is the photocathode current, T is the target mesh transmission, e is the charge of an electron, and Δf is the bandwidth in hertz. The signal-to-noise ratio of the incident beam is

$$(\text{snr})_i = \frac{IT}{\sqrt{2e\Delta f TI}} = \sqrt{\frac{IT}{2e\Delta f}}. \tag{17.5}$$

On striking the target, both the signal and the noise are multiplied by δ, the secondary-electron emission ratio of the target. Due to the fact, however, that the incident current charges and the secondary-emission current discharges the target-mesh capacitor, only a $(\delta - 1)$ portion of the amplified signal and noise is stored on the target. Because of the rms fluctuation of the amplified current that flows to the target mesh, an additional noise component having a value $\sqrt{2e\Delta f \delta TI}$ is also stored on the target. The total rms noise current I_{nt} stored on the target is the sum of the two noise components:

$$I_{nt} = \sqrt{2e\Delta f \delta TI + 2e\Delta f TI(\delta - 1)^2} = \sqrt{2e\Delta f TI(\delta^2 - \delta + 1)}. \tag{17.6}$$

The signal current stored on the target is

$$I_{st} = (\delta - 1)\,TI. \tag{17.7}$$

In order to neutralize the stored charge on the target a scanning beam current having an amplitude given by equation 17.4 must land on the target. The energy of the scanning beam, striking the target, is in the range of zero to a few volts. In this energy range the secondary-electron emission ratio of the electrons from the usual targets is only a few tenths below unity (0.7 to 0.8). Therefore the scanning beam, depending on the secondary-electron emission ratio, must be several times greater than I_{st} to be able to neutralize the stored charge. By defining the beam modulation as the ratio of the signal current to the scanning beam current, the value of the scanning beam I_b becomes

$$I_b = \frac{I_{st}}{m} = \frac{(\delta - 1)TI}{m}. \tag{17.8}$$

The rms noise associated with the beam current is

$$I_{nb} = \sqrt{2e\Delta f(\delta - 1)\,TI/m}. \tag{17.9}$$

The total noise I_{no} at the entrance of the multiplier may be obtained by summing the noise stored on the target and the beam noise. In the field mesh type of image orthicons the field mesh attenuates both the signal and the noise. With field mesh transmission T' then I_{no} is

$$I_{no} = T'\sqrt{2e\Delta f TI\,\{(\delta - 1)/m + \delta/T' + \delta^2 - 2\delta + 1\}}. \tag{17.10}$$

The signal current I_{so} at the entrance of the multiplier is

$$I_{so} = (\delta - 1)T'TI. \tag{17.11}$$

The signal-to-noise ratio is

$$(\text{snr})_o = \frac{I_{so}}{I_{no}} = \sqrt{\frac{I}{2e\Delta f}} \sqrt{\frac{T(\delta - 1)}{\delta - 1 + \delta/T'(\delta - 1) + 1/m}}. \tag{17.12}$$

In the image isocon the signal-to-noise ratio is improved by elimination of the beam noise component by use of scattered electrons with gain mechanism to transmit the stored charge from the target to the multiplier. As pointed out by Weimer, the return beam consists of scattered and reflected electrons. The reflected electrons, in the image isocon, are isolated. The number of scattered electrons is proportional to the charge on the target. Because of the near-unity secondary emission ratio at the target, for each electron which lands on the target several electrons are scattered, giving rise to a gain mechanism. In practice, it is usually difficult to isolate completely the reflected current. Therefore a small dark current I_o may exist at the entrance of the multiplier. The rms noise associated with I_o is

$$I'_{nb} = \sqrt{2e\Delta f I_0}. \tag{17.13}$$

By omitting the $(\delta - 1)/m$ member in equation 17.8 the amplified target noise at the entrance of the multiplier becomes

$$I'_{nt} = T'\alpha\sqrt{2e\Delta f TI(\delta/T' + \delta^2 + 2\delta + 1)}. \tag{17.14}$$

Here α is the scatter gain factor. The noise component of scattered electrons is

$$I_{ns} = \sqrt{2e\Delta f T'T \alpha (\delta - 1) I}. \tag{17.15}$$

The total rms noise current at the entrance of the multiplier is the sum of equations 17.13, 17.14 and 17.15:

$$I'_{no} = T'\alpha\sqrt{2e\Delta f TI[\delta/T' + \delta^2 - 2\delta + 1 + (\delta - 1)(1 - \mu)/T'\alpha\mu + (\delta - 1)/T'\alpha]}. \tag{17.16}$$

Here μ is the beam modulation, which is defined as

$$\mu = \frac{I'_s}{I'_s + I_0}. \tag{17.17}$$

and

$$I_s = T'T \alpha(\delta - 1) I. \tag{17.18}$$

The signal-to-noise ratio is

$$(\text{snr})' = \frac{I'_s}{I'_{no}}$$

$$= \sqrt{\frac{I}{2e\Delta f}} \sqrt{\frac{T(\delta - 1)}{\delta - 1 + \delta/T'(\delta - 1) + (1 - \mu)/T'\alpha\mu + 1/T'\alpha}}. \quad (17.19)$$

The noise improvement of the image isocon, as compared with the image orthicon, may be obtained by dividing the signal-to-noise ratio of the image isocon by the signal-to-noise ratio of the image orthicon. The ratio is

$$R = \sqrt{\frac{\delta - 1 + \delta/T'(\delta - 1) + 1/m}{\delta - 1 + \delta/T'(\delta - 1) + (1 - \mu)/T'\alpha\mu + 1/T'\alpha}}. \quad (17.20)$$

By substitution of typical values for the different parameters in equation 17.20 ($\delta = 4$, $m = 0.25$, $T' = 0.6$, $\mu = 0.8$, $\alpha = 3$), 1.25 is obtained for the value of R. In other words, the image isocon may have about 25% better signal-to-noise ratio than the image orthicon has. It may readily be seen from equation 17.20 that in the dark areas of the picture where m is smaller than 0.1 the improvement may be far greater.

The signal-to-noise ratio given by equations 17.12 and 17.19 is slightly reduced by the noise generated in the electron multiplier. It can be shown that the output signal-to-noise ratio of an electron multiplier is related to the input signal-to-noise ratio in the following manner:

$$(\text{snr})_{\text{out}} = (\text{snr})_{\text{in}}\sqrt{1 - \frac{1}{\delta_d}}. \quad (17.21)$$

Here δ_d is the secondary emission ratio per dynode stage.

In order to prove the validity of equation 17.21, consider an incident electron beam I striking the first multiplier dynode. The rms noise associated with I is $\sqrt{2e\Delta fI}$ and the input signal-to-noise ratio is $\sqrt{I}/\sqrt{2e\Delta fI}$. At the first dynode both the signal and the noise are multiplied by the secondary emission ratio δ so that the signal becomes δI. The noise, however, has an additional component due to the rms fluctuation of the multiplier signal current. By summing the noise components the rms noise current after the first dynode multiplication is

$$I_{n_1} = \sqrt{(\delta\sqrt{2e\Delta fI})^2 + (\sqrt{2e\Delta fI\delta})^2} = \sqrt{2e\Delta f\delta(\delta + 1)}. \quad (17.22)$$

The signal-to-noise ratio is

$$(\text{snr})_1 = \frac{\delta I}{I_{n_1}} = \sqrt{\frac{I}{2e\Delta f}} \sqrt{\frac{\delta}{\delta + 1}}. \quad (17.23)$$

Repeating the same process on the second dynode the signal becomes $\delta^2 I$ and the noise is

$$I_{n2} = \sqrt{[\delta\sqrt{2e\Delta fI\delta(\delta + 1)}]^2 + (\sqrt{2e\Delta fI\delta^2})^2}$$
$$= \sqrt{2e\Delta fI\delta^2[\delta(\delta + 1) + 1]}. \qquad (17.24)$$

The signal-to-noise ratio after the second dynode multiplication is

$$(snr)_2 = \frac{\delta^2 I}{I_{n2}} = \sqrt{\frac{I}{2e\Delta f}} \sqrt{\frac{\delta^2}{\delta^2 + \delta + 1}} = (snr)_{in} \sqrt{\frac{\delta^2}{\delta^2 + \delta + 1}}. \qquad (17.25)$$

Continuing this process for n dynodes, at the output the signal-to-noise ratio becomes

$$(snr)_{out} = (snr)_{in} \sqrt{\frac{\delta^n}{\delta^n + \delta^{n-1} + \delta^{n-2} + \cdots + \delta + 1}}. \qquad (17.26)$$

But

$$\sqrt{\delta^n + \delta^{n-1} + \delta^{n-2} + \cdots + \delta + 1} = \sqrt{\frac{\delta^{n+1} - 1}{\delta - 1}}. \qquad (17.27)$$

Therefore

$$(snr)_{out} = (snr)_{in} \sqrt{\frac{\delta^n(\delta - 1)}{\delta^{n+1} - 1}} \cong (snr)_{in} \sqrt{1 - \frac{1}{\delta}}. \qquad (17.28)$$

17.7 Secondary Electron Conduction Camera Tube

The secondary electron conduction (SEC) tube is a high-sensitivity, wide-dynamic-range, storage-type camera tube used for nighttime outdoor broadcasting at normal stadium levels of illumination and for scientific and industrial applications. The most outstanding feature of this tube is the secondary electron conduction target which has high current gain, good storage properties and low lag, and it enables this tube to operate at low light levels. Good-quality low light level operation was made possible by the noise-free multiplication of the photocathode current by the SEC target, and by the high output signal current available from the high-capacitance target (about 2000-pF target capacitance). The high output current permits the signal to ride over the video amplifier noise to much lower light levels than can be done with the vidicon or with the image orthicon tubes. The good storage characteristics of the SEC target allow this tube to be operated at slow scanning rates as well as at the normal televison scanning rate. An

additional advantage of this device over the more complicated type of camera tubes is the simplicity of operation.

The SEC camera tube consists of three main sections: (1) the image section; (2) the SEC target; and (3) the scanning sections. A cross section of the SEC camera tube is shown in figure 17.13.

The image section, essentially, is an electrostatically focused image tube diode having the SEC target in its image plane. It consists of a semi-transparent photocathode deposited on the inside of the fiber-optic faceplate and an electrostatic image tube lens for focusing the photocathode current on the SEC target. The electron image of the cathode is inverted and it has a less than unity magnification (about 0.64). The electron image is in sharp focus over the entire useful area and the distortion of the image is typically 2%.

Because the image tube lens is an electrostatic image inverting diode, the image section remains in sharp focus with variation of the image tube voltage. This feature provides a convenient means for gain control. Figure 17.14 shows the relative target gain of the SEC target as a function of image tube voltage.

The light image being televised is focused on the photocathode by an optical system. The photoelectrons generated by the light image are accelerated to an energy of about 8 to 10 keV and are sharply focused on the
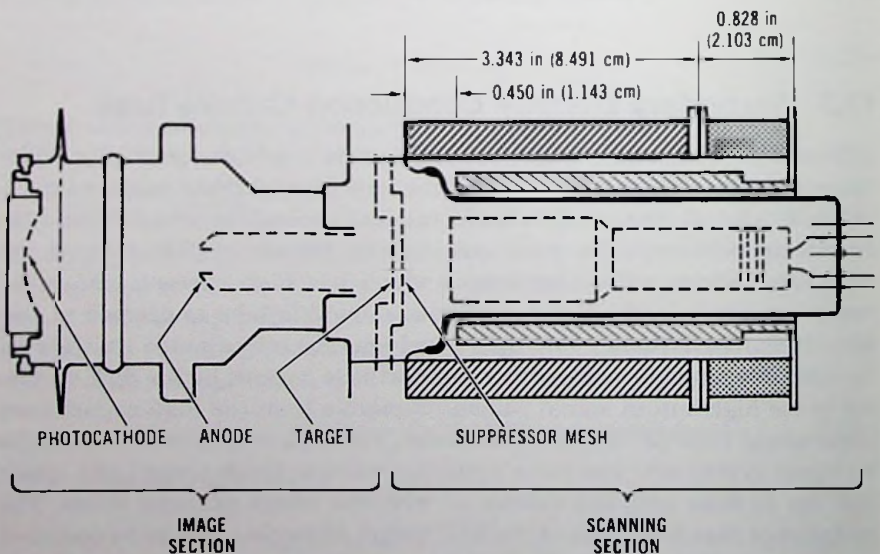
Fig. 17.13   Cross section of the SEC camera tube.
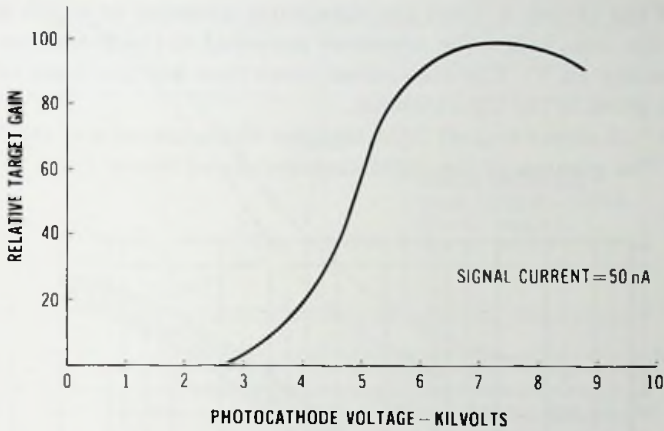
Fig. 17.14   Relative target gain of the SEC target.

target by the image tube lens. After penetration of the aluminum oxide and conductive aluminum layers supporting the secondary electron conduction potassium chloride layer, the photoelectrons dissipate their energy in the potassium chloride layer, creating many low-energy secondary electrons. Since the scan side of the target is stabilized to the gun cathode potential by the low-velocity scanning beam and the conductive aluminum signal plate is at a positive potential, an electronic field exists across the potassium chloride layer. Due to the electric field a secondary-electron conduction occurs discharging the target capacitor. In this manner a charge pattern corresponding to the light image is produced on the target. The relative target gain of the SEC target is shown in figure 17.14.

The video signal is generated by capacitive displacement current during the recharging of the target by the scanning beam. The low-velocity scanning beam returns the potential of the target to the gun cathode potential.

The scanning beam is produced by a low-velocity electron gun consisting of a thermionic cathode, a control grid (grid no. 1), and an accelerating grid (grid no. 2). The beam is brought to sharp focus on the target after several loops by the magnetic field of the external focusing coil and by the potential of the G_3 electrode.

Alignment of the beam is accomplished by transverse magnetic fields produced by external coils located at the gun end of the focusing coil.

Biaxial deflection of the electron beam is achieved by transverse magnetic fields produced by external deflection coils.

A field mesh provides a uniform decelerating electric field to the target.

Another mesh electrode, the suppressor mesh, is placed in close proximity

in front of the target to limit the maximum potential to which the target potential can rise, below the crossover potential of the potassium chloride (approximately 15 V). The suppressor mesh thus has the same role as the stabilizing mesh in the CPS emitron.

Figure 17.15 shows typical light transfer characteristics of the SEC camera tube. The gamma of the light transfer curve varies from nearly 1 at
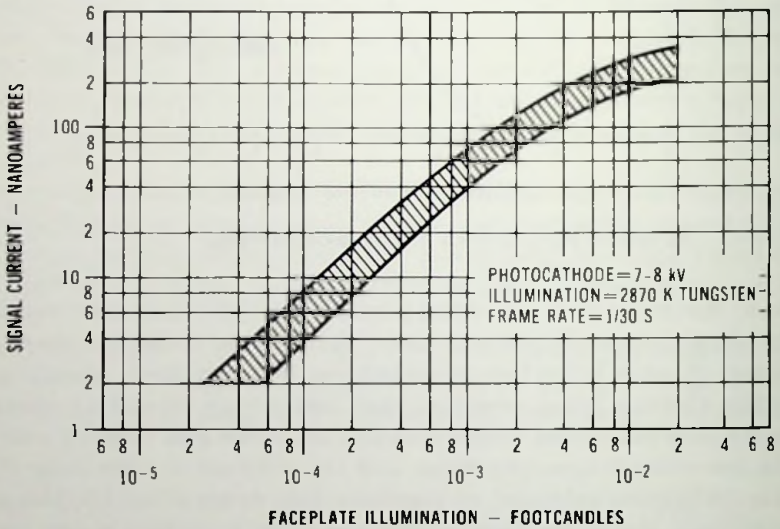
Fig. 17.15   Typical light transfer characteristic of the SEC camera tube.

lower light levels to about 0.6 at higher light levels. At higher light levels the light transfer characteristic has a knee but the light levels associated with the knee may cause burn-in after prolonged exposure. At high illumination, however, the tube may be safely operated by reducing the image tube voltage, thus reducing the target gain.

The range of operation may further be extended toward lower light levels by use of an additional image tube section in front of the SEC camera tube.

Figure 17.16 shows typical square-wave response curves of the SEC camera tube.

The SEC camera tube is relatively free from lag. The so-called third field lag, which is observed, three fields ($\frac{3}{60}$th second) after the light is removed from the tube, is less than 5%. In the first frame, therefore, 95% of the signal is read out, leaving typically 5% to be read out in the second frame. In the third frame the residual signal is imperceptible.

RELATIVE RESPONSE

RESOLUTION — TV LINES PER PICTURE HEIGHT

CENTER

CORNER

NORMAL RASTER SIZE
SIGNAL CURRENT = 150 nA
GRID NO. 3 = 325 V
GRID NO. 5 = 15 V
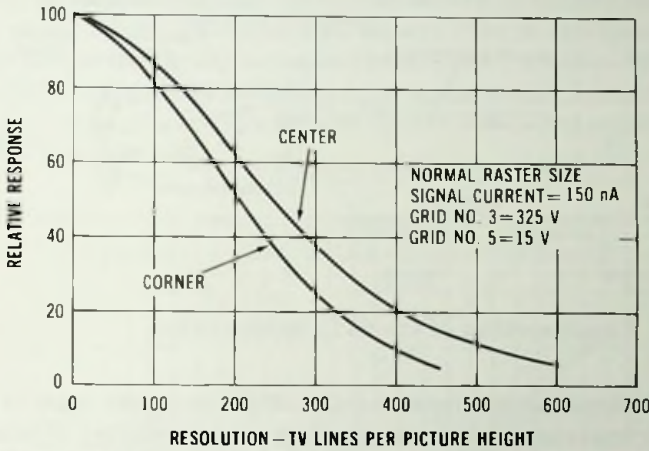
Fig. 17.16   Typical square-wave response curves of the SEC camera
tube.

Under typical operating conditions the tube provides a typical high light signal current of 150 nA. Using a suitable video amplifier the signal-to-noise ratio is about 150, or 43 dB.

17.8   Silicon Intensifier Target Camera Tube

The silicon intensifier target (SIT) camera tube is a very high sensitivity, storage type camera tube that extends the range of operation to very low light levels. The SIT camera tube operates in the same way as the SEC tube. The target, however, consists of a two-dimensional array of diodes formed in a very thin silicon wafer. The silicon diode array provides the SIT tube with a high target gain which may be on the order of 2000 to 2500. The high target gain enables the SIT tube to operate at lower light levels than any of the devices already discussed.

The SIT camera tube, similar to the SEC tube, consists of an electrostatic image inverting diode which has the SIT target in its image plane and of a low-velocity scanning beam section which is again similar in principle to the scanning beam section of the SEC tube. Figure 17.17 shows the cross section of the SIT camera tube.

In operation, the light image being televised is focused on the semi-transparent photocathode by an optical system. The low-velocity photo-electron image corresponding to the light image is accelerated and sharply focused on the SIT target by the electrostatic image tube lens. The energy
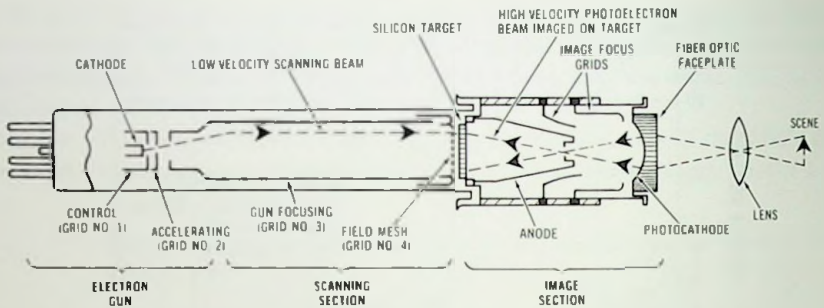
Fig. 17.17   Cross section of the SIT camera tube.

of the photoelectrons impinging on the target is on the order of about 10 keV. The primary photoelectrons produce a large number of hole-electron pairs for each primary photoelectron by interaction with the silicon layer. Because the back plate (signal plate) of the target, facing the image tube, is connected to a small positive potential (5 to 10 V) and the scan side is stabilized at gun cathode potential by the scanning beam, an electric field is present between the two sides of the target. Due to this electric field the holes diffuse to the scan side of the target and discharge the elemental diode capacitors in proportion to the local intensity of the primary photoelectron image. The charge pattern produced this way is read out on the back plate by neutralizing the positive charge by the scanning beam.

The light transfer characteristic of the SIT tube has a linear gamma with a value of unity in the normal operational signal current range. At the usual signal plate voltage of $+8$ V, the maximum signal current is on the order of 700 to 800 nA. The high signal current is realized by the high-capacitance target which is on the order of 4000 pF. Because of the high capacitance, large output signal currents are available for moderately low voltage swings at the target. (Large voltage swing at the target is not desirable, because it may cause beam pulling and defocusing and consequently the loss of resolution.)

Because of the linear gamma characteristics, the signal current I_s may be expressed with the target gain G, photocathode sensitivity S, photocathode illumination E, and the photocathode area A, by the following equation:

$$I_s = G \times S \times E \times A. \qquad (17.29)$$

For example, using the following values for the above parameters, $G = 2500$, $S = 270$ μA/lm, $E = 2 \times 10^{-8}$ lm/cm^2, $A = 7.5$ cm^2, the signal current I_s is 100 nA.

The range of operation may be further extended toward lower light levels

by coupling an additional image intensifier section to the SIT camera tube. The gain of the image intensifier SIT camera tube is sufficiently high to display single electron scintillation on the monitor. Therefore the low light level resolution is primarily limited by the statistical fluctuation of the photoelectron beam. Figure 17.18 shows the low light level resolution of the SIT and I-SIT camera tubes.
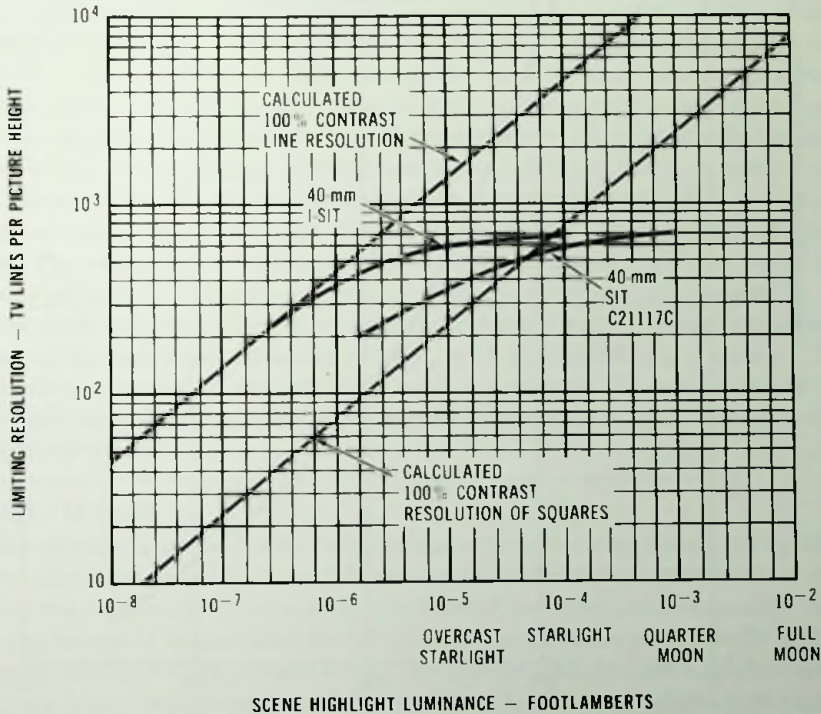
Fig. 17.18   Low light level resolution of the SIT and I-SIT camera tubes.

The high light level resolution of the SIT camera is primarily limited by the electron optics of the scanning and image section of the tube. Other resolution losses are caused by the mosaic structure of the diodes and by the fiber-optic input faceplate. The spacing of the diodes is on the order of 14 μm. Figure 17.19 shows the square-wave response characteristics of the SIT tube.

The spreading of the high light image, or blooming, is a limitation to high-quality imaging in the SIT camera tube that occurs when the light
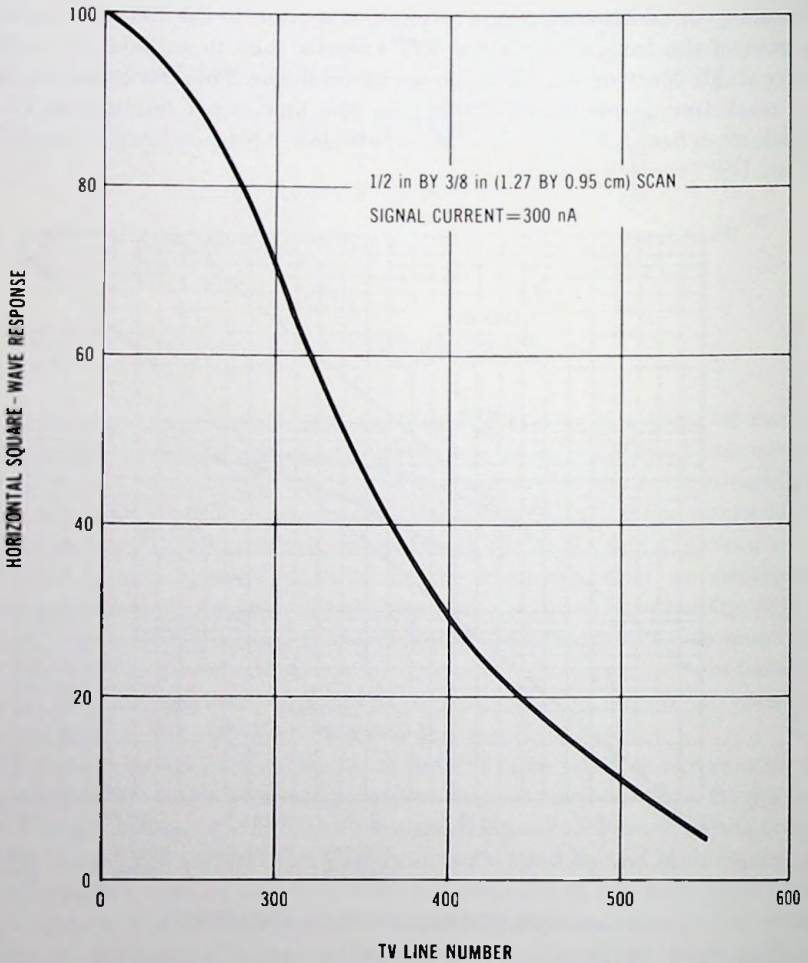
Fig. 17.19   Square-wave response of the SIT tube.

intensity exceeds the operating levels by which the gun side of the target is charged to the signal plate potential. The blooming is caused by the lateral spreading of the excess charge in the target developed by bright spots. Blooming becomes a problem when the light intensity exceeds normal operating levels by about 100 times.

The SIT camera tube is relatively free from lag at high output signal currents. The "third field" lag at 500-nA signal current is less than 5%. At small signal currents (less than 50 nA), however, the lag is quite noticeable.

The dark current of the tube is 5 to 10 nA at normal target voltage of 8 V.

Because of the high signal current in the high light image the SIT tube provides a high signal-to-noise ratio which is limited only by the photo-electron statistics.

17.9   Photoconduction Camera Tubes

The photoconduction storage-type camera tubes operate on the photo-conduction principle. In these devices a thin layer of photoconductor is uti-lized for conversion of the light image to be televised into an electrical charge pattern. As far as operation is concerned the photoconductive layer has a dual function. First, it is the light-sensitive element which converts light into electrical charge. Second, the electrical charge is displaced across the photoconductor, and the charge pattern corresponding to the light image is stored and integrated on the elemental capacitors of the photoconductive layer. The video signal is generated by instantaneous transformation of the charge pattern into electric current by a low-velocity scanning beam.

The three frequently used photoconductive materials for camera tube tar-gets are the antimony trisulfide (Sb_2S_3), lead oxide (PbO), and silicon. The first of these materials is associated with the vidicon, the second is used in the Plumbicon and the third is employed in the silicon diode array target photoconduction tube.

17.9.1   Vidicon

The vidicon is a small size relatively inexpensive and simple to operate television camera tube. It was developed primarily for closed-circuit and industrial television applications. Because of the good picture quality that it can produce, it is also used for television broadcast service, mostly for the reproduction of motion picture films. The vidicon can produce a useful signal at scene illuminations of 1 to 10 000 fc. For a lag-free operation, however, a faceplate illumination of 30 fc is required. The cross-sectional view of a magnetic focus and deflection vidicon is shown in Figure 17.20.

A frequently used target material of the vidicon is the antimony trisulfide overlaid on a transparent signal plate consisting of tin oxide (SnO_2). By evaporation in high vacuum, a solid amorphous layer of antimony trisulfide is obtained. The compact layer obtained this way has a high sensitivity, high dark current, high dielectric constant, long photoconductive lag, and low blue response. It has an inefficient beam acceptance, because it is an efficient secondary electron emitter at relatively low target voltages. Due to the high dielectric constant, the capacitance is about 10^{-8} F/cm^2. The large capacitance causes capacitive lag.

By evaporation in a rare gas (argon) a porous layer of antimony trisulfide
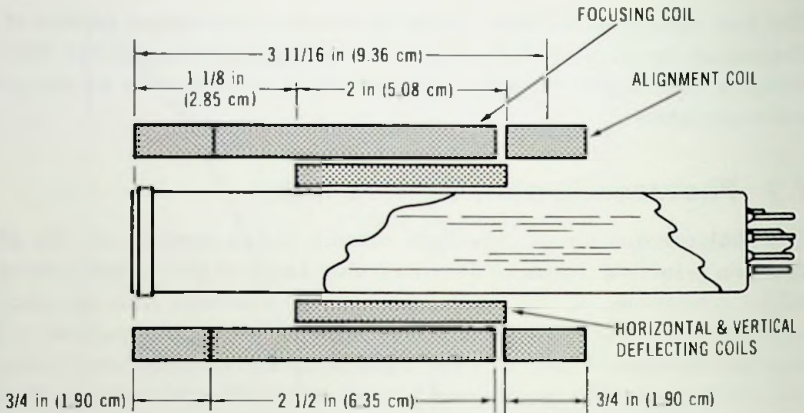
**Fig. 17.20   Location of components for magnetic focus and
deflection vidicon.**

may be obtained which may have one order of magnitude less film density
and capacitance than the solid layer. The porous layer also has an improved
blue response, lower lag, and dark current and a low secondary-electron
emission ratio. In the porous layer the photoconductive lag predominates
over the capacitive lag.

A composite photoconductor may be fabricated by use of a combination of
solid and porous surfaces. For example the SPS target consists of a solid-
porous-solid layer combination. With the composite target, intermediate
results are obtained as the different performance parameters are concerned.
Another example of the composite photoconductor is the high-performance
ASOS target, which is made by coevaporation of antimony sulfide and anti-
mony sulfide oxide in high vacuum.

The primary problems of the Sb_2S_3 vidicon target are the relatively high
and nonuniform dark current which causes nonuniform background, and
the high photoconductive lag at lower light levels. The photoconductive lag
is a function of illumination: the higher the illumination, the less the lag.
Therefore the best use of vidicon is in highly lighted scenes with a limited
amount of motion.

Figure 17.21 shows typical light transfer characteristics of the vidicon
camera tube. Because the rate of recombination of electrons and holes in
the photoconductor increases with the light level, the gamma of the light
transfer characteristics of the vidicon is not linear but it has an average
value of about 0.65. The gamma characteristic of the vidicon thus is comple-
mentary to the picture tube response of the television receiver. Therefore
the picture tones and the gray-scale gradations are properly reproduced on
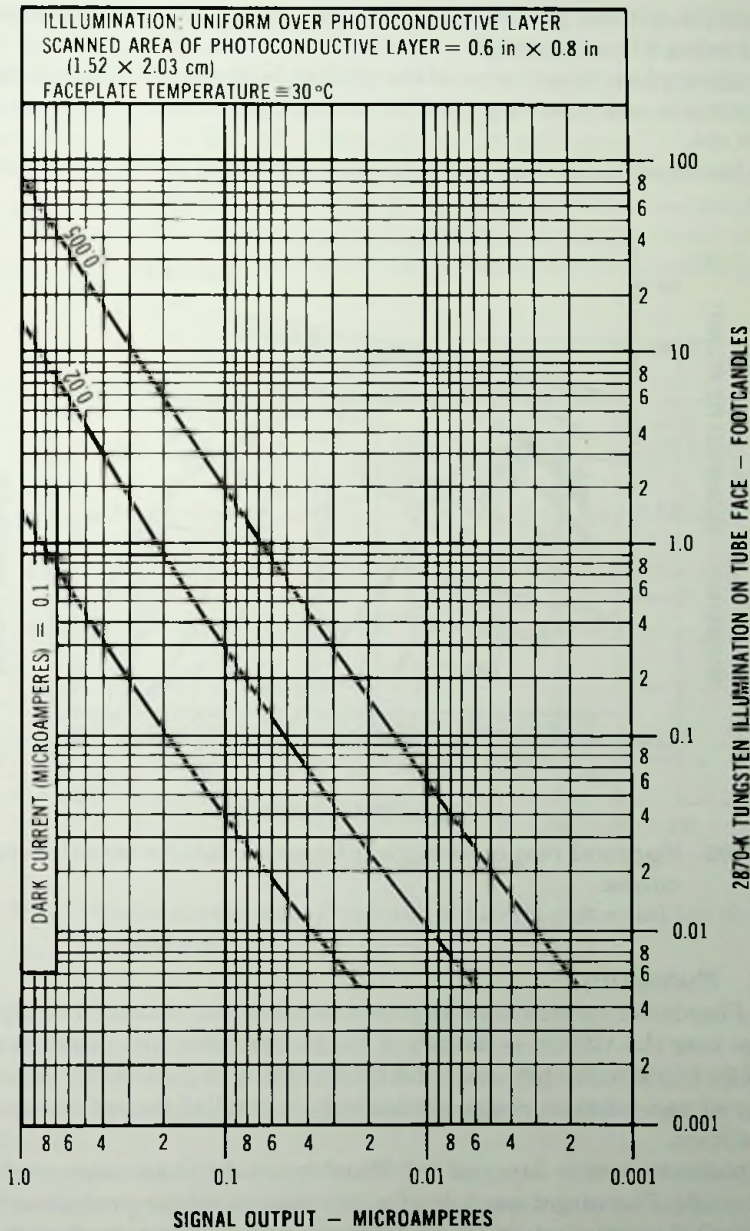
Fig. 17.21 **Typical light transfer characteristic of an antimony trisulfide (Sb_2S_3) vidicon camera tube.**

the receiver without gamma matching circuits necessary with the camera tubes having a linear gamma.

The spectral response curve of the vidicon is shown in figure 17.22. It is panchromatic and it is very similar in shape to the response curve of the human eye.

The luminous sensitivity, in an optimum operation mode, is typically 150 $\mu A/lm$.
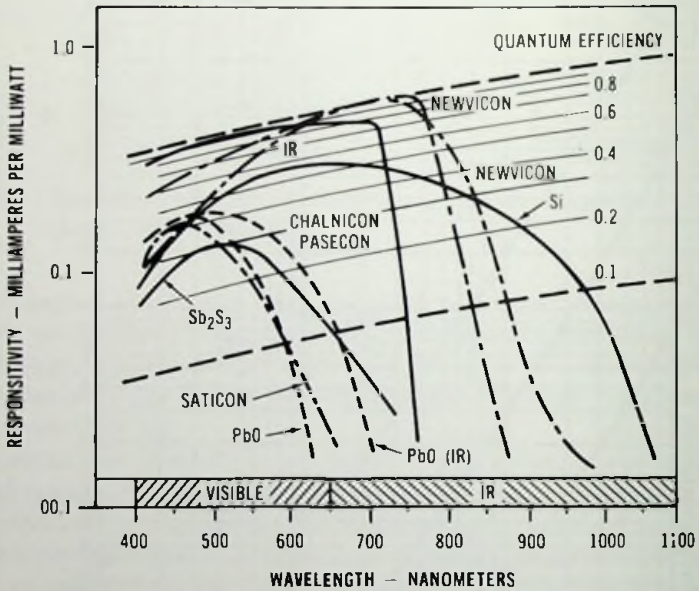
Fig. 17.22 **Spectral responsivity of photoconductive target camera tubes.**

17.9.2 Plumbicon

The Plumbicon camera tube is a lead oxide target vidicon. Its major advantage over the vidicon is its lack of image retention. The Plumbicon tube is used for black-and-white and color broadcasting in applications where the light level and contrast range is adquately controlled for optimum picture transmission.

The photoconductive layer of the Plumbicon tube is an evaporated layer of lead oxide. The target consists of a transparent n-type conduction signal plate (SnO_2 layer) overlaid by an intrinsic and a p-type conduction lead-oxide layer. The thickness of the photoconductor is in the range of 10 to 20 μm, providing high target resolution.

In operation the photoconductor is reverse biased by maintaining the signal plate at a positive potential and the p-type layer on the scan side at ground potential. Due to the blocking contacts at the n-i and i-p interfaces the dark current is less than 5 nA. As a result the dark current variation is very small and the black level uniformity is extremely good.

Figure 17.23 shows the signal current as a function of target potential. The signal current shows the tendency to saturate over a certain target potential. If the tube is used at a target potential where the signal current saturates, beam landing errors should not introduce signal nonuniformities.
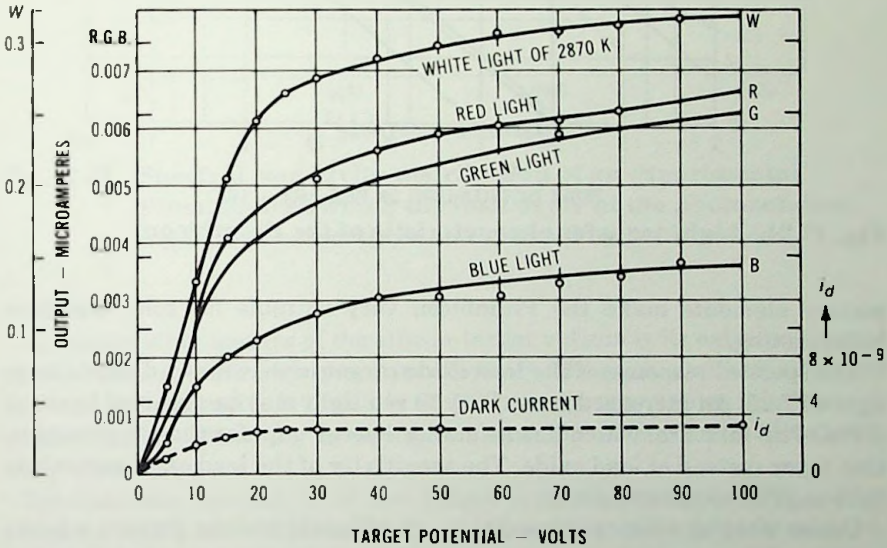
Fig. 17.23   **Photocurrent as a function of target potential for the Plumbicon.**

Figure 17.24 shows the light transfer characteristic of the Plumbicon. The gamma is nearly unity for up to 1 μA signal current.

The lead oxide target is relatively free from lag. The "third field" lag, which is observed three fields after the light is removed from the tube, is less than 5%.

The capacitance of the target is in the range of 1000 to 1500 pF. This capacitance can provide a reasonably large signal current without excessively large target voltage swings which would cause beam pulling and loss of resolution.

The short lag and the independence of the signal from the surrounding
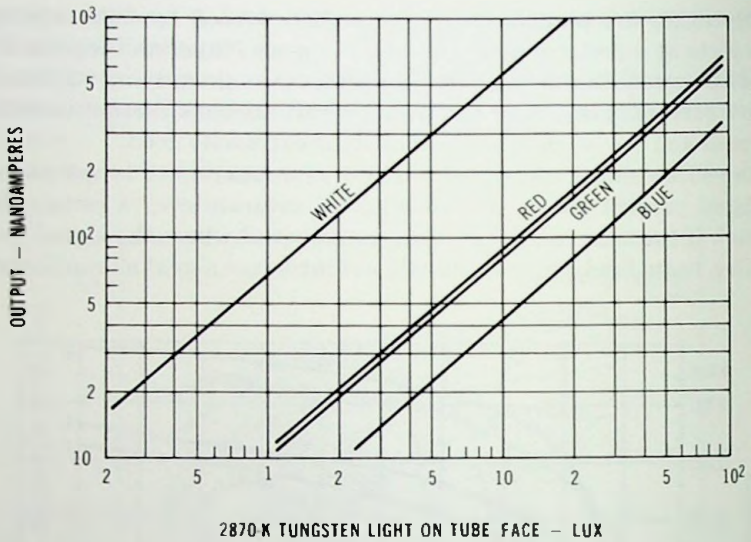
Fig. 17.24   Light transfer characteristic of the Plumbicon.

picture elements make the Plumbicon very suitable for color television broadcasting.

The spectral response of the lead oxide target is shown as a dashed line in figure 17.25. An increased sensitivity to red light may be obtained by use of a PbO-PbS mixture, which has a smaller energy gap, for the p-type conduction layer instead of lead oxide. The sensitivity of the lead oxide target is in the range of 150 to 400 μA/lm.

Under normal operating conditions the Plumbicon can provide a better signal-to-noise ratio than the image orthicon tube. Its use at low light levels, however, is limited by its sensitivity.

17.9.3   Silicon-Target Vidicon

The photoconductive layer of the silicon-target vidicon consists of a two-dimensional array of silicon photodiodes processed in an n-type silicon wafer. It is one of the most sensitive tubes of the vidicon family and it has extremely broad spectral response.

In operation, the target is reverse biased by connecting the n-type wafer to a positive potential (+ 8 V), and maintaining the p side of the diodes at ground potential by the scanning beam. The silicon diode array thus provides a target structure which has a very low dark current (5 to 10 nA) and it is relatively free of lag. The "third field" lag is about 7% at 300 nA signal level.
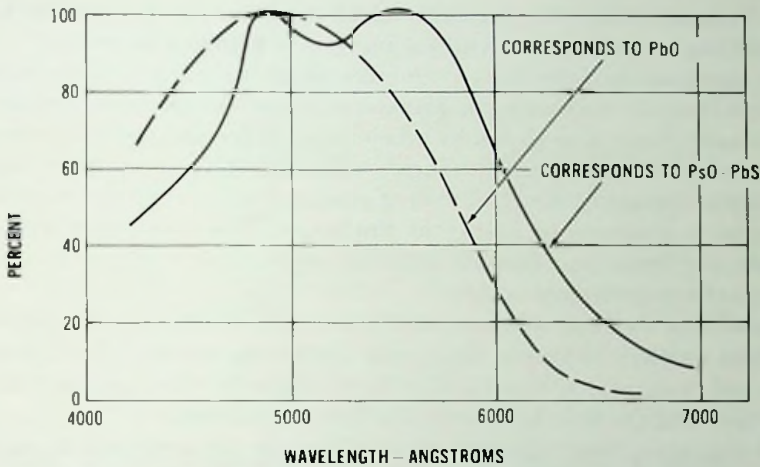
Fig. 17.25   Spectral sensitivity distribution of an experimental
Plumbicon in which the lead oxide of the photoconduct-
ing layer has partly been replaced by lead sulfide.

An outstanding feature of the silicon-target vidicon is its extremely broad
spectral response and high quantum efficiency. The peak quantum efficiency
occurs at 520 nm and it is typically 85%. The response extends into the near
infrared region, gradually dropping to about 50% at 800 nm, and to about
5% at 1100 nm.

The luminous sensitivity of the target is on the order to 4000 μA/lm
measured with a 2854-K transystem source, and it is 900 μA/lm for a source
radiation restricted to the visible spectrum. The sensitivity of the silicon
target thus is much higher than that of the lead oxide or the antimony
sulfide targets.

The silicon target has a linear gamma and the peak signal level range is
200 to 500 nA. The large signal current in the highlights provides a very
high signal-to-noise ratio. The video amplifier noise level is in the range of
3 to 5 nA rms for a bandpass of 5 to 10 MHz. With 300 to 500 nA signal
current the signal-to-noise ratio therefore is 100:1 (40 dB). The amplifier
noise, however, is concentrated at higher frequencies and it is not easily
noticeable to the average viewer. Statistical viewer tests indicate that the
effective signal-to-noise ratio is higher by a factor of 3 than the above figure,
or 300:1 (50 dB).

The resolution of the target is primarily determined by the diode spacing,
which is about 14 μm, and the thickness which is about the same in magni-

tude. Targets with 5/8-in (1.58-cm) useful diameter can provide 700 to 800 tvl limiting resolution with a 40% square-wave response at 400 tvl.

For signal readout the photoconductive target is scanned by a low-velocity electron beam to discharge the target surface to the ground potential. The low-velocity beam is produced by acceleration of the thermionic electrons of an oxide cathode to several hundred volts of electric potential in order to form a narrow-angle, small-diameter electron beam. Then the beam is decelerated to a near-zero energy at the target. The scanning section thus consists of a thermionic cathode, cathode, main and deceleration lenses, and a biaxial beam deflection system.

Concerning focusing and beam deflection, four basic systems are in use. The first employs magnetic focus and deflection, the second electrostatic focus and magnetic deflection, the third magnetic focus and electrostatic deflection, and the fourth electrostatic focus and deflection.

The magnetic focus and deflection system is characterized by superior performance mostly as far as resolution and amplitude response are concerned.

The electrostatic focus and magnetic deflection type is used in applications where small camera size and weight is important. The camera size and weight and power requirements are reduced by elimination of the magnetic focus coil. In addition, the deflection power is one-fourth of that required by the separately connected mesh magnetic focus and deflection system. The performance, meaning resolution, mainly is inferior to the magnetic focus and deflection type.

The magnetic focus and electrostatic deflection is utilized in the FPS vidicon. This system provides very high resolution. It also requires less power than the magnetic focus and deflection type. The beam deflection is done by a deflectron.

The all-electrostatic system (electrostatic focus and deflection) is used where weight, power and size are of primary importance. The performance, however, is inferior to the other types.

In high-resolution vidicons the high resolution is obtained by demagnification of the crossover image. The RCA return-beam vidicon, which is shown in figure 17.26, utilizes a magnetic lens for this purpose. In the FPS (focus projection and scanning) vidicon the crossover is demagnified by partial immersion of the vidicon tube in the focusing magnetic field. As shown in figure 17.27 the focusing coil and the deflection of the FPS vidicon have the same length and axial position. This arrangement provides a magnetic lens which demagnifies the spot size of the scanning beam by a factor of 0.7.

Figure 17.28 shows the square-wave response of photoconduction devices.
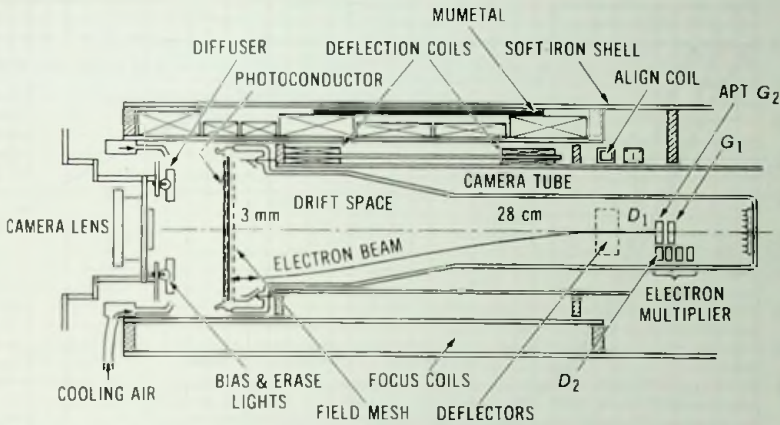
Fig. 17.26   Electron optics of 4½-inch (11.43-cm) return-beam
             vidicon.
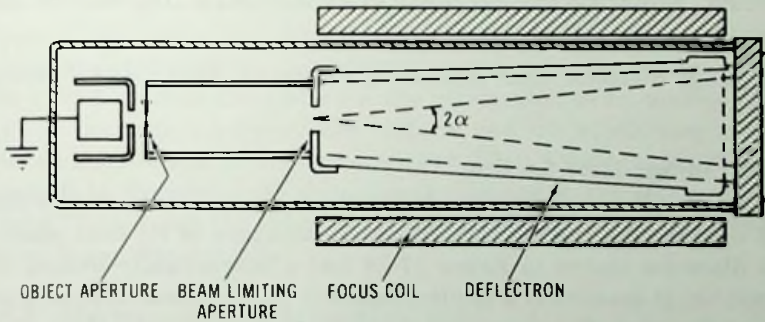
Fig. 17.27   FPS vidicon system, partially immersed.

17.10   Image Dissector Tube

The image dissector tube is a nonstorage type camera tube used primarily
for televising fast image motion, instantaneous readout, and computer di-
rected, localized scanning. The image dissector operates on the principle of
resolving the photoelectron image of a scene by an electron collecting aper-
ture in which the image content is time-sequentially directed by means of
photoelectron beam scanning. Since the resolving aperture collects elec-
trons at each instant only from one resolution element, and the reading of
one resolution element takes a very short time, the image is free of blur
even at very fast scene motions.
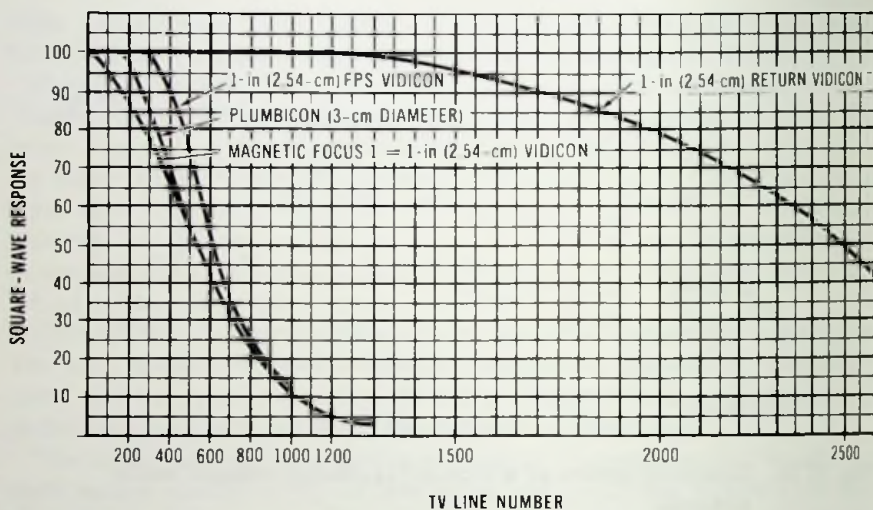
Fig. 17.28   Square-wave response of photoconductive camera tubes.

The image dissector tube consists of an image section and a multiplier section.

17.10.1   Image Tube Section

The image tube section is an electrostatically or a magnetically focused image tube having the electron collecting aperture in its focal plane. The image dissector shown in figure 17.29 has a magnetically focused image tube section. It consists of a semitransparent photocathode deposited on the inside of the glass faceplate, and three accelerating grids which together with the photocathode and the aperture plate establish an axial electric field. An axial magnetic field is supplied by an external focusing coil. Focusing is accomplished by the combined action of the electric and magnetic fields. The electron image of the photocathode is in sharp focus at the aperture plate and for homogeneous electric and magnetic fields, it is erect, and it has unity magnification.

The light image being televised is focused on the photocathode by an optical system. The photoelectrons generated by the light are accelerated to an energy of about 500 eV by the electromagnetic lens. The video signal is then generated by biaxial deflection of the photoelectron image over the electron collecting aperture by transverse magnetic fields produced by external deflection coils. The transverse motion of the photoelectron image allows the aperture to scan and sample the photoelectron image and convert it into a time based video signal.
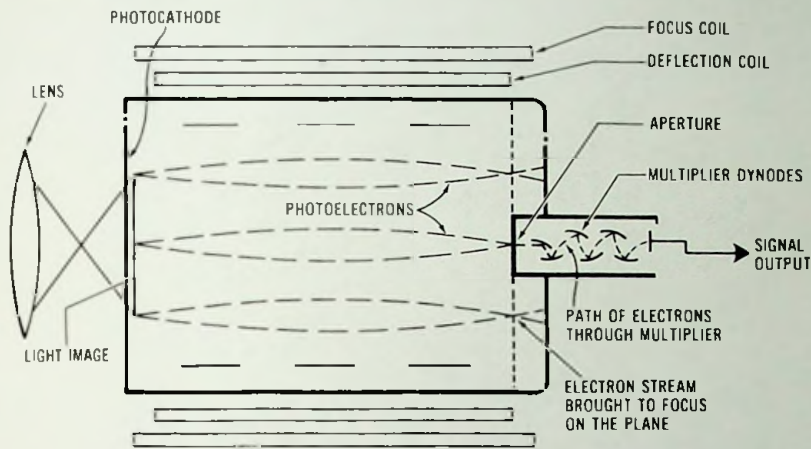
Fig. 17.29   Magnetically focused image dissector tube.

Figure 17.30 shows the magnetic focus and deflection coils and twelve-stage box and grid electron multiplier of the vidisector image dissector tube. In the vidisector tube the electrons are accelerated to an energy of about 500 eV in the region between the cathode and the accelerator mesh (ion barrier mesh) mounted to the focus cylinder. Then, by the action of the axial magnetic field, the photocathode is sharply focused on the aperture plate.

Figure 17.31 shows the cross section of an electrostatically focused and deflected image disector tube.

17.10.2   Electron-Multiplier Section

The sample electrons, continuously taken from the resolution elements of the televised image, are directed to the first dynode of a multistage electro-
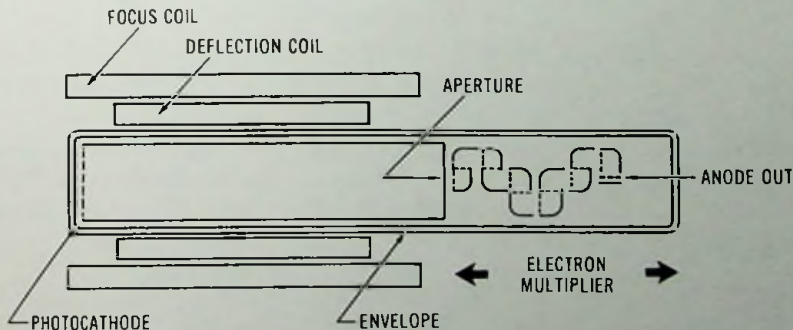
Fig. 17.30   Cross section of the vidisector image dissector tube.

PHOTOCATHODE

FOCUSING ELECTRODE

DEFLECTION PLATES

APERTURE PLATE
APERTURE

MULTIPLIER STRUCTURE
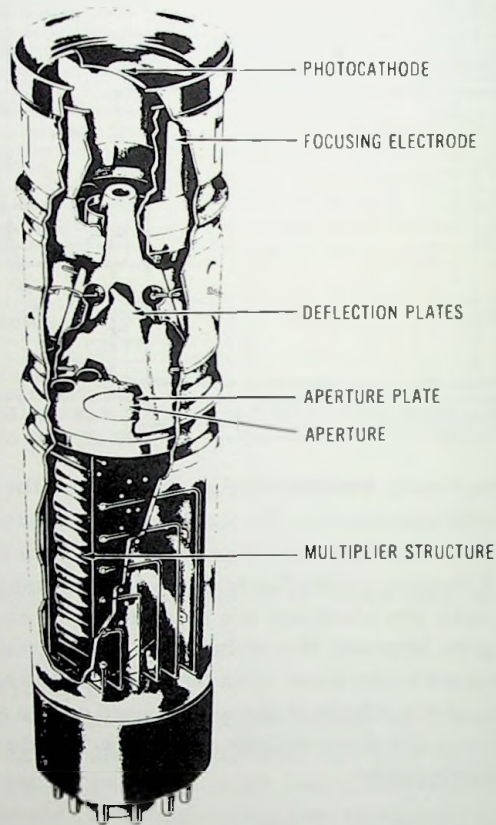
Fig. 17.31   Electrostatically focused and deflected image dissector tube. (*Courtesy CBS Laboratories*)

statically focused electron multiplier. The purpose of electron multiplication is to raise the level of the small signal above the noise level of the first stage of the video amplifier by a relatively noiseless process.

The gamma of the light transfer characteristics is unity because the photocathode current is proportional to the photocathode illumination. The signal current striking the first dynode may be expressed by the following equation:

$$I_s = SEaT/M^2,$$
(17.30)

where I_s is the signal current, S is the luminous sensitivity, E is the photocathode illumination, a is the aperture area, M is the magnification of elec-

tron optics, and T is the transmission of the ion barrier mesh used in the vidisector tube.

The image dissector tubes are used at light levels ranging from the starlight level to very high light levels which may cause photocathode current densities in excess of 1 $\mu A/cm^2$.

The resolution of the image dissector tube is determined by the aperture size. Figure 17.32 shows the square-wave response as a function of aperture size. The defining apertures are ranging from 0.0005 to 0.150 in (12.7 μm to 3.81 mm) in the different type of image dissector tubes.

The usual photocathodes of the image dissector tube are the S-11 and the S-20 photocathodes.
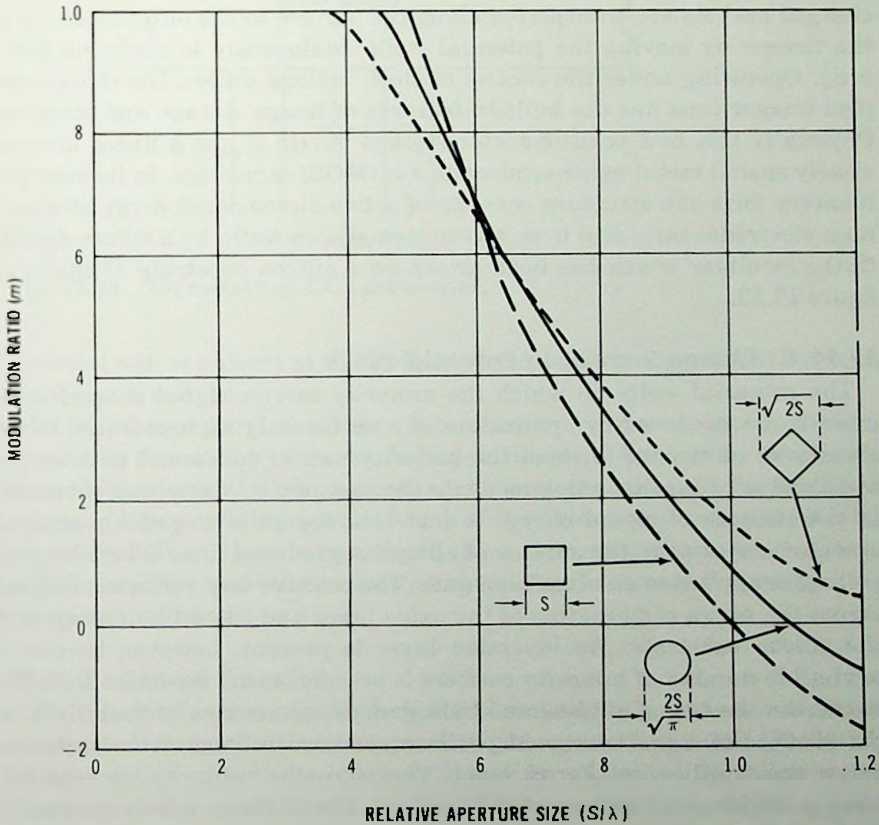
Fig. 17.32   Square-wave response of the image dissector tube as a function of aperture size.

The signal-to-noise ratio of the image dissector is given by the following equation:

$$\text{snr} = \sqrt{\frac{I_s}{2e\Delta f}} \sqrt{\frac{\delta - 1}{\delta}}, \tag{17.31}$$

where e is the charge of the electron, Δf is the bandwidth in hertz, and δ is the secondary emission ratio of the first multiplier dynode.

17.11   Charge-Coupled Imager

The charge-coupled imager (CCI) is a solid-state image sensor in which the charge signal to be televised is stored in potential wells created at the semiconductor surface by clock voltage pulses. To read out the signal the charged packets are transported along the surface to the output location of the imager by moving the potential wells analogously to electronic scanning. Operating under the control of clock voltage pulses, the charge coupled imager thus has the built-in features of image storage and scanning. Physically this new semiconductor storage device is just a linear array of closely spaced metal-oxide-semiconductor (MOS) capacitors. In its most elementary form the structure consists of a two-dimensional array of aluminum electrodes insulated from a very thin silicon wafer by a silicon dioxide (SiO_2) insulator which has been grown on a silicon substrate as shown in figure 17.33.

17.11.1   Charge Storage in Potential Wells

The potential wells, in which the minority carrier signal charges accumulate, are produced by application of a sufficiently high potential to the aluminum electrodes to repel the majority carrier holes and to drive the semiconductor in a depletion mode. In the case of a p-type silicon substrate, in the absence of signal charge a depletion region of negatively charged acceptor states near the surface of silicon is produced after a positive step voltage is applied to an aluminum gate. The positive step voltage is dropped across the series combination of the oxide layer and the depletion region of the silicon substrate. No inversion layer is present, however, because a negligible number of minority carriers is present in the transient state due to the low density of surface and bulk generation centers in the silicon. In the absence of signal charge the silicon conduction band of the surface is below the equilibrium Fermi level. Therefore the minority carriers will have a tendency to gather at the surface. The surface, however, remains depleted for a time interval on the order of seconds before thermally generated minority carriers accumulate in sufficient number to relax the surface. Thus, for times much shorter than the thermal relaxation time, a
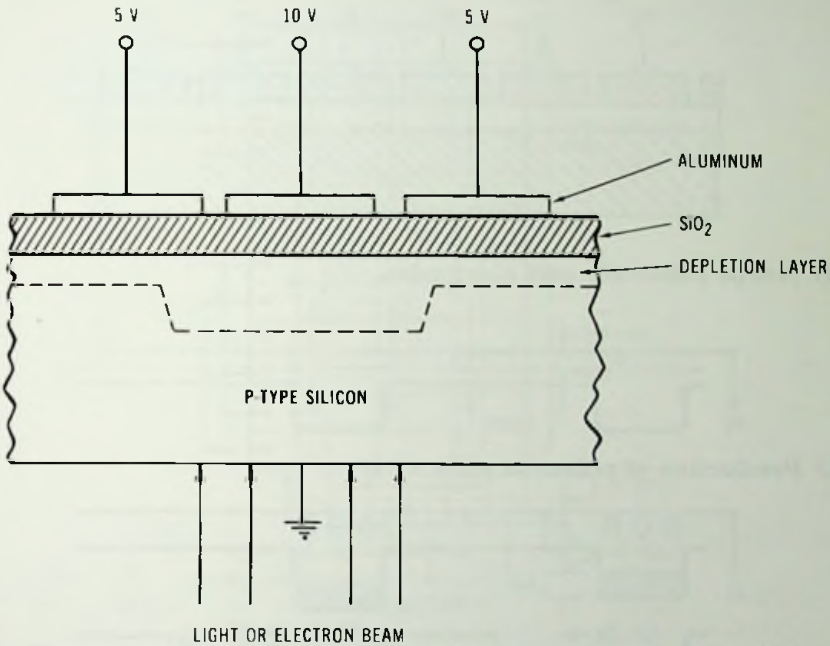
Fig. 17.33   Elementary CCI structure.

potential well is present at the surface whose depth can be altered by chang-
ing the gate voltage.

In the charge-coupled imager the minority carrier generation (signal
charge) in the silicon is accomplished by incident light or by an electron
beam. With accumulation of the minority carrier charges at the surface an
inversion layer residing within 100 Å of the oxide-semiconductor interface
is produced. The charge accumulated there reduces the surface potential at
Si-SiO₂ interface until the surface potential goes to zero and no more charge
can be accumulated.

17.11.2   Charge Transfer

The minority carrier signal charge accumulated in potential wells can be
transported along the surface by moving the potential wells. The charge
transfer action of a three-phase CCI may be explained by following the
diagrams of figure 17.34. In figure 17.34, a sufficiently high negative
voltage has been applied to all electrodes to drive the semiconductor in a
depletion mode. The ϕ_1 clock line voltage, however, is greater than ϕ_2 and
ϕ_3 clock line voltages producing a surface potential variation with potential
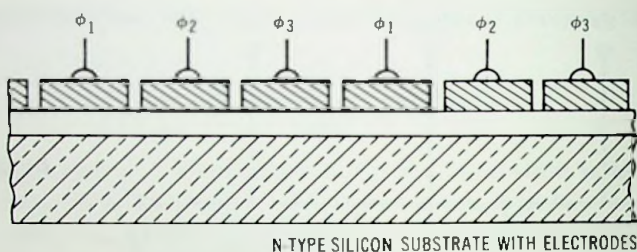
(A) N-type substrate with electrodes.
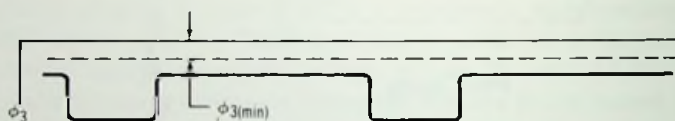
(B) Production of potential wells by ϕ_1.
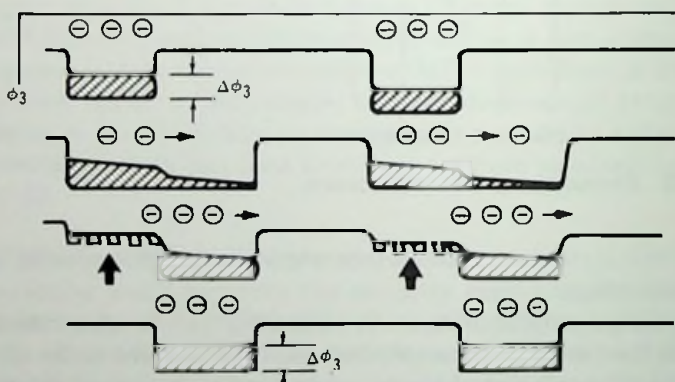
(C) Transfer of charge to right by ϕ_2.

Fig. 17.34 Charge transfer action of a three-phase CCI.

wells along the silicon–silicon dioxide interface as shown in figure 17.34B. By illumination of the silicon substrate with light or by bombardment by an electron beam, minority carriers are generated which will accumulate in the potential wells under the ϕ_1 gate. The accumulated charge is prevented from moving to left or right by the potential barrier present under the ϕ_2 and ϕ_3 gates. The charge is transferred to right to the position under the ϕ_2 gate as shown in figure 17.34C. The charge now is able to move under the ϕ_2 electrodes. The charge transfer is completed by gradually reducing the ϕ_1 voltage to the ϕ_3 value and allowing the charge to move under the ϕ_2
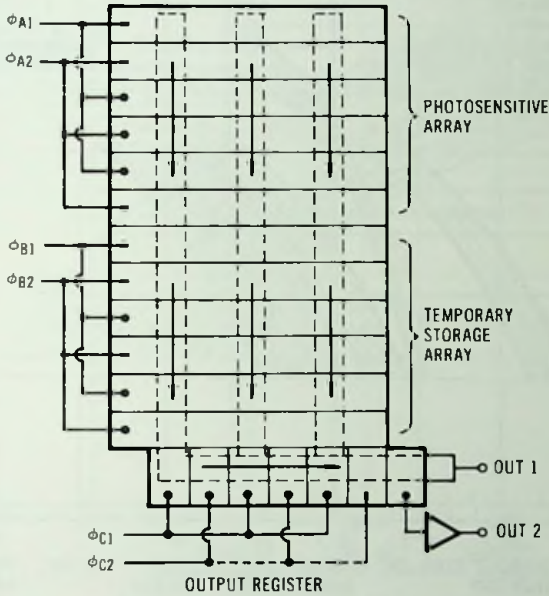
(A) Frame transfer CCI with a temporary storage array.
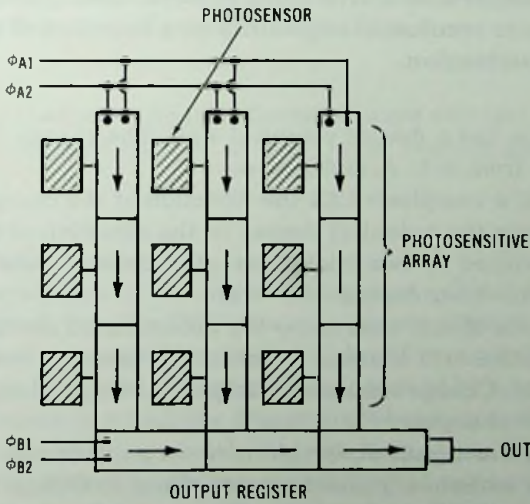
(B) Frame transfer with separated photosensors.

Fig. 17.35   CCI television cameras.

LENS = f:1
T = 80%
IMAGE DIAMETER = 40 mm
SCENE REFLECTANCE = 50%
SCENE CONTRAST = 100–30%

VIDICON (16 mm)   100%
30%

100%
30%

RESOLUTION – TV LINES PER PICTURE HEIGHT

NIGHT SCENE ILLUMINANCE – LUMENS PER SQUARE FOOT

OVERCAST STARLIGHT   QUARTER MOON   FULL MOON   DEEP TWILIGHT   TWILIGHT   VERY DARK DAY   OVERCAST DAY
STARLIGHT
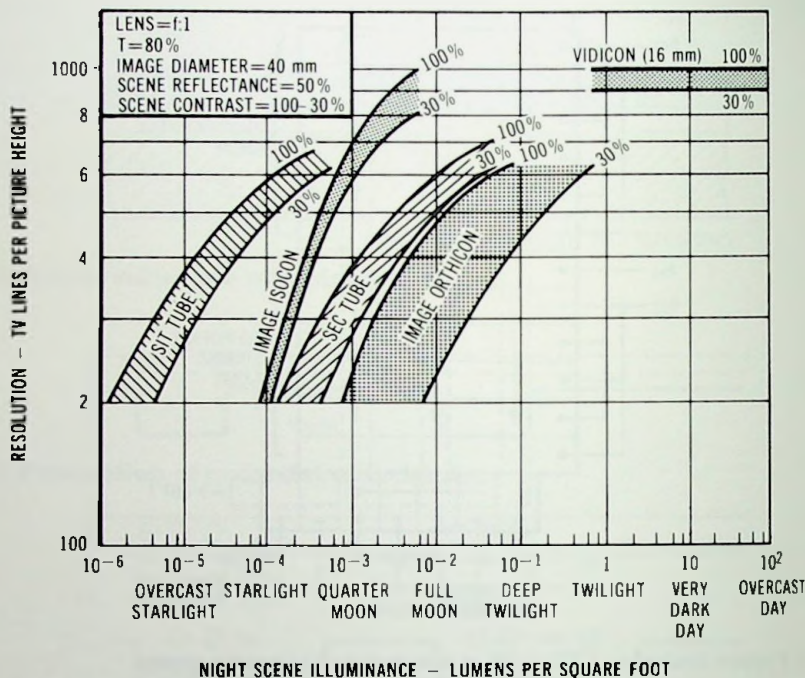
Fig. 17.36   Comparison of five basic camera tube types, showing the static resolution capability as a function of scene illumination.

gate, which now has a deeper potential well. The charge is moved with a similar process from ϕ_2 to ϕ_3 and ϕ_3 to ϕ_1.

In the case of a two-phase CCI the direction of the charge flow is determined by making the potential deeper in the direction of charge transfer. This is accomplished by two thicknesses of oxide under one electrode or by a variation in substrate doping.

There are three effects that cause the accumulated charge to move from one well to another: (1) thermal diffusion, (2) fringing field drift, and (3) charge repulsion. Charge repulsion is important only at large signal charge densities ($\leq 10^{10}$ charges/cm^2).

In order to avoid signal distortion it is very important to complete the charge transfer without significant losses. Since in CCIs a large number of transfers are required, the transfer efficiency per transfer must be very high. The maximum achievable value of transfer efficiency is limited by
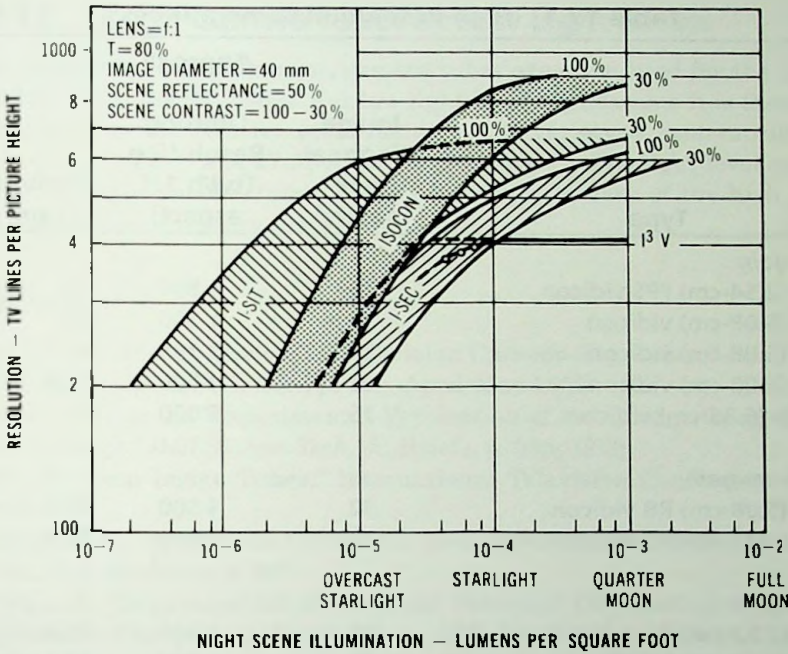
Fig. 17.37   Comparison of the I-SIT, the I-isocon, the I-SEC, and a three-stage image intensifier vidicon for static resolution as a function of scene illumination.

how fast the free charge can be transferred between adjacent gates and how much of the charge gets trapped at every gate location by fast interface states.

17.11.3   CCI TV Cameras

There are several ways for the implementation of a CCI tv camera. Figure 17.35 shows a frame transfer CCI with a temporary storage array and also frame transfer with separated photosensors. In a frame transfer CCI with a temporary storage array the optical image is detected by a two-dimensional array of photosensors in which the charge signal corresponding to the optical image is stored and integrated during a tv frame time. The accumulated charge packets representing the integrated optical image are transferred into the temporary storage array by clocks A and B during the vertical blanking time. From the temporary storage array the charge image pattern

Table 17.1   High-Resolution Camera Tubes*

Type	Image Diagonal (milli-meters)	Approxi-mate Limiting Resolution (tvl/h,1:1 aspect)	Manufac-turer
low gain			
1-in (2.54-cm) FPS vidicon	18	1 800	GE
2-in (5.08-cm) vidicon	36	1 500	GE
2-in (5.08-cm) vidicon	36	2 300	W
2-in (5.08-cm) vidicon	32	4 500	RCA
2.5-in (6.35-cm) vidicon	75	5 000	GE
medium gain			
2-in (5.08-cm) RB vidicon	32	4 500	RCA
4.5-in (11.43-cm) RB vidicon	72	10 000	RCA
high gain			
3-in (7.62-cm) 1-isocon	35	1 200	RCA
2-in (5.08-cm) SIT/I²V	38	2 300	RCA (dev.)
5-in (12.7-cm) SEC	75	3 000	W (dev.)
4.5-in (11.43-cm) SIT/I²V	80	4 500	RCA (dev.)

*From "Study of Photoelectric-Digital Radiology," by Sol Nudelman et al., *Proceedings of the IEEE*, Vol. 70, No. 7, July 1982.

is transferred down one horizontal line at a time into the output register by clock B during the horizontal blanking time. The charge pattern of a horizontal line is then read out from the output register by the high-speed clock C during the horizontal line period.

The frame transfer CCI with separated photosensors is composed of a two-dimensional array of photosensors and vertically oriented charge coupled device (CCD) channels that are not photosensitive. On the photosensors the charge produced by the optical image is integrated during a tv frame time. During the vertical blanking time the integrated charge signal is transferred from the photosensors into the vertical CCD channels. From the CCD channels the charge image pattern is transferred down one horizontal line at a time into the output register by clock A, from where the horizontal line is read out by the high-speed clock B during the horizontal line period.

17.12   Use of Camera Tubes at Low Light Levels

In addition to entertainment, camera tubes are often used for the detection of low light level scenes. For low light level applications it is therefore useful to know the relative performance of the variety of camera tube devices. Figures 17.36 and 17.37 show the comparative low light level resolution of different camera tubes. Table 17.1 is a summary of the high light level resolution of camera tubes.

References

Allard, L. S. "Design Factors in Television Cathode-Ray Tubes," *Proc. Inst. Brit. IEE*, Vol. 99, Part IIIA, p. 499, April-May 1952.

Amelio, G. F., et al. "Experimental Verification of the Charge-Coupled Device Concept," *Bell System Tech. J.*, Briefs, p. 593, 1970.

Ando, T. "Zoom Image Tubes," International Television Conference, June 1962.

Bedford, L. H. "A Note on Davisson's Electron-Lens Formula," *Phys. Soc. Proc.*, Vol. 46, No. 6, p. 882.

Bertram, S. "Determination of the Axial Potential Distribution in Axially Symmetric Electrostatic Fields," *Proc. IRE*, Vol. 28, No. 9, p. 418, September 1940.

Bertram, W. J. "Application of Charge-Coupled Device Concept to Solid State Image Sensors," *Digest of Technical Papers, 1971 IEEE International Convention*, New York, p. 250, March 22-25, 1971.

Beule, R. L.; D. A. Day; and W. E. Turk. "Developments in Television Camera Tubes," *The Royal Television Society Journal*, Vol. 11, p. 254, 1967.

Biberman, L. C., and S. Nudelman, ed. *Photoelectronic Imaging Devices*, Plenum Press, New York and London, 1971.

Boyle, W. S., and G. E. Smith. "Charge-Coupled Semiconductor Devices," *Bell System Tech. J.*, 1970, p. 587.

Carnes, J. E., and W. F. Kosonocky. "Charge-Coupled Digital Units," *IEEE Transactions on Electron Devices*, Vol. ED-19, No. 6, pp. 798–808, 1972.

————, and E. G. Ramberg. "Drift-Aiding Fringing Fields in Charge-Coupled Devices," *IEEE J. Solid State Circuits*, SC-6, p. 322, 1971.

Ceckowski, D. H. "Imaging Devices Using Self-Scanned Arrays Operating in the Electron Bombarded Mode," *Proceedings of the Electro-Optical System Design Conference*, New York, 1976.

Chace, E. T., et al. "Light Sensitive Imaging Tubes," *Electronic Industries*, p. 67, May 1966.

Coltman, J. W. "Fluoroscopic Image Brightening by Electronic Means," *Radiology*, Vol. 51, p. 359, September 1948.

Cope, A. D., and E. Luedicke. "Development of Camera for Recording Astronometric Images," *Advances in Electron Physics*, 22, pp. 175-188, 1966.
———. "Camera Tubes for Recording Stratoscope II Telescope Images," *RCA Review*, 27, p. 41, 1966.

Cope, A. D., and H. Borkan. "Isocon Scan—A Low-Noise, Wide-Dynamic-Range Camera Tube Scanning Technique," *Applied Optics*, Vol. 2, No. 3, p. 253, March 1963.

de Haan, E. F. "The Plumbicon: A Camera Tube With a Photoconductive Lead-Oxide Layer," International Television Conference, June 1962.
———, et al. "The Plumbicon: A New Television Camera Tube," *Philips Technical Review*, Vol. 25, No. 6/7, p. 133, 1964.

El-Kareh, A. B. "Analysis of the 3-Tube Symmetrical Electrostatic Unipotential Lens," *J. Appl. Phys.*, Vol. 42, No. 5, p. 1870, April 1971.

Engler, W. E., et al. "Surface Charge Transport in Silicon," *Appl. Phys. Letters*, Vol. 17, p. 469, 1970.

Engstrom, R. W., et al. "Camera Tubes for Night Vision," *Optical Spectra*, February 1971.
———, et al. "Choose the Tube for LTV," *Electro-Optical Systems Design*, June 1971.
———, et al. "Camera Tubes for Night Vision," *Optical Spectra*, p. 26, February 1971.
———, et al. "Choose the Tube for L'TV," *Electro-Optical Systems Design*, June 1971.

Epstein, D. W. "Electron-Optical System of Two Cylinders as Applied to Cathode-Ray Tubes," *Proc. IRE*, Vol. 24, No. 8, p. 1095, August 1936.

Fink, D. G., ed. *Television Engineering Handbook*, McGraw-Hill Book Co., Inc., New York, 1957.

Francken, J. C., and H. Bruining. "New Developments in the Image Iconoscope," *Philips Technical Review*, Vol. 14, No. 11, p. 327, May 1953.

Francken, J. C., and R. Dorrestein. "Paraxial Image Formation in the Magnetic Image Iconoscope," *Philips Res. Rep.*, Vol. 6, p. 323, 1951.

Gans, R. "Electron Paths in Electron Optics," *Zeit. fur Tech. Phys.*, Vol. 18, p. 41, February 1937.

Goetze, G. W., and A. H. Boerio. "Secondary Electron Conduction (SEC) for Signal Amplification and Storage in Camera Tubes," *Proc. IEEE*, p. 1007, September 1964.

Gray, F. "Electrostatic Electron-Optics," *Bell Sys. Tech. J.*, Vol. 18, No. 1, p. 1, January 1939.

Heiman, B., and W. Heiman. "Television Camera Tubes—Characteristics and Applications," *Fernseh Und Kino-Technik*, 32, Jahrgang, No. 9/10, 1978.

Himelfarb, F. "Principle of Electronic Image Magnification," *RCA Engineer*, October 1964.

Janes, R. B., et al. "Development and Performance of Television Camera Tubes," *RCA Review*, p. 191, June 1949.

Janes, R. B., and A. A. Rotow. "Light-Transfer Characteristics of Image Orthicons," *RCA Review*, Vol. XI, No. 3, p. 364, September 1950.

Johnson, C. B., et al. "RCA Developmental High Resolution 4.5 inch Image Intensifier-Return Beam Vidicon and Camera System," Paper presented at Naecon, Dayton, Ohio, May 19–21, 1969.

Jones, R. C. "Quantum Efficiency of Detectors for Visible and Infrared Radiation," *Advances in Electronics and Electron Physics*, Vol. XI, p. 88, Academic Press, New York, 1959.

Kim, C. K., and M. Lenzinger. "Charge Transfer in Charge-Coupled Devices," *J. Appl. Phys.*, 42, p. 3586, 1971.

Knoll, M. "Electric Electron Lens for Cathode-Ray Tubes," *Arch. Elektrotech*, Vol. 28, p. 1, 1934.

———, and B. Kazan. *Storage Tubes and Their Basic Principles*, John Wiley & Sons, Inc., New York, 1952.

Kosonocky, W. F., and J. E. Carnes. "Two-Phase Charge-Coupled Shift Registers," *Digest of Technical Papers, IEEE International Solid State Circuits Conference*, p. 132, Philadelphia, February 1972.

Kovac, M. G., et al. "Image Sensors Based on Charge Transfer by Integrated Bucket Brigades," International Electron Devices Meeting, Washington, D.C., October 11–13, 1971.

Klemperer, O., and W. D. Wright. "Investigations of Electron Lenses," *Proc. Phys. Soc.*, Vol. 51, Part II, p. 296, March 1939.

Langmuir, D. B. "Theoretical Limitations of Cathode-Ray Tubes," *Proc. IRE*, Vol. 25, No. 8, p. 977, August 1937.

Langmuir, I., and K. T. Compton, "Electrical Discharges in Gasses, Part II," *Rev. Mod. Phys.*, Vol. B, p. 191, April 1931.

Law, R. R. "High Current Electron Gun for Projection Kinescopes," *Proc. IRE*, Vol. 25, p. 954, August 1937.

———. "Factors Governing Performance of Electron Guns in Television Cathode-Ray Tubes," *Proc. IRE*, Vol. 30, p. 103, February 1942.

Leaman, J. R. "Electron Optics of Vidicons," *RCA Engineer*, 1968.

Levitt, R. S. "Infrared Imaging: Heating Up," *Industrial Research*, 1977.

Liebmann, G. "Image Formation in Cathode Ray-Tubes and the Relation of Fluorescent Spot Size and Final Anode Voltage," *Proc. IRE*, Vol. 33, p. 381, June 1945.

Lubszynski, H. G., et al. "Some Problems of Resolution in Low-Velocity Camera Tubes," International Television Conference, June 1962.

McGee. J. D. "A Review of Television Signal Generating Tubes," International Television Conference, June 1962.

Miller. L. D., and B. H. Vine. "Improved Developmental One-Inch Vidicon for Television Cameras," *J. SMPTE*, Vol. 67, p. 154, March 1958.

Morton, G. A. "Electron Guns for Television Application," *Rev. Mod. Phys.*, Vol. 18, No. 3, p. 362, July 1946.

——. et al. "The Brightness Intensifier," *RCA Review*, Vol. IX, No. 3, p. 419, September 1948.

——, and J. E. Ruedy. "The Low-Light-Level Performance of the Image Intensifier Orthicon," *Advances in Electronics and Electron Physics*, Vol. XII, 1960.

Moss. H. "The Electron Gun of the Cathode-Ray Tube—Part 1," *J. Brit. IRE*, January 1945.

——. "A Space Charge Problem," *Wireless Eng.*, Vol. 22, p. 316, July 1945.

——. "The Electron Gun of the Cathode-Ray Tube—Part 2," *J. Brit. IRE*, June 1946.

——. et al. "Dimensional Tolerances in Cathode-Ray Tube Guns," *Proc. IEE*, Vol. 97, July 1950.

Mouser. D. P., et al. "A Practical Television Tube for Low Light Levels," *Roy. Tel. Soc. J.*, Vol. 11, No. 11, p. 261, 1967.

Murray. C. B., Jr., and A. van der Ziel. "Measurements of Noise in Image Orthicons," *IEEE Transactions on Electron Devices*, p. 365, August 1964.

Musselman. E. M. "The New Image Isocon—Its Performance Compared to the Image Orthicon," *Photoelectronic Imaging Devices*, Vol. 2, Plenum Press, 1971.

Neuhauser, R. G. "The Station Color Television Camera Tube," *J. SMPTE*, Vol. 87, pp. 147–151, March 1978.

——. et al. "The Design and Performance of a High-Resolution Vidicon," *J. SMPTE*, p. 833, November 1962.

——. et al. "Beam-Landing Errors and Signal Output Uniformity of Vidicons," *J. SMPTE*, Vol. 67, p. 149, March 1958.

——. "Developments in Electron Optics Produce Two New Lines of Vidicon Tubes," *RCA Engineer*, PE-244, 1964.

——. "Characteristics and Mode of Operation of Image Orthicons," *Proceedings of the Convention of the National Association of Broadcasters*, April 1962.

——; A. A. Rotow; and F. S. Veith. "Image Orthicons for Color Cameras," *Proc. IRE*, p. 161, January 1954.

Niklas, W. F.; C. S. Szegho; and J. Wimpffen. "A Television Picture Tube with Increased Effective Perveance for Cathode Modulation," *J. Tel. Soc.*, Vol. 8, No. 9.

Parker, N. W.; I. P. Csorba; and H. N. Frihart. "Recent Developments in Scan Magnification," *IRE International Convention Record, Part 7, Broadcast and Television Receivers*, New York, p. 167, March 21–24, 1960.

Pierce, J. R., "Limiting Current Densities in Electron Beams," *J. Appl. Phys.*, Vol. 10, p. 775, October 1939.

——. "A Figure of Merit for Electron Concentrating Systems," *Proc. IRE*, Vol. 33, p. 476, July 1945.

Ramberg, E. G. "Optical Factors in the Photoemission of Thin Films," *Applied Optics*, Vol. 6, No. 12, p. 2163, December 1967.

Rogers, R. L., et al. "Silicon Intensifier Target Camera Tube," 1970 IEEE International Solid-State Circuit Conference at University of Pennsylvania, February 20, 1970.

Rogowski, W. "Aberrations of Electron Images," *Archiv. für Electrotechnik*, Vol. 31, No. 9, p. 555, 1937.

Roosmalen, J. H. T. "New Possibilities for the Design of Plumbicon Tubes," Abstracts of Papers from International Electron Devices Meeting sponsored by IEEE, Washington, D.C., p. 64, October 28–30, 1970.

Rose, A. "Television Pickup Tubes and Problem of Vision," *Advances in Electronics and Electron Physics*, Vol. I, 1948.

——, P. K. Weimer; and H. B. Law. "The Image Orthicon—A Sensitive Television Pickup Tube," *Proc. IRE*, p. 424, July 1946.

Schade, O. H. "A Method of Measuring the Optical Sinewave Spatial Spectrum of Television Image Display Devices," *J. SMPTE*, Vol. 67, No. 9, September 1958.

——. "An Evaluation of Photographic Image Quality and Resolving Power," *J. SMPTE*, Vol. 73, p. 81, February 1964.

——. "Electron Optics and Signal Readout of High-Definition Return-Beam Vidicon Camera," *RCA Review*, p. 60, March 1970.

——. "Image Gradation, Graininess and Sharpness in Television and Motion Picture Systems," *J. SMPTE*, Vol. 58, p. 182, March 1952.

Schlesinger, K. "A Mixed-Field Type of Vidicon," *IEEE Transactions on Electron Devices*, Vol. ED-14, No. 3, March 1967.

Schwartz, J. W. "Space-Charge Limitations on the Focus of Electron Beams," *RCA Review*, Vol. 18, p. 3, 1957.

Spangenberg, K. R. *Vacuum Tubes*, McGraw-Hill Book Co., Inc., New York, 1948.

——, and L. M. Fields. "Some Simplified Methods of Determining the Optical Characteristics of Electron Lenses," *Proc. IRE*, Vol. 30, No. 3, p. 138, March 1942.

Sternglass, E. J., et al. "Transmission Secondary Electron Multiplication for High-Speed Pulse Counting," *IRE Transactions on Nuclear Science*, Vol. NS-3, No. 4, p. 29, November 1956.

Thompson, B. J., and L. B. Headrick. "Space Charge Limitations on the Focus of Electron Beams," *Proc. IRE*. Vol. 28, p. 318, July 1940.

Tompsett. M. F. "Charge-Coupled Imaging Devices: Experimental Results," *IEEE Transactions on Electron Devices*, ED-18, p. 992, November 1971.

van Asselt, R. L. "The Image Isocon Camera Tube," *Proceedings of 1967 NAB Broadcast Engineering Conference*, 1967.

Vine. B. H. "Analysis of Noise in the Image Orthicon," *J. SMPTE*, Vol. 70, p. 432, 1961.

Watson. E. E. "The Dispersion of the Electron Beam," *Phil. Mag.*, Ser. 7, Vol. 3, p. 849, April 1927.

Weimer. P. K. "The Image Isocon—An Experimental Television Pickup Tube Based on the Scattering of Low Velocity Electrons," *RCA Review*, p. 366, September 1949.

————. "Measurement of Secondary Emission of Insulators at Low Primary Energies," *Phys. Rev.*, 74, p. 1219, November 1, 1948.

————. and A. Rose, "The Motion of Electrons Subject to Forces Transverse to a Uniform Magnetic Field," *Proc. IRE*, p. 947, November 1947.

Wentworth. J. W. "Camera Tubes for Studio Use—A Semi-Technical Appraisal for Educators," *J. SMPTE*, March 1963.

Wolfe. W. L., and G. J. Zissis. eds. *The Infrared Handbook*, Office of Naval Research. Department of the Navy, Washington, D.C., 1978.

Zworykin. V. K., and G. A. Morton. *Television*. John Wiley & Sons. Inc., New York. 1940.

Zworykin, V. K., and W. H. Painter. "Development of the Projection Kinescope," *Proc. IRE*, Vol. 25, p. 937, 1937.

Zworykin, V. K., and E. G. Ramberg. *Photoelectricity and its Applications*, John Wiley & Sons. Inc., New York. 1949.

18

THE ELECTRON GUN

18.1   Introduction

The electron gun is a vital part of many different types of electronic imaging devices operating in an x-y positioning, time-sequentially, point-by-point imaging mode. With the aid of an electron gun a continuous image may be resolved into its constituent parts by means of electronic scanning. For example, in the case of a camera tube the electronically stored image of a scene may be converted into electrical signals by scanning the storage target with a fine beam of electrons produced by an electron gun. On the other hand, in display tubes the image is reconstructed by a scanned and camera tube signal modulated electron beam. The basic function of the electron gun of imaging devices, therefore, is the production of an electronically deflectable pencil of electron beam that is sharply focused on the target and, in camera tubes, the generation of a beam with low beam temperature for low beam discharge lag. In display tubes, beam intensity modulation is also required. The term "electron gun" covers a broad subject. In this chapter, however, the discussion will be limited to the type of electron guns used in display devices, and to the low-voltage type of guns used in camera tubes.

18.2   Cathode Ray Tube Guns

18.2.1   General Description

The cathode ray tube gun consists of an electron source, which is usually a thermionic cathode, and a focusing system that confines the cathode rays

into a narrow bundle of electron beam and focuses the cathode current into a small spot at the target (phosphor screen, storage target, etc.). Figures 18.1 and 18.2 show the diagrams of conventional electrostatic- and magnetic-focus tetrode guns. The electrons leaving the cathode enter first the cathode lens which is present within the region bounded by the cathode and the G_1 and G_2 electrodes. The G_2 electrode (first anode) is at a positive potential (usually few hundred volts) with respect to the cathode. The potential of G_1 is zero or negative with respect to the cathode. The focusing action of the cathode lens is similar to the focusing action of the image tube lens shown in figure 3.1. The electron bundles, originating at the cathode, form
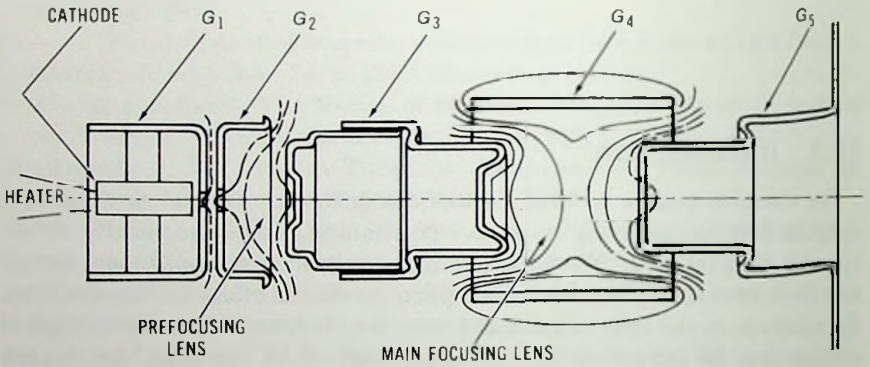
(A) Cross section.
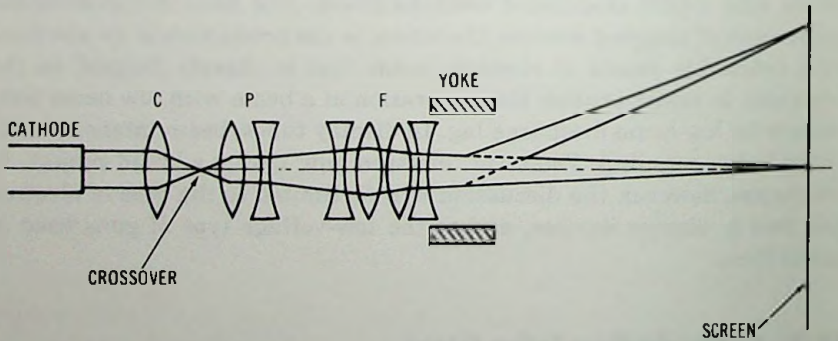
(B) Schematic arrangement of the beam focusing lens.

Fig. 18.1   Conventional electrostatic focus, tetrode-type electron gun.
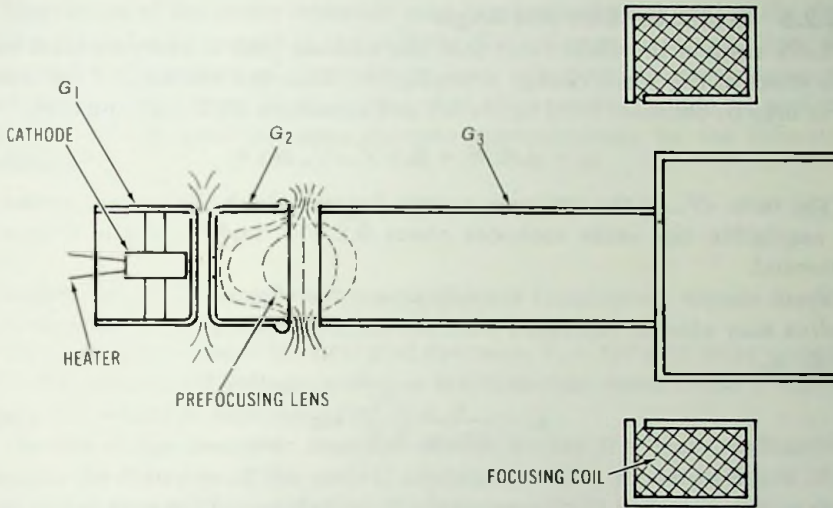
Fig. 18.2   Cross section of a magnetic focus, tetrode-type gun.

a crossover in the vicinity of the G_2 aperture, and behind the G_2 aperture produce a real image of the cathode. The beam current has the smallest diameter and consequently the highest current density at the crossover. Therefore the smallest spot size, corresponding to the highest current density, may be obtained by imaging the crossover on the target. The crossover is imaged by the prefocusing and main focusing lenses.

In figure 18.1B the cathode beam, after leaving the cathode lens C, passes through the prefocusing lens P and is directed toward focusing lens F. The strength of focusing lens F is adjusted so that an image of the crossover is formed at the phosphor screen. The beam is deflected by a deflection yoke.

In figure 18.2 the electron beam, after crossover, passes through the prefocusing lens and is directed toward the magnetic focusing main lens. The strength of the magnetic lens is adjusted so that an image of the crossover is formed at the phosphor screen.

18.2.2   Cathode Lens

As mentioned above, the function of the cathode lens is to confine the cathode current into a small crossover spot and to provide beam modulation. For the design of the cathode lens, therefore, the following properties must be considered: (a) the crossover size and crossover angle, (b) the value of the beam current and the cutoff voltage, and (c) the cathode loading.

18.2.3   Crossover Size and Angle

Let's assume the ideal case: that the cathode lens is aberrationless and the effect of the space charge is negligible. Then the radius ρ of the crossover may be obtained from figure 3.1 and equations 3.22, 3.27 and 3.28.

$$\rho_c = \rho_s R_c / S = R_c \sqrt{V V_{cr}} / V_{cr} \sin \theta. \tag{18.1}$$

The term eV_m is the emission energy beyond which the current emission is negligible (for oxide cathodes about 0.2 eV), and V_{cr} is the crossover potential.

From simple geometrical considerations (see figure 18.3), the crossover radius may also be expressed with the cathode radius r_c and the crossover angle α_{cr}.

$$\rho_c = \frac{r_c}{\sin \alpha_{cr}} \sqrt{\frac{V_m}{V_{cr}}} \sin \theta. \tag{18.2}$$

From equations 18.1 and 18.2 and for a constant value of r_c the crossover size may be reduced by increasing the value of α_{cr}, which on the other hand, is synonymous with decreasing the value of R_c.

As mentioned earlier the location of the crossover is in the vicinity of the G_2 aperture. Therefore the crossover size and angle is greatly influenced by the G_2 electrode to cathode distance; the closer G_2 is to the cathode, the greater α_{cr} becomes.
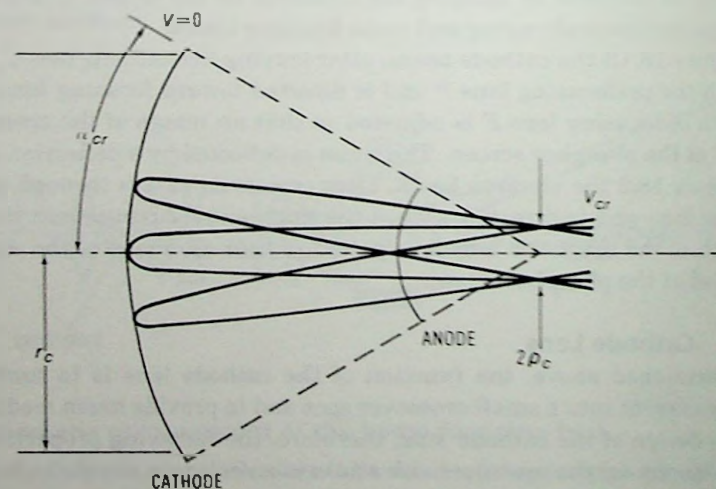
Fig. 18.3   Idealized cathode with spherical field.

Modulation of the beam intensity may be obtained by changing the first grid potential with respect to the cathode. This change, however, alters the potential configuration of the cathode lens, affecting the crossover angle and the emitting area. Moss showed that the crossover angle α_{cr} and the radius r_c of the emitting area changes approximately by the following relations:

$$\alpha_{cr} = \alpha_0 V_d / V_c \qquad (18.3)$$

and

$$r_c = r_0 V_d / V_c. \qquad (18.4)$$

Here r_0 is the radius of the first grid aperture, V_d is the grid drive voltage, V_c is the beam cutoff voltage, and α_0 is the maximum value of the crossover angle that occurs at zero bias ($V_c = V_d$).

The size of the crossover does not change during the beam modulation, because the diameter of the central electron bundles, shown in figure 18.3, does not change with modulation. Modulation affects the crossover so that with increased bias the zonal bundles are detached from the beam decreasing the current density and the angle of the crossover.

In an aberrated system (flat cathode, etc.) the electron bundles originating at different radial zones may not cross the axis at the same axial distance from the cathode. Space charge may also alter the potential configuration. In essence, aberrations and space charge, therefore, may increase the crossover diameter.

The precise analysis of an aberrated cathode lens with space charge condition is possible only by electron trajectory calculations. The theory put forward with the aberrationless cathode lens, however, gives a gross understanding of a cathode lens which, coupled with the cut-and-try methods, enabled the electron gun designers to develop the great majority of present-day cathode ray tube guns.

18.2.4 Beam Current Characteristics

The beam current characteristics are the second factor which must be considered for the cathode lens design. The points of interest are the maximum value of the beam current and the beam current modulation characteristic. The maximum value of beam current is usually obtained at zero potential difference between the first grid and the cathode, and the beam cutoff occurs at a negative potential V_c with respect to the cathode. Beam current modulation may be obtained by varying the potential difference between the cathode and the first grid in the range of 0 to $-V_c$. As far as operation is concerned we may differentiate between grid and cathode modulations. In the case of grid modulation the cathode is grounded, the first

grid is biased negative, and the signal voltage is applied to the first grid, superimposing it on the bias voltage. In order to display the entire modulation characteristic the sum of the bias and signal voltages must vary from 0 to $-V_c$. For cathode modulation, on the other hand, the first grid is grounded and the signal voltage is applied to a positively biased cathode.

The cathode current for grid modulation may be given by the following equation:

$$I = kV_d^m V_c^n, \tag{18.5}$$

where I is the cathode current in amperes, k is a constant having a value of about $3 \times 10^{-6}/V^{m+n}$, V_c is the cutoff voltage, and V_d is the grid drive voltage.

For the exponents m and n, different authors give different values. Moss gives $m = 7/2$ and $n = -2$ for the exponents.

By substitution of the above m and n values in equation 18.5, the space charge limited emission from the cathode at zero bias ($V_d = V_c$), in accordance with the Child-Langmuir space charge law, becomes

$$I_0 = kV_c^{3/2}. \tag{18.6}$$

The cutoff voltage, V_c, is related to the second grid voltage V_2 and the high voltage V_3 by the following equation:

$$V_c = D_2 V_2 + D_3 V_3, \tag{18.7}$$

where D_2 and D_3 are the second grid voltage and high voltage penetration factors, respectively. Voltages D_2 and D_3 are related to the physical structure of the gun. For a gun which has fixed dimensions, V_c changes according to equation 18.7 with changes in V_2 and V_3.

In the case of cathode modulation a steeper modulation characteristic is obtained, because with cathode drive the second grid to cathode voltage is also changing. The advantage of the cathode drive is utilized to full extent in gun designs with low V_2 voltage. If the grid modulation characteristic of a gun is known as a parameter of second grid voltage, then it is also possible to derive the cathode modulation characteristic. The value of the cutoff voltage V_{cc} in cathode modulation is

$$V_{cc} = D_2(V_2 - V_{cc}) + D_3 V_3. \tag{18.8}$$

When a cathode drive V_{dc} is applied, the effective value of drive voltage V_{dc}, from the diagram of figure 18.4, is

$$V_{dc} = V_{dc} + V_{cc} - V_{cc}, \tag{18.9}$$

where V_{cc} is the effective value of cutoff voltage for drive V_{dc}.

$$V_{cc} = D_2[V_2 - (V_{cc} - V_{dc})] + D_3 V_3. \tag{18.10}$$
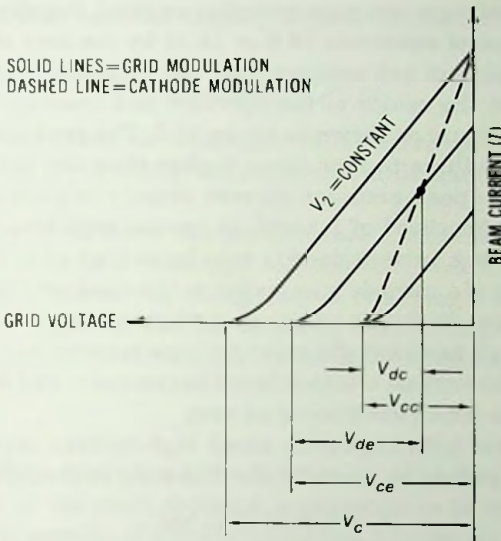
Fig. 18.4   Beam current characteristics for grid and cathode modulations.

By combination of equations 18.8, 18.9, and 18.10, we obtain

$$V_{de} = V_{dc}(1 + D_2).$$ (18.11)

For $V_{dc} = V_{cc}$ (zero bias)

$$V_{ce} = V_c = (1 + D_2)V_{cc}.$$ (18.12)

By substitution of equation 18.12 in equation 18.6, the beam current at zero bias becomes

$$I_0 = k(1 + D_2)^{3/2} V_{cc}^{3/2}.$$ (18.13)

Combining equations 18.8 and 18.10 we also obtain

$$V_{ce} = V_{cc} + D_2 V_{dc}.$$ (18.14)

By substitution of equations 18.11 and 18.14 in equation 18.5, the beam current modulation characteristics for cathode modulation becomes

$$I = kV_{dc}^m (1 + D_2)^m (V_{cc} + D_2 V_{dc})^n.$$ (18.15)

18.2.5   Electron Beam Parameters

As discussed earlier, at zero bias (maximum beam current) the diameter of the emitting area of the cathode equals the diameter of the first grid

aperture. The maximum average emission current density then may be obtained by division of equations 18.6 or 18.13 by the area of the aperture. The cathode emission is not uniform over the emitting area, but it has a maximum value at the center of the aperture and descends to zero at the edge of the grid aperture as shown in figure 18.5. The peak emission current density therefore is three to four times higher than the average emission current density. The peak emission current density in picture tube guns is usually in the neighborhood of 1 A/cm². In special high-resolution cathode-ray tube guns the peak current density may be as high as 3 A/cm².

The performance of a cathode lens, as far as the electron beam parameters are concerned, depends on the physical configuration of the cathode lens electrodes. Moss has analyzed the relationships between the geometry of a cathode lens and the various electron beam parameters, and derived approximate relationships which are presented next.

For gun structures with negligibly small high-voltage penetration ($D_3 \cong$ 0), the cutoff voltage may be given by the following approximate equation:

$$V_c \cong 0.0046\, D^3 V_2 / tbf, \tag{18.16}$$

where D is the diameter of the first grid aperture, t, b, and f are the grid material thickness, G_1-to-cathode spacing, and G_1-to-G_2 spacing, respectively.
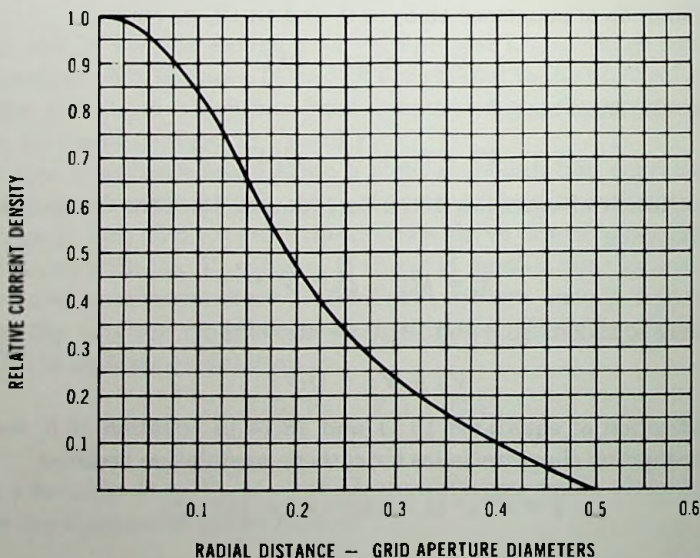
Fig. 18.5 Typical emission current density distribution as a function of radial distance at zero bias.

The value of peak cathode loading may be estimated from the following equation:

$$J_c = 0.0145 \, V_d^{3/2}/D^2, \tag{18.17}$$

where J_c is the peak cathode loading in milliamperes per square millimeter, D is the diameter of the first grid aperture in millimeters, and V_d is the grid drive in volts.

It is often useful to know the performance change due to changing the physical dimensions of a prototype cathode lens. Table 18.1 gives a brief summary of the performance change due to changing the G_1-to-G_2 spacing, the G_1-to-cathode spacing, and the diameter of the first grid aperture. These results are approximate only and accuracy on wide extrapolations must not be expected.

18.2.6 The Main Focusing Lens System

The function of the main focusing lens system is to image the crossover on the target. It consists of a prefocusing lens and the main focusing lens as shown in figure 18.6. The main focusing lens is a thin electrostatic lens or a short magnetic lens. Sharp imaging with the main lens, however, is possible only if the electron beam diameter passing through the main lens is small. Otherwise, because of spherical aberration and deflection defocusing, the main lens does not faithfully reproduce the crossover image. The electron beam is confined to a small diameter by the prefocusing lens that exists between the G_2 and G_3 electrodes. The prefocusing lens is a positive lens having a focal length greater than the prefocusing lens to crossover distance. Therefore the prefocusing lens forms a virtual image of the crossover. By application of the sine law of the geometrical optics to the crossover and its image, the following relation may be obtained between the crossover angle α_{cr} and the prefocused angle α_1:

$$\sin \alpha_1 = \sqrt{\frac{V_{cr}}{V_3}} \, \frac{\sin \alpha_{cr}}{M_P}, \tag{18.18}$$

where M_P is the lateral magnification of the prefocusing lens and the ratio of the square roots of the voltages represents the refraction indexes on the two sides of the lens. For example, if $V_{cr} = 200$ V, $V_3 = 20\,000$ V, $M_P = 1.1$, and $\alpha_{cr} = 20°$, then from equation 18.18 $\alpha_1 = 1.78°$, which produces a 0.062-cm beam diameter spread per centimeter. If the beam diameter is to be limited to 0.31 cm in the main lens, then the main lens should be placed at 15 cm from the virtual image of the crossover.

By application of the sine law to the virtual image of the crossover and the real image of the crossover at the phosphor screen, the following relation

Table 18.1 Beam Characteristics Change Due to Changing the Dimensions of a Cathode Lens*

Operation			Consequences					
independent variable and operation	solve other variable and extent of adjustment to achieve new condition specified	cutoff voltage	crossover diameter	beam angle (α)	total current in beam	current/unit solid angle	cathode loading
	grid material thickness, grid hole diameter and anode/grid spacing all multiplied by k (geometrical similitude)	$\times 1$	$\times k$	$\times 1$	$\times 1$	$\times 1$	$\times \dfrac{1}{k^2}$
cathode grid spacing multiplied by k	grid drive multiplied by k^{-1} to maintain constant beam angle	$\times \dfrac{1}{k}$	$\times 1$	$\times 1$ (postulate)	$\times \dfrac{1}{k^{3/2}}$	$\times \dfrac{1}{k^{3/2}}$	$\times \dfrac{1}{k^{3/2}}$
	anode/grid spacing multiplied by k^{-1} to maintain constant cutoff voltage	$\times 1$ (postulate)	$\times \dfrac{1}{k^m}$ $\left(\times \dfrac{1}{k^{3/4}}\right)$	$\times k^m$ $\left(\times k^{3/4}\right)$	$\times 1$	$\times \dfrac{1}{k^{2m}}$ $\left(\times \dfrac{1}{k^{3/2}}\right)$	$\times 1$
	grid hole diameter multiplied by $\sqrt[n]{k}$ to maintain constant cutoff voltage	$\times 1$ (postulate)	$\times 1$	$\times k^{1/n}$ $(\times k^{1/3})$	$\times 1$	$\times \dfrac{1}{k^{2/n}}$ $\left(\times \dfrac{1}{k^{2/3}}\right)$	$\times \dfrac{1}{k^{2/n}}$ $\left(\times \dfrac{1}{k^{2/3}}\right)$

Table 18.1—cont.   Beam Characteristics Change Due to Changing the Dimensions of a Cathode Lens*

Operation		Consequences					
independent variable and operation	sole other variable and extent of adjustment to achieve new condition specified	cutoff voltage	crossover diameter	beam angle (α)	total current in beam	current/unit solid angle	cathode loading
grid hole diameter multiplied by k	anode/grid spacing, cathode/grid spacing and grid material thickness all multiplied by k to maintain constant cutoff voltage (geometrical similitude)	$\times 1$ (postulate)	$\times k$	$\times 1$	$\times 1$	$\times 1$	$\times \dfrac{1}{k^2}$
	grid drive multiplied by k^{n-1} to maintain constant beam angle	$\times k^{n}$ ($\times k^3$)	$\times 1$	$\times 1$ (postulate)	$\times k^{(3n-7)/2}$ ($\times k$)	$\times k^{(3n-7)/2}$ ($\times k$)	$\times k^{(3n-7)/2}$ ($\times k$)
	cathode/grid spacing multiplied by k^n to maintain constant cutoff voltage	$\times 1$ (postulate)	$\times 1$	$\times k$	$\times 1$	$\times \dfrac{1}{k^2}$	$\times \dfrac{1}{k^2}$
	anode/grid spacing multiplied by k^n to maintain constant cutoff voltage	$\times 1$ (postulate)	$\times k^{mn}$ ($\times k^{9/4}$)	$\times k^{1-mn}$ $\left(\times \dfrac{1}{k^{5/4}}\right)$	$\times 1$	$\times \dfrac{1}{k^{2(1-mn)}}$ ($\times k^{5/2}$)	$\times \dfrac{1}{k^2}$

Table 18.1—cont. Beam Characteristics Change Due to Changing the Dimensions of a Cathode Lens*

	Operation		Consequences					
independent variable and operation	sole other variable and extent of adjustment to achieve new condition specified	cutoff voltage	crossover diameter	beam angle (α)	total current in beam	current/unit solid angle	cathode loading
	grid hole diameter, cathode/grid spacing, grid material thickness all multiplied by k (geometrical similitude)	$\times 1$	$\times k$	$\times 1$	$\times 1$	$\times 1$	$\times \dfrac{1}{k^2}$
anode/grid spacing multiplied by k	cathode/grid spacing, multiplied by $1/k$ to maintain constant cut-off voltage	$\times 1$ (postulate)	$\times k^m$ $\left(\times k^{3/4}\right)$	$\times \dfrac{1}{k^m}$ $\left(\times \dfrac{1}{k^{3/4}}\right)$	$\times 1$	$\times k^{2m}$ $\left(\times k^{3/2}\right)$	$\times 1$
	grid hole diameter multiplied by $k^{1/n}$ to maintain constant cutoff voltage	$\times 1$ (postulate)	$\times k^m$ $\left(\times k^{3/4}\right)$	$\times k^{1/n-m}$ $\left(\times \dfrac{1}{k^{5/12}}\right)$	$\times 1$	$\times \dfrac{1}{k^{2/n-2/m}}$ $\left(\times k^{5/6}\right)$	$\left(\times \dfrac{1}{k^{2/n}}\right)$ $\dfrac{1}{k^{2/3}}$
	grid drive multiplied by k^{m-1} to maintain constant beam angle	$\times \dfrac{1}{k}$	$\times k^m$ $\left(\times k^{3/4}\right)$	$\times 1$ (postulate)	$\times k^{(7m-3)/2}$ $\left(\times k^{9/8}\right)$	$\times k^{(7m-3)/2}$ $\left(\times k^{9/8}\right)$	$\times k^{(3(m-1))/2}$ $\left(\times \dfrac{1}{k^{3/8}}\right)$

*Data from H. Moss, "The Electron Gun of the Cathode-Ray Tube," *J. Brit. IRE*, January 1945.
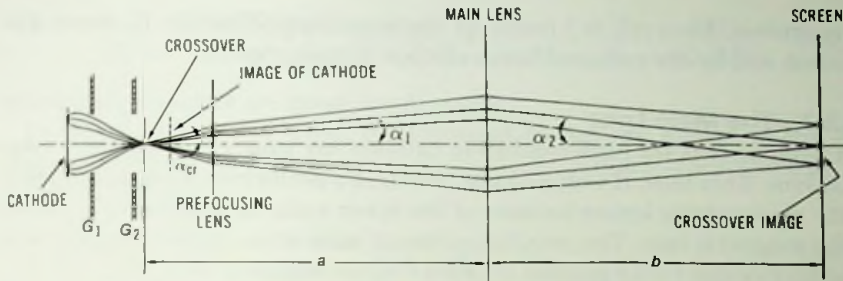
Fig. 18.6   Focusing action in the electron gun.

may be obtained for the main lens magnification:

$$M_L = \sqrt{\frac{V_3}{V_S}}\frac{\sin \alpha_1}{\sin \alpha_2} \cong \sqrt{\frac{V_3}{V_S}}\frac{\tan \alpha_1}{\tan \alpha_2} \cong \sqrt{\frac{V_3}{V_S}}\frac{\alpha_1}{\alpha_2} \cong \sqrt{\frac{V_3}{V_S}}\frac{b}{a}. \qquad (18.19)$$

The total magnification M_T of the main focusing lens system is the product of the main lens and prefocusing lens magnification:

$$M_T = M_L M_P. \qquad (18.20)$$

In order to obtain a small spot size at the target (screen), M_L should be as small as it is practical. Accordingly, α_1 should be small, and α_2 and V_S large. The value of α_2 is determined by the allowable beam diameter and by the main lens to target distance. The target distance, on the other hand, is determined by the target size and the maximum deflection angle. For a given target size, the greater the deflection angle, the smaller is the target distance. The maximum deflection angle is usually limited by the available deflection power or by the deflection focusing error. By inspection of equation 18.18 there are several alternatives to keep α_1 small. For example, by increasing M_P, angle α_1 can be decreased and a increased. However, M_P is present in equation 18.20, and therefore the total magnification would not decrease. By decreasing α_{cr} and V_{cr}, angle α_1 would be also decreased, but the crossover size would increase as may be concluded from equations 18.1 and 18.2, and therefore the spot size at the target would not improve. The only effective alternatives for reduction of α_1 is increasing the voltage V_3 and increasing judiciously the value of a. With an increased value of a a beam diameter limiting aperture may be placed in front of the main focusing lens in order to hold the maximum beam diameter below the allowable value. This way the value of α_1 and the effective value of α_{cr} are decreased at the expense of losing beam current to the G_3 electrode. With this step, if no aberration is present, the spot magnification is decreased proportionally with the decrease of α_1, and the current density in the spot is increased.

This process, however, is limited by the maximum allowable G_3 power dissipation and by the required beam current at the target.

18.2.7 The Main Lens

A popular lens for high-resolution cathode ray tube guns is a short magnetic lens. This lens, if well aligned, provides a performance superior to that of the electrostatic lenses because of the lower value of spherical aberration of the magnetic lens. The smaller spherical aberration of the magnetic lens is primarily due to the greater diameter of the magnetic lens.

The short electromagnetic lens consists of windings enclosed in a soft iron housing as shown in figure 18.7. With the assumption that the windings act as a single turn, the axial distribution of the magnetic flux density B_0 may be given from equation H.2 of appendix H as follows:

$$B_0 = \frac{\mu_0 \, NIR^2}{2(R^2 + z^2)^{3/2}},\tag{18.21}$$

where N is the number of turns of the coil, and $\mu_0 = 1.257 \times 10^{-6}$ H/m is the permeability of free space. By substitution of equation 18.21 in equation E.71 of appendix E, the focal length of the short magnetic lens becomes

SOFT IRON
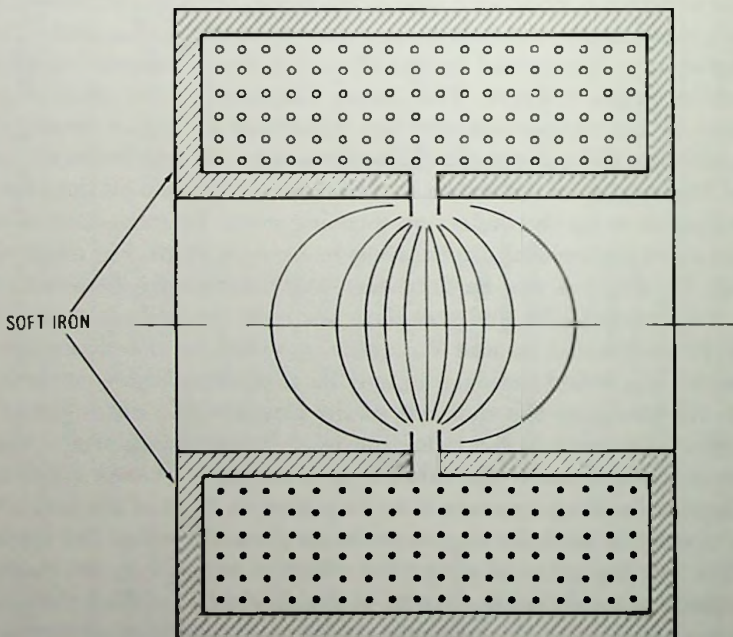
Fig. 18.7 Short magnetic lens.

$$\frac{1}{f} = -\frac{\mu_0^2 e N^2 I^2 R^4}{32 m V} \int_{-\infty}^{+\infty} \frac{dz}{(z^2 + R^2)^3} = \frac{3\pi\mu_0^2}{256V} \frac{e}{m} \frac{N^2 I^2}{R} = \frac{N^2 I^2}{97.9VR}, \qquad (18.22)$$

where all parameters are given in mks units.

For weak fields $N^2 I^2/V < 100$, the principal planes are located at the lens center. Therefore the image and object distances, a and b, are related by the thin lens formula:

$$\frac{1}{a} + \frac{1}{b} = \frac{1}{f}, \qquad (18.23)$$

where a and b are measured from the center of the lens.

The disadvantages of the electromagnetic focusing, besides the alignment problems, are that an additional component with a current supply is needed and that for sharp focusing a stable voltage and current supplies are necessary.

Among the electrostatic lenses, the two-cylinder lens has the lowest value of spherical aberration. Therefore the two-cylinder lens is frequently used in high-resolution electrostatic-focus cathode-ray tubes. The focal lengths and the location of the principal planes of the two-cylinder lens, in addition to the physical structure (gap of the cylinders and diameter ratio), depends on the voltage ratio applied to the cylinders. Figure 18.8 shows the cardinal quantities f_1, f_2, and F_1, and F_2 of three different lens structures as a function of voltage ratio V_2/V_1. The relation between the image and object distance may be obtained by the thick lens formula:

$$\frac{f_1}{a - P_1} + \frac{f_2}{b - P_2} = 1, \qquad (18.24)$$

where P_1 and P_2 give the location of the principal planes measured from the lens center as shown in figure 18.9. The disadvantages of the two-cylinder lens are two separate voltages, V_1 and V_2, and that for sharp focus the voltage ratio must be stable.

The unipotential lens is another electrostatic type of main focusing lens that gained wide application in a variety of cathode-ray tubes, especially in tv picture tubes. Figure 18.10 shows several different types of construction of the unipotential lens. The center electrode is at ground potential and the entrance and the exit electrodes are tied to the anode potential, usually the screen potential. The unipotential lens has several good features: (a) it is economical because only one voltage is applied to it; (b) once the physical structure is adjusted to produce a sharp image at the phosphor screen, the focusing becomes independent of the high-voltage variation and, since the focal length is independent of the value of the high voltage, no high voltage regulation is necessary; and (c) because the entrance electrode (the G_3 elec-

trode of the gun) is at the screen potential the crossover angle is strongly demagnified by the prefocusing lens, thus confining the beam into a narrow angle.

The refractive index is identical on both sides of the lens. Therefore the focal lengths are also identical: $f_1 = f_2$. The unipotential lens acts as a thin lens positioned at the center of the physical structure. The image and object distances, therefore, are related by the thin lens formula given by equation 18.23.
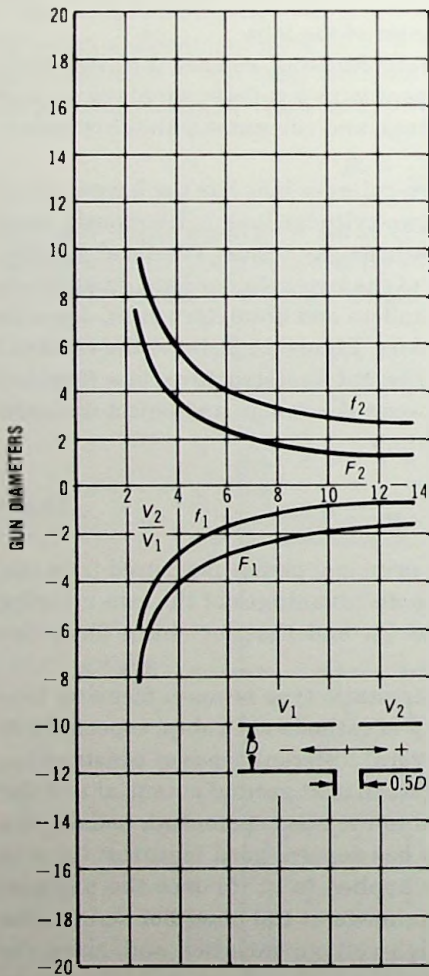
(A) $D_2/D_1 = 1.00$, spacing $= 0.5\ D$.   (B) $D_2/D_1 = 1.00$, spacing $= 0.1\ D$.
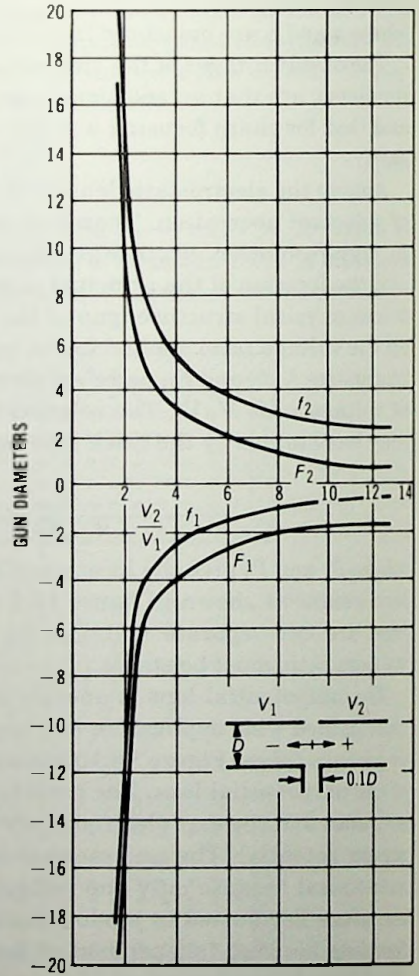
Fig. 18.8   Optical characteristics

18.3   Low-Velocity Electron Guns

18.3.1   Introduction

For signal readout the camera tube target is scanned by a low-velocity electron beam to charge the target to a uniform potential. The required electron beam is usually about 1 μA and its diameter is in the range of 10 to 25 μm, depending on the size of the target and on the resolution require-ments. For a uniform and efficient charging, the electron beam must have a narrow velocity range and the deflected electron beam must land perpendic-

(C) $D_2/D_1 = 1.5$.
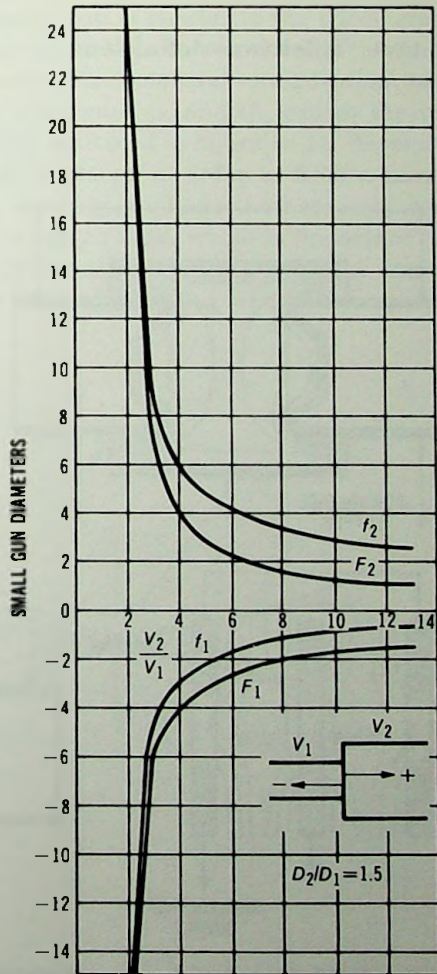
of two-cylinder lenses.
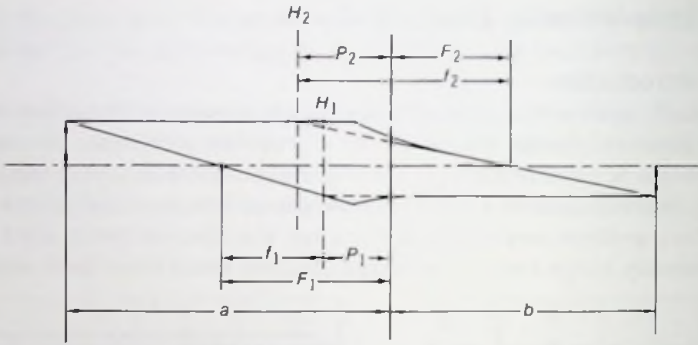
Fig. 18.9   Thick lens definitions.
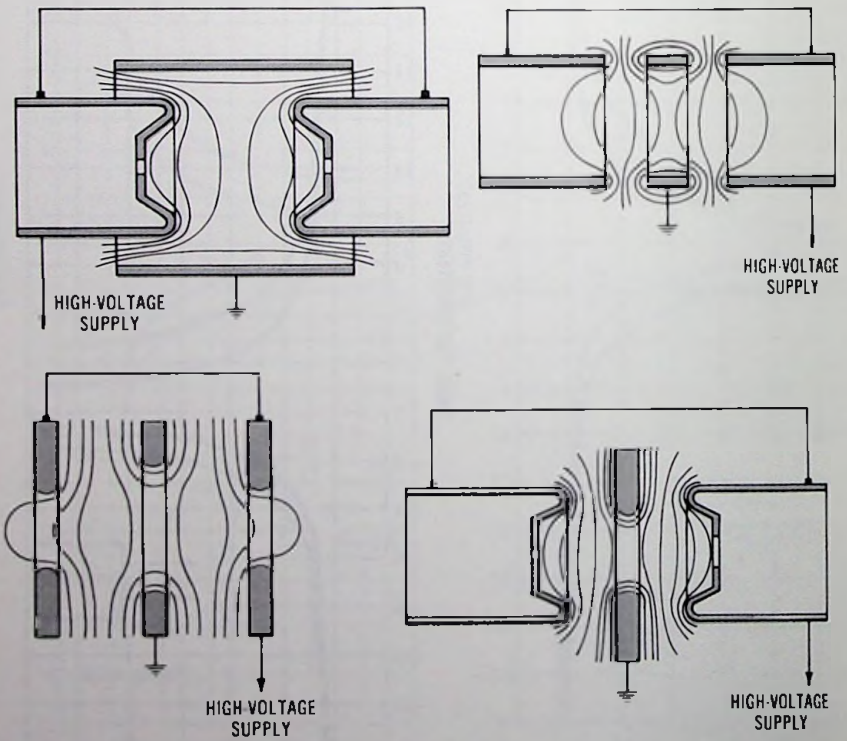
Fig. 18.10   Unipotential type electrostatic focusing lenses.

ularly on the target, or it must have a constant axial energy over the target, to avoid shading. Efficient charging is particularly important in the image orthicon type of tubes, where an acceptable noise figure demands the lowest possible scanning beam current.

The low-velocity beam is usually generated by acceleration of the thermionic electrons of an oxide cathode to a few hundred volts of electric potential, in order to form a narrow-angle, small-diameter, electron beam followed by deceleration of the beam to a near-zero energy at the target.

18.3.2   The Emission Source

The emission source of a low-velocity gun is similar to the triode section of the cathode-ray tube gun already described. It consists of a thermionic cathode and of the G_1 and G_2 electrodes. The potential configuration, in the space bounded by the cathode and electrodes G_1 and G_2, causes the thermionic electrons to form a crossover as indicated in figure 18.11. Beyond the crossover a small limiting aperture is placed in order to form a narrow-angle electron beam. The limiting aperture produces the necessary conditions for ensuring a narrow axial velocity range, which is important for a uniform target charging. The electron beam emerging from the limiting aperture is focused on the target by the main focusing lens system.
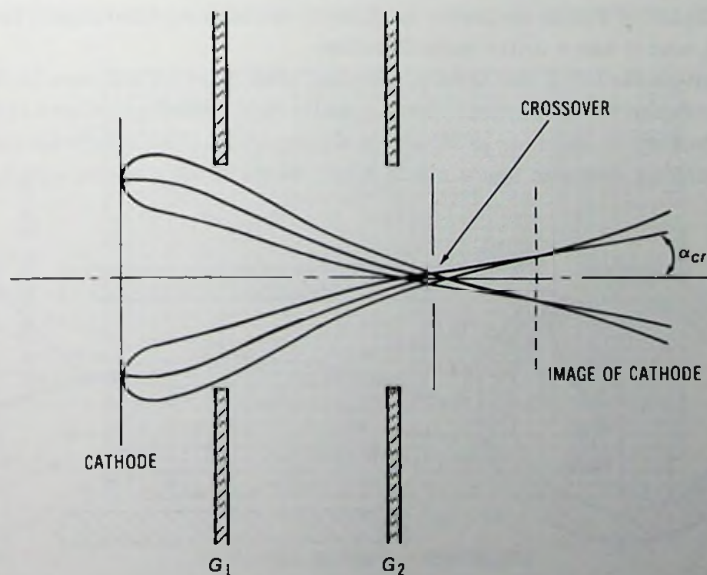
Fig. 18.11   Electron trajectories of a triode emission system.

In conventional electron guns a significant portion of energy spread of electrons is caused by space charge effects which by mutual repulsion speed up some electrons and slow down others and impart radial components of velocity to electrons at the periphery. The space charge effect is most significant in the crossover. The axial emission energy spread of conventional guns can be reduced by reduction of the space charge density in the crossover and by use of a narrow beam angle. The laminar-flow diode gun is the second and a better method for reduction of beam energy spread. The laminar-flow gun avoids the crossover of the triode gun, leading to markedly reduced electron beam temperatures and consequently lower electron beam discharge lag.

18.3.3   The Main Focusing System

The main focusing lens system consists of the main lens and the deceleration or collimation lens near the target. One of the most widely used main lens in camera tubes is the long magnetic lens consisting of an axial homogeneous magnetic field that extends from the thermionic cathode to the target. The magnetic field and the small transverse velocity component of electrons present in the narrow electron beam cause the electrons to move on a circular orbit in the plane perpendicular to the magnetic field. The period T of the circular motion is given by equation 3.10. By adjustment of the transit time of the electrons between the crossover and the target to T or multiples of T, the crossover is sharply focused on the target. The image is erect, and it has a unity magnification.

The short focusing coil lens is another lens used in vidicons to focus the electron beam on the target. The magnetic field distribution and the motion of an electron in the lens is shown in figure 18.12. The magnetic field turns the diverging electron beam along a helical path back to the axis by acting
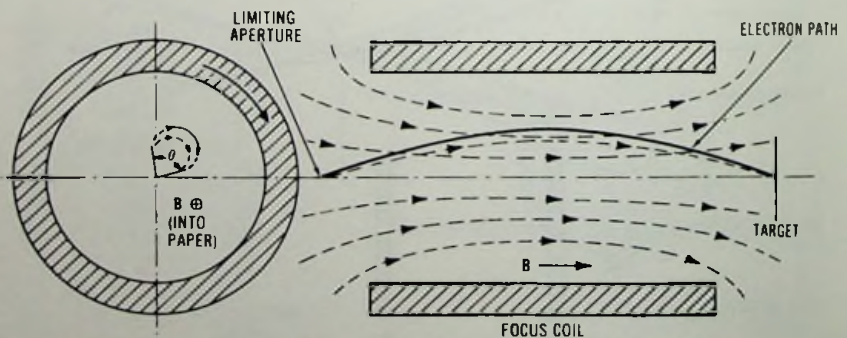
Fig. 18.12   Motion of electrons in a magnetic focus lens.

on the transverse velocity component of the electron beam. The main advantage of magnetic focusing as compared with electric focusing is the low value of the spherical aberration of the magnetic lens. Because of the low value of the spherical aberration, the resolution capability of the magnetic lens is greater than that of the electrostatic lens. Another advantage of magnetic focusing is that it is possible to immerse completely the deflection field in the focus field without serious corner defocusing, thus obtaining a short length tube.

In electrostatically focused vidicons a three-tube lens, such as is shown in figure 18.10, is used to focus the electron beam on the target. A strong focusing lens is formed by connection of the middle tube to a potential lower than the potentials of the entrance and exit tubes. The entrance and exit tubes are then connected together, or the entrance tube is connected to a potential (mesh potential) higher than the potential of the exit tube in order to obtain a stronger prefocusing lens and a narrower electron beam.

In high-resolution vidicons high resolution is obtained by demagnification of the crossover image. A demagnifying magnetic lens may be obtained by reducing the magnetic field at the crossover. Figure 18.13 shows the axial magnetic field strength of the RCA return-beam vidicon. The left-side portion of the lens, where the magnetic field gradually increases, produces a 2:1 demagnification. The uniform field projects the demagnified image over several loops on the target with unity magnification.

In the FPS (focus projection and scanning vidicon) the crossover is demag-
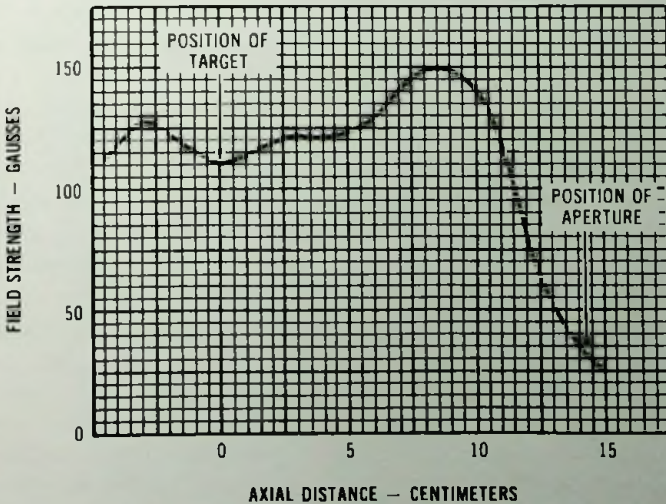
Fig. 18.13   **Focus field plot along tube axis.**

nified by partial immersion of the vidicon tube in the focusing magnetic field as shown in figure 17.27. Partial immersion produces a magnetic lens which demagnifies the spot size of the scanning electron beam by a factor of 0.7 to an effective spot diameter of 10 μm. Another advantage of partial immersion is the greater deflection efficiency that is the result of relaxed magnetic field required to focus. The relaxed magnetic field reduces the scan compression caused by the magnetic immersion.

The deflected electron beam has a helical motion in the region of deflection which, due to the shortness of the focus coil, is only a fraction of the loop and therefore causes beam landing errors. Beam landing errors, fortunately, can be compensated as outlined later in this section.

In its general performance the FPS vidicon compares favorably with a conventional magnetic vidicon. The FPS is, however, smaller in size, power, and weight. As compared with an electrostatic vidicon it is far ahead in resolution and signal current.

The second part of the main focusing system is the deceleration lens. This lens is included to decelerate the electrons and to ensure a uniform charging of the entire target without shading. For uniform target charging the axial velocity component of the deflected electron beam must be uniform over the entire useful target area. In order to be able to charge the target to near zero potential the transverse component of electron velocity must have a small value. This is particularly important in the image orthicon, where the transverse component of electron energy of the landing electrons is about 0.1 eV, in order to produce a large voltage swing at the target.

Ideally, therefore, the deflected beam should land perpendicularly on the target. In the case of an all-magnetic system (magnetic focus, magnetic deflection) the deflected beam moves on a helical path around the magnetic field, which is the vector sum of the focusing and deflecting fields. The undeflected electrons are characterized by an axial motion. The motion in the deflecting field can be visualized by dividing the axial motion into its two components, one component parallel to the magnetic field and the other component perpendicular to the magnetic field. The motion parallel to the magnetic field is unaffected by the magnetic field. The perpendicular velocity component of the motion, however, causes the beam to move on a helical path. In a homogeneous field, after the completion of a circular loop the two components of motion assume the spatial position which the undeflected beam had; that is, at this point, the motion has only an axial component of velocity. Thus a deflection coil whose length is a multiple of the loop focus theoretically could produce a beam deflection with perpendicular landing on the target. In an actual setup of image orthicon tubes, however, the deflected beam may have, in addition to the axial velocity, a radial velocity and a tangential velocity component due to the helical motion. The two

unwanted components may be cancelled by the deceleration lens formed by a short cylindrical electrode and the wall coating. By proper positioning of the deflection coils from the target, and by adjustment of the strength of the deceleration lens, both components of the helical motion may be compensated. In this manner a perpendicular landing of the electron beam may be obtained.

As far as beam landing is concerned, a different situation exists in the vidicon tubes due to different optics used. In the magnetically focused and deflected vidicon the electron beam has a helical motion in the region of deflection. Due to the shortness of the deflection coil, however, the electron beam may complete only a fraction of a loop. At the end of the deflection, therefore, the electrons have, in addition to the axial velocity component, a tangential and a radial velocity component.

In a magnetically compensated system the radial error is compensated by adjustment of the deflection produced helical motion at the end of the deflection coils to a half-loop period. At this point no radial velocity exists. The tangential velocity component is compensated by reduction of the focusing field strength at the target. Reduced field strength results in a radial magnetic field component which deflects the electron beam in the direction opposite to the tangential motion as shown in figure 18.14. Here the radial energy component is zero at the end of the deflection coils. The tangential component of the energy is cancelled by the radial magnetic field component of the focusing coil.
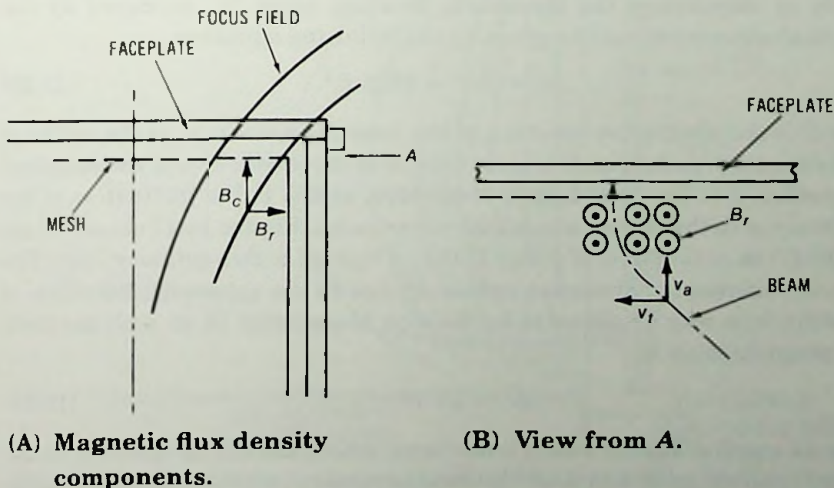
(A) **Magnetic flux density**   (B) **View from A.**
    components.

Fig. 18.14   **Magnetic beam-landing error compensation.**

In a combined electric and magnetic beam-landing error compensation system, an electric collimating lens is used to compensate the radial velocity as illustrated in figure 18.15. The tangential velocity component is compensated by the radial magnetic field component of the focusing coil.

In the electrostatically focused and magnetically deflected vidicon the unwanted velocity component has a radial direction. Perpendicular beam landing in this system therefore may be obtained by using an electrostatic collimating lens as shown in figure 18.16.

An alternate correction method for beam landing errors is the application of a modulation voltage to the cathode of the vidicon tube. In this method the cathode is made more negative as the beam is deflected farther away from the center. As a result the landing beam energy is gradually increased with the deflection. In this manner a compensation for the loss of energy to the radial and tangential components is achieved.

18.4   Spherical Aberration

Spherical aberration is an axial aberration which, in the absence of beam deflection, is the only geometrical aberration that limits the performance of the main focusing lens of a properly aligned gun. The crossover diameter of a cathode ray tube gun may be on the order of 0.1 mm. Therefore the crossover may be regarded as a point source positioned on the axis of the gun. If the potential distribution of a lens is known, the focusing error produced by the spherical aberration may be calculated. From the third-order image theory of aberrations the transverse focusing error Δr_s, produced by the spherical aberration may be given by the following equation:

$$\Delta r_s = S r_a^3 = M C f_1 \theta_1^3. \tag{18.25}$$

Here S is the aberration constant of the focusing system, r_a is the radius of the beam cross section at the main lens, C is the coefficient of the spherical aberration, f_1 is the focal length of the lens, and θ_1 is the inclination of the electron ray to the optical axis at the object point. Figure 18.17 shows values of CD^2/f_1^2 as a function of $[(V_2 - V_1)/(V_2 + V_1)]^2$ of a two-cylinder lens. The apparent increase of crossover radius Δr_c due to the spherical aberration of the main lens may be obtained by division of equation 18.25 with the main lens magnification M:

$$\Delta r_c = (S/M) r_a^3. \tag{18.26}$$

For an equal-diameter two-cylinder lens, which usually is operated in the voltage ratio range of 4 to 6, at the voltage ratios of $V_2/V_1 = 4$, 5, and 6, the quantity SD^2/M has calculated values of 4.5, 5.1, and 5.6, respectively,
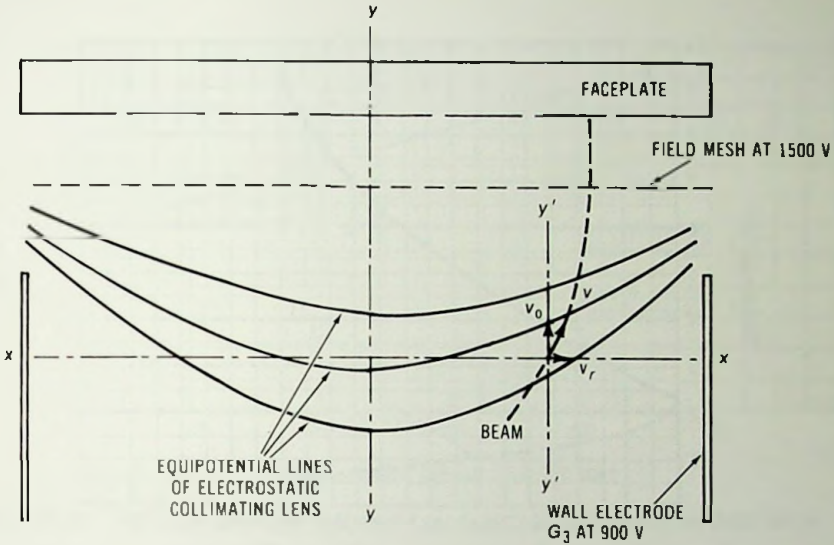
Fig. 18.15   Combined electric and magnetic beam-landing error compensation.
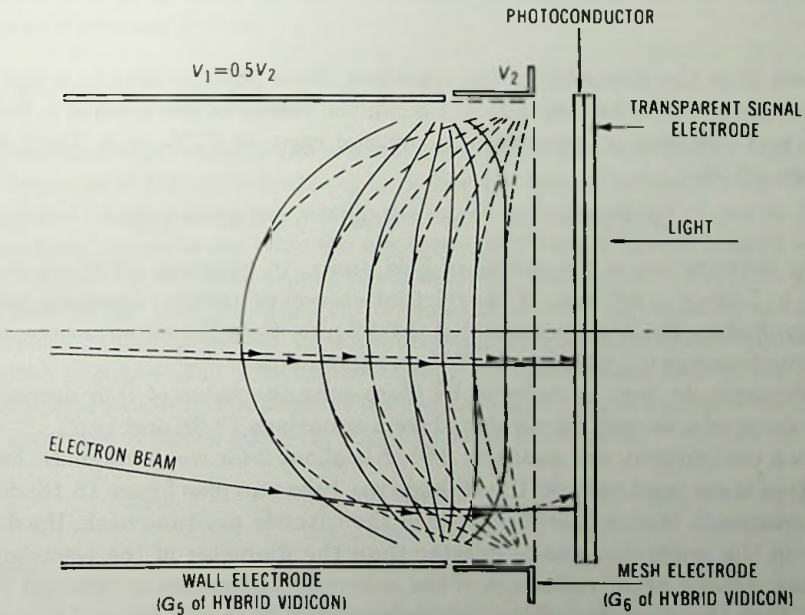
Fig. 18.16   Electrostatic beam-landing compensation in the electrostatically focused and magnetically deflected vidicon.
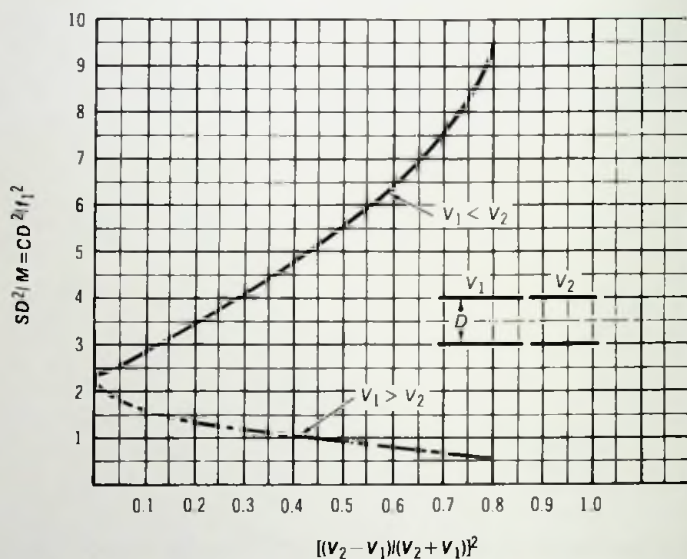
Fig. 18.17   Spherical aberration of a two-cylinder electrostatic lens.

where D is the diameter of the cylinders. Now suppose that in a gun the diameter of the cylinders is $D = 1.5$ cm, the radius of the beam is $r_a = 0.15$ cm, and the lens is operated at a voltage ratio of $V_2/V_1 = 5$. Then, from figure 18.16,

$$(S/M)D^2 = 5.1 \quad \text{or} \quad S/M = 5.1/2.25 = 2.26. \tag{18.27}$$

By substitution of the values of S/M and r_a in equation 18.26 we obtain $\Delta r_c = 7.65 \times 10^{-2}$ mm. If the virtual crossover radius (crossover radius magnified by the prefocusing lens) is 0.02 mm, then the apparent crossover radius becomes $r_{ca} = 0.02 + 0.0765 = 0.0965$ mm.

The term Δr_c may be reduced by increasing the value of D or decreasing the value of r_a as may be concluded from equations 18.26 and 18.27.

As a comparison, the quantity SD^2/M is about 3 for weak magnetic lenses such as those used to focus the cathode ray tube gun (see figure 18.18). Since the magnetic lens is placed outside of the cathode ray tube neck, the diameter of the magnetic lens is greater than the diameter of the electrostatic lenses. Thus a great reduction of the spherical aberration is obtained. Suppose that the diameter of the focusing magnet is $D = 4$ cm and $r_a = 0.15$ cm. Then, with similar calculation as for the electric lens, we obtain
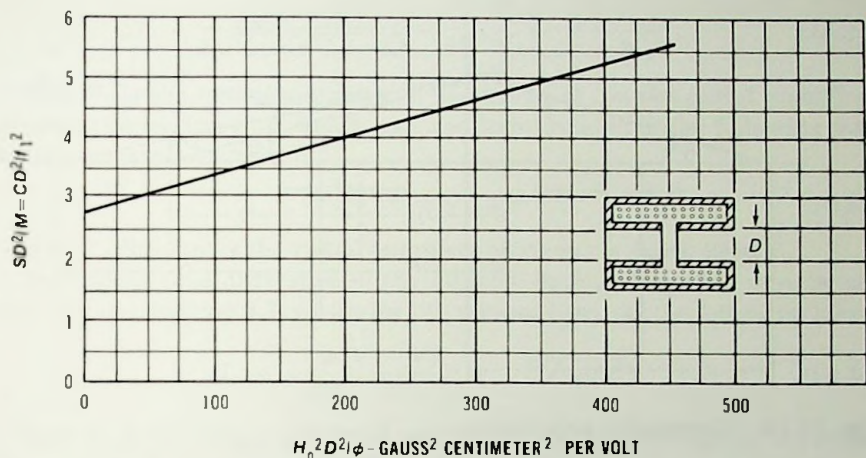
Fig. 18.18   Spherical aberration of a magnetic pole-piece gap lens.

$\Delta r_c = 6.4 \times 10^{-3}$ mm, which is much smaller than the aberration of the electrostatic lens. Here is the advantage of magnetic lens as compared with an electrostatic lens.

18.5   Chromatic Aberration

Chromatic aberration is the second axial aberration which may limit the performance of the main focusing lens. For the type of lenses for which the object and image planes lie outside the focusing fields (short magnetic lens, einzel lens, two-cylinder lens) the electrons that have different kinetic energies incident on the lens experience a different amount of refractions passing through the lens. In figure 18.19 two electrons are refracted by the lens. One electron has energy $e\phi_o$ incident on the lens, and the energy of the other electron is $e(\phi_o + \Delta\phi)$. The higher-energy electron is bent less by the lens. This electron therefore intersects the axis at a greater image distance. From the geometry of figure 18.19 the axial focusing error Δz is

$$\Delta z = f_2' + x_2' - f_2 - x_2 = (f_1 + x_1)\sqrt{\frac{\phi_i}{\phi_o}}(M' - M). \qquad (18.28)$$

Here

$$M' = \frac{f_1'}{x_1'} = \frac{f_1 + \Delta F_1}{x_1 - \Delta F_1} \quad \text{and} \quad M = \frac{f_1}{x_1}. \qquad (18.29)$$
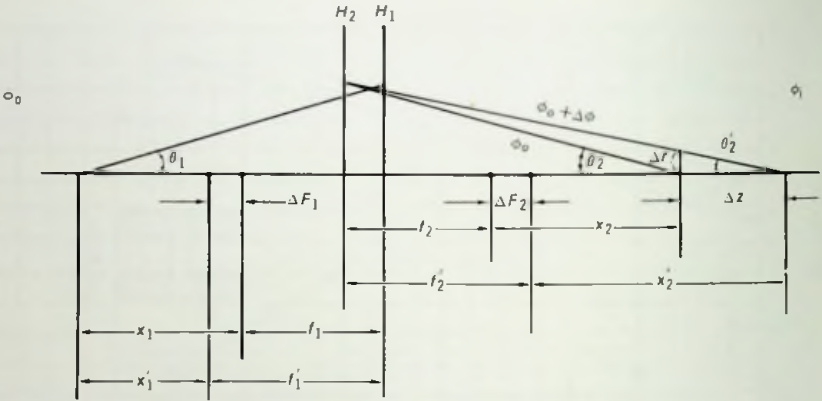
Fig. 18.19 Chromatic aberration.

By substitution of M' and M from equation 18.29 in equation 18.28, Δz becomes

$$\Delta z \cong \Delta F_1 \sqrt{\frac{\phi_i}{\phi_o}} (1 + M)^2 = \frac{dF}{dV_o} \Delta V \sqrt{\frac{\phi_i}{\phi_o}} (1 + M)^2, \qquad (18.30)$$

where ΔF_1, indicates the change of the distance of the focal point from the center of the lens, ΔV is the energy spread of electron incident on the lens, ϕ_i and ϕ_o are the image and object potentials, M is the magnification of the lens and dF/dV_o is a coefficient indicating the rate of focal point change with the lens strength. Values of dF/dV_o multiplied by V/f are shown in figure 18.20 for several lenses.

The transverse focusing error Δr in the Gaussian image plane is

$$\Delta r = \Delta z \theta_2 = \frac{dF}{dV_o} \Delta V \sqrt{\frac{\phi_i}{\phi_o}} (1 + M)^2 \theta_2 = \frac{dF}{dV_o} \Delta V \frac{(1 + M)^2}{M} \theta_1. \qquad (18.31)$$

In the case of a long magnetic focusing main lens the electrons may travel in a field-free region followed by an accelerating or decelerating lens region, and in a uniform decelerating electric field present between the field mesh and the target. Consider the case when the electrons travel in a field-free region of potential V and length L_1 followed by a uniform decelerating electric field region of length L_2. In the field-free region the transit time difference between two electrons, one having a θ and the other θ_f inclination to the optical axis is

$$\Delta T_1 = \frac{L_1}{\sqrt{(2e/m)(V + V_0)} \cos \theta} - \frac{L_2}{\sqrt{(2e/m)(V + V_0)} \cos \theta_f}$$

$$\varDelta T_1 = \frac{L_1(\theta^2 - \theta_f^2)}{2\sqrt{(2e/m)(V + V_0)}} = \frac{L_1(V_r - V_{rf})}{2\sqrt{(2e/m)}(V + V_0)^{3/2}}. \qquad (18.32)$$

Here V_0 is the emission energy of electrons, eV_r is the radial energy of electrons (emerging from the G_2 exit aperture) related in the following way to the energy of electrons:

$$V_r = (V + V_0) \sin^2 \theta, \qquad (18.33)$$

where eV_{rf} designates the radial energy of electrons in sharp focus.

The transit time difference in the uniform decelerating field may be obtained from equation 3.7, which for the present case has the following form:

$$L_2 = -\frac{e}{2m} \frac{V - V_T}{L} t^2 + \sqrt{(2e/m)V_a}\, t. \qquad (18.34)$$

Here V_T is the target potential and eV_a is the axial energy of electrons entering the decelerating field. From equation 18.34 the transit time difference is

$$\begin{aligned}
\varDelta T_2 &= \sqrt{\frac{2m}{e}} \frac{L_2}{V - V_T} (\sqrt{V_{af}} - \sqrt{V_a} + \sqrt{V_a - V + V_T} \\
&\quad - \sqrt{V_{af} - V + V_T}) \\
&= \sqrt{\frac{2m}{e}} \frac{L_2}{V - V_t} \left(\frac{V_r - V_{rf}}{2\sqrt{V}} + \sqrt{V_0 + V_T - V_r} \right. \\
&\quad \left. - \sqrt{V_0 + V_T - V_{rf}} \right). \qquad (18.35)
\end{aligned}$$

The transverse focusing error now becomes

$$\begin{aligned}
\varDelta r &= (\varDelta T_1 + \varDelta T_2)v_r = (\varDelta T_1 + \varDelta T_2)\sqrt{(2e/m)\, V_r} \\
&= \frac{L_1(V_r - V_{rf})\sqrt{V_r}}{2(V + V_0)^{3/2}} + \frac{2L_2}{V - V_T} (\sqrt{V_0 + V_T - V_r} \\
&\quad - \sqrt{V_0 + V_T - V_{rf}})\sqrt{V_r}. \qquad (18.36)
\end{aligned}$$

In the case of demagnifying optics, such as are used in the return beam vidicon, the radial energy after demagnification becomes

$$V_r' = V_r/M^2. \qquad (18.37)$$

The radial energy increase causes an equal amount of axial energy decrease. Therefore the electrons can discharge the target only to a potential

$$V_T \geq \frac{V_0}{M^2} - V_0. \qquad (18.38)$$
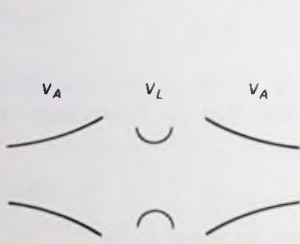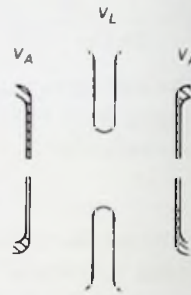
(A) System A.   (B) System B.
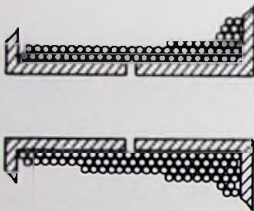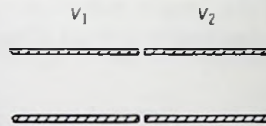
(C) System C.   (D) System D.
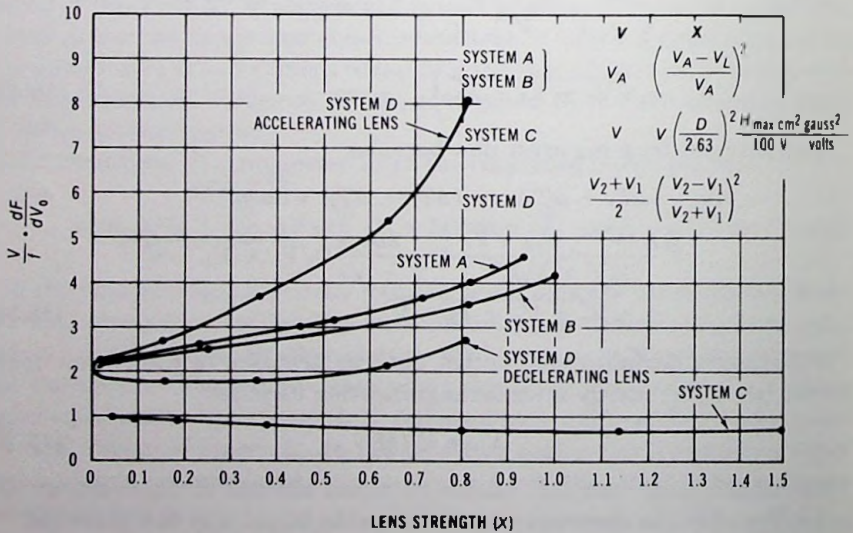
(E) Graph of lens systems A through D.

Fig. 18.20   Variation of chromatic aberration of systems A to D with
            lens strength X. (*Courtesy* Journal of Applied Physics)

By substitution of equations 18.37 and 18.38 in equation 18.36, the transverse focusing error of the demagnifying optics becomes

$$\Delta r = \frac{L_1}{2V^{1/2}M^3}(V_r - V_{rf})\sqrt{V_r} + \frac{2L_2}{VM^2}(\sqrt{V_0 - V_r}$$
$$- \sqrt{V_0 - V_{rf}})\sqrt{V_r}. \tag{18.39}$$

18.6   Off-Axial Aberrations

In addition to chromatic and spherical aberrations, the sharpness of the deflected electron beam off axis may be impaired by off-axial aberrations, such as astigmatism, coma, curvature of field, distortion and deflection aberrations. The first two off-axial aberrations are of little significance unless the optical system is out of alignment. The electron beam is usually aligned by the alignment coils in the vicinity of the G_2 electrode.

Curvature of the field is a more serious problem. In general, the deflected electron beam is in sharp focus on a curved surface, rather than on a flat target. In the case of a flat target, therefore, corner focus deteriorations exist. In electrostatic focus tubes, curvature of field problems are kept to an acceptable level by limitation of the deflection angle and the maximum beam diameter. By limitation of the deflection angle the curvature of field error is reduced, and by limitation of the beam diameter the depth of focus is improved. In the magnetic focus devices, sharp corner focus may be obtained by using a focusing coil in which the axial component of the magnetic field slightly decreases with the radial distance. This way the longer transit time of the deflected electrons is matched by a larger loop period, providing an essentially flat image field at the target.

Linear distortion is another aberration which may be present in the scanning side of camera tubes. One cause of this aberration is geometrical, that is, the raster image lies on a flat surface. Because the deflection distance at the target is proportional to the tangent function of the deflection angle, the deflection sensitivity is greater at the edge than in the center, causing pincushion distortion. Other causes of distortion are nonhomogeneous deflecting fields and aberrations of electric and magnetic lenses. For example, the collimation lens introduces a barrel distortion which may be used to correct pincushion distortion in a way similar to that discussed in chapter 4 in connection of correcting pincushion distortion of image tubes.

In magnetically focused tubes, *spiral distortion* is also present in addition to the linear distortion. Spiral distortion is the result of varying image rotation along a radial line. It is caused by a weak, radially varying, radial magnetic-field component. Therefore the better the homogeneity of the focusing field, the smaller is the spiral distortion. Spiral distortion may be

kept small by using small deflection angles, that is, using only a portion of the diameter of the focusing field.

Deflection aberrations such as deflection focusing and distortion may be kept at an acceptable level by using small deflection angles produced by long and uniform deflection fields.

18.7   Space Charge Limitation of the Beam Diameter

Space charge is a serious limitation to fine focusing at high-intensity beam currents. In the presence of space charge the mutual repulsion between the electrons alters the beam accelerating and focusing fields, and limits the maximum value of current density that may be obtained at a particular potential configuration. The highest current density in the electron gun occurs in the first crossover where the electron beam has the smallest diameter. For a centrally symmetric lens the crossover diameter limited only by the crossover energy may be obtained from equation 18.1. Equation 18.1 gives the minimum radius of the conical beam in the absence of space charge.

The space charge limited beam radius at the crossover may be obtained by considering the space charge flow of two concentric spherical electrodes. As shown by Langmuir and Compton, the space charge limited current I, for the spherical electrodes with cathode radius R_c and anode radius R_a, may be given by the following equation:

$$I = \frac{29.34\ V^{3/2}}{\alpha^2} \times 10^{-6}, \tag{18.40}$$

where V is the potential difference between the spherical electrodes in volts, I is in amperes and α is a function of $u = \ln R_a/R_c$ given by

$$\alpha = u - 0.3u^2 + 0.075u^3 - 0.00143u^4 + 0.0021u^5 - \cdots. \tag{18.41}$$

The space charge limited current in a conical section of semiangle θ from purely geometrical considerations is

$$I_c = \frac{29.34\ V^{3/2}}{\alpha^2} \sin^2(\theta/2) \times 10^{-6}. \tag{18.42}$$

The radius ρ_s of the conical beam at the anode sphere is

$$\rho_s = R_a \sin(\theta/2). \tag{18.43}$$

Figure 18.21 shows ρ_s as a function of the conical beam. As the beam current increases, the space charge limited beam radius also increases. It is interesting to note, however, that the space charge limited current density $I_c/\pi\rho_c^2$ is nearly constant for the range of beam current values shown in figure 18.21.
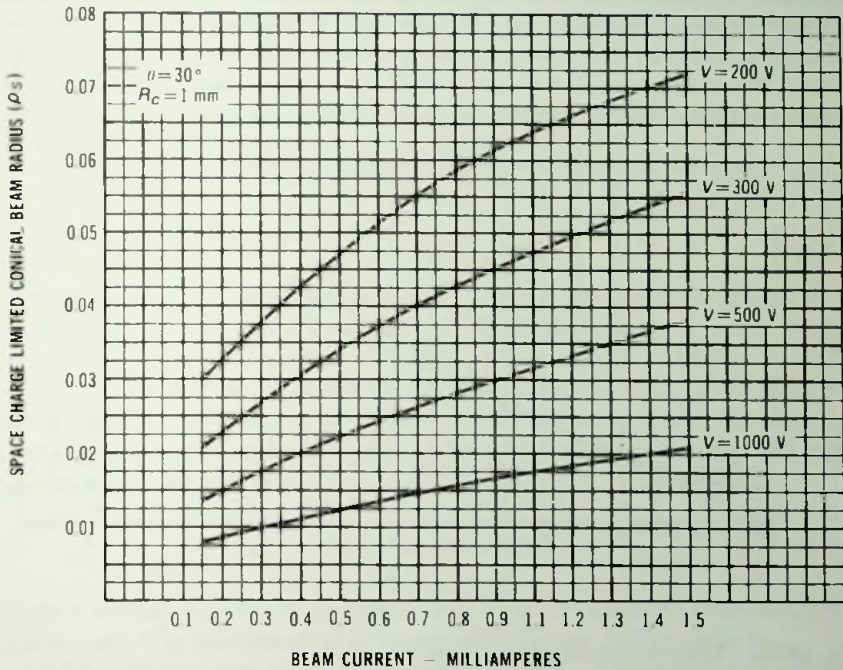
Fig. 18.21   Space-charge limited conical beam radius as a function
            of beam current.

In the above discussion a radial flow of current was assumed. Because of
the emission energy of electrons actual conditions are more complicated,
and precise solutions may be obtained only by electron path calculations in
the presence of accurately described space charge distribution. The results
presented here, however, indicate how the space charge alone limits the
smallest obtainable beam radius.

Space charge may cause a considerable focusing error also in the main
focusing lens, where the electron current is confined into a narrow bundle
of electron beam. Here the mutual repulsion between the electrons causes a
radial acceleration of the beam electrons. When the current density distri-
bution in the cross section of the beam diameter is such that it produces a
force acting on the electron proportional to the radius, then the space charge
effect may be compensated by adjustment of the strength of the main focus-
ing lens. Even in such cases, however, a dynamic adjustment would be nec-
essary to compensate for the beam intensity variation during modulation.
In general, the current density distribution in the cross section of the beam
diameter is such that it produces a radial force which is not proportional to

the radial distance. The focusing error produced under this condition there-
fore cannot be compensated by a simple lens strength adjustment.

In order to avoid the space charge error it is helpful to know the magni-
tude of the uncompensated beam spread for a simple current density distri-
bution in the beam cross section. Figure 18.22 shows the beam spread curve
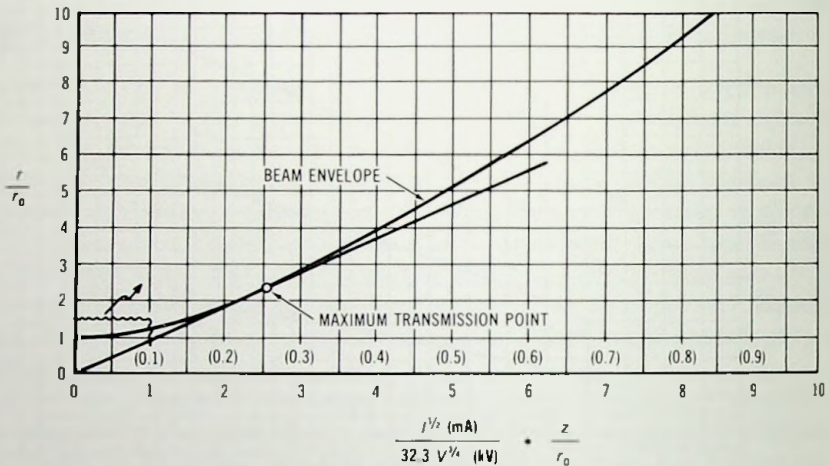
Fig. 18.22   Universal beam-spread curve.

of an initially parallel beam having an initial beam radius r_0 and a uniform
current density in the cross section as a function of beam current I and beam
voltage V and axial distance z. For example, if $r_0 = 1$ mm, $z = 250$ mm,
$V = 10$ kV, $I = 1$ mA, then the value of the abscissa of figure 18.22 is

$$\frac{1}{32.3 \times 10^{3/4}} \cdot \frac{250}{1} = 1.38. \tag{18.44}$$

The relative beam-spread r/r_0, from the graph of figure 18.22, is 1.5. The
space charge therefore increased the beam radius by 50%. Note that by
increasing V and or decreasing I, the spread of the beam may be reduced to
any desired value.

18.8   Upper Limits of Current Density in a Focused Spot

The upper limit of the current density of a focused spot may be obtained
by consideration of the imaging characteristics of an aberrationless and
dissipationless lens. If no aberration exists and no energy is lost to the lens,
then, according to the laws of geometrical optics, the total emission of a
circular object is sharply focused into a circular area whose radius is the

product of the object radius r_o and the magnification M of the lens. Because the object and image currents are identical, the following relation exists:

$$i_o\, \pi r_o^2 = i\pi r^2. \tag{18.45}$$

Here i_o and i are the object and image current density, respectively, and i_o and r are the object and image radius, respectively.

From equation 18.45, the relation between the object and image current density is

$$i = i_o(r_o/r)^2 = i_o/M^2. \tag{18.46}$$

For a Maxwellian emission energy distribution the emission energy of the electrons ranges from zero to infinity. Suppose that the lens has a limiting aperture that limits the exit angle of the electrons to a value of ϕ. In such a system only a fraction of electrons can pass through the limiting aperture. By calculating the fraction of electrons which pass through the aperture, Langmuir showed that the following relation is obtained between the object and image current density:

$$\frac{i}{i_o} = \frac{1}{M^2}\left[1 - (1 - M^2 \sin^2 \phi)\exp(eV/kT)\left(\frac{M^2 \sin^2 \phi}{1 - M^2 \sin \phi}\right)\right] \tag{18.47}$$

where k is the Boltzmann constant and T is the cathode temperature in kelvins, and V is the potential of image with respect to the cathode.

For large M equation 18.47 reduces to equation 18.45. For small values of M the approximate value of equation 18.47 is

$$i_m = i_o[1 + (eV/kT)]\sin^2 \phi, \tag{18.48}$$

where i_m indicates the largest image current density obtainable.

18.9   MTF of Electron Beams

The principal function of scanning electron beams in cameras and display tubes is the resolution of the televised optical image into its constituent parts and the reconstruction of the image by simultaneous scanning of the camera target and display tube phosphor screen. The faithfulness of the televised image is partially determined by the resolution capability of the scanning beam. The resolution of the electron beam is a function of the spot diameter of the beam and the image current density distribution within the spot. The MTF of this imaging process may be given by the following equation:

$$\text{MTF} = \left|\frac{\int_{-\infty}^{+\infty}\int_{-\infty}^{+\infty} J(x, y)e^{-j\omega x}\, dx\, dy}{\int_{-\infty}^{+\infty}\int_{-\infty}^{+\infty} J(x, y)\, dx\, dy}\right|, \tag{18.49}$$

where $J(x, y)$ is the image current density distribution of the electron beam and ω is the spatial circular frequency.

Figure 18.23 shows the MTF of electron beams with a uniform and a Gaussian image current density distribution.

The electron gun obtained its most extensive application in the cathode-ray tubes (crt's) ranging from ½ in (0.635 cm) up to 36 in (91.44 cm) in diameter. The main applications of crt's are in television, large screen projection systems, radar, aerospace programs, avionics systems, military monitor displays and helmet mounted displays for visually coupled systems, and
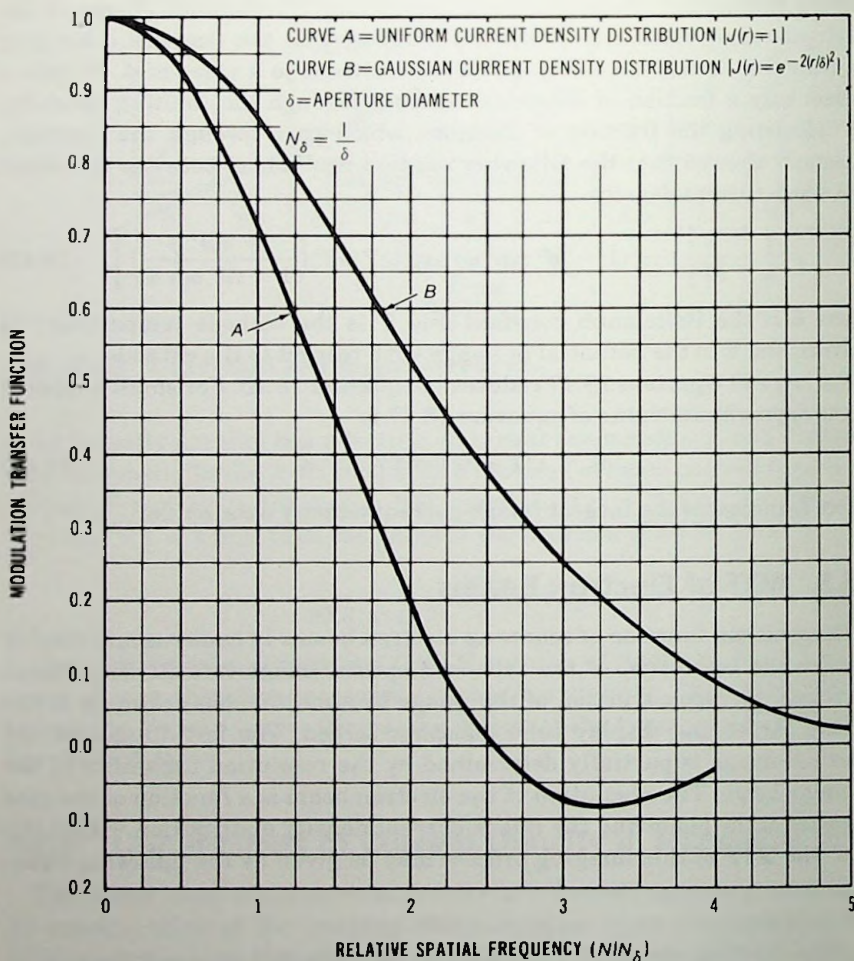
Fig. 18.23   Sine-wave response characteristics of round apertures.

Fig. 18.24   Industrial cathode-ray tubes. (*Courtesy Thomas Electronics, Inc.*)

thermal viewers. Figure 18.24 is a photograph of some special purpose industrial cathode-ray tubes.

References

Allard, L. S. "Design Factors in Television Cathode-Ray Tubes," *Proc. Inst. Brit. IEE*, Vol. 99, Part IIIA, p. 499, April-May 1952.

Ando, T. "Zoom Image Tubes," International Television Conference, June 1962.

Bedford, L. H. "A Note on Davisson's Electron-Lens Formula," *Phys. Soc. Proc.*, Vol. 46, No. 6, p. 882.

Bertram, S. "Determination of the Axial Potential Distribution in Axially Symmetric Electrostatic Fields," *Proc. IRE*, Vol. 28, No. 9, p. 418, September 1940.

Beule, R. L.; D. A. Day; and W. E. Turk. "Developments in Television Camera Tubes," *The Royal Television Society Journal*, Vol. 11, p. 254, 1967.

Brueche, E., and O. Scherzer. *Elektronenoptik*, Julius Springer, Berlin, 1934.

Carré, B. A. "The Determination of the Optimum Accelerating Factor for Successive Over-relaxation," *Computer J.*, Vol. 4, p. 73, 1961.

Cooper, H. G. "Design of a High-Resolution Electrostatic Cathode Ray-Tube for the Flying Spot Store," *The Bell System Technical Journal*, p. 723, May 1961.

de Boer, F., and H. Emmens. "Sedimentation of Fluorescent Screens in Cathode-Ray Tubes," *Philips Technical Review*, p. 232, Vol. 16, February 1955.

de Haan, E. F., et al. "The Plumbicon: A Camera Tube With a Photoconductive Lead-Oxide Layer," International Television Conference, June 1962.

————, et al. "The Plumbicon: A New Television Camera Tube," *Philips Technical Review*, Vol. 25, No. 6/7, p. 133, 1964.

El-Kareh, A. B. "Analysis of the 3-Tube Symmetrical Electrostatic Unipotential Lens," *Journal of Applied Physics*, Vol. 42, No. 5, p. 1870, April 1971.

Epstein, D. W. "Electron Optical System of Two Cylinders as Applied to Cathode-Ray Tubes," *Proc. IRE*, Vol. 24, No. 8, p. 1095, August 1936.

Francken, J. C., and R. Dorrestein. "Paraxial Image Formation in the Magnetic Image Iconoscope," *Philips Res. Rep.*, Vol. 6, p. 323, 1951.

Francken, J. C., and H. Bruining. "New Developments in the Image Iconoscope," *Philips Technical Review*, Vol. 14, No. 11, p. 327, May 1953.

Frankel, S. P. "Convergence Rates of Iterative Treatments of Partial Differential Equations," *Math Tab. Nash.*, IV, Vol. 30, pp. 65–75, April, 1950.

Gans, R. "Electron Paths in Electron Optics," *Zeit. für Tech. Phys.*, Vol. 18, p. 41, February 1937.

Gray, F. "Electrostatic Electron-Optics," *Bell Sys. Tech. J.*, Vol. 18, No. 1, p. 1, January 1939.

Hildebrand, F. F. *Introduction to Numerical Analysis*, McGraw-Hill Book Company, Inc., New York, 1956.

Janes, R. B., et al. "Development and Performance of Television Camera Tubes," *RCA Review*, p. 191, June 1949.

————, and A. A. Rotow. "Light-Transfer Characteristics of Image Orthicons," *RCA Review*, Vol. XI, No. 3, p. 364, September 1950.

Klemperer, O., and W. D. Wright. "Investigations of Electron Lenses," *Proc. Phys. Soc.*, Vol. 51, Part II, p. 296, March 1939.

Knoll, M. "Electric Electron Lens for Cathode-Ray Tubes," *Arch. Elektrotech*, Vol. 28, p. 1, 1934.

Kroeger, F. A., and J. E. Hellingman. "The Blue Luminescence of Zinc Sulfide," *Transactions of the Electrochem. Soc.*, Vol. 93, p. 156, 1948.

———. "Chemical Proof of Presence of Chlorine in Blue-Fluorescent Zinc Sulfide," *J. Electrochem. Soc.*, Vol. 95, p. 68, 1949.

Law, R. R. "High Current Electron Gun for Projection Kinescopes," *Proc. IRE*, Vol. 25, p. 954, August 1937.

———. "Factors Governing Performance of Electron Guns in Television Cathode-Ray Tubes," *Proc. IRE*, Vol. 30, p. 103, February 1942.

Langmuir, D. B. "Theoretical Limitations of Cathode-Ray Tubes," *Proc. IRE*, Vol. 25, No. 8, p. 977, August 1937.

Langmuir, I., and K. T. Compton. "Electrical Discharges in Gasses, Part II," *Rev. Modern Phys.*, Vol. B, p. 191, April 1931.

Leaman, J. R. "Electron Optics of Vidicons," *RCA Engineer*, 1968.

Liebmann, G. "Image Formation in Cathode-Ray Tubes and the Relation of Fluorescent Spot Size and Final Anode Voltage," *Proc. IRE*, Vol. 33, p. 381, June 1945.

Lubszynski, H. G., et al. "Some Problems of Resolution in Low-Velocity Camera Tubes," International Television Conference, June 1962.

McGee, J. D. "A Review of Television Signal Generating Tubes," International Television Conference, June 1962.

Maloff, I. G., and D. W. Epstein. *Electron Optics in Television*, McGraw-Hill Book Co., Inc., New York, 1938.

Miller, L. D., and B. H. Vine. "Improved Developmental One-Inch Vidicon for Television Cameras," *J. SMPTE*, Vol. 67, p. 154, March 1958.

Morton, G. A. "Electron Guns for Television Application," *Reviews of Modern Physics*, Vol. 18, No. 3, p. 362, July 1946.

Moss, H. "The Electron Gun of the Cathode-Ray Tube—Part 1," *Journal Brit. IRE*, January 1945.

———. "The Electron Gun of the Cathode-Ray Tube—Part 2," *Journal Brit. IRE*, June 1946.

———, et al. "Dimensional Tolerances in Cathode-Ray Tube Guns," *Proc. IRE*, Vol. 97, July 1950.

———. "A Space Charge Problem," *Wireless Eng.*, Vol. 22, p. 316, July 1945.

Mouser, D. P., et al. "A Practical Television Tube for Low Light Levels," *The Royal Television Society Journal*, Vol. 11, No. 11, p. 271, 1967.

Murray, C. B., Jr., and A. Van Der Ziel. "Measurements of Noise in Image Orthicons," *IEEE Transactions on Electron Devices*, p. 365.

Neuhauser, R. G. "Developments in Electron Optics Produce Two New Lines of Vidicon Tubes," *RCA Engineer*, PE-244, 1964.

———, et al. "The Design and Performance of a High-Resolution Vidicon," *J. SMPTE*, p. 833, November 1962.

———, et al. "Beam-Landing Errors and Signal Output Uniformity of Vidicons," *J. SMPTE*, Vol. 67, p. 149, March 1958.

———; A. A. Rotow; and F. S. Veith. "Image Orthicons for Color Cameras," *Proc. IRE*, p. 161, January 1954.

Niklas, W. F.; C. S. Szegho; and J. Wimpffen. "A Television Picture Tube with Increased Effective Perveance for Cathode Modulation," *Journal of the Television Society*, Vol. 8, No. 9.

Parker, N. W.; I. P. Csorba; and H. N. Frihart. "Recent Developments in Scan Magnification," IRE International Convention Record Part 7, Broadcast and Television Receivers, New York, p. 167, March 21–24, 1960.

Photomultiplier Manual, RCA Technical Series PT-61.

Phototubes and Photocells, RCA Technical Series PT-60.

Pierce, J. R. "Limiting Current Densities in Electron Beams," *Journal of Applied Physics*, Vol. 10. p. 775, October 1939.

———. "A Figure of Merit for Electron Concentrating Systems," *Proc. IRE*, Vol. 33, p. 476, July 1945.

Rajchman, J. A., and R. L. Snyder. "An Electrically Focused Multiplier Phototube," *Electronics*, Vol. 13, pp. 20, 58, 60, December 1939.

Rogers, R. L., et al. "Silicon Intensifier Target Camera Tube," 1970 IEEE International Solid-State Circuit Conference at University of Pennsylvania, February 20, 1970.

Rose, A.; P. K. Wiemer; and H. B. Law. "The Image Orthicon—A Sensitive Television Pickup Tube," *Proc. IRE*, p. 424, July 1946.

Schade, O. H. "Electron Optics and Signal Readout of High-Definition Return-Beam Vidicon Camera," *RCA Review*, p. 60, March 1970.

———. "Image Graduation, Graininess and Sharpness in Television and Motion Picture Systems," *J. SMPTE*, Vol. 58, p. 182, March 1952.

Schlesinger, K. "Anastigmatic Yokes for Picture Tubes," *Electronics*, Vol. 22, No. 10, p. 102, October 1949.

———. "A Mixed-Field Type of Vidicon," *IEEE Transactions on Electron Devices*, Vol. ED-14, No. 3, March 1967.

Schwartz, J. W. "Space-Charge Limitations on the Focus of Electron Beams," *RCA Review*, Vol. 18, p. 3, 1957.

Spangenberg, K. R. *Vacuum Tubes*, McGraw-Hill Book Co., Inc., New York, 1948.

———, and L. M. Fields. "Some Simplified Methods of Determining the Optical Characteristics of Electron Lenses," *Proc. IRE*, Vol. 30, No. 3, p. 138, March 1942.

Septier, A. *Focusing of Charged Particles*, Academic Press, New York, 1967.

Thompson, B. J., and L. B. Headrick. "Space Charge Limitations on the Focus of Electron Beams," *Proc. IRE*, Vol. 28, p. 318, July 1940.

Vine, B. H. "Analysis of Noise in the Image Orthicon," *J. SMPTE*, Vol. 70, p. 432, 1961.

Watson, E. E. "The Dispersion of the Electron Beam," *Phil. Mag.*, Ser. 7, Vol. 3, p. 849, April 1927.

Weimer, P. K., and A. Rose. "The Motion of Electrons Subject to Forces Transverse to a Uniform Magnetic Field," *Proc. IRE*, p. 947, November 1947.

Wentworth, J. W. "Camera Tubes for Studio Use—A Semitechnical Appraisal for Educators," *J. SMPTE*, March 1963.

Young, D. M. "Iterative Methods for Solving Partial Differential Equations of Elliptic Type," *Trans. Amer. Math. Soc.*, pp. 76, 92-111, 1954.

Zworykin, V. K., et al. *Electron Optics and the Electron Microscope*, John Wiley & Sons, Inc., New York, 1945.

———, and W. H. Painter. "Development of the Projection Kinescope," *Proc. IRE*, Vol. 25, p. 937, 1937.

———, and G. A. Morton. *Television*, J. Wiley & Sons, Inc., New York, 1940.

———, and J. A. Rajchman. "The Electrostatic Electron Multiplier," *Proc. IRE*, Vol. 27, p. 558, September 1939.

19

DEFLECTION OF ELECTRON BEAMS

19.1   Introduction

Image intensifier tubes have numerous applications that require a deflection of the high-energy photoelectron image. For example, in the process of image motion compensation and image stabilization the image motion that is present at the photocathode is made motionless at the phosphor screen by a compensating deflection of the high-energy electron image. In streak mode operation of image tubes the intensity distribution of a fast photoevent is analyzed on a picosecond scale by deflection of the high-energy photoelectron image. The framing type image tube camera is still another example of image deflection; here a varying scene may be photographed several times on a single plate by changing the image position on the phosphor screen by deflection.

In image tubes the photoelectron image may be deflected electrostatically or electromagnetically in a similar fashion as it is done in a cathode-ray tube. In the electrostatically focused image tubes the electron beam must pass through the anode aperture before it can be deflected in order to avoid vignetting of the image by the aperture and to avoid loss of resolution. The deflection (electrostatic or magnetic), therefore, is done in the anode cone region, which is free of focusing fields. In the electromagnetically focused image tubes which use magnetic fields for deflection, no such restrictions exist. Therefore the electron beam in the electromagnetically focused tube can be deflected across the whole length of the tube.

418

19.2   Electrostatic Deflection

Consider first the electrostatic deflection of an electrostatically focused
image tube. In this device a pair of deflection plates are used that are posi-
tioned in the anode cone close to the anode aperture. This is the most suit-
able place because in the vicinity of the anode aperture the beam diameter
is relatively small and, therefore, the separation of defection plates can be
made small without vignetting. Because of the divergence of the undeflected
electron beam it is natural to use tapered plates rather than parallel plates.
For the generality of discussion, however, first let us consider the deflection
in a transverse homogeneous electric field produced by a voltage difference
V_p between two parallel deflection plates positioned along the axis of the
image tube as shown in figure 19.1.
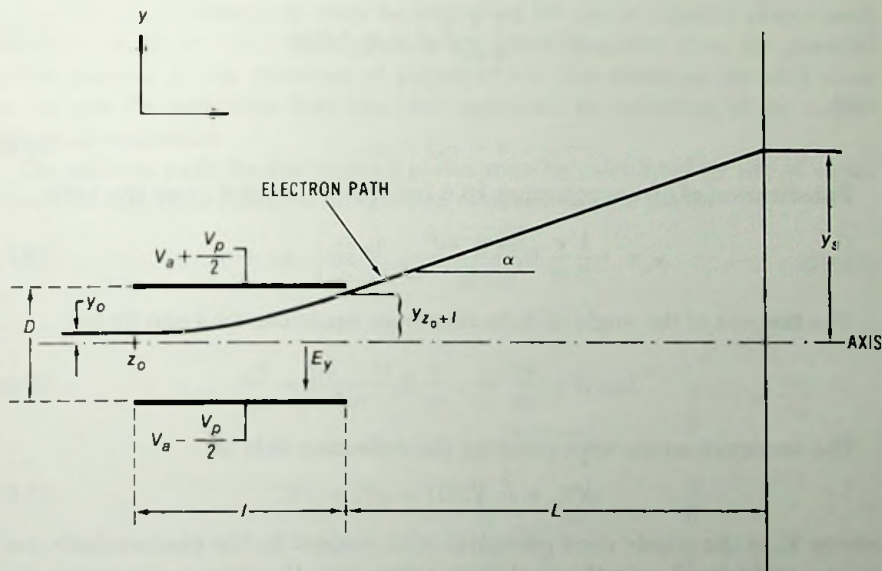
Fig. 19.1   Electron beam deflection by parallel deflection plates.

The intensity of the electrostatic field is $E_y = -V_p/D$, where D is the
separation of the deflection plates. Let an electron enter the deflection field
with the following initial conditions: when $t = 0$ $z = z_0$, $y = y_0$, and $v_z = v_{z0}$
and $v_y = v_{y0}$. The equations of motion then may be given by the following
two equations:

$$m\frac{d^2y}{dt^2} = -eE_y \tag{19.1}$$

and

$$m \frac{d^2 z}{dt^2} = 0.$$ (19.2)

The first integration of equations 19.1 and 19.2 gives

$$v_y = \frac{dy}{dt} = -\frac{e}{m} E_y t + v_{y_0}$$ (19.3)

and

$$v_z = \frac{dz}{dt} = v_{z_0}.$$ (19.4)

The second integration of equations 19.1 and 19.2 gives

$$y = -\frac{1}{2}\frac{e}{m} E_y t^2 + v_{y_0} t + y_0$$ (19.5)

and

$$z = v_{z_0} t + z_0.$$ (19.6)

Substitution of t from equation 19.6 into equation 19.5 gives the path:

$$y = -\frac{1}{2}\frac{e}{m} E_y \frac{(z - z_0)^2}{v_{z_0}^2} + \frac{v_{y_0}}{v_{z_0}} (z - z_0) + y_0.$$ (19.7)

The tangent of the angle of deflection from equations 19.3 and 19.4 is

$$\tan \alpha = \frac{dy}{dz} = -\frac{e}{m} E_y \frac{(z - z_0)}{v_{z_0}^2} + \frac{v_{y_0}}{v_{z_0}}.$$ (19.8)

The energy of an electron entering the deflection field is

$$e(V_a + y_0 V_p/D) = eV_y + eV_z,$$ (19.9)

where V_a is the anode cone potential with respect to the photocathode, and on the right-hand side the first term represents the transverse energy and the second term is the axial energy. The initial transverse and axial velocity then may be expressed as follows:

$$v_{y_0} = \sqrt{(2e/m)\, V_y}$$ (19.10)

and

$$v_{z_0} = \sqrt{(2e/m)\, V_z}.$$ (19.11)

For deflection plates with fringing fields at the edge of deflection plates, values of V_y and V_z are determined by the divergence of the undeflected beam of electrons and by the y and z components of the $ey_0 V_p/D$ energy.

By substitution of equations 19.10 and 19.11 into the equations 19.7 and 19.8, and by substitution of $E_y = -V_p/D$, we obtain

$$y = \frac{1}{4}\frac{V_p}{V_z}\frac{(z - z_0)^2}{D} + \sqrt{\frac{V_y}{V_z}}(z - z_0) + y_0 \qquad (19.12)$$

and

$$\tan \alpha = \frac{1}{2}\frac{V_p}{V_z}\frac{(z - z_0)}{D} + \sqrt{\frac{V_y}{V_z}}. \qquad (19.13)$$

The deflection at the phosphor screen from the geometry of figure 19.1 is

$$y_{z-l+z_0} + L \tan \alpha_{z-l+z_0} = y_{l+z_0} + \frac{1}{2}\frac{V_p}{V_z}\frac{lL}{D} + L\sqrt{\frac{V_y}{V_z}}. \qquad (19.14)$$

The deflection sensitivity may be improved by use of tapered plates such as shown in figure 19.2. These plates are more sensitive than the parallel plates because at the entrance of plates where the electrons are still close to the axis the deflection field has been increased by reduction of the deflection plate separation.

The electron path for the tapered plates may be calculated by use of equations 19.1 and 19.2. The first integration of equation 19.2 yields

$$\frac{dz}{dt} = v_{z_0} = \sqrt{\frac{2eV_z}{m}}. \qquad (19.15)$$
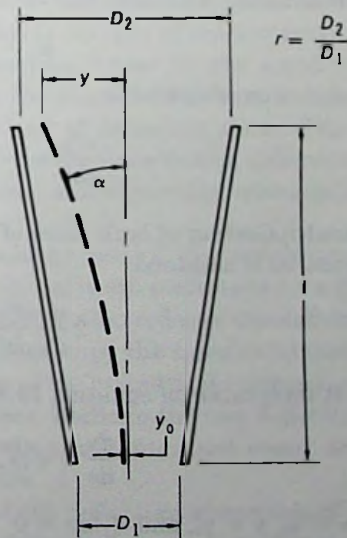
Fig. 19.2   Electron path in tapered deflection plates.

The field strength in the tapered plates is

$$E_y = \frac{V_p}{D_1[1 + (r - 1)(z - z_0)/l]},$$ (19.16)

where D_1, r and l are shown in figure 19.2. Differentiating equation 19.7 twice with respect to z and substituting in it equations 19.11 and 19.16, the equation of motion for tapered plates becomes

$$\frac{d^2y}{dz^2} = -\frac{E_y}{2V_z} = \frac{V_p}{V_z} \frac{1}{2D_1[1 + (r - 1)(z - z_0)/l]}.$$ (19.17)

The first integration of equation 19.17 at $z - z_0 = l$ yields the deflection angle α, and the second integration yields the deflected distance y as given in the following two equations:

$$\frac{dy}{dz} = \tan \alpha = \frac{l}{2D_1} \frac{V_p}{V_z} \frac{\ln r}{r - 1} + \left(\frac{dy}{dz}\right)_{z=z_0}$$ (19.18)

and

$$y = \frac{l^2}{2D_1} \frac{V_p}{V_z} \left[\frac{r \ln r}{(r - 1)^2} - \frac{1}{r - 1}\right] + \left(\frac{dy}{dz}\right)_{z=z_0} z + y_0.$$ (19.19)

Maximum deflection sensitivity can be obtained by use of curved deflection plates which are shaped as shown in figure 19.3. Under these conditions the deflection plate separation along the path is made as small as possible without touching the beam. The field strength in the curved plates is

$$E_y = -V_p/2y.$$ (19.20)

The equation of motion is

$$\frac{d^2y}{dz^2} = -\frac{E_v}{2V_z} = \frac{V_p}{4V_z} \frac{1}{y}.$$ (19.21)

By multiplication of both sides of equation 19.21 with 2 dy/dz the following equation is obtained:

$$2\frac{dy}{dz}\frac{d^2y}{dz^2} = \frac{V_p}{2V_z} \frac{dy}{dz} \frac{1}{y}.$$ (19.22)

The first integration of equation 19.22 yields

$$\frac{dy}{dz} = \sqrt{(V_p/2V_z) \ln y + c}.$$ (19.23)

For $z = z_0$, $y = y_0$, and $dy/dz = 0$

$$\sqrt{(V_p/2V_z) \ln y + c} = 0.$$ (19.24)

and therefore

$$c = -(V_p/2V_z) \ln y_0. \tag{19.25}$$

Substitution of the value of c in equation 19.23 gives

$$\frac{dy}{dz} = \sqrt{(V_p/2V_z) \ln (y/y_0)}. \tag{19.26}$$

After rearranging terms,

$$dz = \sqrt{\frac{2V_z}{V_p}} \frac{dy}{\sqrt{\ln (y/y_0)}}. \tag{19.27}$$

After integration of the last equation we obtain

$$z - z_0 = \sqrt{2V_z/V_p} \int_{y_0}^{y} \frac{dy}{\sqrt{\ln (y/y_0)}}. \tag{19.28}$$

Changing to a new variable $R = y/y_0$, equation 19.28 becomes

$$\frac{z - z_0}{y_0\sqrt{2V_z/V_p}} = \int_{R=1}^{R=y/y_0} \frac{dR}{\sqrt{\ln R}}. \tag{19.29}$$

The right-hand integral is the same as that for space charge spreading in a cylindrical beam. Solutions of equation 19.29 are plotted in figure 19.3.

For biaxial deflection (x and y deflection) two pairs of deflection plates placed along the beam axis in sequence may be used. The x and y deflection plates are rotated $90°$ with respect to one another and are shielded from each other to avoid crosstalk. Major disadvantages of the sequential beam deflection are the lack of common deflection center for the x and y deflections, the increased length required for the biaxial deflection, and, in image tubes, vignetting caused by the second pair of deflection plates. The lack of common deflection center for the x and y deflections causes different deflection sensitivity for the x and y deflections, and vignetting restricts the useful cathode diameter of the image tube.

The above problems may be corrected by use of the *deflectron*. In the deflectron the x and y deflection electrode pairs are positioned on a cylindrical or conical surface. The x and y deflection electrodes of the deflectron, in analogy to the magnetic deflection yokes, occupy the same axial position on the beam axis, but on the circumference of the cylindrical surface the deflection pairs are $90°$ apart from one another. Because the two deflection pairs are physically identical, a common deflection center and equal deflection sensitivity exists for both deflection pairs.

Let us consider briefly the pattern of the deflection electrodes of a cylindrical deflectron. The desired pattern of the deflection electrodes is the pattern that produce a homogeneous E_x and E_y electric field within the
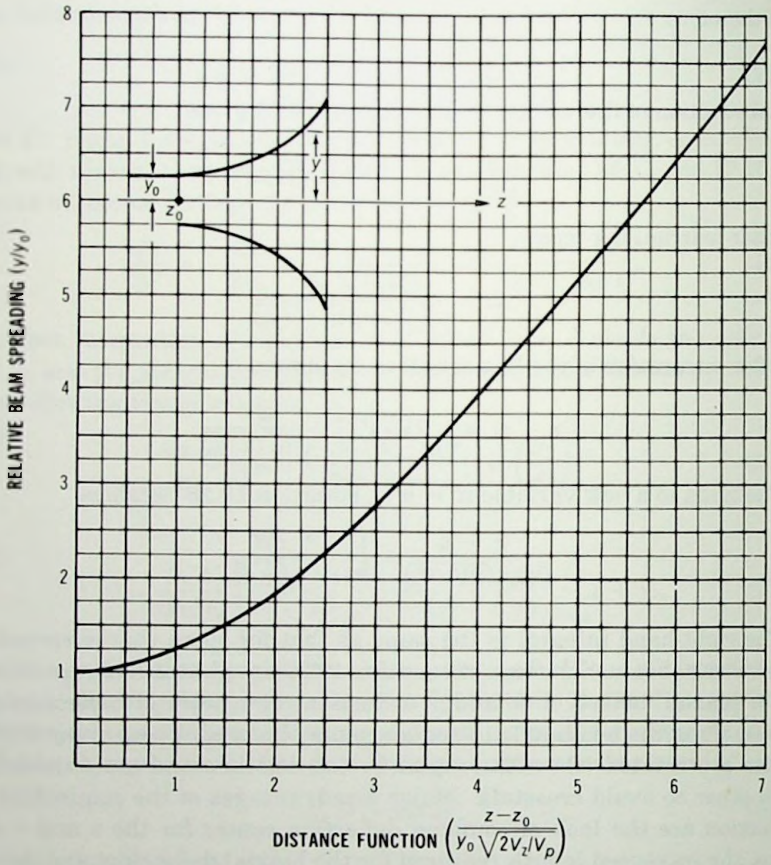
Fig. 19.3   **Separation of maximum sensitivity deflection plates as a function of axial distance.**

boundary of the cylinder when the deflection electrode pairs are connected to balanced deflection voltages V_{x_0} and V_{v_0}, respectively. If homogeneous x and y deflection fields exist, then the boundary potential difference between two points P and P' of the cylindrical surface is from the geometry of figure 19.4,

$$V_a = V_{xa} + V_{ya} = \int_{-x}^{+x} E_x \, dx + \int_{-y}^{+y} E_y \, dy$$

$$= 2xE_x + 2yE_y \tag{19.30}$$

$$= 2RE_x \cos \alpha + 2RE_y \sin \alpha.$$
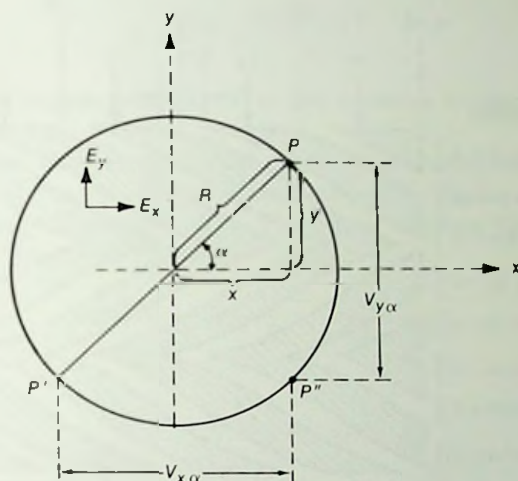
Fig. 19.4   Cross sectional diagram of a cylindrical deflection for the
derivation of boundary potential variation for a homoge-
neous E_x and E_y electric field within the cylindrical sur-
face.

The x and y components of the potential difference, therefore, are

$$V_{x\alpha} = 2RE_x \cos \alpha \qquad (19.31)$$

and

$$V_{y\alpha} = 2RE_y \sin \alpha . \qquad (19.32)$$

From these equations the x component of the boundary potential varies
as the cosine function of α and the y component by sine function of α.

An average boundary potential difference which approximately satisfies
equations 19.31 and 19.32 may be obtained by covering the cylindrical sur-
face with x and y deflection electrode pairs whose axial length varies accord-
ing to $\cos \alpha$ for the x deflection, and $\sin \alpha$ for the y deflection. A 3-cycle
deflection pattern, which has continuity between the cycles, and proper
insulation between the x and y electrodes is shown in figure 19.5.

The difference between the boundary line functions is the effective axial
length of the electrodes. The various boundaries are formulated by

$$\lambda \frac{1 \pm \sin (\alpha \pm \Delta)}{2} \quad \text{and} \quad \lambda \frac{1 \pm \cos (\alpha \pm \Delta)}{2}, \qquad (19.33)$$

where Δ is the angle corresponding to the insulation.

$\alpha = 0$ $\frac{\pi}{2}$ π $\frac{3\pi}{2}$ 2π

$-x$ $+y$ $+x$ $-y$

NO. BOUNDARIES

1. $\frac{1}{2}\left[1+\sin(\alpha+\Delta)\right]$
2. $\frac{1}{2}\left[1+\sin(\alpha-\Delta)\right]$
3. $\frac{1}{2}\left[1-\cos(\alpha+\Delta)\right]$
4. $\frac{1}{2}\left[1-\cos(\alpha-\Delta)\right]$
5. $\frac{1}{2}\left[1-\sin(\alpha+\Delta)\right]$
6. $\frac{1}{2}\left[1-\sin(\alpha-\Delta)\right]$
7. $\frac{1}{2}\left[1+\cos(\alpha+\Delta)\right]$
8. $\frac{1}{2}\left[1+\cos(\alpha-\Delta)\right]$

$\frac{+V_y}{2}$ $\frac{+V_x}{2}$ $\frac{-V_y}{2}$ $\frac{-V_x}{2}$
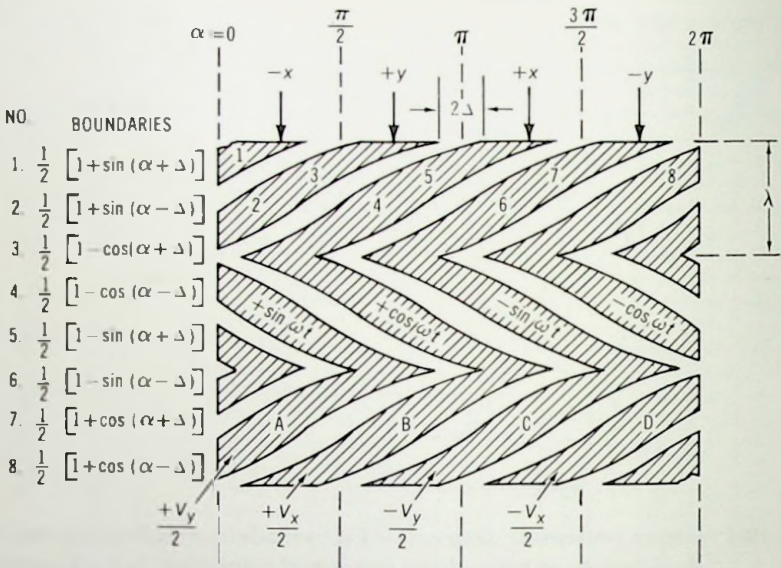
Fig. 19.5 **Three-cycle deflectron deflection pattern.**

19.3   Magnetic Deflection

In the case of magnetic deflection of the electrostatically focused image tube, a pair of deflection yokes similar to that used to deflect the electron beam of a cathode-ray tube is used. The deflection yokes are placed around the cylindrical glass envelope of the image tube. The yokes produce a homogeneous magnetic field that is perpendicular to the axis of the image tube. Good field homogeneity is very important in image tubes. Nonhomogeneous fields not only reduce resolution but also introduce distortion. In the absence of magnetic materials good homogeneity may be obtained with long, air-core yokes having a cosine distribution of turn density or with the so-called linear yoke which is shown in figure 19.6. Image tubes, however, contain magnetic materials, such as kovar, which tend to modify the field distribution. In addition, on short yokes the end effects may alter substantially the homogeneity of the field. Therefore it is often necessary to modify the turn density of cosine and linear yokes by a cut-and-try process, according to the needs, to make the field sufficiently homogeneous.

As discussed in chapter 3, in a homogeneous magnetic field the electron moves on a circular path. The radius of the circular motion from equation 3.9 is

$$R = \frac{mv}{eB} = \frac{\sqrt{(2m/e)V}}{B}, \qquad (19.34)$$

where v is the electron velocity, eV is the electron energy, and B is the magnetic flux density.

In figure 19.7 an electron enters the region of magnetic field (perpendicular to page) along the axis at line A and leaves the region of deflection at line B with a deflection angle of α. The angle between the incident and refracted beam from figure 19.7 is

$$\sin \alpha = \sin \beta = \frac{l}{R} = \frac{lB}{\sqrt{(2m/e)V}} \qquad (19.35)$$

and

$$y_l = R(1 - \cos \alpha). \qquad (19.36)$$
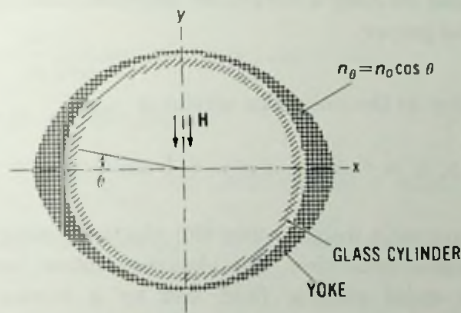
(A) A pair of deflection yokes having a cosine distribution of turn density.
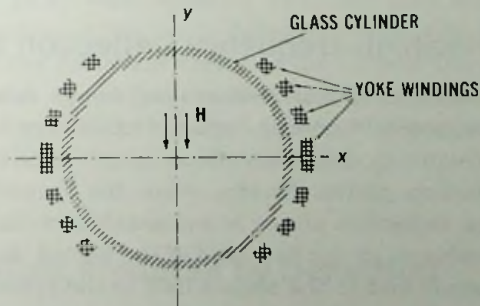
(B) A pair of linear deflection yokes.

Fig. 19.6   Cross section of deflection yokes.
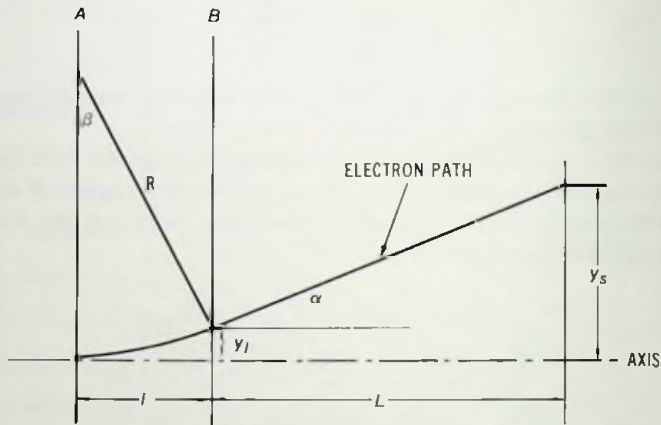
**Fig. 19.7   Electron beam deflection by a homogeneous magnetic
field having a direction perpendicular to the plane of
the paper.**

The deflection at the phosphor screen is

$$y_s = y_l + L \tan \alpha \cong y_l + L \sin \alpha = y_l + \frac{lLB}{\sqrt{(2m/e)V}}. \tag{19.37}$$

In electromagnetic image tubes the electron energy is not constant in the
region of electron deflection. The electron motion here is determined by the
homogeneous axial electric field and by a homogeneous magnetic field,
where the latter is the vector sum of deflecting and focusing fields. This case
is discussed in appendix E, section E.7, "Electron Motion in Combined
Homogeneous Electric and Magnetic Fields."

19.4   Ultrahigh-Frequency Deflection Effects

For the analysis of fast photoevents, image tubes must be operated at
streak velocity of 10^{10} cm/s or higher. At this very high deflection speed the
ultrahigh-frequency deflection effects may reduce the deflection sensitivity
of the deflection plates. Briefly, when the transit time of the electrons
through the deflection plates is comparable to the period of a sinusoidal
deflecting voltage, in the first half of the period the electrons are deflected
in one direction and in the second half in the opposite direction. The same
holds for the Fourier harmonics of a sawtooth waveform. The deflection
sensitivity as a function of frequency may be analyzed by applying a sinu-
soidal voltage $V_p \cos \omega t$ to the parallel deflection plates. Let an electron

enter the deflection field along the axis with $v_{z_0} = \sqrt{2eV_a/m}$ axial velocity. The equations of motion are

$$m\frac{d^2y}{dz^2} = -eE_y \cos \omega t \tag{19.38}$$

and

$$m\frac{d^2z}{dt^2} = 0. \tag{19.39}$$

The transverse velocity at the end of the deflection plates may be obtained by integrating equation 19.38 between the limits t and $t - \tau$, where τ is the transit time between the deflection plates:

$$v_y = -\frac{e}{m}E_y\int_{t-\tau}^{t} \cos \omega t \, dt = -\frac{e}{m}\frac{E_y}{\omega}\{\sin \omega t - \sin\{\omega(t - \tau)]\}, \tag{19.40}$$

so that

$$v_y = \frac{2e}{m}\frac{V_p}{D\omega} \sin(\omega\tau/2) \cos[\omega(t - \tau/2)]. \tag{19.41}$$

The tangent of the angle of deflection is

$$\tan \alpha = \frac{v_y}{v_{z_0}} = \frac{2e}{m}\frac{V_p}{D\omega v_{z_0}} \sin(\omega\tau/2) \cos[\omega(t - \tau/2)]. \tag{19.42}$$

Substituting in the above equation $l = v_{z_0}\tau$, and using the expression $2e/mv_{z_0} = v_{z_0}/V_a$ we obtain

$$\tan \alpha = \frac{lV_p}{2V_aD} \frac{\sin(\omega\tau/2)}{\omega\tau/2} \cos[\omega(t - \tau/2)]. \tag{19.43}$$

Comparing equation 19.43 with equation 19.13 we may note that the factor ahead of sine function is the static deflection sensitivity. In addition, the maximum value of the deflection varies as the ratio of the sine of half the transit angle through the deflection plates to half the transit angle. With increase of ω, the maximum value of deflection decreases. In fact at $\omega\tau = 2k\pi$, where $k = 1, 2, 3, \ldots$, $\tan \alpha$ is zero.

19.5 Focusing Errors Produced by Deflection

Thus far in the preceding discussions only homogeneous electric and magnetic fields were considered. In practice, however, it is not possible to produce homogeneous deflecting fields without end effects. At the end of

deflection plates or deflection yokes the field does not cease to exist but continues as fringing fields. Fringing fields are nonhomogeneous fields.

In the case of an image tube when the cone-shaped electron beam, which seems to originate in the crossover, passes through the nonhomogeneous electric or magnetic fringing fields, regional variations of the field will cause distortion due to the different amounts of deflection at different zonal places. Local variations of the field will distort the circular shape of the electron beam originating from one point of the photocathode by producing a different amount of deflection on the periphery on the circle, thus changing the convergence of the beam. As a result local nonhomogeneity may produce astigmatism, curvature of field, and coma, depending on the nature of the nonhomogeneity. Therefore it is important to keep the deflection effect of fringing fields to a minimum. In magnetic tubes the fringe deflection may be minimized or eliminated by using a yoke longer than the optical length of the tube. In electrostatic deflection the fringe deflection may be reduced (at the expense of losing deflection sensitivity) by increasing the plate separation.

Even in the case of homogeneous fields, an error, the so-called deflection focusing, appears. In the case of electrostatic deflection the deflection focusing is due to the fact that an electron traveling near the positive deflection plate has a higher energy than an electron farther from the plate. The electrons with the higher energy are deflected less. Therefore a convergent beam after deflection becomes more convergent in the direction of deflection.
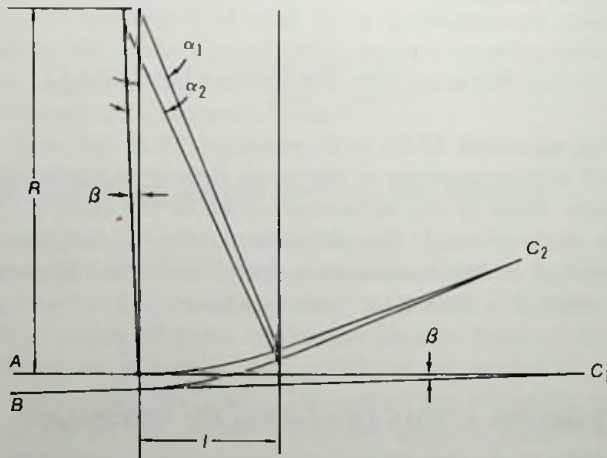
Fig. 19.8   Deflection focusing in a homogeneous magnetic field of length _l_.

This effect may be minimized by increasing the plate length. For purely geometrical reasons deflection focusing is also present in the case of a homogeneous magnetic field, as may be concluded from the geometry of figure 19.8. Here the undeflected rays are converging at point C_1. The deflected rays are converging at point C_2. Both deflected rays are deflected on a circular path having a radius R.

References

Cooper, H. G. "Design of a High-Resolution Electrostatic Cathode-Ray Tube for the Flying Spot Store," *The Bell System Technical Journal*, p. 723, May 1961.

Maloff, I. G., and D. W. Epstein. *Electron Optics in Television With Theory and Operation of Cathode-Ray Tubes*, McGraw-Hill Book Co., Inc., New York, 1938.

Schade, O. H. "Characteristics of High Efficiency Deflection and High Voltage Supply Systems for Kinescopes," *RCA Review*, Vol. 9, No. 1, pp. 98–138, March 1947.

Schlesinger, K. "Anastigmatic Yokes for Picture Tubes," *Electronics*, Vol. 22, No. 10, p. 102, October 1949.

———. "Scanning, Deflection, and Color Registration," Chapter 6 in *Television Engineering Handbook*, McGraw-Hill Book Co., Inc., New York, 1957.

Zworykin, V. K., and G. A. Morton. *Television*, John Wiley & Sons, Inc., New York, 1940.

20

FOCUSING COILS AND PERMANENT MAGNETS

20.1 Introduction

As discussed in chapter 3, for the electromagnetic image tubes a homogeneous axial magnetic field is needed for focusing the photoelectron image on the phosphor screen. The axial magnetic field may be generated by a focusing coil or by a cylindrical permanent magnet. A focusing coil is usually used to vary the magnetic field together with the focusing voltage to change the gain of the image tube or to switch the number of focusing loops; otherwise a permanent magnet is used.

20.2 Focusing Coils

As far as image tube performance is concerned, the primary consideration of a focus coil or a permanent magnet design is the homogeneity of the magnetic field. Consider first the focusing coil. As shown in appendix H, the magnetic field of a long solenoid, whose diameter is negligibly small with respect to its length, is perfectly homogeneous. However, the magnetic flux density B of a short solenoid (which has a length comparable to the length of the image tube) varies considerably along the axis of the solenoid as may be seen from the following equation (see appendix H for the derivation of B):

$$B_s(z) = \mu_0 \times 10^4 \frac{IN}{2l} \left[\frac{l/D + 2z/D}{\sqrt{D^2 + (l/D + 2z/D)^2}} \right.$$

$$+ \frac{l/D - 2z/D}{\sqrt{D^2 + (l/D - 2z/D)^2}} \Bigg].$$

<div style="text-align:right">(20.1)</div>

Here B is the magnetic flux density in gausses along the axis of solenoid, $\mu_0 = 4\pi \times 10^{-7}$ H/m is the permeability of free space, I is the solenoid current in amperes, N is the number of turns of the solenoid and l and D are the length and the diameter of the solenoid in meters, respectively, and z is the axial distance measured from the center of solenoid.

In the center of solenoid ($z = 0$), the magnetic flux density in gausses is

$$B_{sc} = \mu_0 \times 10^4 \, \frac{IN}{\sqrt{D^2 + l^2}}.$$

<div style="text-align:right">(20.2)</div>

Figure 20.1 shows the axial variation of the magnetic flux density for several solenoid length-to-diameter ratios. For the shorter solenoids the homogeneity is satisfactory only in the middle of the solenoid.
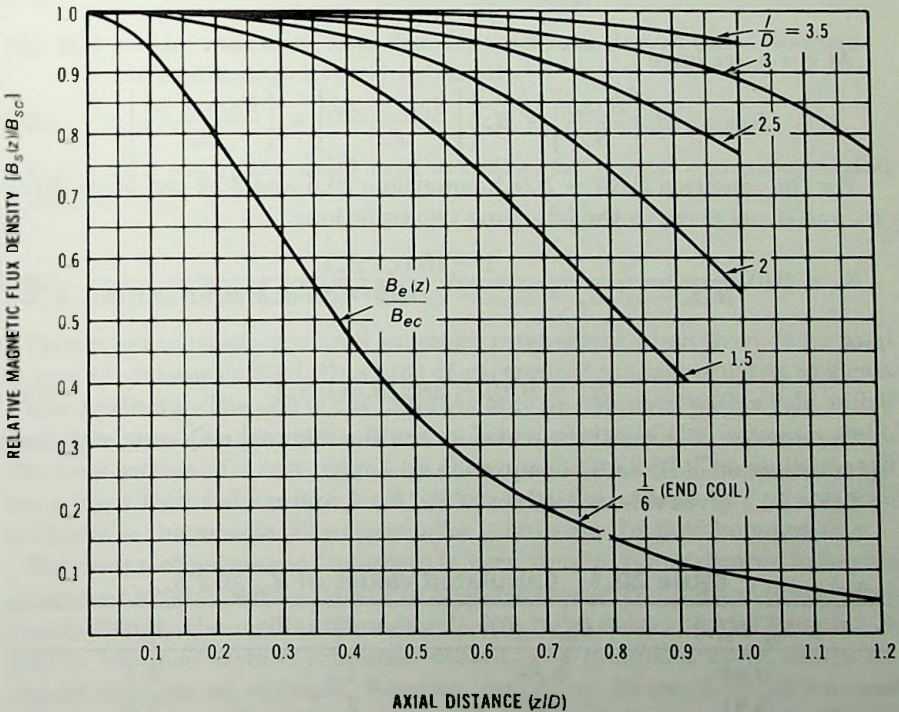
Fig. 20.1   **Axial magnetic flux density as a function of axial distance.**

The homogeneity of the magnetic field along the axis may be improved by the addition of short end coils to each end of the solenoid. The composite field $B_t(z)$ of the solenoid and end coils may be given by the following equation:

$$B_t(z) = B_s(z) + B_e(z_0 - z) + B_e(z_0 + z). \tag{20.3}$$

Here B_e is the magnetic flux density produced by the end coils positioned at a distance z_0 from the middle of the solenoid. Equation 20.3 may also be given in the following form:

$$B_t(z) = B_{sc}\left[\frac{B_s(z)}{B_{sc}}\right] + B_{ec}\left\{\left[\frac{B_e(z_0 - z)}{B_{ec}}\right] + \left[\frac{B_e(z_0 + z)}{B_{ec}}\right]\right\}. \tag{20.4}$$

Here the terms in the square brackets represent the normalized magnetic flux density of the solenoid and the end coils as shown in figure 20.1, and B_{ec} is the magnetic flux density in the center of an end coil.

In the middle of the solenoid ($z = 0$) we have from equation 20.4

$$B_t(0) = B_{sc} + 2B_{ec}\left[\frac{B_e(z_0)}{B_{ec}}\right]. \tag{20.5}$$

At $z = z_p$ we have

$$B_t(z_p) = B_{sc}\left[\frac{B_s(z_p)}{B_{sc}}\right] + B_{ec}\left\{\left[\frac{B_e(z_0 - z_p)}{B_{ec}}\right] + \left[\frac{B_e(z_0 + z_p)}{B_{ec}}\right]\right\}. \tag{20.6}$$

For the condition $B_t(0) = B_t(z_p)$, equations 20.5 and 20.6 can be solved for B_{ec} and B_{sc} as given in the following two equations:

$$B_{ec} = B_t(0) \frac{1 - [B_s(z_p)/B_{sc}]}{B_e(z_0 - z_p)/B_{ec} + B_e(z_0 + z_p)/B_{ec} - 2[B_e(z_0)/B_{ec}][B_s(z_p)/B_{sc}]} \tag{20.7}$$

and

$$B_{sc} = B_t(0) - 2B_{ec}[B_e(z_0)/B_{ec}]. \tag{20.8}$$

The number of turns of the end coils and the solenoid may now be obtained by substitution of B_{ec} or B_{sc} in equation 20.2.

Table 20.1 gives relative values of B_{sc}, B_{ec}, l, and z_p.

Table 20.1 Calculated Values of B_{sc} and B_{ec}

$B_{sc}/B_t(0)$	$B_{ec}/B_t(0)$	l/D	z_p/D
0.84	0.26	1.5	0.4
0.91	0.24	2	0.6
0.97	0.22	3	1
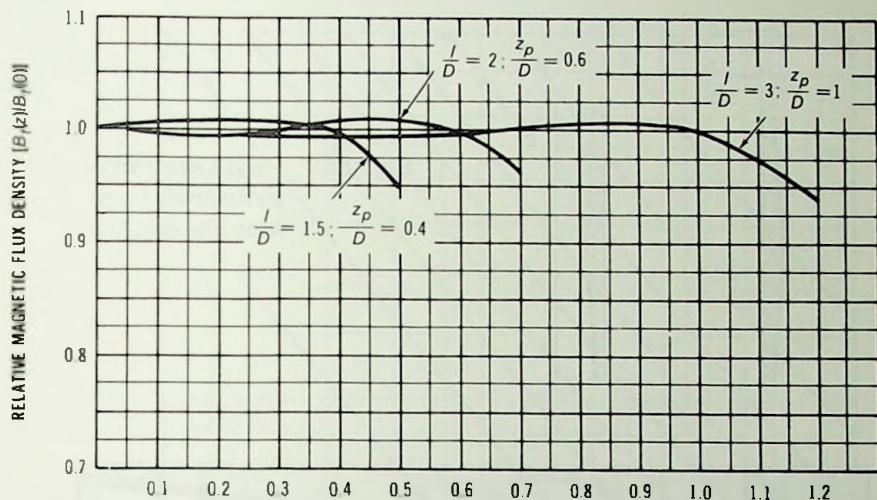
Fig. 20.2 **Axial magnetic flux density as a function of axial distance of end-compensated solenoids.**

Figure 20.2 shows the axial field variation for several end-compensated solenoids.

20.3 Permanent Magnets

Permanent magnets are used in image intensifiers when there is no need to vary the magnetic field. One type of permanent magnet consists of a cast alnico 5 cylinder. The end of the cylinder may be equipped with a cold-rolled steel pole piece for improving the end homogeneity of the magnetic field. The cross section of a cast magnet is shown in figure 20.3. The magnet wall has a taper that reduces the wall thickness at the ends to 60% of the wall thickness in the middle. The taper is for improving the field homogeneity.

The design of permanent magnets is very simple. If one desires to have a permanent magnet with a length L, inside diameter D_1, and a magnetic flux density B, only the median diameter D_2 has to be determined. Diameter D_2 may be obtained from a graphical design. The method may be easily explained through an example. Suppose that $D_1 = 10$ cm, $L = 25$ cm, and $B = 370$ gausses ($H = 370$ oersteds). Then, as a first step, find the 370-Oe point on the horizontal axis of figure 20.4 and draw a vertical line at this
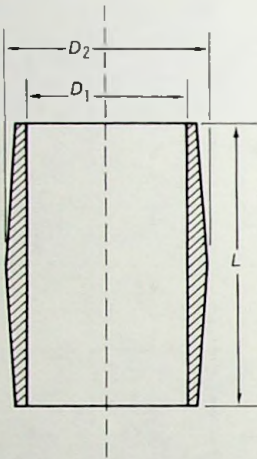
Fig. 20.3   Cross section of a
cylindrical per-
manent magnet.
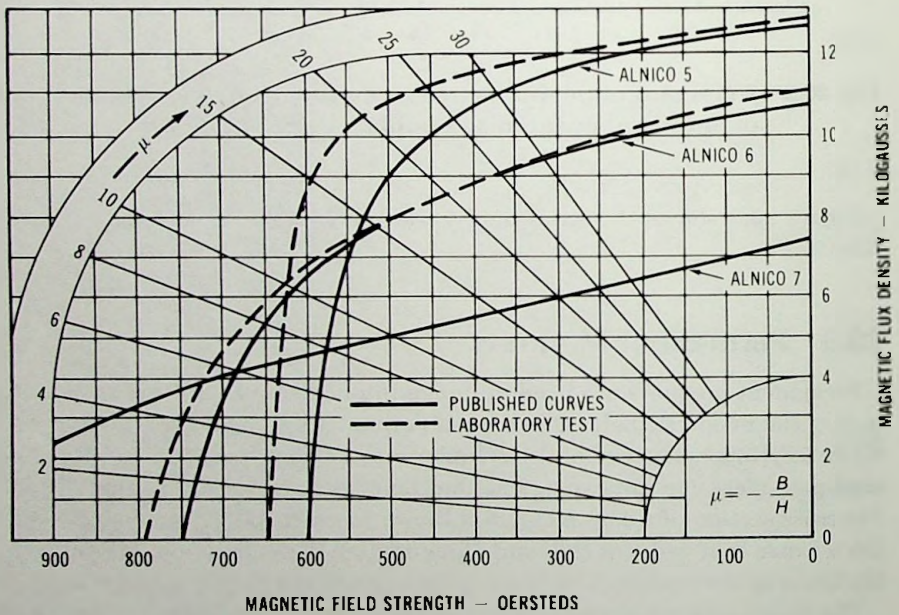
Fig. 20.4   Demagnetization curves of permanent magnet alloys.

point. The vertical line intersects the alnico 5 curve at $\mu = 30$. Next, go to figure 20.5 and find the intersection of $\mu = 30$ and $D_1/L = 10/25 = 0.4$. At the intersection we find $\rho = 0.85$. Therefore $D_2 = D_1/\rho = 10/0.85 = 11.7$ cm. For the origin of the graphic design the reader is referred to the M. S. Glass paper given in the references.
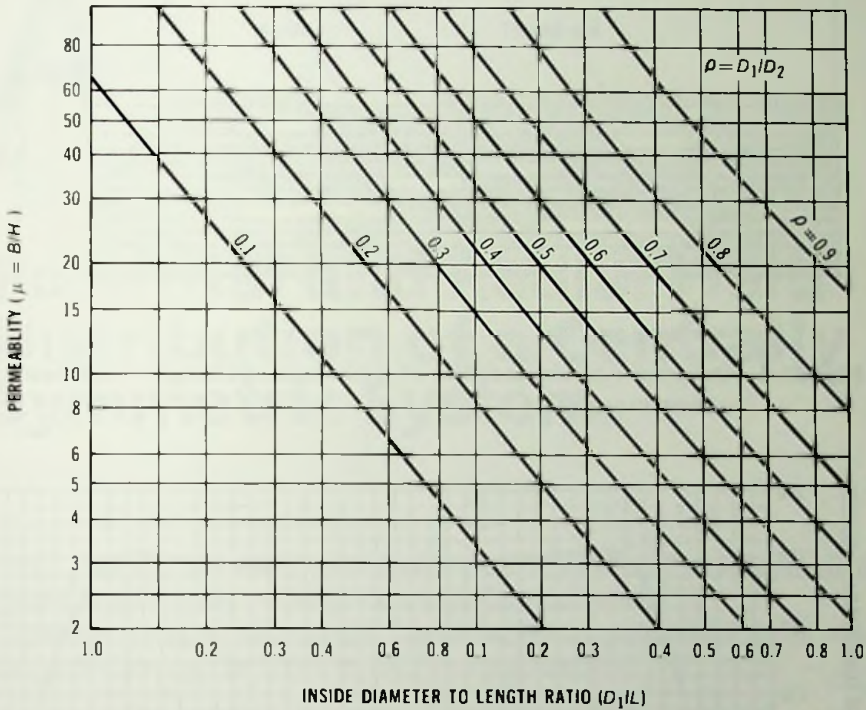
Fig. 20.5   **Permeability $\mu = B/H$ as a function of permanent magnet dimensions.**

In another type of cylindrical permanent magnet the wall consists of longitudinal bar magnets which are fixed to an aluminum or a nonmagnetic type stainless-steel cylinder. This magnet is handmade and it is designed by a cut-and-try method. The magnetic field strength is determined again by the dimensions and by the wall thickness (bar thickness) of the magnetic cylinder. However, both the uniformity and field strength may be modified by using two or three bars instead of a single bar along the length of the cylinder. With two or three bars along the cylinder length the magnetic field produced by the composite bar may be adjusted by insertion of suitable air gaps between the component bars. Figure 20.6 shows the quarter-section module of a 25 cm long, 12.5 cm inside diameter, permanent magnet. The module is repeated four times on the circumference. Figure 20.7 shows the magnetic field variation along the length of the cylindrical magnet.
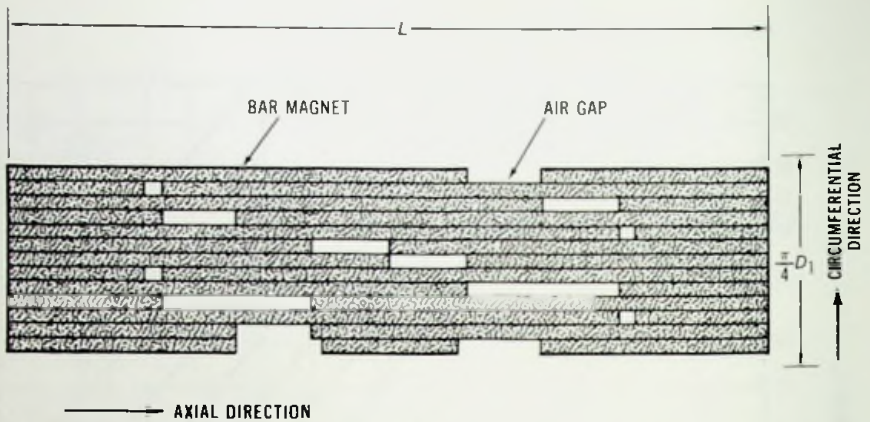
Fig. 20.6   Quarter-section module of a permanent magnet consisting of bar magnets.
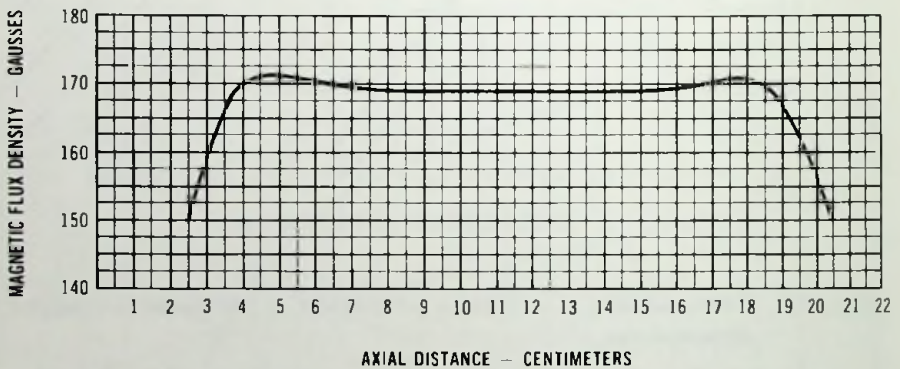
Fig. 20.7   Axial magnetic flux density variation of a permanent magnet consisting of bar magnets.

References

Bozorth, R. M., et al. "Demagnetizing Factors of Rods," *Journal of Applied Physics*, p. 320, Vol. 13, May 1942.

Glass, M. S. "Strait-Field Permanent Magnets of Minimum Weight for TWT Focusing. Design and Graphic Aids in Design," *Proc. IRE*, p. 1100, August 1957.

A

Potential and Radial Field Distribution of a Centrally Symmetric System

The potential and radial field distribution of a system of two concentric spheres is essentially the same as of a single point charge.

Consider a single point charge. The radial electric field distribution, from Coulomb's law, may be given by the following equation:

$$E_r = \frac{q}{4\pi\epsilon_0 r^2},$$ (A.1)

where ϵ_0 is the dielectric constant and r is the radial distance.

The potential difference between two spherical surfaces, shown in figure A.1, is

$$V_a - V_c = \Delta V = -\int_{R_c}^{R_a} E_r\, dr = -\int_{R_c}^{R_a} \frac{q}{4\pi\epsilon_0 r^2}\, dr = \frac{q}{4\pi\epsilon_0}\left(\frac{R_c - R_a}{R_a R_c}\right).$$ (A.2)

The potential difference between the c sphere and a sphere having a radius r is

$$V_r - V_c = \Delta V_r = -\int_{R_c}^{r} E_r\, dr = \frac{q}{4\pi\epsilon_0}\left(\frac{R_c - r}{R_c r}\right).$$ (A.3)

By division of equation A.3 by equation A.2, we obtain for the potential distribution

$$\Delta V_r = \Delta V \frac{R_a}{R_c - R_a}\left(\frac{R_c - r}{r}\right).$$ (A.4)
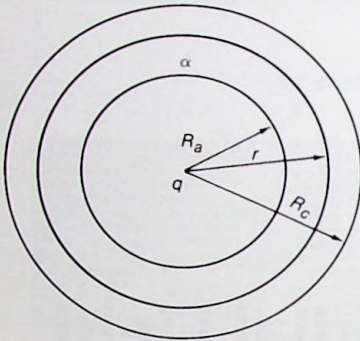
Fig. A.1   A point charge q and two imaginary concentric spheres a and c.

By division of equation A.1 by equation A.2, the radial electric field distribution becomes

$$E_r = \Delta V \frac{R_a R_c}{(R_c - R_a)r^2} \tag{A.5}$$

From equation A.5, the electric field strengths at the spheres a and c, respectively, are

$$E_a = \Delta V \frac{R_c}{(R_c - R_a) R_a} \tag{A.6}$$

and

$$E_c = \Delta V \frac{R_a}{(R_c - R_a) R_c} \tag{A.7}$$

B

Relationship Between the Sine-Wave Response, Square-Wave Response and Elliptic-Wave Response Factors of Imaging Systems

The relationship between the square-wave response $r(n)$ and sine-wave response $R(n)$ may be obtained by Fourier analysis. The Fourier series $F(x)$ of the input square-wave pattern is

$$F(x) = B_1 + B_1(4/\pi)[\cos(2\pi nx/\delta) - (1/3)\cos[3(2\pi nx/\delta)] + (1/5)\cos[5(2\pi nx/\delta)] - (1/7)\cos[7(2\pi nx/\delta)] + \cdots], \qquad (B.1)$$

where n is the number of cycles in a unit distance δ.

By imaging the square-wave pattern, each term in the brackets of equation B.1 is attenuated by the sine-wave response factor $R(kn)$ corresponding to the spatial frequency kn of the particular component; here, $k = 1, 3, 5, 7$. The output wave, therefore, may be obtained by multiplication of each term of the input wave by the sine-wave response $R(kn)$ that corresponds to the line frequency kn. At the maximums and minimums of the output wave all cosines are either unity or -1; therefore the square-wave response factor $r(n)$ is

$$r(n) = (4/\pi)[R(n) - R(3n)/3 + R(5n)/5 - R(7n)/7]. \qquad (B.2)$$

441

By use of similar series for $r(3n)$, $r(5n)$, ..., $r(kn)$, the above series can be solved for $R(n)$ as follows:

$$R(n) = (\pi/4)[r(n) + r(3n)/3 - r(5n)/5 + r(7n)/7$$
$$- r(9n)/9 + r(11n)/11 - \cdots]. \tag{B.3}$$

The relationship between the elliptic-wave response and sine-wave response may be obtained in a similar way. For $\pi/2 < x < \pi$, the input elliptic-wave pattern may be given by the following equation:

$$f(x) = -\sqrt{1 - (2 - 2x/\pi)^2}. \tag{B.4}$$

With substitution of

$$2 - 2x/\pi = \cos u \tag{B.5}$$

we obtain

$$\left.\begin{array}{l} f(u) = -\sin u, \\ dx = (\pi/2)\sin u\, du. \end{array}\right\} \tag{B.6}$$

The Fourier coefficient a_n is

$$a_n = \int_0^{\pi/2} \sin^2 u\, \{\cos\,[(n\pi/2)\cos u] - \cos\,[(n\pi/2)(2 - \cos u)]\}\, du \tag{B.7}$$

and so

$$a_n = 0 \text{ for } n \text{ even,}$$
$$= \int_0^{\pi/2} \sin^2 u \cos\,[(n\pi/2)\cos u]\, du = (2/n)\, J_1(n\pi/2) \text{ for } n \text{ odd.} \tag{B.8}$$

The Fourier series $F(x)$ of the input elliptical-wave pattern then becomes

$$F(x) = B_1[1 + 2J_1(\pi/2)\cos(2\pi nx/\delta) + (2/3)\,J_1(3\pi/2)\cos(6\pi nx/\delta)$$
$$+ (2/5)\,J_1(5\pi/2)\cos(10\pi nx/\delta) + \cdots]$$
$$= B_1 + B_1(2\sqrt{3}/\pi)\{\cos(2\pi nx/\delta) - (0.51/3)\cos[3(2\pi nx/\delta)]$$
$$+ (0.38/5)\cos[5(2\pi nx/\delta)] - (0.32/7)\cos[7(2\pi nx/\delta)]$$
$$+ (0.25/9)\cos[9(2\pi nx/\delta)] - \cdots\}. \tag{B.9}$$

The output wave may be obtained by multiplication of each term of the input wave by the sine-wave response $R(kn)$:

$$r(n) = (2\sqrt{3}/\pi)[R(n) - (0.51/3)R(3n) + (0.38/5)R(5n)$$
$$- (0.32/7)R(7n) + (0.25/9)R(9n) - \cdots]. \tag{B.10}$$

See figure B.1.

$r = \Delta B/B_2$

$$F(x) = B_1\left(1 + \sqrt{1 - \left(\frac{4x}{T}\right)^2}\right) ; \quad -\frac{T}{4} < x < \frac{T}{4}$$

$$F(x) = B_1\left(1 - \sqrt{1 - \left(\frac{4x}{T} - 2\right)^2}\right) ; \quad \frac{T}{4} < x < \frac{3}{4}T$$

$F(x)$

B_1

T

B_2

ΔB

$x \longrightarrow$

OUTPUT WAVE $(\delta = nT)$

$x \longrightarrow$
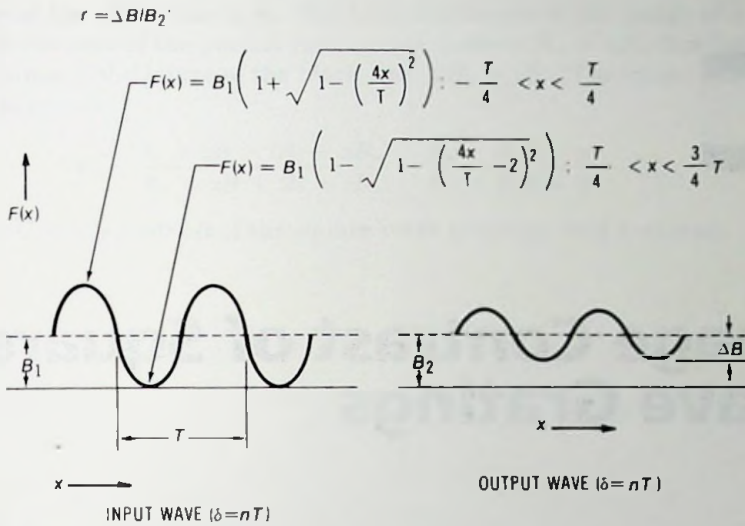
INPUT WAVE $(\delta = nT)$

Fig. B.1   Input and output waves of an elliptic-wave pattern.

By use of similar series for $r(3n)$, $r(5n)$, . . . , $r(kn)$, the above series can be solved for $R(n)$ as follows:

$$R(n) = (\pi/2\sqrt{3})[r(n) + (0.51/3)r(3n) - (0.38/5)r(5n) \\ + (0.32/7)r(7n) - \cdots] \tag{B.11}$$

C

Image Contrast of Square-Wave Gratings

In a 100% contrast square-wave grating the light passes through the white lines without significant attenuation; no light passes through the black lines. When this pattern is imaged by an optical system, such as glass optics or an image intensifier, the image contrast or contrast transfer C_i is given by

$$C_i = \frac{B_w - B_b}{B_w + B_b},$$ (C.1)

where B_w and B_b are the luminance of the image of white and black lines, respectively.

The sum of $B_w + B_b$, the denominator of equation C.1, is essentially constant for all spatial frequencies because the contrast loss is caused by the light spread from the white lines into the black lines. If B_w and B_b are expressed as a fraction of the luminance of the white line at zero spatial frequency, and the luminance of the white line at zero spatial frequency is unity, the following equation holds for all spatial frequencies:

$$B_w + B_b = 1 \quad \text{or} \quad B_b = 1 - B_w.$$ (C.2)

In the image of a less than 100% contrast pattern, light diffuses from both the white lines and the black lines into adjacent lines. If the fraction of light transmission of a black line is denoted by x, equation C.2 can be modified to give the partial luminance of the image of a white line resulting from light diffusion from a black line as $x(1 - B_w) = xB_b$. The partial luminance of the

image of the white line is B_w. The total luminance of the image of a white line is the sum of the partial luminances, namely $B_w + xB_b$. Similarly, the luminance of the image of the black line is $B_b + xB_w$. The image contrast C then becomes

$$C = \frac{B_w + xB - (B_b + xB_w)}{B_u + xB + B_b + xB_w} = \frac{B_u - B_b}{B_{u'} + B_b}\frac{1 - x}{1 + x} = C_iC_f,$$ (C.3)

where C_i is the contrast of the square-wave gratings (field contrast).

D

Resolution of the Mica-Coupled Image

At moderate input illumination levels a serious limitation to the resolution of a cascaded image tube exists as a result of the thickness (5 to 10 μm) of the mica spacer. The spacer serves as a support for the interstage phosphor screen and photocathode and also couples the light image from the phosphor screen to the photocathode. The resolution of the mica-coupled image may be obtained by tracing light paths through the mica, as shown in figure D.1. Assuming a Lambertian light emission of phosphor screens, the illumination dI of the screen side of the mica spacer produced by a small excited area (ΔA) of the screen is given by

$$dI = \frac{i_0}{\pi} \frac{\Delta A}{(d')^2} \cos^4 \alpha_2, \qquad (D.1)$$

where i_0 is the luminous emittance of the phosphor screen, d' is the distance of ΔA from the mica, and α_2 is the angle of incidence of light. The light flux within the incremental angle $\Delta \alpha_2$ illuminates the screen side of the mica over an annular element $dA = 2\pi r_1 dr_1$. The same light flux illuminates an annular element $dA' = 2\pi r dr$ on the cathode side of the mica. Consequently the illumination of the cathode side with respect to the screen side is reduced by a factor ρ, as follows:

$$\rho = \frac{dA}{dA'} = \frac{r_1 dr_1}{r dr}. \qquad (D.2)$$
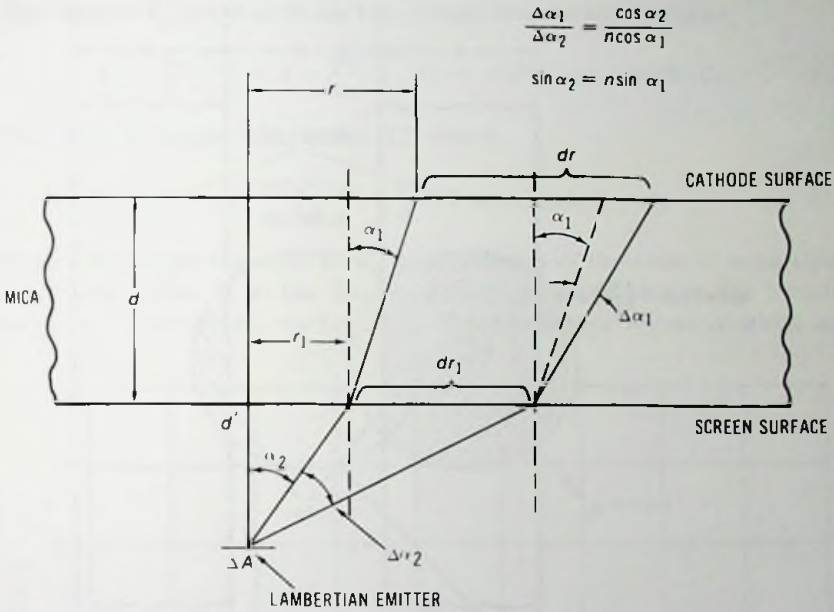
Fig. D.1　A mica spacer illuminated by a Lambertian emitter.

From figure D.1,

$$\rho = \frac{(d')^2 n^2 \cos^4 \alpha_1}{(d \cos^3 \alpha_2 + d'n \cos^3 \alpha_1)(nd' \cos \alpha_1 + d \cos \alpha_2)}.$$ (D.3)

The illumination on the cathode side of the mica spacer is calculated as the product of equations D.2 and D.3. For $d' << d$ the illumination on this surface becomes

$$dI' = \frac{i_0 \Delta A n^2}{\pi d^2} \cos^4 \alpha_1 = \frac{i_0 \Delta A n^2}{\pi d^2} (1 + r^2/d^2)^{-2}.$$ (D.4)

(This simplified analysis does not consider light from the phosphor in optical contact with the mica and light reflected back to the phosphor screen by the photocathode.)

On illumination of the mica spacer through a resolution pattern that is in contact with the screen side of the mica ($d' << d$), the illumination of the cathode side in the center of a black or white line may be obtained as shown in figure D.2, where points C_1 and C_2 are on the cathode side of the mica. Because of the refraction at the screen side of the mica, a point on the cathode side may receive illumination only from those points on the screen

$A_2 = (r_m{}^2\pi) - A_1$
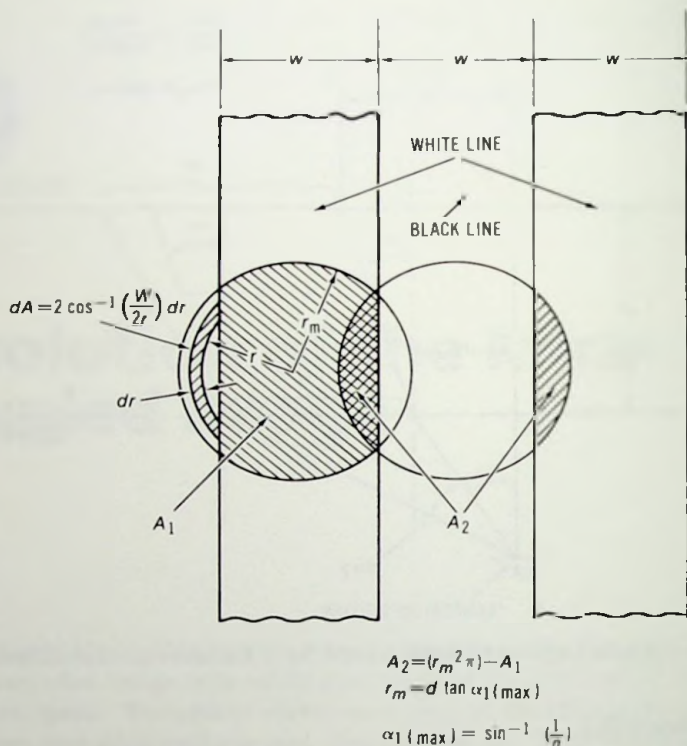
$r_m = d \tan \alpha_1 (\max)$

$\alpha_1 (\max) = \sin^{-1} \left(\frac{1}{n}\right)$

Fig. D.2 Two white lines and a black line of a resolution pattern in contact with the screen side of the mica spacer.

side that are within a circular area having a radius $r_m = d \tan \alpha_{1(\max)}$ where $\alpha_{1(\max)} = \sin^{-1} (1/n)$, d is the thickness of the mica, and n is the index of refraction.

Therefore the illumination in the mica-coupled image of the white line (I_w) at point C_1 of figure D.2 may be obtained by integrating dI' over the area A_1:

$$I_w = \frac{i_0 n^2}{\pi d^2} \int_{A_1} (1 + r^2/d^2)^{-2} \, dA$$

$$= i_0 - \frac{4 i_0 n^2}{\pi d^2} \int_{w/2}^{r_m} r(1 + r^2/d^2)^{-2} \cos^{-1} (w/2r) \, dr. \qquad (D.5)$$

The illumination I_B in the image of the black line at C_2 is given by

$$I_B = \frac{i_0 n^2}{\pi d^2} \int_{A_1} (1 + r^2/d^2)^{-2} \, dA = 4 \frac{i_0 n^2}{\pi d^2} \int_{w/2}^{r_m} r(1 + r^2/d^2)^{-2} \cos^{-1} (w/2r) \, dr. \qquad (D.6)$$

The contrast C' between these two images may be expressed as

$$C' = \frac{I_w - I_b}{I_w + I_b} = 1 - \frac{8n^2}{\pi d^2} \int_{w/2}^{'_m} r(1 + r^2/d^2)^{-2} \cos^{-1}(w/2r) \, dr. \quad (D.7)$$

The range is limited in equation D.7, where

$$\frac{\tan \alpha_{1(max)}}{1.5} < \frac{w}{d} < 2 \tan \alpha_{1(max)}. \quad (D.8)$$

Figure D.3 shows the contrast C' as a function of the ratio of mica thickness to line width. If, at the line frequency corresponding to the limiting resolution, a sinusoidal variation of the luminance across a white and
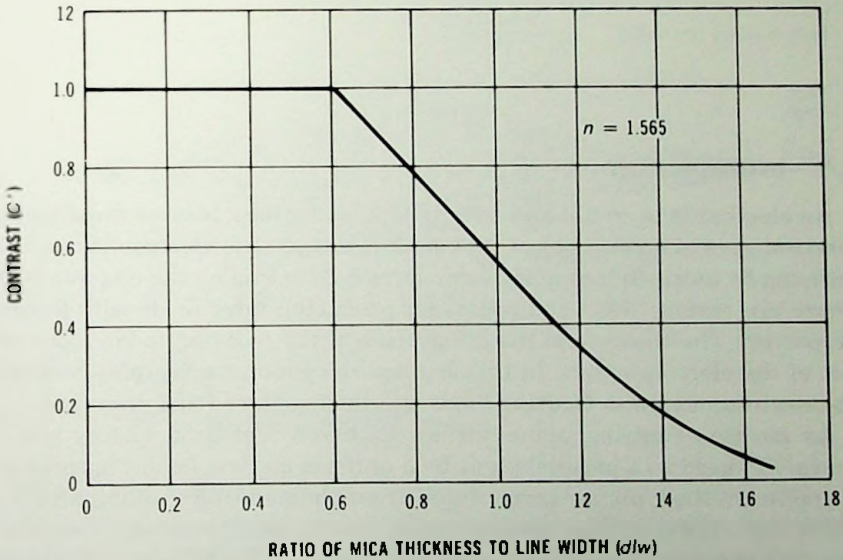
Fig. D.3 Contrast as a function of the ratio of mica thickness to line width.

a black line is assumed, then at 3% average luminance difference, C' is $0.03/0.637 = 0.047$. Because the value of d/w is 1.60 at $C' = 0.047$, the limiting resolution R_l is

$$R_l = \frac{1}{2w} = \frac{1}{2(0.625d)} = \frac{0.80}{d} \text{ lp/mm,} \quad (D.9)$$

where d is the thickness of the mica spacer in millimeters.

E

Optical Principles

E.1   Introduction

An electron lens, in analogy to a light focusing lens, focuses the divergent electron rays of a point object into a point image. The electron lens attains focusing by an electric or a magnetic force field acting on the electron beam. There are various ways and means for producing force fields with focusing properties. The theory and the description of the focusing fields is the subject of the electron optics. In this chapter the general principles governing the electron motion in focusing fields will be introduced and discussed.

An electron-emitting plane surface with zero emission energy may be sharply imaged on a parallel plane by a uniform electric field. This principle is applied in the biplanar image tube. From photoemitters illuminated with white light the electrons, however, may emerge with substantial emission energies ranging from zero to a few electronvolts. Each point of the photo-cathode emits electrons to all directions of the hemisphere, producing a divergent electron beam. In such a case, only proximity focusing may be obtained by a uniform electric field alone. Busch has shown that, in analogy to light optics, divergent electron beams can be made convergent by axially symmetric electric and magnetic fields. Such fields, therefore, constitute an electron lens. The axially symmetric electron lens is built of elements having cylindrical boundaries and positioned along the axis of symmetry as shown in figure E.1. Note that in light optics the light beam is converged by two spherical refracting surfaces, whereas in electron optics the refraction is smooth in the region of the lens. A good example of an axially symmetric electron lens is the electron gun of cathode-ray tubes.

450
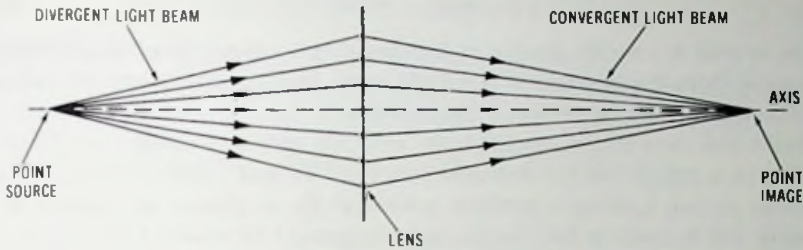
(A) Light optics.
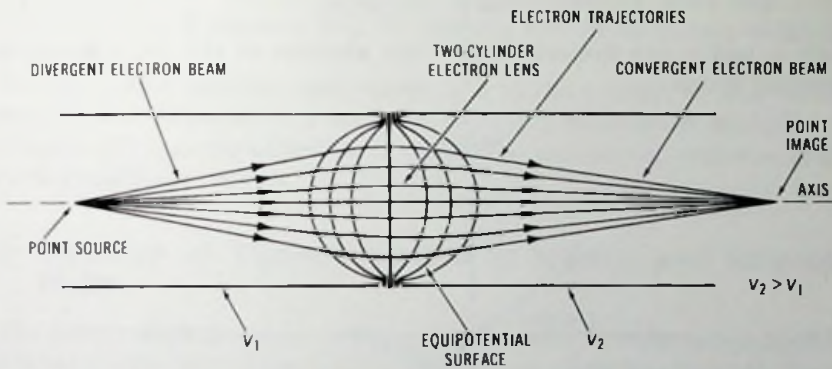
(B) Electron optics.

Fig. E.1 Axially symmetric lenses.

With axially symmetric lenses, however, sharp focusing is obtained only along the axis of the system; off axis, geometric aberrations are present which may degrade the quality of imaging.

In image tubes the requirement is to focus electron beams of large cross section with as little aberration as possible. The two most frequently used image tube lenses which meet this requirement are the electromagnetic lens, consisting of homogeneous axial electric and magnetic fields, and the centrally symmetric electrostatic lens (also called point symmetric lens). Both lenses, in ideal conditions, are free from geometrical aberrations.

E.2 Snell's Law

The analogy between focusing light and electron rays can be shown by considering Snell's law of refraction from which all properties of physical lenses can be deduced. Snell's law for glass optics is

$$n_1 \sin \theta_1 = n_2 \sin \theta_2, \qquad\qquad (E.1)$$

where θ_1 and θ_2 are the angles of incidence and refraction of the light rays measured from the normal to the light rays, and n_1 and n_2 are the indexes of refraction on the two sides of the boundary.

Snell's law has its counterpart in electron optics. Consider an electron moving in a region with a uniform potential V_1 and suddenly crossing into a second region having a uniform potential V_2, as shown in figure E.2. In crossing the boundary the tangential component of velocity is unchanged, but the normal component of velocity is increased. By equating the tangential components of velocity we obtain

$$v_1 \sin \theta_1 = v_2 \sin \theta_2, \qquad\qquad (E.2)$$

where v_1 and v_2 are the velocities of the electron on the two sides of the refracting plane.
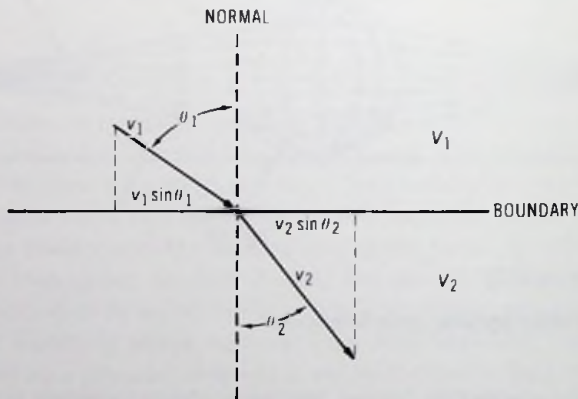
Fig. E.2   Electron refraction at the boundary between potentials V_1 and V_2.

By comparing equations E.1 and E.2 it becomes clear that in electron optics the electron velocity is analogous to the refraction index in light optics.

The relationship between the electron velocity and its energy may be given by the following equation:

$$\tfrac{1}{2}mv^2 = e(V + V_i), \qquad\qquad (E.3)$$

where e and m are the electron charge and mass, respectively, eV_i is the emission energy, and V is the electric potential with respect to the cathode. From equation E.3 the velocity is

$$v = \sqrt{(2e/m)(V + V_i)} = 5.93 \times 10^5\sqrt{V + V_i}, \tag{E.4}$$

where V and V_i are in volts and v is in meters per second.

By expressing v_1 and v_2 in equation E.2 with the electron emission energy eV_i and the potentials V_1 and V_2, the following equation is obtained:

$$\sqrt{(2e/m)(V_1 + V_i)} \sin \theta_1 = \sqrt{(2e/m)(V_2 + V_i)} \sin \theta_2. \tag{E.5}$$

After rearrangement of terms,

$$\frac{\sin \theta_1}{\sin \theta_2} = \sqrt{\frac{V_2 + V_i}{V_1 + V_i}}. \tag{E.6}$$

In light optics the path of a light ray may be traced by using Snell's law. Similarly, by use of equation E.6, the electron path in an electric field may be traced.

One difference between light optics and electron optics is that in the former, light is refracted only on a few refracting surfaces; in the latter, in the region of a lens the refraction is continuous because the variation of the potential field is continuous.

E.3   Equation of Electron Motion in Electric and Magnetic Fields

The motion of electrons in electric and magnetic fields is determined by the fundamental laws of mechanics. The general equation of motion, therefore, from Newton's second law, is:

$$m\frac{d\mathbf{v}}{dt} = -e\mathbf{E} - e(\mathbf{v} \times \mathbf{B}), \tag{E.7}$$

where $\mathbf{E}$ is the vector electric field, $\mathbf{B}$ is the magnetic flux density, and $\mathbf{v}$ is the velocity of the electron. The first term on the right-hand side of equation E.7 represents the electric force, while the second term is the Lorentz force. When the distribution of E and B are known in a region the electron path may be determined by solving equation E.7.

E.4   Motion in Centrally Symmetric Gravitational Fields

The vector equation E.7 may be written in different forms in different coordinate systems. For the centrally symmetric system, which may be used to describe the planetary motion around the sun, the equations of motion in the plane of orbital motion are

$$m\left(\frac{dr^2}{dt^2} - r\left(\frac{d\phi}{dt}\right)^2\right) = -F(r) \tag{E.8}$$

and

$$m\left(2\frac{dr}{dt}\frac{d\phi}{dt} + r\frac{d^2\phi}{dt^2}\right) = 0,$$ (E.9)

where $F(r)$ is the gravitational force of attraction, m is the mass of the planet, and r and ϕ are the spherical coordinates of the centrally symmetric system.

Multiplying equation E.9 by r/m gives

$$\frac{d}{dt}\left(r^2\frac{d\phi}{dt}\right) = 0.$$ (E.10)

By integration of equation E.10 we obtain

$$r^2\frac{d\phi}{dt} = c,$$ (E.11)

where c is a constant. Equation E.11 is known as Kepler's second law of planetary motion. As shown in chapter 3 the same law may be used to describe the motion of a free electron in vacuum in a central field.

E.5 Electron Motion in Axially Symmetric Electric Fields

From Newton's second law, the equations of motion, in two-dimensional cylindrical coordinates, are

$$-eE_r = m\frac{d^2r}{dt^2}$$ (E.12)

and

$$-eE_z = m\frac{d^2z}{dt^2},$$ (E.13)

where r and z are the radial and axial coordinates, respectively, and E_r and E_z are the radial and the axial components of the electric field. By writing

$$\frac{d}{dt} = \frac{dz}{dt}\frac{d}{dz}$$ (E.14)

we obtain

$$-eE_r = m\frac{d}{dt}\left(\frac{dr}{dt}\right) = m\frac{dz}{dt}\frac{d}{dz}\left(\frac{dr}{dz}\frac{dz}{dt}\right)$$
$$= m\left[\left(\frac{dz}{dt}\right)^2\frac{d^2r}{dz^2} + \frac{dr}{dz}\frac{dz}{dt}\frac{d}{dz}\left(\frac{dz}{dt}\right)\right]$$ (E.15)

and

$$-eE_z = m\frac{d}{dt}\left(\frac{dz}{dt}\right) = m\frac{dz}{dt}\frac{d}{dz}\left(\frac{dz}{dt}\right). \tag{E.16}$$

Multiplying equation E.16 by $-dr/dz$ and adding it to equation E.15 we obtain

$$e\left(E_z\frac{dr}{dz} - E_r\right) = m\left(\frac{dz}{dt}\right)^2\frac{d^2r}{dz^2}. \tag{E.17}$$

The electron energy is

$$\tfrac{1}{2}mv^2 = \frac{m}{2}\left[\left(\frac{dr}{dt}\right)^2 + \left(\frac{dz}{dt}\right)^2\right] = e(V + V_t), \tag{E.18}$$

where eV_t is the emission energy and V is the electric potential with respect to the cathode.

By substitution of $(dz/dt)^2$ from equation E.18 into equation E.17 we obtain an equation having a term containing $(dr/dt)^2$. This term may be expressed in terms of E_z, E_r, and dr/dz by multiplying equation E.17 by $(dr/dz)^2$ and using the relation $dr/dt = (dz/dt)(dr/dz)$. This gives the general differential equation of the electron path:

$$2(V + V_t)\frac{d^2r}{dz^2} = \left(E_z\frac{dr}{dz} - E_r\right)\left[1 + \left(\frac{dr}{dz}\right)^2\right]. \tag{E.19}$$

Point-by-point computation of equation E.19 gives the electron path.

Most digital computers have subroutines available for solving ordinary differential equations. They may be used to solve equations E.12 and E.13.

E.6 Electron Motion in Axially Symmetric Electric and Magnetic Fields

In a more general case the electron lens may consist of combined axially symmetric electric and magnetic fields. The equations of motion, for this case, are given by the following equations (see appendix G):

$$m\frac{d^2z}{dt^2} = e\left(-r\frac{d\phi}{dt}\frac{\partial A}{\partial z} + \frac{\partial V}{\partial z}\right), \tag{E.20}$$

$$m\left[\frac{d^2r}{dt^2} - r\left(\frac{d\phi}{dt}\right)^2\right] = e\left(-\frac{d\phi}{dt}\frac{\partial(rA)}{\partial r} + \frac{\partial V}{\partial r}\right), \tag{E.21}$$

$$\frac{m}{r}\frac{d}{dt}\left(r^2\frac{d\phi}{dt}\right) = e\left(\frac{dz}{dt}\frac{\partial A}{\partial z} + \frac{1}{r}\frac{dr}{dt}\frac{\partial(rA)}{\partial r}\right) = \frac{e}{r}\frac{d(rA)}{dt}. \tag{E.22}$$

In the case of axial symmetry the magnetic vector potential **A** at a radial distance r_0 is equal to the ratio of the magnetic flux ϕ_{mag} through the circular area πr_0^2 about the axis divided by the circumference of the circle $2\pi r_0$ (see equation E.30).

The magnetic vector potential **A** is related to the magnetic field components in the following way:

$$B_r = -\frac{\partial A}{\partial z}, \tag{E.23}$$

$$B_z = \frac{1}{r}\frac{\partial(rA)}{\partial r}, \tag{E.24}$$

$$B_\phi = 0. \tag{E.25}$$

By integration of equation E.22 the following equation is obtained:

$$\frac{m}{e}\left(r^2\frac{d\phi}{dt} - r_0^2\frac{d\phi_0}{dt}\right) = rA - r_0 A_0, \tag{E.26}$$

where r_0, ϕ_0 and A_0 designate the cylindrical coordinates and the magnetic vector potential of a fixed point.

By rearrangement of equation E.26, the following is obtained:

$$\frac{m}{e}\frac{d\phi}{dt} = \frac{A}{r} + \left(\frac{m}{e}r_0^2\frac{d\phi_0}{dt} - r_0 A_0\right)\frac{1}{r^2} = \frac{rA + C}{r^2}, \tag{E.27}$$

where

$$C = \frac{m}{e}r_0^2\frac{d\phi_0}{dt} - r_0 A_0 = \frac{m}{e}r^2\frac{d\phi}{dt} - rA = \text{constant.} \tag{E.28}$$

Equation E.27 can now be used to eliminate $d\phi/dt$ from equations E.20 and E.21. Let us introduce the function

$$Q(r,z) = -\frac{e}{2m}\left(\frac{rA + C}{r}\right)^2 + V(r,z), \tag{E.29}$$

where

$$A = \frac{\phi_{mag}}{2\pi r_0} = \frac{1}{r_0}\int_0^{r_0} B_z r\, dr. \tag{E.30}$$

The partial derivatives of $Q(r,z)$ with respect to z and r are identical with the right-hand sides of equations E.20 and E.21, respectively. Therefore equations E.20 and E.21 are identical with the following two equations:

$$m\frac{d^2z}{dt^2} = e\frac{\partial Q}{\partial z} \tag{E.31}$$

and

$$m \frac{d^2r}{dt^2} = e \frac{\partial Q}{\partial r}. \tag{E.32}$$

By comparing equations E.30 and E.31 with equations E.12 and E.13, it becomes clear that $Q(r,z)$ is a modified potential whose gradient describes the force field acting on an electron.

The energy equation may be obtained by multiplying equation E.31 by dz/dt and equation E.32 by dr/dt and adding and integrating:

$$m\left(\frac{d^2z}{dt^2}\frac{dz}{dt} + \frac{d^2r}{dt^2}\frac{dr}{dt}\right) = \frac{m}{2}\frac{d}{dt}\left[\left(\frac{dz}{dt}\right)^2 + \left(\frac{dr}{dt}\right)^2\right]$$

$$= e\left(\frac{\partial Q}{\partial z}\frac{dz}{dt} + \frac{\partial Q}{\partial r}\frac{dr}{dt}\right) = e\frac{dQ}{dt}. \tag{E.33}$$

By integration of the last equation the following equation is obtained:

$$\frac{m}{2}\left[\left(\frac{dz}{dt}\right)^2 + \left(\frac{dr}{dt}\right)^2\right] = e(Q + V_i). \tag{E.34}$$

By combination of equations E.27, E.28 and E.34, the kinetic energy of an electron becomes

$$\tfrac{1}{2}mv^2 = \frac{m}{2}\left[\left(\frac{dz}{dt}\right)^2 + \left(\frac{dr}{dt}\right)^2 + r^2\left(\frac{d\phi}{dt}\right)^2\right] = e(V + V_i). \tag{E.35}$$

From equations E.31, E.32, and E.34, the differential equation of the electron path in the rotating meridian plane may be obtained in a similar way as in the case of pure electrostatic field by elimination of time as a parameter. The result is

$$2(Q + V_i)\frac{d^2r}{dz^2} = \left(\frac{\partial Q}{\partial r} - \frac{dr}{dz}\frac{\partial Q}{\partial z}\right)\left[1 + \left(\frac{dr}{dz}\right)^2\right]. \tag{E.36}$$

Equation E.36 is identical in form with equation E.19, with Q taking the place of the potential distribution.

By combination of equations E.27, E.29 and E.34, the following differential equation may be obtained for the rotation of the meridian plane:

$$r^2\left(\frac{d\phi}{dt}\right)^2 = \frac{V - Q}{V_i + Q}\left[\left(\frac{dr}{dt}\right)^2 + \left(\frac{dz}{dt}\right)^2\right]. \tag{E.37}$$

From equation E.37, the rotation is

$$\phi = \phi_0 + \int_{z_0}^{z}\frac{1}{r}\sqrt{\frac{V - Q}{V_i + Q}\left[\left(\frac{dr}{dz}\right)^2 + 1\right]}\,dz. \tag{E.38}$$

The magnetic potential $A(r,z)$ and the electrostatic potential $V(r,z)$ may be expressed in terms of the axial magnetic field B_0 and axial potential V_0 in the following way:

$$V(r,z) = V_0(z) - \frac{V_0^{(2)}(z) \, r^2}{2^2} + \frac{V_0^{(4)}(z) \, r^4}{2^2 \, 4^2}$$
$$+ \cdots + \frac{(-1)^n \, V_0^{(2n)}(z)}{(n!)^2} \left(\frac{r}{2}\right)^{2n} + \cdots \qquad (E.39)$$

and

$$A(r,z) = B_0(z)\frac{r}{2} - B_0^{(2)}(z)\frac{r^3}{16} + \cdots + \frac{(-1)^n B_0^{(2n)}(z)}{n!(n+1)!} \left(\frac{r}{2}\right)^{2n+1} + \cdots \qquad (E.40)$$

If these series are substituted in equation E.29, and only the terms of lowest order in r and dr/dz are retained (we regard C of the order of r^2), the following two equations are obtained from equations E.36 and E.38 for the paraxial case:

$$\frac{d^2r}{dz^2} = -\frac{dr}{dz}\frac{V_0'}{2(V_0 + V_i)} - r\left(\frac{V_0''}{4(V_0 + V_i)} + \frac{eB_0^2}{8m(V_0 + V_i)}\right.$$
$$\left. - \frac{eC^2}{2mr^4(V_0 + V_i)}\right) \qquad (E.41)$$

and

$$\phi = \phi_0 + \int_{z_0}^{z} \sqrt{\frac{e}{2m(V_0 + V_i)}} \left(\frac{C}{r^2} + \frac{B_0}{2}\right) dz. \qquad (E.42)$$

On the axis $r_0 = 0$ and $C = 0$. Therefore equations E.41 and E.42 reduce to

$$\frac{d^2r}{dz^2} = \frac{dr}{dz}\frac{V_0'}{2(V_0 + V_i)} - \frac{r}{4(V_0 + V_i)}(V_0'' + eB_0^2/2m) \qquad (E.43)$$

and

$$\phi = \sqrt{\frac{e}{8m}} \int_{z_0}^{z} \frac{B_0}{\sqrt{V_0 + V_i}} \, dz. \qquad (E.44)$$

E.7 Electron Motion in Combined Homogeneous Electric and Magnetic Fields

In the case of combined homogeneous electric and magnetic fields, the electron motion can be resolved into two components: one motion occurring parallel to the magnetic field and the other motion in the plane perpendicular to the magnetic field. For the analysis of the motion the electric field

and the velocity vector may be expressed by their components: one compo-
nent parallel to the magnetic field and the other two components perpendic-
ular to the magnetic field as shown in figure E.3. Here the z coordinate is
aligned with the direction of the magnetic field **B**, the electric field **E** is
aligned with the z,y plane, and the velocity vector **v** has components in the
x, y, and z directions.
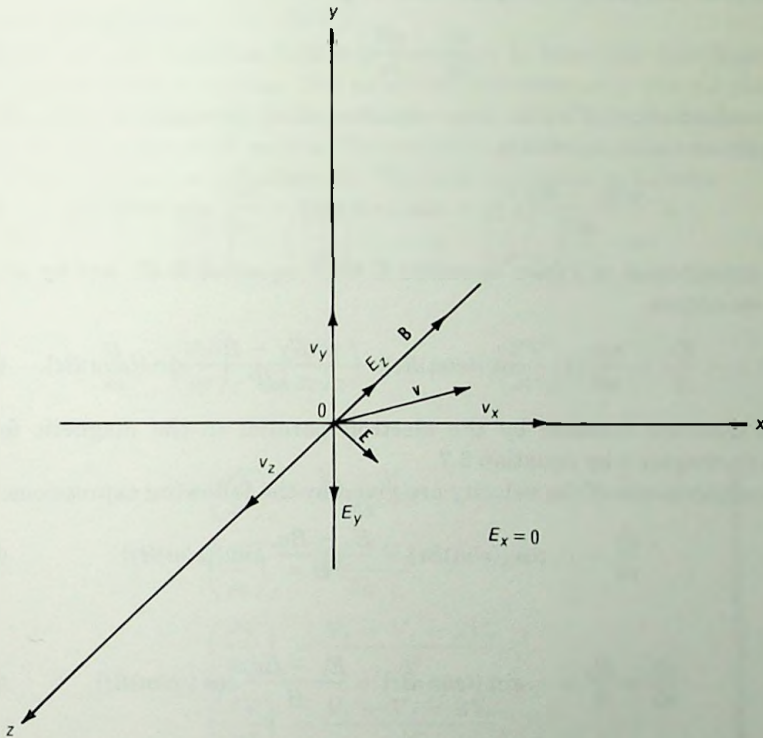
Fig. E.3   Three-dimensional diagram of vectors B, E, and v.

Parallel to the direction of the magnetic field the electron is accel-
erated only by the E_z component of electric field. This case is discussed in
chapter 3.

In the plane perpendicular to the magnetic field the motion may be de-
scribed by the following differential equations:

$$m \frac{d^2y}{dt^2} = eE_y - eB \frac{dx}{dt} \qquad (E.45)$$

and

$$m \frac{d^2x}{dt^2} = eB \frac{dy}{dt}. \tag{E.46}$$

Equations E.45 and E.46 may be solved with the following initial conditions: when t is 0, y and x are 0 and $dy/dt = v_y$, $dx/dt = v_x$.

The first integration of equation E.46 gives

$$\frac{dx}{dt} = \frac{eB}{m} y + v_x. \tag{E.47}$$

By substitution of dx/dt from equation E.47 in equation E.45, and by integration twice, we obtain

$$y = \frac{m(E_y - Bv_x)}{eB^2} \{1 - \cos[(e/m)Bt]\} + \frac{mv_y}{eB} \sin[(e/m)Bt]. \tag{E.48}$$

By substitution of y from equation E.48 in equation E.47, and by integration, we obtain

$$x = \frac{E_y}{B} t + \frac{mv_y}{eB} \{1 - \cos[(e/m)Bt]\} - \frac{m(Ey - Bv_x)}{eB^2} \sin[(e/m)Bt]. \tag{E.49}$$

The distance traveled by the electron parallel to the magnetic field is given in chapter 3 by equation 3.7.

The components of the velocity are given by the following expressions:

$$\frac{dy}{dt} = v_y \cos[(e/m)Bt] - \frac{E_y - Bv_x}{B} \sin[(e/m)Bt] \tag{E.50}$$

and

$$\frac{dx}{dt} = \frac{E_y}{B} + v_y \sin[(e/m)Bt] - \frac{E_y - Bv_x}{B} \cos[(e/m)Bt]. \tag{E.51}$$

E.8 Numerical Solution of Differential Equations of Electron Motion

As we already have seen earlier the electron path in a meridian plane of axially symmetric fields may be obtained by numerical solution of equations E.19 or E.36. In general, however, the electron emission occurs in all directions of a hemisphere. Therefore, to image a point in the presence of geometrical aberrations it is necessary to calculate the electron path in three dimensions rather than in a plane. In the case of axial symmetry, if the z coordinate of the cartesian coordinates is aligned with the axis of symmetry, the equations of motion for pure electrostatic fields become

$$\frac{d^2x}{dt^2} = -\frac{e}{m} E_x = \frac{e}{m} \frac{x}{r} \frac{\partial V}{\partial r},$$

$$\frac{d^2y}{dt^2} = -\frac{e}{m} E_y = \frac{e}{m} \frac{y}{r} \frac{\partial V}{\partial r},$$

$$\frac{d^2z}{dt^2} = -\frac{e}{m} E_z = \frac{e}{m} \frac{\partial V}{\partial z}.$$

(E.52)

In the above equations, $r = \sqrt{x^2 + y^2}$.

In order to solve equation E.52 it is necessary to know the distribution of the potential in the r,z plane. The potential distribution in the r,z plane is usually obtained by iterative methods. (See appendix F.) Hence the potential is known only at the mesh points. The potential gradient about a mesh point (r_0, z_0), however, can be calculated by Taylor's expansion as follows:

$$\frac{\partial V}{\partial r} = \left(\frac{\partial V}{\partial r}\right)_0 + \left(\frac{\partial^2 V}{\partial r^2}\right)_0 (r - r_0) + \left(\frac{\partial^2 V}{\partial r \partial z}\right)_0 (z - z_0) \qquad (E.53)$$

and

$$\frac{\partial V}{\partial z} = \left(\frac{\partial V}{\partial z}\right)_0 + \left(\frac{\partial^2 V}{\partial r \partial z}\right)_0 (r - r_0) + \left(\frac{\partial^2 V}{\partial z^2}\right)_0 (z - z_0), \qquad (E.54)$$

with

$$\left(\frac{\partial V}{\partial r}\right)_0 = \frac{V_3 - V_4}{2h},$$

$$\left(\frac{\partial V}{\partial z}\right)_0 = \frac{V_1 - V_2}{2h},$$

$$\left(\frac{\partial^2 V}{\partial r^2}\right)_0 = \frac{V_3 + V_4 - 2V_0}{h^2},$$

$$\left(\frac{\partial^2 V}{\partial z^2}\right)_0 = \frac{V_1 + V_2 - 2V_0}{h^2},$$

$$\left(\frac{\partial^2 V}{\partial r \partial z}\right)_0 = \frac{V_5 - V_6 - V_7 + V_8}{4h^2}.$$

(E.55)

The derivatives at the mesh point (r_0, z_0) were calculated by applying equations E.53 and E.54 to the neighboring mesh points as shown in figure E.4.

Second-order differential equations of special form (such as the simultaneous equations E.52)

$$\frac{d^2y}{dt^2} = \ddot{y} = G(t,y) \qquad (E.56)$$
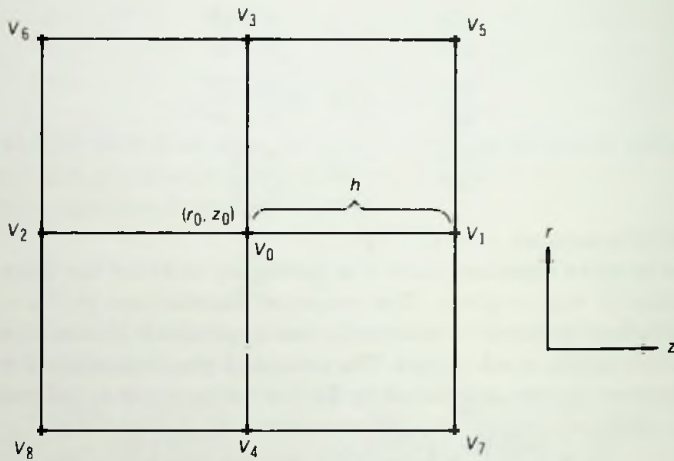
Fig. E.4   The (r_0, z_0) mesh point and eight neighboring mesh points
used for the calculation of the potential gradient.

in which $\dot{y}$ is not explicitly involved, may be solved by repeated calculation
of the following formulas:

$$y_{n+1} = y_n + y_{n-2} - y_{n-3} + 3(\Delta t)^2 \left(1 - \nabla + \frac{5}{12}\nabla^2 + 0\nabla^3 \right.$$

$$\left. + \frac{17}{720}\nabla^4 + \frac{17}{720}\nabla^5 + \cdots \right)\ddot{y}_n \tag{E.57}$$

and

$$y_{n+1} = 2y_n - y_{n-1} + (\Delta t)^2 \left(1 - \nabla + \frac{1}{12}\nabla^2 + 0\nabla^3 \right.$$

$$\left. - \frac{1}{240}\nabla^4 - \frac{1}{240}\nabla^5 + \cdots \right)\ddot{y}_{n+1}, \tag{E.58}$$

where the symbol ∇ indicates backward differences and Δt is the time incre-
ment.

By retaining only the second differences the following formulas are ob-
tained:

$$y_{n+1} = y_n + y_{n-2} - y_{n-3} + \frac{(\Delta t)^2}{4}\left(5\ddot{y}_n + 2\ddot{y}_{n-1} - 5\ddot{y}_{n-2}\right) \tag{E.59}$$

and

$$y_{n+1} = 2y_n - y_{n-1} + \frac{(\Delta t)^2}{12}\left(\ddot{y}_{n+1} + 10\ddot{y}_n + \ddot{y}_{n-1}\right). \tag{E.60}$$

Milne's method employs equation E.59 to predict y^n_{n+1} and equation E.60 as a basic formula to be solved for y_{n+1} by iteration.

The values of y_n, y_{n-1}, y_{n-2}, y_{n-3}, and $\dot{y}_n$, $\dot{y}_{n-1}$, and $\dot{y}_{n-2}$ needed in formulas E.59 and E.60 can be calculated from the initial conditions y_0, $\dot{y}_0$, $\ddot{y}_0$, and t_0 by use of laws of uniform motion:

$$\dot{y}_{n+1} = \dot{y}_n + \Delta t \ddot{y}_n \tag{E.61}$$

and

$$y_{n+1} = y_n + \Delta t \dot{y}_n + \frac{1}{2}(\Delta t)^2 \ddot{y}_n. \tag{E.62}$$

The last two formulas can give as accurate a result as desired by choosing a sufficiently small time interval. There are other methods to solve second-order differential equations. One popular method which has been used is the Runge-Kutta method.

E.9   Thin Lenses

For pure electric fields, from equation E.41 (B_0, C, $V_i = 0$), the differential equation of motion of a paraxial electron becomes

$$\frac{d^2 r}{dz^2} + \frac{V'_0}{2V_0}\frac{dr}{dz} = -\frac{V''_0}{4V_0}r. \tag{E.63}$$

An alternative form of equation E.63 is

$$\frac{d}{dz}\left(\sqrt{V_0}\frac{dr}{dz}\right) = -\frac{V''_0 r}{4\sqrt{V_0}}. \tag{E.64}$$

Integration of equation E.64 between the limits z_1 and z_2, as shown in figure E.5, gives

$$\left[\sqrt{V_0}\frac{dr}{dz}\right]_{z_1}^{z_2} = -\frac{1}{4}\int_{z_1}^{z_2}\frac{r\,V''_0}{\sqrt{V_0}}\,dz. \tag{E.65}$$

The left-hand side of equation E.65 is the difference of the product of the square root of the axial potential (V_0) and the electron path slope (dr/dz) at points z_2 and z_1.

A thin lens, by definition, is a lens whose dimensions are short compared with the focal length. In the case of a very short lens the value of r changes very little. Therefore r in equation E.65 can be regarded as a constant and placed ahead of the integral sign. If the axial potential at z_2 is V_2, then for a ray entering the lens parallel to the axis ($dr/dz = 0$ at z_1) at a radial distance r, equation E.65 reduces to

$$\left(\frac{dr}{dz}\right)_{z_2} = -\frac{r}{4\sqrt{V_2}}\int_{z_1}^{z_2}\frac{V''_0}{\sqrt{V_0}}\,dz. \tag{E.66}$$
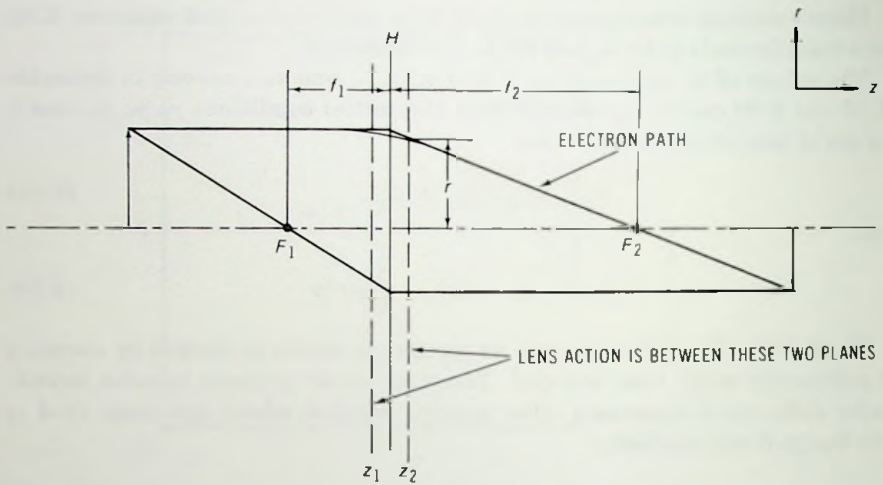
Fig. E.5   Image formation by parallel rays.

Equation E.66 gives the slope of an electron at coordinates (r, z_2). The focal length then may be given from simple geometrical considerations of figure E.5:

$$\frac{1}{f_2} = -\left(\frac{dr}{dz}\right)_{z_2} \Big/ r = \frac{1}{4\sqrt{V_2}} \int_{z_1}^{z_2} \frac{V''_0}{\sqrt{V_0}}\, dz \, . \tag{E.67}$$

With similar considerations as above, the first focal length of the lens becomes

$$\frac{1}{f_1} = -\frac{1}{4\sqrt{V_1}} \int_{z_1}^{z_2} \frac{V''_0}{\sqrt{V_0}}\, dz \, , \tag{E.68}$$

where V_1 is the axial potential at point z_1. It should be remembered that the above equations are strictly valid only for very thin lenses. The results, however, are also applicable to a thick lens if we regard the thick lens as consisting of a series of thin lenses in cascade.

For a pure magnetic field, again from equation E.41, the differential equation of motion of a paraxial electron becomes

$$\frac{d^2 r}{dz^2} = -\frac{eB_0^2}{8mV}\, r \, . \tag{E.69}$$

For a thin lens the slope of an electron entering the lens parallel to the axis at a radial distance r may be obtained by integration of equation E.69:

$$\left(\frac{dr}{dz}\right)_{z_2} = -\frac{er}{8mV} \int_{z_1}^{z_2} B_0^2\, dz \, . \tag{E.70}$$

The focal lengths, from equation E.70 with the same reasoning as in the electrostatic lens, are

$$\frac{1}{f_1} = -\frac{1}{f_2} = -\frac{e}{8mV} \int_{z_1}^{z_2} B_0^2 \, dz. \tag{E.71}$$

The image rotation from equation E.42 is

$$\phi = \frac{\sqrt{e}}{2\sqrt{2mV}} \int_{z_1}^{z_2} B_0 \, dz. \tag{E.72}$$

F

Numerical Calculation of the Potential Distribution of Axially Symmetric Electric Fields

The potential distribution in a region may be obtained by solving Poisson's equation. Poisson's equation in cylindrical coordinates (r,z) is of the form:

$$\frac{\partial^2 V}{\partial r^2} + \frac{1}{r}\frac{\partial V}{\partial r} + \frac{\partial^2 V}{\partial z^2} = -\frac{\rho}{\epsilon_0},$$

(F.1)

where ϵ_0 is the dielectric constant, and ρ is the charge density.

Consider a mesh point (r_0, z_0) with potential V_0 and with its four equidistant adjacent neighbors with potentials V_1, V_2, V_3, and V_4 arranged as shown in figure F.1. By Taylor's expansion of the potential V about the mesh point (r_0, z_0) the following is obtained:

$$V_1 = V_0 + \left(\frac{\partial V}{\partial z}\right)_0 h + \frac{1}{2}\left(\frac{\partial^2 V}{\partial z^2}\right)_0 h^2 + \frac{1}{6}\left(\frac{\partial^3 V}{\partial z^3}\right)_0 h^3 + \cdots,$$

(F.2)

$$V_2 = V_0 - \left(\frac{\partial V}{\partial z}\right)_0 h + \frac{1}{2}\left(\frac{\partial^2 V}{\partial z^2}\right)_0 h^2 - \frac{1}{6}\left(\frac{\partial^3 V}{\partial z^3}\right)_0 h^3 + \cdots,$$

(F.3)

$$V_3 = V_0 + \left(\frac{\partial V}{\partial r}\right)_0 h + \frac{1}{2}\left(\frac{\partial^2 V}{\partial r^2}\right)_0 h^2 + \frac{1}{6}\left(\frac{\partial^3 V}{\partial r^3}\right)_0 h^3 + \cdots,$$

(F.4)

466
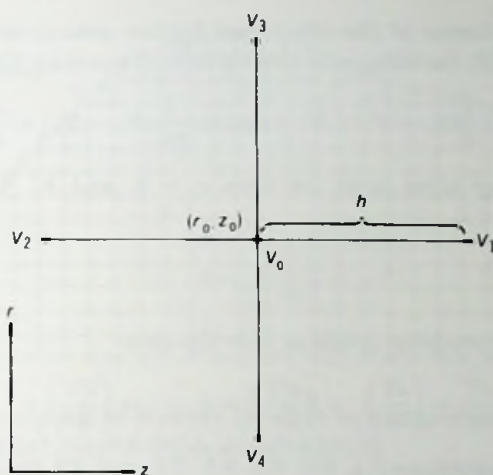
(A) Equidistant points.
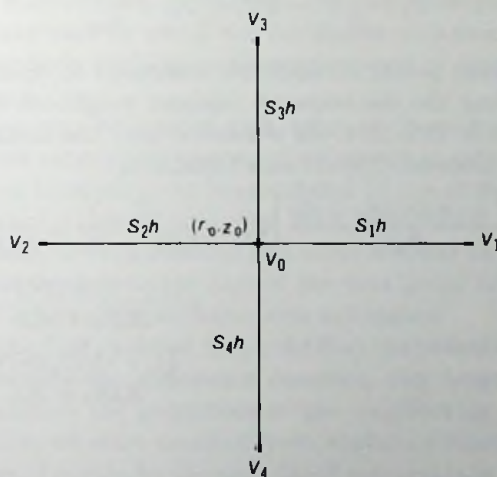
(B) Nonequidistant points.

Fig. F.1   The (r_0, z_0) mesh point and four neighboring mesh points used for the calculation of the difference equation.

and

$$V_4 = V_0 - \left(\frac{\partial V}{\partial r}\right)_0 h + \frac{1}{2}\left(\frac{\partial^2 V}{\partial r^2}\right)_0 h^2 - \frac{1}{6}\left(\frac{\partial^3 V}{\partial r^3}\right)_0 h^3 + \cdots. \tag{F.5}$$

By neglecting terms of the third and higher orders, and by combining equations F.1 to F.5, the difference analog form of equation F.1 is obtained:

$$V_0 = \frac{1}{4}(V_1 + V_2 + V_3 + V_4) + \frac{h}{8r_0}(V_3 - V_4) + \frac{\rho h^2}{4\epsilon_0}. \tag{F.6}$$

When the center point is on the axis, $r = 0$, and $V_4 = V_3$. Because of symmetry,

$$\left(\frac{\partial V}{\partial r}\right)_0 = 0. \tag{F.7}$$

We have for the potential gradient near the axis

$$\frac{\partial V}{\partial r} = \left(\frac{\partial V}{\partial r}\right)_0 + \left(\frac{\partial^2 V}{\partial r^2}\right)_0 r + \cdots \cong \left(\frac{\partial^2 V}{\partial r^2}\right)_0 r. \tag{F.8}$$

By combining equations F.1, F.3, F.4, F.5, F.7, and F.8 the difference equation along the axis becomes

$$V_0 = \frac{1}{6}(V_1 + 4V_3 + V_2) + \frac{\rho h^2}{6\epsilon_0}. \tag{F.9}$$

For nonequidistant points an equation analogous to equation F.6 may be obtained by writing the distances of adjacent neighbors in place of h in equations F.2 to F.5. This formula is needed near the boundary where the distances may be unequal. The off-axis formula is

$$\left[\frac{1}{S_1 S_2} + \frac{1 + (h/2r_0)(S_4 - S_3)}{S_3 S_4}\right]V_0 = \frac{V_1}{S_1(S_1 + S_2)} + \frac{V_2}{S_2(S_1 + S_2)}$$
$$+ \frac{[1 + (h/2r_0)S_4]V_3}{S_3(S_3 + S_4)}$$
$$+ \frac{[1 + (h/2r_0)S_3]V_4}{S_4(S_3 + S_4)} \tag{F.10}$$

and on the axis

$$\left[\frac{1}{S_1 S_2} + \frac{2}{S_3^2}\right]V_0 = \frac{V_1}{S_1(S_1 + S_2)} + \frac{V_2}{S_2(S_1 + S_2)} + \frac{2V_3}{S_3^2}. \tag{F.11}$$

In equations F.10 and F.11, S_1, S_2, S_3, and S_4 are related to h as indicated in figure F.1.

In the process of calculating the potential distribution the region of interest is broken up into a square grid (see figure F.2). In order to obtain a unique solution the potential must be given on the boundary. The corresponding difference equations hold for each point of the grid. If there are n interior mesh points, there are n linear algebraic equations for n unknown
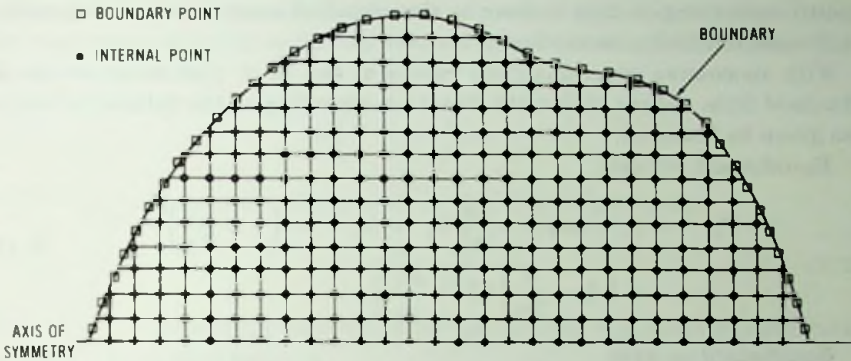
Fig. F.2   The network of square meshes in a region in which the
potential distribution is calculated.

potentials. There are exact methods for solving such algebraic equations. However, these methods are impractical even for a computer. Instead, iterative processes are used by which the residue at each point is progressively reduced in an orderly fashion until convergence is reached to a desired degree of accuracy.

The calculation may be started with arbitrary potentials at the interval points that do not satisfy the system of difference equations. Next, the potential of the first internal point is calculated by use of the difference equation. The arbitrary value of potential then is replaced by the calculated value. The calculation is carried out in a same manner for the next internal point using the calculated potential of the first point and so on until the potentials of all internal points have been calculated.

At the end of the first cycle we may note that the potentials of the internal points do not satisfy the difference equation any longer because in the process of calculation the potentials of the neighboring points have been changed. Therefore we start another cycle, replacing successively the potentials of the internal points by the calculated potentials in a same fashion as in the first cycle. This process is repeated many times until convergence is reached to a desired degree of accuracy.

The rate of convergence of this procedure is very low even for fast computers. By considering the potential of a fixed point during several cycles we may note that the potential gradually changes in the direction of the final solution. (The potential either gradually increases or decreases.) Therefore a faster convergence may be obtained by using instead of potential values given by the difference equation another potential that may be obtained by extrapolation in the direction of the expected change. The pro-

cedure operating in this fashion is the so-called successive overrelaxation (extrapolated Liebman method).

With successive overrelaxation values at the $(n + 1)$st iteration can be obtained from values at the nth iteration according to the following formulas given by Kulsrud.

Equidistant off-axis:

$$V_0^{(n+1)} = (1 - \omega)V_0^{(n)} + \frac{\omega}{4}\left[V_1^{(n)} + V_2^{(n+1)} + \left(1 + \frac{h}{2r_0} \right)V_3^{(n+1)} \right.$$
$$\left. + \left(1 - \frac{h}{2r_0} \right)V_4^{(n)} + \frac{\rho h^2}{\epsilon_0} \right], \tag{F.12}$$

Equidistant on-axis:

$$V_0^{(n+1)} = (1 - \omega)V_0^{(n)} + \frac{\omega}{6}\left(V_1^{(n)} + V_2^{(n+1)} + 4V_3^{(n+1)} + \frac{\rho h^2}{\epsilon_0} \right), \tag{F.13}$$

Nonequidistant off-axis:

$$V_0^{(n+1)} = (1 - \omega)V_0^{(n)} + \frac{\omega}{k_1}\left\{ \frac{V_1^{(n)}}{S_1(S_1 + S_2)} + \frac{V_2^{(n+1)}}{S_2(S_1 + S_2)} \right.$$
$$\left. + \frac{[1 + (h/2r_0)\,S_4]V_3^{(n+1)}}{S_3(S_3 + S_4)} + \frac{[1 - (h/2r_0)\,S_3]V_4^{(n)}}{S_4(S_3 + S_4)} + \frac{\rho h^2}{\epsilon_0} \right\}, \tag{F.14}$$

where

$$k_1 = \left\{ \frac{1}{S_1 S_2} + \frac{[1 + (h/2r_0)(S_4 - S_3)]}{S_3 S_4} \right\}. \tag{F.15}$$

Nonequidistant on-axis:

$$V_0^{(n+1)} = (1 - \omega)V_0^{(n)} + \frac{\omega}{k_2}\left(\frac{V_1^{(n)}}{S_1(S_1 + S_2)} \right.$$
$$\left. + \frac{V_2^{(n+1)}}{S_2(S_1 + S_2)} + \frac{2V_3^{(n+1)}}{S_3{}^2} + \frac{\rho h^2}{\epsilon_0} \right), \tag{F.16}$$

where

$$k_2 = \frac{1}{S_1 S_2} + \frac{2}{S_3{}^2}. \tag{F.17}$$

The convergence of the iteration is speeded by proper choice of ω, the overrelaxation factor. The value of ω must be chosen carefully. If it is too small, the rate of convergence is low. If it is too large, the extrapolation goes too far and the rate of convergence is again low. The overrelaxation procedure is convergent for $1 < \omega < 2$. The optimum value of ω depends on the boundary configuration and the number of internal mesh points.

Young has shown that the optimum relaxation factor ω_0 is related to μ, the maximum eigenvalue for the method of simultaneous displacement, in the following way:

$$\omega_0 = \frac{2}{1 + \sqrt{1 - \mu^2}}. \tag{F.18}$$

The value of μ may be calculated from the following equation:

$$\mu^2 = \frac{(\lambda + \omega - 1)^2}{\omega^2 \lambda}. \tag{F.19}$$

Here λ is the maximum eigenvalue for the method of successive over relaxation at a relaxation factor ω.

The value of λ is experimentally determined by starting at some $\omega < \omega_0$ (a good starting value is $\omega = 1.6$), performing a certain number of cycles of iteration at this ω and calculating λ from the following relation:

$$\lambda = \frac{\sum_{i=1}^{n} V_i^{(m)} - V_i^{(m-1)}}{\sum_{i=1}^{n} V_i^{(m-1)} - V_i^{(m-2)}}. \tag{F.20}$$

Knowing λ and ω, from equation F.19 we can calculate μ, and then from equation F.18, ω_0.

In general, however, one is not assured of getting the optimum ω_0 on the first try. The problem of determining ω_0 has been discussed by Carré and Kulsrud. In their method λ is calculated several times at a given ω. The λs calculated in this fashion have a statistical distribution. Taking the average value of λ, from equations F.19 and F.18, ω can be calculated. The terms ω_0 and λ_0 must satisfy the following relation:

$$\lambda_0 = \omega_0 - 1 \tag{F.21}$$

If λ is less than $\omega - 1$, we back off on ω and the calculation is repeated. In this way the procedure for estimating ω is made stable.

References

Carré, B. A. "The Determination of the Optimum Accelerating Factor for Successive Overrelaxation," *Computer J.*, Vol. 4, p. 73, 1961.

Frankel, S. P. "Convergence Rates of Iterative Treatments of Partial Differential Equations," *Math Tab. Nash.*, IV, Vol. 30, pp. 65–75, April 1950.

Gruche, E., and O. Scherzer. *Elektronenoptic*, Julius Springer, Berlin, 1934.

Hildebrand, F. F. *Introduction to Numerical Analysis*, McGraw-Hill Book Company, Inc., New York, 1956.

Kulsrud, H. E. "A Programming System for Electron Optical Simulation," *RCA Review*, Vol. 28, p. 351, June 1967.

————. "A Practical Technique for the Determination of the Optimum Relaxation Factor for the Successive Overrelaxation Method," *Comm. of the ACM*, Vol. 4, No. 4, p. 184, April 1961.

Maloff, I. G., and D. W. Epstein. *Electron Optics In Television*, McGraw-Hill Book Company, Inc., New York, 1938.

Septier, A. *Focusing of Charged Particles*, Academic Press, New York, 1967.

Young, D. M. "Iterative Methods for Solving Partial Differential Equations of Elliptic Type," *Trans. Amer. Math. Soc.*, Vol. 76, pp. 92–111, 1954.

Zworykin, V. K., et al. *Electron Optics and the Electron Microscope*, John Wiley & Sons, Inc., New York, 1945.

G

Acceleration in Plane Polar Coordinates and Cylindrical Coordinates

G.1   Polar Coordinates

It is assumed that the motion of a particle occurs under the action of a central force whose position is chosen as the origin of the r,θ plane polar coordinates. The motion of the particle can be resolved into two components: one motion occurring in the radial direction and the other motion normal to the radial direction. For the purpose of calculation two mutually perpendicular unit vectors $\mathbf{e}_r$ and $\mathbf{e}_\theta$ are introduced which have their directions in the increasing r and increasing θ, respectively. The derivative of a unit vector is perpendicular to the vector, as shown in figure G.1. Therefore, since $|\mathbf{e}_r| = 1$ and $|\mathbf{e}_\theta| = 1$,

$$\frac{d\mathbf{e}_r}{dt} = \mathbf{e}_\theta \frac{d\theta}{dt} \quad \text{and} \quad \frac{d\mathbf{e}_\theta}{dt} = -\mathbf{e}_r \frac{d\theta}{dt}. \tag{G.1}$$

The radius vector is

$$\mathbf{r} = r\mathbf{e}_r. \tag{G.2}$$

The velocity vector is the first derivative of $\mathbf{r}$:

$$\mathbf{v} = \frac{d\mathbf{r}}{dt} = \frac{dr}{dt}\mathbf{e}_r + r\frac{d\mathbf{e}_r}{dt} = \frac{dr}{dt}\mathbf{e}_r + r\mathbf{e}_\theta \frac{d\theta}{dt}. \tag{G.3}$$
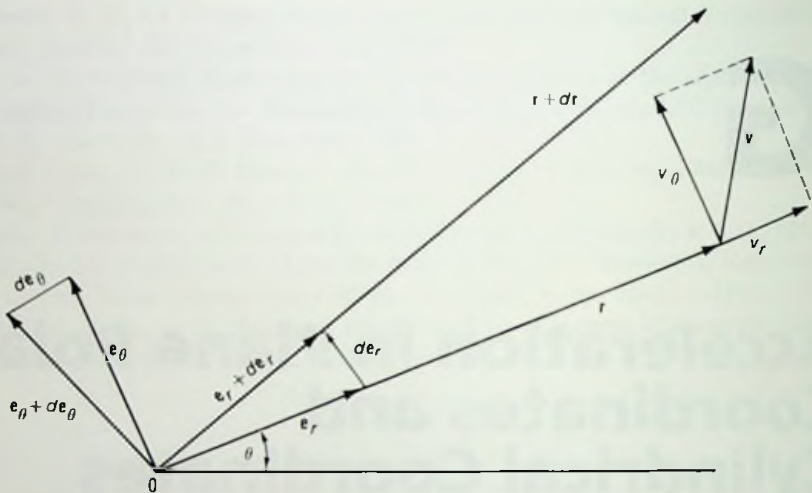
Fig. G.1 Motion in polar coordinates.

The acceleration is obtained by differentiation of **v**:

$$\mathbf{a} = \frac{d\mathbf{v}}{dt} = \frac{d^2r}{dt^2}\mathbf{e}_r + \frac{dr}{dt}\frac{d\mathbf{e}_r}{dt} + r\mathbf{e}_\theta\frac{d^2\theta}{dt^2} + \frac{dr}{dt}\mathbf{e}_\theta\frac{d\theta}{dt} + r\frac{d\theta}{dt}\frac{d\mathbf{e}_\theta}{dt}$$

$$= \left[\frac{d^2r}{dt^2} - r\left(\frac{d\theta}{dt}\right)^2\right]\mathbf{e}_r + \left[r\frac{d^2\theta}{dt^2} + 2\frac{dr}{dt}\frac{d\theta}{dt}\right]\mathbf{e}_\theta. \tag{G.4}$$

Hence

$$a_r = \frac{d^2r}{dt^2} - r\left(\frac{d\theta}{dt}\right)^2 \tag{G.5}$$

and

$$a_\theta = r\frac{d^2\theta}{dt^2} + 2\frac{dr}{dt}\frac{d\theta}{dt}. \tag{G.6}$$

G.2 Cylindrical Coordinates

It is assumed that the motion of a particle occurs under the action of a force having components in the r, ϕ, and z directions. See figure G.2. The velocity vector then may be given by the following equation:

$$\mathbf{v} = \frac{dr}{dt}\mathbf{e}_r + r\frac{d\phi}{dt}\mathbf{e}_\phi + \frac{dz}{dt}\mathbf{e}_z. \tag{G.7}$$
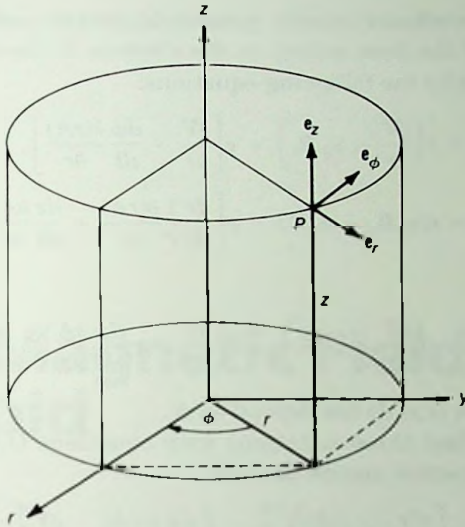
Fig. G.2   Cylindrical coordinate system.

Here $\mathbf{e}_r$, $\mathbf{e}_\phi$, and $\mathbf{e}_z$ are three mutually perpendicular unit vectors having directions in the r, ϕ and z directions.

The acceleration is

$$\mathbf{a} = \frac{d\mathbf{v}}{dt} = \frac{d^2r}{dt^2}\,\mathbf{e}_r + \frac{dr}{dt}\frac{d\mathbf{e}_r}{dt} + \frac{dr}{dt}\frac{d\phi}{dt}\,\mathbf{e}_\phi + r\,\frac{d^2\phi}{dt^2}\,\mathbf{e}_\phi$$

$$+ r\,\frac{d\phi}{dt}\frac{d\mathbf{e}_\phi}{dt} + \frac{d^2z}{dt^2}\,\mathbf{e}_z + \frac{dz}{dt}\frac{d\mathbf{e}_z}{dt}. \tag{G.8}$$

Using the relations obtained in equation G.1 ($d\mathbf{e}_z/dt = 0$, because the direction of $\mathbf{e}_z$ is constant) finally we have

$$\mathbf{a} = \left[\frac{d^2r}{dt^2} - r\left(\frac{d\phi}{dt}\right)^2\right]\mathbf{e}_r + \left[2\frac{dr}{dt}\frac{d\phi}{dt} + r\frac{d^2\phi}{dt^2}\right]\mathbf{e}_\phi + \frac{d^2z}{dt^2}\,\mathbf{e}_z. \tag{G.9}$$

thus

$$a_r = \frac{d^2r}{dt} - r\left(\frac{d\phi}{dt}\right)^2, \tag{G.10}$$

$$a_\phi = \frac{1}{r}\frac{d}{dt}\left(r^2\frac{d\phi}{dt}\right), \tag{G.11}$$

and

$$a_z = \frac{d^2z}{dt^2}. \tag{G.12}$$

In the case of combined axially symmetric electric and magnetic fields, the components of the force acting on the electron in the r, ϕ, and z directions may be given by the following equations:

$$F_r = e\left(\frac{\partial V}{\partial r} - v_\phi B_z\right) = e\left[\frac{\partial V}{\partial r} - \frac{d\phi}{dt}\frac{\partial(rA)}{\partial r}\right], \tag{G.13}$$

$$F_\phi = e(v_r B_z - v_z B_r) = e\left[\frac{dr}{dt}\frac{1}{r}\frac{\partial(rA)}{\partial r} + \frac{dz}{dt}\frac{\partial A}{\partial z}\right], \tag{G.14}$$

and

$$F_z = e\left(\frac{\partial V}{\partial z} + v_\phi B_r\right) = e\left(\frac{\partial V}{\partial z} - r\frac{d\phi}{dt}\frac{\partial A}{\partial z}\right), \tag{G.15}$$

where $V(r,z)$ and $A(r,z)$ do not depend on ϕ.

Combining the last three equations with equations G.10 through G.12, the equations of electron motion become

$$m\left[\frac{d^2r}{dt^2} - r\left(\frac{d\phi}{dt}\right)^2\right] = e\left[\frac{d\phi}{dt}\frac{\partial(rA)}{\partial r} + \frac{\partial V}{\partial r}\right], \tag{G.16}$$

$$\frac{m}{r}\frac{d}{dt}\left(r^2\frac{d\phi}{dt}\right) = e\left[\frac{dz}{dt}\frac{\partial A}{\partial z} + \frac{1}{r}\frac{dr}{dt}\frac{\partial(rA)}{\partial r}\right] = \frac{e}{r}\frac{d(rA)}{dt}, \tag{G.17}$$

and

$$m\frac{d^2z}{dt^2} = e\left(-r\frac{d\phi}{dt}\frac{\partial A}{\partial z} + \frac{\partial V}{\partial z}\right). \tag{G.18}$$

H

Axial Magnetic Field of a Solenoid

The axial magnetic field produced by a circular loop current I may be obtained by use of Biot-Savart law. Accordingly, an elemental length dl of the circular loop produces an axial magnetic field, dH_a (see figure H.1):

$$dH_a = \frac{I}{4\pi} \frac{dl \times r}{r^3} \cos \alpha = \frac{I}{4\pi} \frac{dl}{r^2} \cos \alpha. \tag{H.1}$$

$$dH = \frac{I}{4\pi} \frac{dl \times r}{r^3}$$
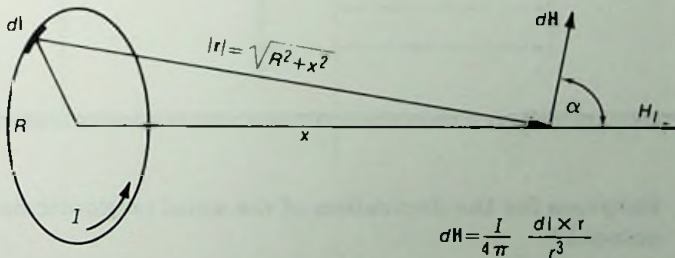
Fig. H.1   Magnetic field of a circular loop current.

The axial magnetic field H_l produced by the circular loop current, from the geometry of figure H.1, is

$$H_l = \oint dH_a = \frac{I}{4\pi} \oint \frac{dl \cos \alpha}{r^2} = \frac{I}{4\pi} \oint \frac{R\, dl}{(R^2 + x^2)^{3/2}} = \frac{I}{2} \frac{R^2}{(R^2 + x^2)^{3/2}}. \tag{H.2}$$

The axial magnetic field H_z of a solenoid of N turns now may be obtained by integration of equation H.2:

$$H_z = \int \frac{R^2}{(R^2 + x^2)^{3/2}} \frac{dI}{2} = \frac{IN}{2l} \int \frac{R^2 \, dx}{(R^2 + x^2)^{3/2}}. \tag{H.3}$$

From the geometry of figure H.2, the following also holds:

$$\sqrt{R^2 + x^2} \, d\alpha = \sin \alpha \, dx \tag{H.4}$$

and

$$R/\sqrt{R^2 + x^2} = \sin \alpha. \tag{H.5}$$
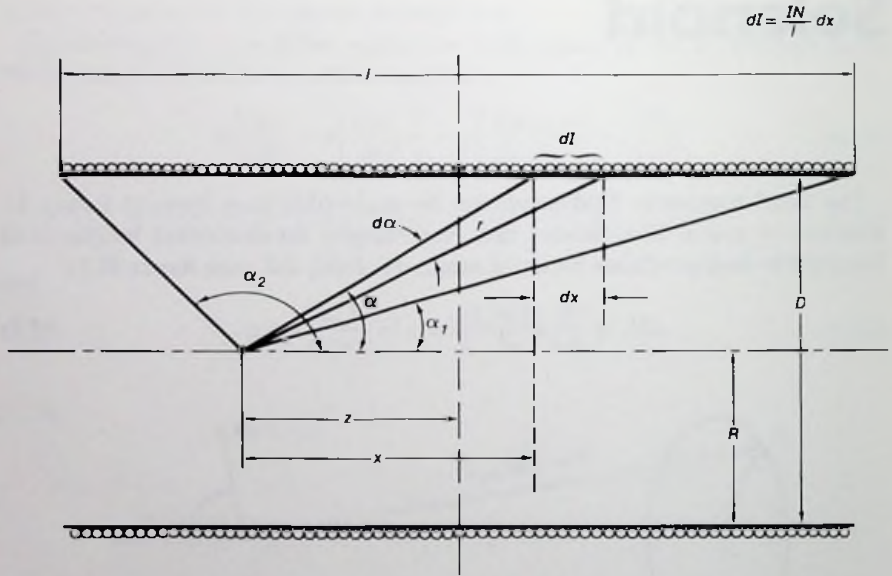
Fig. H.2 **Diagram for the derivation of the axial magnetic field of a solenoid.**

Combining equations H.3, H.4, and H.5 we obtain

$$H_z = \frac{IN}{2l} \int_{\alpha_1}^{\alpha_2} \sin \alpha \, d\alpha = \frac{IN}{2l} (\cos \alpha_1 - \cos \alpha_2)$$

$$= \frac{IN}{2l} \left[\frac{l + 2z}{\sqrt{4R^2 + (l + 2z)^2}} + \frac{l - 2z}{\sqrt{4R^2 + (l - 2z)^2}} \right]. \tag{H.6}$$

In the center of solenoid ($z = 0$) the magnetic field becomes

$$H_{sc} = IN/\sqrt{4R^2 + l^2}.$$ (H.7)

For a very long cylinder $\cos \alpha_1 = 1$ and $\cos \alpha_2 = -1$. Therefore, from equation H.6 the homogeneous magnetic field has a value of

$$H_h = IN/l.$$ (H.8)

INDEX

480

SAMS

Image Tubes

Image Tubes is an excellent source and highly original guide for engineers, managers, industrialists or anyone studying or working with electron optics, imaging and image intensification systems. This broad-based volume teaches all aspects of image tube design and construction, reinforcing its valuable and hard-to-find data with a solid grounding in tube components and theory.

Image Tubes describes the design and operation of camera tubes, fluorescent screens and power supplies plus components that include photocathodes, photoconductors, fiber optic and microchannel plates and secondary electron emitters. Separate chapters cover photomultiplier tubes and electron guns while 8 appendixes contain additional material related to imaging and electron optics.

Another in Sams Professional Reference Series, **Image Tubes** is written by scientist-engineer Illes P. Csorba, designer of the familiar 19-inch rectangular black-and-white television picture tube and a man of numerous electronic accomplishments.

bliothee